University of Southampton

Faculty of Engineering and Physical Sciences

Mechanical Engineering

The development of high-resolution crack monitoring methods to investigate the effect of the local weld toe geometry on fatigue crack initiation life.

by

Somsubhro Chaudhuri

ORCID ID 0000-0001-9849-5766

Thesis for the degree of **Doctor of Philosophy**

September, 2019

University of Southampton

Abstract

Faculty of Engineering and Physical Sciences

Engineering Materials

Thesis for the degree of **Doctor of Philosophy**

The development of high-resolution crack monitoring methods to investigate the effect of the local weld toe geometry on fatigue crack initiation life by

Somsubhro Chaudhuri

The effect of weld toe geometry on the fatigue performance of welded joints is investigated, with a primary focus on the fatigue crack initiation (FCI) life of the joints. Available standards prescribe global approaches for estimating total life and crack propagation life, as FCI life has historically been considered to be negligible. However, experimental results from the literature show that FCI can take up a significant portion of the total life of welded joints, especially in the case of good quality welds under high-cycle fatigue loading conditions.

Weld toe fatigue crack initiation is highly dependent on the local weld toe stress-concentrating geometry, including the inherent flaws such as undercuts, spatter, cold-laps and inclusions. Such flaws, as well as the inhomogeneous geometry, promote premature fatigue crack initiation. Thus, it is essential to investigate methods of resolving such flaws and characterising them in terms of their geometry and stress concentration. The weld toe stress concentration factor (SCF) is an important parameter for characterising the stress-concentrating features that act as fatigue crack initiation sites.

In this work, interrupted fatigue tests were performed on arc-welded joints manufactured by different welders with different electrodes to obtain a variety of weld toe geometries. To obtain fatigue crack initiation lives (corresponding to the growth of a technical crack of depth 250 μm), a novel multi-probe array of alternating current potential drop (ACPD) probes and strain gauges were positioned across the weld toe. These bespoke systems also located fatigue cracks. The effect of stress on the ACPD measurements was observed to influence results, and once cracks approached through-thickness they were difficult to characterise using this method. Further research to investigate this phenomenon has been identified. Both crack growth monitoring techniques (ACPD and strain gauges) were seen to correlate well with crack depth for isolated cracks. However, due

to the large number of crack coalescence events in high stress-range fatigue loading conditions, both techniques proved inconsistent at the onset of crack coalescence.

FCI lives and early crack propagation rates were correlated with the local weld toe stresses, which were obtained from a high-resolution (5-10 μm) stress analysis. 3D linear-elastic and elastic-plastic finite element models were developed from X-ray micro-Computed Tomography (μ-CT) scans of each fatigue tested weld toe. From these models, over 5000 SCFs were extracted for approximately every 50 mm of weld toe, thus providing comprehensive SCF distribution maps for each of the interrupted-fatigue tested and scanned weld toes.

In obtaining FCI lives in welded joints, the local notch stress-strain approach has been used from the available literature. In this study, multiple variations of the approach have been investigated to potentially identify improvements to the approach when using state-of-the-art technology (industrial μ-CT) for resolving the weld toe geometry and bespoke data-rich crack monitoring techniques. The SCF distribution maps, along with the experimental FCI data, were used to identify the robustness of each of the variations in the literature. The use of fatigue notch factor (K_f) is seen to give significantly non-conservative results when combined with high-resolution SCF data. Elastic-plastic SCF data was observed to give satisfactory results in terms of predicting the FCI lives. However, more computation time is required to get elastic-plastic SCF distributions compared to linear-elastic stress analysis. The number of tests performed was low and so were not statistically significant to draw firm conclusions but provide an indication of the methods that have the most potential.

I may not have gone where I intended to go, but I think I have ended up where I needed to be.

Douglas Adams

Table of Contents

Table of Contents ..... **i**

List of Tables ..... **v**

List of Figures ..... **vii**

Research Thesis: Declaration of Authorship ..... **xv**

Acknowledgements ..... **xvii**

Definitions and Abbreviations ..... **xix**

Chapter 1 Introduction **1**

1.1 Motivation 1

1.2 Weld fatigue - Overview 1

1.3 Research objectives 4

1.4 Thesis structure 5

Chapter 2 Background and literature review **7**

2.1 Fatigue as a failure mechanism 7

2.2 Arc welding of steel 11

2.3 Fatigue of welded joints 22

2.4 Literature review – Summary 28

Chapter 3 High-resolution Weld Toe Stress Analysis using Micro-Computed Tomography (μ-CT) and 3D Finite Element Analysis (FEA) **31**

3.1 Motivation 31

3.2 Introduction 32

3.3 Methodology 43

3.4 μ-CT Data Analysis 54

3.5 Three-Dimensional (3D) Finite Element Analysis (FEA) 77

Chapter 4 Multi-Probe ACPD Method for Detecting Fatigue Crack Initiation **103**

4.1 Motivation 103

4.2 Introduction to APCD 103

4.3 Review of Notable ACPD Applications 107

4.4 Methodology – Fatigue Testing with ACPD Crack Detection 111

4.5 Results and Discussion - Fatigue Testing with ACPD Crack Detection..... 118
4.6 Validation of 3D finite element stress analysis using ACPD and serial metallography 144
4.7 Summary 151
4.8 Conclusion and future work..... 151

Chapter 5 Strain Gauge Array Technique for FCI Detection 153

5.1 Motivation..... 153
5.2 Use of strain gauges for crack growth – Review..... 153
5.3 Uniaxial fatigue testing using strain gauges (experiment set 2) - Methodology... 156
5.4 Uniaxial fatigue testing using strain gauges (experiment set 2) - Results and discussion 165
5.5 Summary 186
5.6 Conclusion and future work..... 187

Chapter 6 Local Notch Stress-Strain Approach to Fatigue Lifing 189

6.1 Motivation..... 189
6.2 Local notch stress-strain approach – Review 190
6.3 Notch stress-strain approach – Methodology 200
6.4 Notch stress-strain approach – Results and Discussion 205
6.5 Notch stress-strain approach – Summary 231

Chapter 7 Conclusions and future work.....235

7.1 Conclusions 235
7.2 Future work..... 238

Appendix A (Chapter 3).....241

A.1 2D Weld Toe Geometry Extraction 241
A.2 3D FEA CT Volume Pre-processing..... 251
A.3 Simpleware ScanIP automated mesh creation script (Python) 255
A.4 Script for converting mesh input file into ABAQUS analysis input file (Python) ... 258
A.5 Different types of flaws counted and measured 260
A.6 Script for submitting ABAQUS jobs to IRIDIS (University of Southampton HPC) for solving (BASH) 262

A.7 Script for converting ABAQUS analysis output (.ODB) files into report (.RPT) files for specific quantities (Python) 263
A.8 Script for extracting SCF distribution from ABAQUS input and output report files (MATLAB) 264
A.9 Specimen-wise elastic SCF distributions from 3D FE analysis 269
A.10 Specimen-wise elastic-plastic SCF and strain distributions from 3D FE analysis ... 276

Appendix B (Chapter 4) 283

B.1 Fatigue test loading data for experiment set 1 283
B.2 Fatigue testing ACPD data for experiment set 1 284

Appendix C (Chapter 5) 287

C.1 Fatigue test loading data for experiment set 2 287
C.2 Static loading data from experimental set 2 288
C.3 Fatigue testing Strain Gauge data for experiment set 2 294

Appendix D (Chapter 6) 297

D.1 Flowchart of the application of notch stress-strain approach 297
D.2 FCI Prediction Distribution 298

References (Numbered) 301

List of Tables

Table 2.1 Alloying Elements commonly added to C-Mn steel and their effects [31]

Table 3.1 SCF distribution obtained from simplified weld profiles.

Table 3.2 Methods used in the open literature to capture the true weld profile.

Table 3.3 SCF distributions obtained for true weld profiles.

Table 3.4 Use of μ-CT on steel.

Table 3.5 Chemical composition of S355 J2+N structural steel.

Table 3.6 Tensile properties of S355 J2+N structural steel.

Table 3.7 Typical chemical composition and mechanical properties of the electrodes.

Table 3.8 Average Welding parameters for Set 1.

Table 3.9 Average welding parameters for Set 2.

Table 3.10 Details of μ-CT scans performed.

Table 3.11 Scan settings for each set.

Table 3.12 Sub-volume size for each CT scan set.

Table 3.13 Mesh refinement parameters for scan set 1.

Table 3.14 Mesh refinement parameters for scan set 2.

Table 3.15 Maximum stress for each specimen.

Table 4.1 Parameters for SONATS NOMAD UNP system.

Table 4.2 Fatigue test results.

Table 4.3 FCI as % of total fatigue life for each probe.

Table 4.4 Plastic zone size estimates based on LEFM for probe 2 and probe 7 cracks at 220,000 cycles.

Table 4.5 Interrupted test data (probe-wise) for Test 6 (MA_MAG_I_2_L, also HQ_T06).

Table 4.6 Interrupted test data (probe-wise) for Test 7 (SM_MAG_I_1_R, also HQ_T07).

Table 4.7 Interrupted test data (probe-wise) for Test 8 (SM_MAG_I_1_L, also HQ_T08)

Table 4.8 Test-7 (Scan Set 1) - Crack Depth versus PD Change.

Table 5.1 Distribution of membrane and bending stresses across the test specimens.

Table 5.2 Loading parameters for elastic strain range analysis.

Table 5.3 Fatigue test results.

Table 5.4 HQ_T13 - Details of beach marking stages.

Table 5.5 HQ_T13 - Crack under SG #5 - Strain range drop and crack depth analysis.

Table 5.6 LQ_T14 - Details of beach marking stages.

Table 6.1 Tensile properties of S355 J2+N structural steel (from Section 3.3.1.1).

Table 6.2 Range of hardness values (in HV) of scan set 1, taken from [9].

Table 6.3 Range of hardness values (in HV) of scan set 2.

Table 6.4 Comparison of predicted FCI life versus actual (experimental) FCI life for HQ_T7 – UML_C1 - elastic S_{11} K_t – BM Hardness.

Table 6.5 HQ_T7 – UML_C1 - elastic S_{11} K_t – Comparison of predicted FCI lives based on different hardness values.

List of Tables

Table 6.6 Comparison of predicted FCI life versus actual (experimental) FCI life for HQ_T7 – UML_C2 - elastic S_{11} K_t – BM Hardness.

Table 6.7 HQ_T7 – UML_C2 - elastic S_{11} K_t – Comparison of predicted FCI lives based on different hardness values.

Table 6.8 Comparison of predicted FCI life versus actual (experimental) FCI life for HQ_T7 – NEWMAT_C3 - elastic S_{11} K_t – BM Hardness.

Table 6.9 HQ_T7 – NEWMAT_C3 - elastic S_{11} K_t – Comparison of predicted FCI lives based on different hardness values.

Table 6.10 Comparison of predicted FCI life versus actual (experimental) FCI life for HQ_T7 – COMPOSITE_C4 - elastic S_{11} K_t – BM Hardness.

Table 6.11 HQ_T7 – COMPOSITE_C4 - elastic S_{11} K_t – Comparison of predicted FCI lives based on different hardness values.

Table 6.12 Comparison of predicted FCI life versus actual (experimental) FCI life for HQ_T7 – NEWMAT_C5 – weld toe geometry based elastic S_{11} K_t – BM Hardness.

Table 6.13 Comparison of predicted FCI life versus actual (experimental) FCI life for HQ_T7 – NEWMAT_C6 – weld toe geometry based elastic S_{11} K_t – BM Hardness.

Table 6.14 Comparison of predicted FCI life versus actual (experimental) FCI life for HQ_T7 – COM1 – BM Hardness.

Table 6.15 Comparison of predicted FCI life versus actual (experimental) FCI life for HQ_T7 – COM2 – BM Hardness.

Table 6.16 Comparison of predicted FCI life versus actual (experimental) FCI life for HQ_T7 – COM3 – BM Hardness.

Table 6.17 HQ_T7 – COM3 - Comparison of predicted FCI lives based on different hardness values.

Table 6.18 Comparison of predicted FCI life versus actual (experimental) FCI life for HQ_T7 – COM4 – BM Hardness.

Table 6.19 HQ_T7 – COM4 - Comparison of predicted FCI lives based on different hardness values.

Table 6.20 Summary of variations and combinations used.

Table 6.21 Comparison of experimental FCI lives for technical crack with FCI lives based on the first indication of the crack detection technique.

Table 6.22 Fatigue life data

List of Figures

Figure 1.1 SN plot for parent metal and non-load carrying fillet welded joint showing the reduction in fatigue strength due to welding. Taken from [11].

Figure 1.2 Images of the cross-section of a fillet weld showing a) the multiple microstructural zones and the macro-sized stress concentration at the interface of the fusion boundary and base metal at the weld toe (marked with a red arrow); b) micro-sized stress concentrating features. Images from present work.

Figure 1.3 Flowchart of the thesis' structure.

Figure 2.1 Typical logarithmic *da/dN* versus *ΔK* plot showing the three distinct regimes of crack growth. Adapted from [19]. Not drawn to scale.

Figure 2.2 Different types of arc welding, chosen based on material and application [24].

Figure 2.3 Schematic of MAG welding. Adapted from [27].

Figure 2.4 Micrograph of an etched cross-section of S355 steel arc fillet-welded joint. Image from current work.

Figure 2.5 Schematic of the transverse residual stress field in a fillet welded joint. Inset of the distribution of the transverse residual stress field initially (as-welded), and after a tensile load has been applied. Residual stress data taken from [11].

Figure 2.6 Schematic of the mathematically simplified geometry. a) Global weld toe geometry; b) Local weld toe geometry; c) Flaw at weld-toe. Adapted from [9].

Figure 2.7 Challenges of mathematically representing the weld toe profile – a) A smooth weld toe profile which is relatively easier to numerically represent as an ideal weld toe geometry, as compared with b) a profile with an overlap, where the ideal geometry is unable to represent the flaw.

Figure 2.8 Micrograph of a weld toe subjected to fatigue cycling, showing flaws and the initiation of fatigue cracking from one such flaw. Image from current work.

Figure 2.9 Photo-elasticity based SCF determination. From [64].

Figure 2.10 Silicone replica of the weld profile in a profile projected for WTR and WTA measurements. From [71]

Figure 2.11 a) 3D stress profile of the weld geometry using laser scanning, from [72]; b) weld toe topography scan using a 3D optical profiler, from [73]; c) 3D profile of a fillet welded joint using the FARO laser scanning system, from [75].

Figure 2.12 SN Plot for Class F (BS7608) [6] non-load carrying fillet weld joint for load ratio 0.1. Additional relevant experimental data are taken from [81].

Figure 2.13 Schematic of weld toe stress approaches - nominal, hot-spot and notch stress. Adapted from [9].

Figure 2.14 Comparison of experimental FCI lives obtained in the literature. Data taken from [9, 88-92]

Figure 3.1 Schematic of the mathematically simplified geometry showing the features that make up the: a) Global weld toe geometry; b) Local weld toe geometry; c) Weld toe flaw geometry.

Figure 3.2 Schematic of the serial sectioning technique.

Figure 3.3 Image of the laser-scanning done by Hou [72] – a) 3D capture of the weld using laser scanning; b) image of the actual weld. Taken from [72].

List of Figures

Figure 3.4 3D capture of a fractured welded joint showing both the weld bead and fracture surface at the weld toe.
Figure 3.5 Schematic of μ-CT. Taken from [116]
Figure 3.6 Schematic of the partial volume effect.
Figure 3.7 Schematic of beam hardening.
Figure 3.8 Stress-strain curves for S355 J2+N structural steel.
Figure 3.9 Schematic of a MAG welded-joint after welding and a specimen extracted after welding.
Figure 3.10 Cross-section of electrodes – a) solid-core; b) metal-core. Adapted from [9].
Figure 3.11 Manual MAG welder position before arc generation. From [9].
Figure 3.12 Semi-automated MAG welding – a) Arc-position; b) operator adjustment. From [9]
Figure 3.13 Schematic of MAG single side welded joints. Top – as-welded; bottom – after specimen cutting.
Figure 3.14 A) image of a weld toe before; B) after UIT
Figure 3.15 Photographs taken of a specimen from each of the three scan sets.
Figure 3.16 Photographs of the replica process whilst the welded specimen is in the servo-hydraulic testing machine – A) The holder for the encapsulant mix around the weld bead; B) curing of the encapsulant mix.
Figure 3.17 A summary of the analysis steps involved in qualitatively and quantitatively assessing the μ-CT scan data.
Figure 3.18 Distribution of flaws in scan set 1 across 150 mm of weld toe length.
Figure 3.19 Flaw size distribution for scan set 1. MA – Semi-automated metal-core electrode weld; SM – Manual solid-core electrode weld. Note - the results from two SM specimens and one MA specimen have been presented.
Figure 3.20 Distribution of flaws in scan set 2 across a total of approximately 200 mm of weld toe.
Figure 3.21 Example of an LQ and HQ specimen.
Figure 3.22 Flaw size distribution for scan set 2. HQ – High-Quality Weld; LQ – Low-Quality Weld.
Figure 3.23 Image from the volume of scan set 3 showing the distribution of air pockets.
Figure 3.24 A) Original μ-CT image slice taken from the reconstructed volume; B) The same image after cropping showing the key features of the weld toe are retained.
Figure 3.25 Image processing steps from μ-CT slice to a single pixel line profile for subsequent MATLAB analysis - A) Minimum Error threshold; B) Flood Fill; C) Find Edges; D) Skeletonize; E) Analyze Particles; F) Invert image.
Figure 3.26 HQ smooth weld toe profile - A) Original single-pixel weld profile obtained from ImageJ processing; B) Weld toe geometry extraction after MATLAB processing.
Figure 3.27 Distribution of errors in WTC identification.
Figure 3.28 HQ weld profile with small cold-lap defect - A) original single-pixel weld profile; B) weld toe geometry extraction after MATLAB processing.
Figure 3.29 HQ weld profile with large cold-lap defect - A) original single-pixel weld profile; B) weld toe geometry extraction after MATLAB processing.
Figure 3.30 HQ weld profile with severe cold-lap defect - A) original single-pixel weld profile; B) weld toe geometry extraction after MATLAB processing.

Figure 3.31 LQ steep weld bead profile - A) original single-pixel weld profile; B) weld toe geometry extraction after MATLAB processing.
Figure 3.32 LQ steep weld bead profile with a deep undercut defect- A) original single-pixel weld bead profile; B) weld toe geometry extraction after MATLAB processing.
Figure 3.33 LQ steep weld bead profile - A) original single-pixel weld bead profile; B) weld toe geometry extraction after MATLAB processing.
Figure 3.34 Schematic depicting angle check - angle between WTA line fit and WTC back gradient.
Figure 3.35 Histogram of entire WTA distribution.
Figure 3.36 Box and whisker plot of entire WTA distribution.
Figure 3.37 Specimen-wise histogram of WTA distribution. Please note that the count scale for HQ_T11, HQ_T15, LQ_T10 and LQ_T12 is different from the bottom three plots.
Figure 3.38 Specimen-wise box and whisker plot of WTA distribution.
Figure 3.39 WTR determination using Lieurade circle fit, by fitting the smallest circle between weld profile coordinates a set distance from the identified WTC. From [9].
Figure 3.40 WTR determination using least mean-squared Pratt's circle, by fitting the smallest circle to the weld profile coordinates within a small arc of a circle. From [9].
Figure 3.41 Histogram of WTR distribution based on the method used in the algorithm.
Figure 3.42 Box and whisker plot of WTR distribution based on the method used in the algorithm.
Figure 3.43 Specimen-wise histogram of the minimum WTR from the two methods. Please note that the count scale for HQ_T11, HQ_T15, LQ_T10 and LQ_T12 is different from the bottom three plots.
Figure 3.44 Specimen-wise box and whisker plot of WTR distribution.
Figure 3.45 Image processing steps - a) slice from the original volume (cropped); b) processed image after ImageJ processing; c) image extended in MATLAB; d) the final shape of the image which is representative of a quarter of the test specimen. The inset shows that the actual geometry has been retained in the final shape.
Figure 3.46 Steps involved in FE analysis of scanned weld toe geometries.
Figure 3.47 Stress-strain curves obtained from tensile tests on the base metal (Structural steel S355 J2+N).
Figure 3.48 Illustration of the von Mises yield surface for each kind of constitutive hardening model in the principal stress space. From [154].
Figure 3.49 3D sub-volume rendered in ScanIP. The inset highlights the presence of the true geometry at the weld toe.
Figure 3.50 Schematic of the two types of quadratic tetrahedral elements - Straight edges (left) and curved edges (right).
Figure 3.51 Mesh refinement zones in the form of four concentric cylinders, each of different element sizes - a) isometric view of the four mesh refinement cylinders; b) side view; c) schematic of the mesh refinement zones on a binarized CT image.
Figure 3.52 Mesh validation - choice of element size.
Figure 3.53 Mesh validation and optimisation study - cylinder 1 size.
Figure 3.54 Geometric parameters to define mesh refinement cylinder - a) position of the centre of the 3D cylinder and thickness; b) rotation of the 3D cylinder about each of the three axes.

List of Figures

Figure 3.55 Final meshed sub-volume containing a spatter-like defect at the weld toe. The different mesh refinement cylinders have been marked.

Figure 3.56 Entire weld volume with the irregular weld toe path highlighted in yellow. Specimen - T15.

Figure 3.57 Need to divide the entire volume further to cover the entire weld toe in the mesh refinement zone with the smallest element size.

Figure 3.58 Schematic of applied pressure load on the input mesh.

Figure 3.59 Image of the mesh after applying symmetry boundary conditions. LEFT - X-axis and Y-axis symmetry as only a quarter of the specimen was modelled in ABAQUS. RIGHT - Z-axis symmetry as sub-models were solved, representative of the entire weld.

Figure 3.60 Flowchart describing the MATLAB code for extracting the distribution of the maximum output variable.

Figure 3.61 Schematic of how the maximum value of the data variable is extracted based on the user-defined resolution for extraction.

Figure 3.62 Box-Whisker distribution of maximum elastic S_{11} (top), S_{PS} (bottom-left) and S_{MISES} SCF (bottom-right).

Figure 3.63 Weld toe geometry of a section with a gradual "chamfer-like" weld bead.

Figure 3.64 Box-Whisker plot of maximum elastic S_{11} (top), S_{PS} (bottom-left) and S_{MISES} SCF (bottom-right) for scan set 2 specimens.

Figure 3.65 Examples of sections from the same specimen showing the different in the shape of the intentionally created undercut - A) Deep and sharp intentional undercut; B) intentional undercut in the shape representative of toe grinding.

Figure 3.66 Box-Whisker distribution of maximum elastic-plastic stress parameters for the entire scanned volume – $S_{EL\text{-}PL\text{-}MISES}$ (Left) and $S_{EL\text{-}PL\text{-}11}$ (Right) SCF. Please note the difference in scales.

Figure 3.67 Box-Whisker distribution of maximum elastic-plastic strain parameters for the entire scanned volume – $E_{EL\text{-}PL\text{-}PEEQ}$ (Left) and $E_{EL\text{-}PL\text{-}11}$ (Right).

Figure 3.68 Box-Whisker distribution of maximum elastic-plastic stress parameters for scan set 2 – $S_{EL\text{-}PL\text{-}MISES}$ (Left) and $S_{EL\text{-}PL\text{-}11}$ SCF (Right). Please note that the scales are different for both plots.

Figure 3.69 Box-Whisker distribution of maximum elastic-plastic strain parameters for scan set 2 – $E_{EL\text{-}PL\text{-}PEEQ}$ (Left) and $E_{EL\text{-}PL\text{-}11}$ (Right).

Figure 3.70 Material plastic behaviour input parameters for ABAQUS FE solving.

Figure 4.1 Schematic of ACPD and DCPD crack monitoring setups showing the relative difference in current paths for a compact tension specimen. Adapted from [160].

Figure 4.2 Schematic of a basic ACPD set-up for a single edge notched specimen showing the “skin-effect” at the surface and around the crack.

Figure 4.3 Schematic of ACPD setup without (left) and with (right) current focusing implemented.

Figure 4.4 Phasor Diagram showing the effect of varying $V_{p/up}$ signal on the measured voltage. Adapted from [160].

Figure 4.5 Relation between PD and applied load on C-Mn steel (BS4360 43A). PD showed a decrease with increase in loading, an effect of stress on the electrical resistance of the material. Adapted from [162]

Figure 4.6 Schematic of the Krautkramer U8 Crack Microgauge crack monitoring system. From [89].

Figure 4.7 Schematic of ACPD crack growth monitoring probe pair setup at the weld toe. From [63].

Figure 4.8 Relation between change in PD and crack size. Adapted from [113].

Figure 4.9 Cross-section of the welded joints and the magnitude of axial misalignment - a) metal-core electrode manual (MM); b) solid-core electrode manual (SM). Taken from [9].

Figure 4.10 Images of the SONATS NOMAD UNP System and the result of peening on a welded specimen.

Figure 4.11 The Matelect CGM-7 ACPD system.

Figure 4.12 Schematic of voltage wires layout.

Figure 4.13 Schematic of current wires with voltage wires.

Figure 4.14 Specimen after wiring, ready for fatigue testing.

Figure 4.15 a) Schematic of specimen setup in fatigue testing machine; b) Annotated photograph of the specimen loaded in the testing machine at TWI Ltd.

Figure 4.16 Plot of Static Loading ACPD data for Active Probes on weld toe.

Figure 4.17 Plot of Static Loading ACPD data for reference probes on the base metal.

Figure 4.18 a) The different static test set-ups; b) the change in PD for each of the cases.

Figure 4.19 Active Probe - PD vs Fatigue Cycles Plot for T4_SM_MAG_I_2_L, tested to failure (787,788 cycles).

Figure 4.20 Reference Probe-PD vs Fatigue Cycles for T4_SM_MAG_I_2_L, tested to failure.

Figure 4.21 Normalised Data-PD vs Fatigue Cycles for T4_SM_MAG_I_2_L, tested to failure.

Figure 4.22 T4_SM_MAG_I_2_L - Active probe 2 ΔPD in fatigue loading, with raw and smoothed values of data.

Figure 4.23 T4_SM_MAG_I_2_L - Normalised probe 2 ΔPD in fatigue loading, with raw and smoothed values of data.

Figure 4.24 Schematic of the specimen being broken at the fracture plane to get two fracture surfaces - the transverse joint and the leg.

Figure 4.25 T4_SM_MAG_I_2_L - 3D scans of the cruciform section of the fractured specimen. Images were taken in the Alicona Infinite Focus Microscope.

Figure 4.26 T4_SM_MAG_I_2_L – b) and c) are SEM images of the FCI site under probe 2. EDX showed crack caused by Nickel wire spot welding spatter.

Figure 4.27 EDX data - a) SEM-EDX image with points of measurement; b) Table with EDX data for each point.

Figure 4.28 T4_SM_MAG_I_2_L - Active Probes 2 and 7 Actual PD.

Figure 4.29 T4_SM_MAG_I_2_L - Normalised Probes 2 and 7 PD.

Figure 4.30 T4_SM_MAG_I_2_L - Active Probes 2 and 7 ΔPD.

Figure 4.31 T4_SM_MAG_I_2_L - Normalised Probes 2 and 7 ΔPD.

Figure 4.32 T4_SM_MAG_I_2_L - Active Probes 1-12 ΔPD.

Figure 4.33 T4_SM_MAG_I_2_L – Active Probes – 500,000 cycles onward 1-12 ΔPD.

Figure 4.34 T4_SM_MAG_I_2_L - Alicona Infinite Focus Microscope scan of the transverse joint fracture surface highlighting probes 6-8.

Figure 4.35 a) Failed weld toe (Optical Camera); b) Cracks propagating along weld ripple resulting in multiple ratchet marks (Optical Camera); c) SEM image of a weld defect – undercut; d) SEM image of a weld defect – Porosity.

Figure 4.36 Active PD vs Fatigue Cycles Plot for T8_SM_MAG_I_1_L, interrupted test (179,457 cycles).

Figure 4.37 Active PD vs Fatigue Cycles Plot for T8_SM_MAG_I_1_L Probes 4 and 7, showing an increase of at least 2 mV.

Figure 4.38 T4_SM_MAG_I_2_L - Combined active PD and ΔPD plot for probe 2 and probe 7, highlighting the point at which the crack propagation stopped.

Figure 4.39 T4_ SM_MAG_I_2_L – Crack Depth versus PD Analysis

Figure 4.40 T3_ MA_MAG_I_2_R – Crack Depth versus PD Analysis

Figure 4.41 Schematic of a mounted specimen.

Figure 4.42 Test7 - S_{11} and S_{PS} maximum SCF values plotted along the length of the weld toe.

Figure 4.43 Test-7 - ACPD data for selected probes along with the point of initiation in the overall life of the specimen.

Figure 4.44 Sections with different features – a) fatigue crack exhibiting bifurcation located at the weld toe; b) expected fatigue crack growth – transverse to the stress axis; c) fatigue cracking from an overlap defect at the weld toe; d) two fatigue cracks which eventually coalesced in further sections.

Figure 4.45 Comparison of S_{11} SCF (maximum) distribution with crack size distribution obtained from serial metallography.

Figure 4.46 Plots A and B represent the crack depth with maximum S_{11} SCF distribution for the regions that have been subject to serial metallography.

Figure 5.1 Use of strain gauges for fatigue crack detection and monitoring on welded joints – A) Strain gauge array used by Otegui et al. [69, 88, 105]; B) Miniature strain gauges used by Verreman et al. [195]; C) Micro-strain gauges used by Janosch [196].

Figure 5.2 Schematic of Experiment Set 2 specimen. Left - as-welded; right - after specimen cutting.

Figure 5.3 Schematic of stress distribution and application of strain gauges on the baseplate of the fatigue specimen away from the stress concentration zone of the weld toe. Adapted from [5].

Figure 5.4 Schematic of the strain gauge setup for measuring weld misalignment in terms of bending stresses.

Figure 5.5 Schematic of the two types of fatigue test specimens - HQ and LQ - with the different weld toes marked for UNP treatment and strain gauge attachment.

Figure 5.6 Images of the SONATS NOMAD UNP System and the result of peening on a welded specimen.

Figure 5.7 Actual images of the two kinds of specimens tested - HQ (high-quality) and LQ (low-quality).

Figure 5.8 Actual strain gauge applied to the surface of a specimen.

Figure 5.9 Schematic of the strain gauge setup (right), relative to the ACPD setup (left). Images are not drawn to scale.

Figure 5.10 Comparative schematic of strain gauge setup in both HQ (top) and LQ (bottom) specimens.

Figure 5.11 a) Schematic of specimen setup in fatigue testing machine; b) actual photograph of specimen gripped in the testing machine.

Figure 5.12 A) Schematic of the positioning of the strain gauge and the measuring gage length relative to the weld toe; B) locally magnified zone from A); C) dimensions from applied strain gauge.

Figure 5.13 Schematic of the representative model used for 2D FE analysis in ABAQUS and the simulated crack.

Figure 5.14 HQ_T15 - Membrane stress evaluation.

Figure 5.15 HQ_T15 - Bending stress evaluation.

Figure 5.16 HQ_T15 – Static data plots of strain gauges (SG) #1-12 attached near the weld toe.

Figure 5.17 HQ_T15 – Elastic S_{11} maximum SCF distribution along the weld toe.

Figure 5.18 Effect of WTA on the estimated elastic strain range drop for different crack depths.

Figure 5.19 Elastic strain rang drop for varying crack depths across different load ratios. Please note that only the crack depths for which strain range drop was evaluated have been shown.

Figure 5.20 HQ_T11 - Strain range drop data. Smoothing done using Loess algorithm.

Figure 5.21 HQ_T11 - Strain range drop data for SG #1-9.

Figure 5.22 HQ_T11 - Change in strain range drop (dSR_{LOESS}) for all strain gauges.

Figure 5.23 HQ_T11 - Actual image of the specimen with the strain gauge array. Left to Right - SG#1 to #12.

Figure 5.24 HQ_T13 - Strain range drop data. Smoothing done using Loess algorithm.

Figure 5.25 HQ_T13 – a magnified plot of strain range drop, highlighting Zone A. Inset is the overall strain range drop plot for SG #5.

Figure 5.26 HQ_T13 - Change in strain range drop (dSR_{LOESS}) for all strain gauges.

Figure 5.27 HQ_T13 - Strain range distribution across the multiple beach-marking stages.

Figure 5.28 HQ_T13 - Fracture surface of the baseplate end of the specimen, highlighting multiple cracking. The middle image is optimised (brightness and contrast) for visualising the fatigue crack fronts. The bottom image is a schematic of how the specimens were labelled after complete fracture.

Figure 5.29 HQ_T13 - Fatigue crack under SG #5 annotated with the crack depths at different beach marking stages.

Figure 5.30 HQ_T13 - Crack under SG #8.

Figure 5.31 LQ_T14 - Strain range distribution across the multiple beach-marking stages.

Figure 5.32 LQ_T14 - Fracture surface showing an edge crack detected by SG #24, amongst other fatigue cracking left of the edge of the specimen.

Figure 6.1 Elastic stress concentration factor calculated using FEA and fatigue notch factor of a specific butt weld geometry for two different structural steels. Adapted from [16], originally from [221].

Figure 6.2 Schematic of the local notch strain approach where the stress-strain behaviour at the vicinity of the notch root is considered to be the same as that of a smooth specimen of the same material properties. Adapted from [16].

Figure 6.3 SN curve depicting the experimentally derived FCI lives, based on the methodologies described in Chapters 4 and 5.

Figure 6.4 Top - FCI prediction distribution in HQ_T7 based on UML_C1 and elastic $S_{11}K_t$ and BM hardness data. Bottom – Distribution of elastic $S_{11}K_t$ along the same weld toe. The FCI location that was indicated by the crack detection method used – ACPD (Chapter 4) – has been highlighted.

Figure 6.5 Comparison of the predicted FCI lives using the variations and combinations of the notch stress-strain approach with the experimentally obtained FCI life for each scanned specimen.

Figure 6.6 Box-whisker distribution of the deviation factor *f* for each attempted variation and combination of the notch stress-strain approach.

Figure 6.7 Specimen-wise distribution of deviation factor *f.*

Figure 6.8 Box-whisker distribution of the deviation factor *f* based on adjusted experimental FCI life (Table 6.21).

List of Figures

Figure 6.9 Specimen-wise distribution of deviation factor *f* based on adjusted experimental FCI life (Table 6.21).

Figure 6.10 Log SN Curve for comparing FCI lives obtained for the growth of a technical crack, adjusted FCI based on the first indication of crack detection techniques and the predictions from variation COM2.

Figure 6.11 Fatigue notch factor distribution with variation in critical distance a^* and notch radius for two values of stress concentration factor, K_t.

Figure 6.12 Fatigue notch factor distribution based on weld geometry based elastic stress concentration factor analytical solutions of Crump, 2017 [9] (used in variation C5).

Figure 6.13 SCF K_t versus estimated FCI life (COM2) plot for BM (top) and HAZ (bottom) hardness maps for scan set 2. Specimens tested in scan set 2 have been indicated with their maximum value K_t and estimated COM2-based FCI life.

Figure 6.14 SN Curve depicting the total life obtained in Table 6.22 compared with the standard BS7608 [6] Class F SN curve. SD is the standard deviation distribution for class F.

Research Thesis: Declaration of Authorship

Print name:	Somsubhro Chaudhuri

Title of thesis:	The development of high-resolution crack monitoring methods to investigate the effect of the local weld toe geometry on fatigue crack initiation life

I declare that this thesis and the work presented in it are my own and has been generated by me as the result of my own original research.

I confirm that:

1. This work was done wholly or mainly while in candidature for a research degree at this University;
2. Where any part of this thesis has previously been submitted for a degree or any other qualification at this University or any other institution, this has been clearly stated;
3. Where I have consulted the published work of others, this is always clearly attributed;
4. Where I have quoted from the work of others, the source is always given. With the exception of such quotations, this thesis is entirely my own work;
5. I have acknowledged all main sources of help;
6. Where the thesis is based on work done by myself jointly with others, I have made clear exactly what was done by others and what I have contributed myself;
7. Parts of this work have been published as:

    a) S. Chaudhuri, J. Crump, P. A. S. Reed, and B. G. Mellor, "High-resolution 3D weld toe stress analysis and ACPD method for weld toe fatigue crack initiation," Welding in the World, 2019.

Signature:		Date:	14/09/2019

Acknowledgements

I am quite surprised being in the position that I am now, finishing the last section of my thesis. Five years ago, I never thought that this is where I would be. That 'Somsubhro' dismissed the possibility of doing a PhD as something impossible with these precise words, "PhD? I can't write a thesis!!" Now that I have written one, it is not lost on me that this involved the contribution and support of a lot of people whom I should acknowledge and thank.

First and foremost, I would like to thank my academic supervisor Professor Philippa Reed who made this PhD possible for me, in every sense of the word. Without her support and guidance, none of this would have been possible. I would like to thank my secondary supervisor Professor Brian Mellor for his support and expertise during the supervisory meetings, and his stories about his time in India. I also would like to thank Dr Jenny Crump, my industrial supervisor, whose guidance was invaluable during the course of this PhD. I cannot thank her enough for helping me to quickly integrate into the working environment at TWI Ltd and tell me about all the little tricks to get one's work done as soon as possible. For all the discussions and brain-storming during the supervisory meetings, I am deeply grateful to Philippa, Brian and Jenny. I genuinely thank you for having faith in me, giving me this opportunity and supporting me from day one.

I would like to acknowledge and thank the sources of funding of my PhD: EPSRC (grant number EP/M508147/1), the University of Southampton, National Structural Integrity Research Centre (NSIRC) and TWI Ltd. I would also like to thank Matthew Waitt and Adam Wojcik from MATELECT Ltd. for their support with the CGM-7 ACPD system.

I would like to thank my friends at the University of Southampton who have given me a lot of memories (happy, strange, weird and peculiar) in the past four years. Mike for being the only guy I could discuss cricket with, Andreu to discuss gaming rigs with, Alex for teaching me how to use the machines in the metallography lab, Chao for teaching me the basics of ABAQUS, Rong for teaching me how to use Instron 2, Binyan for showing how one can smile even if one's roof is on fire, Angelos to discuss whether he is Angelos or Evangelos, Pawee to discuss dodgy vegetables, Sebastian for being my first ever gym trainer (until I gave up), Aleks for his MATLAB skills and quirkiness, Charlie for showing how one could be royal and humble at the same time, Alvaro for making myself feel relieved that I do not have to polish Aluminium for my PhD, Junqing for inspiring me to work at least 50% as hard as he did, Kim for the K-jokes and enunciation lessons, Songsong for his company when working late in the office, Diego for being a fellow Madridista and metal-borrowing expert, Ben for his lessons in the physiology of greyhounds and generally being the nicest guy (ever) in 05/3021, Antonio and Chiara for being relatively quick "Niccceeee" enthusiasts, Maria for her dedication to

volleyball, Alina for the purest Palinka ever, Madina for the lovely dinners, Dan for ensuring that I still have access to the fast machines at Southampton from Cambridge, Corentin for his willingness to be a shooting target, and Saran for his questions about everything. I would also like to thank Mark Mavrogordato and everyone at μ-VIS for their help with getting my specimens scanned. Sue and Katherine's patient and warm handling of the random needs of PhD students could not be appreciated enough. Also, this PhD led me to meet Dr Ion Palamarciuc, who came to the University of Southampton as an exchange. I did not know that salvaging old cycles could be so much fun and an everlasting memory.

I have been lucky to also spend 50% of my PhD at NSIRC, TWI Ltd, where I met a lot of wonderful people who made my stay there truly memorable. Dibakor for his knowledge on residual stresses and how to get papers published; Rosa for all the awesome cakes she brought to work and fed her fellow students; Kuveshni for the lovely Diwali dinner; Ashley, Diana and Catherine for having faith in me to work a bit longer than usual; Alan, Martin, Stuart and Tom for making me feel like spending all my time in the fatigue lab to educate myself about England, cakes and Norfolk; Lisa, Alexandre, Cui, Kostas (both), Berenika, Mike, Gowtham, Emre, Jazeel, Usama, Juvaria, Pedro, Karan, Mahesh for their friendship and making the time at work much more enjoyable and exciting. I would also like to mention my flatmate in Cambridge, Markel Bilbao, with whom I had some very interesting conversations about aeroplanes, fatigue damage, and cooking.

None of this would have been possible without the support of my Baba (father), Ma (mother) and Gaischand (sister). They have been constant pillars of strength throughout my life, and I dedicate everything that I have achieved or will ever achieve to them. We may have many artificial constructs in our society, but one construct that we share with most organisms, is family. To this family, I have joyfully added a new member, my wife, Tanya. Thank you for having so much confidence in me, even when I could not find any myself. Our relationship transpired during the course of this PhD, which is another reason why I can truly say that the past four years were the best years of my life. I have learned and gained an incredible lot and realise how privileged I am to be in this position.

In the end, I would like to finally thank two extremely important people without whom I would have never even come to the UK, my friend Rohit Mahlawat and his father Virender Mahalawat. They made a lot of sacrifices to help me, and I possibly could never thank them enough.

Thank you / धन्यवाद / ধন্যবাদ

Somsubhro Chaudhuri / शोमशुभ्रो चौधूरी / সোমশুভ্র চৌধুরী

Definitions and Abbreviations

$\Delta\varepsilon$	Total local strain range
$\Delta\sigma$	Total local stress range
μ_{MP}	Magnetic permeability
$\mu\varepsilon$	microstrain
$2c$	Surface crack length OR major axis of semi-elliptical surface crack
a	Initial crack length OR depth of semi-elliptical surface crack (semi-minor axis)
a^*	Critical distance
a_i	Initial crack depth
b	Fatigue strength exponent or Basquin exponent.
c	Half flaw width
c	Fatigue ductility exponent
dR/R	Change in measured resistance, output signal of the strain gauge
dSR_{LOESS}	Change in the Loess smoothened strain range drop
$d\varepsilon$	Change in strain of the measurement specimen
E	Young's (elastic) Modulus
e	Axial misalignment or eccentricity
f	AC frequency
H	Heat Input
I	Current
k	Strain gauge factor
K	Static strength coefficient
K'	Cyclic strain-hardening coefficient
K_f	Fatigue notch factor
K_I	Mode I crack opening stress intensity factor
K_t	Elastic stress concentration factor
L	Leg attachment length
n	Static strain-hardening exponent
n'	Cyclic strain-hardening exponent
N_f	Load reversals to failure (fatigue crack initiation)
P	Primary Stress
P_b	Bending stress – the stress induced due to misalignment, and is considered to be superimposed on P_m
$PD_{crack\ growth}$	Change in PD due to crack propagation

$PD_{effect\ of\ stress}$	Change in PD due to increased stress in remaining ligament of the fatigue specimen
P_m	Membrane stress – mean stress through the cross-section of the tested specimen that is required to maintain its equilibrium.
q	Notch sensitivity index
r_p	Radius of plastic zone
S_{EL-11}	Elastic stress in the direction of applied tensile stress
$S_{EL-MISES}$	Elastic Von Mises Stress
S_{EL-PS}	Elastic Maximum Principal Stress
T	Plate thickness
V	Voltage
V_{acpd}	ACPD voltage
V_{meas}	Measured ACPD voltage
$V_{p/up}$	Induced pick-up voltage
V_{res}	Resistive voltage
α	Weld toe angle
Δ	ACPD Skin depth
ΔK	Stress intensity factor range
ΔK_{th}	Threshold stress intensity factor range
ΔPD	Change in measured potential drop
$\Delta\sigma_{nom}$	Nominal stress range
ε	Total local strain (Chapter 6)
$\varepsilon_{ELASTIC}$	Elastic component of true strain
$\varepsilon_{ENGINEERING}$	Engineering strain
ε_f'	Fatigue ductility coefficient
ε_k	Maximum notch strain in elastic-plastic stress state
$\varepsilon_{PLASTIC}$	Plastic component of true strain
ε_{TRUE}	True strain
η	Process efficiency factor
v	Travel speed
v	Poisson's Ratio
ρ	Weld toe radius (Chapter 3)
ρ	Notch radius (Chapter 6)
ρ_c	Critical notch radius
ρ_{RES}	Electric resistivity
σ	Instantaneous value of stress at any point along the cyclic far-field stress distribution
σ	Total local stress (Chapter 6)

σ_a	Stress amplitude for nonzero mean stress
$\sigma_{a\|\sigma\_(m=0)}$	Stress amplitude (for a finite life) for full-reversed loading
$\sigma_{ENGINEERING}$	Engineering stress
σ_f'	Fatigue strength coefficient (approximately equal to the fracture strength of the material)
σ_{HSS}	Hot-spot stress
σ_k	Maximum notch stress in elastic-plastic stress state
σ_m	Mean stress
σ_{NOM}	Nominal stress
σ_{NS}	Notch stress
σ_{res}	Initial residual stress
σ_{TRUE}	True stress
σ_{UTS}	Ultimate tensile strength
σ_{ys}	Uniaxial yield stress

µ-CT	Micro-computed tomography
2D	Two-dimensional
3D	Three dimensional
ACPD	Alternating Current Potential Drop
BM	Base metal
C-Mn	Carbon-manganese
CPU	Central Processing Unit
DCPD	Direct current potential drop
EBSD	Electron back scatter diffraction
EDM	Electrical Discharge Machining
EDX	Energy dispersive X-ray spectroscopy
EPD	Electric potential drop
FCI	Fatigue Crack Initiation
FEA	Finite Element Analysis
FSW	Friction stir weld
HAZ	Heat Affected Zone
HB	Brinell Hardness
HFMI	High-frequency mechanical impact
HPC	High-Performance Cluster
HSS	Hot-spot stress
HV	Vicker's Hardness
IIW	International Institute of Welding
LEFM	Linear elastic fracture mechanics
LOF	Lack of fusion
MA_MAG	Metal Core Electrode Semi-Automated
MAG	Metal active gas (welding)
MM_MAG	Metal Core Electrode Manual
NDT	Non-destructive testing
PD	Potential drop
PEEQ	Plastic Equivalent Strain
RMS	Root mean squared
ROI	Region-of-interest
SA_MAG	Solid Core Electrode Semi-Automated
SCF	Stress concentration factor
SEM	Scanning electron microscopy

SG	Strain gauge
SIF	Stress intensity factor
SM_MAG	Solid Core Electrode Manual
TIG	Tungsten Inert Gas
UIT	Ultrasonic Impact Treatment
UML	Uniform Material Law
WIA	Weld Impression Analysis
WM	Weld Metal
WTA	Weld Toe Angle
WTC	Weld Toe coordinate
WTR	Weld Toe radius

Chapter 1 Introduction

1.1 Motivation

Potential modes of failure of components and structures need to be accounted for in their structural design bearing in mind: the chosen material, manufacturing process (including joining or assembly), dimensions and loading conditions. Fatigue damage should be considered if the loading conditions involve cyclic loading (constant- or variable-amplitude). Failure due to fatigue is one of the most common mechanical failure modes in structures or components [1]. Designing against fatigue failure in welded joints is of critical concern to engineers, therefore fatigue in welded joints (and methods of improving the fatigue performance of welds) has historically been an important topic of research [2]. Standards are available [3-8] which provide thoroughly researched procedures and methods which could potentially lead to fewer fatigue failures, lower material costs (due to savings in manufacturing and repair expenditures) and, most importantly, safer structures/components. However, they do not cover all the aspects associated with welded joint fatigue, especially fatigue crack initiation life. Due to the large number of variables associated with fatigue crack initiation, a standardised procedure is yet to be published for welded joints. This project aims to investigate the prediction methods for fatigue crack initiation life using fatigue crack initiation life data obtained from welded joints using novel crack-detection methods and stress analysis.

1.2 Weld fatigue - Overview

In most engineering applications, it is not possible to make an entire engineered structure from a single piece of material. In such cases, some form of material joining process needs to be used to design and build complex structures. Before the development of welding, riveting and bolting techniques were used, but these often proved relatively slow and inefficient compared to welding. The benefit of the greater efficiency of welding over other available joining methods, as well as the ability to have weld lengths from 0.1 mm to several metres in length has made welding popular in industrial practice. Apart from the conventional arc welding techniques, other welding techniques have been developed and optimised over the years. Some notable examples are friction stir welding, electron beam welding, laser welding and resistance welding. However, arc welding processes and the use of steel continues to be one of the most popular choices for the construction and oil and gas industries[9, 10]. This is primarily why conventional C-Mn arc welded joints were chosen for this PhD project.

Despite the considerable benefits of welding, any design involving welding needs to address the effects of the process on damage tolerance of the structure. Understanding and predicting the fatigue behaviour of welded structures is crucial as the fatigue strength of a welded joint is significantly lower than that of the parent metal [11, 12], as illustrated by the SN plot in Figure 1.1. The stress-concentrating geometry inherent to the welding process is one of the primary causes of the poor fatigue performance of welds, along with tensile residual stress fields and inhomogeneous microstructural and hardness zones. The geometrical stress concentrations readily act as sites of crack initiation from which fatigue cracks propagate, meaning that often the majority of the life of welded joints is spent in the crack propagation regime[11, 12].

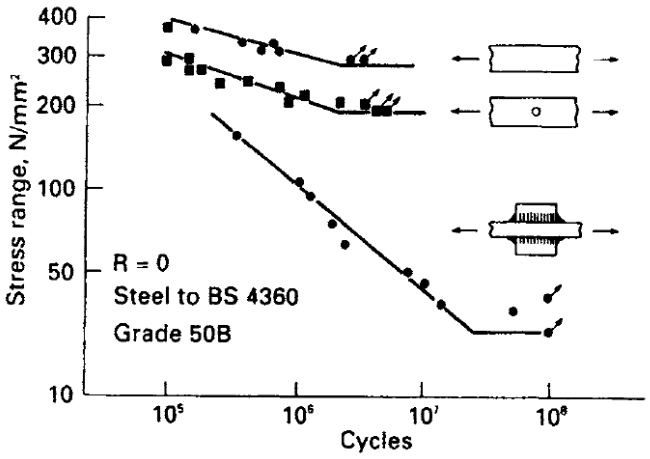

Figure 1.1 SN plot for parent metal and non-load carrying fillet welded joint showing the reduction in fatigue strength due to welding. Taken from [11].

These stress concentrations can be broadly classified based on their relative size as macro-sized stress concentration regions, i.e. the weld bead, and micro-sized stress concentration regions, i.e. weld toe flaws, as shown in Figure 1.2. The role of these stress concentrations in fatigue crack initiation is similar to the behaviour of sharp notches in unwelded specimens [13].

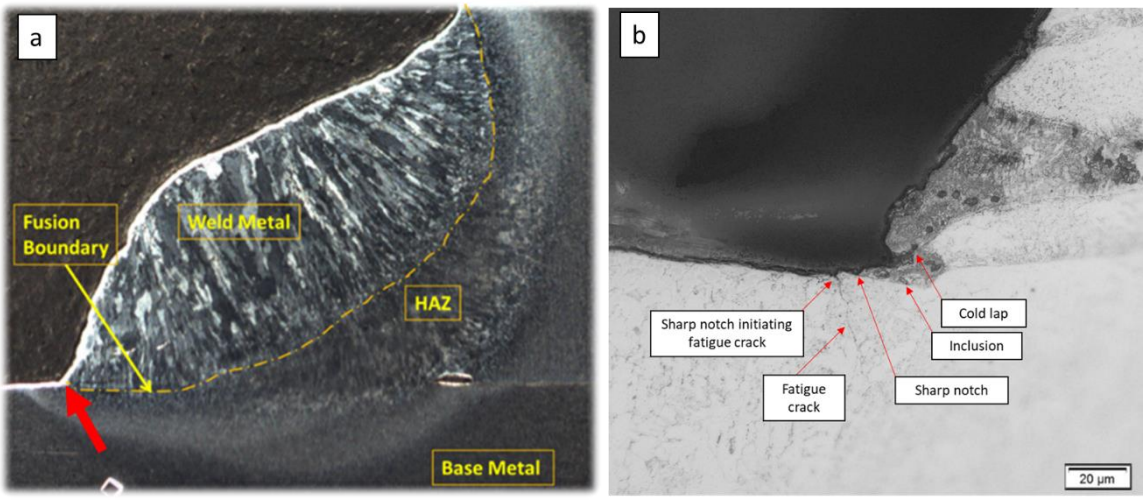

Figure 1.2 Images of the cross-section of a fillet weld showing a) the multiple microstructural zones and the macro-sized stress concentration at the interface of the fusion boundary and base metal at the weld toe (marked with a red arrow); b) micro-sized stress concentrating features. Images from present work.

Inherent stress-concentrating flaws are always present in arc-welded joints; even in good quality welds, flaws up to depths of 100 µm have been observed. Consequently, post-weld treatments have been developed in attempts to minimise their influence on fatigue crack initiation and thus either maximise or extend the life of welded joints. Some post-weld treatments are described further in [2, 11], the most popular ones are burr grinding, plasma dressing and peening. The basic premise behind them involve reducing the stress concentrating effect by physically removing the flaws and increasing the radius at the weld toe and introducing compressive residual stresses directly at the weld toe. Although post-weld toe treatments can significantly improve fatigue life, they involve an additional cost in terms of equipment, consumables and labour. Therefore, the ideal solution to improve fatigue life is to either select welding parameters that will result in the best quality welds possible, or to improve fatigue life prediction methods to reduce any current conservatism.

This PhD project focusses on the latter approach. Many years of research on the prediction of weld fatigue life have resulted in procedural standards published by the British Standards Institution (BSI) [4-6] and the International Institute of Welding (IIW) [8], amongst others. These standards/recommendations aim to provide a foundation for the design and analysis of welded structures and components in order to avoid failure due to fatigue. Each standard clearly states its limitations in order to avoid application of the wrong procedure in a particular scenario. It is currently recommended that all commercial weld fatigue analyses are carried out based on these standards.

The total fatigue life, N_t, of a component can be divided into the life taken to initiate a crack, which is the fatigue crack initiation life (FCI), N_i, and the life taken for the crack to propagate to final failure, N_p [14]. Broadly there are two kinds of approaches for weld fatigue analysis – global and local approaches[15]. Global approaches are primarily the nominal stress approach and the structural hot-spot stress approach. The nominal stress approach considers the far-field stress in a stressed component and does not take into account any changes in stress due to structural discontinuity (the result of the welded joint). The hot-spot structural stress approach considers both the far-field stress as well as the increase in stress due to the structural discontinuity. Both approaches ignore the notch stress, which is the local stress due to the presence of smaller notch-like stress concentration features at the weld toe itself [2]. Standards on weld fatigue design provide methodologies for implementing the global approaches, where different types of welded joints are categorised into classes, and an SN curve (based on experiments performed on similar welds) is provided for each of these classes [6]. Although global approaches have proven to be robust and widely applicable, they are more conservative due to the large scatter seen experimentally in the SN curves. Also, these approaches are used for estimating the total fatigue life and do not differentiate between the crack initiation or propagation life. By using local approaches which consider the effects of notch-like features at the weld toe on the local stress and strain distributions it is possible to estimate the crack initiation and propagation life separately, using a two-step approach – notch stress or notch stress-strain approach for predicting initiation, and the crack propagation approach for predicting the crack propagation life after initiation [16]. Due to the complexities involved in capturing the local stress-strain distributions and the inherent microstructural variations at the weld toe, local approaches are not yet standardised, but a considerable amount of research has been performed on this problem [15-17]. This PhD project focuses on the use of the local notch stress-strain approach in predicting the fatigue crack initiation lives of welded joints.

1.3 Research objectives

The primary aim of this PhD project is to further investigate the potential of industrial X-Ray micro-computed tomography (μ-CT) to capture the three-dimensional (3D) local weld toe geometry for high-resolution 3D stress-strain analysis. The primary benefit of using μ-CT is that it is non-destructive and has the ability to differentiate between metal and slag, as slag could potentially mask notch-like features when using other non-destructive topographical or optical techniques for resolving the local weld toe geometry. Also, sub-surface flaws (resulting from the welding process) that act as stress concentrations can be captured non-destructively. Further, the application of the

local 3D stress-strain analysis in local approaches for fatigue crack initiation estimation will be explored.

Following on from the primary aim and to validate the results obtained from the μ-CT and FCI estimations, the secondary aim of the project is to investigate ways of improving the experimental techniques available for fatigue crack detection. Data-rich variations of two non-destructive in-situ fatigue crack detection techniques – Alternating current potential drop (ACPD) and a strain gauge array method – will be investigated to obtain accurately the location of fatigue crack initiation as well as the fatigue crack initiation life.

To deliver on these aims of the research project, the following objectives have been identified:

Objective 1: Resolve and define weld toe geometry for high-resolution three-dimensional stress analysis of the inherent weld toe flaws during cyclic fatigue loading.

Objective 2: Accurately detect in-situ fatigue crack initiation life and location using two data-rich fatigue crack monitoring techniques:

Objective 2a: The use of *Alternating Current Potential Drop (ACPD)*.

Objective 2b: The use of an *array of strain gauges*.

Objective 3: The use of the local notch stress-strain approach for the estimation of fatigue crack initiation life and, subsequently, the total life of a welded joint with local stresses obtained from 3D FE stress analysis of the true weld geometry, followed by validation of the results with data-rich experimental methods of crack growth monitoring.

1.4 Thesis structure

Figure 1.3 presents the structure of the thesis in the form of a flowchart. Apart from the current introductory chapter and concluding chapters containing references and appendices, the thesis is divided into six main chapters:

Chapter 2 provides an overview of the background and literature available on relevant topics to provide the context for the work done in this project.

Chapter 3 focuses on objective 1 and provides a detailed review of why μ-CT was chosen as opposed to other techniques that have been used in capturing the true weld toe geometry. The methodology that was developed to capture the weld toe geometry and obtain the local stress-strain distributions has been described, along with the results obtained.

Chapter 4 focuses on objective 2a, which is the use of ACPD as a data-rich fatigue crack monitoring technique. A brief overview of the work previously done using ACPD is provided, and the possibility of using ACPD for the purpose of accurately detecting FCI is investigated.

Chapter 5 focuses on objective 2b, which is the use of a strain gauge array as a data-rich fatigue crack monitoring technique. Very similar to Chapter 4 in terms of structure, it explores the use of strain gauges (as compared to ACPD in Chapter 4).

Chapter 6 focuses on objective 3, which is the use of the local notch stress-strain approach for predictions of FCI lives. It provides a brief overview of the literature available on the topic in order to substantiate the methods adopted for the purpose of estimations. Results from Chapter 3, 4 and 5 are used to validate the results obtained.

Chapter 7 presents the conclusions drawn from the results obtained in the studies performed for this project, followed by the further questions that the study has raised. It ends with the author's recommendations for future work based on the conclusions.

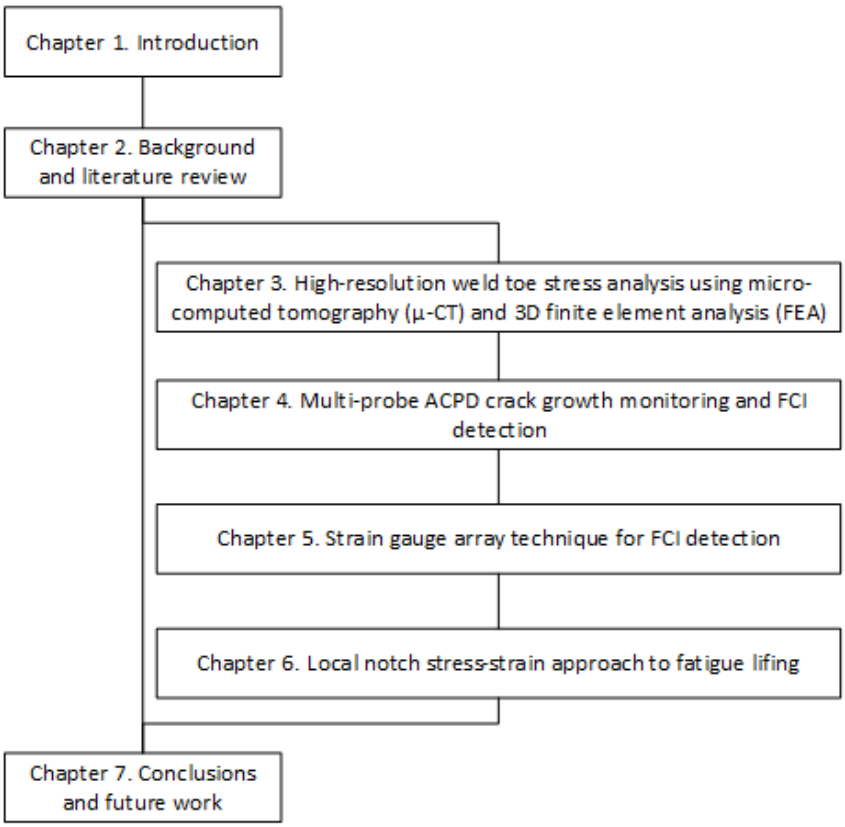

Figure 1.3 Flowchart of the thesis' structure.

Chapter 2 Background and literature review

This chapter provides the foundation upon which this PhD study is based. It presents a comprehensive review of the literature behind this research and describes similar research that has been considered in the development of this work. It should be noted that in each experimental Chapter (Chapters 3 to 6) a brief review of relevant literature is also provided that extends on that in this Chapter.

2.1 Fatigue as a failure mechanism

Fatigue damage occurs in structures subject to fluctuating and dynamic stresses, often at levels below the proof strength of the material [18]. The fatigue properties of a structure or material are dependent upon the microstructure, loading conditions, component geometry, crack or notch geometry and environmental conditions [14]. In assessing fatigue performance, fatigue properties are broadly characterised as fatigue life and fatigue strength. Fatigue strength is the magnitude of an applied load that causes failure after a certain number of loading cycles. Fatigue life is the number of cycles of an applied load that leads to fatigue failure. The fatigue life can also be denoted as total life (N_t), which is the sum of the number of cycles required to initiate a fatigue crack (N_i) and the number of cycles for propagating the crack until failure (N_p). Fatigue damage generally progresses through the following stages:

a. Fatigue crack initiation
b. Fatigue crack propagation

2.1.1 Fatigue crack initiation

Microscopic fatigue crack initiation and propagation in materials is dependent on the slip behaviour, characteristic microstructural dimensions, near-crack tip plasticity and applied stresses. In nominally defect-free or un-notched components or specimens, crack initiation from a smooth surface generally occurs due to repeated cyclic straining leading to varying amounts of net slip on different crystallographic glide planes and the formation of persistent slip bands (PSBs). Due to the cyclic straining occurring as a result of the loading cycle, the resultant irreversible slip creates intrusions or extrusions at the free surface. These act as microscopic notches and can act as stress concentration sites for additional slip and fatigue crack nucleation.

In the case of engineering components, fatigue crack initiation primarily occurs at sites of impurities, inclusions or constituent particles and geometrical stress concentrations such as

scratches, machining imperfections or corners within the component geometry. Such features can act as notches, similar to notched specimens. However, the presence of a notch or notch-like stress concentrations under cyclic loading may produce a lower stress concentration effect than that predicted by linear elastic theory. This is called the microstructural notch support effect and is dependent on the notch geometry and material properties. This is discussed in greater detail in Chapter 6, where life assessment approaches based on local geometry containing notch-like features are investigated.

When distinguishing between life to crack initiation, there is some debate about what is defined as fatigue crack initiation. If defined in terms of material behaviour, it could be termed as the nucleation of a flaw at PSBs. However, in engineering terms, it is challenging to detect initiation at such a small scale. Therefore, it is easier to define fatigue crack initiation as the life taken to initiate a fatigue crack to a specific depth. Fatigue assessment approaches often use the latter definition when estimating fatigue crack initiation life [16].

2.1.2 Fatigue crack propagation

The process of fatigue crack propagation can be classified in terms of the different mechanisms that control crack growth (Figure 2.1):

Regime A (Stage 1)

Regime A considers near threshold crack propagation corresponding to crack propagation that is barely measureable and may arrest. Crack propagation in this regime is strongly influenced by the load ratio, microstructure, the crack geometry, slip characteristics of the metal and the environment. The crack and the plastic zone surrounding the crack tip are within a few grain diameters.

Regime B (Stage 2)

In Regime B or stage 2 crack growth at higher ΔK values such as 300 to 1000 N/mm$^{3/2}$, the plastic zone at the crack tip encompasses many grains and the requirement for their compatible plastic deformation results in simultaneous dislocation movement along multiple slip systems. This leads to an overall crack growth path that is perpendicular to the applied stress. This regime of crack growth is largely independent of the microstructure. The fracture surface in many engineering alloys exhibits fatigue striations due to this stage 2 type crack propagation. Striations are formed due to repeated opening and blunting of the crack tip under an applied load and subsequent re-sharpening of the crack tip on load reversal. The spacing between adjacent striations can be correlated to the average crack growth rate per cycle.

Regime C – Stage 3

In Regime C or stage 3 crack growth, the value of the maximum stress intensity factor approaches the fracture toughness value of the metal, thus leading to local fracture events. Crack growth is unstable in this regime with bursts of monotonic failure contributing to a much faster crack growth rate.

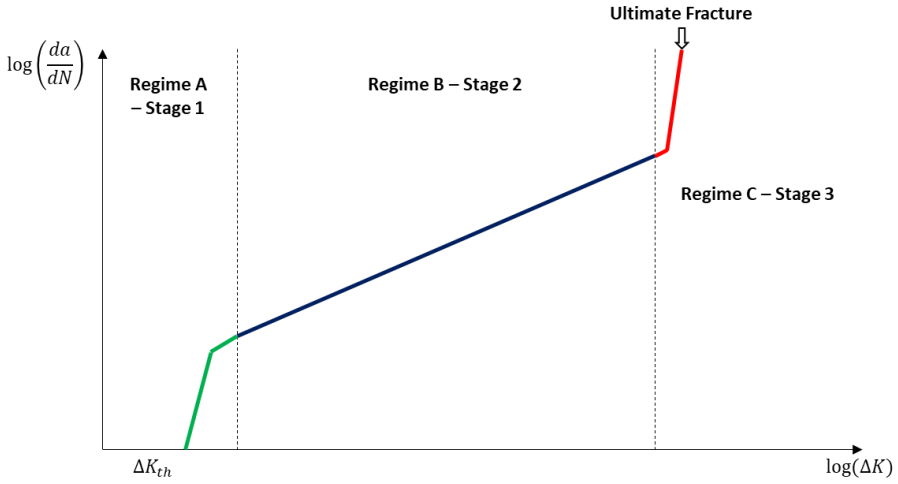

Figure 2.1 Typical logarithmic *da/dN* versus *ΔK* plot showing the three distinct regimes of crack growth. Adapted from [19]. Not drawn to scale.

Linear elastic fracture mechanics (LEFM) is widely used for quantifying fatigue crack growth as it allows the quantification of stresses at the crack tip in terms of the crack and specimen geometry, and applied loading conditions. These are used to calculate *ΔK* using Equation 2-2. The current study focusses on the tensile opening mode (Mode I) of failure.

$$\Delta K = K_{max} - K_{min} \quad 2\text{-}1$$

$$\Delta K = f\left(\frac{a}{W}\right)\Delta\sigma\sqrt{\pi a} \quad 2\text{-}2$$

Where,

K_{max}	Stress intensity factor at maximum applied load
K_{min}	Stress intensity factor at minimum applied load
a	Crack length
$f\left(\frac{a}{W}\right)$	Geometrical correction factor
$\Delta\sigma$	Applied stress range

One of the primary assumptions involved in using LEFM is that there is no crack tip plasticity, which results in LEFM predicting a stress singularity at a sharp crack tip. However, this is not the case in reality as stresses at a sharp crack tip are redistributed due to plasticity ahead of the crack tip in the

plastic zone. The size of the plastic zone (r_p) can be approximated for plane strain conditions using Equation 2-3 [20]. For LEFM to apply, the use of *K* is limited to what is known as small scale yielding, i.e. the plastic zone is very small compared to the bulk of the elastically responding material. Therefore, Equation 2-4 must be satisfied [21]. As long as these validity criteria are satisfied the K-concept provides similitude, as different cracks of different sizes in different structural geometries will behave identically and have the same crack tip plastic zone sizes for the same value of K.

$$r_p = \frac{1}{3\pi}\left(\frac{K}{\sigma_y}\right)^2 \quad 2\text{-}3$$

$$W - a, a, B > 2.5\left(\frac{K_{1C}}{\sigma_y}\right)^2 \; approx\; 50\; times\; the\; plastic\; zone\; size \quad 2\text{-}4$$

Where,

σ_y	Yield strength
K_{1C}	Plane strain fracture toughness
W	Sample width
$W - a, a, B$	Remaining ligament length

Although LEFM provides the basis for understanding the fracture behaviour of most materials in common engineering situations, it is not possible for the plastic zone size validity requirement to be met in all cases. This is more relevant in the case of characterising the behaviour of short cracks, which tend to propagate faster than longer cracks at a particular *ΔK*, and also exhibit more scatter compared with long cracks [22]. In such cases, the application of Elastic-Plastic Fracture Mechanics (EPFM) is more appropriate, which has two parameters to define the crack tip driving force: Crack tip opening displacement (CTOD or δ_t) and the J-integral. CTOD is used to describe the crack blunting that occurs due to large plastic zones ahead of an advancing sharp crack tip. An accepted definition of CTOD is the distance between two points on the lower and upper crack faces where two 45° lines drawn from the deformed crack tip intercept the two crack faces [19]. CTOD can be used to rank fracture toughness behaviour and to describe fatigue crack growth behaviour. J-integral was developed as the strain energy release rate based on non-linear elasticity (as compared with LEFM). It is defined as a path-independent line integral along a contour around the crack tip for a linear or non-linear elastic material [23]. Under LEFM conditions, it is possible to relate both parameters to stress intensity factor *K* using Equations 2-5 and 2-6 (*E* is elastic modulus).

$$\delta_t = \frac{K^2}{\sigma_y E} \quad 2\text{-}5$$

$$J = \frac{K^2}{E} \quad 2\text{-}6$$

2.2 Arc welding of steel

Arc welding has existed for more than 100 years, with multiple variations of the technique being developed throughout the years based on continuous research on joint quality, material evolution both in terms of parent metal and welding consumables (electrodes and shielding gas) and cost [24-26]. Generally, in arc welding, an electrode is used to create the arc, provide the filler metal and a 'shield' from atmospheric contamination during the welding process. In some cases, the gas shield is supplied separately. Based on specific manufacturing requirements such as strength, choice of the parent metal, type of weld, etc., a range of variations of the arc welding process have been developed over the years. Logistical concerns such as cost, availability, portability of welding equipment, etc. also play a significant role in the choice of arc welding process selected for a specific application. The range of arc welding processes is shown in Figure 2.2. For this study, Gas Metal Arc, also known as Metal Active Gas (MAG) arc welding was used.

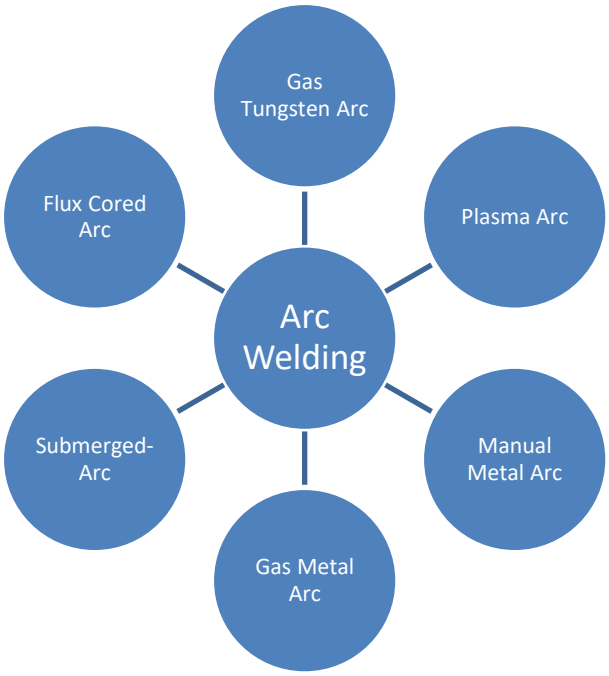

Figure 2.2 Different types of arc welding, chosen based on material and application [24].

2.2.1 Metal Active Gas (MAG) welding

In Metal Active Gas Welding (MAG), fusion is created using an arc as a source of heating between the filler metal (supplied by the electrode) and parent metal, and shielding gas is supplied externally. The heat generated from the arc melts the surface of the parent metal and the tip of the electrode, where the molten metal travels through the arc to the parent metal to become the deposited weld metal. The electrode could either be solid or contain a core containing metal powder or powdered-flux. Shielding from the atmosphere is obtained by either using an externally

supplied inert gas (MIG) or an active gas (MAG). A schematic of MAG welding is given in Figure 2.3. MAG became popular as a welding process due to its versatility, high utilisation of filler material and ease of automation. Compared to another commonly used arc welding process, manual metal arc (MMA), MAG provided larger deposition rates with less smoke and fumes [26].

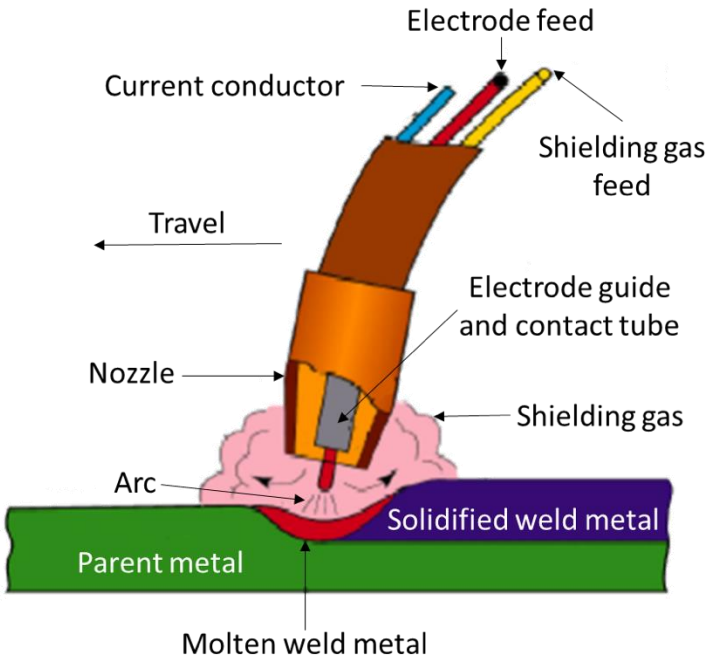

Figure 2.3 Schematic of MAG welding. Adapted from [27].

2.2.2 Weld Microstructure

Due to the nature of the welding process where spatial variation in solidification and cooling of the molten weld metal occurs, the sequence of phase transformations in different regions causes a variation in the microstructure of the metal. This variation in microstructure is generally described by the following zones: parent/base metal, heat-affected-zone (HAZ) and weld metal (WM) with the fusion zone boundary separating the HAZ and WM, Figure 2.4. The precise microstructure of each of these regions is dependent on the heat input and cooling rates during the welding process, as well as the chemical composition of the filler and parent metal. The resulting microstructure can influence the strength and toughness properties of the welded joint and in particular its corrosion resistance [24, 26, 28].

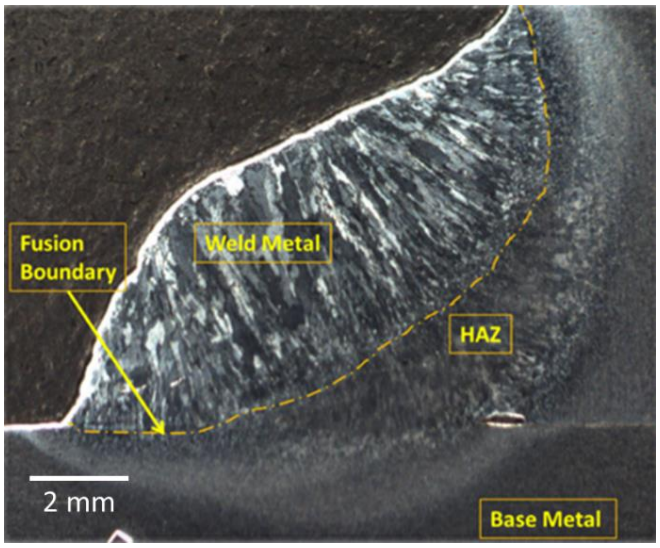

Figure 2.4 Micrograph of an etched cross-section of S355 steel arc fillet-welded joint. Image from current work.

2.2.2.1 Microstructure – Parent metal

A structural Carbon manganese (C-Mn) low-alloy steel was chosen for this project due to its widespread use in the transport and construction industries, where welding is a crucial aspect of structural design [29]. Properties such as toughness, strength, corrosion resistance, ease of thickness reduction, formability and weldability are often desired from structural steels, as an improvement over conventional carbon steel. The carbon content in structural steel is generally 0.05-0.25% to allow formability and weldability. C-Mn steels are commonly used as structural steels with manganese contents up to 2%. Other micro-alloying additions such as aluminium, silicon, chromium are used in certain compositions to achieve specific properties. C-Mn steels are utilised in a variety of applications such as offshore structures, bridges, building beams, oil and gas pipelines, automobile parts and components, etc. [30].

Table 2.1 Alloying Elements commonly added to C-Mn steel and their effects [31]

Alloying Element	Approx. content (in wt.%)	Alloying effects
Manganese (Mn)	0.25 – 1.70	Increases the strength of ferrite by solid solution strengthening, reduces solidification cracking, increases the hardenability of steel as it reduces the critical cooling rate to obtain martensite by stabilising the austenite phase. Combines with sulphur to form manganese sulphides or MnS, which is a soft inclusion thus increasing machinability (and reduces atomic S at grain boundaries, improving toughness).
Silicon (Si)	<0.4	Primarily used as a deoxidiser in steel as it has a greater affinity for oxygen when compared to iron, provides solution strengthening. High amounts of Si not desirable, especially during welding as silicon oxides can make weld metal brittle and may induce cracking.
Aluminium (Al)	<0.1	Acts as a deoxidiser, enables grain refinement by forming aluminium nitrides which prevent austenitic grain growth (similar to the effect of titanium, vanadium and niobium).

2.2.2.2 Microstructure – HAZ and WM and fusion boundary

Since the effect of the microstructure of the welded joints (and the regions formed as a result of the welding process) on fatigue performance of the weld has not been investigated in this study, it will not be discussed in detail in this thesis. Detailed descriptions can be found in Lancaster, 1999 [28]. However, for the purpose of fatigue life predictions carried out in this study (Chapter 6), the variation in mechanical properties across the welded joint was characterised empirically based on the micro-hardness of each of these regions.

2.2.3 Impact of welding on mechanical properties

As described in the previous sections, variations in weld mechanical properties are inevitable, and the challenge for the engineer is to be able to quantify these and determine if quantification is necessary. A common method to characterise the weld microstructure is via hardness measurements and a number of previous studies have developed empirical relations to obtain mechanical properties such as tensile and yield strength [32-34], and cyclic material parameters [34-41] from these. Based on the empirical relations thus proposed, numerous studies have been carried out which have attempted to correlate the hardness measurements with the fatigue

performance of welded joints [34-36, 40-48]. Fatemi and Roessle, 2000 [34] used hardness distributions and strain-controlled fatigue data of different steels to develop empirical relations using the local notch strain approach for fatigue estimation. Similar work was carried out for lifing estimations by Ye and Wang, 2001 [48], Li et al., 2015 [36] and Ladinek et al., 2018 [42, 43]. In an alternative approach, Remes, 2008 [40] and Zubko et al., 2015 [35] presented direct relationships between hardness measurements and fatigue estimations and reported an increase in fatigue performance with increasing microhardness. A more detailed discussion of such work can be found in Chapter 6, Section 6.2.

2.2.4 Weld residual stress

Residual stresses are a consequence of the weld thermal cycle and can approach yield point magnitude in typical arc welded joints. This occurs as the contraction of the cooling weld metal, and the adjacent HAZ is limited due to the restraining effect of colder adjacent parent metal, leading to the weld adjusting to its "new" length by plastic strain. This also causes compressive residual stress in the adjacent metal and a varying through-thickness residual stress field [2, 5, 11, 49, 50]. A schematic of typical transverse residual stresses in a fillet welded joint is shown in Figure 2.5. It is important to highlight that the initial residual stress system-induced due to the welding process may change as a result of shakedown from applied static or cyclic loading [51, 52] and is depicted in the inset of Figure 2.5. The stress system before and after the application of an applied load shows relaxation in the residual stress field. Such a phenomenon was documented by Iila and Takanashi, 1998 [53]. In the experimental work of this project, a possible combination of relaxation and/or redistribution of residual stresses was observed on specimen cutting, which has been observed and studied previously [54-56]. Numerical modelling of the relaxation was also attempted along with experimental validation for both fillet and butt welds [57, 58].

Although welding-induced residual stresses play a significant role in the fatigue strength of a welded joint [2, 11, 12, 49], they are not the focus of this study and, therefore, have not been further investigated.

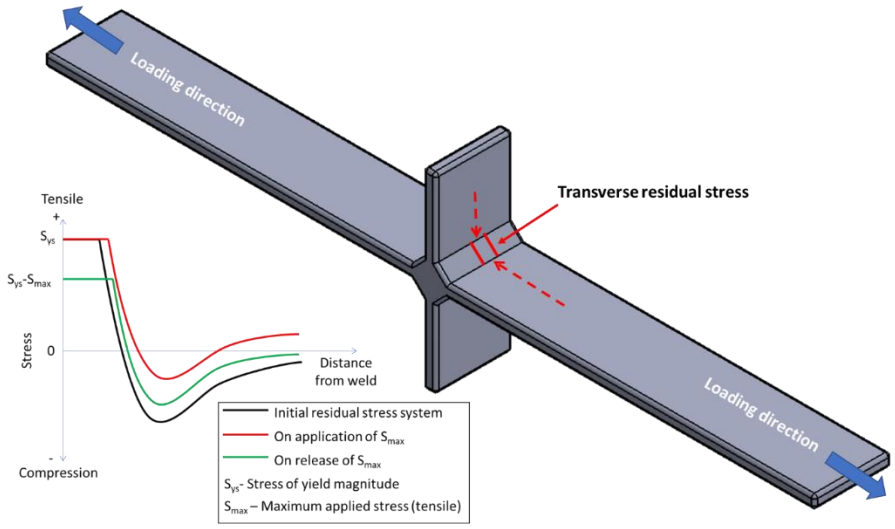

Figure 2.5 Schematic of the transverse residual stress field in a fillet welded joint. Inset of the distribution of the transverse residual stress field initially (as-welded), and after a tensile load has been applied. Residual stress data taken from [11].

2.2.5 Weld toe geometry

Stress-concentrating geometrical features inherent to welding are one of the primary causes of the low fatigue strengths of welded joints compared to unwelded material. The stress concentrating features can be broadly classified as macro- or micro-sized; the former considers the weld bead geometry as described by the plate thickness, leg attachment length and weld toe angle and radius, Figure 2.6, whilst the latter considers weld toe flaws, which typically consist of undercuts and spatter. The role of the inherent flaws in fatigue crack initiation is similar to the behaviour of sharp notches in unwelded material [13], and it has been shown that [59] even in high-quality welds, flaws can have depths of 0.1 mm.

Due to the inherent inhomogeneity of welding processes, varying weld toe geometries can result, and it is currently not possible to economically identify and measure the morphology and distribution of inherent micro-sized flaws [60-62]. Hence, a mathematically simplified or "perfect" weld toe geometry is assumed for weld toe stress and integrity assessments with the initial flaws being considered as initial cracks, with depth, *a*, and length *2c* [5], Figure 2.6c.

Chapter 3, Section 3.2.1 highlights some important work available in the literature which has investigated the various methods of capturing and mathematically representing the weld toe geometry. An example of the challenges involved is shown in Figure 2.7, where an attempt is made to represent the true geometry numerically as ideal weld toe geometries. For the smooth weld toe profile in Figure 2.7a, the idealisation is an acceptable representation of the actual weld geometry. However, in Figure 2.7b, the presence of an overlap flaw is not truly represented in the idealisation.

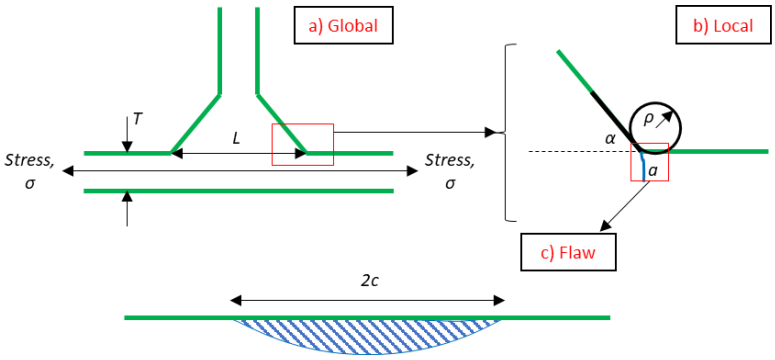

L	Leg attachment length
T	Plate thickness
α	Weld toe angle
ρ	Weld toe radius
a	Crack depth
c	Half flaw width

Figure 2.6 Schematic of the mathematically simplified geometry. a) Global weld toe geometry; b) Local weld toe geometry; c) Flaw at weld-toe. Adapted from [9].

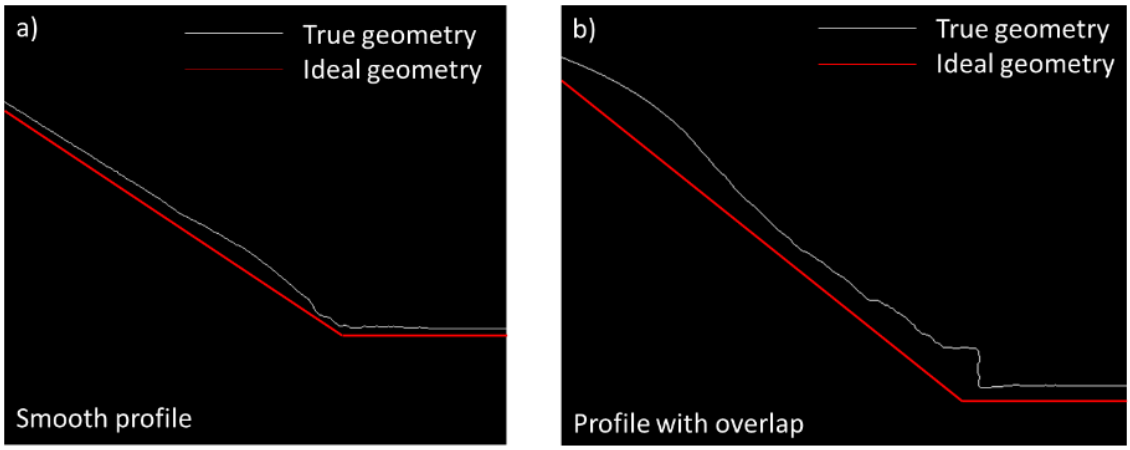

Figure 2.7 Challenges of mathematically representing the weld toe profile – a) A smooth weld toe profile which is relatively easier to numerically represent as an ideal weld toe geometry, as compared with b) a profile with an overlap, where the ideal geometry is unable to represent the flaw.

Figure 2.8 depicts flaws present at the weld toe. Weld toe flaws can range from non-metallic inclusions formed due to the weld thermal cycle, as well as undercuts, cold-laps and overlaps, which are all defects from welding. An undercut occurs due to the reduction of the thickness of parent metal at the weld toe [63]. A cold lap forms when complete fusion between the molten weld metal and the previously cooled parent metal fails to occur [28].

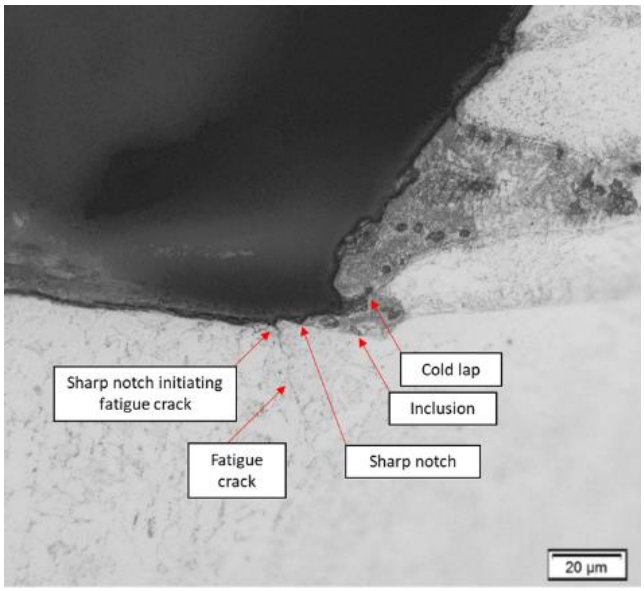

Figure 2.8 Micrograph of a weld toe subjected to fatigue cycling, showing flaws and the initiation of fatigue cracking from one such flaw. Image from current work.

2.2.5.1 Weld geometry characterisation

For fatigue estimation of welded joints, one of the important steps involved in almost all of the available prediction methodologies involves the characterisation of the weld geometry [8]. This is especially important for local fatigue estimation approaches [16]. Characterisation techniques that have been used historically can be broadly categorised into photo-elasticity, metallography, replication, optical profilometry and radiography. The use and success of each of these techniques have continuously evolved as each technique has developed over the years.

Photo-elastic methods were used by Cherry, 1941 [64] to evaluate elastic stress concentration factors (SCFs) due to the geometry of welded stiffeners for non-load carrying welds (Figure 2.9), by Kenyon et al., 1966 [65] for SCFs of load-carrying welded joints, and Hayes and Maddox, 1972 [66] for stress intensity factors (SIFs) estimations for fillet welds. The geometry was, therefore, characterised in terms of the generated SCF and SIF.

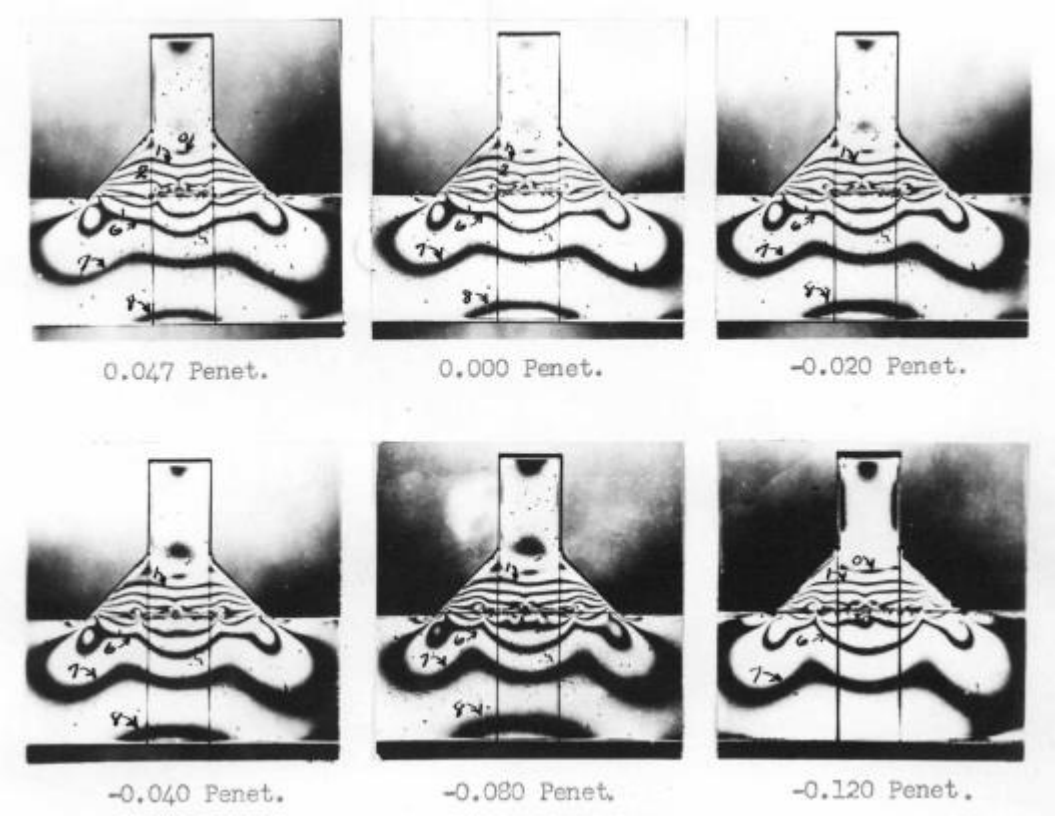

Figure 2.9 Photo-elasticity based SCF determination. From [64].

Ferreira and Branco, 1989 [67] used sectioning to characterise the geometry of fillet welds on the basis of the weld toe radius (WTR). The weld toe angle (WTA) was assumed to be constant at 45°. The study involved investigating the influence of varying WTR on the SIF-based fatigue life prediction methods. Due to the limitations of the technique in terms of the resolution of resolving the geometry, the weld toe radius for cruciform joints ranged from 1-3.5 mm. Weld toe flaws were not accounted for.

A similar sectioning technique was used by Branco et al., 1999 [68] for evaluating the WTR and WTA of tungsten inert gas and plasma butt welds in thin sections for comparison with the geometry of manual metal arc (MMA) welds and correlating this with their respective fatigue performance. Otegui et al., 1991 [69] used sectioning and rubber replicas for determining the weld toe radius and weld angle to study the inhomogeneity of the weld bead and the resultant variation in SCF. A larger average weld toe radii and distribution were observed in the manual welds as compared to the automatic welded joints. The range of WTR was between 0.18-0.65 mm, indicating that sharp features at the weld toe were successfully captured. Lee et al., 2009 [70] used a moulding/replica process for weld geometry characterisation to study the effect on fatigue life of the different weld toe geometries that were tested. WTR values ranged from 0.4-2.2 mm and WTA of 15-85 degrees. The fatigue results obtained agreed well with the general understanding of the influence of WTR and WTA, that increasing WTR and decreasing WTA improve the fatigue performance of non-load

carrying fillet welded joints. Barsoum and Jonsson, 2011 [71] used silicone replicas for replicating the weld profile and a profile projector for measuring WTR and WTA, Figure 2.10, as well as laser scanning. WTR values ranged from 0.3-4 mm, and WTA values ranged from 30-65 degrees for load-carrying fillet welded joints. A comparison was made between the two methods used, and although both the replica and laser scanning gave the similar ranges of data for WTR, the scatter in the data was lower in the recommended laser scanning technique.

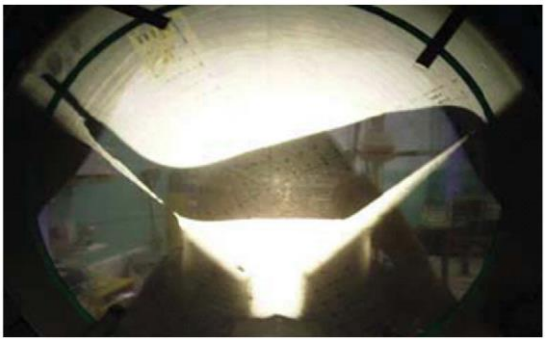

Figure 2.10 Silicone replica of the weld profile in a profile projected for WTR and WTA measurements. From [71]

Apart from replication systems, 3D optical profilometry and laser scanning systems have also been used to characterise the weld toe geometry, primarily for their ability to characterise as-welded joints, without any machining. Some laser scanning systems, however, may require a masking agent to aid the scanning process. Hou, 2007 [72] used 3D laser scanning to create a 3D profile of the welded joints. SCF distributions were generated using FE modelling and the 'true' weld toe geometry, Figure 2.11a. The distribution was compared with the actual fracture surfaces of the fatigue-tested specimens to study the correlation between the crack locations and the regions of maximum SCF determined from the FE modelling. White paint was used as a masking agent, which could potentially mask microscopic flaws or irregularities in the geometry. Alam et al., 2010 [73] combined plastic replica methods for determining the WTR and WTA distributions at a macro-scale with the capture of the topography or micro-geometry of the weld toe using a 3D optical profiler, Figure 2.11b. The data obtained from the two techniques were used to evaluate the SCF distribution of 2D profiles of laser hybrid welded eccentric fillet joints. Lang et al., 2016 [74] and Lener et al., 2018 [75] used a FARO® mobile laser scanning system for characterising the weld toe geometry in 3D for stress analysis, and consequently using the stress data for fatigue estimations using local approaches.

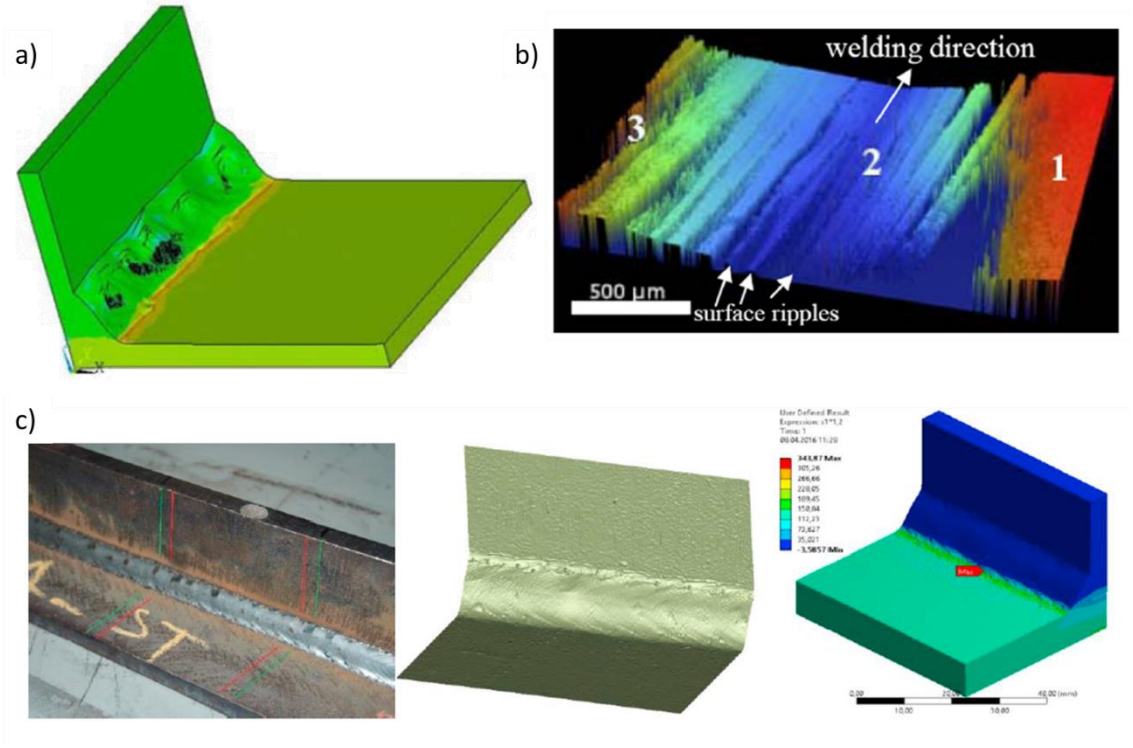

Figure 2.11 a) 3D stress profile of the weld geometry using laser scanning, from [72]; b) weld toe topography scan using a 3D optical profiler, from [73]; c) 3D profile of a fillet welded joint using the FARO laser scanning system, from [75].

X-ray micro-computed tomography (µ-CT) was employed in work performed by Crump, 2017 [9], which formed the basis of choosing µ-CT for this study. A detailed description of this technique is given in Chapter 3, Section 3.2.2.

2.2.6 Weld misalignment

Misalignment caused by the welding process in the case of transverse fillet welded joints is another source of stress concentration and potential cause of poor fatigue strength of welded joints [76-80]. Jakubczak and Glinka, 1986 [78] studied the axial misalignment in the form of an additional bending stress and found that the fatigue crack initiation lives of the welded joints were significantly reduced in the case of large misalignments. Andrews, 1996 [77] did a similar study on axial misalignments and found that the reduction in fatigue strength due to misalignment (and resulting secondary bending stress) was only apparent in welded joints under axial tension loading; no effect was observed in the case of bending loading. Ottersböck et al., 2019 [76] looked at the effect of axial misalignment in the fatigue performance of ultra-high-strength steel butt joints and as expected found a detrimental impact. Fatigue estimations incorporating the misalignments were carried out using global and local approaches, and the possible impact of post-weld treatment such as high-frequency impact treatment (HFMI) on axially misaligned specimens was observed.

IIW Guidelines [8], BS7608 [6] and BS7910 [5] provide solutions for evaluating the misalignment in the form of angular and axial misalignments for their application in the fatigue design of different kinds of welded joints. For the purpose of this study, misalignment was characterised by a secondary bending stress, as detailed in BS7910 [5].

2.3 Fatigue of welded joints

The fatigue performance of welded joints is primarily dependent on weld toe geometry, residual stresses, microstructure, loading conditions, and environment. Design standards are available which provide fatigue assessment methods, and solutions for incorporating most of the above-mentioned factors [6-8]. The methods can be grouped into continuum and damage tolerant methods. The continuum method is typically used at the design stage to estimate the total life (N_t), whereas the damage tolerant methods are typically used in the presence of flaws for estimating the remaining crack propagation life (N_p), Equation 2-7. Both methods are discussed in Sections 2.3.1 and 2.3.2.

$$N_t = N_i + N_p \tag{2-7}$$

2.3.1 Continuum approach

The total-life approach for welds is used to estimate the total fatigue life, N_t, from S-N curves obtained for a specific weld-detail. S-N curves for various weld-details are given in Classes and are obtained using linear regression analyses of available experimental data obtained using constant-amplitude loading. The variation in weld-details differs in terms of welding processes, material properties, joint configuration and size, the orientation of weld to applied stress, residual stress field and post-weld treatment [6-8]. Figure 2.12 presents the S-N curve for a non-load carrying joint with loading transverse to the weld. The X-axis (number of cycles) has been drawn up to the endurance limit for welded joints, i.e. 10^7 cycles. The lower standard deviation bound of the S-N curve is used typically for fatigue design assessment because it accounts for the scatter in experimental data. Two standard deviations are used when the data set is large. Otherwise, the number of SDs that give a confidence level of 95% must be computed. For each class of welded joint, BS7608 provides a method to calculate the mean curve and respective design curve. It is based on Equation 2-8. The standard provides the values of the slope (m), intercept (C) and standard deviation (SD) used in the Equation 2-8. d is the number of standard deviations that the user of the curves may wish to use.

$$log_{10}N = log_{10}C - mlog_{10}\Delta\sigma - dSD \tag{2-8}$$

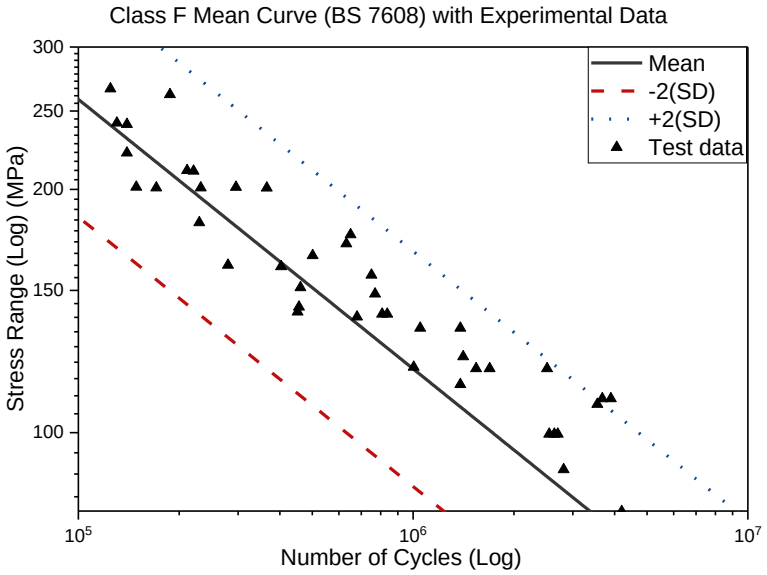

Figure 2.12 SN Plot for Class F (BS7608) [6] non-load carrying fillet weld joint for load ratio 0.1. Additional relevant experimental data are taken from [81].

Different approaches are available to evaluate the stress range to be used in the fatigue estimation of welded joints, specifically non-load carrying transverse welded joints. Figure 2.13 is a schematic of the different stress ranges that are applicable to such a welded joint. It is important to note the variation in the maximum value of each of the stress ranges and the degree to which each of them considers the specimen geometry.

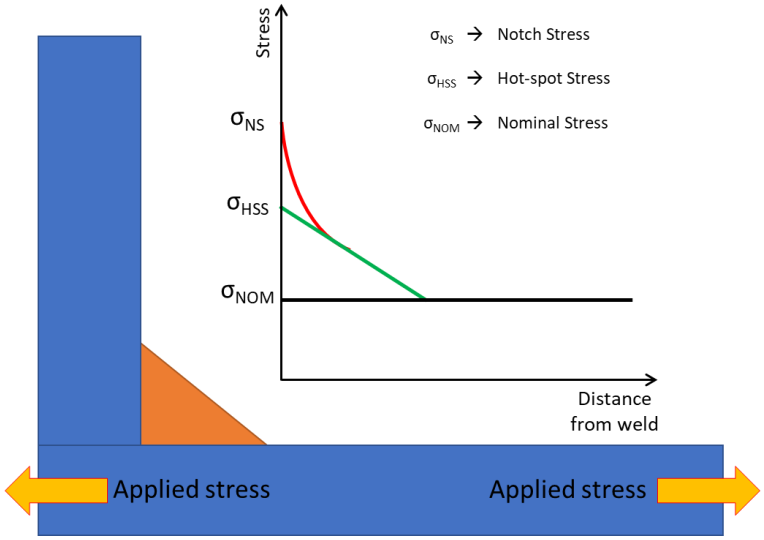

Figure 2.13 Schematic of weld toe stress approaches - nominal, hot-spot and notch stress. Adapted from [9].

A. Nominal stress approach - In the nominal stress approach, the stress range is estimated using conventional engineering analysis methods, without considering the effect of the weld on the stress field or the effect of stress concentration due to the local geometry. It can be easily

calculated for simple axially loaded specimens or simple specimens in bending. Although it remains a popular approach (as the simplest of the three approaches), for welded structures, hot-spot stresses are generally preferred, as this accounts for the changes in geometry [2, 6, 8, 16].

B. Hot-spot stress (HSS) approach - The HSS approach, also called the structural stress approach [8], can be used in the fatigue design of welded joints when potential fatigue initiation is considered likely at the weld toe. HSS includes the macroscopic stress concentration due to the macroscopic weld profile but not the local peak stresses caused by notches at the weld toe. The hot-spot stress at the weld toe can be estimated by the extrapolation from the surface stresses at locations near the weld, and this technique is called surface stress extrapolation [8, 82, 83]. This method is based on the assumption that the extrapolation to the weld toe from measured surface stresses at two distinct reference points away from the weld toe matches the HSS. The stress analysis can either be by experimental strain measurement or validated finite element analysis; a comparison of different methods for the latter has been presented in a study by Poutiainen et al., 2004 [84]. The choice of the location of the reference points can be defined by the kind of meshing that was performed during the finite element stress analysis [8]. Compared to the nominal stress approach where the effect of different structural geometries are covered using different fatigue classes, the HSS approach already incorporates these effects, and therefore a single design S-N curve can potentially be used for each weld type [2]. Stress concentration due to linear or angular misalignment is accounted for in HSS as surface strain measurements (using strain gauges) will pick up additional stress fields affected by misalignments [2]. It is important to note that the HSS does not actually exist; it is a theoretical value. It has been successful in making relatively less conservative fatigue life predictions and reducing the spread in predicted fatigue data as compared with the nominal stress approach.

C. Notch stress approach - In the notch stress approach, stress concentration due to the local weld toe geometry is considered. The fundamental idea behind this approach is the modelling of the weld toe with a reference radius, to estimate the local principal stress or von Mises stress [85, 86]. Recommendations for the application of the notch stress approach have been published by the International Institute of Welding (IIW) [17]. The approach is discussed in greater detail in Chapter 6, Section 6.2.2.

The continuum approach is widely popular because of the relative simplicity involved in implementing available standardised procedures for industrial applications. S-N curves based on these stress analyses will account for residual stress fields, misalignment, fatigue crack initiation and crack propagation. However, drawbacks exist for the continuum approach, which need consideration during implementation. It is limited to welds assigned to a specific classification and

the assumptions involved within each class. Joints that cannot be classified are assigned the classification with the lowest quality, therefore making very conservative life estimations in such cases. The standardised global approaches – Nominal and HSS approach – that employ the continuum approach do not provide any information about the fatigue crack initiation (FCI) life. This has led to local approaches being developed in the literature [16] and also their investigation in this PhD study. More detailed information on the continuum approaches can be found in these resources [2, 6, 8].

2.3.2 Damage tolerant approach

In the presence of a flaw, the damage tolerant approach is applied for fatigue analysis, especially in cases where accurate measurements of the flaw are possible using non-destructive testing (NDT) techniques. LEFM is used with the assumption of stable crack propagation from a flaw for calculating the number of cycles (N_p) required to propagate the crack to a critical size. The application of LEFM is based on the description given in Section 2.1.2. Stable crack propagation is characterised by the stress intensity factor, K. BS7910 [5] and IIW recommendations [8] provide solutions for calculating the value of K for specific external loading conditions, welded joints, residual stress, component geometry, detected flaw characteristics, material parameters and operating environment [5, 8, 87]. As described previously in Section 2.1.2, microstructurally independent crack growth in Stage 2 or the Paris Regime leads to the power-law relationship given in Equation 2-9, also known as the Paris Law. Integration of the Paris Law from initial crack length a_i to final crack length a_f provides the number of cycles needed for crack propagation (N_p) from a_i to a_f, Equation 2-10.

$$\frac{da}{dN} = C(\Delta K)^m \qquad 2\text{-}9$$

$$N_p = \frac{1}{C}\int_{a_i}^{a_f} \frac{1}{(\Delta K)^m}\, da \qquad 2\text{-}10$$

In this study, the application of the damage tolerant approach has been limited to basic assumptions of material properties (C and m in Equation 2-10) and accounting for secondary bending stresses due to axial misalignment. This approach can be found in Chapter 6. Further detail on the damage tolerant approach and SIF solutions for welded joints can be found here [5, 8, 87].

2.3.3 Fatigue crack initiation

In Sections 2.3.1 and 2.3.2, standardised methods for estimating total life (N_t) and the crack propagation life (N_p) have been discussed. Methods for the estimation of fatigue crack initiation

life, N_i, in welded joints are still not standardised due to a large number of variables that result in large scatter in the results found for the same nominal specimen geometry [43]. Radaj et al., 2006 [16] provide a comprehensive review of the local approaches used for FCI estimation.

For high stress range testing in welds, the contribution from the FCI life can be assumed to be negligible. However, at lower stress ranges, FCI life has been seen experimentally to take up a significant proportion of the total life of a welded joint. It is important to note that the indication of FCI life in the different studies that present experimental data is based on their individual definition of crack initiation. The definition of crack initiation is dependent on the sensitivity of the NDT or crack growth monitoring technique. In engineering terms, it is primarily defined as the growth of a technical crack to a certain depth. Post-weld treatments like stress-relief and peening have been seen to have a significant effect on delaying the FCI. A range of experimental FCI lives as a function of their total lives for as-welded and post-weld treated welds are shown in Figure 2.14. The results from Otegui et al., 1989 [88], Lassen, 1990 [89], Bell et al., 1993 [90], Chappetti et al., 1997 [91, 92] are based on an FCI life for a particular technical crack length, a_i, based on the crack growth monitoring technique implemented. The FCI results from the work of Crump, 2017 [9] are based on the first indication of the crack growth monitoring technique used. The size of the crack at the time of the first indication of fatigue crack initiation will be different for each technique. For the as-welded joints, the FCI lives obtained ranged from 6%-50% of total fatigue life, with an average of 26%. For the specimens with post-weld treatments, the FCI lives ranged from 24%-80% of total fatigue life, with an average of 45%. The comparison of the above two ranges highlights the impact of post-weld treatments on delaying the FCI lives of welded joints, and has been investigated in great detail (with recommendations) in the literature [2, 8, 11, 93, 94].

It is important to highlight that these studies have used a wide range of equipment, and therefore the data will be highly dependent on the implementation of the techniques and their respective obtainable resolutions. However, the varying portion of the fatigue life spent in initiating a technical crack, therefore highlights the importance of investigating the available approaches for its estimation.

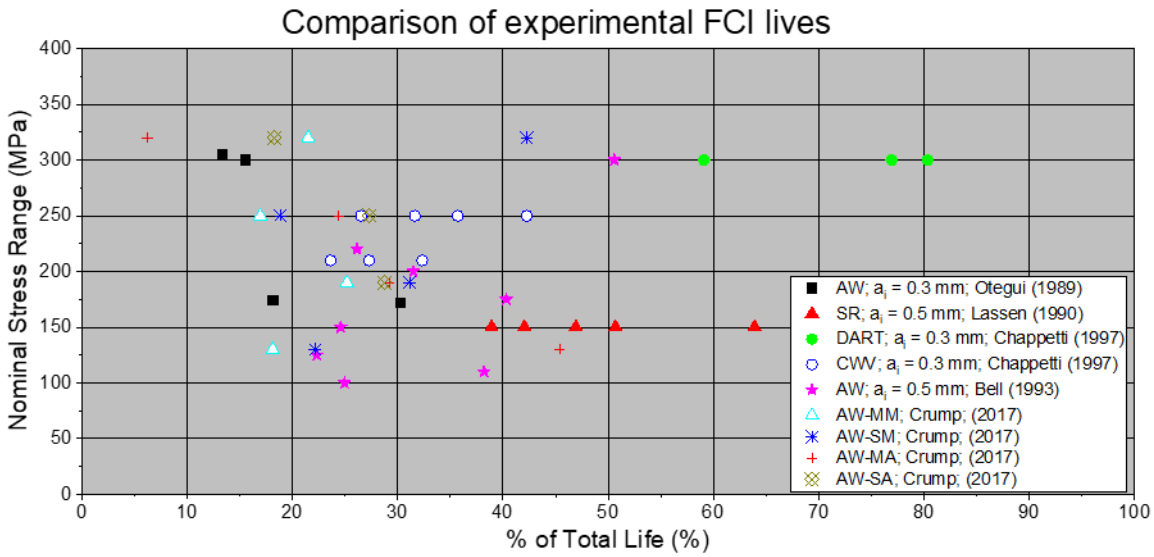

AW: As-welded	SR: Stress-relieved	DART: Double arc rotating technique	CWV – Controlled weld waviness
AW-MM: As-(manually)welded metal-core electrode	AW-MM: As-(manually)welded solid-core electrode	AW-MA: As-(semi-automatic)welded metal-core electrode	AW-SA: As-(semi-automatic)welded solid-core electrode

Figure 2.14 Comparison of experimental FCI lives obtained in the literature. Data taken from [9, 88-92]

2.3.4 Capturing fatigue crack initiation

There are a variety of relatively easy and low-cost non-destructive techniques that are prescribed in the standards for the purpose of crack detection [95, 96], such as dye-penetrant and magnetic particle inspection. These visual NDT techniques provide information on surface-breaking crack lengths, not crack depth. For the application of a damage tolerant fatigue estimation approach, obtaining flaw or crack depth is essential, and this can also be approximated from surface crack length by assuming a crack aspect ratio within a safety design limit [87]. Although dye-penetrant and magnetic particle inspection are relatively low-cost and less labour-intensive, their resolution is limited. Strain gauges and electric potential drop (EPD) techniques are relatively more costly both in terms of equipment cost and labour, but they are capable of providing crack depth information at better resolutions than the visual NDT techniques and have been used extensively [9, 96]. EPD techniques are available in two versions - alternating current AC and direct current DC, both with their specific advantages and disadvantages [96, 97]. Strain gauges have also found application in the investigation of fatigue crack growth in welded joints. The primary concern during the implementation of both techniques is their dependency on the location of the strain gauge or ACPD probe with respect to an initiating crack. In the case of un-notched specimens, it is not always certain where initiation would occur, especially in the case of as-welded joints. Therefore, multiple

measuring units are recommended in both techniques to not miss a crack initiation event [63, 88, 98]. Chapter 4, Section 4.2, provides a comprehensive review of the use of ACPD in previous research. Chapter 5, Section 5.2, provides a review of the use of strain gauges for welded joints.

2.4 Literature review – Summary

The purpose of this chapter was to introduce briefly the fundamentals that form the backbone of this study and contextualise why specific techniques and methodologies were implemented. The experimental work that has been performed for this PhD study has been discussed in the specific following chapters, and each of these chapters has a tailored introductory literature review section.

The role of the weld toe geometry in the fatigue performance of a welded joint has been investigated extensively in the literature. The techniques that have been used to capture and characterise the true weld geometry have consistently increased in resolution over the past 50 years. Apart from geometrical parameters such as weld toe radius and weld toe angle, weld toe geometries have also been empirically characterised in terms of the degree of stress concentration they offer. This defines the context for this study, which attempts to capture the weld geometry using high-resolution X-ray micro-computed tomography and to characterise the weld toe in terms of both geometrical parameters and stress distribution, the latter using 3D FE analysis. Such a study has only been performed once in the work of Crump, 2017 [9], where the stress distribution study was based on 2D FE analysis.

Global approaches that are standardised for the purpose of predicting total fatigue life and crack propagation life do not give predictions for FCI lives, which can be a sizable portion of the total fatigue life. Approaches for FCI estimations have been investigated in the literature with limited success. The methods of obtaining the large number of essential variables for the FCI-based approaches vary significantly in the literature. An attempt has therefore been made in this PhD study to compare the different approaches that have been used in the literature with the results obtained in this study to investigate their shortcomings and potentially identify the optimum methodology for such predictions.

In order to validate the estimations, experimental FCI data is critical. Previous experimental methodologies for estimating fatigue crack initiation have been briefly discussed. ACPD and strain gauges were chosen to be used in this PhD study to allow assessment of their specific advantages (and consideration of their respective limitations). Recent use of the ACPD approach (with the improvement in ACPD electronics design) has been limited to single probes for welded joints; a novel multiple probe approach has been used in this study. Miniature strain gauges have been used

previously in an array-based arrangement on welded joints before but limited to the centre of the weld. In this PhD study multiple strain gauges have been used to monitor the entire weld toe.

Chapter 3 High-resolution Weld Toe Stress Analysis using Micro-Computed Tomography (μ-CT) and 3D Finite Element Analysis (FEA)

3.1 Motivation

Alongside tensile residual stresses of yield point magnitude, welding-induced geometrical features and their associated stress concentrations are a key cause of the relatively low fatigue performance of a welded joint compared to an unwelded uniform specimen of the same material. These stress concentrations can be broadly classified based on their relative size as macro-sized stress concentration regions, i.e. the weld bead geometry and micro-sized stress concentration regions, i.e. weld toe flaws. The role of these stress concentrations in fatigue crack initiation is similar to the behaviour of sharp notches in parent material [13]. A study by Grover [59] showed that even high-quality welds contain micro-sized flaws which can reach depths of 0.1 mm.

The geometry and the flaws can be characterised using Serial Sectioning, but this technique is very slow, and most importantly, destructive. In industry, non-destructive testing (NDT) techniques are available for detecting flaws, each with their respective limitations, which can be categorised into the following [5] –

a) Techniques for sub-surface flaws –
    i. Ultrasonic testing,
    ii. radiography,
    iii. electric potential drop methods,
    iv. eddy current.
b) Techniques for surface-breaking flaws –
    i. visual inspection,
    ii. magnetic particle inspection (ferromagnetic material only),
    iii. dye penetrant,
    iv. and the methods already listed for sub-surface flaws.

Due to the inherent inhomogeneity of the welding process resulting in varying weld geometries, it is not always possible to measure every flaw using the above techniques [60-62]. These limitations prompted Crump [9] to explore the use of industrial X-ray micro-computed tomography (μ-CT) to characterise the weld toe geometry and defects. μ-CT non-destructively provides high-resolution

through-thickness imaging of the weld, and therefore allows us to accomplish the following aim of this PhD project –

> **"Resolve and define weld toe geometry for high-resolution three-dimensional stress analysis of the inherent weld toe flaws during cyclic fatigue loading."**

This chapter discusses the use of μ-CT and Finite Element Analysis (FEA) to deliver the above objective and is the first focus of the experimental work performed in this thesis. Some parts of the work described in this Chapter have been published in a peer-reviewed journal:

S. Chaudhuri, J. Crump, P. A. S. Reed, and B. G. Mellor, "High-resolution 3D weld toe stress analysis and ACPD method for weld toe fatigue crack initiation," Welding in the World, 2019/08/08 2019, doi: 10.1007/s40194-019-00792-3.

3.2 Introduction

3.2.1 Weld Profile Characterisation for Stress Analysis - Review

Accurately characterising the weld toe geometry using increasingly local approaches for fatigue lifing has been well documented in the literature [15, 16, 99]. Due to the resolution capabilities of the readily available characterisation methods, a mathematically simplified or "perfect" weld toe geometry is often assumed at both the global and local scale for weld toe stress and integrity assessments. This geometry (Figure 3.1) is described by plate thickness T, leg attachment length L, weld toe angle α and weld toe radius ρ. The inherent flaws are considered as sharp notches and are described by c and a, which are the half flaw length and flaw depth.

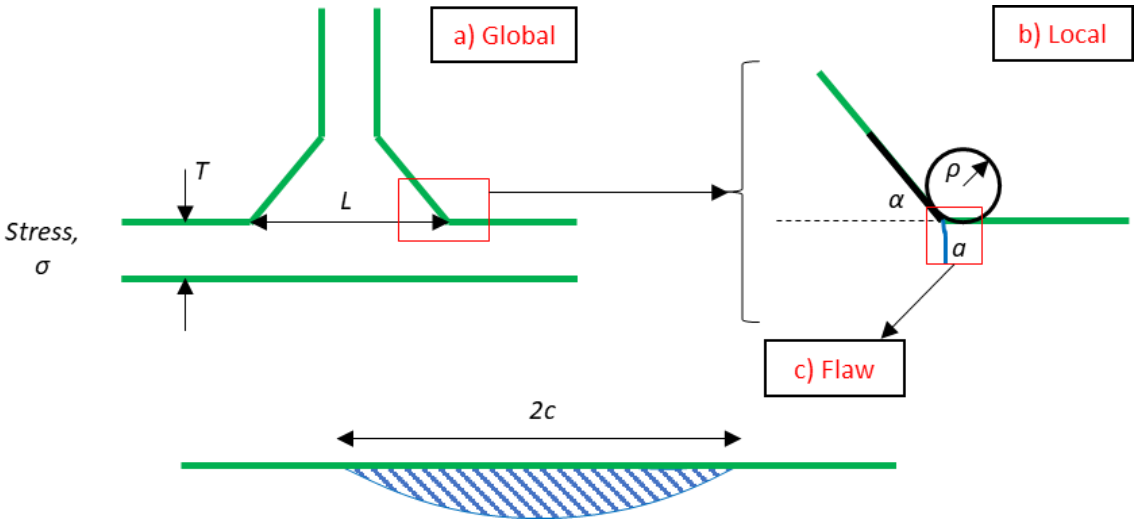

Figure 3.1 Schematic of the mathematically simplified geometry showing the features that make up the: a) Global weld toe geometry; b) Local weld toe geometry; c) Weld toe flaw geometry.

In estimating stress concentration factors (SCFs) for a particular simplified weld profile, various parametric solutions can be found in the literature, with certain validity limits in terms of weld toe geometry [100, 101]. The influence of the actual weld toe geometry stress concentrations on stress concentration factor (SCF) parameters calculated using idealised weld profiles has been documented by Niu and Glinka [100, 101], Martins Ferreira and Moura Branco [67], Brennan et al. [102], Hobbacher [103], Hellier et al. [104], amongst others. The literature on fatigue assessment of welds using linear elastic fracture mechanics (LEFM) has used simplified weld toe geometries to obtain the distribution of SCFs given in Table 3.1.

Table 3.1 SCF distribution obtained from simplified weld profiles.

Reference	**SCF Distribution**	**Type of specimen**	**Reason for SCF distribution**
Otegui et al., 1991 [105]	2.5 – 3.3	2D finite element model of a T-joint	Different weld toe radii
Pedersen et al., 2010 [106]	2.35	3D finite element analysis of a transverse loaded welded joint	Only one geometry has been evaluated
Fricke, 2012 [17]	2.4-2.6	2D finite element model of a non-load carrying weld toe	Element type and method of evaluation
Kim et al., 2015 [107]	1.7-2.3	3D finite element analysis (hot-spot stress) of transverse loaded welded joints	Variation in the geometries of the tested welded joints
Savaidis et al., 2016 [108]	2.31	A fictitious radius of 1 mm was used to model the weld toe	Only the SCF in tension loading has been mentioned
Shiozaki et al., 2018 [109]	1.4 – 2.49	2D finite element analysis of a lap fillet welded joint, with geometric parameters taken from actual weld toe measurements	Varying weld toe radius (based on the post-weld treatment of toe machining).

To incorporate the true weld toe geometry into fatigue assessments, various methods have been used in the literature to capture the local geometrical parameters of real welded joints, Table 3.2.

Nykänen et al. obtained the local geometrical parameters based on published experimental data and used Linear Elastic Fracture Mechanics (LEFM) to report their influence on the fatigue behaviour of transverse non-load carrying fillet welded joints [110]. Table 3.3 lists the studies that have used local geometrical parameters to evaluate the resultant linear elastic SCFs using FEA.

Table 3.2 Methods used in the open literature to capture the true weld profile.

Reference	**Methods used**
Otegui et al., 1991 [105]	Sectioning and rubber replica
Branco et al., 1999 [68]	Weld sectioning and microscopy
Hou, 2007 [72]	3D laser scanning
Lee et al., 2009 [70]	Rubber replica
Alam et al., 2010 [73]	Rubber replica and 3D optical profiling
Barsoum et al., 2011 [71]	Rubber replica and 3D optical profiling
Harati et al., 2015 [111]	Weld Impression Analysis (WIA) [111, 112] (A combination of replica and laser scanning)
J. Raujol-Veillé et al., 2015 [113]	3D laser scanning
Lang et al., 2016 [74, 114]	3D laser scanning
Crump, 2017 [9]	X-ray micro-computed tomography (µ-CT)
Lener et al., 2018 [75]	3D laser scanning
Shiozaki et al., 2018 [109]	Non-contact 3D measurement system (Keyence VR-3100) – Laser scan system

Table 3.3 SCF distributions obtained for true weld profiles.

Reference	**SCF Distribution**	**Resolution**	**Type of Specimen**
Branco et al., 1999 [68]	1.098 – 1.624 (distribution of maximum SCF from different specimens)	37.5 – 60 µm	3D FE model of butt welded and transverse non-load carrying fillet welded joints
Hou, 2007 [72]	1.9 – 4.0, only 2% of all SCFs above 3.0. Values are maximum values at each location along the weld toe	25 µm	3D FE model of non-load carrying cruciform joint

Alam et al., 2010 [73]	Mean SCF – 3.09. SCF>4 ignored	0.92 µm	2D FE model of laser hybrid welded eccentric fillet joints
J. Raujol-Veillé et al., 2015 [113]	Normalised SCF relative to mean SCF provided	10^{-3} relative to flange thickness	3D FE model of welded T-joints
Crump, 2017 [9]	2.45 – 8.70 (distribution of maximum SCFs obtained for each section)	10 µm	2D FE model of transverse non-load carrying fillet welded joints
Lener et al., 2018 [75]	4.0 (Maximum SCF)	50 µm	3D FE model of T-joint (transverse non-load carrying fillet welded joints)

In Table 3.2 and Table 3.3, the maximum values of SCF obtained from actual weld toe geometries are noted to be relatively higher than the values obtained from idealised weld profiles, highlighting the possible non-conservatism in using the latter for fatigue assessment.

3.2.2 Introduction to µ-CT

To characterise the true weld toe geometry, the following methods were considered, and their advantages and disadvantages were compared to choose the optimum method –

a) **Serial Sectioning** – Serial sectioning involves the repeated removal of a known amount of material via grinding and polishing and taking optical-micrographs of each prepared section. An example of a section of a welded specimen containing a fatigue crack is shown in Figure 3.2. Although the method produces high-resolution images also detailing cracks and microstructure, it has the following disadvantages –
    a. labour intensive and thus costly and time-consuming,
    b. Destructive technique requiring relatively small specimens
    c. can miss small flaws located in the intervals between sections.

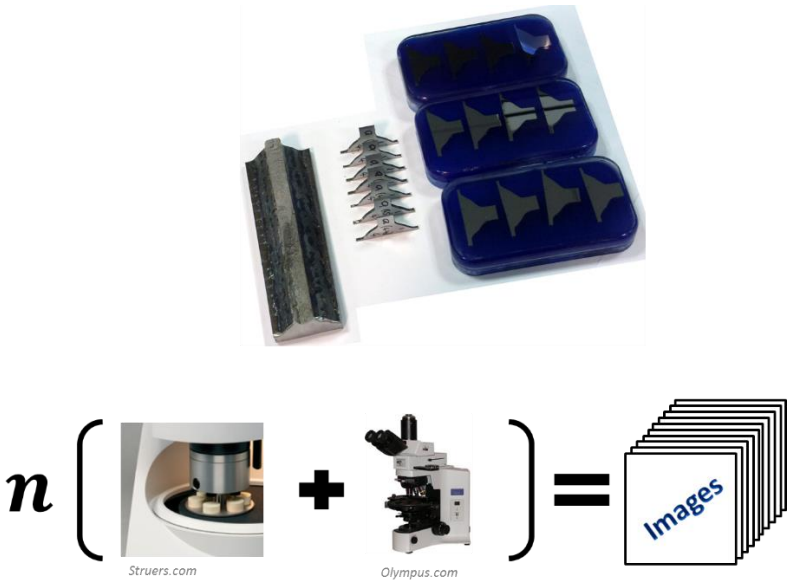

Figure 3.2 Schematic of the serial sectioning technique.

b) **Laser Scanning** – Laser scanning involves scanning the surface of a specimen with a laser to characterise its surface topography. Most systems characterise the distance at specific locations on a specimen using time of flight principles. More sophisticated systems incorporate bespoke software that allows for specific geometrical parameters to be defined post-scanning, such as weld toe angle and radius. An example of a 3D scan obtained using laser scanning is shown in Figure 3.3. This method has the advantages of being non-destructive and can be used on large components in service within a timely manner. However, it has the following disadvantages –

   a. the resolution of the scan is related to the quality of the laser being used. For a high-resolution scan (on the same scale as that of optical and tactile techniques), the required laser could be very expensive.
   b. No through-thickness information is obtained, as only the surface of the weld is scanned. Also, subsurface flaws and flaws exhibiting high re-entrant angles will be missed.
   c. In the laser scanning systems that have been used in the works listed in Table 3.2, the surface had to be painted to optimise the scanning process. The process of painting could mask sharp weld toe flaws.

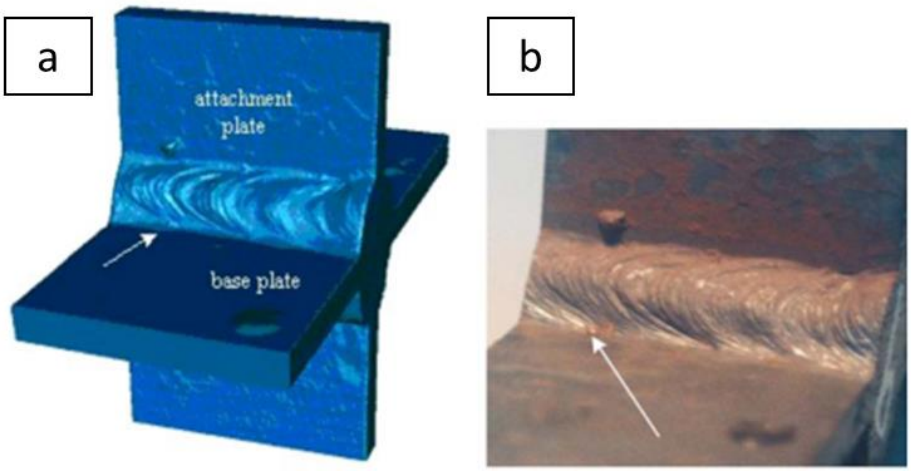

Figure 3.3 Image of the laser-scanning done by Hou [72] – a) 3D capture of the weld using laser scanning; b) image of the actual weld. Taken from [72].

c) **Tactile Techniques** – Tactile techniques are economical and non-destructive, but again are purely surface-based methods with no through thickness information obtainable. Also, the resolution of the profiles obtained are a function of the probe size.

d) **Optical infinite focus microscopy** – This is performed generally using an optical microscope with infinite focus, thus being able to create a 3D representation of the weld surface. Although this technique cannot be performed on specimens in service or in test machines, the specimens tested for this work could be scanned without requiring any cutting. Again, it is a purely surface-based method with no through thickness information. Figure 3.4 is an example of the fracture surface and weld bead of a joint captured using infinite focus microscopy.

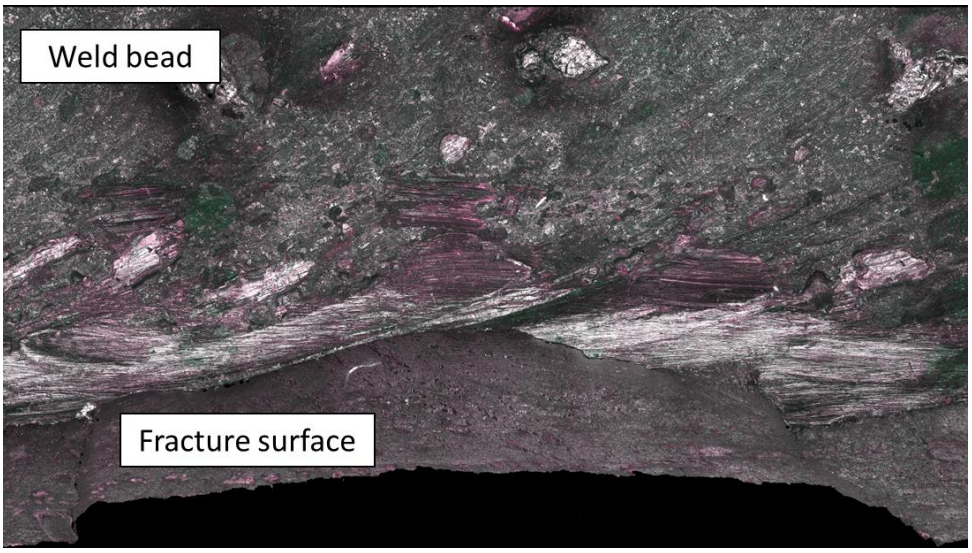

Figure 3.4 3D capture of a fractured welded joint showing both the weld bead and fracture surface at the weld toe.

The disadvantages with the available methods mentioned above were considered with the need to resolve the weld toe geometry at high-resolutions capable of capturing both surface and embedded flaws. Consequently, X-ray µ-CT was chosen for this project. X-ray µ-CT is a non-destructive radiographic method for three-dimensional (3D) imaging, allowing visual observation of the internal and external features of a scanned metallic or non-metallic object.

During a CT scan, there is a relative rotation between the X-ray source and detector and the specimen, i.e. either the specimen is rotated, and the X-ray source and detector remain stationary, or vice versa. A series of 2D images are taken at specific rotations, which are then mathematically reconstructed to create a 3D image where each voxel (3D pixel) represents the X-ray absorption at that point. As the X-ray absorption depends on material density, it is possible to create a 3D volume where internal features, with different densities, can be differentiated.

A schematic of the process is given in Figure 3.5. X-Ray photons are generated in the X-Ray source by accelerating electrons towards a target material producing X-rays via Bremsstrahlung radiation or k-Shell emission [115]. In Bremsstrahlung emission, X-Ray photons result from a loss of energy of accelerated electrons as they are deflected around the target atom's nucleus. In k-Shell emission, X-Ray photons result from accelerated electrons knocking k-shell electrons out of their energy state, resulting in outer shell electrons moving into the gaps to minimise the energy of the atom. A notable difference in these two types of emissions is that Bremsstrahlung can release X-Rays with varying intensities, whereas the X-Rays of k-Shell emission are entirely dependent on the characteristic of the k-Shell energy level of a target material. A scintillator then converts the X-Rays into visible light, and a photodetector converts this to a digital image, known as a radiograph.

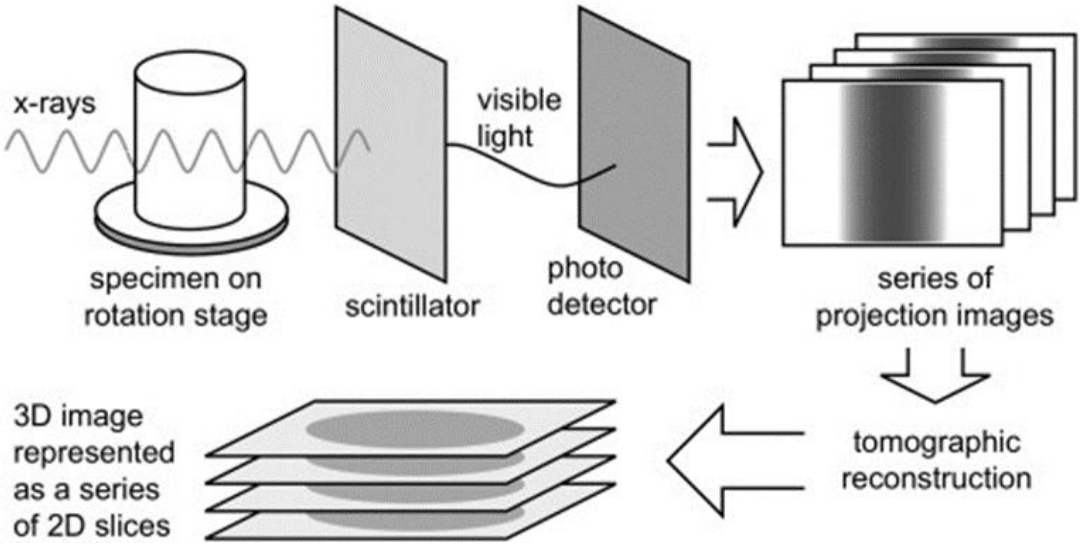

Figure 3.5 Schematic of µ-CT. Taken from [116]

To obtain good quality µ-CT scans, a small X-Ray focal spot size, a short source to specimen length and a high number of detecting elements are required. The source to specimen length and number of detector elements are dependent on the actual scanning system. The focal spot size however, can be optimised and is a function of the scanning parameters, i.e. the current and beam energy.

The optimum scan parameters are dependent on the specimen size and material density and should be optimised before a full 3D scan is commenced. For example, increasing the current increases the X-Ray flux resulting in a stronger signal arriving at the detector. However, this can increase the signal to noise ratio as well as the focal spot size and therefore reduce spatial resolution. Furthermore, increasing the voltage increases the mean energy and therefore, the penetrability of the X-rays. Beyond an optimum voltage, the contrast of the scan is compromised, making it challenging to distinguish between different material types.

In addition to scan parameters, scan artefacts can also influence the scan quality. Possible artefacts can result due to beam-hardening, the partial volume effect, ring artefacts, photon starvation, motion blur and cone beam effects. Further information on these artefacts can be found in [117]. For high-resolution scans of steel weld toes, the most important artefacts to consider are probably the partial volume effect and beam-hardening.

The partial volume effect is a result of a voxel containing multiple materials. As each material has a different density, the resulting voxel will be an average of the different intensities of X-rays [118], as illustrated in Figure 3.6. If the size of the region of interest is similar to the scan resolution (voxel size), the edge can appear blurred.

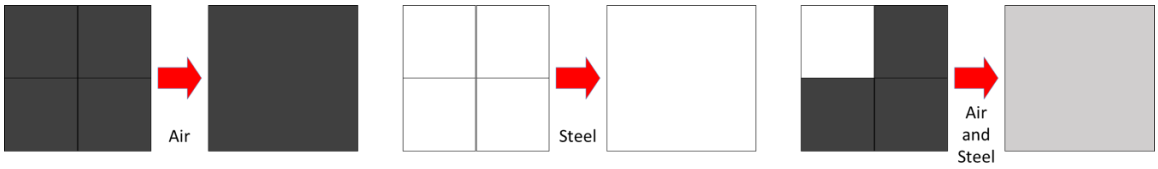

Figure 3.6 Schematic of the partial volume effect.

Beam-hardening occurs when lower energy X-rays from a polychromatic X-ray suffer more attenuation in the thicker regions of an object, generally at the centre where the through-thickness is greater than at the edges. This results in a darker artefact in the centre of the scan as compared to the edges. To mitigate this issue, copper or tin plates are commonly used to remove the lower energy X-rays (schematic in Figure 3.7). For the scan performed in this study, tin plates were used due to their relatively higher absorption compared with copper.

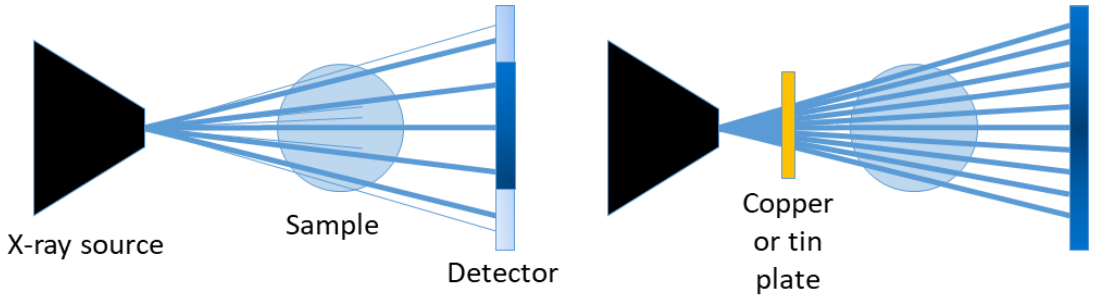

Figure 3.7 Schematic of beam hardening.

With the development and availability of better µ-CT facilities, it has become more widely used in characterisation of both metallic and non-metallic materials [119]. The challenge with steel is its relatively high density (typically 7850 kg/m^3), compared to other materials more commonly characterised using µ-CT e.g. composites or aluminium alloys. The high density of the steel results in increased X-ray attenuation and noise in the detected signal. This challenge has been somewhat overcome in the various studies that have involved µ-CT scanning of steel by using very small specimens and/or synchrotron X-ray facilities (which also require very small specimens); the latter makes use of a high-power monochromatic source of X-rays resulting in lower attenuation and noise, thus improving spatial resolution. Applications are generally the characterisation of internal features within the material, such as corrosion pits and cracks, fatigue cracking, inclusions and porosity. Table 3.4 lists some of the relevant studies performed on steels using µ-CT in recent years.

Table 3.4 Use of µ-CT on steel.

Reference	**Material**	**Purpose**	**CT Equipment**	**Voxel size**
Connolly et al., 2006 [120]	3Ni–Cr–Mo–V steam turbine disk steel	Transition from pitting to stress corrosion cracking.	High-resolution desktop µ-CT system (Skyscan 1072)	3.9 µm – specimen thickness of 3 mm.
Shiozawa et al., 2007 [121]	Stainless steel (JIS SUS 630)	Fretting fatigue crack observation	Synchrotron X-ray µ-CT (SPring-8, Japan)	0.9 µm – scanned cross-section of 300 µm x 300 µm
Kastner et al., 2010 [122]	Carbon steel	Comparison of different tomography techniques	µ-CT cone beam devices (GE Inspection & Sensing Technologies)	3.5 µm – maximum specimen diameter of 0.5 mm

Jovanović et al., 2012 [123]	Low carbon steel (S235JR)	Examination of metal arc gas (MAG) weld defects	NANOMEX CT system (Phoenix X-ray Company)	10 µm – 5 mm x 5 mm cubed specimen
Gamboa et al., 2014 [124]	X65 low-carbon steel	Examination of stress corrosion cracking in a 30-year-old subsea pipe	Xradia ® µ-CT imaging system	2.19 µm – 4 mm diameter cylinders,
Ziółkowski et al., 2014 [125]	Additively manufactured 316L stainless steel	Detection of discontinuities and porosities	Carl Zeiss X-ray CT machine	37 µm – scanned cylindrical cross-section of 4 mm diameter.
Meng et al., 2015 [126]	Hadfield high manganese steel	In-situ observation of fatigue crack morphology and crack growth	Synchrotron X-ray µ-CT (SSRF, China)	0.74 µm – scanned cross-section of 0.5 mm x 0.5 mm.
Seo et al., 2015 [127]	Free-cutting steel (JIS SUM24L)	Investigation of void coalescence	Synchrotron X-ray µ-CT (SPring-8, Japan)	0.5 µm – scanned cross-section of 600 µm x 600 µm.
An et al., 2015 [128]	Super duplex stainless steel	Study of the application of µ-CT in-situ inspection of butt welds in subsea umbilical tubes	X-ray µ-CT	Not given (feasibility study). Smallest detectable defect sized at 240 µm (4.3% of wall-thickness)
Crump, 2017 [9]	Carbon-manganese steel (S355)	Characterisation of weld toe defects and weld toe geometry	X-ray µ-CT	6 – 17 µm – a range of different specimen sizes were scanned

Farhad et al., 2018 [129]	X65 low-carbon steel	In-situ corrosion fatigue testing and characterisation of fatigue cracks	Xradia ® µ-CT imaging system	3.75 µm

In terms of the use of µ-CT on welded specimens, it was recently used to detect defects in aluminium friction stir welded (FSW) lap joints in the work by Hamade et al., 2019 [130]. In terms of steel welds, it was used by Jovanović et al., 2012 [123] to characterise lack of fusion (LOF) features and pores in steel MAG welds. The characterisation of steel weld toe defects and the weld toe geometry using µ-CT was carried out by Crump [9]. The works mentioned above used conventional micro-CT systems which are limited in resolution by the weight and size of the specimen.

In an attempt to make the µ-CT technique more industry relevant and to investigate its potential to replace or extend radiography inspection, Piazza et al., 2018 [131] developed a portable CT system capable of resolving flaws in pipeline seam welds. A prototype of a portable pipeline CT scanner was developed and specific regions of interest, determined to contain defects based on other NDT techniques such as magnetic particle inspection (MPI), were scanned. The results obtained were validated using serial metallography. The information presented on the validation was limited. Developing the portability of µ-CT scanning systems is undoubtedly required and is being pursued, as this NDT technique provides a potentially good method to characterise both surface and embedded flaws in metals, compared to the other industrially accepted techniques.

3.3 Methodology

3.3.1 Materials and Welded Joints

3.3.1.1 Material Specification

Structural carbon-manganese (C-Mn) S355 steel complying with BS EN10025-2 S355 J2+N [132] of 8 mm plate thickness was used for the two sets of experiments performed in this Chapter. The work described in Chapters 4 and 5 also used this material, but the material used was from a different batch.

The steel arrived in the hot-rolled and normalised condition (to avoid excess hardening during welding and to improve its ductility and toughness). The chemical composition of the material (as given by the supplier test certificate) is given in Table 3.5. Tensile tests were performed in accordance with BS EN ISO 6892-1:2016 [133], the results of which are given in Table 3.6. This data

was used for FE modelling, discussed in Section 3.5.3. Stress-strain curves are presented in Figure 3.8.

Table 3.5 Chemical composition of S355 J2+N structural steel.

Elements	**C**	**Mn**	**Si**	**Al**	**P**	**S**	**Cr**	**Mo**	**Ni**	**Cu**	**Nb**
Weight%	0.14	1.42	0.41	0.033	0.013	0.007	0.02	0.001	0.02	0.011	0.028

Table 3.6 Tensile properties of S355 J2+N structural steel.

Young's Modulus	**Yield Strength (0.2% proof)**	**Ultimate Tensile Strength (UTS)**	**Elongation**
190 GPa	383 MPa	535 MPa	27.5%

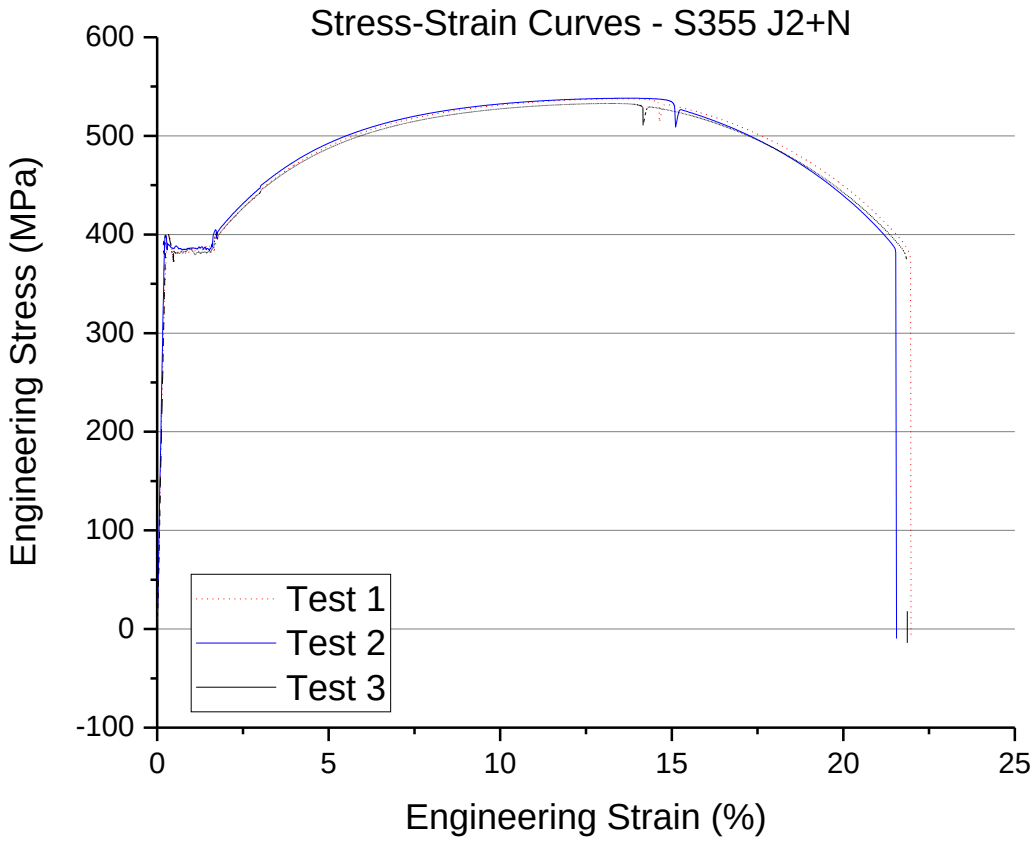

Figure 3.8 Stress-strain curves for S355 J2+N structural steel.

3.3.1.2 Welding Specification

The two sets of experiments performed in this project used metal active gas (MAG) welded joints, which were manufactured with different welding parameters and dimensions.

Welding Parameters – Experiment Set 1 (data taken from [9])

Four MAG double-sided transverse non-load carrying joints comprising of four single pass fillet welds 1200 mm long with an attachment length of 60 mm were fabricated at TWI Ltd from the S355 plates. On completion of all welds, 20 specimens of length 50 mm were then extracted from each joint using a band saw with cooling fluid. A schematic of the complete welded joint and subsequent specimen extraction is shown in Figure 3.9.

Prior to welding, the plates were ground and tacked into position with the attachment plates and practice runs were carried out to determine the optimum welding parameters. Pen marks were made on the baseplate every 100 mm to aid the welding process, and two cameras were used to monitor the arc position and welding parameters (voltage, current and wire feed).

The four different MAG welding process parameters selected, and their abbreviations used in this thesis, were:

1. Manual welding using a metal core electrode (MM_MAG),
2. Semi-automated welding using a metal core electrode (MA_MAG),
3. Manual welding using a solid core electrode (SM_MAG),
4. Semi-automated welding using a solid core electrode (SA_MAG).

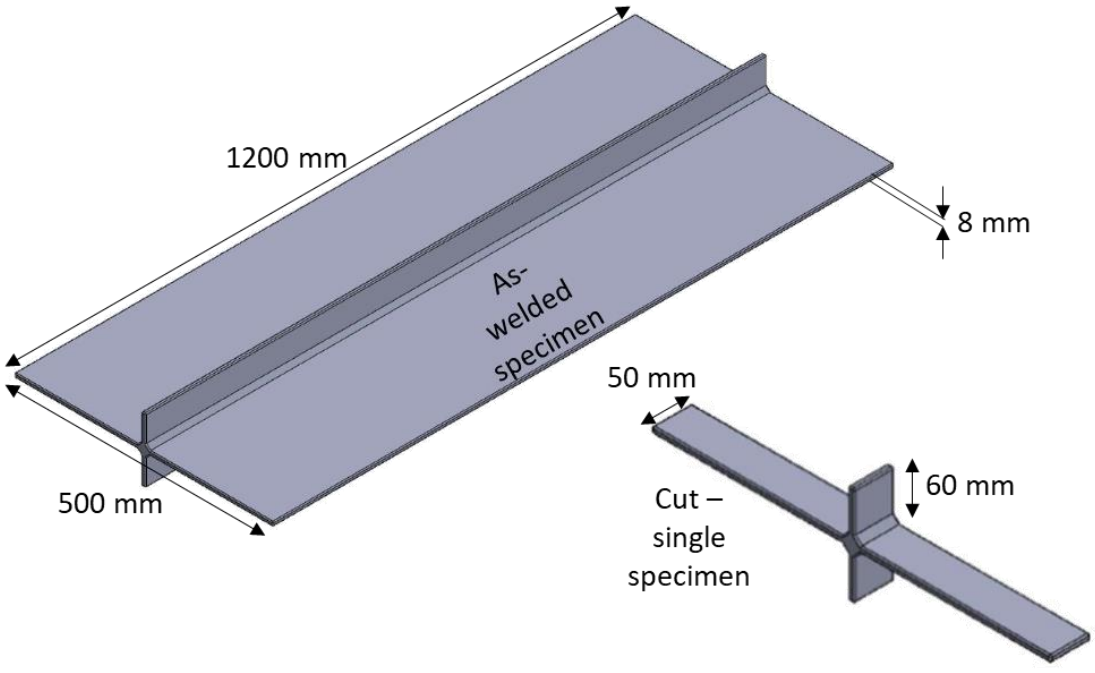

Figure 3.9 Schematic of a MAG welded-joint after welding and a specimen extracted after welding.

Metal-core electrodes were 1 mm diameter ESAB OK Tubrod 14.12 electrodes complying with BS EN ISO 17632:2015 [134]. Solid-core electrodes were 1 mm diameter SIFMIG SG 3 (also designated G4Si1 – grade) copper coated double-deoxidised electrodes complying with BS EN ISO 14341:2011 [135]. The cross-sections of the electrodes taken under an optical microscope can be seen in Figure 3.10 and the chemical composition and mechanical properties of both electrodes (as given by [3, 135]) are presented in Table 3.7.

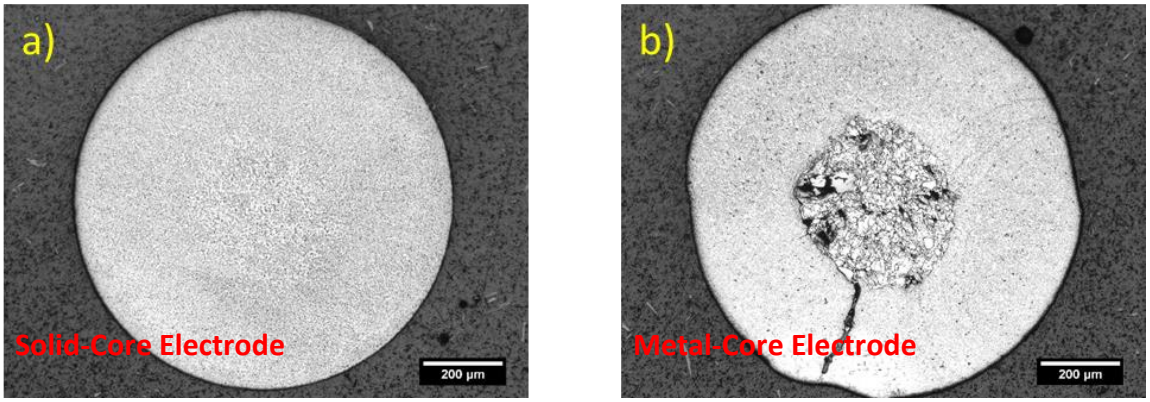

Figure 3.10 Cross-section of electrodes – a) solid-core; b) metal-core. Adapted from [9].

Table 3.7 Typical chemical composition and mechanical properties of the electrodes.

Electrode	**Composition (Wt. %)**			**Mechanical Properties**	
	C	**Si**	**Mn**	**Tensile Strength (MPa)**	**Elongation (%)**
Metal Core	0.1	1.0	1.75	550-600	24
Solid Core	0.07	0.6	1.3	510-640	22

Both types of welds, manual and semi-automated were produced using an ESAB MIG U5000i welding plant with ESAB 3004 wire feed unit. The welding torch was held at 45° to the base plate. The electrode stick-out length was 16-18 mm and the shielding gas used throughout was 80 % Argon/20 % CO_2 supplied by Air Products Coogar and complying with ISO 14175:M26.

Manual welds were carried out by a trained welder (ID: 263) with two weld runs just over 600 mm in length for each side of the weld, as seen in Figure 3.11. The welded sides were numbered from 1 to 4 in order of the welding. Individual weld runs were labelled a, b and c, if necessary. Weld sides 2 and 4 were ground and tacked before welding.

Figure 3.11 Manual MAG welder position before arc generation. From [9].

Semi-automated welds were produced using a Gullco Auto-Weld KAT travel carriage at a constant travel speed of 290.4 mm/min, as seen in Figure 3.12. To account for plate contraction, manual horizontal and vertical adjustment of arc position was applied during the weld run. One weld run was carried out for each weld side, as no stop/start was needed for welder position adjustment. All weld sides were ground and tacked before welding.

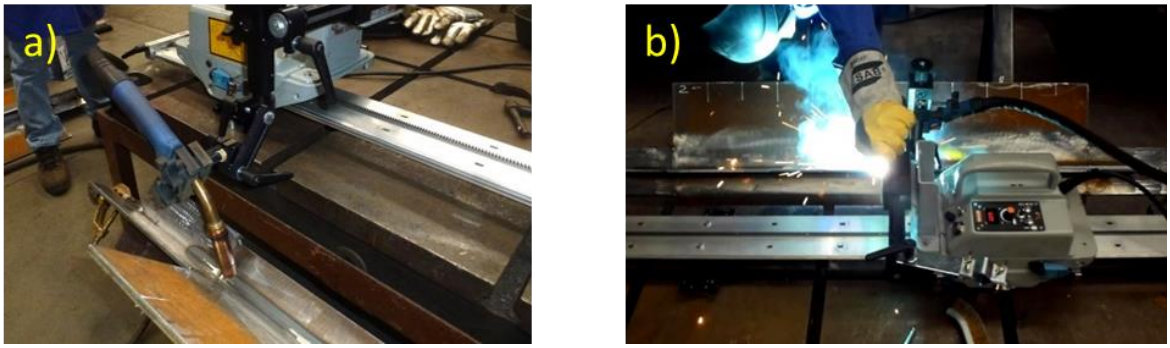

Figure 3.12 Semi-automated MAG welding – a) Arc-position; b) operator adjustment. From [9]

Once the welding was performed, the specimens were cut to a width of 50 mm, and the edges were chamfered using a pneumatic rotary grinder with #180 and #320 grit size. Three of the four weld toes were ultrasonically peened to promote fatigue crack initiation (FCI) from the as-welded toe, i.e. the weld toe that would be monitored for fatigue crack growth. A SONATS NOMAD Ultrasonic Impact Treatment (UIT) system was used to perform the ultrasonic peening. An ultrasonic frequency of 20 kHz was used with a vibration amplitude setting of 60 µm (peak to peak) and an impact needle of 1.5 mm diameter.

Welding parameters – voltage, current and electrode wire feed rate – were monitored throughout each weld run. Heat input was calculated using equation 3-1. The process efficiency factor, η, was taken to be 0.8 for MAG welds [3]. Travel speed was calculated using weld run length over time per weld run. Table 3.8 shows the average welding parameters and heat input for each weld. The first

weld run was performed at ambient temperature and subsequent weld runs were performed at an interpass temperature near to 70°C.

$$HI = \eta \frac{VI}{v} \quad 3\text{-}1$$

Where,

H Heat Input (J/mm)

η Process efficiency factor

V Voltage (volts)

I Current (ampere)

v Travel speed (mm/s)

Table 3.8 Average Welding parameters for Set 1.

Weld	Side/Toe	Runs	Current (Amps)	Voltage (V)	Travel Speed (mm/sec)	Heat Input (kJ/mm)	Interpass Temperature (°C)
SM_MAG	1	a, b, c	230	30	4.69	1.17	70
	2	a, b	230	30	4.36	1.26	65
	3	a, b	230	30	4.18	1.32	68
	4	a, b	230	30	4.56	1.21	Ambient
SA_MAG	1	a	236	30	4.89	1.15	51
	2	a	236	30	4.89	1.15	46
	3	a	236	30	4.89	1.15	76
	4	a	236	30	4.89	1.15	Ambient
MM_MAG	1	a, b	245	30	4.62	1.27	51
	2	a, b	245	30	4.71	1.25	142
	3	a, b	245	30	4.88	1.22	67
	4	a, b	245	30	4.41	1.33	Ambient
MA_MAG	1	a	245	30	4.89	1.2	65
	2	a	245	30	4.89	1.2	101

	3	a	245	30	4.89	1.2	67
	4	a	245	30	4.89	1.2	Ambient

Welding Parameters – Experiment Set 2

Manual MAG single-sided transverse non-load carrying joints comprising of two single pass fillet welds 500 mm long with attachment length of 60 mm were fabricated at TWI Ltd from S355 plates and an E7018 solid-core electrode. Figure 3.13 shows a schematic of the as-welded plate and a specimen subsequently extracted from it.

Prior to welding, the plates were ground and tacked into position with end plates and some trial welds were performed to determine optimum parameters. The parameters were selected to obtain two types of weld, high-quality (HQ) and low-quality (LQ), with the latter targeting to give weld toes with a high-density flaw distribution.

The parameters for each welding run are given in Table 3.9. Once the welding was performed, the specimens were cut to a width of 50 mm (as shown in Figure 3.13), and the edges were chamfered using a pneumatic rotary grinder with #180 and #320 grit size.

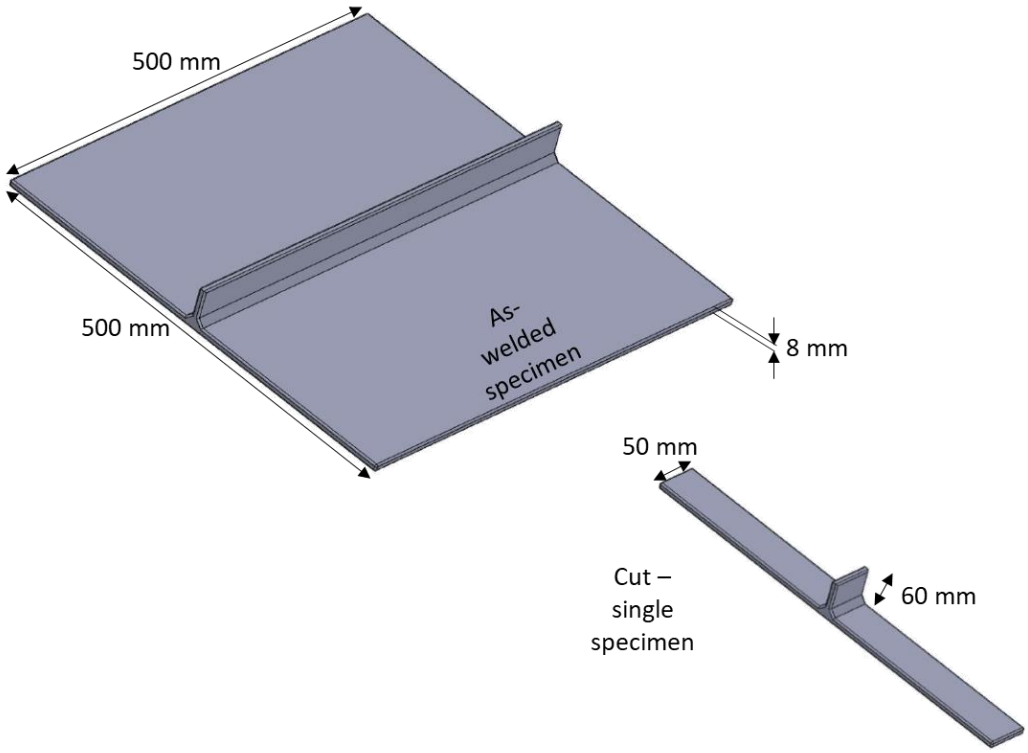

Figure 3.13 Schematic of MAG single side welded joints. Top – as-welded; bottom – after specimen cutting.

Table 3.9 Average welding parameters for Set 2.

Weld	Side/Toe	Runs	Current (Amps)	Voltage (V)	Travel Speed (mm/sec)	Heat Input (kJ/mm)	Interpass Temperature (°C)
HQ (High Quality)	1	a	185	17	5.7	0.54	Ambient
	2	a	179	17	6.1	0.49	Ambient
LQ (Low Quality)	1	a	270	17	7.5	0.69	Ambient
	2	a	265	17	7.5	0.66	Ambient

One of the two weld toes of the HQ specimens were ultrasonically peened as per the above section to facilitate fatigue crack initiation (FCI) occurring first at the as-welded toe (as this was the toe that was to be monitored for fatigue crack growth). The weld toes for the LQ specimens were left as-welded as the depth of the intentionally created undercuts would not allow for proper UIT [136]. Figure 3.14 shows an example of an as-welded toe and a weld toe after ultrasonic peening.

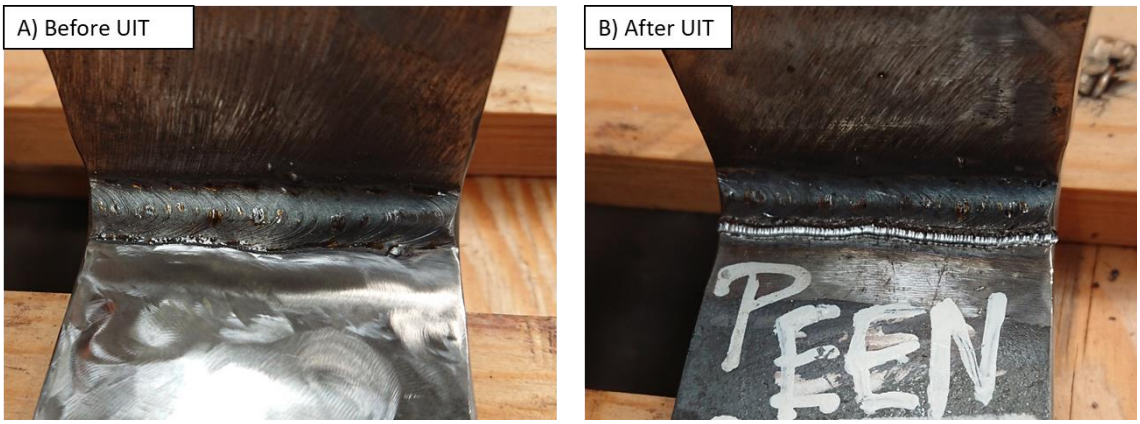

Figure 3.14 A) image of a weld toe before; B) after UIT

3.3.2 Scan Methodology

All X-ray µ-CT scans in this thesis were carried out by Dr Mark Mavrogordato at the µ-VIS X-ray Imaging Centre, University of Southampton. Two scan systems were used: a 225 kV Nikon/Xtek HMX (HMX) and a custom 450 kV HUTCH system (HUTCH). Several software packages were used to analyse the scanned data, namely CT3DPRO, VG Studio, Simpleware ScanIP, MATLAB and ImageJ.

Three sets of scans were performed, each set on different specimens, the results of which are presented and discussed in this chapter. Table 3.10 provides details of the three sets of scans, and Table 3.11 shows the scanning parameters for each set.

Table 3.10 Details of µ-CT scans performed.

Scan Set	**Scanning System**	**Type of Specimen**	**Number of Specimens**	**Objectives of scan**
1	HMX	**Weld Toe Matchstick** C-Mn steel specimens containing at least one fatigue crack of approximately 200 – 400 µm. **Cross-section** – 3 x 3 mm. **Length** – 50 mm.	3	1. Resolve weld toe geometry and inherent flaws. 2. Quantitative flaw analysis. 3. Additional validation of alternating current potential drop (ACPD) crack growth (crack depth) monitoring technique.
2	HUTCH	**Weld Bead** C-Mn steel specimens containing fatigue crack of approximately 200-500 µm. **Cross-section** – 10 x 10 mm. **Length** – 50 mm.	4	1. Resolve weld toe geometry. 2. Quantitative flaw analysis. 3. Additional validation of strain gauge array technique for crack growth (crack depth) monitoring.
3	HMX	**Weld Bead Replica (in-situ)** Silicone replica of the weld bead in the testing machine. **Cross-section –** 10 x 10 mm. **Length** – 50 mm.	1	1. Assess the quality of replication of in-service welded joints for the µ-CT application.

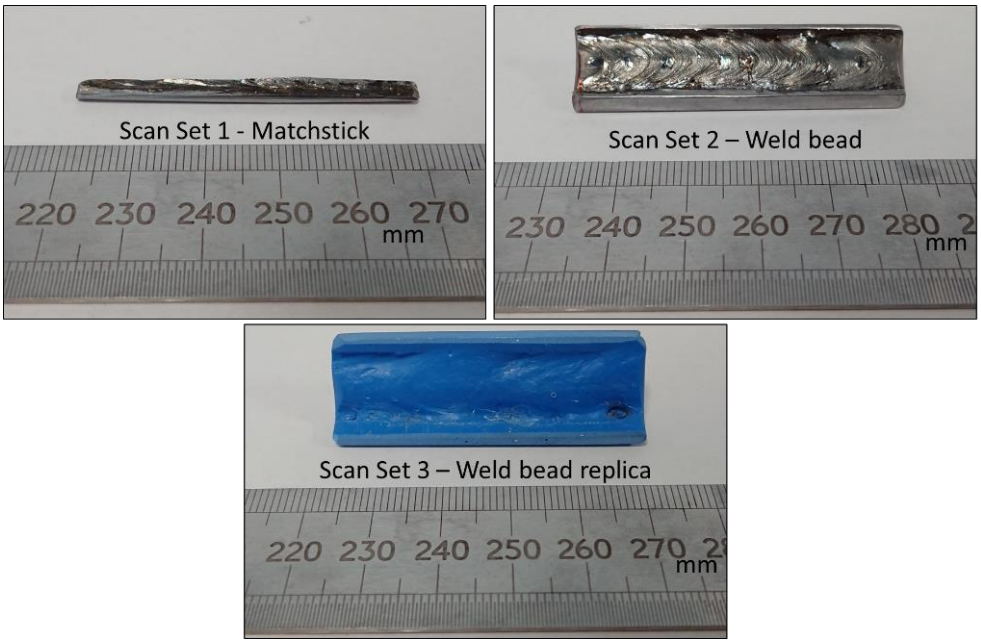

Figure 3.15 Photographs taken of a specimen from each of the three scan sets.

Table 3.11 Scan settings for each set.

Scan parameter	**Scan Set**		
	Set 1	**Set 2**	**Set 3**
Scanner	HMX	HUTCH	HMX
Target	Reflection	Reflection	Reflection
Beam Energy (kV)	200	200	200
Beam Intensity	175 µA	160 µA	85 µA
Filter Material	Tin	Not used	Not used
Filter Thickness	0.25 mm	Not used	Not used
Exposure	0.177 seconds	0.177 seconds	0.25 seconds
Gain	5	3	4
Projections	1801	3142	3142
Frames per Projection	16	4	4
Voxel Size	4.9 µm	10 µm	14 µm
Approximate Scan Time (per specimen)	15 hours	8 hours	3.5 hours

3.3.2.1 Scan Set 1

Three specimens were scanned in total; the scanning parameters were determined based on the results obtained previously using the same scanning system and specimen size and material [9]. 3x3 mm matchstick specimens were extracted at the weld toe using Electric Discharge Machining (EDM). The specimens were stacked vertically using foam and masking tape in a Perspex tube to enable overnight scanning of all specimens. A resolution of 4.9 µm was achieved for the three scans.

3.3.2.2 Scan Set 2

Four specimens were scanned in total, and the scan parameters were determined using the same criteria as described in Section 3.3.2.1. Of the two available weld runs on each specimen, only one was scanned and analysed. The chosen weld bead was extracted from the larger specimen using precision rotary saw cuts with cooling fluid. Again, the specimens were vertically stacked using foam and masking tape in a Perspex tube to enable overnight scanning. A resolution of 10 µm was achieved for the four scans.

3.3.2.3 Scan Set 3

One specimen was scanned in this set, and the scanning parameters were determined using the experience of the µ-VIS operators and [137]. It was a silicone replica of a weld bead, and it was done while the specimen was in the hydraulic testing machine (Figure 3.16). The specimen was produced using silicone encapsulant Silicoset 105, manufactured by acc® silicones Europe. This process produced a mould of the weld bead. Rencast® FC 54 polyurethane casting resin was used to create a cast of the weld bead, which was to be the scanned specimen. According to the experience of the technician who performed the procedure, it has been proven to achieve resolutions of up to 1 µm (no such information was provided by the manufacturer or the technical data sheet).

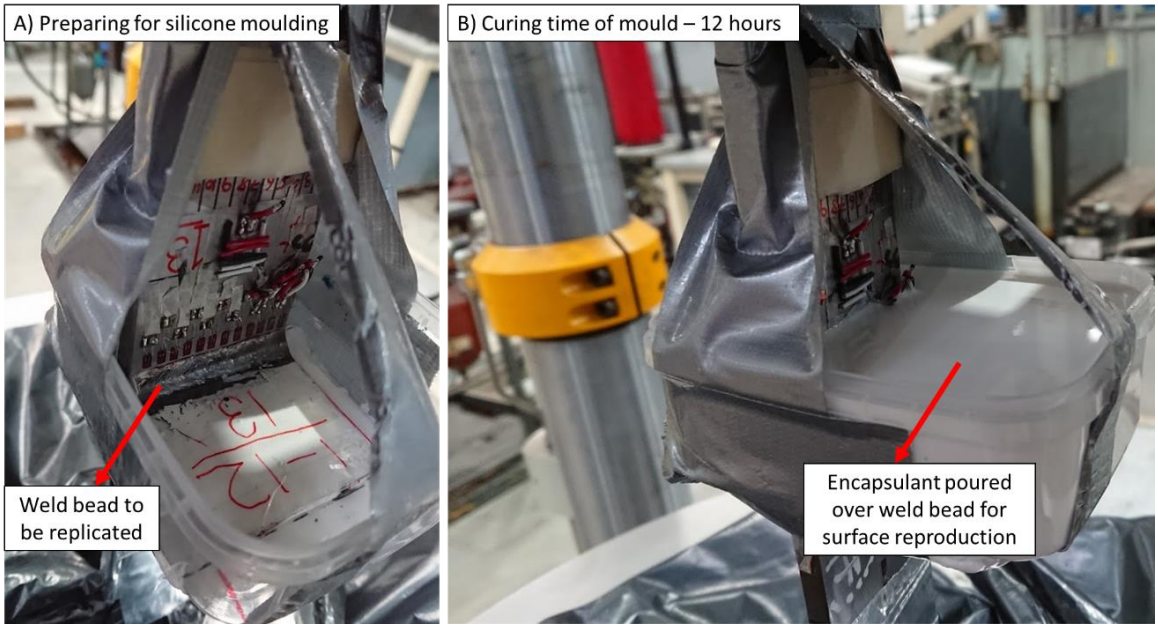

Figure 3.16 Photographs of the replica process whilst the welded specimen is in the servo-hydraulic testing machine – A) The holder for the encapsulant mix around the weld bead; B) curing of the encapsulant mix.

3.4 µ-CT Data Analysis

A total of eight weld toes were subjected to µ-CT scanning during this PhD project, each resulting in a volume file size of approximately 150 GB. A series of analysis steps were performed on each scan volume, which are summarised in Figure 3.17. These are described in more detail in this Section, and the results are later used in fatigue life predictions, presented in Chapter 6.

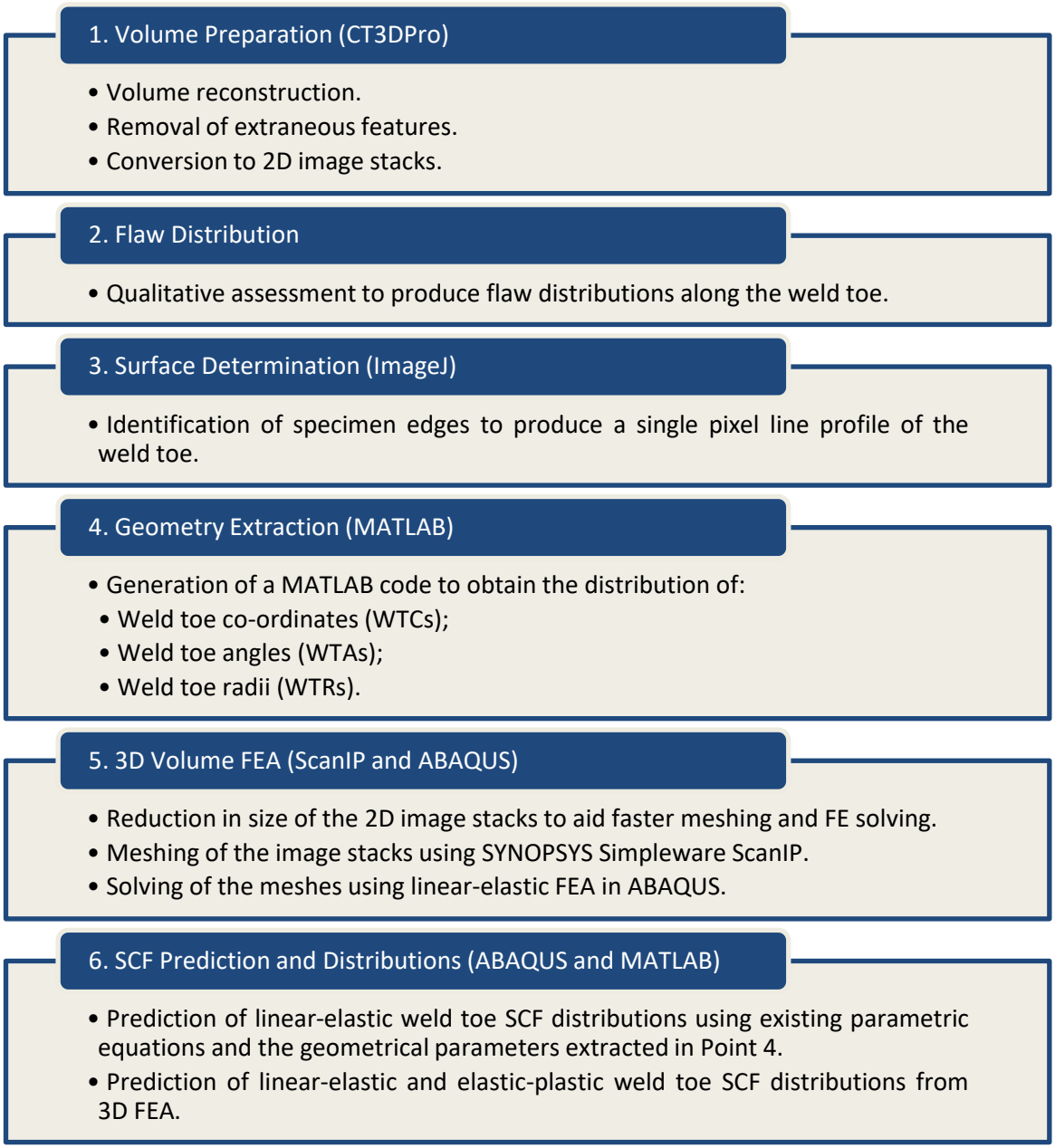

Figure 3.17 A summary of the analysis steps involved in qualitatively and quantitatively assessing the μ-CT scan data.

3.4.1 Volume Preparation

The scans were reconstructed using back-filtered projected in the software CT3DPro to create a 3D volume. This was imported into ImageJ for the removal of extraneous areas to reduce file size and computing time. This was converted to a stack of 2D images, to be analysed in the next steps.

3.4.2 Flaw Distribution

A qualitative study was performed to obtain the flaw distribution for each scanned weld toe. This involved visually inspecting each 2D image slice in the 3D volume stack in order to determine:

a) The number of visible flaws;
b) The type of each flaw;
c) The size of each flaw.

Flaws were classified as the following types, and examples of each type and how they were measured has been presented in Appendix A.5 –

A) Notch-like flaws, often also known as undercuts;
B) Internal flaws, often also known as embedded flaws;
C) Cold laps;
D) Spatter.

The results from each scan set are provided separately below as each had a different resolution and were of welds fabricated using different welding parameters. Due to the different resolutions and the partial volume effects at the specimen edges, each scan set is likely to have a different error associated with the measured flaw depths.

The size measured is the observable vertical depth of each flaw (maximum diameter for internal flaws). It is important to note that due to resolution issues and the number of pixels depicting the edge of the metallic specimen, there is an amount of error in these measurements which is a function of the scan quality. The partial volume effect in the scans analysed extended over distances of about one pixel. The size of this pixel, the resolution of the scan, can therefore be estimated to be the error and the limit of the flaw depth detection.

3.4.2.1 Results - Scan Set 1

The frequency of all flaws (number of individual flaws observed) observed at the weld toes of the three specimens scanned for Set 1 is shown in Figure 3.18. The distribution of the sizes of the flaws is segregated in terms of the two different types of welded joints that were scanned and is shown in Figure 3.19.

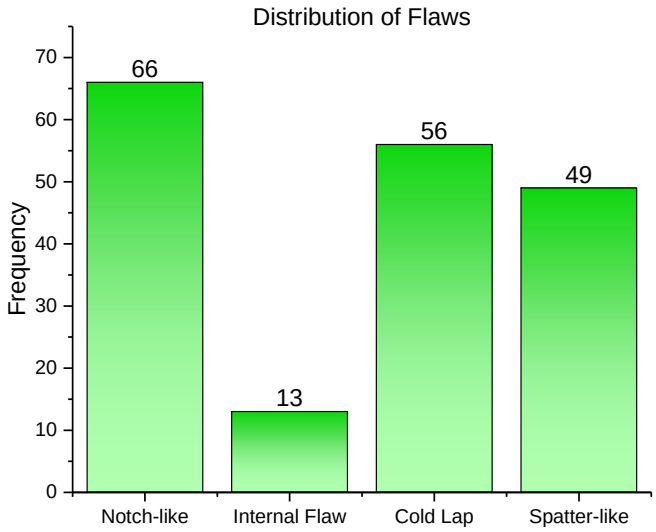

Figure 3.18 Distribution of flaws in scan set 1 across 150 mm of weld toe length.

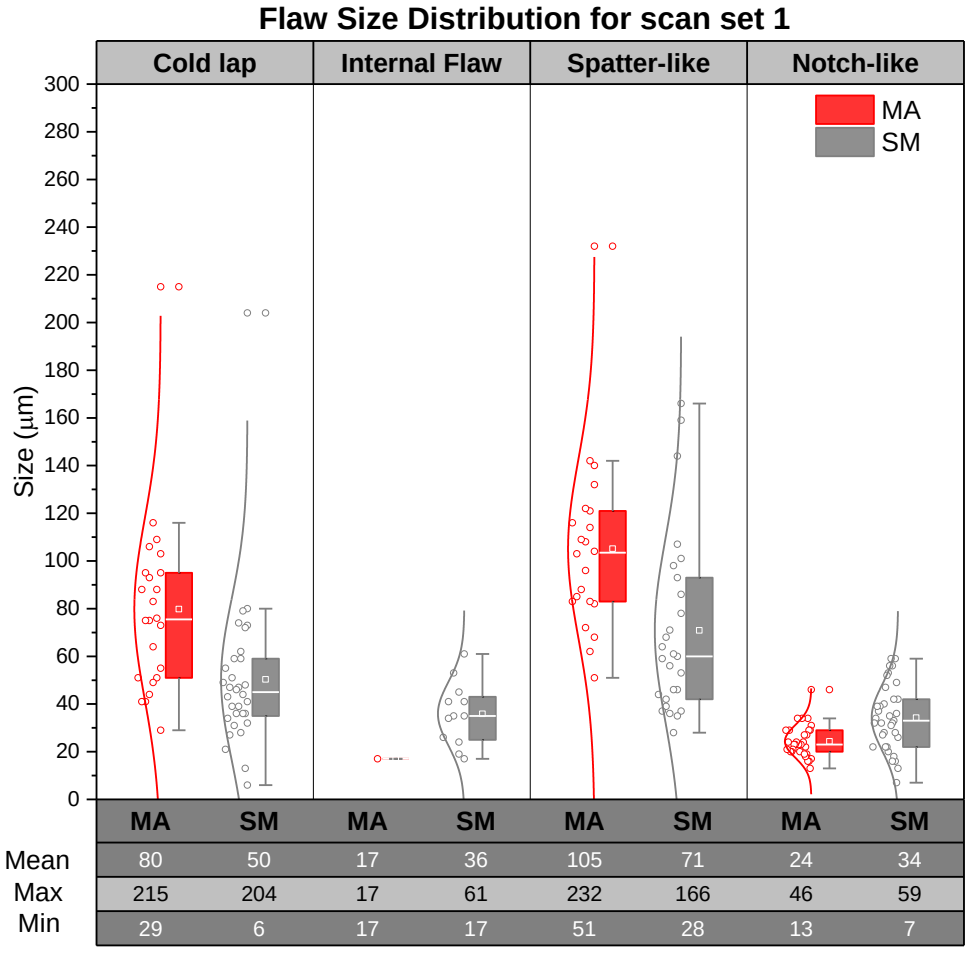

Figure 3.19 Flaw size distribution for scan set 1. MA – Semi-automated metal-core electrode weld; SM – Manual solid-core electrode weld. Note - the results from two SM specimens and one MA specimen have been presented.

Notch-like flaws at the weld toe were the most in number, but their depths were relatively smaller than the other flaws, which were considered to be more surface flaws. Such flaws were primarily observed at weld ripple junctions, however more tests would be required to make a correlation. Surface flaws such as spatter-like defects and cold laps were seen uniformly across the scanned welds. Certain cold laps also showed a lack of fusion with the parent plate. It is important to note that these voids or slag below a cold lap would be missed by most of the techniques used for capturing the true weld toe profile given in Table 3.2 except µ-CT and serial metallography, with the latter being a destructive process. More internal subsurface flaws were observed in the manual welds, with only one being captured in the semi-automated welds. This could be attributed to the fact that semi-automated welds have a pre-defined path for the welding torch which is consistent for the entire weld bead, leading to a more uniform weld penetration for the entire weld run.

3.4.2.2 Scan Set 2

Two scans each of HQ and LQ welds were performed. Figure 3.20 shows the distribution of flaws in the specimens. The LQ specimens were purposely made of low quality. Figure 3.21 presents images of each specimen as an example. Therefore, the distribution has been categorised into LQ and HQ. Figure 3.22 shows the distribution of the flaw depths.

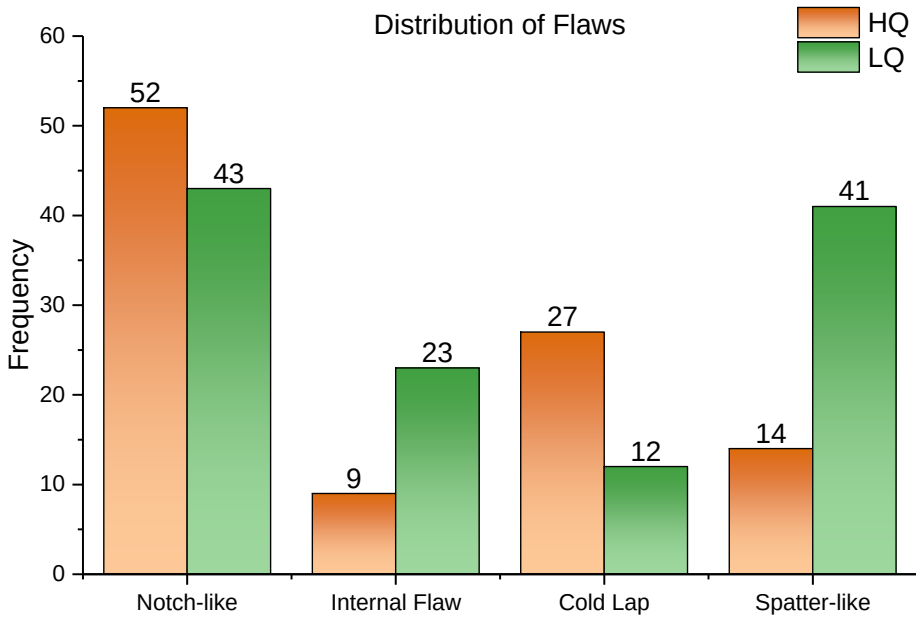

Figure 3.20 Distribution of flaws in scan set 2 across a total of approximately 200 mm of weld toe.

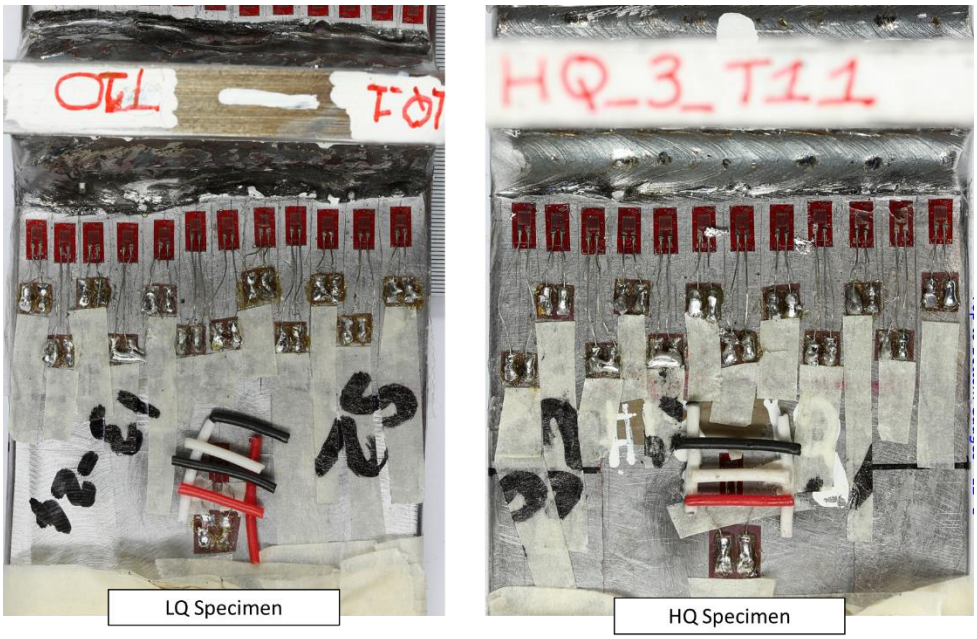

Figure 3.21 Example of an LQ and HQ specimen.

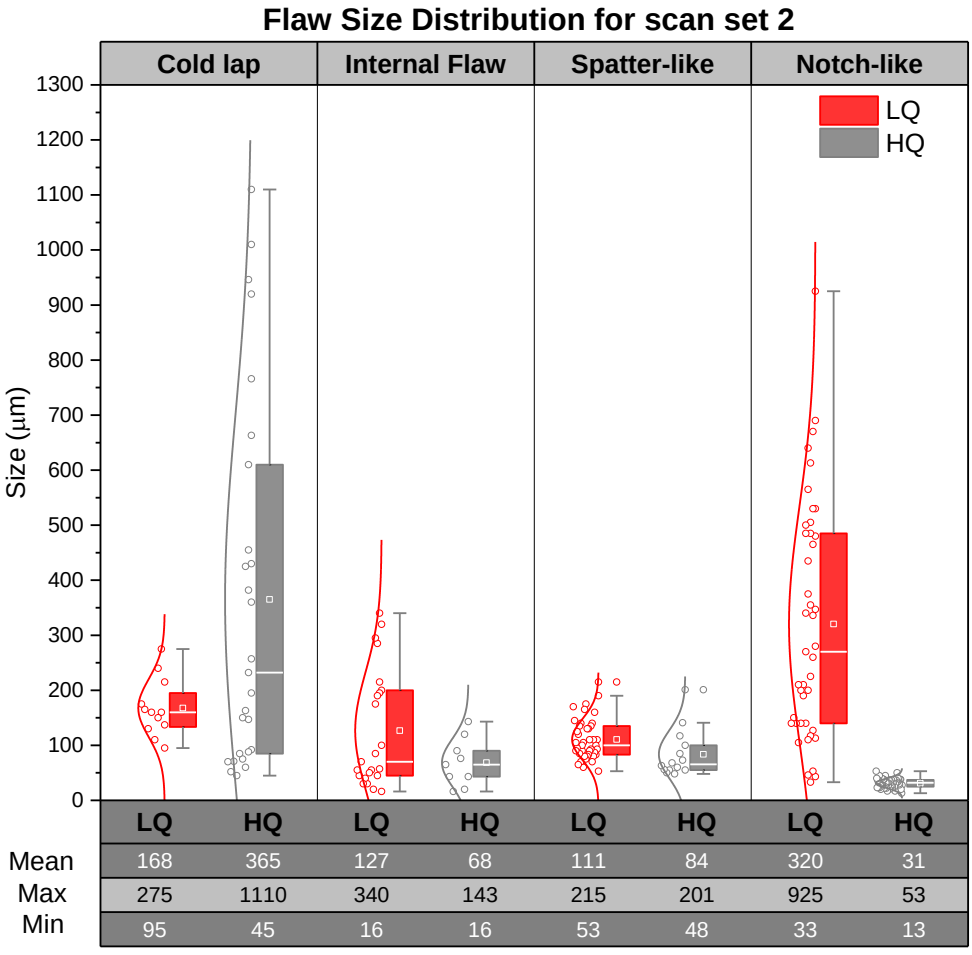

Figure 3.22 Flaw size distribution for scan set 2. HQ – High-Quality Weld; LQ – Low-Quality Weld.

The primary change in the welding parameters to manufacture the LQ specimens was the high current and thus heat input, which had the aim of creating deeper notch-like features and a higher

flaw density across the weld. A difference can, therefore, be seen for each kind of flaw, with the most substantial contrast in the notch-like defects. These flaws were much larger in the LQ specimens, even though they were more abundant in the HQ specimens. The numerical count alone does not reflect the critical defect distribution as the larger notches in the LQ specimens were only counted once (irrespective of the size of the flaw). The deeper notches were present along a more substantial length of the weld toe as compared to relatively smaller notches. For example, the typical length of a large undercut was 2 mm and that of a small notch like feature was only 200 µm.

The non-optimum welding process also resulted in larger internal subsurface flaws in the LQ specimens, with the largest extending for 1100 µm in the horizontal direction (only the vertical length was captured for Figure 3.22). More spatter-like flaws were also observed in the LQ specimens, possibly due to the excessive heat input. Cold laps were larger in the HQ specimens. This could be because the deposition rate of the electrode was not enough to encourage the formation of cold laps, which require an excess of weld metal that overflows over the weld bead and onto the baseplate.

3.4.2.3 Scan Set 3

In scan set 3, the quality of the µ-CT scan was affected by the replica taking process. Typically, these replication procedures are done on samples which can be kept in a vacuum chamber where the air can be evacuated. However, this was not performed for these specimens. Figure 3.23 is an image from the volume scanned, showing the distribution of air pockets in the replica, these were in the bulk and were surface breaking. Air pockets at the surface near the weld toe make it difficult to distinguish between them and an actual weld flaw. Consequently, no defect study was performed for this scan set.

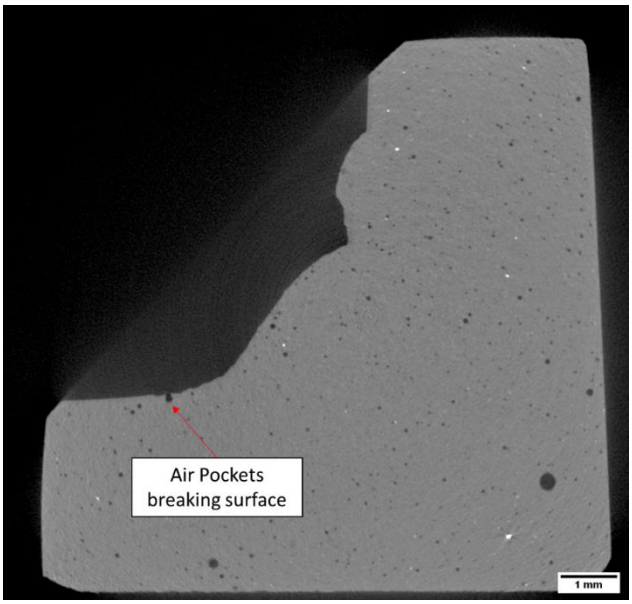

Figure 3.23 Image from the volume of scan set 3 showing the distribution of air pockets.

3.4.2.4 Conclusion

An extensive study on the capability of µ-CT to capture weld toe flaws was performed by Crump [9], which gave a detailed review of the flaw distribution that could be qualitatively obtained from CT scans as well as the impact of having either low- or high-resolution scans. In this work, the study of flaw distribution is not of the same exhaustive nature, as it is only intended to give a brief overview of the kind of flaws that exist in the tested as-welded joints.

From the study of flaw distributions as observed qualitatively from the scans, it can be concluded that µ-CT scanning is a good NDT technique for characterising flaws in welds, with the critical disadvantage that these scans could not be done in-situ. This study also provides an understanding of the size of flaws present in as-welded joints that can be detected using µ-CT scanning. This can prove to be useful for improvement or validation of the approximations of initial flaw sizes used in standards for fatigue crack propagation in welds. A statistically significant number of specimens would need to be scanned for this and this has been discussed further in Chapter 7. Given the subjective judgment factor in this study, the statistics obtained were not used for subsequent FEA and fatigue predictions. It does however highlight the need for using an automated process to capture the weld toe geometry that is consistent and adequately validated.

3.4.3 Surface Determination

ImageJ, an image manipulation software, was used to create a 2D single-pixel profile of the weld toe on each 2D image slice from the µ-CT volumes. A number of analysis steps were involved to achieve this, which needed to be applied to over 47,900 images. Hence, a macro was developed in ImageJ to automate the process and make it consistent across all µ-CT volumes processed. The macro is provided in Appendix A.1.

First, the reconstructed volumes were cropped to minimise file size and thus subsequent processing time, Figure 3.24. Next, the minimum error threshold method developed by Kittler et al. [138], was used to identify the specimen volume and thus the surface resulting in a binary image, Figure 3.25A. A number of global thresholding methods were investigated within ImageJ, however, the minimum error method was found to best capture the inherent flaws, particularly at notches, where some alternative thresholding methods resulted in more rounded flaw roots. Any space irrelevant to the weld toe, was removed using the 'Flood Fill' tool in ImageJ, Figure 3.25B, then the 'Find Edges' plugin, based on the Sobel-Feldman Operator [139], was applied to detect the edges in each image. This plugin works by using two 3x3 convolution kernels to identify sharp changes in pixel intensity, Figure 3.25C. Next, the 'Skeletonize' plugin (developed by I. Arganda Carreras using a thinning algorithm from Lee et al. [140]) was used to create a single-pixel profile of the weld toe, Figure 3.25D. The 'Analyze Particles' plugin was then used to remove any profiles below 300 µm^2, Figure 3.25E. The profiles removed were primarily from subsurface flaws, which are not part of the current study, particularly those located away from the weld toe. Finally, the 'Invert' tool was used to flip each binary image in the stack, ready for analysis in MATLAB, Figure 3.25F.

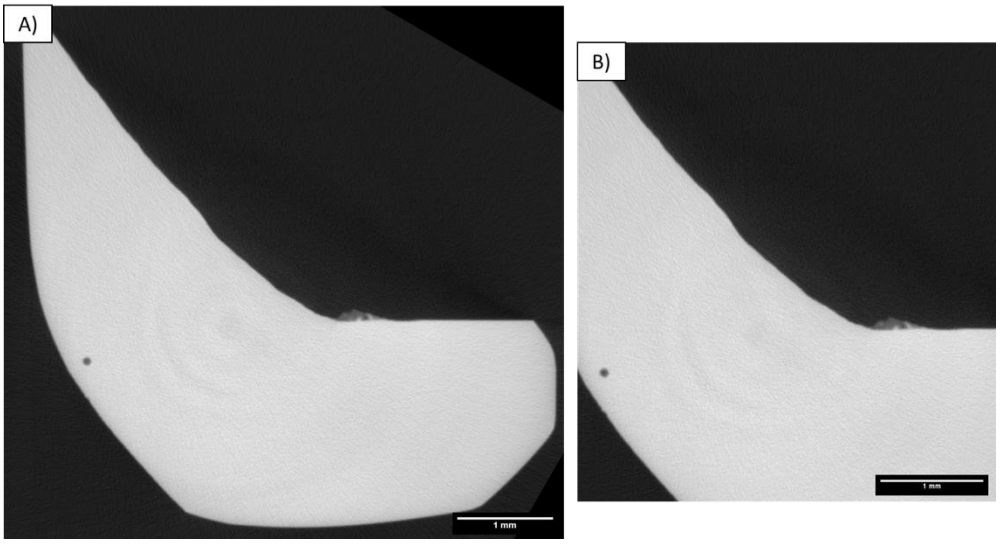

Figure 3.24 A) Original µ-CT image slice taken from the reconstructed volume; B) The same image after cropping showing the key features of the weld toe are retained.

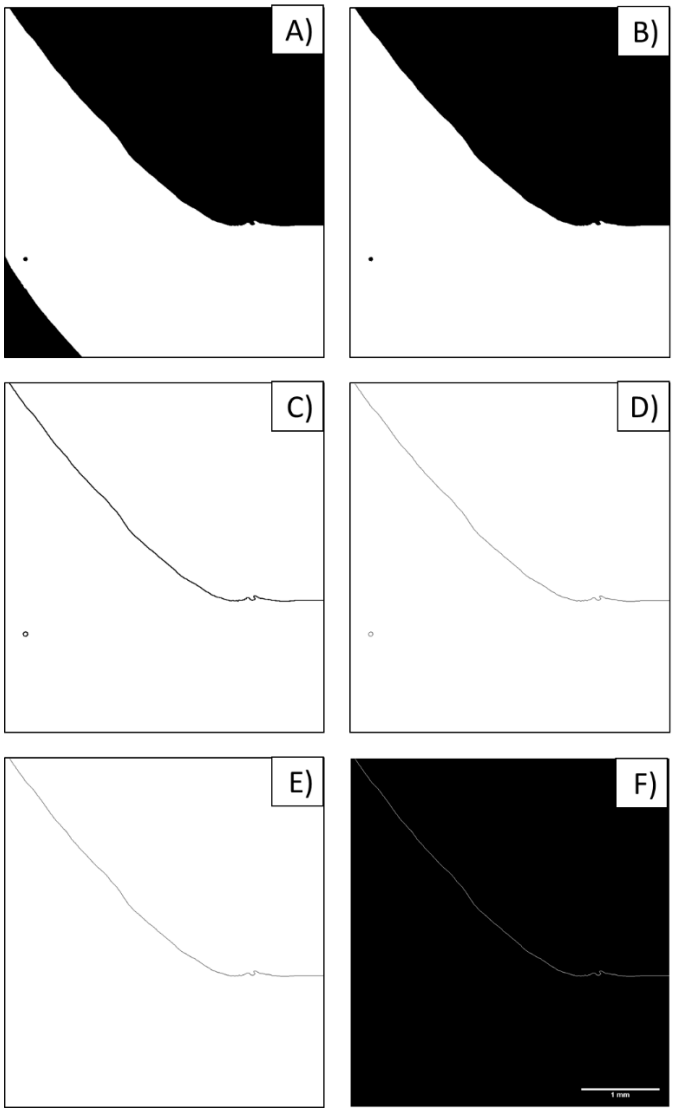

Figure 3.25 Image processing steps from µ-CT slice to a single pixel line profile for subsequent MATLAB analysis - A) Minimum Error threshold; B) Flood Fill; C) Find Edges; D) Skeletonize; E) Analyze Particles; F) Invert image.

3.4.4 Geometry Extraction

Crump developed a program in MATLAB for weld toe geometry extraction from similar types of 2D image stacks. For each image, the program identified the weld toe coordinate (WTC) and from this point, the weld toe angle (WTA) and weld toe radius (WTR). In this study, Crump's MATLAB program has been further modified to be applicable to the specimens scanned in this project and has been made more informative in terms of visually representing each weld toe measurement. The main algorithms used in the program were kept the same and more detail on these can be found in [9].

3.4.4.1 Weld Toe Coordinate (WTC) Identification

The WTC defines the point at which the weld bead meets the base plate and it is needed in order to subsequently determine the WTR and WTA parameters. The same algorithm is used in this study as that in the original MATLAB program [9].

An example of correct WTC identification for a relatively smooth profile with no weld flaws (HQ welded specimen) is given in Figure 3.26. Figure 3.26A) shows the single-pixel weld toe profile and Figure 3.26B) shows the WTC position (blue triangle) identified by the MATLAB program (in addition to the other geometrical parameters). The solid red lines are the vectors that are fitted to the profiles of the weld bead and baseplate either side of the WTC; the angle between these is used to determine the WTC as they are fitted at each pixel along the weld profile.

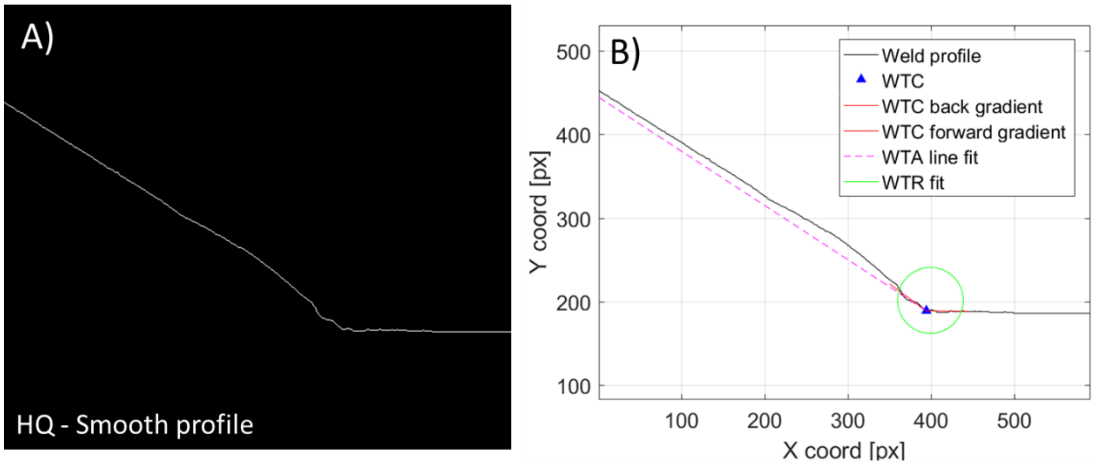

Figure 3.26 HQ smooth weld toe profile - A) Original single-pixel weld profile obtained from ImageJ processing; B) Weld toe geometry extraction after MATLAB processing.

For testing the robustness and accuracy of the algorithm, it was run on all 2D image stacks, i.e. over 47,900 images from seven µ-CT volumes. A manual check was performed on each processed image using visual inspection and the number of images where the WTC was determined to be misplaced were recorded. The results are presented in Figure 3.27. For each weld toe scanned, the WTC identification error varied between 3% and 26%; errors were highest for the LQ welded joints. From the two LQ specimens scanned, the average error was 25%, whilst the average error for the five HQ welded joints was 12%. The larger errors for the LQ specimens were attributed to the rougher weld toe profiles and the increased number of larger flaws, particularly spatter and notch-like ones. In addition, the relatively high error in specimen HQ T-07 compared to other HQ specimens, was attributed to the smaller amount of weld bead profile available for analysis as a consequence of the matchstick specimen machining, as well as a relatively higher density of flaws amongst the HQ specimens. Examples of WTC identification errors are provided below.

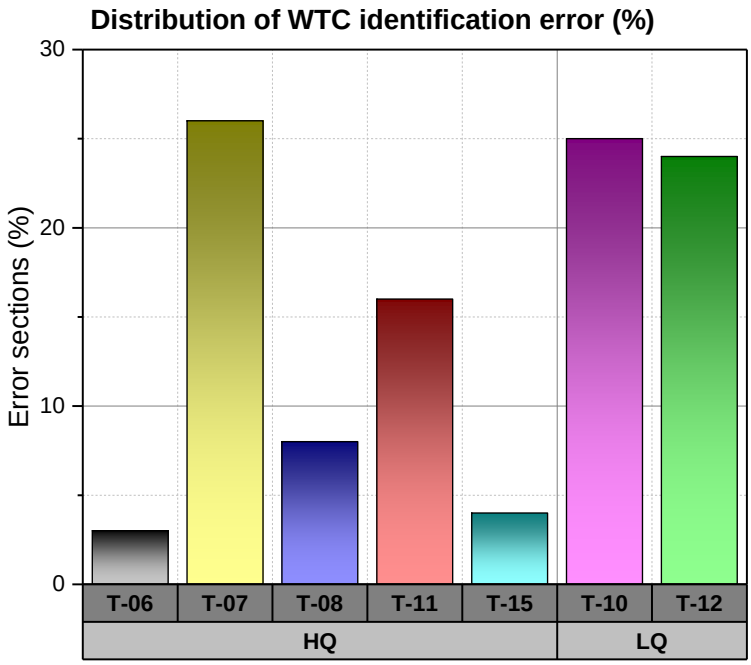

Figure 3.27 Distribution of errors in WTC identification.

Figure 3.28 shows a weld toe profile, where a cold-lap is developing in an HQ weld (the cold-lap gets larger in subsequent images). Here, the algorithm accurately identifies the WTC, however, once the cold-lap becomes larger, the algorithm struggles and identifies it incorrectly, Figure 3.29 and Figure 3.30.

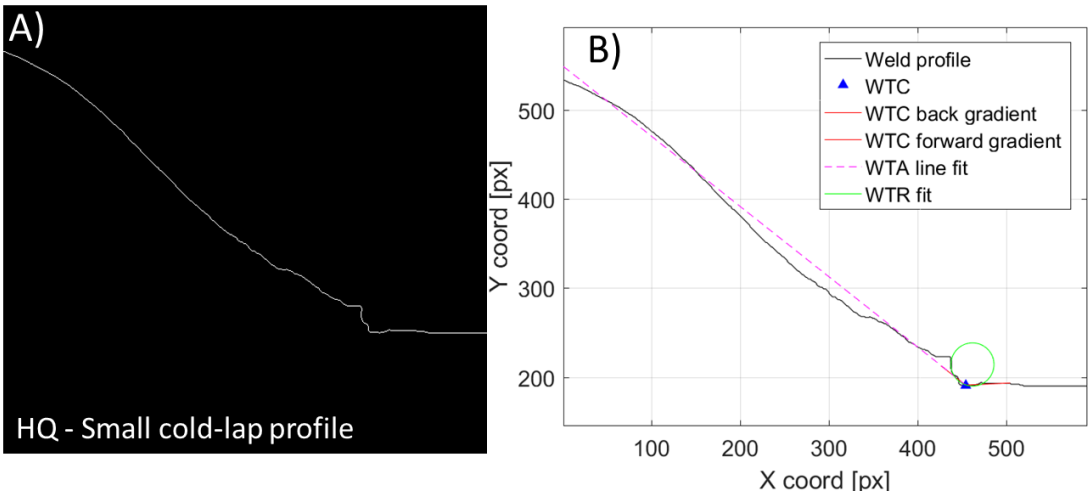

Figure 3.28 HQ weld profile with small cold-lap defect - A) original single-pixel weld profile; B) weld toe geometry extraction after MATLAB processing.

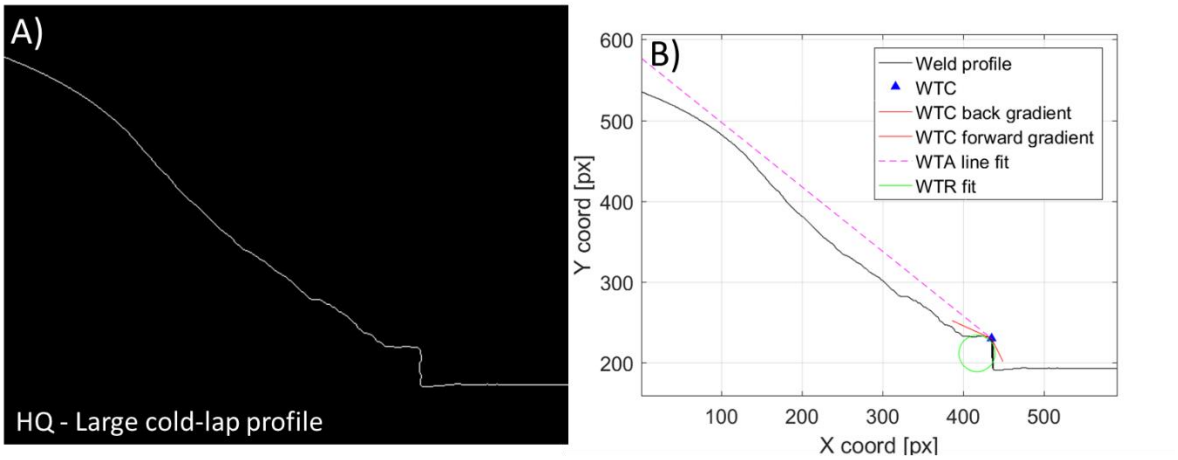

Figure 3.29 HQ weld profile with large cold-lap defect - A) original single-pixel weld profile; B) weld toe geometry extraction after MATLAB processing.

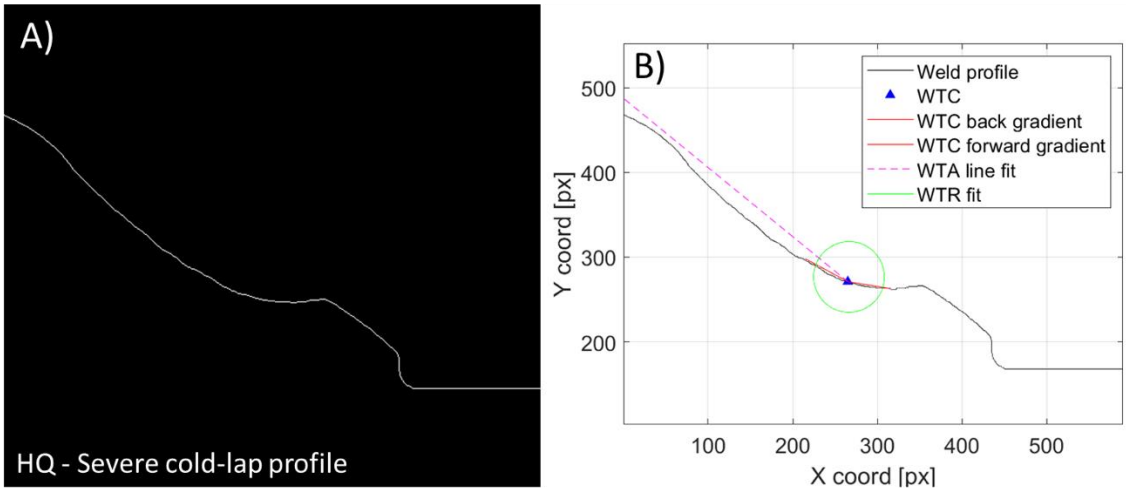

Figure 3.30 HQ weld profile with severe cold-lap defect - A) original single-pixel weld profile; B) weld toe geometry extraction after MATLAB processing.

Figure 3.31 shows a weld toe profile, from an LQ weld, where the profile is steep, and the WTC is correctly defined. In subsequent images, an undercut forms, initially the WTC is identified correctly, Figure 3.32 but as it gets deeper and steeper, the WTC is misplaced, Figure 3.33.

It is clear that the WTC identification struggles to correctly identify the WTC in the presence of flaws in both the LQ and HQ welded joints. The algorithm is dependent on a number of parameters, i.e. length of profile used for computing the best fit vectors at each pixel and the region of interest analysed, which is set on the WTC position from the previous image. The errors are not too dissimilar to those initially observed by Crump [9] for welded joints similar to the HQ welds in this work. For vector path lengths between 500 µm and 1000 µm, Crump observed an average WTC position error of 12% across 800 images.

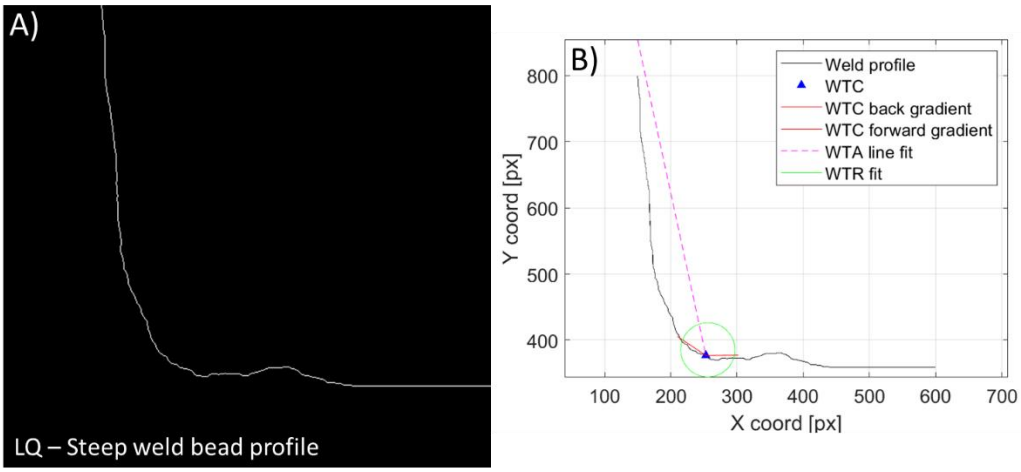

Figure 3.31 LQ steep weld bead profile - A) original single-pixel weld profile; B) weld toe geometry extraction after MATLAB processing.

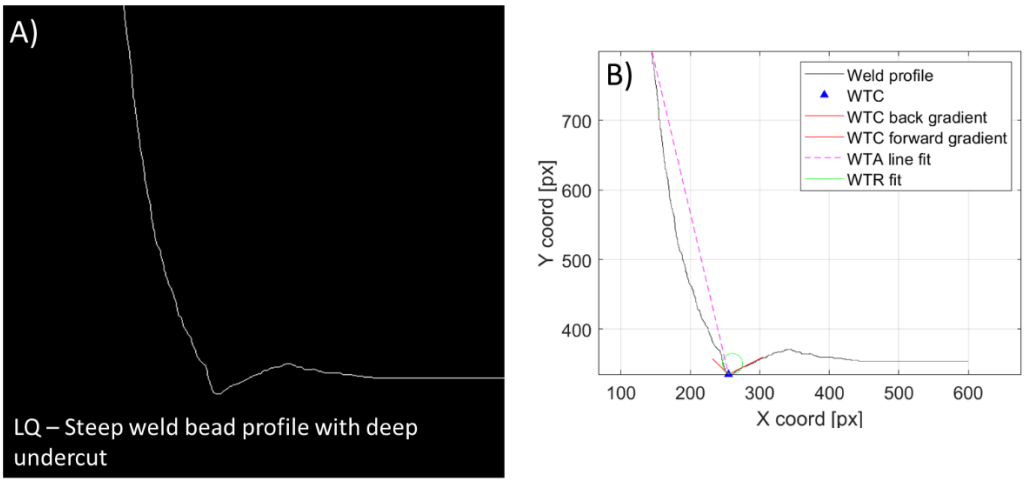

Figure 3.32 LQ steep weld bead profile with a deep undercut defect- A) original single-pixel weld bead profile; B) weld toe geometry extraction after MATLAB processing.

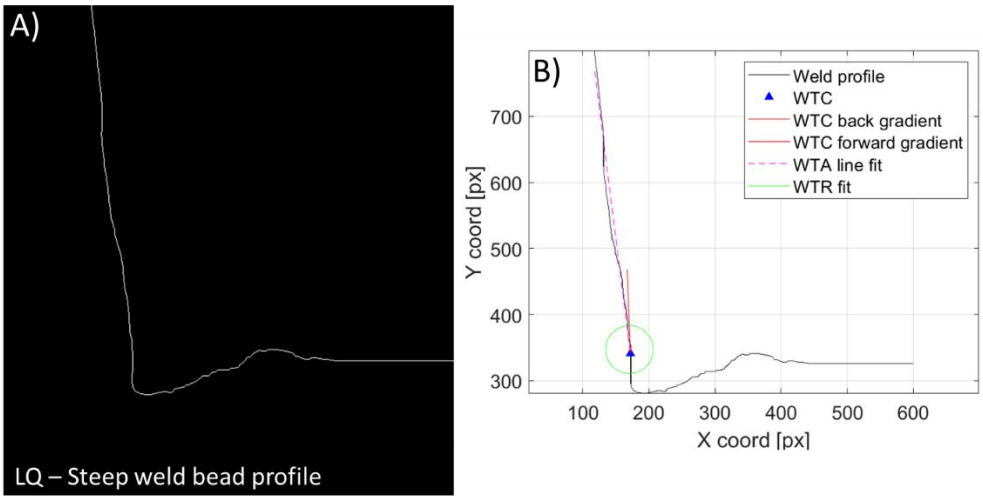

Figure 3.33 LQ steep weld bead profile - A) original single-pixel weld bead profile; B) weld toe geometry extraction after MATLAB processing.

3.4.4.2 Weld Toe Angle (WTA)

The WTA (α in Figure 3.1) is calculated by evaluating the angle between two lines, one fitted to the weld bead and one to the baseplate, with the baseplate assumed to be horizontal. The weld bead line was fitted using the linear best-fit 'Polyfit' function in MATLAB, considering points on the weld bead up to a vertical distance from the identified WTC of 1.75 mm. This distance was selected from [9], it should however be noted that for the matchstick specimens, the vertical distance was reduced to 0.75 mm as the weld bead height in each image was less than 1.75 mm.

When computing WTA, a modification was made to the processing algorithm by introducing a new parameter, referred to as the 'angle check'. This is the angle between the WTA line fit and the WTC back gradient (vector), see Figure 3.34. The purpose of this parameter was to improve the WTC positioning in image slices that resulted in erroneous results (this was included in the data given in section 3.4.4.1). It worked by identifying the deviation in the global WTA (considering up to 1.75 mm of the weld bead) and the local WTA (considering up to 0.5 mm of the weld bead).

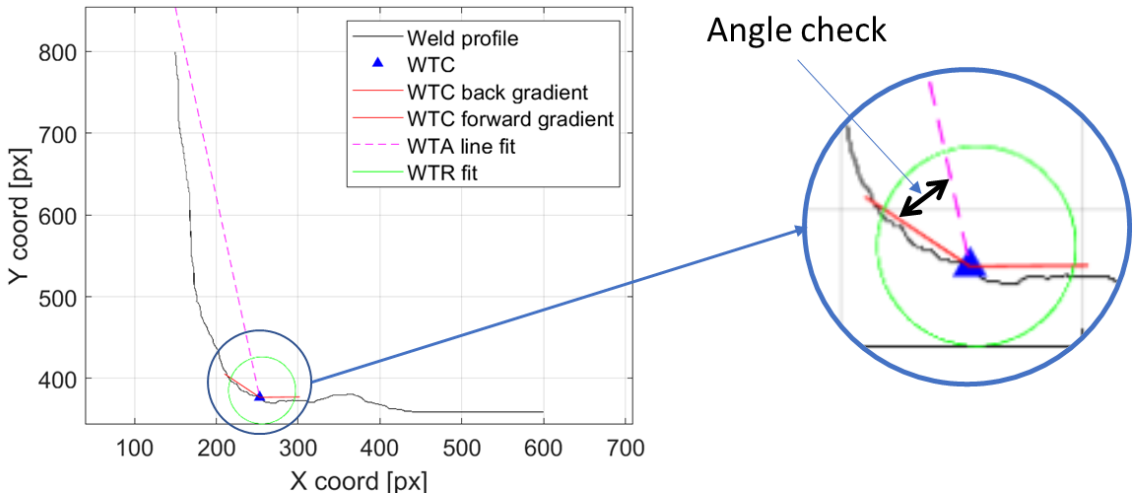

Figure 3.34 Schematic depicting angle check - angle between WTA line fit and WTC back gradient.

The WTA results are provided as a histogram in Figure 3.35 and as a box and whisker plot in Figure 3.36. Results are given for 40,920 image slices; 6980 image slices were not included in the analyses as their WTC positions were deemed incorrect. The majority (>60%) of WTAs were between 35°-50° and the median WTA was just less than 45°, which is the angle often assumed in assessments when the weld toe is mathematically simplified.

Individual specimen WTA distributions are presented in histograms in Figure 3.37 and in box and whisker diagrams in Figure 3.38. It should be noted that the count scale (y-axis) for specimens T10, T11, T12 and T15 in the histograms is different from T6, T7 and T8 as they are from scan sets of different resolutions. For example, T10 is from Scan Set 2, which has approximately half the resolution of T6 from Scan Set 1, thus the volumes from Scan Set 1 will have approximately twice as many image slices associated with them (for the same length of weld toe). From both visual representations, it is evident that the LQ welds have consistently and significantly larger WTAs compared to those of the HQ specimens. For the LQ welds, the median WTA's for each specimen were 64° and 68°, in comparison, for the HQ welds, the median WTA's for each specimen were between 35° and 45°.

The LQ specimens had significantly larger WTAs as compared to the HQ specimens, which is thought to be a consequence of the welder intentionally increasing the weld torch angle during welding to create a steep weld bead.

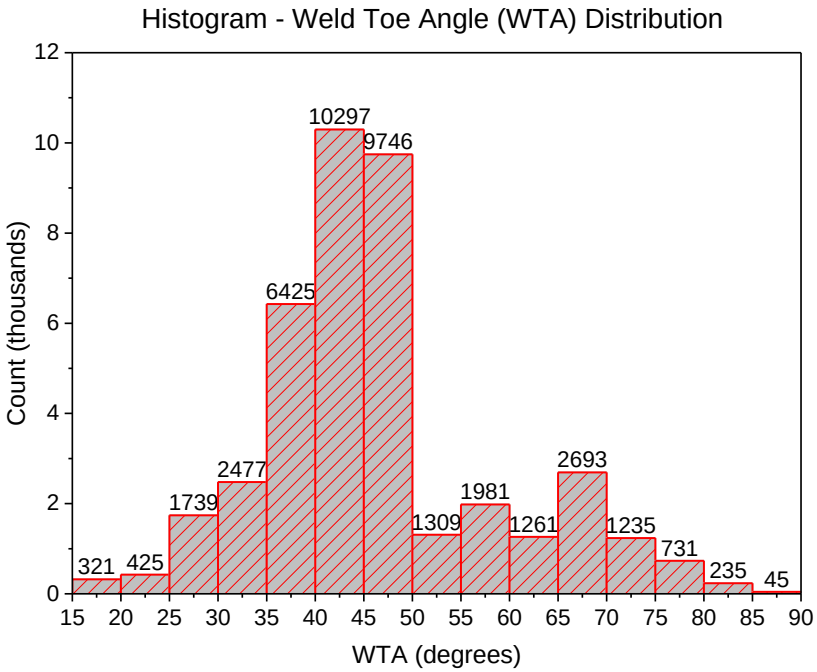

Figure 3.35 Histogram of entire WTA distribution.

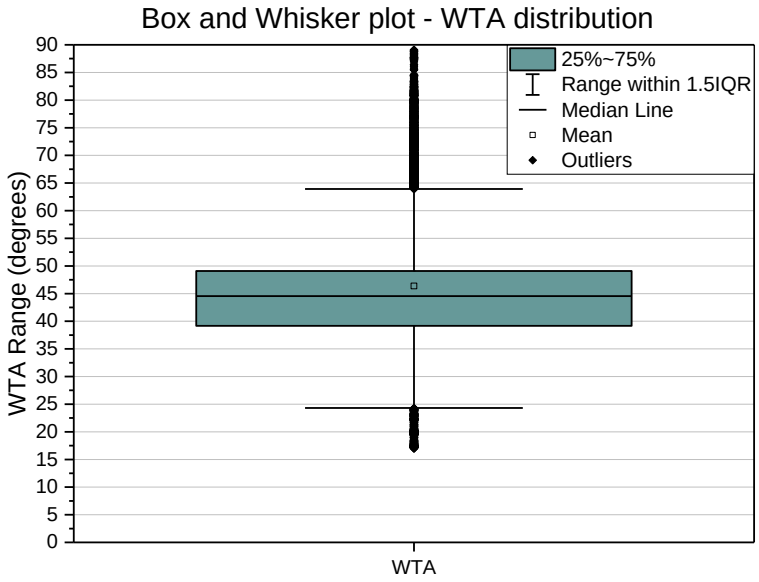

Figure 3.36 Box and whisker plot of entire WTA distribution.

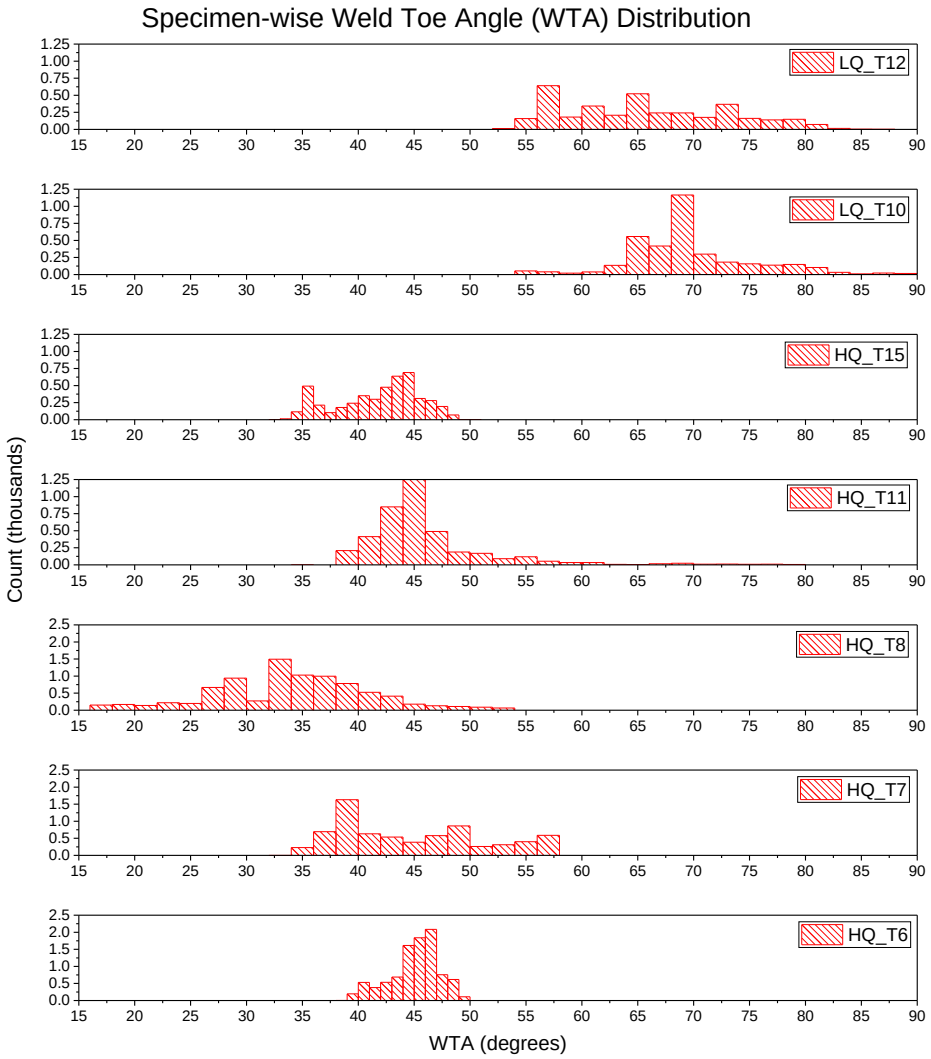

Figure 3.37 Specimen-wise histogram of WTA distribution. Please note that the count scale for HQ_T11, HQ_T15, LQ_T10 and LQ_T12 is different from the bottom three plots.

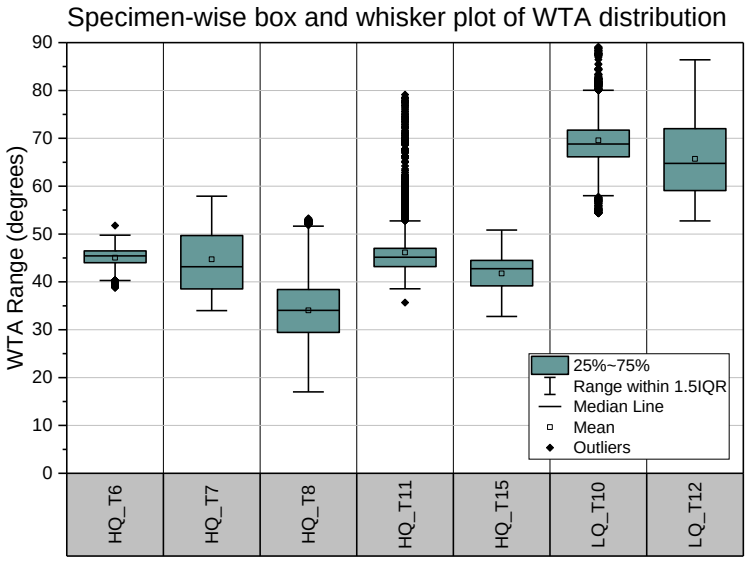

Figure 3.38 Specimen-wise box and whisker plot of WTA distribution.

3.4.4.3 Weld Toe Radius (WTR)

It has been known that lower values of WTR (independent of WTA) result in severe stress concentration at the weld toe [63, 68, 70, 109, 110, 141, 142]. The difficulty of accurately measuring the WTR in addition to not having a consistent measurement method due to the complex weld toe geometry has also been highlighted in previous literature [142]. Significant improvements in techniques of capturing the true weld toe geometry have increased the possibility of measuring lower and therefore more severe values of WTR. In most industrially accepted fatigue lifing approaches of welds [4, 15, 17, 143, 144], an ideal geometry with a fixed WTR is considered. PD ISO/TR 14345:2012 provides three of methods to calculate local weld toe geometry, from using welding or a radius gauge to measuring the least radius by fitting the smallest circle to at least three points on the weld profile [4].

The MATLAB algorithm uses two methods to calculate the WTR [9]. The first method, the Lieurade circle fit, fits the smallest circle possible between two weld profile coordinates, each at a given distance both sides of the identified WTC [145], Figure 3.39. This distance is chosen based on a qualitative assessment done by the author of the algorithm. The second method is called the least mean-squared Pratt's circle fit [146]. This method is based on fitting a circle to the weld profile coordinate points that exist within a small arc of a circle, as shown in Figure 3.40. Both methods were implemented on each specimen to get two values of WTR. For obtaining conservative results, the lowest of the two calculated WTR values were chosen for each section.

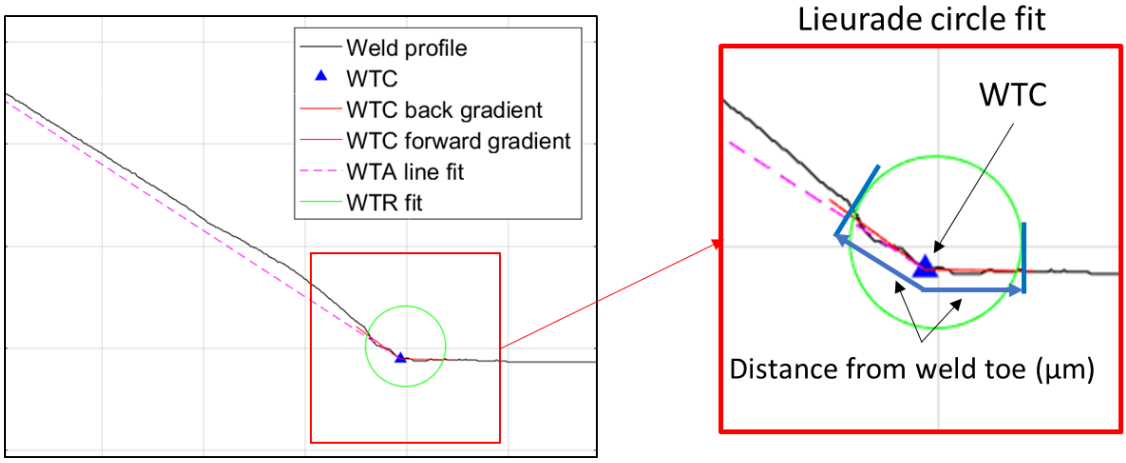

Figure 3.39 WTR determination using Lieurade circle fit, by fitting the smallest circle between weld profile coordinates a set distance from the identified WTC. From [9].

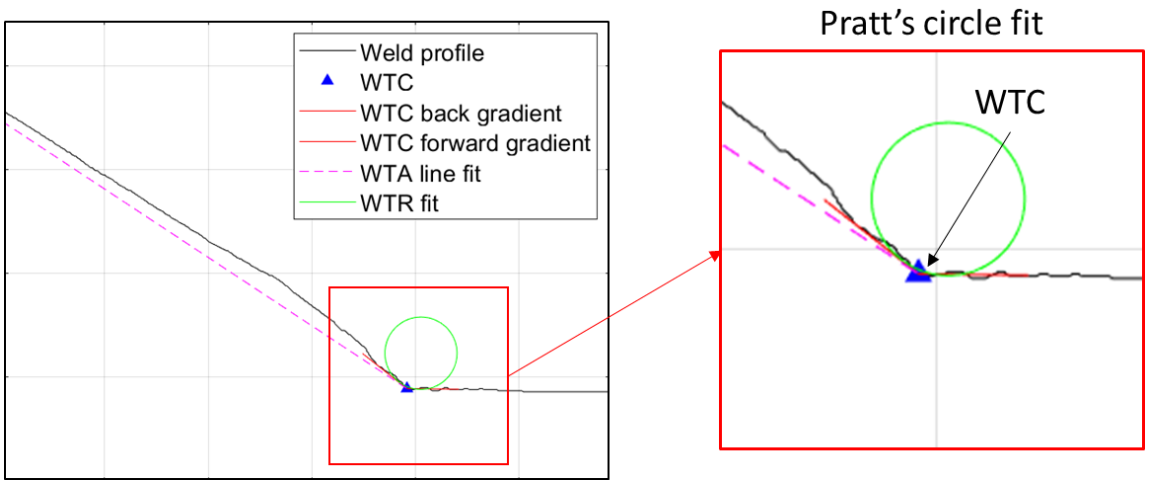

Figure 3.40 WTR determination using least mean-squared Pratt's circle, by fitting the smallest circle to the weld profile coordinates within a small arc of a circle. From [9].

The distribution of obtained WTR values using both methods is shown in a histogram in Figure 3.41 and box and whisker plot in Figure 3.42. Using the Lieurade method, the values were concentrated around 0.425 mm as this method is heavily dependent on the pre-determined distance chosen before the evaluation of WTR. The Pratt's circle method suffered from erroneous calculations, and therefore any WTR values larger than 2 mm have been discarded from the histogram. The specimen-wise distribution of minimum WTR obtained from both methods has been presented as a histogram in Figure 3.43 and a box and whisker plot in Figure 3.44. The highest concentration of values was around the pre-determined path length, but lower and therefore more severe values of WTR have been recorded. From the plots, the low-quality (LQ) samples had the most severe WTR values due to the deep undercuts that were intentionally created during the welding process.

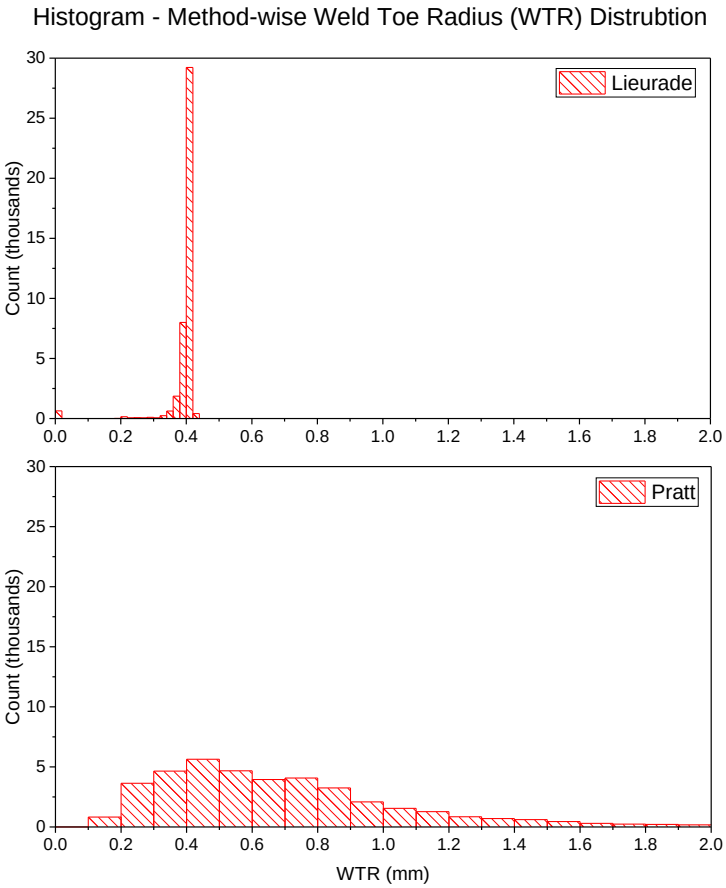

Figure 3.41 Histogram of WTR distribution based on the method used in the algorithm.

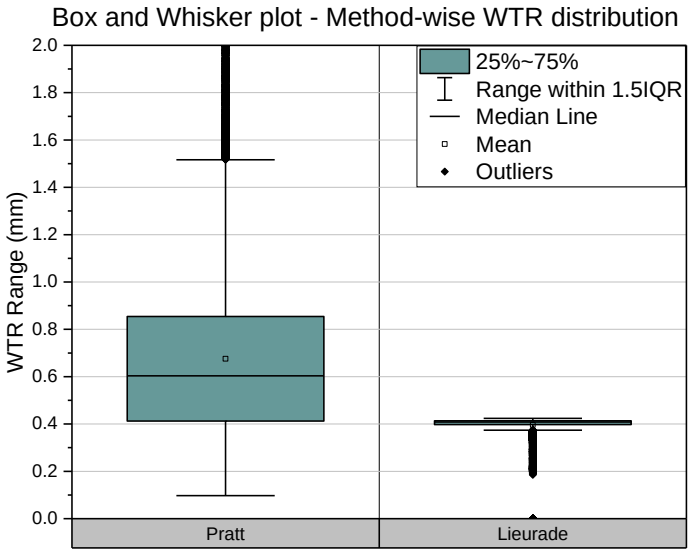

Figure 3.42 Box and whisker plot of WTR distribution based on the method used in the algorithm.

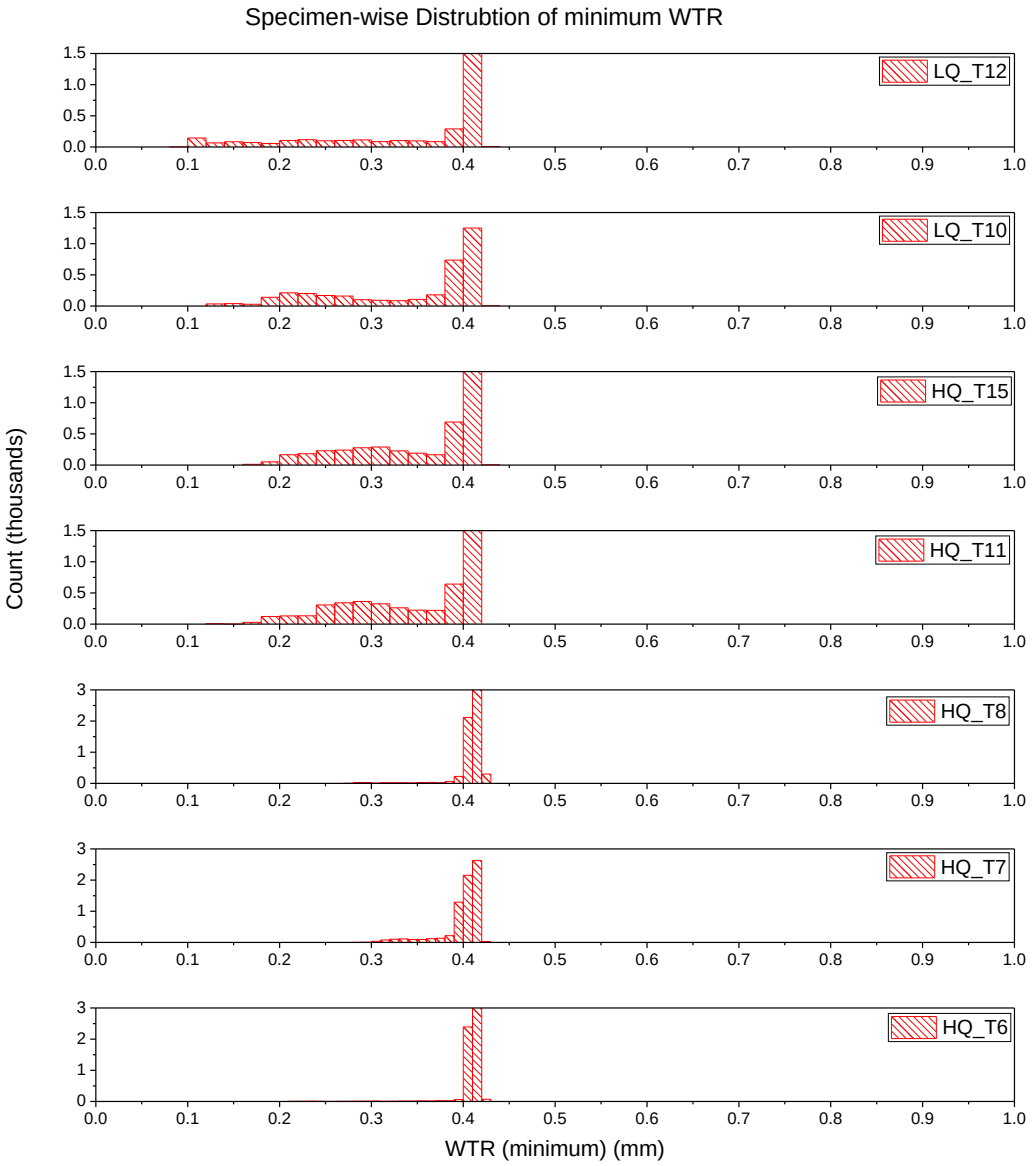

Figure 3.43 Specimen-wise histogram of the minimum WTR from the two methods. Please note that the count scale for HQ_T11, HQ_T15, LQ_T10 and LQ_T12 is different from the bottom three plots.

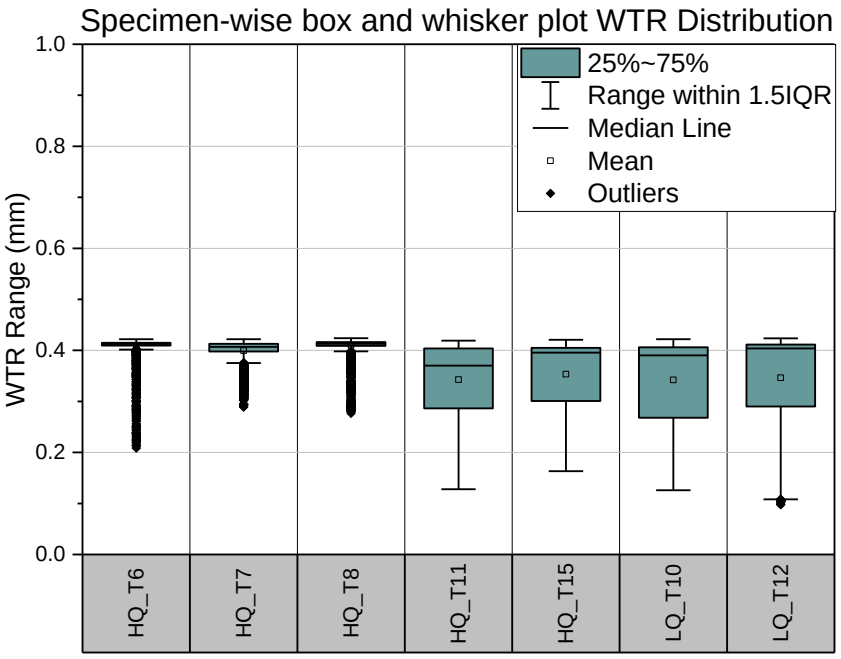

Figure 3.44 Specimen-wise box and whisker plot of WTR distribution.

3.4.5 3D Volume Preparation for Finite Element Analysis (FEA)

CT scan sets 1 and 2 were prepared for 3D FEA. The scan volumes were converted into a series of 2D images, which were cropped to the region of interest to reduce the file size further (Figure 3.45a) and then processed in ImageJ using the MinError(I) thresholding algorithm [138] to obtain the surface profile of the weld (Figure 3.45b). An algorithm was written in MATLAB to extend each image making it representative of the full weld bead (Figure 3.45c). Figure 3.45d shows the final image which is a symmetric representative of the actual test specimen (symmetry was used in the FEA to reduce meshing and analysis time). The inset in Figure 3.45d shows that the true geometry of the weld has been retained in the final shape. The ImageJ macro and the MATLAB code for image processing has been provided in the Appendix A.2. The processed image volumes were used for FE stress analysis, which will be discussed in detail in Section 3.5.

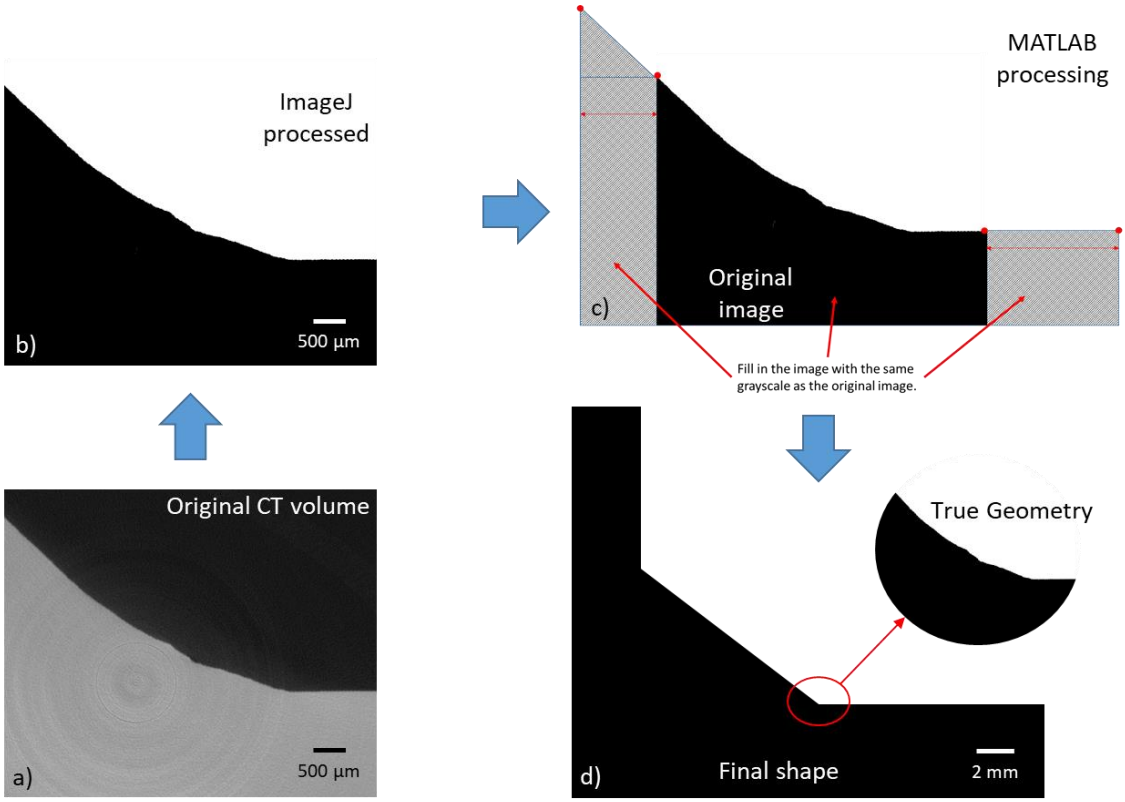

Figure 3.45 Image processing steps - a) slice from the original volume (cropped); b) processed image after ImageJ processing; c) image extended in MATLAB; d) the final shape of the image which is representative of a quarter of the test specimen. The inset shows that the actual geometry has been retained in the final shape.

3.4.6 CT Scan Data Analysis – Summary

The processes involved in preparing the CT scan volumes for FE stress analysis are discussed in this section. The process of geometry extraction was based on using an improved version of a previously developed algorithm [9] on specimens tested during this project. The results will be used to analytically evaluate the elastic SCF at the weld toe, which is used later in Chapter 6 for fatigue life estimations. Preparation of volumes for 3D stress analysis has been briefly discussed. This work will be elaborated upon in much greater detail in section 3.5.

3.5 Three-Dimensional (3D) Finite Element Analysis (FEA)

Section 3.2.1 provided a background to the work that was performed to develop an understanding of the impact of weld toe geometry on the stress distribution, particularly stress concentrations at fatigue-prone regions i.e. the weld toe. Studies involving both ideal and true geometries were identified and discussed in detail in Section 3.2.1. Section 3.4.4 provided a distribution of weld toe geometry parameters extracted from a MATLAB algorithm. It was seen that the data was still

dependent on the initial choice of parameters required by the algorithm. In addition, parametric equations available in the literature for calculating values of SCF at the weld toe are based on ideal weld geometries [102, 104, 147-149]. WTA and WTR values obtained using the algorithm did not all fall within the limits of the available parametric equations. For this purpose, Crump provided two sets of modified parametric equations for SCF evaluation [9]. These modifications are based on the range of weld toe geometry parameters and 2D FEA solutions of the same weld sections that were obtained in the EngD thesis of J. Crump [9]. The SCF results thus obtained gave a more conservative SCF distribution compared with those calculated from the previous parametric equations given in the literature. This was primarily due to the improvements in the resolution at which the weld toe geometry was extracted (X-Ray μ-CT scanning). The limitation of this work was that as the weld bead geometry and the defects have a three-dimensional shape, the 2D model would not be able to capture adequately the stresses at the weld toe. It was therefore considered that a 3D FE stress analysis should be carried out with suitable solving elements and boundary conditions to represent the actual test conditions.

This section therefore discusses the method used to generate 3D FE models of the weld toe geometry as captured by the X-Ray μ-CT scans described in Section 3.4. The objective of each model is to generate a high-resolution stress distribution map of the weld toe that takes into account the effect of the inherent flaws. A “true” representative distribution (compared with what has been achieved in the previous literature, (Table 3.1) of SCFs could help in improving the estimates of the fatigue strength of such welds and so comparing welding parameters to optimise welded joints. The work in this section has been divided into steps as shown in Figure 3.46. ABAQUS was used as the FE solver, Simpleware ScanIP was utilised for meshing, and ImageJ and MATLAB were employed to create volumes from the processed stack of CT images.

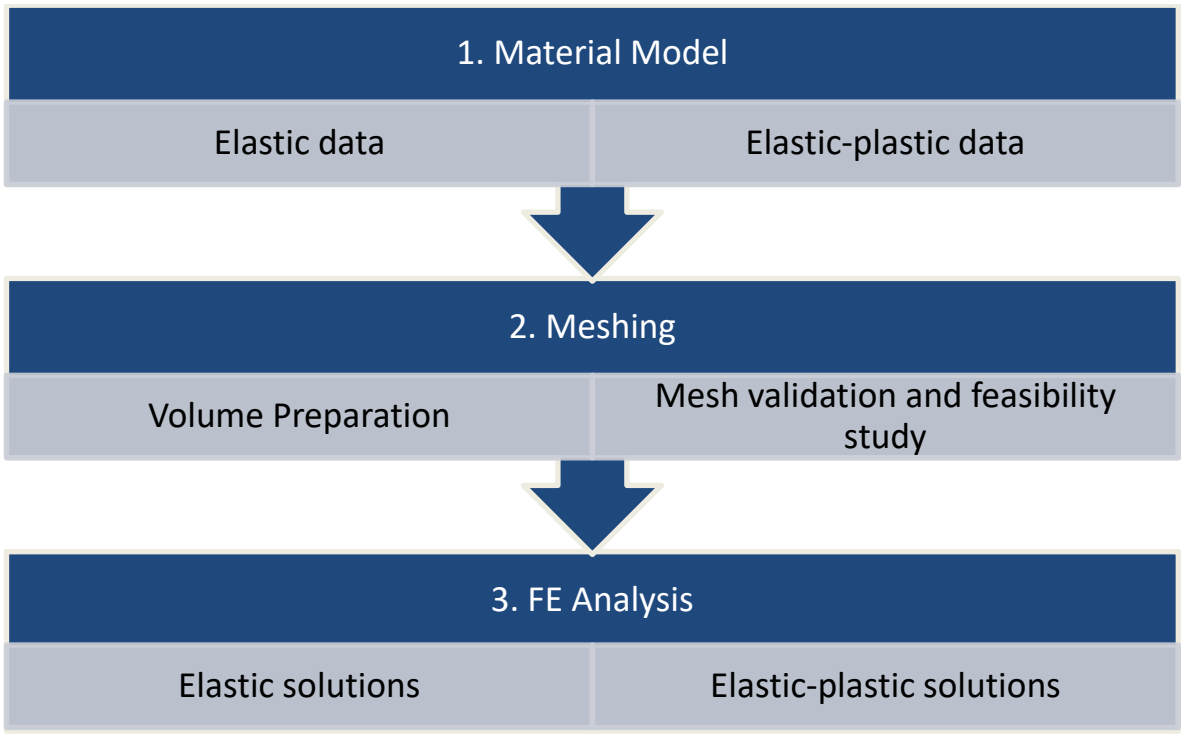

Figure 3.46 Steps involved in FE analysis of scanned weld toe geometries.

3.5.1 Material Model

For elastic as well as elastic-plastic FE analysis, material properties were taken from the C-Mn parent material complying with BS EN10025-2 S355 J2+N [132]. These properties were assumed for the heat affected zone (HAZ) and weld metal (WM) as it was not possible to incorporate multi-material models in ScanIP without different grayscales for the different materials. No distinguishable grayscale variation was observed in the CT scan volumes since the densities of each microstructural zone are very similar.

For elastic stress-strain calculations, a Young's Modulus (E) of 190 GPa and Poisson's ratio (v) of 0.3 were used. Young's Modulus was obtained from the uniaxial tensile tests described in Section 3.3.1.1. It is important to note that the value for Young's Modulus for structural steel is generally found to be higher than 200 GPa (203 GPa as per BS7910 [5]). However, the value of 190 GPa, as was obtained from the tensile tests, was used for the evaluation as this would give relatively conservative results compared to those obtained using a higher Young's Modulus.

For the elastic-plastic stress-strain calculations, both elastic as well as plastic material properties were necessary. Elastic properties were the same as mentioned above, and the plastic material properties were taken from the plastic region of the stress-strain curves (Figure 3.8). The true stress and true strain were first evaluated from the engineering stress-strain data from the tensile test, based on Equation 3-2 and Equation 3-3. The elastic component of true strain was subtracted from

the total (true) strain to obtain the plastic component of true strain, based on Equation 3-4 and Equation 3-5. The stress-strain curves depicting the engineering, true and plastic stress-strain data is shown in Figure 3.47. Values beyond the point at which engineering stress reached the ultimate tensile stress (UTS) were not considered.

$$\sigma_{TRUE} = \sigma_{ENGINEERING}(1 + \varepsilon_{ENGINEERING}) \quad 3\text{-}2$$

$$\varepsilon_{TRUE} = \ln(1 + \varepsilon_{ENGINEERING}) \quad 3\text{-}3$$

$$\varepsilon_{PLASTIC} = \varepsilon_{TRUE} - \varepsilon_{ELASTIC} \quad 3\text{-}4$$

$$\varepsilon_{ELASTIC} = \frac{\sigma_{TRUE}}{E} \quad 3\text{-}5$$

Where,

σ_{TRUE}	True stress
$\sigma_{ENGINEERING}$	Engineering stress
ε_{TRUE}	True strain
$\varepsilon_{ENGINEERING}$	Engineering strain
$\varepsilon_{PLASTIC}$	Plastic strain component of true strain
$\varepsilon_{ELASTIC}$	Elastic strain component of true strain
E	Young's modulus

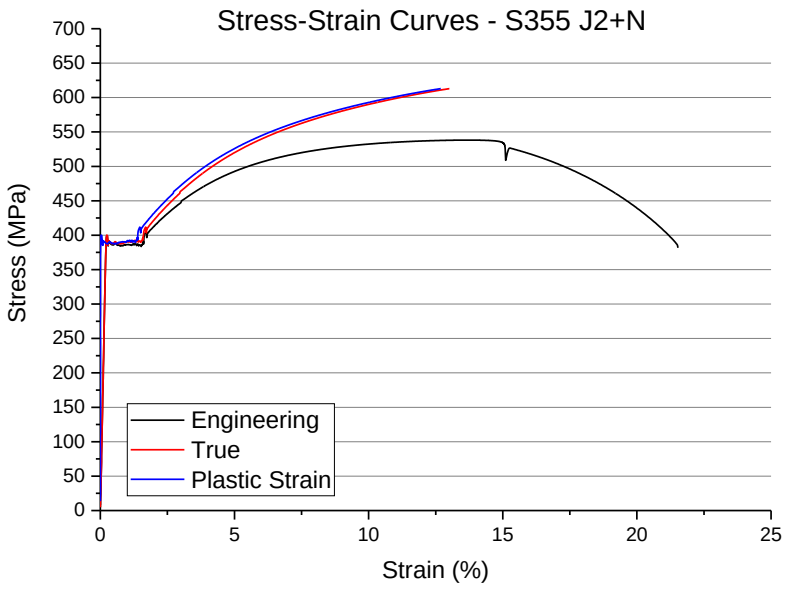

Figure 3.47 Stress-strain curves obtained from tensile tests on the base metal (Structural steel S355 J2+N).

To model the material softening/hardening behaviour in response to mechanical loading, several constitutive models are available [150], some of which are available for selection within the FE

software used in this project, ABAQUS [151]. The isotropic and kinematic hardening models and the combined constitutive model of the two were available for selection. Each model has certain capabilities based on how the model predicts the monotonic and cyclic deformation response of the material. These responses include but are not limited to: elastic shakedown, the Bauschinger effect, cyclic hardening/softening before a stable hysteresis loop develops (in low-cycle fatigue LCF strain-control testing), amongst others [14].

The yield surface concept can be used to describe the different constitutive models that were available for selection in this work [14]. In a principal stress space, if the stress state lies within the von Mises yield surface, material behaviour is elastic. If the stress state lies on the yield surface, the material is deemed to have reached its yield point and exhibits plastic deformation. As plastic deformation occurs, the stress state continues to lie on the yield surface, although the yield surface itself may undergo change in its shape and size. Isotropic hardening is represented by the yield surface changing size uniformly in all directions with plastic straining. No change in shape occurs. Isotropic hardening can also be used in the case of materials which exhibit strain softening (the yield surface will uniformly reduce in size) or hardening followed by softening. Translation of the yield surface in the direction of the outward normal is representative of the kinematic hardening model and the FE software, ABAQUS, uses kinematic hardening to model the cyclic loading of metals [151]. If the translation is without any change in shape or size, it is referred to as linear kinematic hardening. A combined isotropic and kinematic hardening model is also available in FE software which covers for certain limitations of isotropic and kinematic hardening models. Namely, the Bauschinger effect cannot be modelled by a perfectly isotropic hardening model; the linear kinematic hardening model is inadequate for modelling elastic shakedown [14]. Figure 3.48 presents the differences between these models in a principal stress space with the von Mises yield surface assumed to be circular. This is adequately documented by the common use of the combined hardening model in recent literature on modelling cyclic material behaviour [152-154].

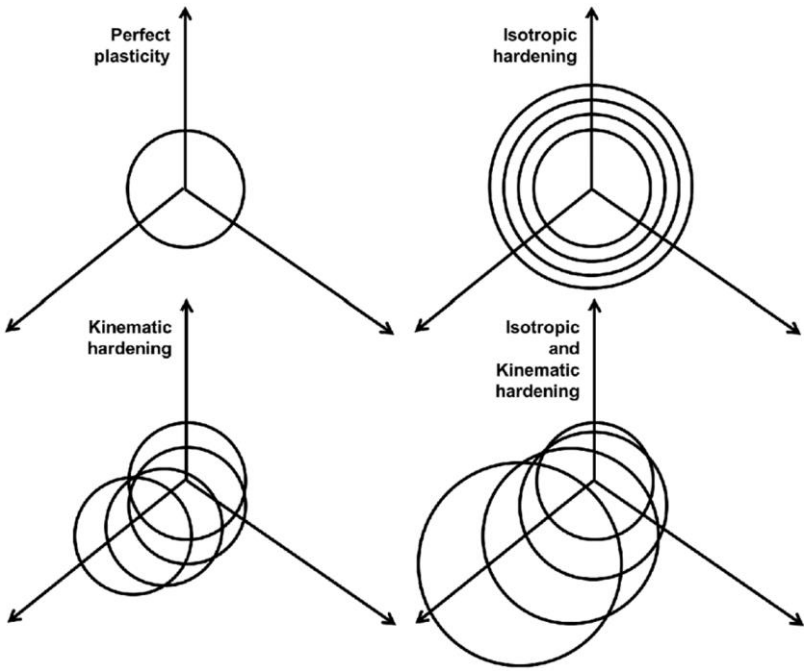

Figure 3.48 Illustration of the von Mises yield surface for each kind of constitutive hardening model in the principal stress space. From [154].

For this project, only monotonic loads were applied since the large number of elements used in each model would have made cyclic loading analysis too computationally demanding. Therefore an isotropic hardening model was used instead of a kinematic hardening model (as this is usually used for cyclic hardening). For increased accuracy, the combined isotropic and kinematic hardening model should have been chosen, but its implementation would have required additional low-cycle fatigue (LCF) tests to be carried in order to obtain the constitutive hardening model parameters.

3.5.2 Meshing

The CT scan volumes were processed as described in Section 3.4.5. To obtain representative results and mesh convergence, a high density of elements was required at the weld toe and the region surrounding the weld toe. This would not be possible if the entire volume of each weld section was treated as a single 3D entity for meshing (in terms of both computational time and ability). Therefore, each CT scan volume was divided into sub-volumes (based on meshing time and final mesh size), and these sub-volumes were then meshed and solved. The size of each sub-volume was constant for each scanned weld but was different between the two scan sets, as shown in Table 3.12. The difference in the size was due to the different scan resolutions (approximately 5 µm for Scan Set 1 and 10 µm for Scan Set 2). Therefore, the number of slices representing the same geometrical distance is different for each set.

Table 3.12 Sub-volume size for each CT scan set.

Parameter	Scan Set 1	Scan Set 2
Number of slices	150	100
Weld toe length	0.73 mm	1 mm
Total sub-volumes covering the entire weld toe	62-64	48-50

The sub-volumes were converted to 3D meshed models for FEA using the proprietary meshing software - ScanIP, shown in Figure 3.49. ScanIP offers meshing algorithms which allow for very fine meshing of irregular weld bead geometries. ScanIP offers two mesh creation algorithms – "+FE Grid" and "+FE Free". Although both are equally adept at meshing complex geometries, the "+FE Free" mesh creation algorithm was used because it offers better control over the number of elements by allowing feature-based mesh refinement. Feature-based mesh refinement permits the preservation of small features at a user-defined ROI (the weld toe in this case) while allowing for increased element size elsewhere [155].

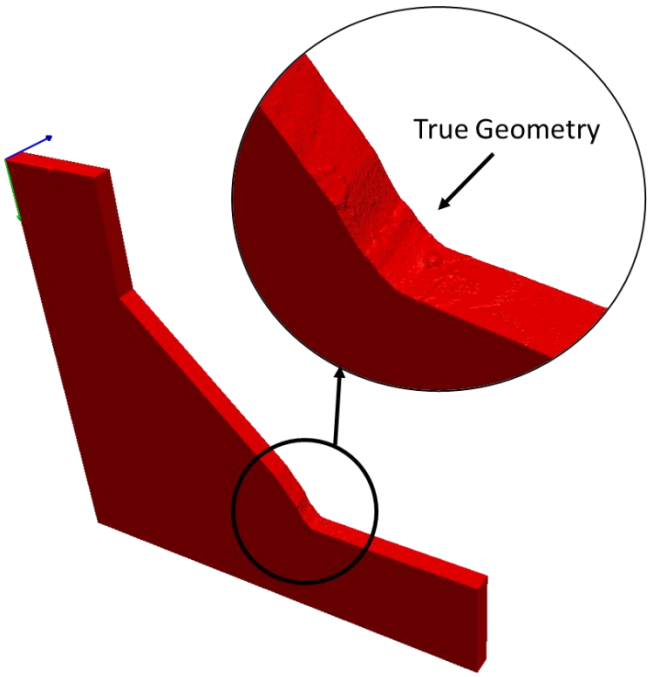

Figure 3.49 3D sub-volume rendered in ScanIP. The inset highlights the presence of the true geometry at the weld toe.

Two different types of elements were available in the "+FE Free" meshing algorithm -

1. Linear tetrahedral (C3D4) – The simplest of the available options. Gives faster meshing time for the same level of accuracy, but for accurate results, a vast number of elements are required [151], increasing the meshing time considerably.
2. Quadratic tetrahedral (C3D10) – Quadratic tetrahedral elements are the best available option in ScanIP for meshing the irregular weld geometry in terms of meshing time, solving time and accuracy of an FE solution. ScanIP offers two types of quadratic tetrahedral elements which differ in the initial position of the nodes (also shown in Figure 3.50) –
    a. Straight edges – The mid-side nodes are added but are not moved from their original position, thus leaving a straight-edged quadratic tetrahedron.
    b. Curved edges – The mid-side nodes are snapped to the input surface (the geometry of the weld), thus creating tetrahedra with curved edges.

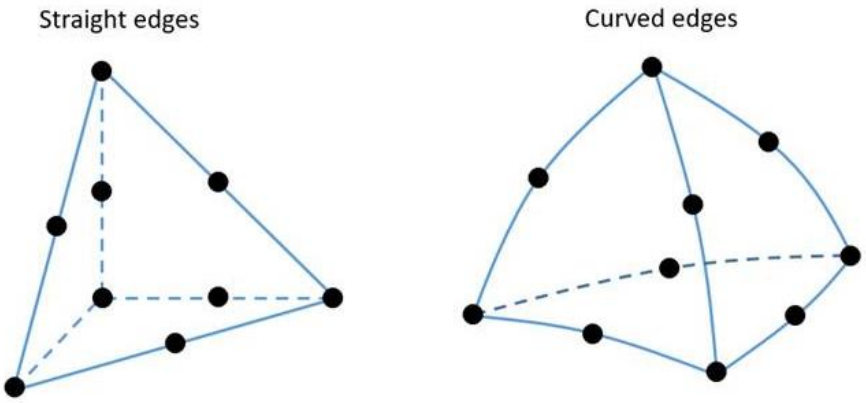

Figure 3.50 Schematic of the two types of quadratic tetrahedral elements - Straight edges (left) and curved edges (right).

The curved edge quadratic tetrahedral elements were chosen as they would result in the lowest loss of high-resolution surface information. For stress concentration features, they provide more accurate results as compared to linear tetrahedral elements [151].

A mesh validation study was performed to determine the optimum mesh density for the local weld toe models that can be achieved within acceptable meshing times (less than 2 hours per sub-model). With quadratic elements, the number of nodes generated per element is higher (relative to linear tetrahedral elements), and the FE software ABAQUS is not able to solve efficiently problems with more than 6 million nodes within a practical amount of time (considered to be 6 hours of solving time). These factors make a mesh density study critical to obtain analysis results within a timely manner especially when numerous models are to be run.

Mesh refinement was applied at the local weld toe geometry in the form of four concentric cylinders centred at the weld toe, as shown in Figure 3.51. In the case of overlapping regions, the mesh size of the inner cylinder was given preference. For example, Cylinder 1 is overlapped by Cylinder 2. But, the properties of the elements within Cylinder 1 will be controlled by the user-defined properties of Cylinder 1.

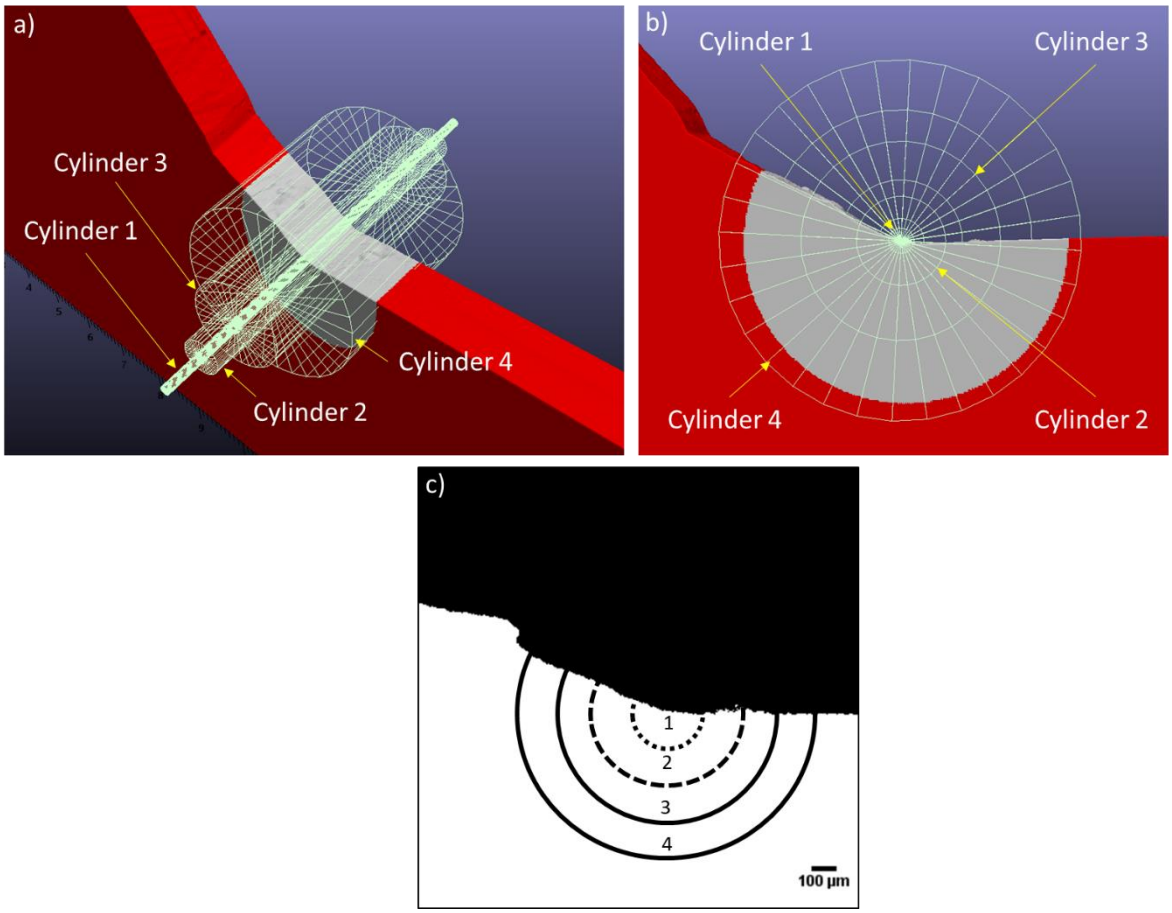

Figure 3.51 Mesh refinement zones in the form of four concentric cylinders, each of different element sizes - a) isometric view of the four mesh refinement cylinders; b) side view; c) schematic of the mesh refinement zones on a binarized CT image.

Mesh validation and optimisation studies were conducted to ascertain the optimum meshing parameters for FEA and convergence. This was based on changing the following parameters in the meshing software -

1. Element Size - The smallest element size (cylinder 1 of the four mesh refinement cylinders) for each scan was chosen to be the resolution of the X-Ray µCT scan. Smaller elements were also considered, but the mesh converged at the value of the CT scan resolution, and the relative time penalty was very high. Figure 3.52 represents the mesh validation done on a particular sub-volume with the smallest element size (and CT scan resolution) of 4.9 µm,

and a cylinder 1 radius of 0.2 mm. Outside the mesh refinement zones, the element size was allowed to increase up to a maximum element size of 0.2 mm for all the CT volumes.

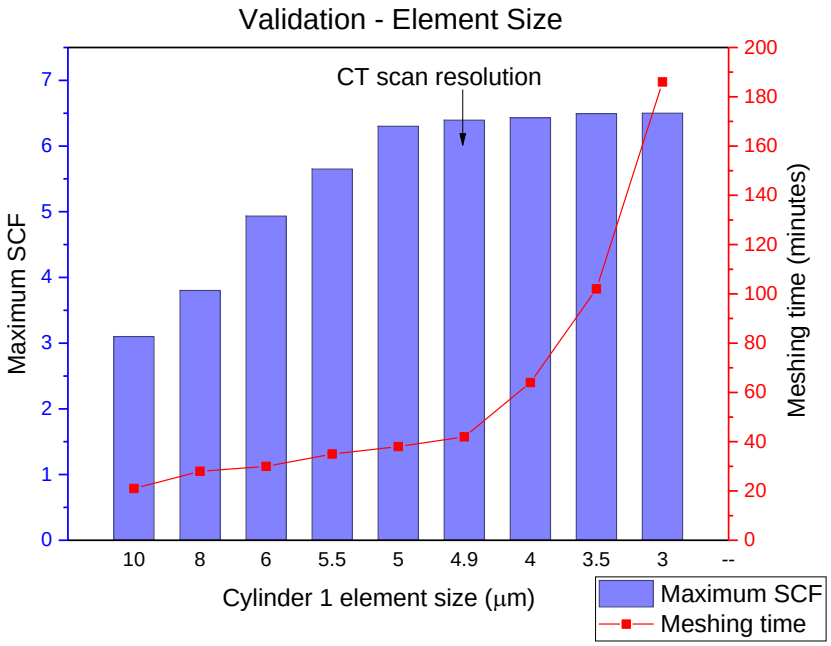

Figure 3.52 Mesh validation - choice of element size.

2. Cylinder 1 size – Cylinder 1 of the four mesh refinement cylinders has the smallest element size. It was, therefore, essential to choose the optimum size of the cylinder for covering the irregular weld toe geometry, solving accuracy, meshing time and the total number of elements and nodes. The size of the cylinder was given as the radius of the cylinder. Figure 3.53 shows the results from the same sub-volume as shown in Figure 3.52, but the meshes were all generated with an element size of 5 μm. The maximum SCF converged at a cylinder radius of 0.2 mm and did not change further (with increasing cylinder radius) as the most severe stress concentrating feature was already captured within the 0.2 mm radius cylinder.

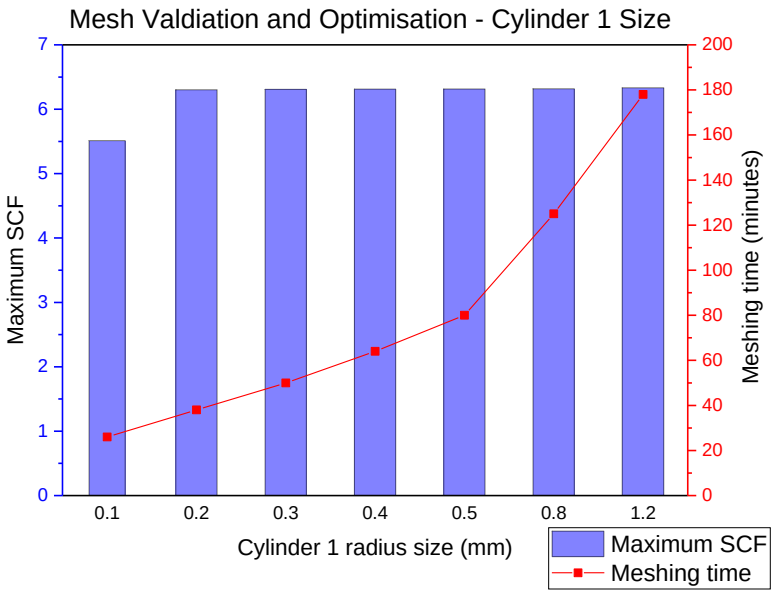

Figure 3.53 Mesh validation and optimisation study - cylinder 1 size.

Once the cylinder 1 radius was optimised, the sizes of mesh refinement cylinders 2, 3 and 4 were progressively increased both in geometry and element size. The final mesh refinement parameters for each of the two scan sets are presented in Table 3.13 and Table 3.14. In addition to defining the size of the mesh refinement cylinders, it was also necessary to define the coordinates of the centre of the cylinder both in terms of the circular cross-section as well as the thickness, as demonstrated in Figure 3.54. Figure 3.54a) represents the centre of the cylinder in the three coordinates as well as the thickness in the Z or through-thickness coordinate. The thickness was chosen large enough to cover the entire weld bead in each sub-volume. Figure 3.54b) shows the possibility of adjusting the cylinder for any waviness in the weld toe by adjusting the rotation of the centre of the cylinder about the three axes. Figure 3.55 presents an example of a meshed sub-volume containing a spatter-like defect. The different mesh refinement zones have also been marked on the figure. This mesh contained a total of 2 million quadratic elements and 2.9 million nodes.

Table 3.13 Mesh refinement parameters for scan set 1.

Parameters	Scan Set 1 (T6, T7, T8)				
	Cylinder 1	**Cylinder 2**	**Cylinder 3**	**Cylinder 4**	**Rest of the Model**
Radius of cylinder (mm)	0.2	0.3	0.5	1.0	NA
Maximum Element size (µm) within refinement zone	4.878 (for T7) & 4.9 (for T6 and T8)	10	20	40	200

Table 3.14 Mesh refinement parameters for scan set 2.

Parameters	Scan Set 2 (T10, T11, T12, T15)				
	Cylinder 1	**Cylinder 2**	**Cylinder 3**	**Cylinder 4**	**Rest of the Model**
Radius of cylinder (mm)	0.2	0.3	0.5	1.0	NA
Maximum Element size (µm) within refinement zone	10	15	20	40	200

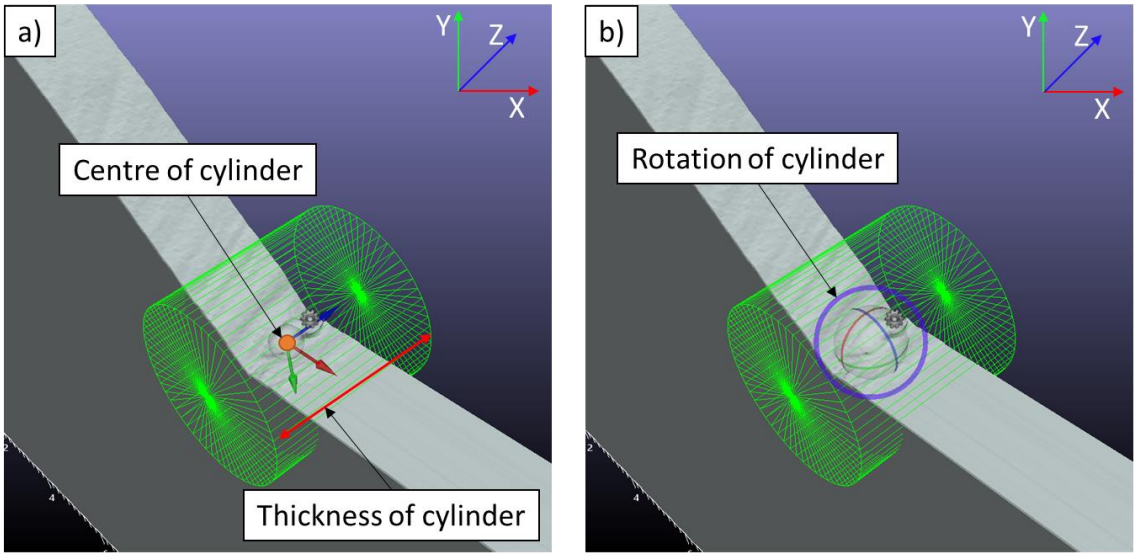

Figure 3.54 Geometric parameters to define mesh refinement cylinder - a) position of the centre of the 3D cylinder and thickness; b) rotation of the 3D cylinder about each of the three axes.

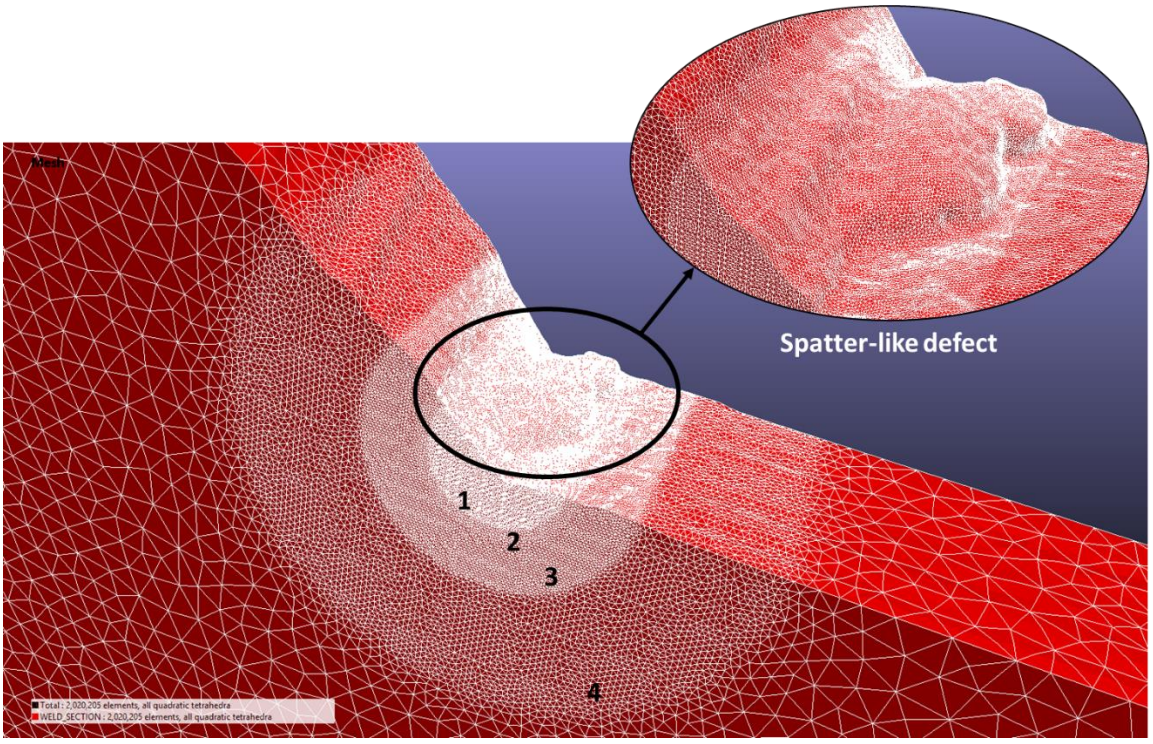

Figure 3.55 Final meshed sub-volume containing a spatter-like defect at the weld toe. The different mesh refinement cylinders have been marked.

For each welded specimen, the length of the entire weld bead was approximately 48-50 mm. Due to the waviness of the weld bead and the resultant irregular weld toe path (shown in Figure 3.56), it was not possible to capture the entire weld toe within a straight cylinder of radius 0.2 mm (cylinder 1 mesh refinement zone). Therefore, it was necessary to further divide the weld bead into sections so that the whole length of the weld toe could be covered. This was manually done by placing the smallest mesh refinement cylinder and observing the extent to which it enveloped the weld toe. This is illustrated in Figure 3.57. The vertical yellow dotted line in the figure defines the volume to the left of that line for which the current cylinder geometry was valid. For the volume to the right of the yellow line, the cylinder geometry will have to be redefined. The coordinates for each of the mesh refinement cylinders were defined accordingly, and a script was written for ScanIP to automate the meshing process. The script has been included in Appendix A.3.

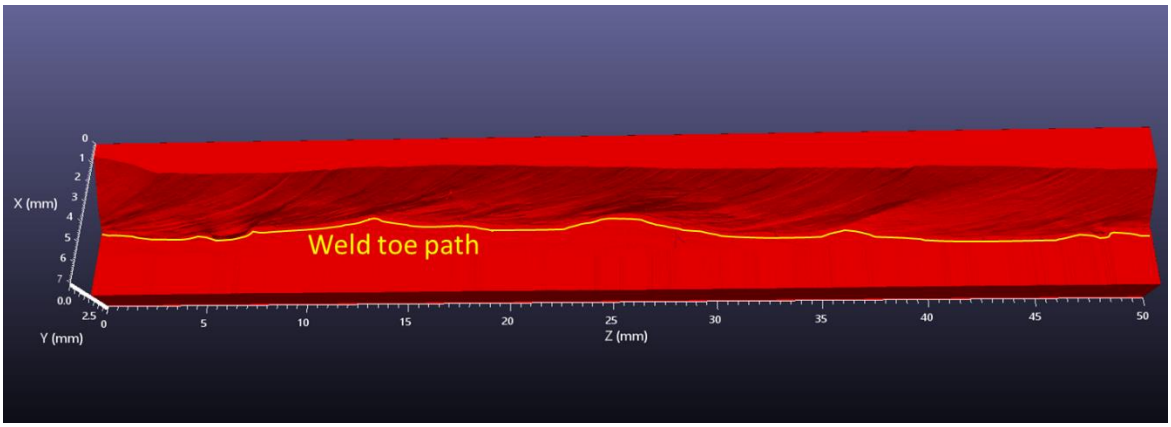

Figure 3.56 Entire weld volume with the irregular weld toe path highlighted in yellow. Specimen - T15.

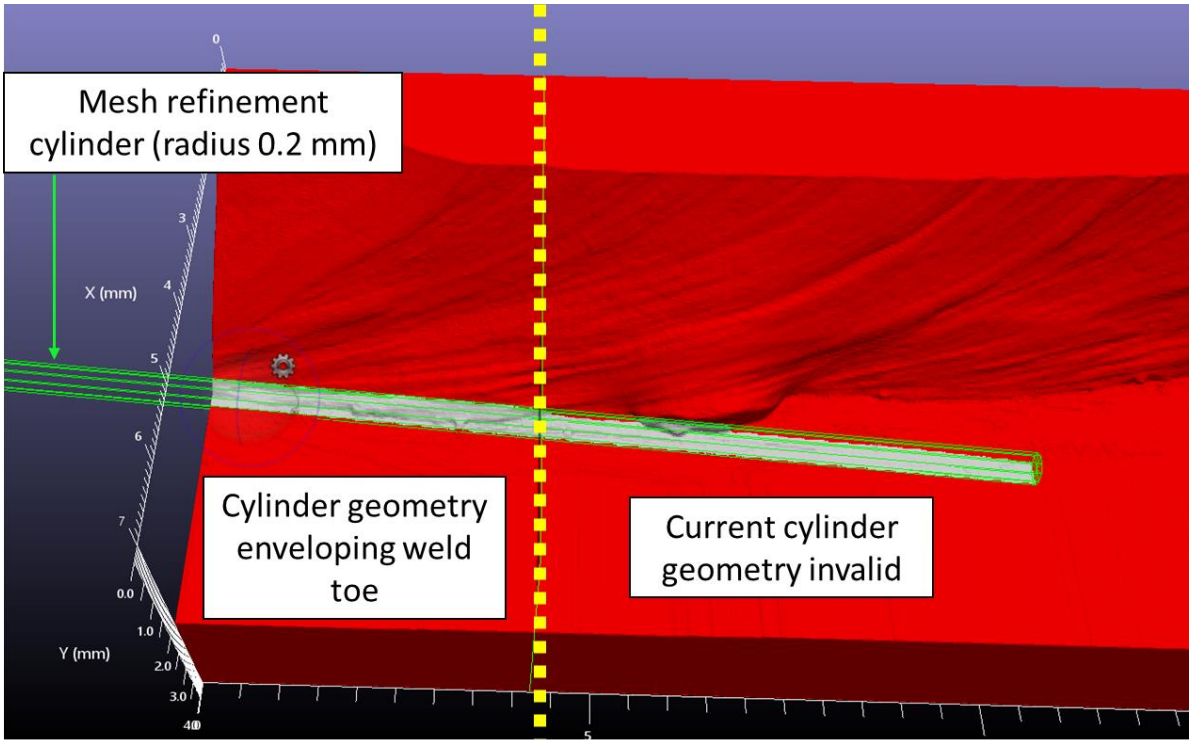

Figure 3.57 Need to divide the entire volume further to cover the entire weld toe in the mesh refinement zone with the smallest element size.

3.5.3 FE Analysis

The meshes created in ScanIP were exported as orphan meshes to import into ABAQUS. A script was written to automatically add the necessary properties and conditions to the input mesh for solving, available in Appendix A.4. Each step of the FE modelling process is discussed below.

3.5.3.1 Material

Material properties were chosen as per the data obtained in Section 3.5.1. For linear elastic solutions, only the elastic properties were considered. For elastic-plastic solutions, both elastic and plastic properties were considered.

3.5.3.2 ABAQUS Steps

Static loading steps were applied where the load was ramped up to the maximum value from an initial value of 10% of the maximum load. The number of increments to maximum load was carried out automatically by the FE solver (default algorithm) based on the number of iterations to convergence at each increment [151].

3.5.3.3 Loads

A tensile pressure load simulating the actual test conditions was applied to the model, as shown in Figure 3.58. The value of the pressure load was taken as the maximum applied stress used during fatigue tests in this work, Table 3.15. For specimens tested in Scan Set 1 (T6, T7 and T8), the maximum applied stress was taken to be the maximum nominal stress applied using the servo-hydraulic machine. For Scan Set 2 specimens (T10, T11, T12 and T15), the maximum applied stress was taken to be the sum of the maximum membrane stress and the maximum bending stress as per BS7910 [5]. Due to the distortion produced by the welding process, an additional bending stress was induced in the specimen once it was held in an axially aligned hydraulic testing machine grips. The bending stress was measured using strain gauges attached 30 mm away from the weld toe either side of the specimen. This was to ensure that the strain gauges were not influenced by the stress-concentrating weld geometry. This has been discussed in further detail in Chapter 5, Section 5.3.

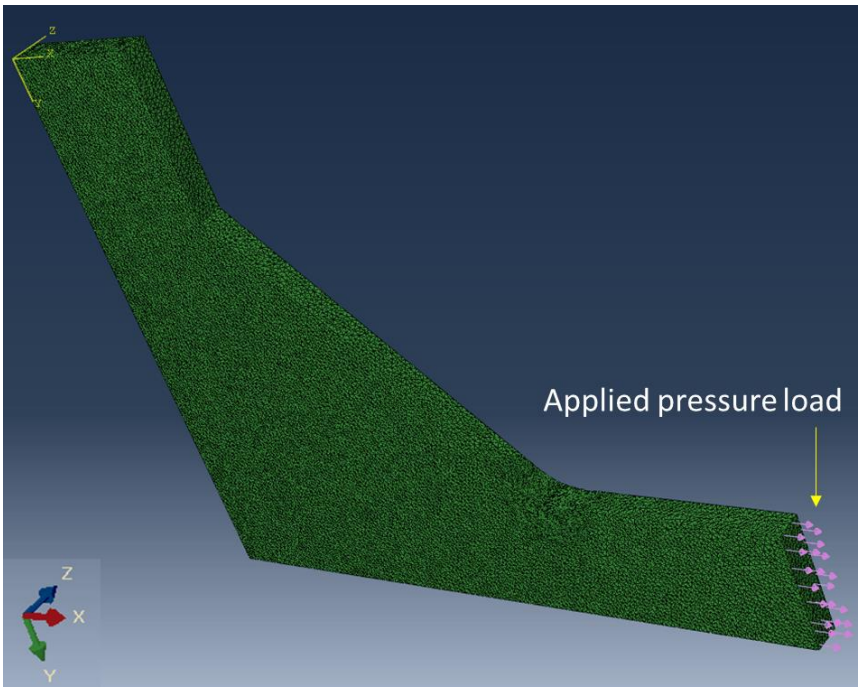

Figure 3.58 Schematic of applied pressure load on the input mesh.

Table 3.15 Maximum stress for each specimen.

	Scan Set 1			
	T6	**T7**	**T8**	
Applied Stress (MPa)	300	300	300	
	Scan Set 2			
	T10 (LQ)	**T11 (HQ)**	**T12 (LQ)**	**T15 (HQ)**
Applied Stress (MPa)	341	296	341	296

3.5.3.4 Boundary Conditions

The boundary conditions were chosen to emulate the conditions of the actual tensile test. A symmetric section of the specimen was considered to reduce the number of elements representing the weld toe geometry, therefore considerably reducing the FE solving time. For this reason, symmetric boundary conditions were taken along the X- and Y-axis (Figure 3.59). As the entire weld section was divided into sub-models (explained in Section 3.5.2), symmetry was also taken along the Z-axis to maintain plane-strain conditions throughout each sub-model and avoid plane-stress effects at the edges of each sub-model.

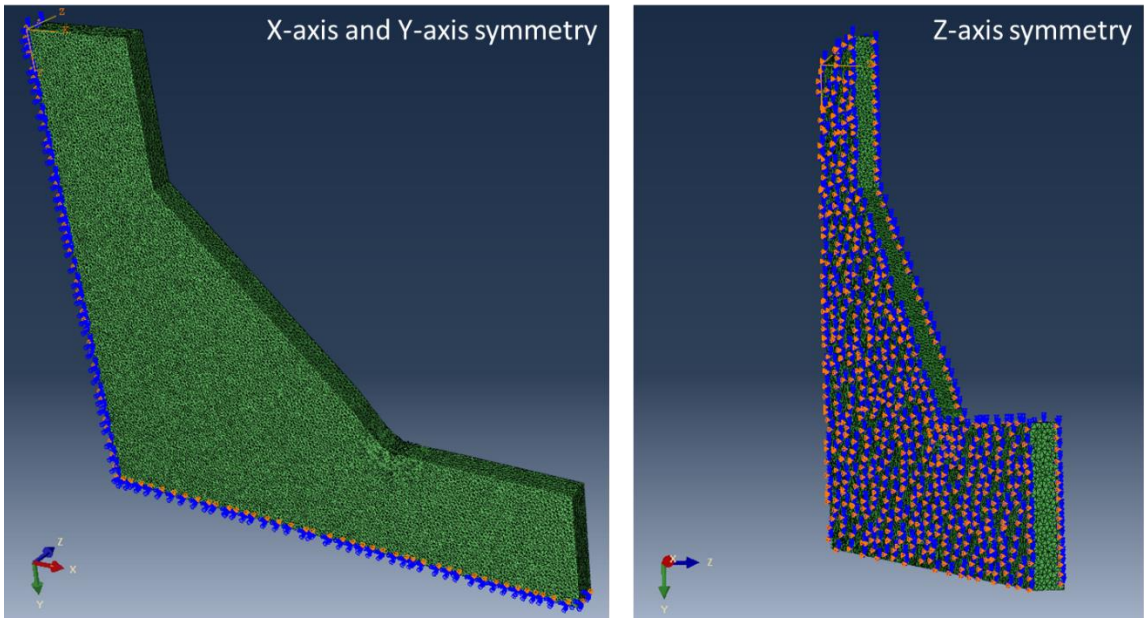

Figure 3.59 Image of the mesh after applying symmetry boundary conditions. LEFT - X-axis and Y-axis symmetry as only a quarter of the specimen was modelled in ABAQUS. RIGHT - Z-axis symmetry as sub-models were solved, representative of the entire weld.

3.5.3.5 Output Values

For both elastic and elastic-plastic solutions, elastic stress and strain components were solved and saved in the generated output files. Additionally, for the elastic-plastic solutions, plastic strain components and the equivalent plastic strain (PEEQ) were also solved and saved. ABAQUS software has a default setting of output fields. If the number of elements and nodes are high, it is beneficial to manually choose only those output fields that are required for post-processing. This provides additional saving in terms of FE-solving time, as the number of parameters computed by the FE solver are reduced (compared with the default computed parameters), and there is less data to write to a file. Also, if the output file size is reduced, post-processing speed is also increased because the developed code (described in Section 3.5.4.1) has smaller files to read and process.

3.5.3.6 FE Analysis - Solving

IRIDIS 5, the High-Performance Cluster (HPC) Supercomputer at the University of Southampton was used to carry out the FE solving. IRIDIS 5 allows the division of the FEA job into multiple nodes, with each node consisting of multiple CPU cores. Using the HPC drastically reduced the solving time that would result from using a stand-alone computer. Once the modelling steps were completed in ABAQUS using the script, input files were generated (.inp) for solving on IRIDIS 5. Scripts were written in bash, which is a Unix shell and command language for the GNU operating system [156]. A template script has been added to the Appendix A.6.

3.5.3.7 FE Analysis – Solution

Once the FE analysis was complete, the data was extracted from the output files in a report file (.rpt). The data was recorded at each node of the model and a script was written to create output variable specific report files, Appendix A.7. These report files were used for further processing of the output data.

3.5.4 FEA Results

This section discusses how the resulting data from the FE analysis was extracted and analysed to obtain statistically significant weld toe stress distributions.

3.5.4.1 Data Extraction

The report files generated from each FE analysis contained the output data for each node of the model but not the spatial coordinates of each node. These were instead contained in the orphan mesh input file generated in ScanIP.

In order to link the FE analysis output data to the spatial coordinates, a code was written in MATLAB which identifies the spatial coordinates of the node in each plane along the weld toe that corresponds to the maximum value of the required output variable. The process behind the code is illustrated in Figure 3.60. As the resolution of the µ-CT scan is generally quite high (up to 4.9 µm), the number of values could run up to 10,000, which could be considered too many values to describe just 50 mm of weld toe. Therefore a 'resolution' input parameter was added to the MATLAB code, which effectively defines the X-Y plane thickness across the weld toe from which output values are obtained. For example, if the total length of the µ-CT scan volume is 48 mm and the chosen "maximum value extraction" resolution is 1 mm, the code will provide 48 maximum values of the output data variable. This is shown in a schematic in Figure 3.61. The script is available in the Appendix A.8.

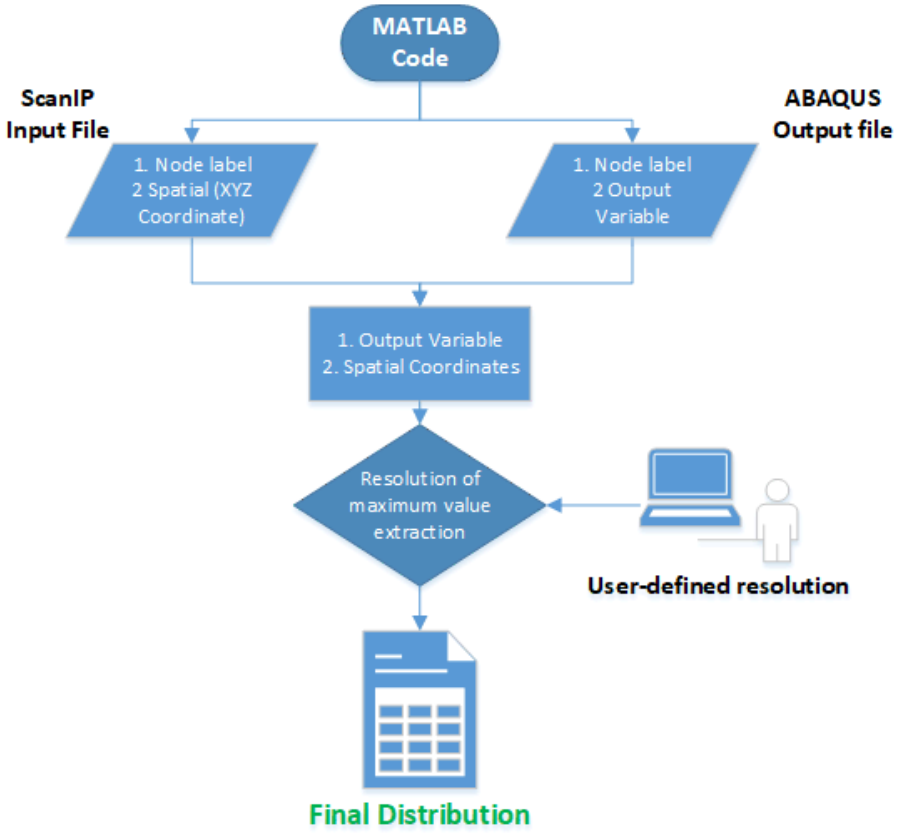

Figure 3.60 Flowchart describing the MATLAB code for extracting the distribution of the maximum output variable.

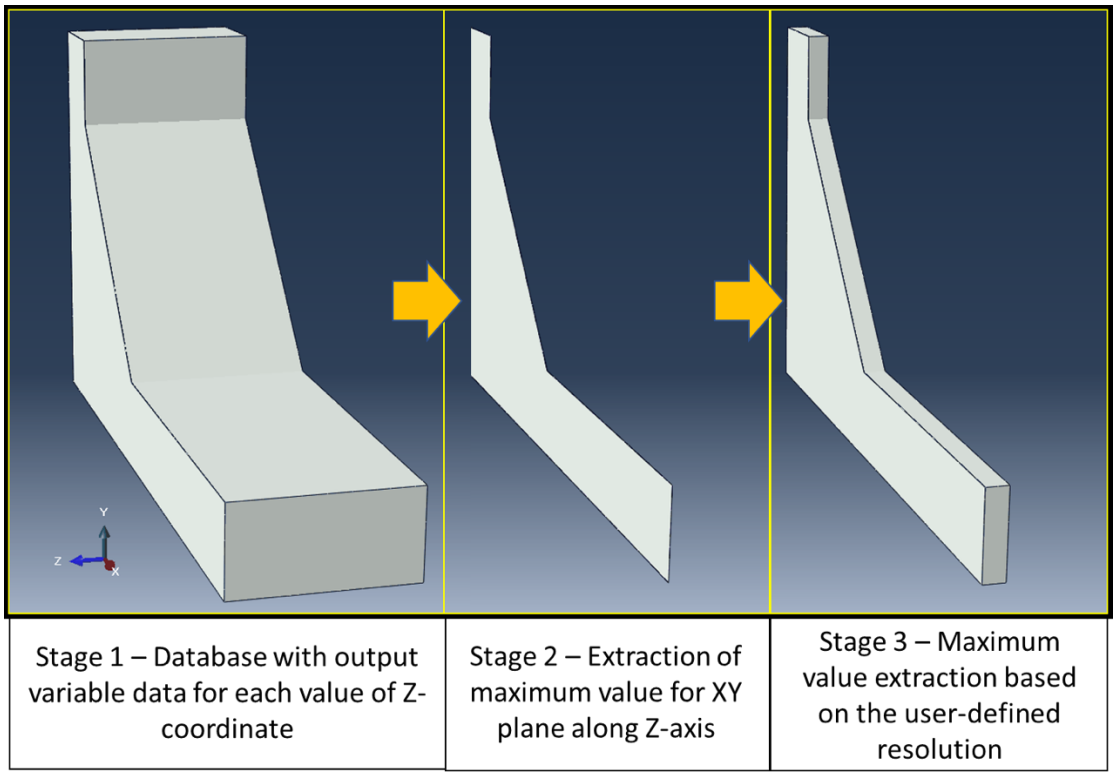

Figure 3.61 Schematic of how the maximum value of the data variable is extracted based on the user-defined resolution for extraction.

3.5.4.2 Statistical Distribution

Distribution of the chosen output variables was obtained for each of the scanned specimens in scan set 1 and scan set 2. The distribution is mainly divided into elastic and elastic-plastic analysis.

Elastic - For the linear elastic stress analysis, distributions of the maximum principal stress ($S_{EL\text{-}PS}$), the von Mises stress ($S_{EL\text{-}MISES}$) and the stress in the direction of the applied tensile stress ($S_{EL\text{-}11}$) were extracted along the weld toe. The SCF for each of these stresses was calculated based on the applied stress shown in Table 3.15. Plots of each of the extracted linear elastic SCFs for each scan/specimen are presented in the Appendix A.9. Box and Whisker distributions of the SCFs for each scan set are given in Figure 3.62.

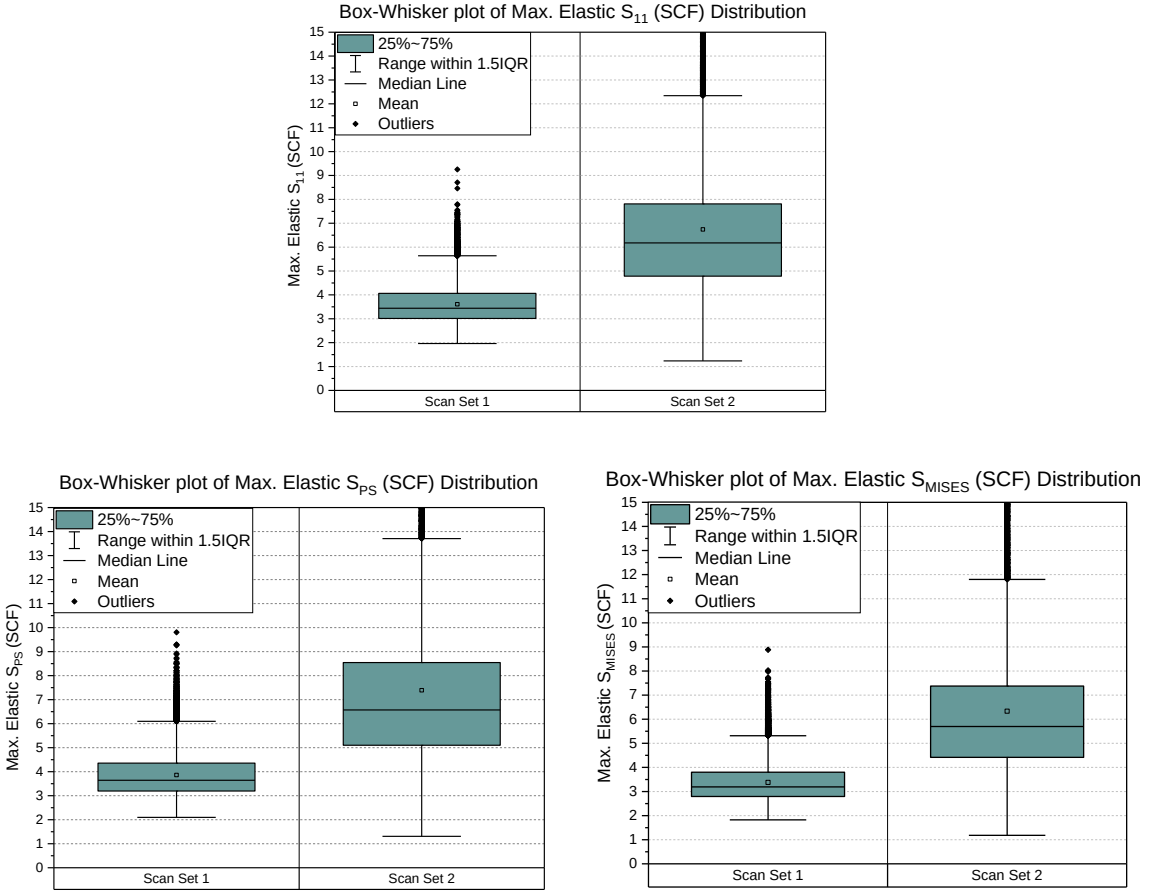

Figure 3.62 Box-Whisker distribution of maximum elastic S_{11} (top), S_{PS} (bottom-left) and S_{MISES} SCF (bottom-right).

As the solution is entirely elastic, the value of stress is not limited by the UTS of the material. The distribution of the different components of stress for each set of scans is therefore similar (shape of the box-whisker plot). From the box and whisker distributions, the distribution of the SCFs for scan set 1 is consistently in a lower band of values compared with scan set 2. This could be attributed to a several factors –

- The geometry of the scanned specimens in scan set 1 were matchstick specimens which were given an average weld angle of 45 degrees during image manipulation (Section 3.4.5), whereas for the scan set 2 specimens, the whole weld bead was scanned. However, this effect should not be very prominent as it has been seen that any geometry further than 2 mm from the weld toe does not have a significant impact on the stress concentration (also considered in Section 3.3.2.1).
- Scan set 1 consisted of sections where there was a gradual increase in the weld toe angle (chamfer-like), instead of the typical sudden steep weld bead which results in higher SCFs at the weld toe. An example is given in Figure 3.63. The distribution of such sections was arbitrary, as it was not intentional.
- Scan set 1 included a semi-automated weld as well, which would be expected to have a lower SCF distribution as compared to specimens in scan set 2, which were all manually welded.
- Two specimens from scan set 2 were deliberately manufactured to be low-quality welds, and their SCF distribution was in a significantly higher band compared to the other specimens.
- The welders for both sets were different, which possibly plays a role in the quality of the final weld.

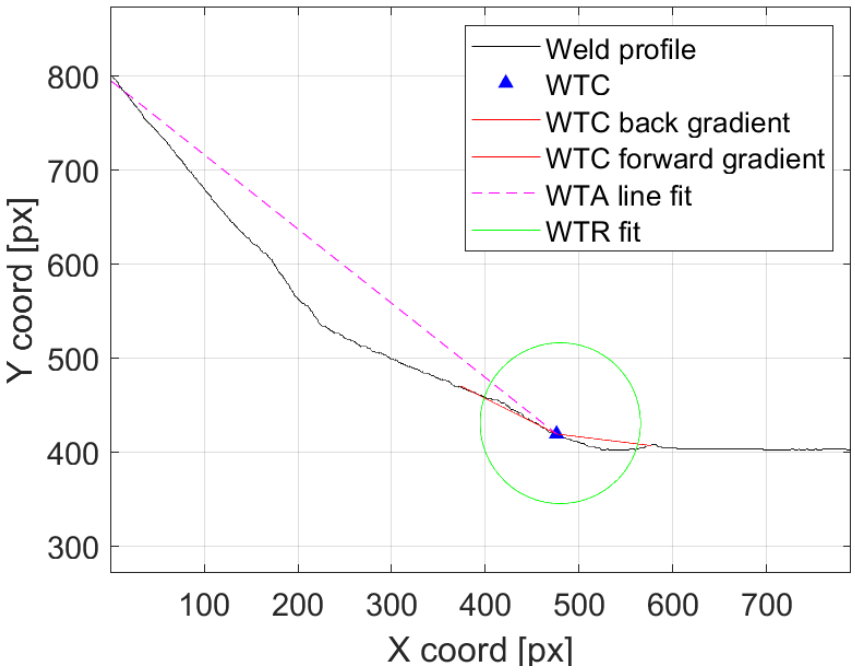

Figure 3.63 Weld toe geometry of a section with a gradual "chamfer-like" weld bead.

Figure 3.64 gives the box-and-whisker distribution of maximum SCFs in the specimens from scan set 2. The mean value for the low-quality (LQ) specimens is, as expected, higher as compared to the high-quality (HQ) specimens. This is attributed to the extensive distribution of severe undercuts in

the LQ specimens that push the mean higher. The median value on the other hand, is lower for the LQ specimens. This is also attributed to the intention of creating detrimental undercuts. In some cases, very deep undercuts (to the order of 1 mm in depth) had a similar morphology to weld toe grinding, which is a post-weld treatment used to remove stress concentrations at the weld toe. Figure 3.65 presents an example of the above-mentioned two cases.

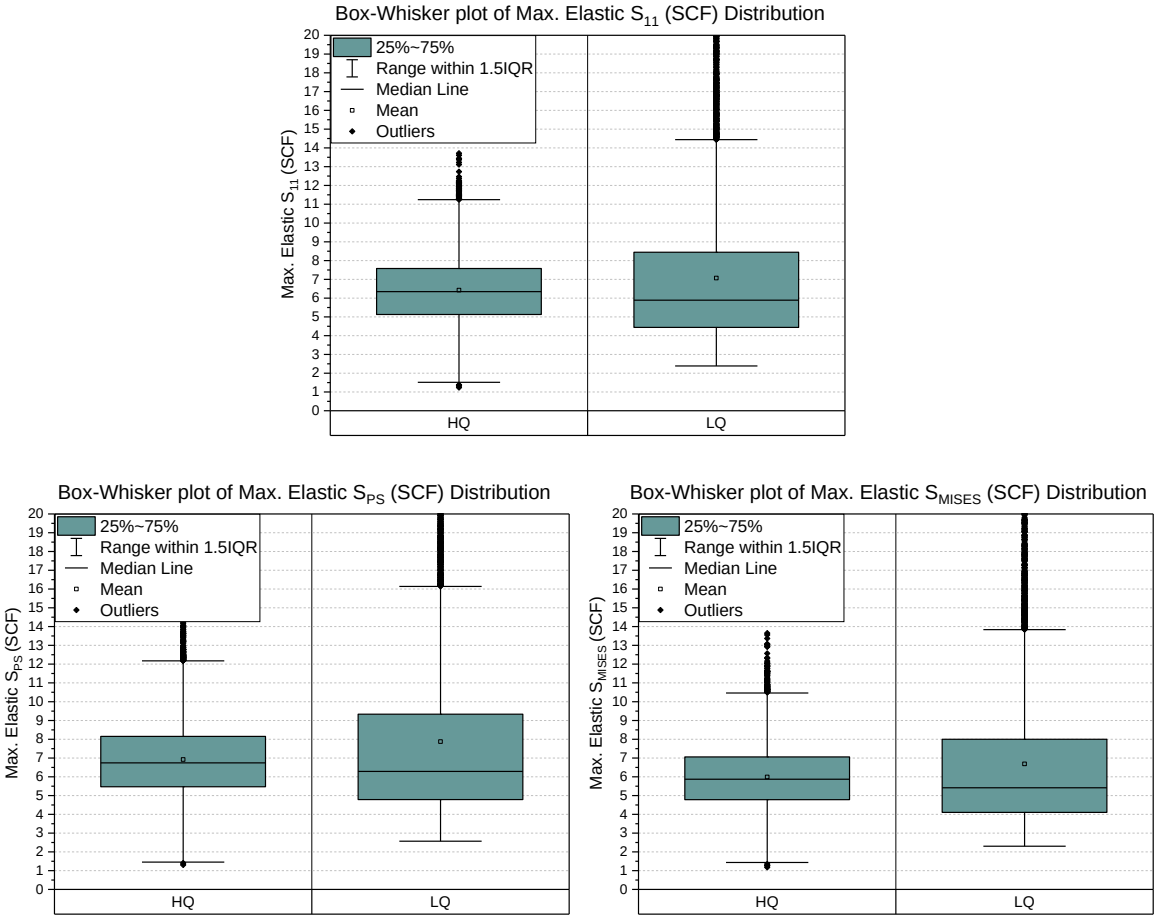

Figure 3.64 Box-Whisker plot of maximum elastic S_{11} (top), S_{PS} (bottom-left) and S_{MISES} SCF (bottom-right) for scan set 2 specimens.

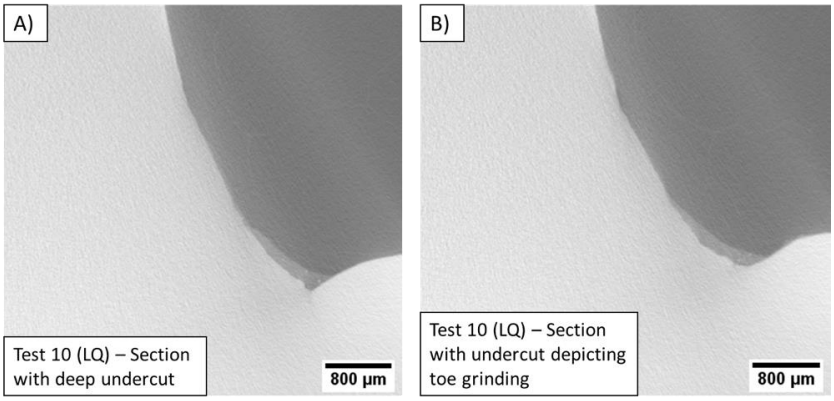

Figure 3.65 Examples of sections from the same specimen showing the different in the shape of the intentionally created undercut - A) Deep and sharp intentional undercut; B) intentional undercut in the shape representative of toe grinding.

Elastic-Plastic – For the elastic-plastic analysis, the von Mises component of stress ($S_{ELPL\text{-}MISES}$) and the equivalent plastic strain (E_{PEEQ}) distribution was primarily extracted. In addition, the stress and strain component in the direction of the applied tensile stress, $S_{EL\text{-}PL\text{-}11}$ and $E_{EL\text{-}PL\text{-}11}$ respectively were also extracted. The SCF for the stress values was calculated based on the maximum applied stress shown in Table 3.15. Plots of each of these extracted elastic-plastic SCFs as well as the elastic-plastic strain for each scan/specimen are presented in the Appendix A.10. Box and Whisker distributions of the stress and strain components of the two scan sets are shown in Figure 3.66 and Figure 3.67. $S_{EL\text{-}PL\text{-}MISES}$ for elastic-plastic calculations is limited by the UTS of the material, and therefore the mean and median of the distribution is as expected lower than the elastic stress distribution. A trend similar to what was seen in Figure 3.62 has been seen here as well, with the distribution of scan set 1 being lower than scan set 2. This can again be attributed to the reasons described previously.

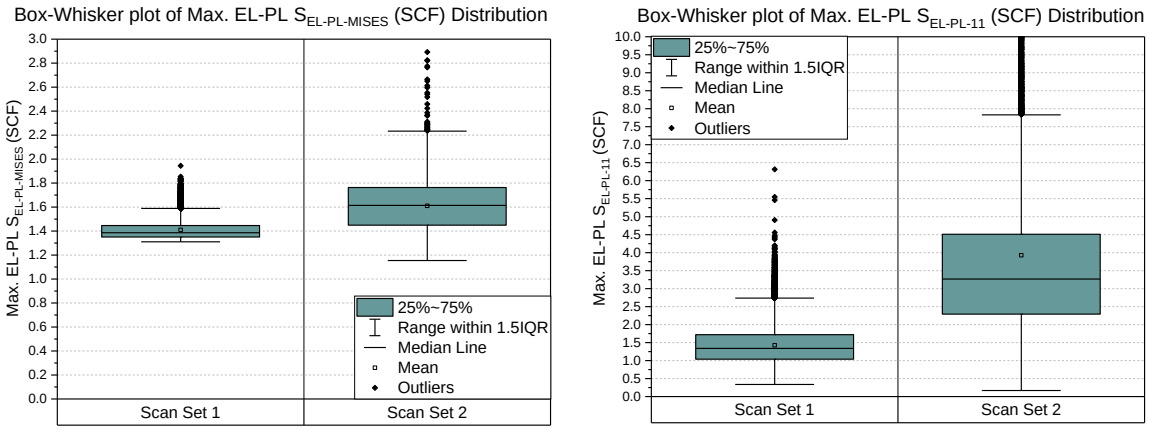

Figure 3.66 Box-Whisker distribution of maximum elastic-plastic stress parameters for the entire scanned volume – $S_{EL\text{-}PL\text{-}MISES}$ (Left) and $S_{EL\text{-}PL\text{-}11}$ (Right) SCF. Please note the difference in scales.

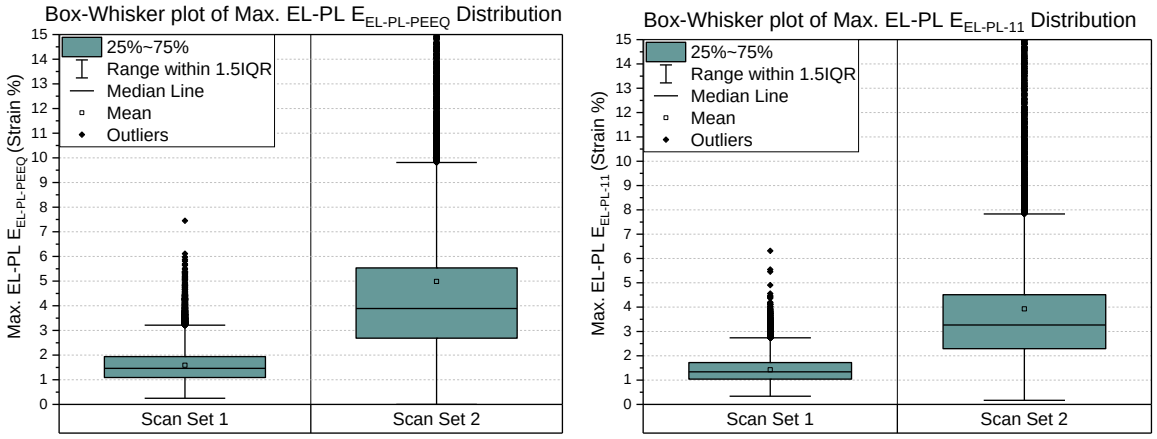

Figure 3.67 Box-Whisker distribution of maximum elastic-plastic strain parameters for the entire scanned volume – $E_{EL-PL-PEEQ}$ (Left) and $E_{EL-PL-11}$ (Right).

Figure 3.68 and Figure 3.69 are box and whisker distribution plots of maximum elastic-plastic SCF and strain components from scan set 2. The stress components for the HQ specimens show a relatively higher distribution as compared to the LQ specimens. The strain components, on the other hand, show a quantitatively larger distribution for the LQ specimens. This can be attributed to the way ABAQUS solves for stress and strain for elastic-plastic solutions. The solver linearly interpolates between the data points provided for plastic material behaviour and assumes that the material response is constant beyond the range defined by the input data, in this case, the UTS of the material [151]. This is shown in Figure 3.70. The cases of outliers where stresses have gone beyond the UTS are possibly caused by stress singularities, which lead to deformed elements.

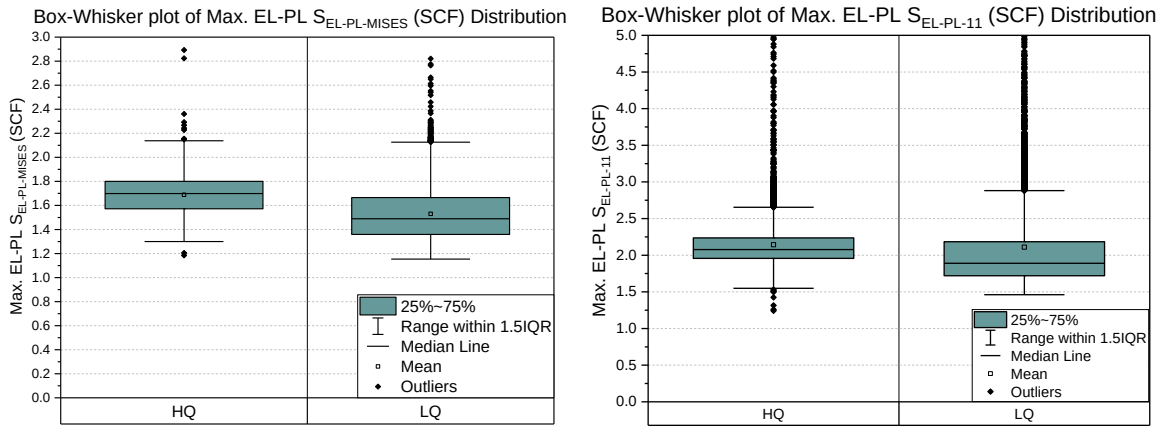

Figure 3.68 Box-Whisker distribution of maximum elastic-plastic stress parameters for scan set 2 – $S_{EL-PL-MISES}$ (Left) and $S_{EL-PL-11}$ SCF (Right). Please note that the scales are different for both plots.

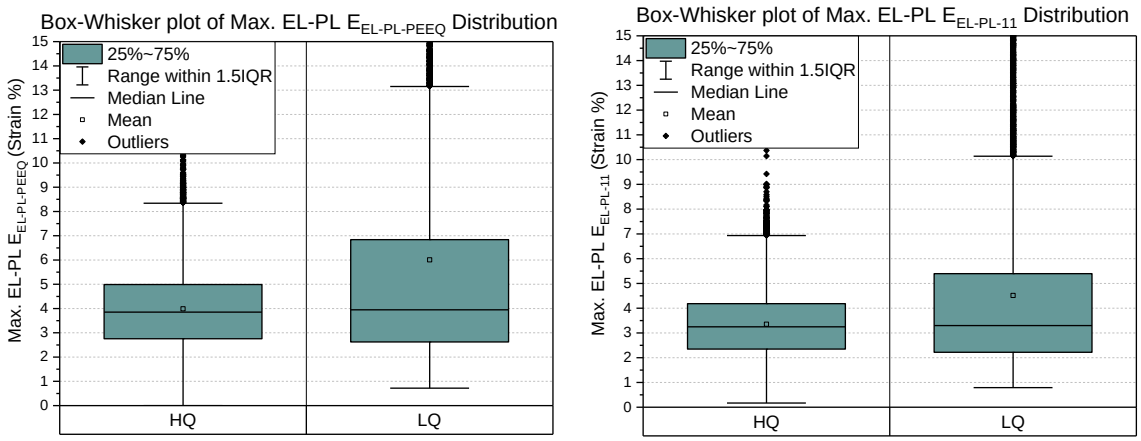

Figure 3.69 Box-Whisker distribution of maximum elastic-plastic strain parameters for scan set 2 – $E_{EL-PL-PEEQ}$ (Left) and $E_{EL-PL-11}$ (Right).

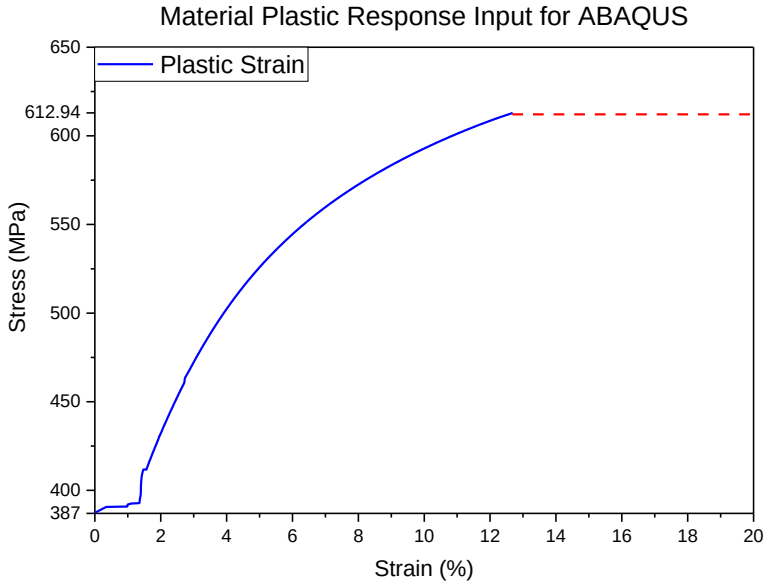

Figure 3.70 Material plastic behaviour input parameters for ABAQUS FE solving.

3.5.5 Three-dimensional (3D) Finite Element Analysis (FEA) – Summary

In this section, the processes involved in developing the 3D FEA were discussed along with their respective challenges. A 3D model improved upon a 2D model as it represented defects in their true spatial form. However, the 3D modelling of the weld toe geometry was subject to various simplifications due to computational limits. They could be listed as follows:

1. Single material model (Section 3.5.1).
2. Creation of sub-models (Section 3.5.2).
3. Use of isotropic hardening model instead of a combined kinematic and isotropic hardening model (Section 3.5.1).

4. Small mesh refinement zones (Section 3.5.2).
5. Lack of residual stress implementation.
6. SCF distribution based on monotonic loading (Section 3.5.3.2).

It is important to note that although an HPC was used for FE solving, there is no linear relationship between the number of processors involved in solving and the solving time. Beyond a certain number of processors, there is no discernible improvement in processing speed.

Stress and strain distributions were obtained for each of the μ-CT scanned specimens. The correlation and validation of the obtained distributions with the crack growth monitoring experimental results will be discussed in Chapter 4 and Chapter 5. The use of the distributions of stress and strain parameters obtained in Section 3.5.4 along with the SCFs from geometry extraction in Section 3.4.4 for fatigue life estimations will be discussed in detail in Chapter 6.

Chapter 4 Multi-Probe ACPD Method for Detecting Fatigue Crack Initiation

4.1 Motivation

In order to correlate the weld toe geometry with its fatigue crack initiation life, a method was required to capture the fatigue crack initiation point of the welded specimens without damaging the weld toe so that they could be subsequently subjected to μ-CT for stress analysis (Chapter 3). The primary aim of this Chapter of work was to therefore meet objective 2a of this PhD study:

"Accurately detect in-situ fatigue crack initiation life and location using a data-rich fatigue crack growth monitoring technique."

BS ISO 12108:2018 is the recognised Standard for conducting crack propagation tests on specific specimen types using either DCPD or ACPD to monitor the crack [96]. Conventional industry practice involves using DCPD to monitor crack propagation in test specimens that are already cracked and have the crack propagating from one location in one direction. In this work, the welded specimens added two complications to this: the precise crack initiation location was unknown, and the specimens did not contain an initial crack, i.e. crack initiation detection was also required.

Both ACPD and DCPD methods were considered, but ACPD was chosen for this study. Differences between the two methods are described in [96, 157-160], however it was the advantageous 'skin effect' of ACPD that made it preferential for this work. The "skin effect" is described further in Section 4.2.1 and basically means that the method is theoretically more sensitive to surface crack initiation.

In this Chapter, the ACPD method for crack monitoring is introduced and its advantages and disadvantages are summarised. The methodology adopted to implement a multi-probe ACPD system to the weld toe is then described and the results from the fatigue tests presented. The results are then interpreted and compared with those from the FE stress analysis described in Chapter 3 and suggestions are discussed to improve the methodology going forward.

4.2 Introduction to APCD

The basic premise of using a potential drop method (AC or DC) for fatigue crack growth monitoring involves the passing of a constant electric current through a test specimen and measuring the change in voltage or electrical potential across the crack plane caused by crack propagation. The

propagating crack effectively reduces the cross-sectional area (remaining ligament length) of the specimen causing the electrical resistance and thus the voltage to increase, as per the simple relationship: $voltage = current \times resistance$. The change in voltage can then be related to the crack depth via calibration equations, which are specific to particular specimen geometry's and can be developed from performing tests that induce beach marks on the fracture surface allowing for a series of crack depth measurements to be correlated with PD values [96, 157].

For AC, the electrical resistance is described by impedance, which is measured as a function of three components: the capacitive, inductive and resistive components. AC also has a frequency, in general, low frequency AC (10 Hz to 100 Hz) operates in a similar manner to DC, but the high frequency AC (5 kHz to 500 kHz) allow for the 'skin-effect' phenomenon to be utilised to increase its sensitivity to surface cracking. A more detailed comparison between the two methods for flaw and crack detection and monitoring with examples of application is provided in [97]. Key features of the method are described below, which include the "skin-effect", current focusing and induced pick up voltage.

4.2.1 The Skin-Effect

The "skin-effect" refers to localising the AC flow at the surface of the specimen, effectively creating a thin "skin" of localised current that increases sensitivity to surface breaking flaws and cracks. In comparison, DC flows in a relatively uniform manner through the remaining cross-section of the specimen, which is one reason why larger currents are required for DCPD crack monitoring. A schematic showing the relative difference in current paths for AC and DC for a typical compact tension specimen is provided in Figure 4.1.

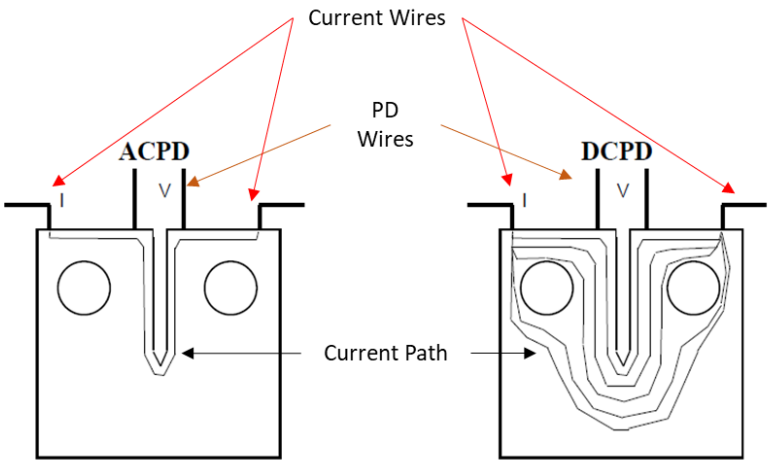

Figure 4.1 Schematic of ACPD and DCPD crack monitoring setups showing the relative difference in current paths for a compact tension specimen. Adapted from [160].

The “skin-effect” can be characterised by the skin depth (Δ), which is the depth of the “skin” from the surface of the specimen, Figure 4.2. It is a function of the AC frequency (f) and the electric resistivity (ρ_{RES}) and magnetic permeability (μ_{MP}) of the material being tested (Equation 4-1).

$$\Delta = \sqrt{\frac{\rho_{RES}}{\pi \mu_{MP} f}} \qquad 4\text{-}1$$

Where,

Δ	Skin depth (m)
ρ_{RES}	Electric resistivity (Ω.m)
μ_{MP}	Magnetic permeability (N.A^{-2})
f	AC frequency (Hz)

The magnetic permeability and electrical resistivity are functions of the material and thus the skin depth can be changed during a test by altering the AC frequency. The skin depth is inversely proportional to the AC frequency, i.e. it reduces as frequency is increased. Reducing the skin depth, increases the sensitivity to surface breaking crack initiation, however, reducing the skin depth too much can reduce the sensitivity to subsequent crack propagation as the crack grows out of the “skin”.

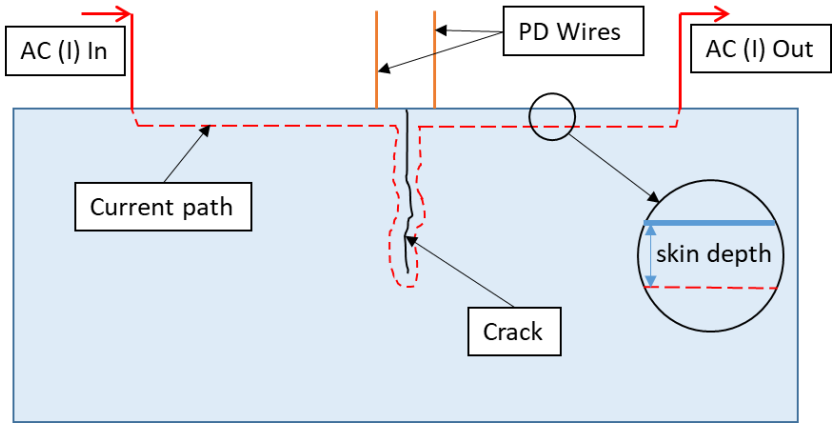

Figure 4.2 Schematic of a basic ACPD set-up for a single edge notched specimen showing the “skin-effect” at the surface and around the crack.

4.2.2 Current Focusing

The “skin-effect” should theoretically direct the current to flow in a uniform layer at the specimen surface. In practice though, this uniform layer can be perturbed by the positioning of the current wires with respect to the surface and influenced by surface breaking and near surface flaws and cracks. These factors can have a significant effect on the resulting ACPD signal measured. The

importance of maintaining a uniform current field distribution and necessary corrections have been documented in previous work [63, 161, 162].

Current focusing, magnifies the sensitivity of ACPD measurement in regions of interest and eliminates the need to maintain a uniform current field and corrections around flaws and cracks. The method was developed by MATELECT Ltd, and is described further in [160, 163]. The correct implementation of the method involves careful positioning of the insulated current wires at regions of interest (ROIs) at the specimen surface. This perturbs the current flow in the specimen so that it mainly flows directly below the current wires and along their length in a well-defined narrow band as illustrated in Figure 4.3.

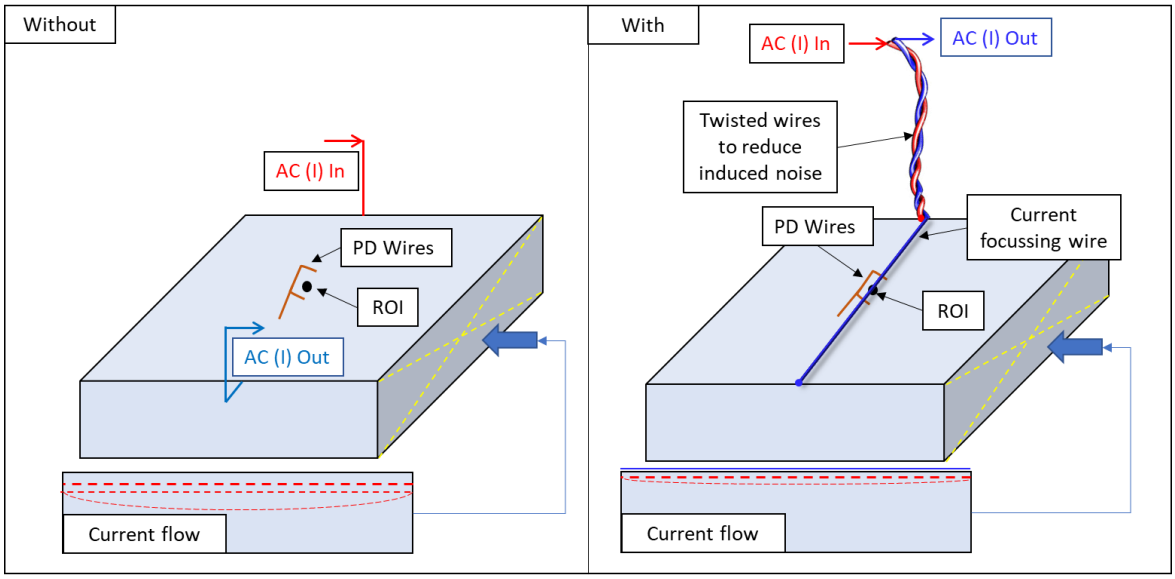

Figure 4.3 Schematic of ACPD setup without (left) and with (right) current focusing implemented.

4.2.3 Induced Pick-Up Voltage

Induced pick-up voltage ($V_{p/up}$) is an unwanted component of the ACPD signal that occurs due to the interaction of the voltage lead signal with the magnetic fields of the AC [96, 160]. It is a vector component of the signal output and varies in both magnitude and phase with respect to the actual ACPD voltage (V_{acpd}), the resistive voltage (V_{res}) and the measured ACPD voltage (V_{meas}). Therefore, it is not possible to simply subtract $V_{p/up}$ from the measured signal.

The induced pick-up voltage is represented in phasor diagrams in Figure 4.4. Two examples of possible $V_{p/up}$ are shown, which differ due to the relative positions of the current and voltage wires, which also causes the value of V_{meas} to change.

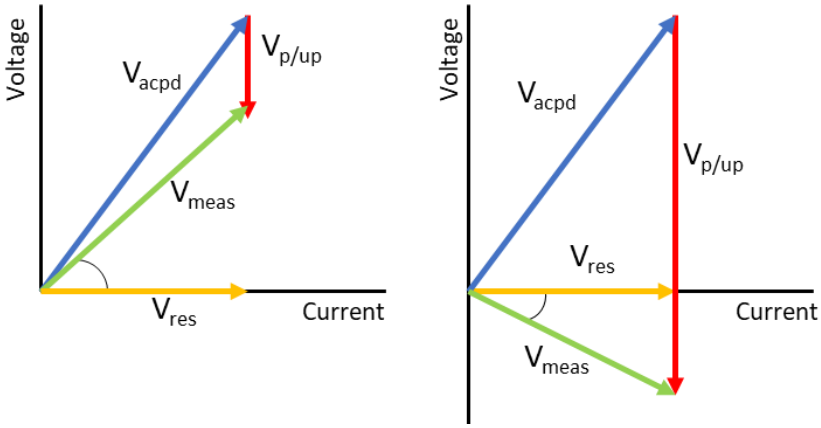

Figure 4.4 Phasor Diagram showing the effect of varying $V_{p/up}$ signal on the measured voltage. Adapted from [160].

An electronic method of dealing with the induced pick-up voltage is implemented in the MATELECT ACPD system used in this study and involves monitoring V_{res}. V_{res} is the real component of the ACPD signal and shares the same phase as the specimen current vector; it therefore does not change with respect to $V_{p/up}$, as illustrated in Figure 4.4.

It is clear from this Section and Section 4.2.2 that wire positioning and relative wire movements can influence the ACPD signal and associated noise, therefore to reduce undesirable signals; two practices should be implemented in an ACPD set-up:

1. Connections should be as rigid as possible and lead movement minimised during each test to reduce any interaction between voltage and current wires;
2. Current wires (input and output) should be tightly twisted to minimise the movement of the wires relative to each other.

The voltage or PD values obtained from the ACPD primarily contains two components – the real and imaginary component. The real component corresponds to the resistive component of the induced voltage, whereas the imaginary component corresponds to the combined capacitive and inductive component of the induced voltage. For the purpose of crack growth, the real component is measured, as the resistive component remain unaffected by effects of $V_{p/up}$, as seen in Figure 4.4.

4.3 Review of Notable ACPD Applications

Venkatasubramanian and Unvala, 1984 [164] outlined the design of an ACPD system and discussed its use and the beneficial role of the skin-effect for crack depth monitoring and measurement. They highlighted the effect of current and voltage wire positioning and the specimen tensile stress on the value of ACPD obtained. They found that in the case of steel, the ACPD output increased with

respect to crack depth but decreased as the tensile stress in the specimen increased. This indicates that the ACPD signal output is not only a function of the crack depth for a particular specimen geometry, but also the magnitude of the applied load.

Okumura et al., 1981 [165] used ACPD for detecting crack initiation and monitoring crack extension during stable tearing to obtain J-integral vs R-curves, with R being resistance to crack growth under monotonically increasing loads. The initiation toughness J_i was evaluated by extrapolating to zero crack extension and assuming that crack initiation occurred at the minimum PD signal and subsequent increases in PD were linearly related to crack extension.

Gibson, 1987 [162] conducted a similar test to Okumura [165] using a Matelect ACPD system and observed that the minimum PD does not always correspond to crack initiation, and that the J-R curves were also dependent on the frequency of the AC at small crack extensions. Gibson suggested using the onset of deviation from the linear relation between the J-integral and PD to be the point of crack initiation. Gibson also observed the effect of tensile stress on the PD signal, which caused the PD to fluctuate during loading and unloading cycles. Figure 4.5 shows the relationship between PD and the applied load, qualitatively it was similar to that observed in [164]. This relationship was obtained by the authors during the loading and unloading cycles in order to correct the data before obtaining the J-R curves.

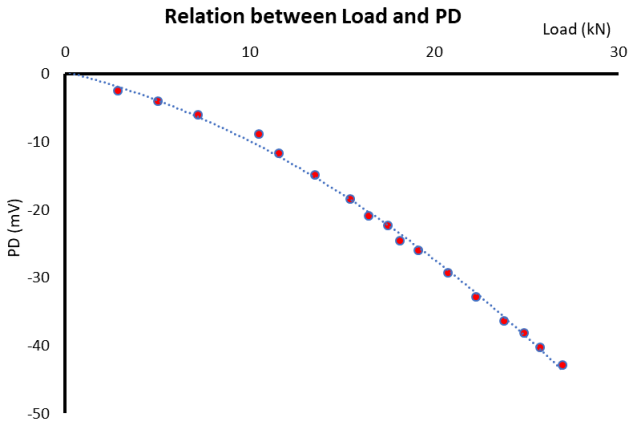

Figure 4.5 Relation between PD and applied load on C-Mn steel (BS4360 43A). PD showed a decrease with increase in loading, an effect of stress on the electrical resistance of the material. Adapted from [162]

An interesting concept was used by Wojcik et al., 2017 [166], in which both ACPD and DCPD were used in combination for creep damage monitoring and end of life warning for high-temperature components.

In terms of welded joints, one of the earliest recorded uses of ACPD was found in the work of Dover et al., 1984 [167] and Collins et al., 1985 [168] where a portable ACPD instrument called the Krautkramer U8 Crack Microgauge was used [169]. The same system was also used by Lassen, 1990 [89] for detecting crack initiation with multiple probes and a switching unit. A schematic for a single probe pair set-up is shown in Figure 4.6 and a similar test set-up using multiple probe pairs is shown in Figure 4.7. The latter is from the work of Bell et al., 1989 [63], who used the system to detect weld toe crack propagation under cyclic loading.

ACPD crack monitoring using a portable Karl Deutsch RMG 4015 hand-held ACPD Probe was used by Crump, 2017 [9]. The probe was practical to use and provided an economical alternative to more elaborate multi-probe permanent installations, however it was found to have limitations, particularly at the crack depths of interest in this work. Firstly, the probe did not offer continuous monitoring and thus measurements were made when the specimen was held under a constant load at several intervals during the fatigue tests. Secondly, as also identified by Wojcik et al., 2017 [166], the obtained ACPD values were prone to differences in the contact angle and contact pressure of the probes on the specimen surface, which was further complicated by the presence of oxides at the weld toe, which act as an insulator to the probes. Lastly, the resolution and accuracy of the portable probe was not suitable for early crack monitoring, i.e. it had a resolution of 100 μm with a reported accuracy of 3-15%.

A Matelect ACPD system with a single probe pair was used at the weld toe of C-Mn steel fillet welds in the work of Raujol-Veillé et al., 2015 [113]. The ACPD signal was used to detect crack initiation and early propagation under cyclic loading. A potential drop of 2 mV was estimated to correspond to a crack depth of 500 μm, as shown in Figure 4.8. It is unknown from the work however where the initiated crack was located with respect to the PD probe pair at the weld, which is likely to influence the ACPD signal.

More recently, Mikulski and Lassen, 2019 [141] used a multi-probe ACPD system based on the Krautkramer U8 Crack Microgauge for monitoring crack propagation in non-load carrying C-Mn steel T-joints of 25 mm plate thickness. The authors used a linear relationship between voltage drop and crack depth and accounted for current and environmental fluctuations via reference probes positioned in an uncracked region of each specimen. The system was used on several specimens, and was able to consistently determine fatigue crack initiation lives to a crack depth of 0.05 mm. Interestingly, the results from this study showed fatigue crack initiation lives (to a crack depth of 0.05 mm at a stress range of 150 MPa) to take an average of 24% total life with a coefficient of variability of 0.40 thus highlighting the importance of the initiation life on the scatter in total fatigue lives of these welded joints.

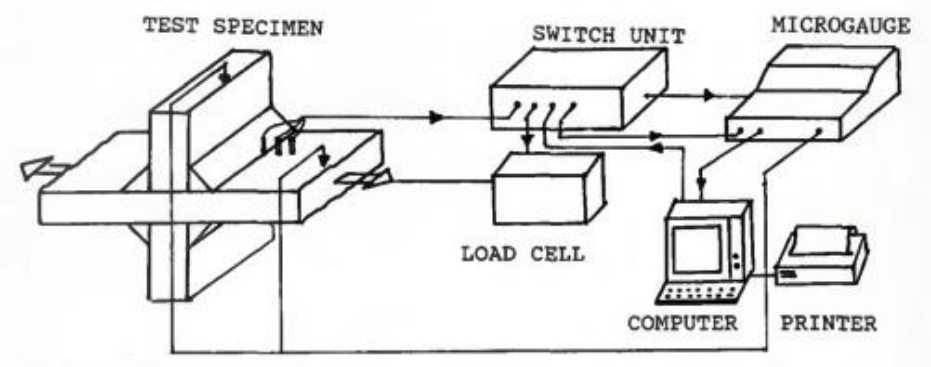

Figure 4.6 Schematic of the Krautkramer U8 Crack Microgauge crack monitoring system. From [89].

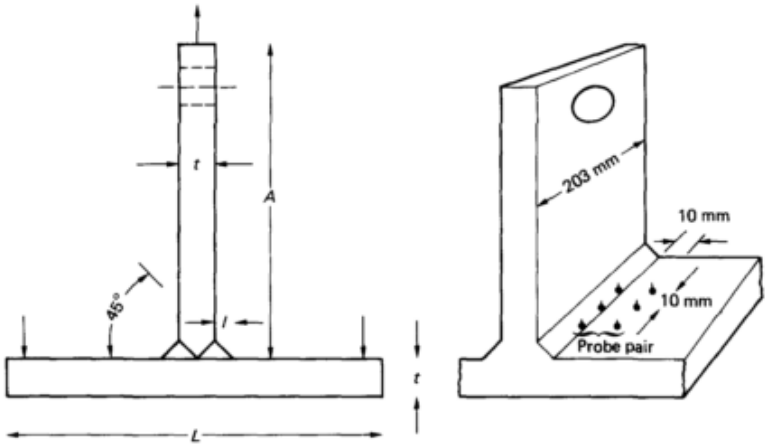

Figure 4.7 Schematic of ACPD crack growth monitoring probe pair setup at the weld toe. From [63].

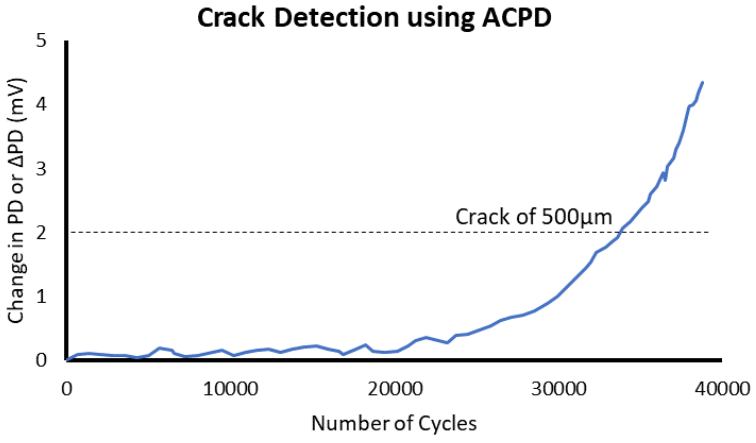

Figure 4.8 Relation between change in PD and crack size. Adapted from [113].

4.4 Methodology – Fatigue Testing with ACPD Crack Detection

4.4.1 Welded Specimens

Three C-Mn steel welded specimens as described in Chapter 3 Section 3.3 and with IDs HQ_T06, HQ_T07 and HQ_T08 were used with ACPD for crack monitoring in this chapter of work. The weld toe length of each specimen was 50 mm and the mechanical properties of the parent material are given in Table 3.6.

As the specimens contained four welds (total length of ≈ 200 mm), three weld toes were ultrasonically peened to prevent fatigue crack initiation from them and to maximise the number of probe pairs that could be utilised on the weld toe most likely to first undergo fatigue crack initiation. To further maximise the likelihood of capturing fatigue crack initiation, weld misalignment measurements were made on the specimens to identify the weld toe most likely to experience the highest stress during uniaxial loading and this toe was left in the as-welded condition.

Weld toe misalignment arises from the way in which the plates are clamped during welding (i.e. their constraint) and their subsequent displacement when specimens are extracted by cutting, due to residual stress relaxation. Figure 4.9 presents two macrographs of the manual weld and semi-automated weld, which depict how the misalignment (e) was measured, in accordance with BS 7910-2013 [5]. The weld misalignment results correlated well with results from the fatigue tests performed by Crump [9] on specimens extracted from the same welded plates. In Crump's work, 73% of weld toe failures occurred at the weld toe subjected to the highest tensile stress during uniaxial cyclic loading.

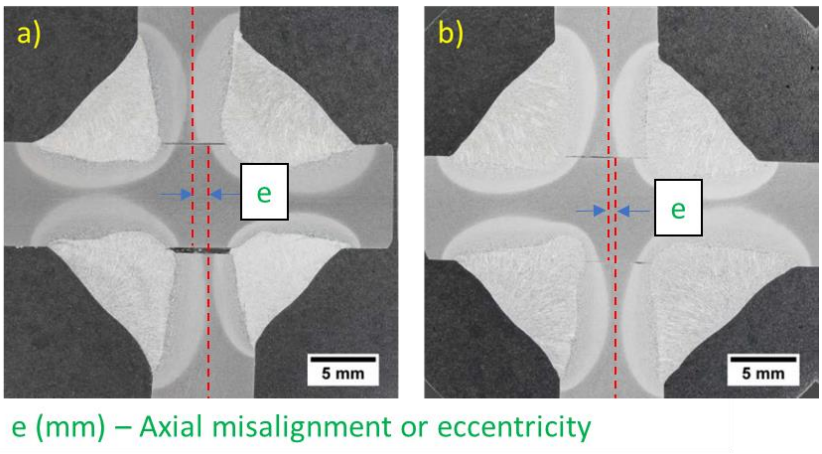

Figure 4.9 Cross-section of the welded joints and the magnitude of axial misalignment - a) metal-core electrode manual (MM); b) solid-core electrode manual (SM). Taken from [9].

Ultrasonic weld toe peening was performed by TWI using a SONATS Stressonic® NOMAD Ultrasonic Needle Peening (UNP) system. The technique is also known as high-frequency mechanical impact (HFMI) treatment and ultrasonic impact treatment (UIT) and can be used to improve or extend the fatigue life of welded joints [93, 170-172]. For example, Yildrim and Marquis, 2012 [172] state an improvement of $[40 + (355 - \sigma_y) \times 0.08]\%$ for mild steel fillet welded joints, where σ_y is the yield strength of the material. Figure 4.10 provides an image of the system and needle along with a welded joint with an as-welded toe and a UNP-treated weld toe. The parameters chosen for the peening process were based on the documentation made available by the manufacturer [136] and the experience of the technician, Table 4.1.

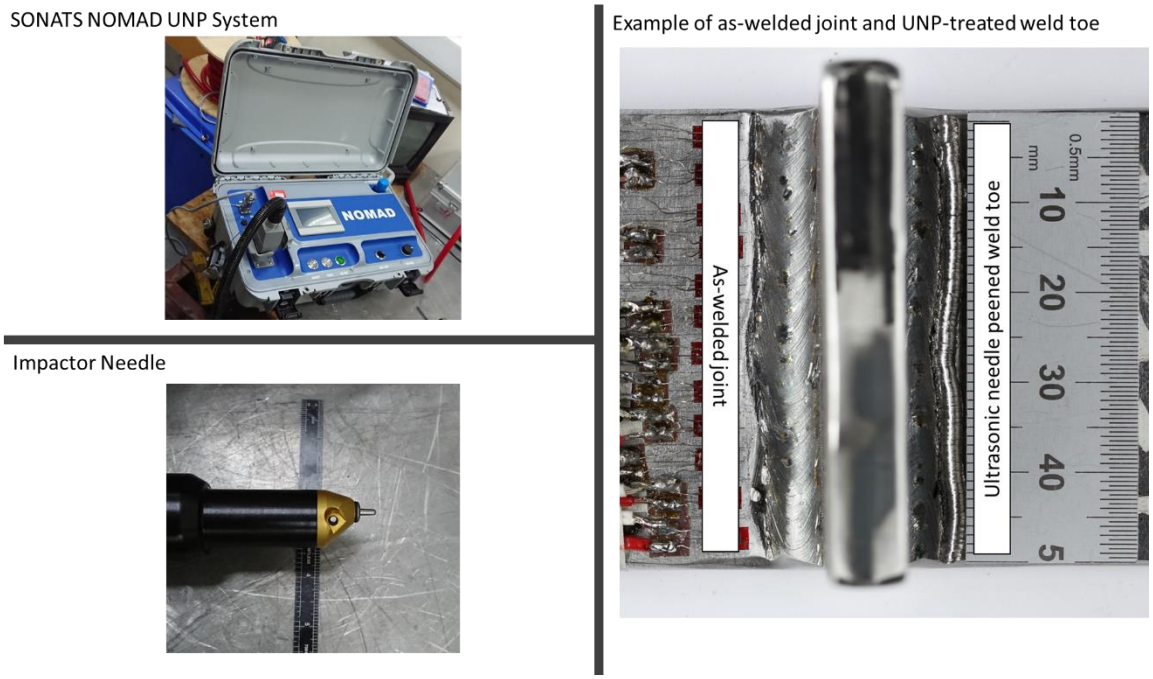

Figure 4.10 Images of the SONATS NOMAD UNP System and the result of peening on a welded specimen.

Table 4.1 Parameters for SONATS NOMAD UNP system.

Parameters	**Value**
Amplitude	60 µm (peak to peak)
Frequency	20 kHz
Impactor size	1.5 mm radius

After weld toe peening, each specimen was chamfered at its edges using a hand-held pneumatic grinder to remove any sharp edges and provide a radius to reduce stress concentrations at the edge. The specimen surface adjacent to the as-welded toe was then polished using a handheld

rotary machine with polishing pads and diamond paste in order to maximise the connection quality of the PD probes with the specimen surface.

4.4.2 ACPD Probe and Wiring Set-Up

A Matelect CGM-7 ACPD crack growth monitoring system (shown in Figure 4.11) was used to detect fatigue crack initiation and monitor crack propagation at one weld toe of each of the three specimens. The system allowed for twenty-four PD probes (twelve pairs of active and reference probes) and current focussing wires and came with signal amplifiers to boost the ACPD signal and minimise the influence of noise caused by unavoidably long wires.

For each PD measurement point, the wiring essentially consisted of six points: two for current, two for PD measurement across the weld toe (active signal) and two for PD measurement in an uncracked region (reference signal). High quality electrical contacts were made to the specimen using spot welding. Soldering or threaded connections could have also been used but spot welding was deemed most feasible for this work. Consequently, regular copper wires were not used, as their high conductivity would not allow for efficient spot welding. Thus, enamelled nickel studs were used for the wire connections to the specimen.

To implement current focusing, the input and output current wires were twisted together and positioned along the specimen surface so that they pass across the region of interest (between each probe pair). This enabled the specimen current to follow its path as explained in Section 4.2.2 to increase the sensitivity of the ACPD signal at the probes. The current wires were regular PTFE coated copper wires, which were soldered to the nickel studs. Efforts were made to minimise cable impendence, and this was further achieved by the current source having a fixed voltage compliance, thus allowing the maximum current to be available for the test.

Figure 4.11 The Matelect CGM-7 ACPD system.

For each specimen, twelve active pairs of ACPD probes were attached across the weld toe with twelve reference pairs of ACPD probes 10 mm below, as shown in Figure 4.12. The manufacturers of the ACPD system suggested a minimum distance of 4 mm between two probe pairs to minimise interference between the focussed current at each probe pair. For each specimen, the probe pairs were distributed evenly at 4-4.5 mm intervals.

Reference probes were attached on the baseplate where the cyclic loading would not cause any fatigue cracking. The primary purpose of the reference probes was to allow normalising of the data to remove any effect of the surrounding environment (i.e. temperature), fluctuations in current, or any other recorded noise. Thus, meaning the normalised ACPD signal would only be influenced by fatigue crack propagation.

The layout of the current wires is presented in Figure 4.13, where input and output current wires were on the same path, they were twisted to prevent interference and the output current wire was passed across the spot-welded PD probes enable current focusing. An image of the specimen after wiring is presented in Figure 4.14.

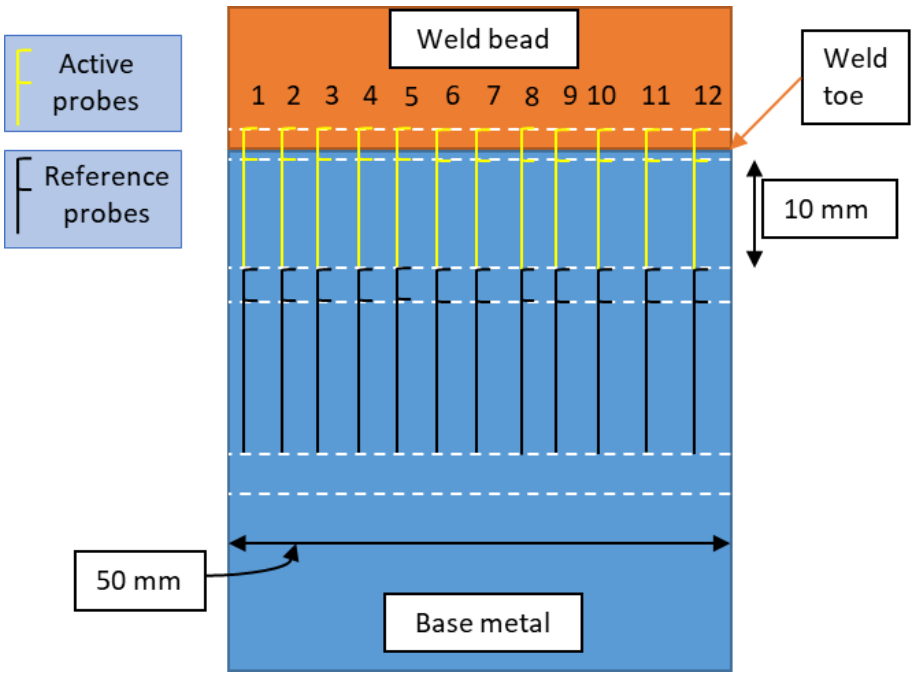

Figure 4.12 Schematic of voltage wires layout.

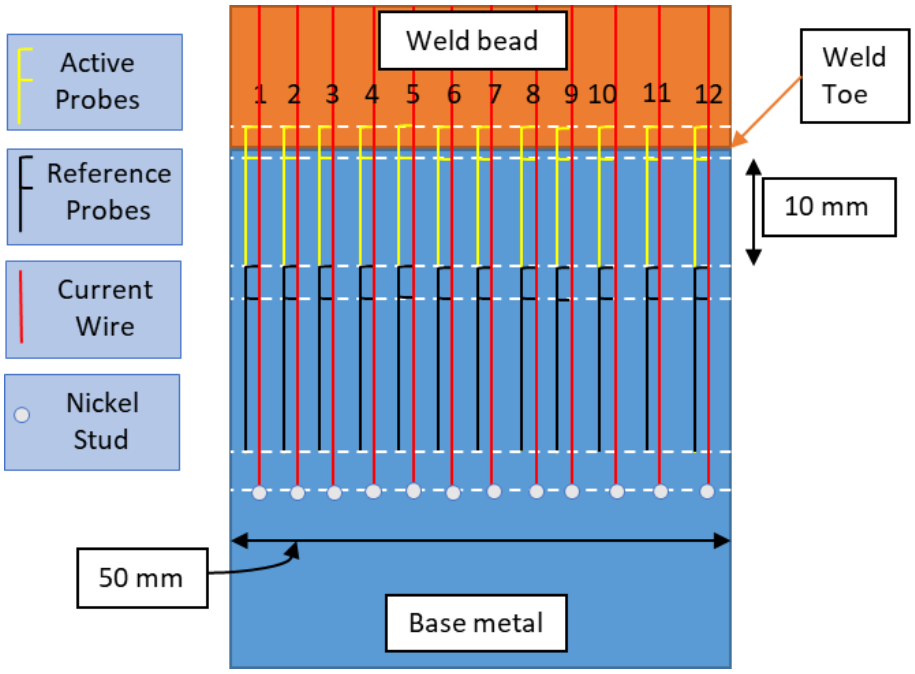

Figure 4.13 Schematic of current wires with voltage wires.

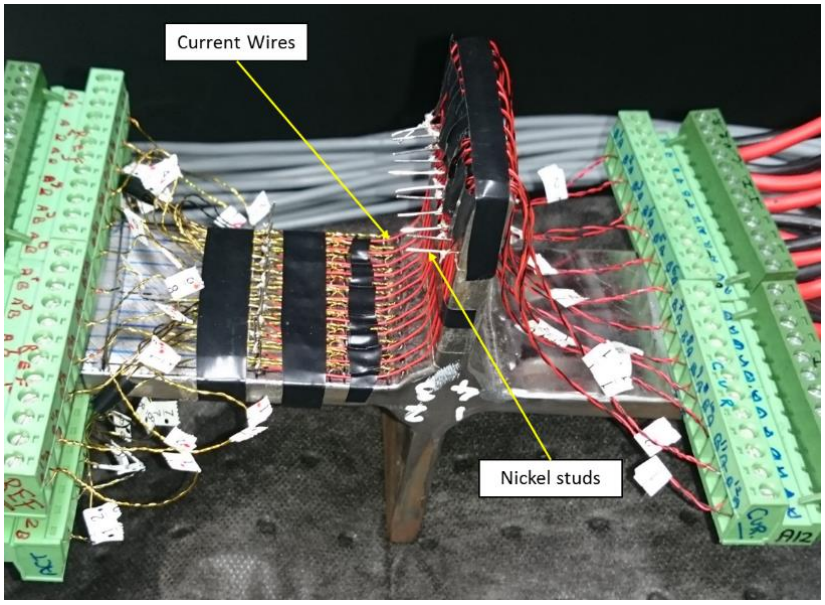

Figure 4.14 Specimen after wiring, ready for fatigue testing.

Once all wires were secured, a noise-cancelling filter was also applied within the ACPD system, which removed noise in the output signals above a defined frequency. In this work, the test frequencies used were between 1-5 Hz and thus a filter of 0.1 Hz was chosen.

Care was also taken to ensure that the current passing at the probes had fully stabilised before the PD output was measured. When the current is applied, it does not settle in the specimen instantaneously; i.e. it requires a certain number of seconds to stabilise at the desired value. Therefore, to get an accurate and stable reading, a delay period of 30 seconds was applied before recording each PD probe value. This resulted in a total of 6 minutes to obtain a complete data set

across the entire set of twelve probe pairs across the weld toe. This needed consideration when selecting the test frequency as this influences the number of cycles between each PD data point at each probe pair location. For example, at 1 Hz there would be 360 cycles between each PD data point and at 10 Hz there would be 3600 cycles between each data point.

4.4.3 Influence of Stress on ACPD Signal

Before the specimens were tested under cyclic loading, the response of each PD probe pair with respect to the applied tensile stress was investigated. The purpose was to provide calibration data similar to that obtained by Gibson [162]. Each specimen was held under a series of static loads, which covered the range of the applied stress range used for the subsequent cyclic loading. Four readings were taken at each load for each PD probe pair, to understand if there were any potential instabilities associated with the ACPD set-up.

Static tests were done in two sets. The first set was carried out before the fatigue test of each specimen at TWI Ltd and the second set was carried out (on different specimens, but of the same geometry) in the Testing Structures Research Laboratory (TSRL) at the University of Southampton. The purpose of the second test set was to provide further validation regarding the anomalies observed in the first set and the static loads were not followed by cyclic loading. The setup of all testing in this Section was similar and is shown in Figure 4.15a.

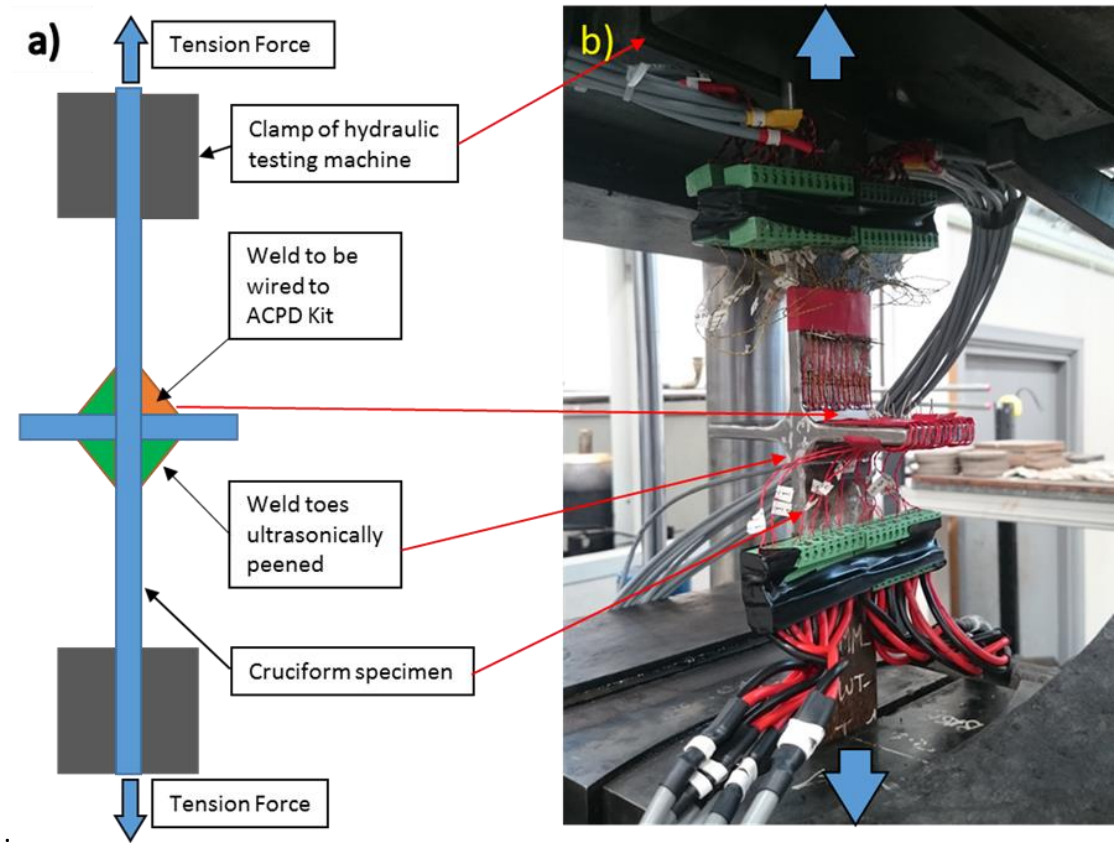

Figure 4.15 a) Schematic of specimen setup in fatigue testing machine; b) Annotated photograph of the specimen loaded in the testing machine at TWI Ltd.

4.4.4 Fatigue Testing

Fatigue testing was performed in load-control using a sinusoidal waveform in a Mayes servo-hydraulic test machine at TWI Ltd. The test machine had a load cell capacity of ±350 kN and was operated at frequencies between 1-5 Hz throughout the test programme. A frequency of 1 Hz was applied at the test start and this was stepped up to 5 Hz as the test progressed.

For each test, a nominal stress range of 270 MPa was chosen to give fatigue lives of at least 10^5 cycles. This was determined using the Class F design curve in BS7608 [6], which corresponds to a 97.5% probability of survival. A stress-ratio of 0.1 was applied, resulting in minimum and maximum nominal stresses of 30 MPa and 300 MPa respectively. The applied loads for each test are provided in Appendix B.1. A total of five tests were performed, two tests were to failure and three were interrupted:

Tests to failure – Two tests were performed to failure, which was indicated by a displacement change of 0.5 mm beyond the initial displacement at maximum load in each cycle. The life beyond this was considered negligible. The purpose of the tests was to correlate the crack depths measured on the fracture surfaces with the ACPD signals.

Upon failure of each specimen, it was broken open after immersion in liquid nitrogen to induce brittle fracture and provide a contrast in the fracture surface morphology with the fatigue cracks. The crack depths were then measured under the microscope.

Interrupted tests – Three tests were performed that were interrupted with the aim of stopping the test with cracks having depths less than 1 mm. Based on the work of Raujol-Veillé et al., 2015 [113] who used a single-probe ACPD set-up with Matelect equipment, a change in PD of 2 mV corresponded to a crack depth of 0.5 mm. Hence, the interrupted fatigue tests herein were stopped once a PD probe pair first indicated this same voltage change. These specimens were then used in the subsequent μ-CT and FE analysis work discussed in Chapter 3.

4.5 Results and Discussion - Fatigue Testing with ACPD Crack Detection

4.5.1 Influence of Stress on ACPD Signal

ACPD data was recorded at eight loads in the range of 0 kN to 130 kN (the load corresponding to a maximum nominal tensile stress of 300 MPa). For each load, four PD values were recorded for each probe pair and the average calculated. The average PD values obtained at each load level are plotted against the applied nominal stress in Figure 4.16 for the active probes across the weld toe and Figure 4.17 for the reference probes on the baseplate. The PD values presented in both plots have all been tared to start from zero, in order to simplify comparison.

At the active probes across the weld toe, the PD values of each probe increased as the stress increased. Up to 300 MPa, the change in PD at each probe varied between 0.005 mV and 0.019 mV. In comparison, at the reference probes, the PD values of each probe decreased as the stress increased. Up to 300 MPa, the change in PD at each probe varied between -0.009 mV and -0.023 mV. Although opposite in sign, the change in PD values for both active and reference probes were of similar magnitudes and both exhibited the same range. Overall, the same trend was seen in all the test specimens, i.e. an increase in PD at the active probes and a drop in PD at the reference probes.

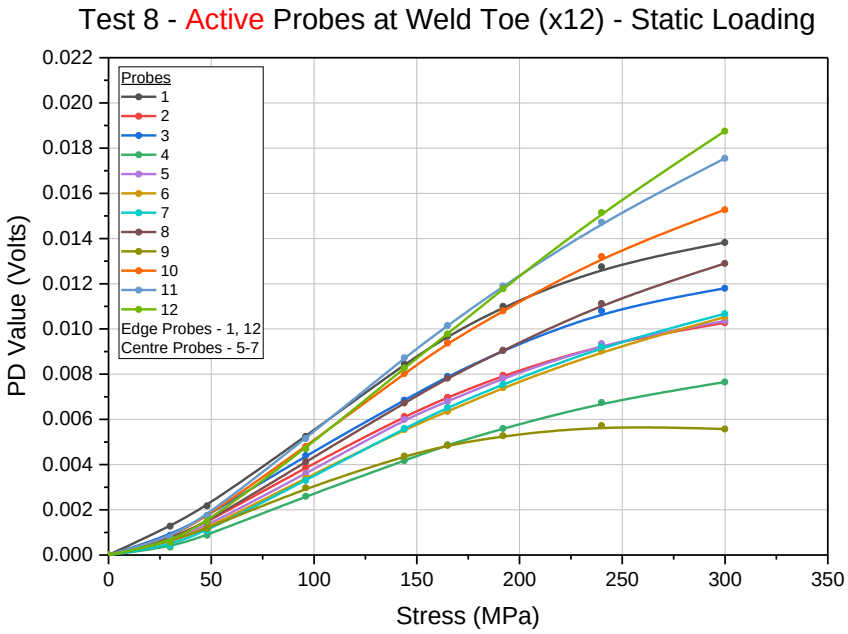

Figure 4.16 Plot of Static Loading ACPD data for Active Probes on weld toe.

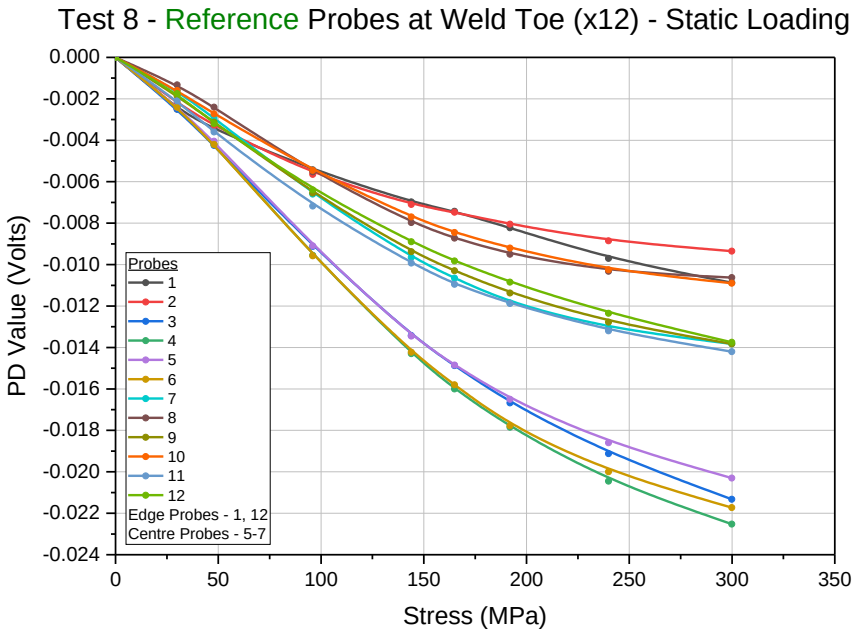

Figure 4.17 Plot of Static Loading ACPD data for reference probes on the base metal.

The increase in PD at the active probes across the weld toe goes against the general trend of PD decreasing as tensile stress (strain) increases, as has been observed in [162, 164-166] and for the reference probes herein. This observation prompted further investigation, which involved looking at how the relative position of the PD probes with respect to the current path and weld toe influences the PD values obtained under a tensile stress. The set-ups investigated are shown in Figure 4.18a and the change in PD as observed at maximum load (average of all measurements) for each case is provided below the schematics in Figure 4.18b.

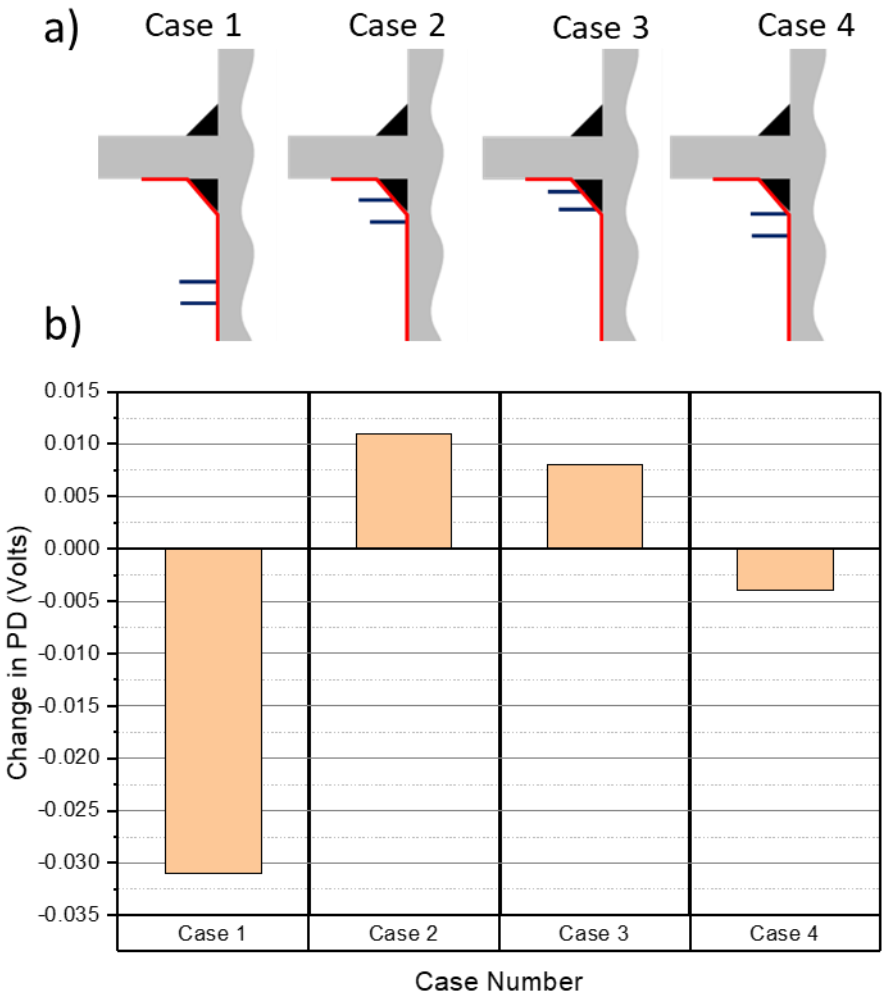

Figure 4.18 a) The different static test set-ups; b) the change in PD for each of the cases.

Interestingly, the change in PD seems to increase as the stress concentration increases and principal stress direction changes; stress concentrations are known to be highest directly at the weld toe (Case 2). The relationship between stress (strain) and change in PD is a complex phenomenon in ferritic steels, as elastic and plastic strains are known to influence both the material resistivity and magnetic permeability, which in turn influence the skin depth (Equation 4-1) of the current flow [162, 165, 166, 173, 174]. Increasing the elastic strain is known to decrease the resistivity of the material and thus cause PD to decrease; this is observed at the reference probes where the material remains below the material yield stress. In the presence of an initial crack or flaw, increasing the load, causes crack tip opening and blunting followed eventually by propagation; all of which cause the current path between the two probes to increase and thus cause PD to increase. In the case of the welds in this work, initial cracks are assumed not to be present and thus these are unlikely to account for the increase in PD signal observed at the weld toe. As described in [165], the magnetic permeability of iron is highly sensitive to plastic deformation and decreases rapidly under plastic strain to reach a steady state value. Such plastic deformation will be present at the weld toe, where stress concentration factors of 1.5-4.0 are common and this will have the effect of increasing the

skin depth as per Equation 4-1. This in turn would theoretically increase the current path and thus cause an increase in PD signal. This hypothesis is supported by the change in PD data obtained at the lower stress levels at the weld toe, where the total change in PD up to a stress of 100 MPa is less than that at the reference probes; 0.003 V to 0.005 V as opposed to -0.005 V to -0.010 V. Thus, suggesting that the effect of elastic strains on resistivity is still counteracting the influence of magnetic permeability on the current flow.

Due to the number of variables influencing the effect of stress on the change in PD, a simple correction could not be derived, and it was determined that further tests would be required to provide sufficient data for such a correction. Despite this, the change in PD values associated with an increasing stress, were observed to be relatively small compared to the change in PD values associated with crack initiation and propagation and hence it was decided to progress with fatigue testing, without accounting for stress effects. In order to minimise the influence of stress during tests, the ACPD system was connected to the servo-hydraulic test machine and PD measurements were only taken whilst the specimen was at maximum load. This was performed by the ACPD system capturing the maximum value of PD in a set of values at each instant of data recording (method of data capture previously explained in Section 4.4.2).

4.5.2 Fatigue test results

Six fatigue tests were performed after two trials were carried out to test the set-up and equipment. The remaining six tests have been analysed in this Section, out of which two specimens were tested to failure, and three specimens were interrupted once a change in PD of 2 mV was seen. The details of these tests in terms of number of cycles to either failure or desired PD change are shown in Table 4.2. Correlations between ACPD data and the actual crack and fracture surface are discussed further in this Section. Representative specimens will be discussed individually.

Table 4.2 Fatigue test results.

Test Number	Specimen	Number of Cycles	
		Tested to Failure	Interrupted
3	**T3_MA_MAG_I_2_R**	357,391	NA
4	**T4_SM_MAG_I_2_L**	787,788	NA
5	**T5_MM_MAG_I_1_L**	1,529,764	NA
6	**T6_MA_MAG_I_2_L**	NA	348,380
7	**T7_SM_MAG_I_1_R**	NA	84,344
8	**T8_SM_MAG_I_1_L**	NA	179,457

4.5.2.1 Tested to failure

According to BS7608 Class F [6] fatigue lives should be between 32,109 cycles and 239,667 cycles within plus and minus two standard deviations of the mean. Considering the fatigue results obtained from Crump's thesis [9] for welded specimens from the same heat and joints, equivalent fatigue lives are expected to fall between 80,533 cycles and 257,900. Therefore, all specimens exhibited higher than expected lives. For T5_MM_MAG_I_1_L, failure occurred in the baseplate held in the clamp of the testing machine. Due to this clamping issue which occurred due to misalignment in the jaws during the tightening process (the clamping was done mechanically), a very large fatigue life was obtained for this specimen for a relatively large nominal stress range.

The data for the two specimens tested to failure are presented in Appendix B.2 (results of Test-4 will be discussed in this Section). Figure 4.19 shows the plots (Recorded PD versus number of cycles) of the active probes for specimen T4_SM_MAG_I_2_L – Test-4 that was tested to failure. Specimen T4_SM_MAG_I_2_L failed at 787,788 cycles. As the recorded data was AC voltage, two values were measured – the real and imaginary component. In the plots to follow, only the real component has been depicted as this represents the resistive part of the measured ACPD voltage. This is done to eliminate the induced pick-up voltage issue that has been explained in Section 4.2.3. The values of PD from each probe have been tared to zero, in order to simplify data comparison and so only show the increase in PD with initiation and propagation of a fatigue crack. The values seen on the vertical axis are the change in recorded PD in millivolts. The top limit of the PD axis has been capped to magnify the variation in the data at lower PD values. From the plot, it can be clearly observed that the different PD probes are able to capture FCI and early crack growth rates. A notable result is the difference of the slope of the curve for probe 2 compared with the remaining probes. Probe 2

indicates FCI much earlier (12.3% of total fatigue life) compared with the rest of the probes, Table 4.3. Although for the first 100,000 cycles, probe 2 showed similar crack growth rates as the rest, the gradient of the curve changed to indicate the retardation of crack growth. This was deemed not be an effect of being closer to the edge of the specimen as such behaviour was not seen in the other probes that were closer to the edge (probes 1, 11 and 12). To understand this behaviour, it was necessary to study the crack growth rate data in further detail. For this purpose, the change in PD (ΔPD) was evaluated and is discussed in detail in Section 4.5.2.1.1.

Table 4.3 FCI as % of total fatigue life for each probe.

FCI as % of total fatigue life for each probe											
P1	**P2**	**P3**	**P4**	**P5**	**P6**	**P7**	**P8**	**P9**	**P10**	**P11**	**P12**
88%	12.3%	82%	54%	45%	22%	26%	39%	45%	45.5%	54%	69%

Figure 4.20 depicts the data recorded at the reference probes. Variation in the reference probes is minimal (fluctuations within ±1 mV) suggesting that the test environment did not vary during the course of the test. Some noise was observed in the probes just before final failure. Normalised data were also evaluated (ratio of active to reference voltage) to eliminate noise in the recorded data, shown in Figure 4.21. Normalised data was also not used for analysis, as it does not account for the differences in stress effect which is even more relevant in the presence of cracks and increased stresses in net sections.

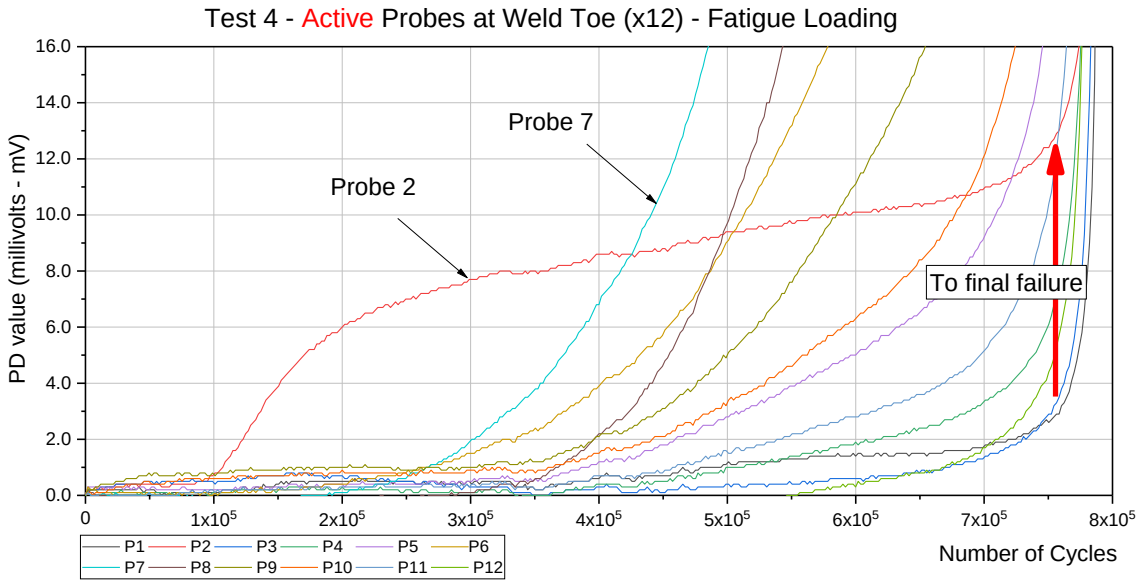

Figure 4.19 Active Probe - PD vs Fatigue Cycles Plot for T4_SM_MAG_I_2_L, tested to failure (787,788 cycles).

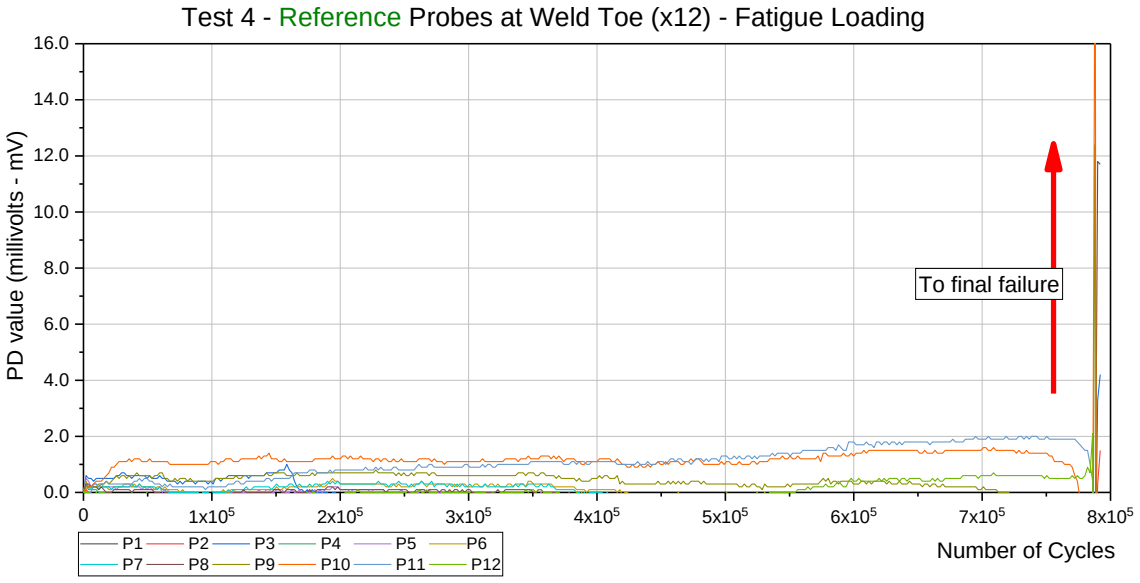

Figure 4.20 Reference Probe-PD vs Fatigue Cycles for T4_SM_MAG_I_2_L, tested to failure.

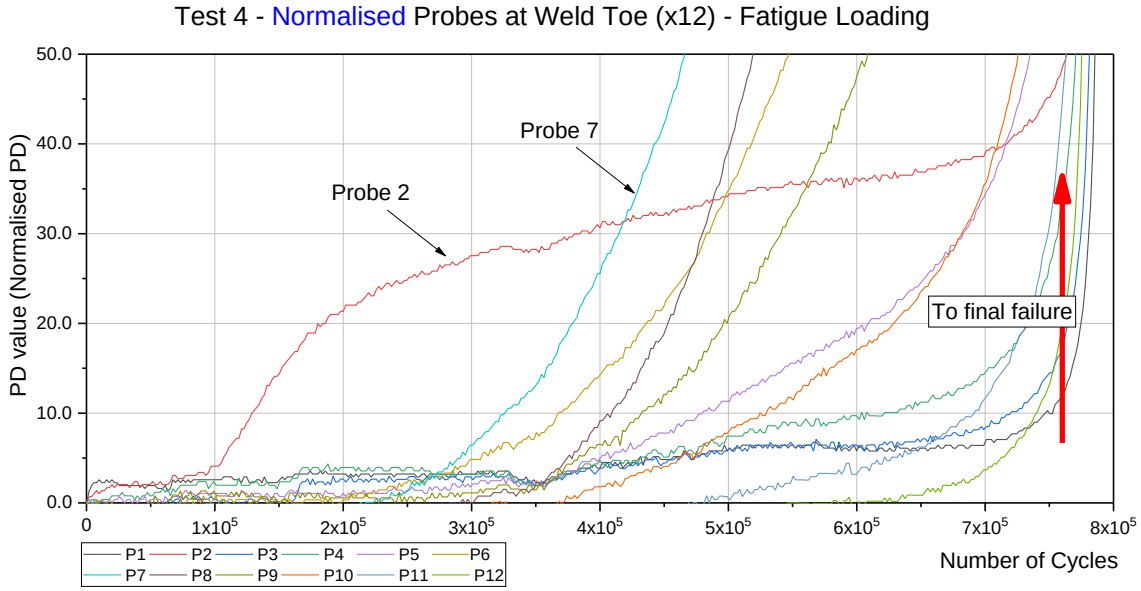

Figure 4.21 Normalised Data-PD vs Fatigue Cycles for T4_SM_MAG_I_2_L, tested to failure.

4.5.2.1.1 Arrested crack growth – Probe 2 in Test 4

Probe 2 is indicated in Figure 4.19, which suggests initiation occurring earlier as compared to that at the other PD probes. Observing the fracture surface once the test was completed showed that the ACPD data for probe 2 indicated the presence of a fatigue crack. Apart from looking at the raw data, the change in PD recorded after data point (interval due to the way the ACPD system recorded PD, described in Section 4.4.2) was plotted against the number of cycles to identify events causing changes in crack propagation at different intervals in the fatigue life of the specimen. Figure 4.22 depicts the variation of ΔPD with life. The resolution of the ACPD crack growth monitoring system is 0.1 mV. To compensate for noise in the PD data due to electrical noise at the signal resolution,

the data has been smoothed to allow for better visualisation of the small changes in ΔPD. Both a moving-point average (six points) smoothing technique and the Loess smoothing technique with a span of 5% (of total points recorded) were used [175]. Figure 4.23 is the normalised representation of the same data showing the same behaviour as the active probes, it shows that the recorded behaviour is not significantly influenced by environmental changes or any noise that may be present in the current flow.

At approximately 89,000 cycles, a sharp increase was recorded, Figure 4.22, which is considered to indicate crack initiation. After crack growth rate peaked at 131,000 cycles, retardation was observed until crack growth was negligible around 250,000 cycles (this can also be seen in the plateau shape of probe 2 plot after 250,000 cycles). Another increase was seen in ΔPD for probe 2 close to final failure due to increased compliance (possibly to do with the increased stress around the crack tip causing increased plasticity due to the smaller net section taking the load) of the specimen in the last stage of its fatigue life (due to a larger crack elsewhere in the specimen). Post fatigue testing, the specimens were broken open using liquid nitrogen to visualise the fatigue fracture surface better and possibly obtain a relation between recorded ACPD voltage and crack depth. Figure 4.24 depicts how the samples were broken. Liquid nitrogen enables brittle cleavage failure of steel, thus making it easy to distinguish between a propagating fatigue crack front and subsequent brittle failure.

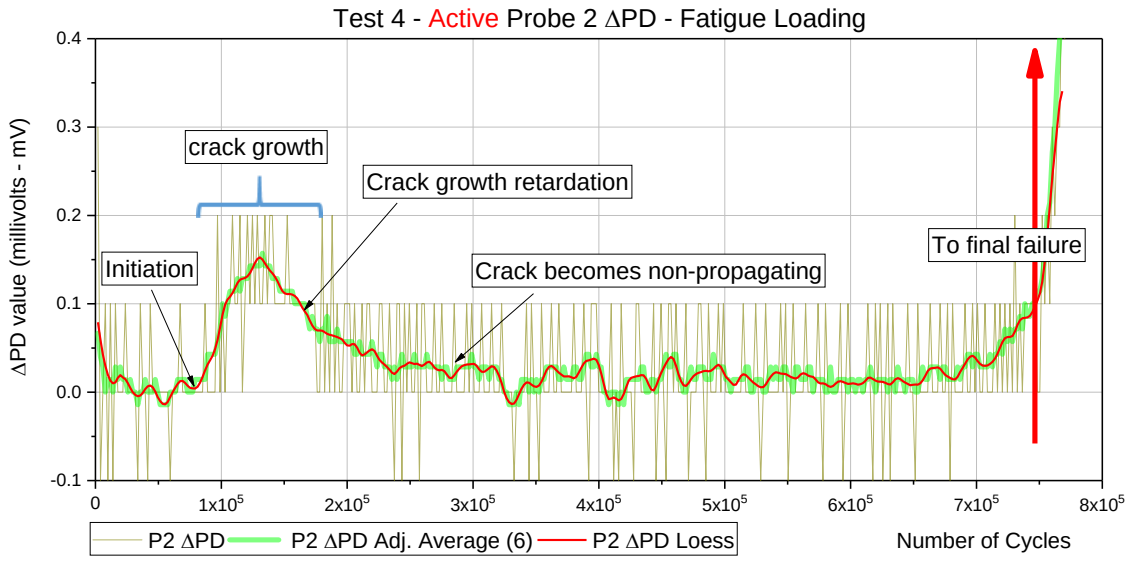

Figure 4.22 T4_SM_MAG_I_2_L - Active probe 2 ΔPD in fatigue loading, with raw and smoothed values of data.

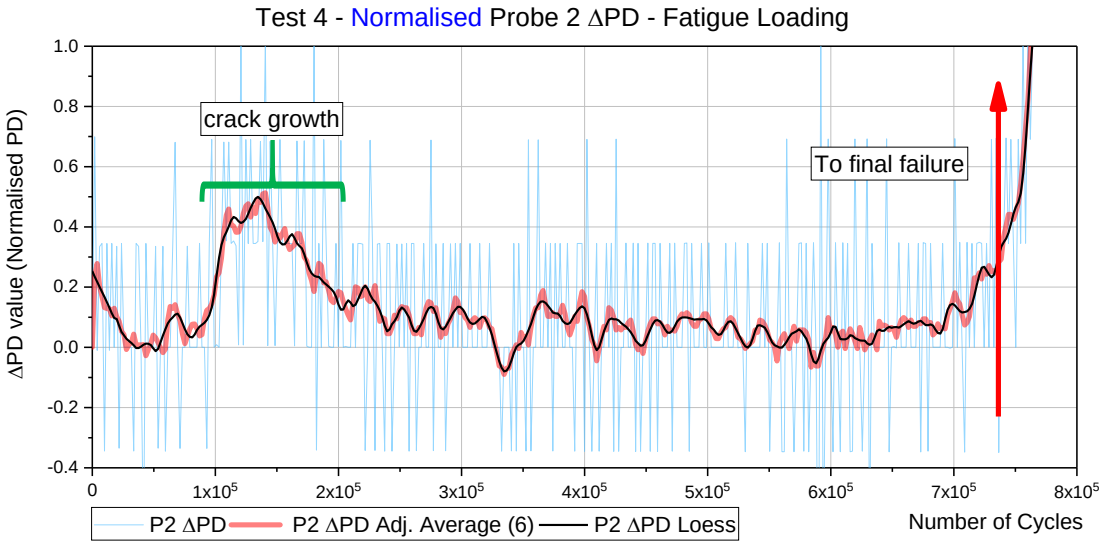

Figure 4.23 T4_SM_MAG_I_2_L - Normalised probe 2 ΔPD in fatigue loading, with raw and smoothed values of data.

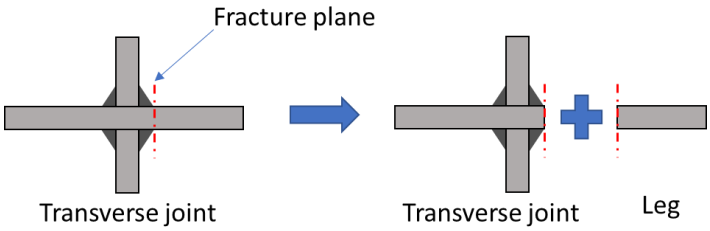

Figure 4.24 Schematic of the specimen being broken at the fracture plane to get two fracture surfaces - the transverse joint and the leg.

In order to obtain a macroscopic 3-dimensional view of the fracture surface, images were taken using the Alicona Infinite Focus Microscope, which enabled the visualisation of the entire fracture surface without requiring any image stitching. Figure 4.25 shows the images of the transverse joint section of the fractured sample. Figure 4.25a is the front view of the fracture surface, with the active probes numbered 12 to 1 from the left to the right of the image. The arrested crack growth depicted in Figure 4.22 is below probe 2 (highlighted in Figure 4.25a, magnified in Figure 4.25b. The crack can be seen to have stopped growing, as brittle fracture (due to cracking in liquid nitrogen) can be seen below the crack. Figure 4.25c is the top view of the weld toe showing the waviness of the fracture profile. Crack depth in line with probe 2 was 670 µm, and the maximum crack depth was measured to be 870 µm (the latter approximately 750 µm away from the line of probe 2). To the right of probe 2, a shallower crack can be seen below Probe 1. Both cracks seem to have coalesced, and multiple ratchet marks are identifiable across the crack front.

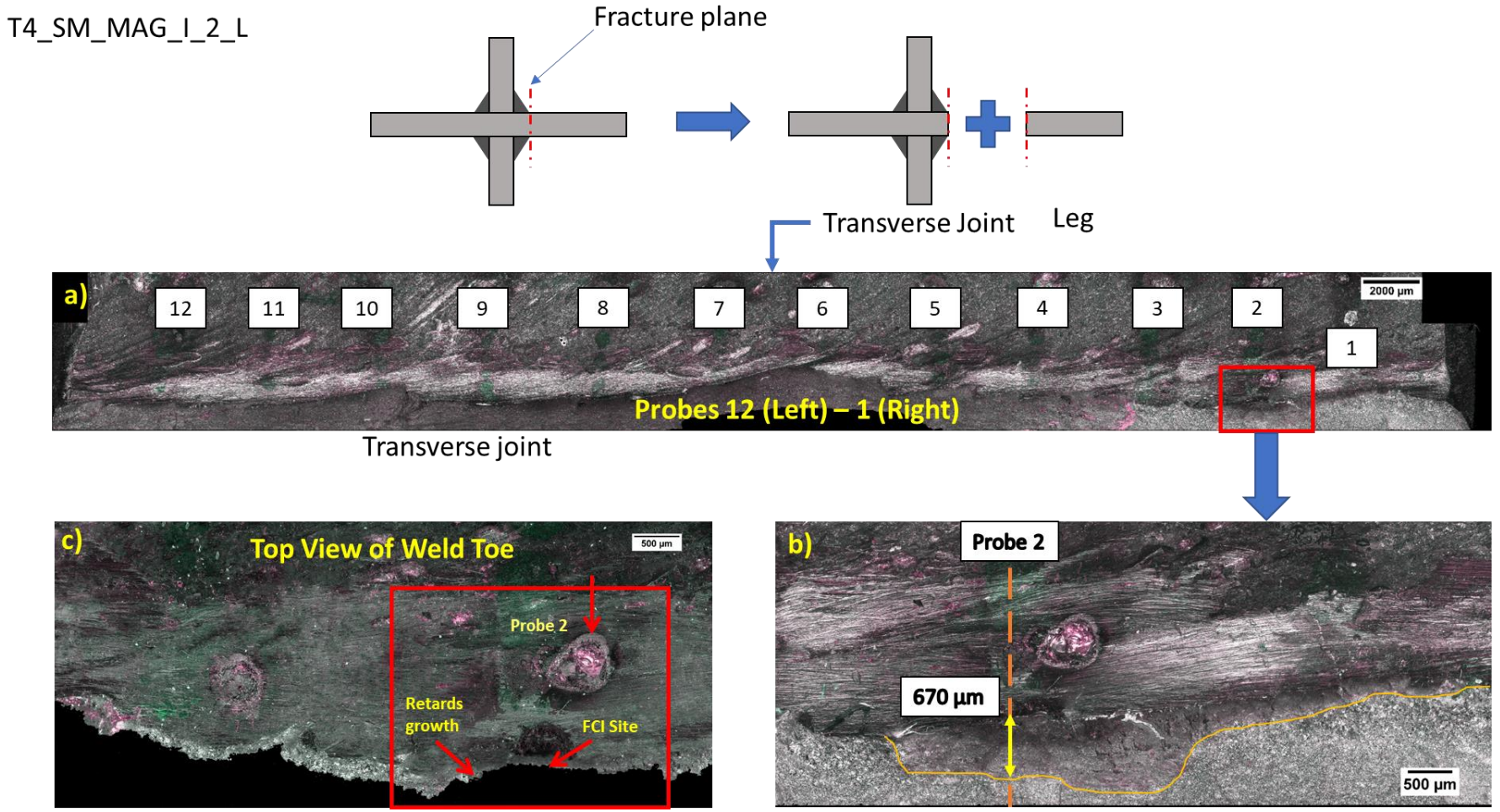

Figure 4.25 T4_SM_MAG_I_2_L - 3D scans of the cruciform section of the fractured specimen. Images were taken in the Alicona Infinite Focus Microscope.

The initiation of the crack under probe 2 was due to spatter from an ACPD probe wire spot welding residue. Figure 4.26b and Figure 4.26c are scanning electron microscopy (SEM) images taken of the arrested crack. The feature seen above the crack is nickel wire spot welding residue, confirmed by using Energy Dispersive X-ray Spectroscopy (EDX). The EDX data has been provided in Figure 4.27.

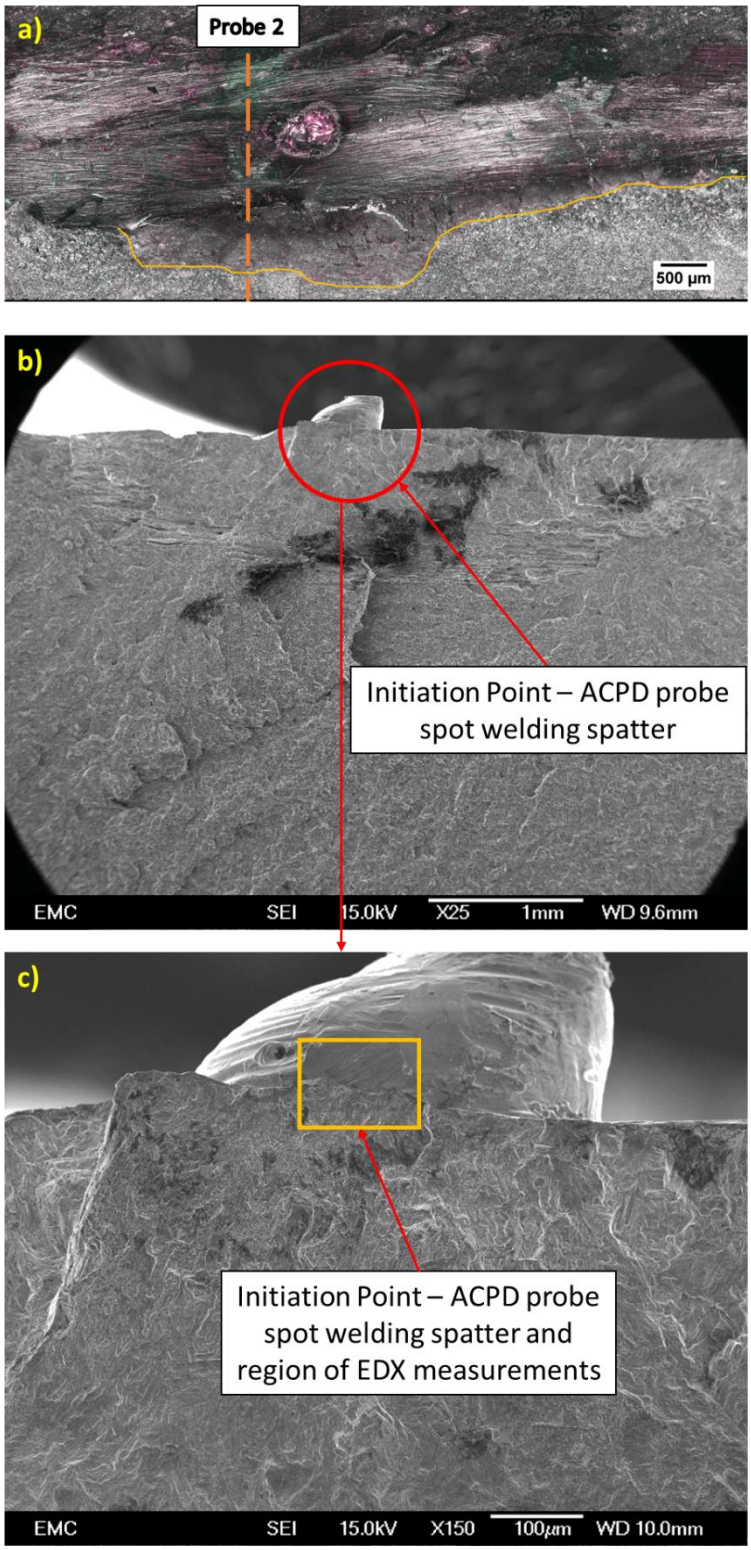

Figure 4.26 T4_SM_MAG_I_2_L – b) and c) are SEM images of the FCI site under probe 2. EDX showed crack caused by Nickel wire spot welding spatter.

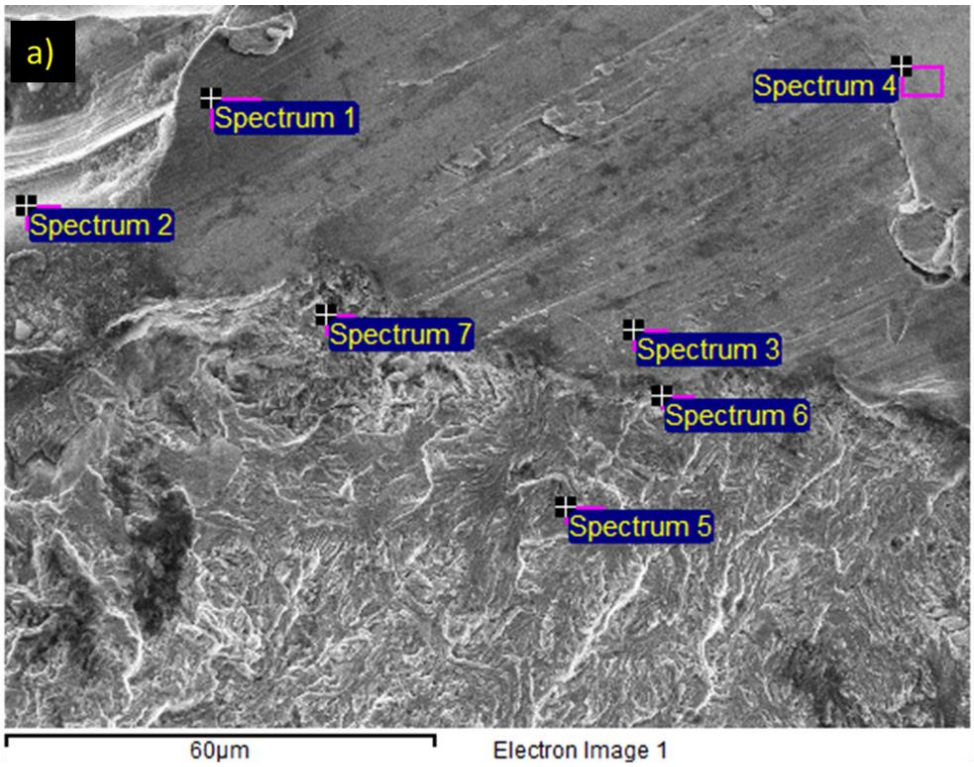

b)

Element / Spectrum ID	O	Fe	Ni	Total
Spectrum 1	1.55%	24.56%	73.89%	100.00%
Spectrum 2	2.68%	8.47%	88.86%	100.00%
Spectrum 3	3.88%	48.76%	47.37%	100.00%
Spectrum 4	NA	15.53%	84.47%	100.00%
Spectrum 5	NA	100.00%	NA	100.00%

Figure 4.27 EDX data - a) SEM-EDX image with points of measurement; b) Table with EDX data for each point.

The reason for crack retardation and arrest is not clear but could be linked to the proximity of the crack to the edge of the specimen, variation in the weld bead profile or crack closure. The specimens tested were in the as-welded condition. Crump, 2017 [9] carried out residual stress measurements on the same batch of specimens. Without cutting, longitudinal residual stresses were tensile and ranged between 397 – 644 MPa. Transverse residual stresses were slightly compressive and ranged between -20 – -67 MPa. For the equilibrium of the structure, it would be expected that these stresses would be counterbalanced by stresses of opposite magnitude away from the point of measurement (weld centre); for e.g. longitudinal tensile residual stress would be counterbalanced by compressive residual stress in the longitudinal direction away from the centre of the specimen, possibly through the thickness [11]. It was observed that cutting the specimens resulted in a drop in the longitudinal residual stress (250 – 500 MPa) and an increase in the transverse residual stress (150 – 200 MPa) [9]. Thus, the residual stress close to the edge of the sample would differ from that

at the centre as a result of lesser constraint as compared to the centre of the specimen which is in plane strain. Due to an increase in the transverse tensile residual stress, a similar increase of counterbalancing transverse compressive residual stress would be expected from the centre of the specimen, in the through-thickness. This could possibly cause crack retardation as the crack at probe 2 first initiated due to applied transverse loading and the presence of a stress concentration, but subsequently progresses to a stress field which has a compressive stress distribution. In the specimens during this PhD project, the dominant cracks in each specimen were all found to be initiating and coalescing approximately at the centre of the specimen.

It also may be that the variations in local crack profile caused local crack closure, but no such discernible changes in microstructure at the crack front were observed. A change in plane of the principal stress field may also cause retardation.

Apart from the FCI under probe 2, FCI was also detected under probe 7. Figure 4.28 to Figure 4.31 are plots of the raw and normalised PD values of probe 2 and probe 7. It can be seen in the plots that the point in the fatigue life of the specimen at which FCI under probe 7 crack is observed and crack growth retardation under the probe 2 occurs coincide, it could be argued that the change in compliance due to crack initiation at probe 7 resulted in changes in the far-field nominal stress distribution around probe 2 to cause crack arrest. However, the crack under probe 2 had a maximum depth of 870 μm, which should not affect the stiffness of the material enough to affect the far-field nominal stress distribution. The distance between these two probes was approximately 20 mm, 40% of the length of the specimen. At early initiation stages, it can be safely assumed that the stress field in front of the initiating crack below probe 7 would not be large enough to cause crack shielding, leading to crack retardation [14]. This can be further checked by calculating the plastic zone size.

The plastic zone size can be estimated using analytical solutions available in the literature [20, 176-179]. The plastic zone size under monotonic loading was initially developed by Irwin, 1960 [20] and later adapted by Schijve, 1964 [178] and Rice, 1965 [177], Equation 4-2. Monotonic loading was considered as it would give the largest estimate of plastic zone size for a conservative result, as cyclic loading plastic zone size has been observed to be smaller in size for the same maximum load [14].

$$r_p = \frac{1}{3.2\pi}\left(\frac{K_I}{\sigma_{ys}}\right)^2 \qquad 4\text{-}2$$

Where,

r_p Radius of plastic zone (m)

K_I Mode I stress intensity factor (N.m$^{-3/2}$)

σ_{ys} Uniaxial yield stress (N.m^{-2})

The monotonic stress intensity factor for Mode I crack opening, K_I can be defined as in 4-3 –

$$K_I = f(y)\sigma\sqrt{\pi a} \quad 4\text{-}3$$

Where,

$f(y)$ *Geometrical correction factor*

σ *Applied stress (N.m^{-2})*

a *Crack length (m)*

Solutions for geometrical correction factor, *f(y),* for the geometry used in these experiments can be found in Murakami, 1987 [180]. Based on the above equations, the plastic zone (r_p) size (based on LEFM) can be estimated for both cracks and is presented in Table 4.4. For a distance of 20 mm between the two probes, the plastic zone sizes are not big enough to have any influence on each other.

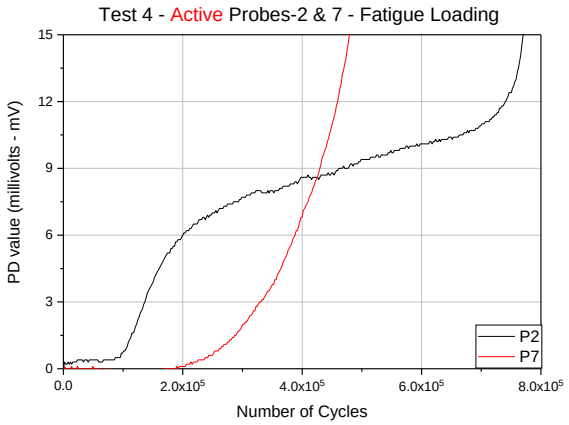

Figure 4.28 T4_SM_MAG_I_2_L - Active Probes 2 and 7 Actual PD.

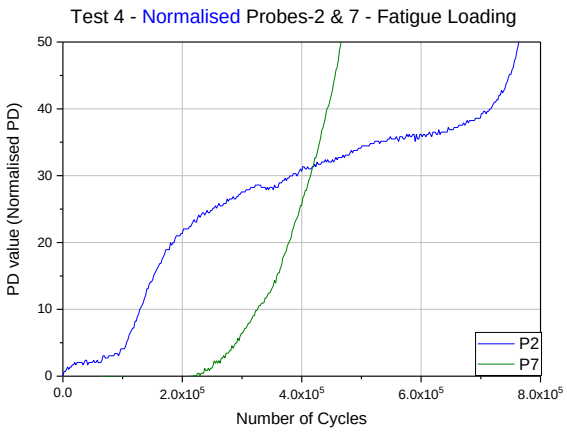

Figure 4.29 T4_SM_MAG_I_2_L - Normalised Probes 2 and 7 PD.

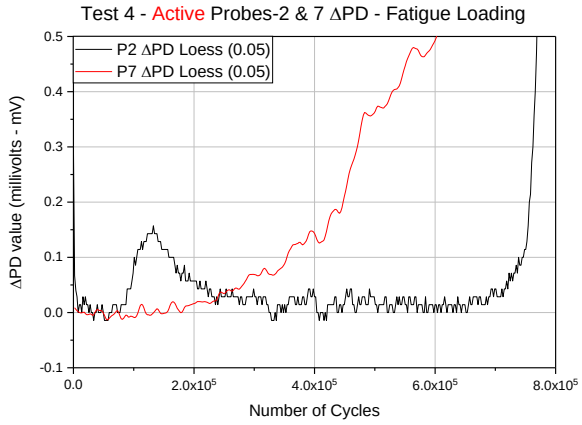

Figure 4.30 T4_SM_MAG_I_2_L - Active Probes 2 and 7 ΔPD.

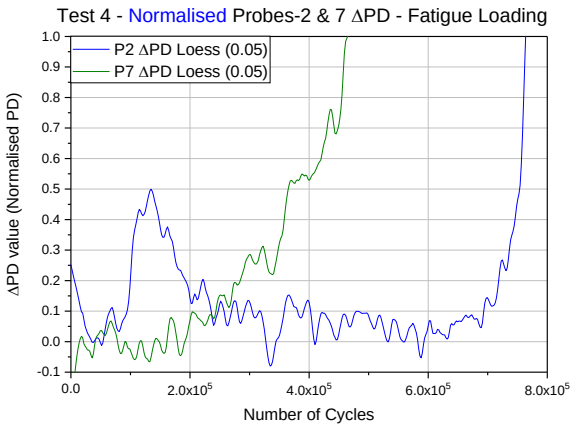

Figure 4.31 T4_SM_MAG_I_2_L - Normalised Probes 2 and 7 ΔPD.

Table 4.4 Plastic zone size estimates based on LEFM for probe 2 and probe 7 cracks at 220,000 cycles.

Parameters	Probe 2	Probe 7
Crack Depth, a (mm)	0.87	0.1
Aspect ratio, a/2c	0.2	0.2
Far-field nominal stress (MPa)	300	300
Geometrical correction factor, f(y)	1.7	1.7
Plastic zone size, r_p (mm)	0.47 mm	0.05 mm

The behaviour of multiple cracks and their influence on each other has been documented in the literature. Forsyth, 1983 [181] discussed the link between the crack tip plastic zone sizes of different cracks and their respective crack growth rates and morphology. Ochi et al., 1985 [182] advanced upon the work of Forsyth and gave an analytical relation for obtaining the minimum distance between two crack tips for coalescence, which also involved crack growth retardation due to coalescence. For the crack sizes seen in this study (given in Table 4.4), the distance would have to be approximately 100-200 µm. In this case, it was approximately 19.5 mm. Wang et al., 1995 [183] looked at the behaviour of multiple stress corrosion cracks experimentally and observed their interaction as a function of their relative distance. For cracks that were 20 mm apart (similar to what is being discussed for probe 2 and probe 7), no crack shielding was ascertained. Such cracks were seen to be growing individually and subsequently coalescing. An empirically derived relation was stated in this work, which relates the maximum value of lateral separation (y) between two cracks with the crack length ($2a$) for achieving coalescence, Equation 4-4.

$$y \leq 0.143(2a) \quad \text{4-4}$$

Therefore, it is difficult to determine the precise reason for the retardation and subsequent arrest of crack growth for the crack under probe 2, as well as the reason for the time of both probe 2 crack arrest and probe 7 crack initiation to be similar. Different approaches were discussed, but not enough evidence is available to attribute the cause to an approach.

4.5.2.1.2 Crack propagation to failure

Probe 7 picked up the first sign of crack growth that formed part of the crack causing final failure, followed by probe 6 and probe 8. Figure 4.32 depicts the active ΔPD data and Figure 4.33 depicts the active ΔPD data only after 500,000 cycles, with a larger cap on the ΔPD values (y-axis) to better highlight the data at final failure. The three probes that recorded initiation first have been marked. Initiation was first recorded at probe 7 at approximately 230,000 cycles, 29% of total fatigue life. Probe 6 and probe 8 recorded a change in PD at approximately 280,000 cycles, 6% of total fatigue life after initiation at probe 7.

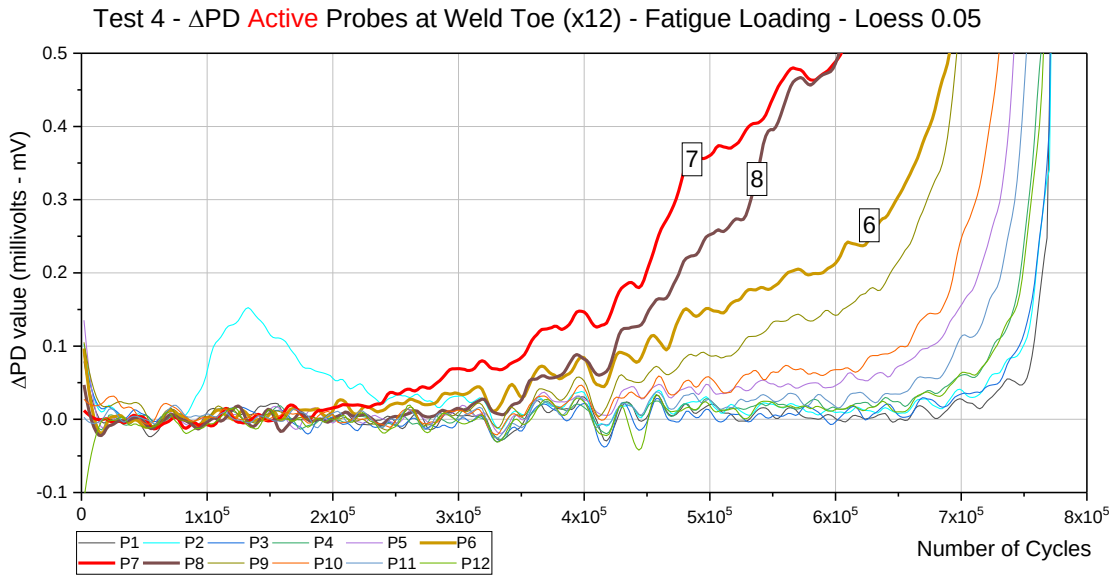

Figure 4.32 T4_SM_MAG_I_2_L - Active Probes 1-12 ΔPD.

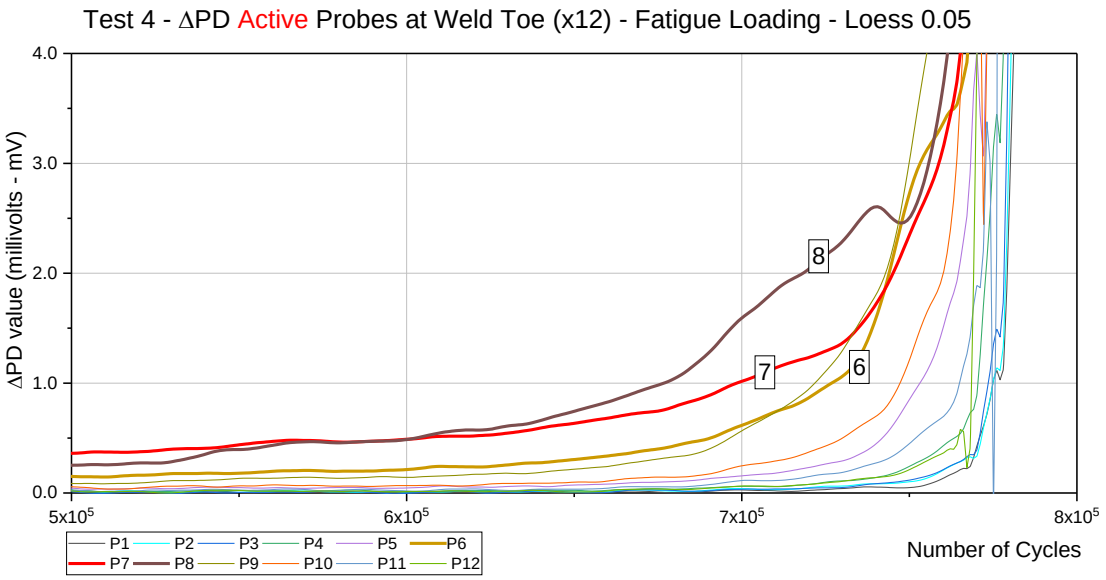

Figure 4.33 T4_SM_MAG_I_2_L – Active Probes – 500,000 cycles onward 1-12 ΔPD.

Figure 4.34 shows the fracture surface of the transverse joint-end of the broken specimen. The failure path observed on the fractured specimens was a result of multiple cracks initiating at different locations across the weld toe, confirmed by a large number of ratchet marks on the fracture surface. Evidence of individual cracks propagating along a weld ripple were also found; Figure 4.35a and Figure 4.35b. Weld defects such as undercuts and porosities act as stress concentrating features and have been observed to initiate cracking, shown in Figure 4.35c-d.

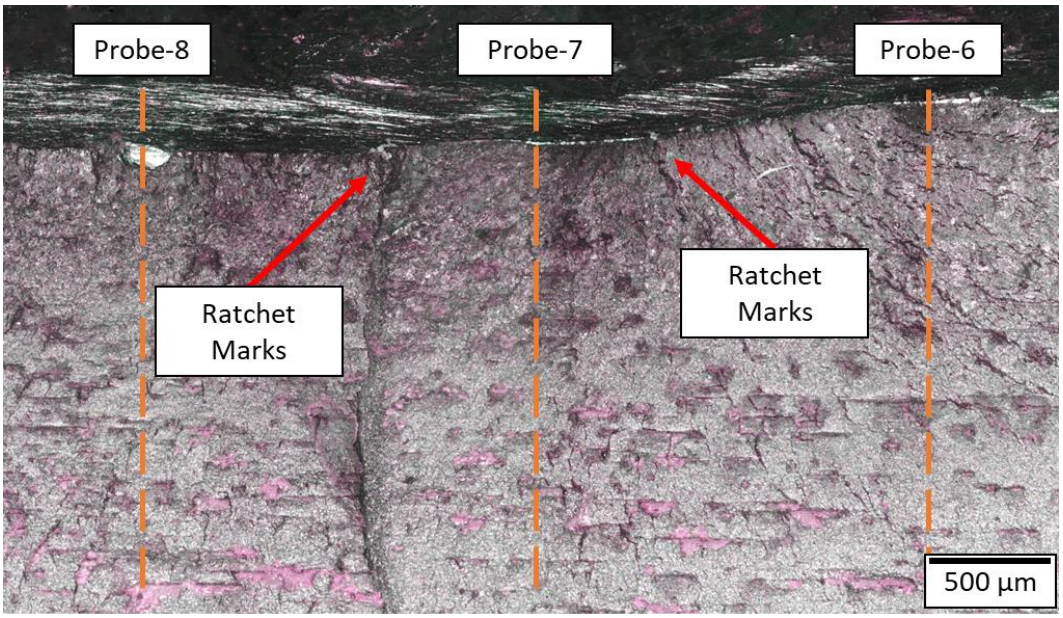

Figure 4.34 T4_SM_MAG_I_2_L - Alicona Infinite Focus Microscope scan of the transverse joint fracture surface highlighting probes 6-8.

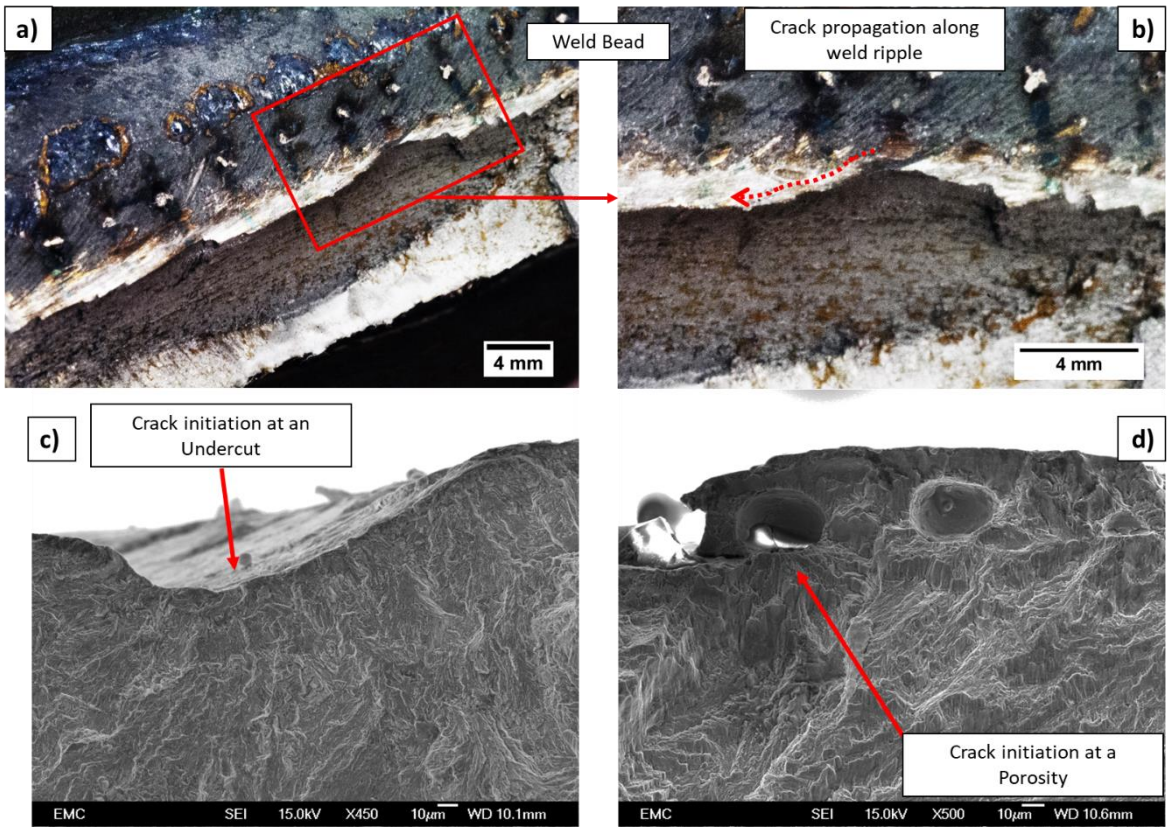

Figure 4.35 a) Failed weld toe (Optical Camera); b) Cracks propagating along weld ripple resulting in multiple ratchet marks (Optical Camera); c) SEM image of a weld defect – undercut; d) SEM image of a weld defect – Porosity.

4.5.2.2 Interrupted tests

Three specimens were interrupted to once a change of at least 2 mV was observed in the recorded actual PD. The data from each test has been shown below.

Table 4.5 Interrupted test data (probe-wise) for Test 6 (MA_MAG_I_2_L, also HQ_T06).

Test 6 (MA_MAG_I_2_L)		
Probe Number	**Overall PD Change (mV)**	**FCI as % of total interrupted life**
P1	No change observed	
P2		
P3		
P4		
P5	2	72%
P6	1	80%

P7	0.5	92%
P8	No change observed	
P9		
P10		
P11		
P12		

Table 4.6 Interrupted test data (probe-wise) for Test 7 (SM_MAG_I_1_R, also HQ_T07).

Test 7 (SM_MAG_I_1_R)		
Probe Number	**Overall PD Change (mV)**	**FCI as % of total interrupted life**
P1	No change observed	
P2		
P3		
P4	1.6	50%
P5	3.9	49%
P6	2	58%
P7	1.3	72%
P8	No change observed	
P9		
P10		
P11		
P12		

Table 4.7 Interrupted test data (probe-wise) for Test 8 (SM_MAG_I_1_L, also HQ_T08)

Test 8 (SM_MAG_I_1_L)		
Probe Number	**Overall PD Change (mV)**	**FCI as % of total interrupted life**
P1	No change observed	
P2		
P3	0.3	75%
P4	2.7	56%
P5	1.3	63%
P6	0.7	66%
P7	3	37%
P8	0.7	81%
P9	No change observed	
P10		
P11		
P12		

In this Section, the results of Test 8 (labelled Test8_SM_MAG_I_2_L), Table 4.7, are presented as representative of the interrupted fatigue tests using ACPD crack growth monitoring technique. Test-8_SM_MAG_I_2_L was tested until 179,457 cycles, and the first indication of initiation was observed at 67,000 cycles at probe 7, shortly followed by detection at probes-4, 5, and 6. Figure 4.36 shows the active data for probes 2-12. Probe 1 has not been shown, as the joint of the probe to the weld toe was not consistent over the whole test resulting in erroneous data. Figure 4.37 shows the change of at least 2 mV in probe 4 and probe 7. A maximum change of 3 mV occurred for probe 7, indicating a crack depth (a) of approximately 300 μm (based on PD vs crack depth analysis in Section 4.5.3).

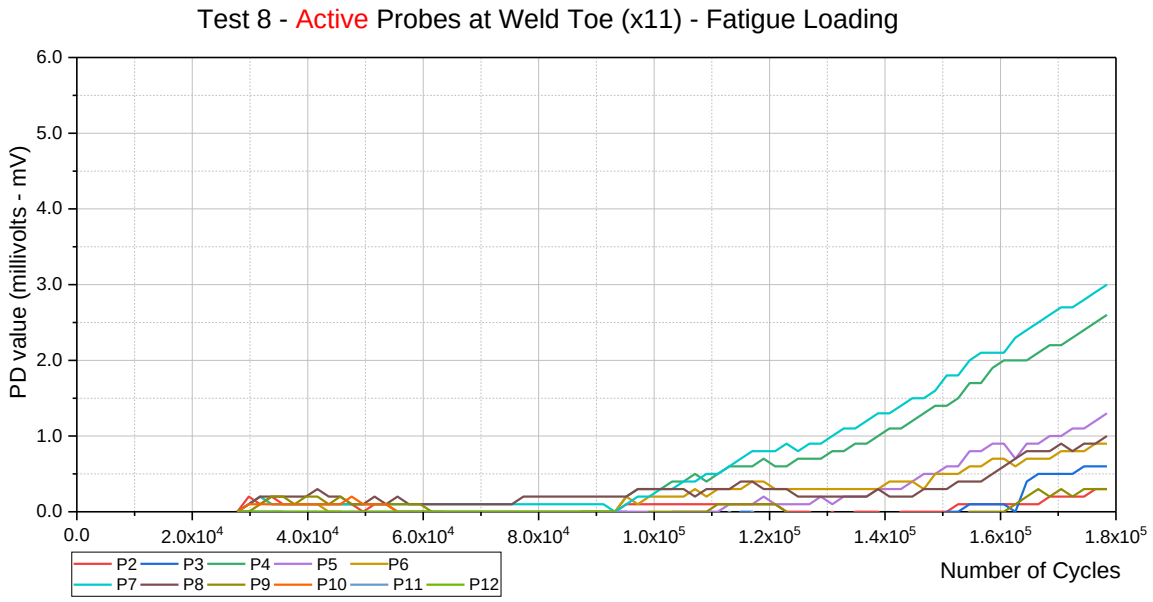

Figure 4.36 Active PD vs Fatigue Cycles Plot for T8_SM_MAG_I_1_L, interrupted test (179,457 cycles).

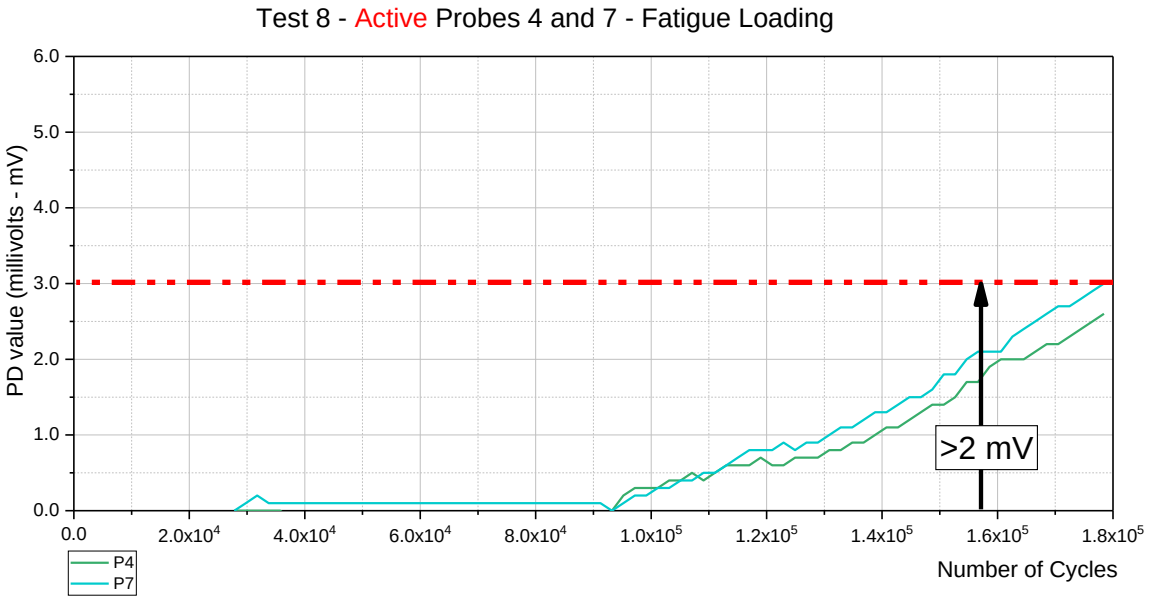

Figure 4.37 Active PD vs Fatigue Cycles Plot for T8_SM_MAG_I_1_L Probes 4 and 7, showing an increase of at least 2 mV.

4.5.3 Crack depth vs PD voltage – Analysis

To be able to utilise the ACPD technique for crack growth monitoring, it the voltage signal obtained needs to be calibrated with the corresponding crack depths. Although changes in PD can be used to qualitatively compare crack growth relatively, linking this with actual crack size would also provide quantitative information about crack propagation. In this project, three specimens have been tested to failure to assess whether it is possible to obtain this relationship. Qualitatively, it can

be concluded that PD with loading cycles presented in Section 4.5.2.1 have clearly shown variations in recorded PD (both actual and normalised data) with number of cycles and therefore provide measurable crack propagation.

4.5.3.1 Test-4 (HQ_T04) – Analysis of arrested crack (discussed previously in Section 4.5.2.1.1)

Figure 4.38 represents the data from Test 4. The figure combines both the active PD and ΔPD in a multiple Y-axis line plot. The purpose of the plot is to be able to ascertain a $\frac{Crack\ Depth}{PD\ Change}$ relation and discuss the challenges that are associated with obtaining such a relation. The plot gives data for Probe 2 and probe 7. The data for probe 2 represents the arrested crack discussed previously in Section 4.5.2.1.1, and the data for probe 7 represents a crack which propagated to failure. As discussed previously, probe 7 was also the first PD probe (except probe 2) to indicate crack growth.

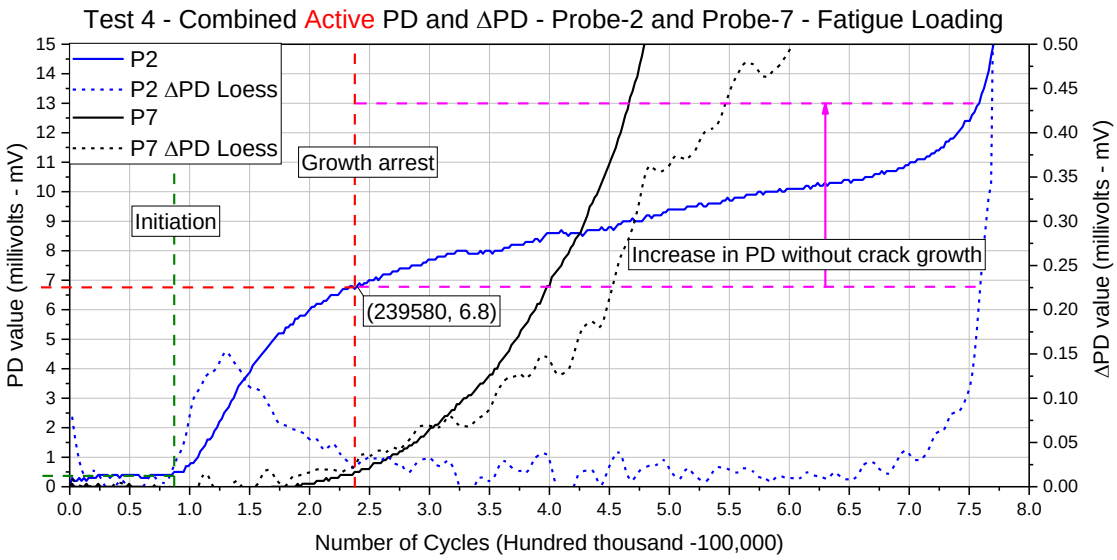

Figure 4.38 T4_SM_MAG_I_2_L - Combined active PD and ΔPD plot for probe 2 and probe 7, highlighting the point at which the crack propagation stopped.

Figure 4.38, the plot of probe 2 (P2) ΔPD (smoothed using Loess function with 5% span), shows that the crack under probe 2 initiated at approximately 83,000 cycles and stopped propagating at approximately 240,000 cycles. Although some variation can still be seen beyond 240,000 cycles, the ΔPD value ranges between 0-0.05 mV. This can be ascertained to be a result of the Loess smoothing as the resolution of the ACPD is 0.1 mV. At this point, the active probe 2 PD change due to crack propagation between 83,000 to 240,000 cycles (crack propagation life of 157,000 cycles) is seen to be 6.3 mV. The maximum depth of the crack observed below probe 2 was 870 µm. Based on the above two values, the approximate value of $\frac{Crack\ Depth}{PD\ Change}$ can be calculated to be 138 µm/mV assuming a linear correlation between PD and crack depth. This is a 45% difference compared to

the previously achieved resolution of 250 µm/mV using the same Matelect ACPD system in the work of Raujol-Veillé et al., 2015 [113] (it is not possible to identify the specific reason for this improvement, as the available literature did not provide adequate test information for a comparison). However, there is a discrepancy that needs to be addressed in the active PD plot of probe 2. From the ΔPD data for probe 2, the crack has become non-propagating beyond 240,000 cycles. However, the value of PD continues to increase beyond 240,000 cycles by at least a further 4 mV, up to the last stages of the fatigue life of the specimen (beyond 720,000 cycles, final failure occurred at 787,788 cycles). This mismatch of crack growth information between the PD and ΔPD data can be attributed to the effect of stress on ACPD, as discussed in Section 4.4.3. The effect of stress on ACPD becomes more prominent as the net cross-section of the specimen reduces, thereby increasing the stress (proportionately with decrease in net cross-section) in the remaining ligament in a load-control fatigue test. The PD and ΔPD values of probe 7 show that a crack is propagating from 220,000 cycles and this propagating crack will have a considerable impact on the net cross-section (other probes also detect crack propagation, as shown previously in Figure 4.32). The PD signal can therefore be described by Equation 4-5.

$$Total\ PD = PD_{crack\ growth} + PD_{effect\ of\ stress} \quad \text{4-5}$$

Where

$Total\ PD$	Overall measured PD
$PD_{crack\ growth}$	Change in PD due to crack propagation
$PD_{effect\ of\ stress}$	Change in PD due to increased stress in the remaining ligament of the fatigue specimen

In Equation 4-5, it is difficult to obtain an exact relation for $PD_{effect\ of\ stress}$ as the value of the change in PD not only varies with stress, but also with the effect of stress, strain, crack tip opening and blunting on the skin depth and material properties such as magnetic permeability and resistivity, explained previously in Section 4.5.1. In Figure 4.39, the maximum crack depth under each probe for Test 4 has been given. The red line-symbol plot represents the change in PD that occurred from the initiation of a crack (the first initial increase in PD from stable PD signal) below each probe until the end of the test at 787,788 cycles, the total number of cycles that the specimen was tested for until a displacement of 0.5 mm was recorded in the testing machine (a displacement of 0.5 mm in the testing machine was used to stop the testing machine).

The FCI life detected at each probe (the first initial increase in PD from stable PD signal) has been provided at the bottom of the figure. It can be seen that the curve representing the change in overall PD for each probe follows the shape of the curve representing maximum crack depth (except Probe 3, which possibly picked up changes in PD from the surrounding crack propagation events). This is

also seen in Figure 4.40, which depicts the same information of ACPD and final (maximum) crack depth for Test 3. It is important to note that for Test 3, no PD data was available for Probe 1 as the joint of the probe with the specimen was compromised, and therefore no PD data could be obtained. Without further analysis into the phenomena involved with effects of stress on ACPD, it would be difficult to break the PD value into the variables on the right-hand side of Equation 4-5.

For Test 4, the $\frac{Crack\ Depth}{PD\ Change}$ relation ranged between 12 and 37 µm/mV, with a standard deviation of 7.7. For Test 3, the data ranged between 10 and 21 µm/mV, with a standard deviation of 3.9. The value (denoted by the blue line in both Figure 4.39 and Figure 4.40) is, therefore, is less scattered for Test 3 as compared with Test 4. It is not entirely certain why this occurs, but an important difference between the two specimens is the arrested crack in Test 4, and the region of no fatigue cracking at Test 4 Probe 3. The $\frac{Crack\ Depth}{PD\ Change}$ for Probes 6-12 for Test 4 ranged between 12.5-20 µm/mV, whereas it was only within 20-21 µm/mV for Test 3. This variation in the relative scatter of each specimen could be attributed to the different final crack fronts of each specimen and more importantly, the different in the final PD values at each probe. Test 4 recorded relatively higher values of final PD for similar values of crack depth. This could be attributed to the effect of stress and associated phenomena (discussed in Section 4.5.1) and could also be an effect of residual stress profiles (especially in the region of uncracked ligament). However, both plausible explanations would require further testing, which was not carried out in this PhD project.

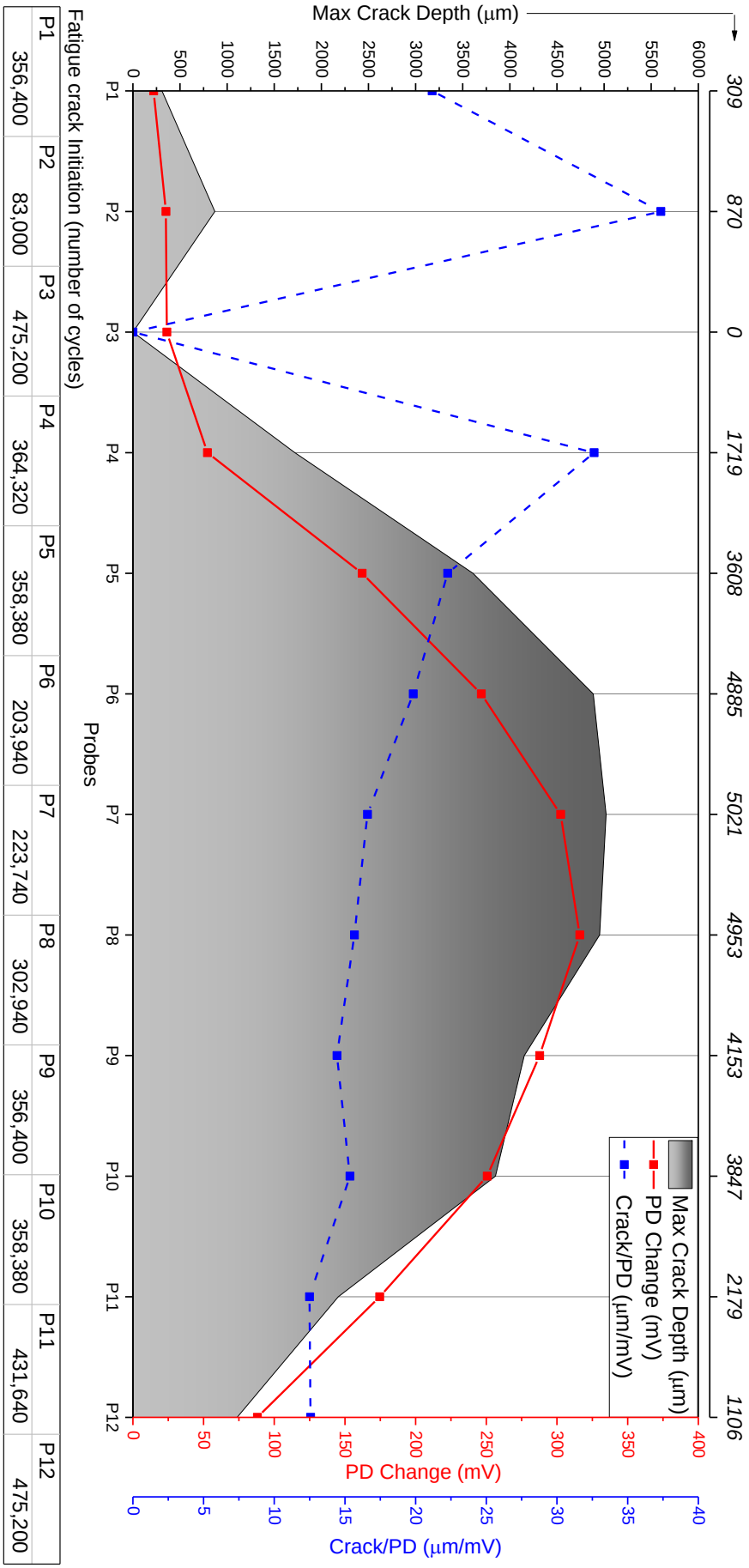

Figure 4.39 T4_ SM_MAG_I_2_L – Crack Depth versus PD Analysis

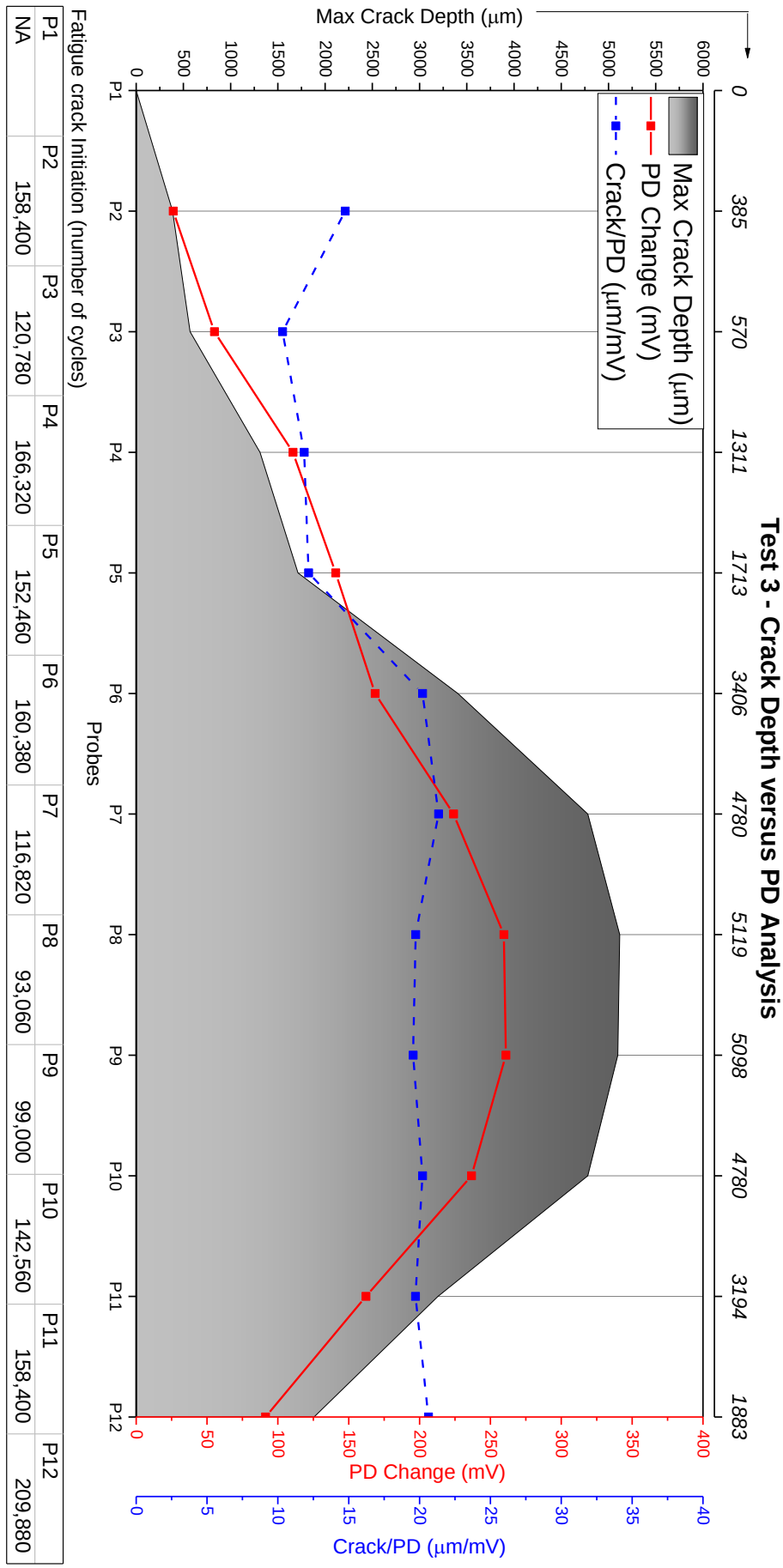

Fatigue crack Initiation (number of cycles)

P1	P2	P3	P4	P5	P6	P7	P8	P9	P10	P11	P12
NA	158,400	120,780	166,320	152,460	160,380	116,820	93,060	99,000	142,560	158,400	209,880

Figure 4.40 T3_ MA_MAG_I_2_R – Crack Depth versus PD Analysis

4.5.3.2 Crack depth vs PD voltage analysis – Conclusions

The analysis of crack depth versus PD voltage highlights the disadvantages of ACPD well beyond fatigue crack initiation. If the relation of $\frac{Crack\ Depth}{PD\ Change}$ is to better defined (as available for other standard fatigue crack growth techniques in ASTM E647 [157]), further tests would be required. A value of critical crack depth could be defined for validation limitations (obtained as a relation to the measured ACPD skin depth for the material and test setup (ACPD skin effect and associated skin depth have been discussed in Section 4.2.1). This would allow for a better choice of ACPD parameters such as the value of the current applied and its frequency. Based on the results obtained in this project, it could be concluded that ACPD crack growth monitoring system should primarily be used for FCI detection, and crack size monitoring of small cracks where the size of small cracks is comparable to the ACPD skin depth for a particular test setup. Work done by Wojcik et al., 2017 [166] is an excellent example of the combination of ACPD for FCI determination and DCPD for crack propagation measurements. The limitations of the tests performed in this part of the project (described in Chapter 4) were identified, and adequate measures were taken to avoid such issues in the next set of experiments, described in Chapter 5.

4.6 Validation of 3D finite element stress analysis using ACPD and serial metallography

Chapter 3 Section 3.5 described the 3D FE analysis of the fatigue-tested welded specimens from X-ray CT scanned volumes. ACPD results and Serial Metallography were used to validate the 3D FE stress analysis results, and the validation process for one such specimen will be discussed in this Section.

4.6.1 Methodology

The validation described in Section 4.6 involves 3D FE analysis, ACPD crack growth monitoring and serial metallography. 3D FE analysis has been discussed extensively in Section 3.5; the methodology for ACPD crack growth monitoring was discussed in Section 4.4. The methodology for the serial metallography is discussed below.

Serial metallography is a commonly used destructive experimental technique of visualising cracks. It is used with optical microscopy, SEM, electron back-scatter diffraction (EBSD) and focused ion beam (FIM) [184-188]. For this project, serial metallography was implemented using optical microscopy to capture two-dimensional (2D) images of fatigue cracks in the fatigue-tested welded specimens. Serial metallography involved grinding and polishing to remove material for producing

sections. Microscopic images were taken of each section, and the amount of material removed was measured.

The specimen was mounted in resin as shown in Figure 4.41 to make it easier to process the weld specimen. Initially, hot-mounting resin Bakelite was chosen as it produces a mount in approximately 10 minutes. However, it was observed that Bakelite does not adhere sufficiently well to the irregular weld bead surface, thus resulting in gaps at the weld bead mount interface. During the serial sectioning process, alcohol and soap (used for cleaning the surface after polishing) accumulated in these gaps and were difficult to remove (even after drying). These affected the quality of the images taken for analysis. To mitigate this issue, cold-mount Struers Epoxy Resin (Struers EpoFix) was used. Although this requires a much higher curing time of 12 hours, it is of a lower viscosity than hot mount Bakelite, and thus gaps between the non-uniform wavy weld bead and the curing mount-resin were significantly reduced. Another advantage of Struers EpoFix over Bakelite was that the former creates a transparent mount, enabling a better visual inspection of the welded specimen as the serial sectioning proceeds. Once the specimens had been mounted, it was necessary to identify the amount of grinding (in terms of time and grit size) and polishing (in terms of time and polishing solution particle size) that was required to remove a certain amount of material during each sectioning process. A micrometre was used to measure the thickness of the mounted specimen to identify the amount of material removed. To check the accuracy of using a micrometre for this purpose, the weld specimen was removed from the mount, and the amount of material removed based on the micrometre readings of the mounted specimen was compared to the actual amount of material removed. The average error was with an acceptable range of ±100 µm or ±0.1 mm. The resolution of the micrometre used was 10 µm or 0.01 mm.

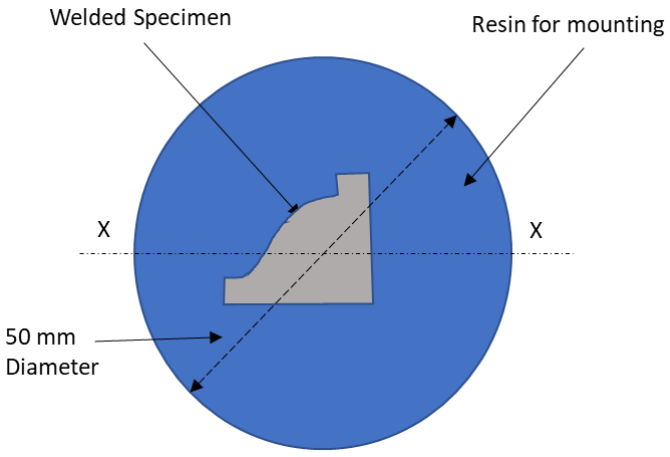

Figure 4.41 Schematic of a mounted specimen.

4.6.2 Validation analysis

For the purpose of validation, data for Test-7 of Scan Set 1 was chosen. The 3D FE linear-elastic stress distribution, the ACPD data from the interrupted fatigue tests and the crack size distribution from the serial metallography was collated to identify any correlations.

4.6.2.1 3D FE stress analysis

Figure 4.42 presents the maximum S_{11} and S_{PS} SCF values for the length of the weld toe of Test-7 of Scan Set 1 (46.9 mm) plotted at 5 µm intervals. The maximum values were plotted based on the algorithm described in Chapter 3 Section 3.5.4.1. The ACPD probe distribution along the weld toe has also been shown in the figure. Over 9300 SCF values were obtained for this specimen.

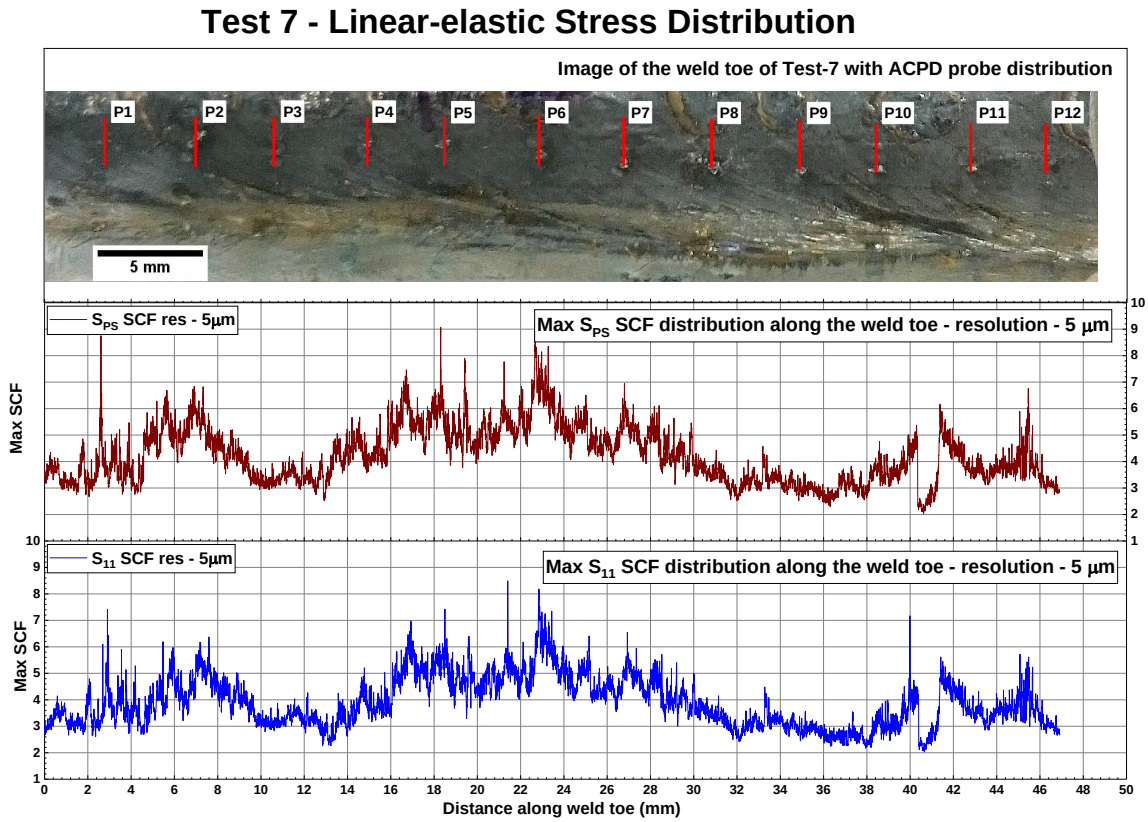

Figure 4.42 Test7 - S_{11} and S_{PS} maximum SCF values plotted along the length of the weld toe.

4.6.2.2 ACPD fatigue crack growth monitoring

The interrupted fatigue test for Test-7 was performed up to 84,344 cycles, which corresponded to a PD drop of 4 mV at probe 5. PD drops (between 0.5 mV and 2 mV) were observed at six of the other twelve PD probes. and no PD drops were observed at the remaining five PD probes. To represent this data graphically, the absolute potential drop (PD) value detected by the probes has been represented in Figure 4.43 in millivolts (mV). The FCI life was evaluated based on the onset of PD drop in probe 5.

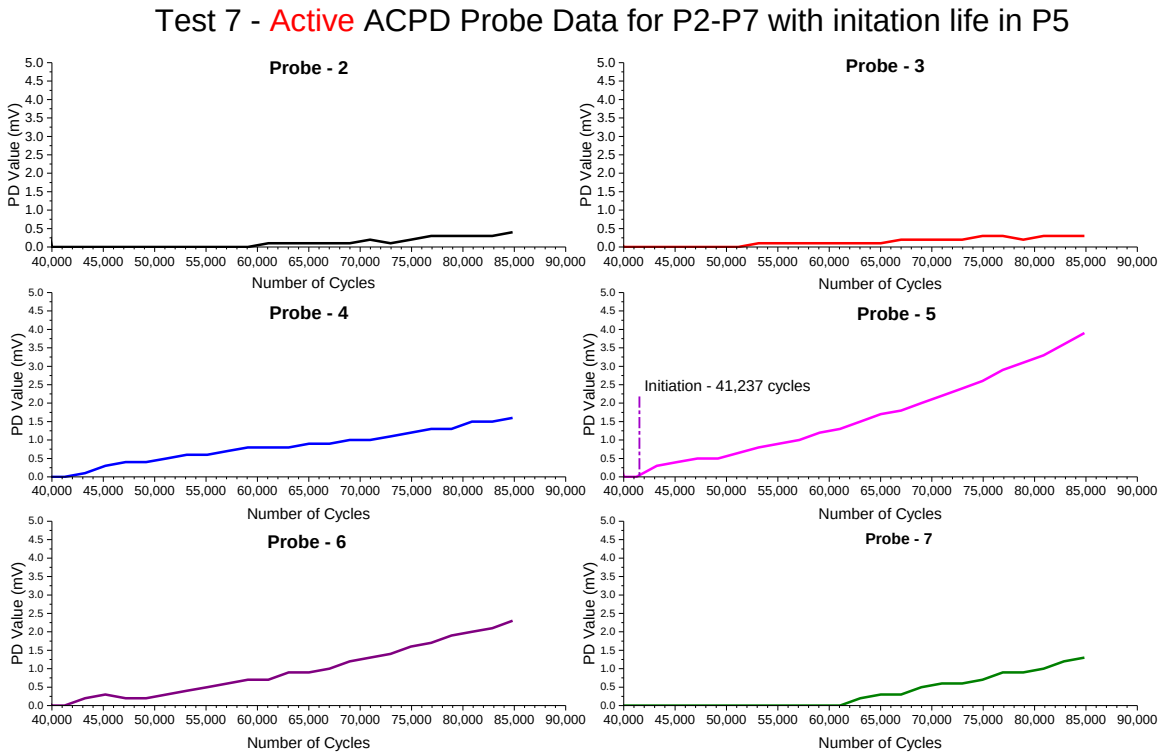

Figure 4.43 Test-7 - ACPD data for selected probes along with the point of initiation in the overall life of the specimen.

4.6.2.3 Serial metallography results

Serial metallography, as described in Section 4.6.1, was conducted at regions of interest along the weld toe to capture the crack depth and morphology to understand if it related well with the FE (as shown in Section 4.6.2.1) and could be calibrated with the ACPD results (as presented in Section 4.6.2.2). A controlled metallography methodology was developed to remove material transverse to the weld toe at 50 µm and 200 µm intervals. The sections provided information on fatigue crack depth, crack morphology and the number of cracks. Figure 4.44 features four such obtained sections. Figure 4.44a shows a fatigue crack with bifurcation occurring possibly around grains. Figure 4.44c shows a fatigue crack initiated at an overlap defect at the weld toe. Figure 4.44d shows the presence of three fatigue cracks that are growing on two different planes adjacent to each other. A total of 210 sections have been taken at regions of interest, to cover a total of approximately 25 mm of the total weld toe length of 46.9 mm. The crack depths of nine different cracks are represented along with the S_{11} maximum SCF distribution plot in Figure 4.45. 7.2.C, 7.3.SH.C and 7.3.LO.C represent the mounts into which the specimen was cut for serial metallography. The number after .C (for example 1 in 7.2.C1) represents the serial number of the crack. Results from this plot will be further analysed in Section 4.6.2.4.

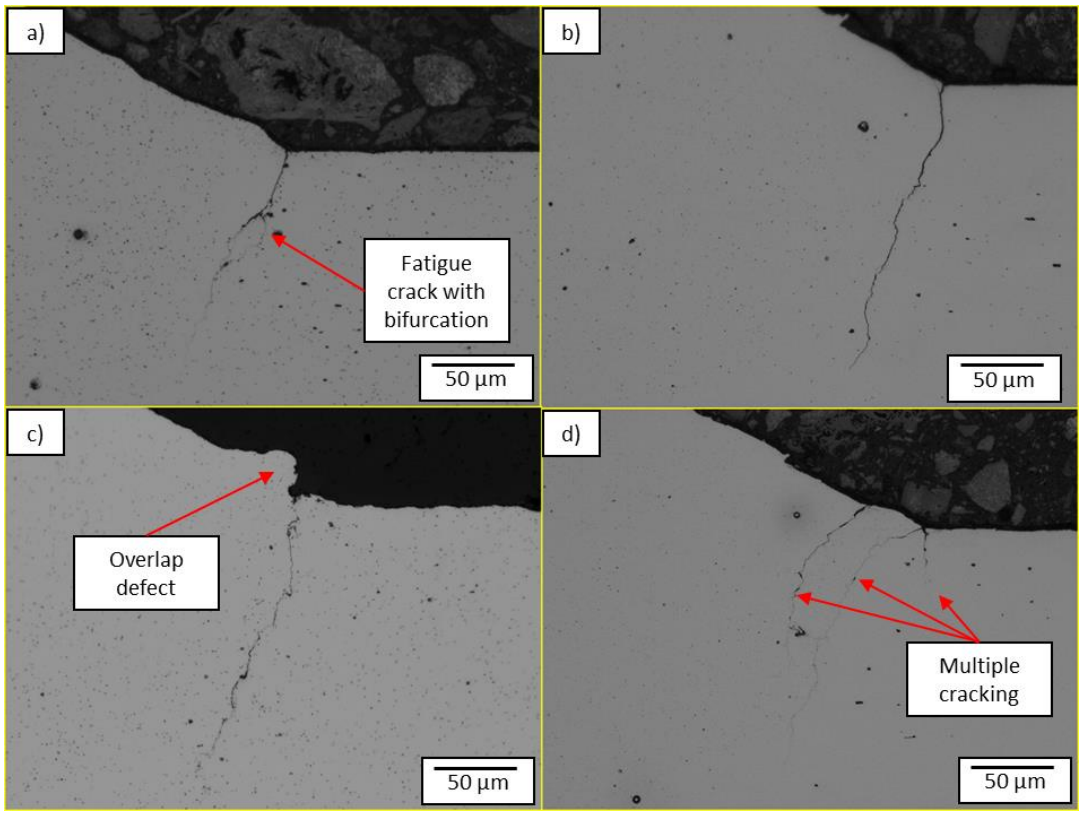

Figure 4.44 Sections with different features – a) fatigue crack exhibiting bifurcation located at the weld toe; b) expected fatigue crack growth – transverse to the stress axis; c) fatigue cracking from an overlap defect at the weld toe; d) two fatigue cracks which eventually coalesced in further sections.

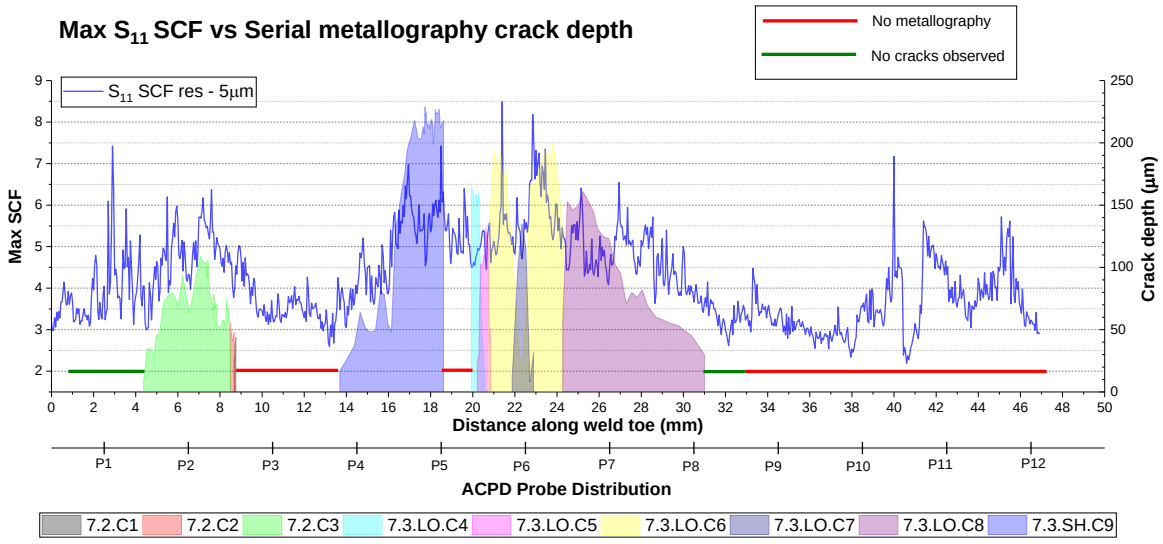

Figure 4.45 Comparison of S_{11} SCF (maximum) distribution with crack size distribution obtained from serial metallography.

4.6.2.4 Discussion

Figure 4.45 presents the observed crack depth at regions identified using the ACPD probe data in Figure 4.43. Multiple cracking was observed at the weld toe. Figure 4.46 contains two magnified plots from Figure 4.45 and are the regions subjected to serial metallography. Some smaller cracks; with depths between 5 and 50 µm and lengths (along the weld toe for which the crack was observed) between 20 and 200 µm were removed from the plots for clarity. The deepest cracks are in the regions with the maximum change in ACPD data. This area also corresponds to the area of consistently large S_{11} SCF observed in the FE analysis. In terms of the real weld bead, this corresponds to a location where two weld ripples meet to create a region of stress concentrating geometry. Crack depth is seen to follow the SCF distribution. However, the ACPD probe 2 and probe 3 have not shown the same degree of change as Probes-4-6. This could be due to a resolution issue with the ACPD or an edge effect; more tests would be required to ascertain the cause. It is also important to note that fatigue crack initiation is not always associated with regions of higher SCFs, but also occurs at surface spatter which exhibited S_{11} SCF from 3.00-6.40.

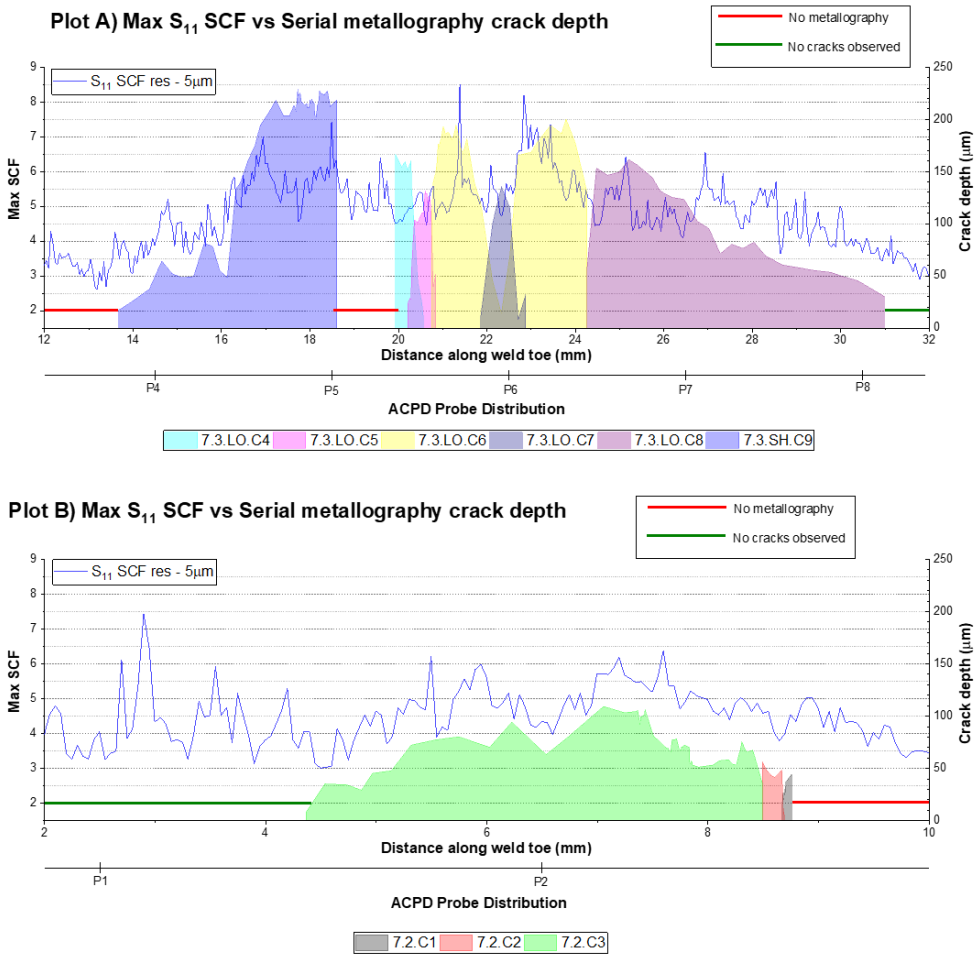

Figure 4.46 Plots A and B represent the crack depth with maximum S_{11} SCF distribution for the regions that have been subject to serial metallography.

Looking at probe 5 ACPD data and the maximum crack depth observed at the same location, the $\frac{Crack\ Depth}{PD\ Change}$ value is approximately 59 µm/mV – for a maximum crack depth of 229 µm and change in PD of 3.9 mV. This value is less than 50% of the value observed in Section 4.5.3.1. Table 4.8 presents the same relation for the other probes that have detected crack propagation. Except for probe 2, Probes 3-7 show much lower $\frac{Crack\ Depth}{PD\ Change}$ compared to the value seen in Section 4.5.3.1 (138 µm/mV). This could be attributed to the size of the crack for which the relation was calculated. In Section 4.5.3.1, the crack depth was 870 µm, i.e. it extended well beyond the approximate skin depth for the current test setup (approximately 200-300 µm). The cracks observed in this section and shown in Table 4.8 have crack depths that are within or similar to the skin depth. Therefore, the sensitivity of the ACPD system is higher for these cracks and because of the small size of the cracks, the effect of stress on ACPD (increase in stress causing a reduction in the measured ACPD, detailed in Section 4.5.1 due to a reduction in net cross-section would not be significant. However, comparing the values of $\frac{Crack\ Depth}{PD\ Change}$ for Probes 4-7, there is a visible variation, and the cause for this is not clear. Further tests would be required to identify the reason for this instability.

Table 4.8 Test-7 (Scan Set 1) - Crack Depth versus PD Change.

Parameters	**Test-7 Active Probes**					
	Probe 2	**Probe 3**	**Probe 4**	**Probe 5**	**Probe 6**	**Probe 7**
Maximum Crack Depth (µm)	63	No crack depth data	81	229	177	123
Maximum PD Change (mV)	0.4		1.6	3.9	2.3	1.3
$\frac{Crack\ Depth}{PD\ Change}$ **(µm/mV)**	157.5		50.6	58.8	76.9	94.6

Fatigue cracking (revealed from serial metallography) has occurred at the locations of high stress concentration observed in the 3D FE stress analysis. The ACPD probes information used to indicate fatigue crack growth location and life have further validated this.

4.7 Summary

The work done in Chapter 4 on combining Alternating Current Potential Drop NDT technique with fatigue testing of welded specimens can be summarised in the following points –

- ACPD crack growth monitoring technique has been implemented in a high-resolution data-rich setup where multiple probes were connected across the weld toe to capture fatigue crack growth in-situ.
- A data-rich approach allows for multiple parameters to be extracted from the experiment – life to fatigue crack initiation, location of fatigue crack initiation, fatigue crack growth rates and an estimate of fatigue crack size.
- Variation in stress is seen to have an effect on the measured ACPD. Conventionally, an increase in stress reduces the measured ACPD, and vice-versa. However, this relation between stress and ACPD voltage is not constant; it also depends on the effects of crack tip plasticity, strain and crack tip blunting on material properties such as magnetic permeability and resistivity (which directly affect the skin depth of the ACPD system). More tests would be required to accurately quantify this effect for calibration of the ACPD system for crack growth sizing.
- Results show that ACPD technique is sensitive to surface crack initiation, but once a crack has reached a specific critical size such that the specimen becomes significantly compliant to the applied (constant) load spectrum, the value of the measured ACPD is subjected to stress effects. Again, further tests would be required to establish the critical crack length for accurate ACPD measurement.
- The ACPD results and serial metallography were used in conjunction to validate the linear elastic stress analysis performed using 3D FEA. Considerable agreement was seen between the data from the three techniques.

4.8 Conclusion and future work

To conclude, the use of ACPD has been improved upon what had previously been done in literature. A novel approach of applying the ACPD technique to a welded specimen was developed. Limitations of the system have been identified, but they were not all addressed in this project. Further testing would be required to understand better the effect of stress on ACPD and calibration of the ACPD system to obtain a consistent $\frac{Crack\ Depth}{PD\ Change}$ relation, in order to predict the size of a crack without performing any destructive procedure.

It is evident from the observed limitations of ACPD that it is a very useful technique for surface crack detection. The in-situ implementation of the technique has successfully managed to identify the location of a crack, the time of crack initiation as a function of the operational life or fatigue life, and early crack growth rates. This can prove to be very useful for assemblies that predominantly suffer from surface cracking such as welds or parts with surface modification such as holes, threading, machining, etc. This sensitivity can be further enhanced by implementing current focusing which effectively reduces the net cross-section across which the ACPD monitors for cracking, therefore increasing sensitivity. However, as a crack front grows beyond the region under the influence of skin effect, the ACPD technique struggles to provide satisfactory monitoring of the crack depth. Crack growth can still be picked up, but the exact depth of the crack front is affected by the stress effect and therefore constant adjustment would need to be made to the ACPD measurements for accurate crack depth information. These adjustments would be very difficult to make as the change in nominal stress due to a reduction in cross-section caused by crack growth can only be measured if the crack depth is known. For crack size determination-based applications, DCPD is a better technique as it does not suffer from stress effects as the ACPD. A combination of these two techniques has been suggested [166] and if the two techniques can be implemented in a portable electronic kit, it would be a very powerful in-situ NDT method.

Chapter 5 Strain Gauge Array Technique for FCI Detection

5.1 Motivation

The motivation for the work described in Chapter 5 is similar to what was described in Chapter 4 – capture FCI life and location non-destructively – for developing a quantitative correlation between the weld toe geometry and the FCI life. Strain gauges can be used for this purpose as a change in compliance of a specimen with the initiation, and subsequent propagation of a fatigue crack can be extracted from the strain data [96]. To emulate the fatigue crack growth monitoring setup of the ACPD in Chapter 4, strain gauges were used. An array of twelve strain gauges was connected next to the weld toe for crack detection, matching the twelve ACPD probes array used previously. The stress effect on ACPD was the primary deterrent for not using the ACPD technique. Also, in the available high-resolution techniques, strain gauges were the easiest to implement for their availability and cost. Therefore, the use of strain gauges allows the accomplishing the same aim as Chapter 4 :

> **"Accurately detect in-situ fatigue crack initiation life and location using a data-rich fatigue crack growth monitoring technique."**

This chapter will introduce the use of strain gauges for fatigue crack growth monitoring and its advantages and disadvantages. The methodology of implementing an array of strain gauges for fatigue crack monitoring will be discussed along with a discussion on the obtained results.

5.2 Use of strain gauges for crack growth – Review

5.2.1 Introduction

Strain gauges were invented independently by two different people within a period of 2 years, Simmons, 1942 [189] and Ruge, 1944 [190]. The basic working principle of the strain gauge is that the changes in the strain on the measurement specimen results in a change in strain of an electrical conductor bonded to the surface of the measurement specimen, resulting in a change in electrical resistance of the conductor. This change in resistance is measured by the strain gauge monitoring equipment and is interpreted as a change in strain of the measured specimen [191]. The sensitivity of the strain gauge is defined by the ratio of the change in the input signal (the strain in the measurement specimen) and the resulting output signal (change in measured resistance of the

strain gauge) [191]. This ratio is defined by a parameter called Gauge Factor, given in Equation 5-1. The value of the gauge factor is provided by the manufacturer of the strain gauge and is critical for the interpretation of the strain gauge output signal.

$$k = \frac{\frac{\Delta R}{R}}{\Delta \varepsilon} \qquad 5\text{-}1$$

Where,

k	*Strain Gauge Factor*
$\frac{\Delta R}{R}$	*Change in measured resistance, the output signal of the strain gauge*
$\Delta \varepsilon$	*Change in the strain of the measurement specimen*

With the development of strain gauges, the possibility of strain gauges measuring dynamic strain, i.e. in the case of cyclic/fatigue loading was explored and established [191-193]. This led to their use in transducers or load cells for the analysis of the strength of materials and components under static or dynamic loading conditions [194].

5.2.2 Use of strain gauges for fatigue crack growth monitoring

The possibility of being able to use strain gauges in dynamic loading conditions with accurate specimen compliance readings enables the use of strain gauges for fatigue crack growth monitoring. Otegui et al. 1989-1991 [69, 88, 105] used an array of strain gauges for fatigue crack growth monitoring on welded specimens, shown in Figure 5.1A. Multiple strain gauges were bonded 2 mm away from the weld toe of the specimen, and the change in compliance was interpreted as an indication of crack initiation and early crack growth. Strain gauges were combined with ink marking, as well as beach marking by reducing the cyclic load. This creates an indication of crack development on the fracture surface. Verreman et al., 1991 [195] used miniature strain gauges (gauge length of 0.2 mm) for the same purpose on cruciform fillet welded joints, with the only difference being the positioning of the miniature strain gauges as physically close to the stress concentrating weld toe as possible, shown in Figure 5.1B. The specimens contained non-load carrying welded joints. Therefore, cracks would be expected to initiate at the weld toe. A similar approach was taken in this project and will be explained in detail in Section 5.3.

Janosh, 1993 [196] used micro-strain gauges for fatigue crack growth monitoring of fillet welded assemblies subjected to tensile and bending loads, shown in Figure 5.1C. Based on the available approaches for fatigue life estimation of welded joints (will be discussed in detail in Chapter 6a), Takeuchi, 2012 [98] suggested ways of implementing strain gauges for calculating the mechanical response of the tested material as well as crack detection. Lukashevich et al., 2015 [197] used

differences in measured strain amplitude and a phase difference (between two strain gauges attached across the region of interest) process for an indication of crack growth near welds of low-carbon steel butt welded joints. Crump, 2017 [9] used strain gauges for capturing fatigue crack initiation as well as structural hot spot stress in non-load carrying welded joints.

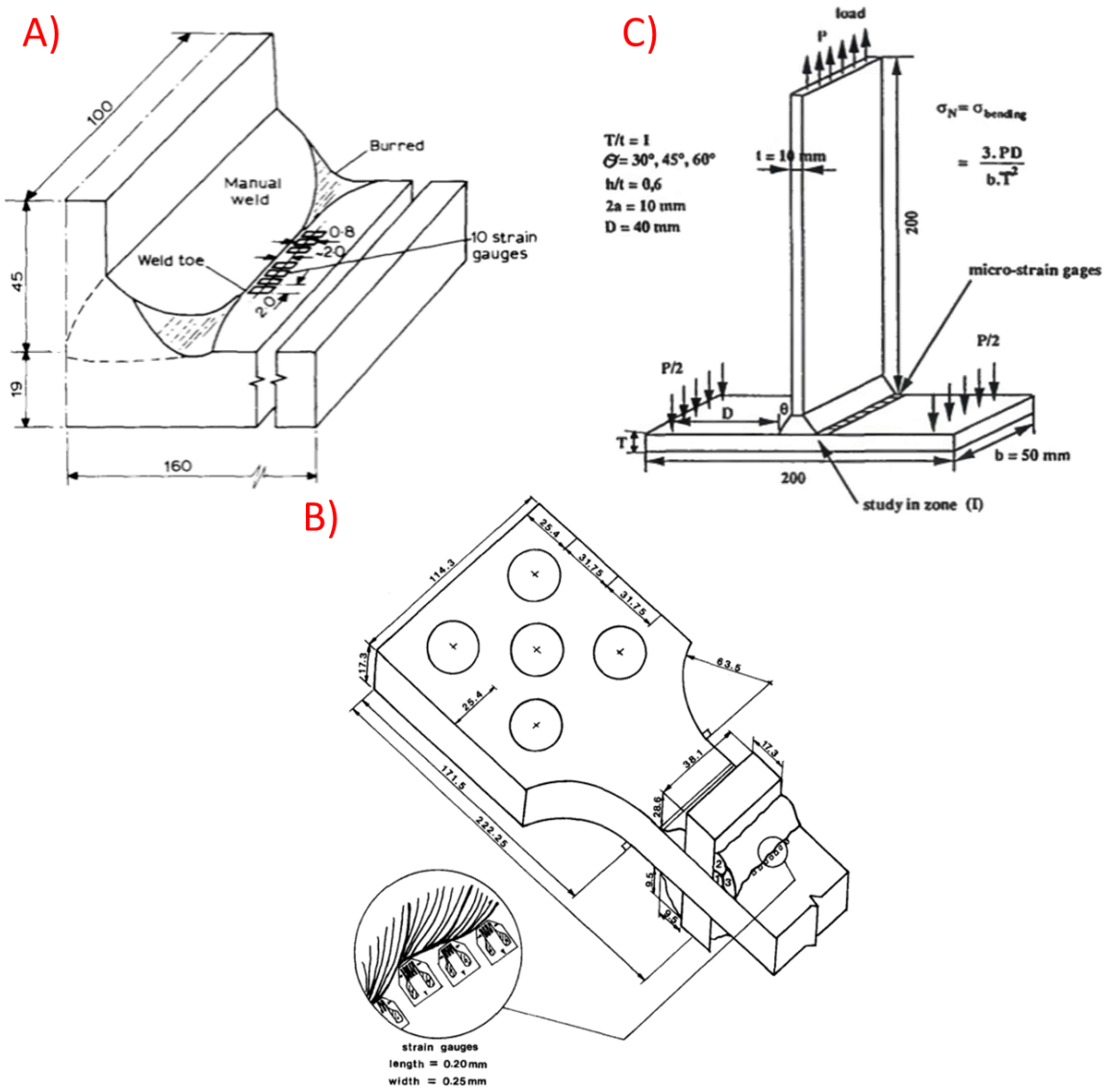

Figure 5.1 Use of strain gauges for fatigue crack detection and monitoring on welded joints – A) Strain gauge array used by Otegui et al. [69, 88, 105]; B) Miniature strain gauges used by Verreman et al. [195]; C) Micro-strain gauges used by Janosch [196].

5.2.3 Summary

Results from previous work provide enough evidence and validation of the use of strain gauges for crack growth monitoring given that proper validation is done (in this case, beach marking followed with fractography). Later sections in this chapter will discuss the methodology adopted (Section 5.3) and the results obtained (Section 5.4).

5.3 Uniaxial fatigue testing using strain gauges (experiment set 2) - Methodology

This Section will provide a detailed description of the processes involved in setting up the strain gauges for in-situ application during uniaxial tensile load fatigue testing on fillet non-load carrying welded joints. The primary aim of the methodology of applying strain gauges was to emulate the ACPD setup in order to implement high-resolution data-rich crack growth monitoring for the detection of FCI location and life, crack propagation rates.

5.3.1 Material and specimen

Structural C-Mn steel single-sided transverse non-load carrying joints were manufactured by metal active gas (MAG) welding. Details of the material properties are provided in Chapter 3, Section 3.3.1.1, and exact specimen dimensions are provided in Section 3.3.1.2. This test refers to Experiment Set 2 from Section 3.3. Figure 5.2 provides a schematic of the geometry of the tested specimens. Two variations of welds were produced – High Quality (HQ) and Low Quality (LQ).

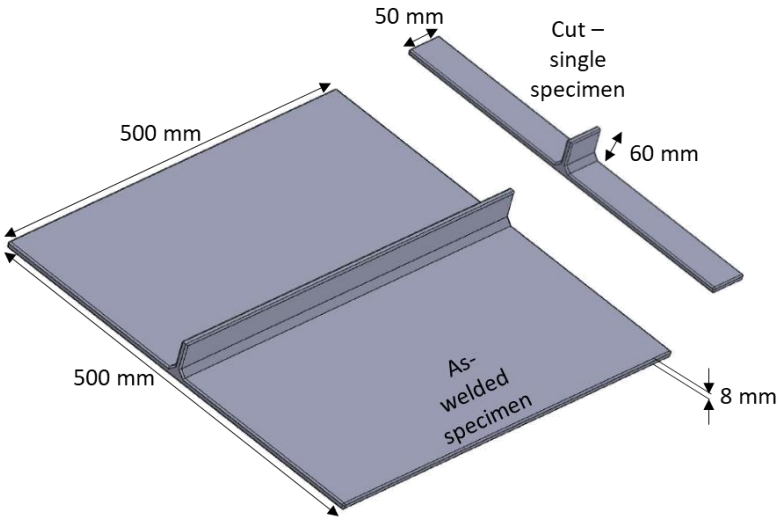

Figure 5.2 Schematic of Experiment Set 2 specimen. Left - as-welded; right - after specimen cutting.

5.3.2 Experimental methods – Fatigue test setup

5.3.2.1 Mechanical properties

The material that was used for carrying out the tests discussed in this chapter is the same as the one used in Chapter 4. For the purpose of experiments carried out in this project, only base metal

properties were considered for the purpose of modelling, as detailed in Chapter 3 Section 3.5.1. Therefore, only weld misalignment methodology and results are used.

1. **Weld misalignment**

   Weld misalignment in these specimens was present prior to testing, primarily from the clamping of the baseplate and stiffener during welding and from residual stress relaxation during specimen cutting. Misalignment in the specimen induces a bending stress at the weld during uniaxial fatigue testing, which is summated with the membrane stress to give the resulting primary stress on the specimen. (described in Equation 5-2) BS 7910:2013 [5]. Figure 5.3 presents a schematic of the application of strain gauges on the baseplate of the material (away from the stress concentration zone of the weld toe; 30 mm for the testing performed in this project) to measure the two components of primary stress (P) – membrane stress (P_m) and bending stress (P_b) – using Equations 5-3 and 5-4. Figure 5.4 highlights the positioning of the strain gauges used for bending stress measurement on an actual test specimen.

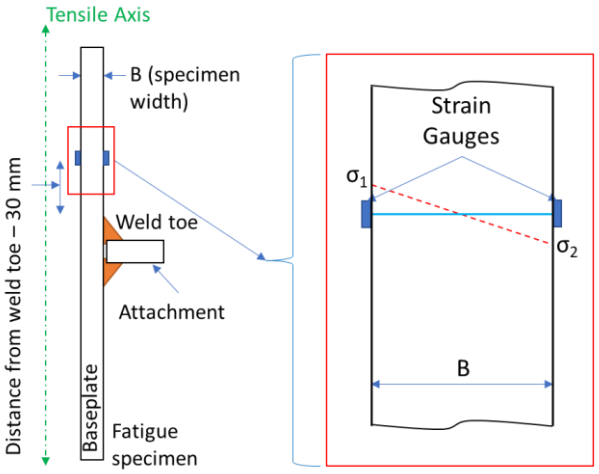

Figure 5.3 Schematic of stress distribution and application of strain gauges on the baseplate of the fatigue specimen away from the stress concentration zone of the weld toe. Adapted from [5].

$$P = P_m + P_b \quad \text{5-2}$$

$$P_m = \frac{\sigma_1 + \sigma_2}{2} \quad \text{5-3}$$

$$P_b = \frac{\sigma_1 - \sigma_2}{2} \quad \text{5-4}$$

Where,

P *Primary Stress*

P_m *Membrane stress – mean stress through the cross-section of the tested specimen*

P_b *Bending stress – the stress induced due to misalignment, and is considered to be superimposed on* P_m

σ_1 *Stress obtained from strain gauge shown in* Figure 5.3

σ_2 *Stress obtained from strain gauge on the other side of the baseplate relative to* σ_1 *shown in* Figure 5.3

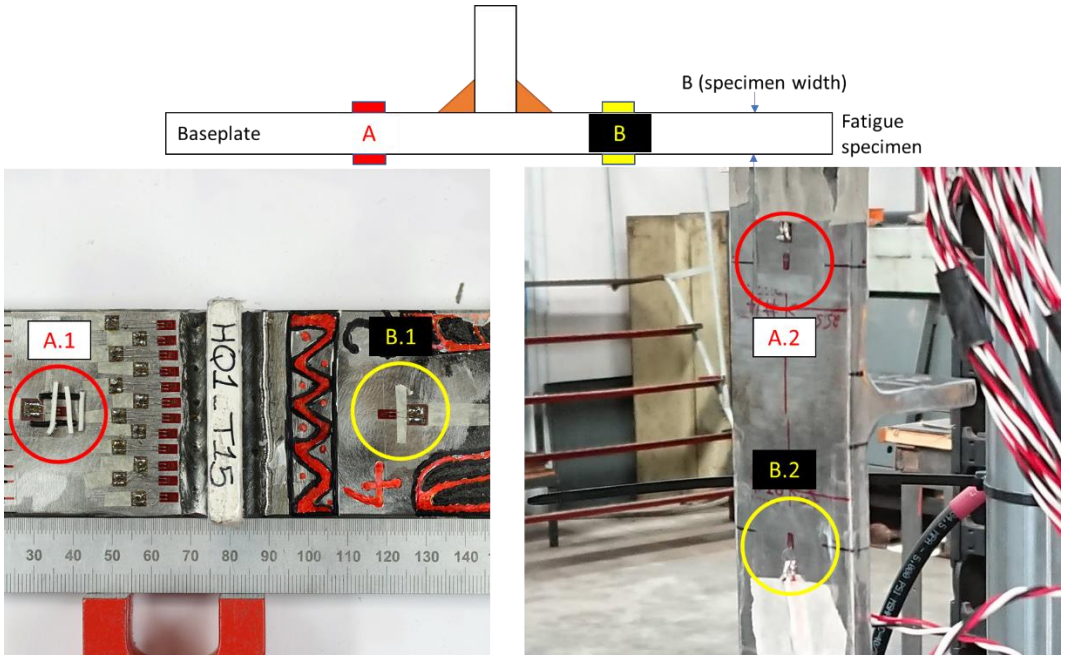

Figure 5.4 Schematic of the strain gauge setup for measuring weld misalignment in terms of bending stresses.

When loaded uniaxially, the calculated membrane stress (from Equation 5-3) should be equal to the applied nominal stress. The axial alignment of the hydraulic testing machine will cause the misaligned specimen to straighten along the tensile axis (as shown in Figure 5.3), resulting in bending stress through the cross-section of the baseplate.

5.3.2.2 Specimen preparation

For the HQ specimen, one weld toe was equipped with 1 mm (gauge length) TML uniaxial strain gauges, and the second weld toe was ultrasonically needle peened by Thomas Jackson (TWI Ltd) using SONATS Stressonic® NOMAD Ultrasonic Needle Peening (UNP) system using the same methodology and parameters as described in Chapter 4 Section 4.4. For the LQ specimens, it was not possible to carry out any UNP treatment as the intentionally created undercuts at both weld toes meant that the peening process may not have been effective. In the LQ specimens, both

available weld toes were monitored using strain gauges as it was not possible to predict otherwise which weld toe would develop a fatigue crack first. Figure 5.5 shows a schematic of the welded specimen setup for both HQ and LQ specimens. Figure 5.6 presents images of the UNP system and the final peened weld toe. Actual images of the two kinds of specimens have been presented in Figure 5.7.

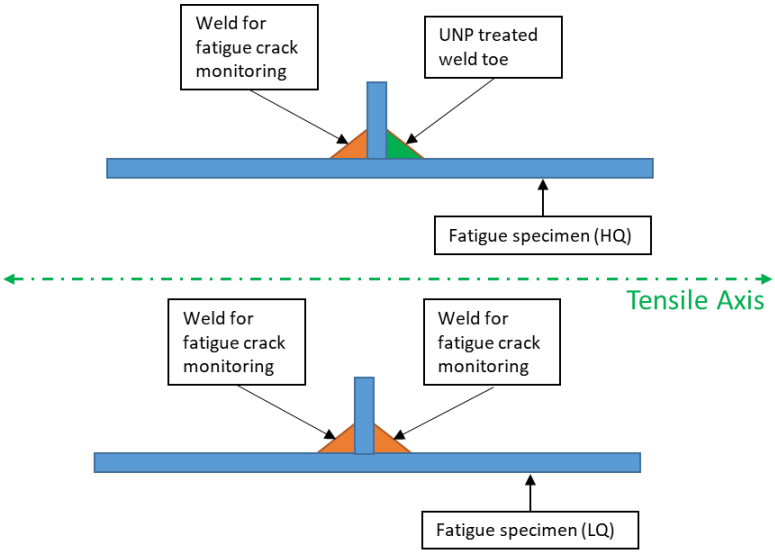

Figure 5.5 Schematic of the two types of fatigue test specimens - HQ and LQ - with the different weld toes marked for UNP treatment and strain gauge attachment.

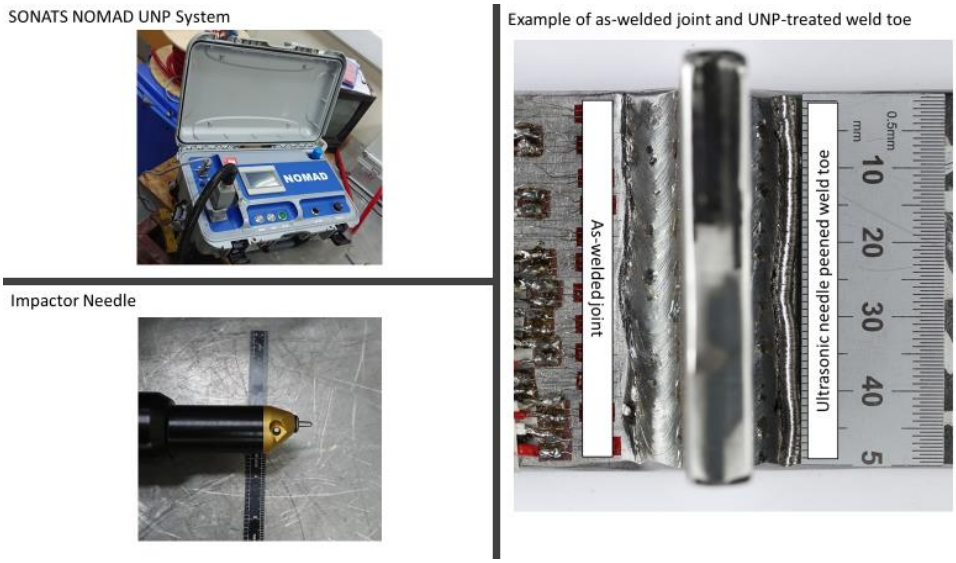

Figure 5.6 Images of the SONATS NOMAD UNP System and the result of peening on a welded specimen.

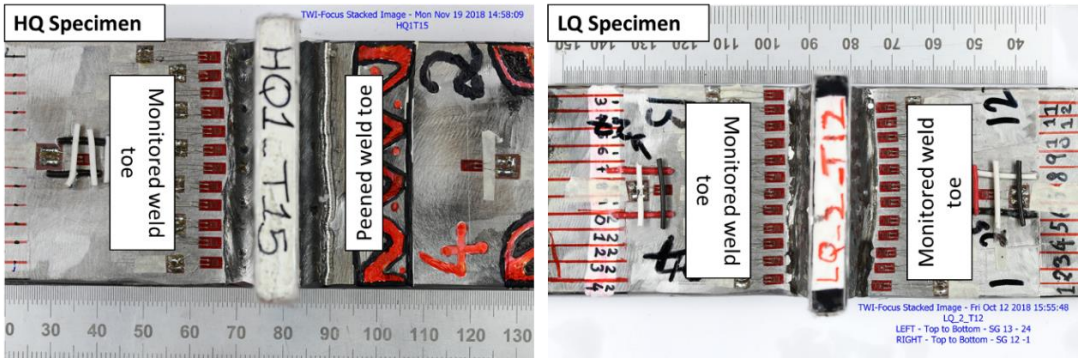

Figure 5.7 Actual images of the two kinds of specimens tested - HQ (high-quality) and LQ (low-quality).

Post cutting and UNP treatment, the specimens were chamfered using a hand-held rotary pneumatic grinder to remove any sharp edges that would act as stress concentration zones. The specimen surface to which strain gauges would be attached was prepared as per the manufacturer's recommendations, as suggested in BS 6888:1988 [198].

5.3.2.3 Strain gauge array

During the ACPD crack growth monitored fatigue test, approximately 50 mm of weld toe length was monitored using twelve PD-measuring probes. To emulate the same system, an equal number of strain gauges were connected across 50 mm of weld toe length. Also, the average distance between the centreline of each ACPD probe, 4 mm, was kept between the centreline of each of the 12 strain gauges. As the applied load was purely tensile and uniaxial, uniaxial strain gauges were selected, specifically FLAB-1-11, manufactured by Tokyo Measuring Instruments Lab (TML), as shown in Figure 5.8. The resistance of these strain gauges was 120 Ω. A schematic of the layout of the strain gauges is shown in Figure 5.9, relative to the ACPD setup. Figure 5.10 shows a comparative schematic of both HQ and LQ specimens. Figure 5.7 presents the actual images of an HQ and LQ specimen.

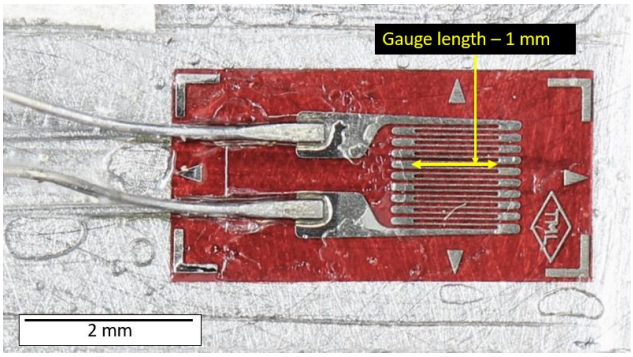

Figure 5.8 Actual strain gauge applied to the surface of a specimen.

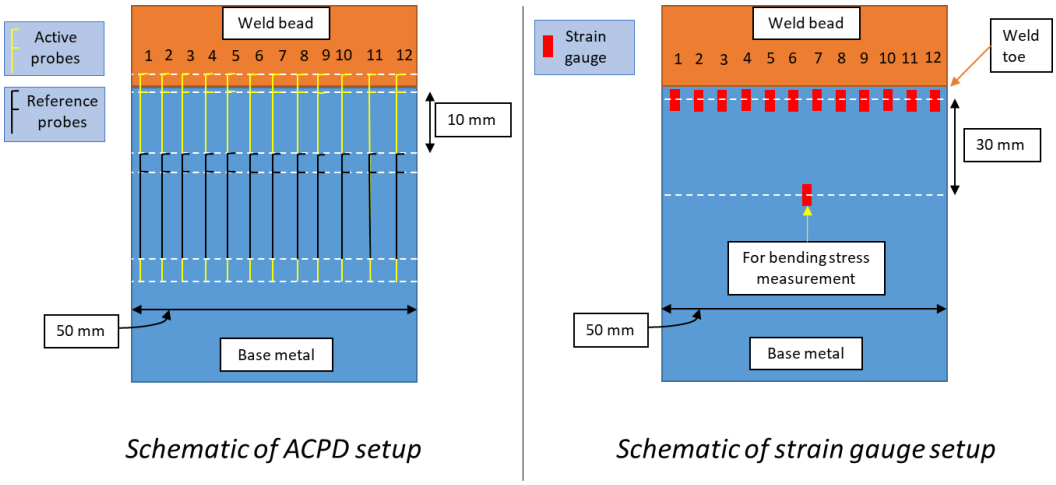

Figure 5.9 Schematic of the strain gauge setup (right), relative to the ACPD setup (left). Images are not drawn to scale.

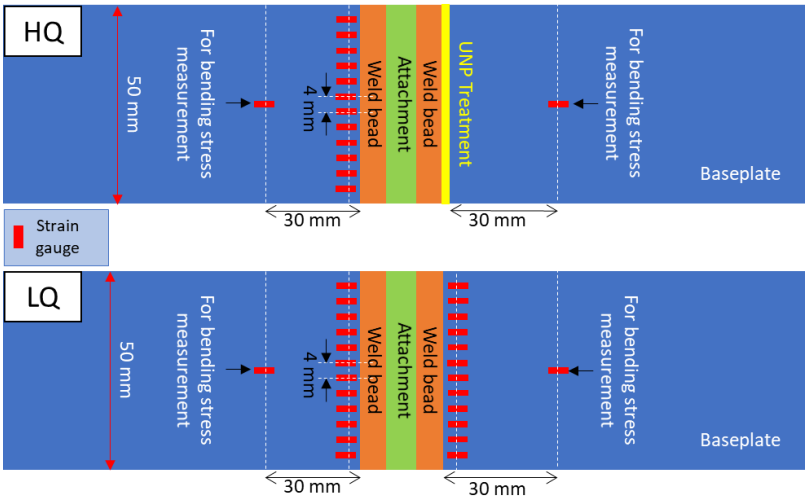

Figure 5.10 Comparative schematic of strain gauge setup in both HQ (top) and LQ (bottom) specimens.

The position of the strain gauge in terms of its distance from the weld toe was based on an FE elastic strain study performed using FE software ABAQUS. It has been discussed in detail in Section 5.3.2.6.

5.3.2.4 Static test – Evaluation of membrane and bending stress

Before each specimen was tested under cyclic loading, the membrane and bending stress in the specimen was determined during the application of static load steps up to the maximum nominal stress. Applied loads were determined from a simple equation $Stress = \frac{Force}{Area}$, where area is that of the baseplate excluding the weld. The schematic of the test is shown in Figure 5.11a and a photograph of the test in 5.11b.

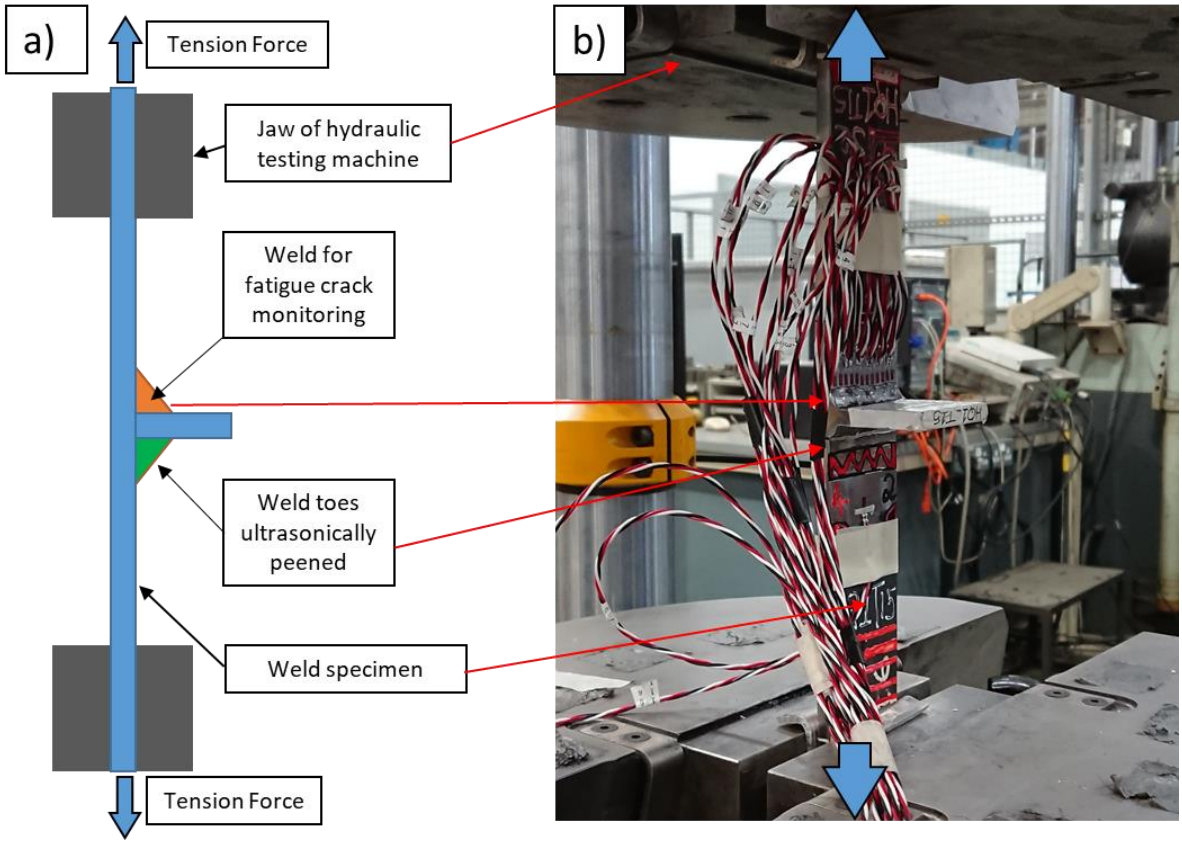

Figure 5.11 a) Schematic of specimen setup in fatigue testing machine; b) actual photograph of specimen gripped in the testing machine.

5.3.2.5 Fatigue testing

Load-control fatigue testing was performed in a servo-hydraulic Instron test machine at TWI Ltd. The specimens were hydraulically gripped, and the load cell has a capacity of ±1000 kN. The fatigue tests were performed at frequencies between 5-6 Hz. The test frequency was stepped up with a step size of 0.5 Hz from an initial frequency of 0.5 Hz to the maximum test frequency over the first approximately 1000 cycles, to 'warm up' the machine. The load ratio, R, was 0.1, and a nominal stress range of 150 MPa was chosen to give fatigue lives around 10^6 cycles according to class F curve in BS7608 [6] for a 97.5% probability of survival. The same stress range was selected for both HQ and LQ specimens. Because of the large intended flaws in the LQ specimens, it was assumed that the LQ specimens would give lower fatigue than the HQ specimens. If a higher nominal stress range was chosen (270 MPa was the selected nominal stress range for the fatigue tests described in Chapter 4), the LQ specimens could exhibit low fatigue crack initiation lives with multiple cracking events. The loading values for each specimen are provided in the Appendix C.1.

For observing the behaviour of the strain gauge array as an FCI detection technique, it would be ideal to have FCI lives greater than 50,000 cycles. This allows the observation of a period in the fatigue life (using strain gauges) of the specimen where no cracking occurs, allowing fatigue growth

initiation to be determined as a deviation from the observed strain values. The strain logging software used was developed internally at TWI Ltd on LabView. It records the number of load cycles, and the minimum and maximum strain, ram displacement and load for each cycle. It also provides in-situ logging of the strain range for each cycle, i.e. the difference of maximum and minimum strain. A further benefit of the software is the possibility of a user-defined test-interrupt based on any of the monitored parameters. Once the interrupt is triggered, the software sends a configured signal to the hydraulic testing machine through a relay, which the testing machine has been programmed to interpret as an instruction to stop the test. How the test is stopped (whether stopped immediately and held at the load at the instant of the signal, unload to zero load, hold at mean load, etc.) can also be defined.

Two types of fatigue tests were performed in this study –

A. Interrupted tests

Four interrupted fatigue tests were performed; two on HQ specimens and two on LQ specimens. The tests were interrupted once a strain range drop of 60 microstrains (με) was observed in any of the strain gauges. A drop of 60 με was determined to be equivalent to a crack depth of 0.2 mm from a strange range validation study carried out using FE elastic strain analysis, described in Section 5.3.2.6. The interrupted samples were later used for X-Ray μ-CT 3D FE Stress Analysis described in Chapter 3.

B. Tests to failure

Two tests to failure were performed: one on an HQ specimen and one on an LQ specimen. The purpose of these tests was to obtain a relation between crack depth and strain range drop and compare this with the FE models described in Section 5.3.2.6. Beach marking on the fracture surface was achieved by changing the load ratio at pre-determined intervals in the fatigue life of the specimen similar to that described in Branco et al., 2012 [199]. The load ratio was changed to 0.5 at regular intervals until a further pre-determined drop in strain range was observed. The value of the strain range drop is based on the methodology described in 5.3.2.6. Post-failure fractography was used to determine the crack depth at each beach mark created on the fracture surface.

5.3.2.6 Strain range validation using FE elastic strain analysis

2D linear-elastic FE analysis on a T-joint with an ideal weld toe was performed in ABAQUS to provide a correlation between weld toe crack depth and surface strain to simulate the tests performed in this Chapter of work. The weld toe cracks were modelled as seam cracks and to simulate the strain

gauge output, the average strain was computed across 1mm length of baseplate at a distance between 1.7 mm and 2.7 mm from the weld toe, Figure 5.12.

In ABAQUS Standard, this was achieved by creating a line path in the output model and calculating the average strain over the defined path length. A schematic of the model, the simulated crack and the average strain path is shown in Figure 5.13. Models were created at different values of weld toe angle (WTA) – from 30, 45 and 60 degrees.

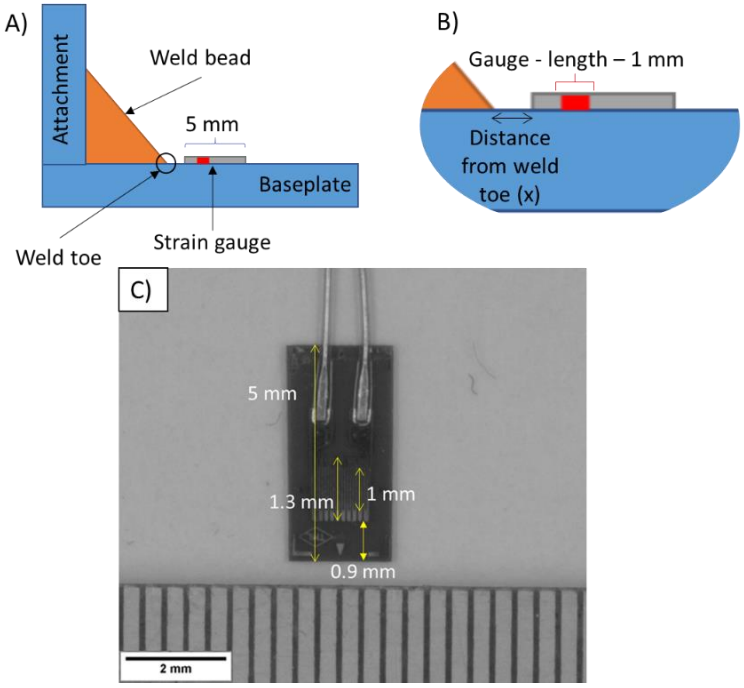

Figure 5.12 A) Schematic of the positioning of the strain gauge and the measuring gage length relative to the weld toe; B) locally magnified zone from A); C) dimensions from applied strain gauge.

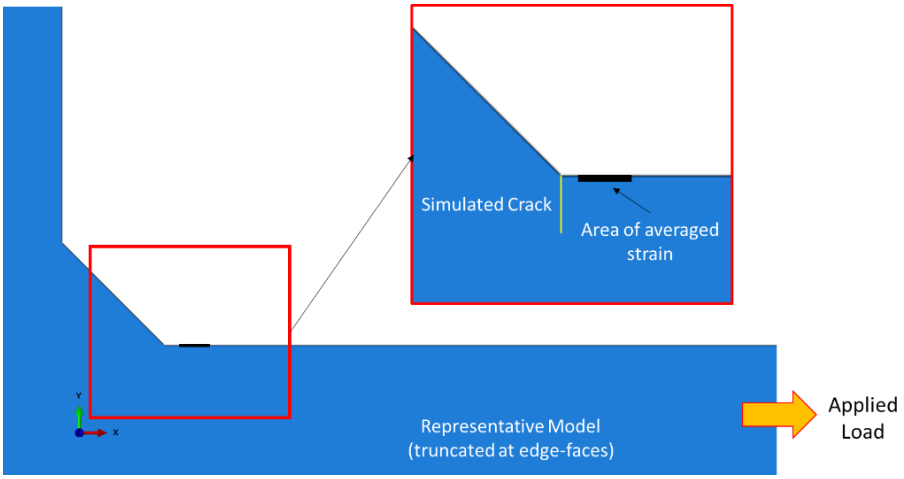

Figure 5.13 Schematic of the representative model used for 2D FE analysis in ABAQUS and the simulated crack.

Values of average strain were taken at the maximum and minimum loads that were applied to the specimens during testing. The crack depth was also varied, and the following depths were modelled: no crack, 0.2 mm, 0.4 mm, 0.6 mm, 0.8 mm, 1.0 mm, 2.0 mm, 3.0 mm.

Using this analysis, it was possible to obtain an estimate of the value of strain range drop (corresponding to the desired crack depth) that should be used in the strain logging software for configuring an interrupt in the fatigue test.

5.4 Uniaxial fatigue testing using strain gauges (experiment set 2) - Results and discussion

This Section will detail the results obtained from the testing methods described in the order of methodology Sections 5.3.2.4, 5.3.2.6 and 5.3.2.5 (to follow a chronological order as performed while carrying out the experiments).

5.4.1 Static testing

Once each specimen was prepared and placed in the fatigue test machine, it was initially tested at static loads before being cycled. The static test results for all the test specimens are given in the Appendix C.2. In this section, the results of one specimen will be presented in detail (HQ_T15). The static steps were carried out at the following test machine load inputs – 0 kN, 10 kN, 20 kN, 30 kN, 37.95 kN (mean load), 40 kN, 50 kN, 60 kN and 69 kN (maximum load). In total, 7 cycles of static loading were performed. This was to capture any cyclic hardening/softening effects or shakedown after the first loading cycle in the strain gauges attached next to the weld toe and also the reliability of the strain gauges attached away from the weld toe for membrane and bending stress evaluation.

5.4.1.1 Membrane (P_m) and bending (P_b) stress evaluation

Two pairs of strain gauges were attached on the baseplate each side of the welded attachment to give two sets of P_m and P_b values, evaluated as per the methodology described under 'Weld misalignment' in Section 5.3.2.1.

Figure 5.14 shows the distribution of P_m observed in each of the two pairs, named side #1 and side #2. The blue line in the plot highlights the ideal case where P_m is equal to the applied stress. Based on this plot, it can be assumed that the strain gauges being used for calculating P_m and P_b are attached properly as the obtained P_m deviates from the applied stress within an average error of 3.5%. An error would be expected as the exact positioning of the strain gauges, and their attachment was performed manually, without any high-precision instruments (such as laser-

assisted dimensioning, etc.). As the strain gauges were attached away from the stress concentrating zone of the weld toe, no hardening or shakedown effects were observed.

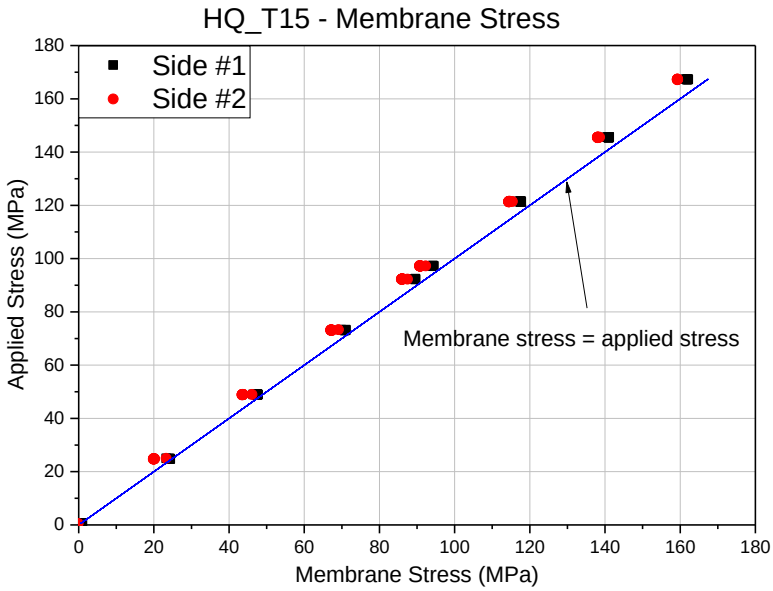

Figure 5.14 HQ_T15 - Membrane stress evaluation.

Figure 5.15 presents the distribution of P_b for HQ_T15 induced as the misaligned weld sample is straightened in the test machine, the latter being aligned along the direction of the applied tensile load. Again, no hardening or shakedown effects were observed, similar to the evaluation of P_m. It can be seen from the plot that the minimum P_b at zero applied load for side #2 is different from that of side #1. This behaviour was consistent in all the HQ specimens that were tested. This could be attributed to how the specimen was gripped in the test machine. There could possibly be a difference in the distance of the clamping in the jaw to the strain gauge attached on the baseplate. L-shaped thick sheet aluminium buffers were used between the hydraulic clamp of the test machine and the specimen to avoid any stress concentration in the clamping area caused by misaligned jaws. With repetitive use, these L-shaped aluminium packers do not retain their initially machined flat surface and may cause the positioning of the gripping surface to change, resulting in the variations observed in P_b at zero load. As the applied load is increased, the two obtained P_b values converge to maximum P_b values within 0.8% of each other. The values of P_b clearly show a significant misalignment in the specimen. The minimum and maximum P_b are 54% and 77% of the maximum applied nominal stress, respectively.

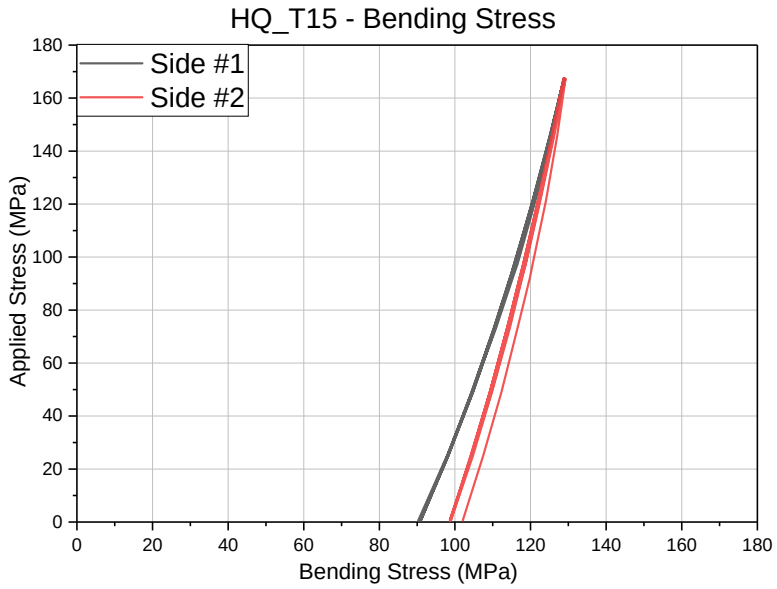

Figure 5.15 HQ_T15 - Bending stress evaluation.

Table 5.1 is a distribution of the maximum P_m and P_b for all the six specimens tested; three each of HQ and LQ. The maximum P_m for all specimens fall within ±5% of the maximum applied nominal stress at which the maximum P_m was measured, indicating that the data from the strain gauges for P_m and P_b are reliable. Comparing both minimum and maximum P_b for the LQ specimens to that of the HQ specimens highlight the relative high severity of misalignment in the LQ specimens. The maximum P_b is consistently higher than the maximum applied nominal stress for the LQ specimens. Apart from the severe stress concentrating features that have been intentionally induced during the welding process of the LQ specimens, large P_b will also contribute in lowering the fatigue lives of the LQ specimens compared to that of the HQ specimens, and this is observed during the fatigue tests of these specimens at the same loading conditions (discussed in Section 5.4.3).

Table 5.1 Distribution of membrane and bending stresses across the test specimens.

Specimen	**HQ**			**LQ**		
	HQ_T11	**HQ_T13**	**HQ_T15**	**LQ_T10**	**LQ_T12**	**LQ_T14**
Maximum applied nominal stress (MPa)	*166.7*	*166.7*	*166.7*	*166.7*	*166.7*	*166.7*
Maximum membrane stress (MPa)	160	174	162	171	171	167
Maximum membrane stress as % of maximum applied nominal stress	96.0%	104.4%	97.5%	102.6%	102.6%	100.2%

Minimum bending stress (MPa)	98	102	90	126	136	127
Minimum bending stress as % of maximum applied nominal stress	58.8%	61.2%	54%	75.6%	81.6%	76.2%
Maximum bending stress (MPa)	136	138	129	174	184	174
Maximum bending stress as % of maximum applied nominal stress	81.6%	82.8%	77.4%	104.4%	110.4%	104.4%

The P_m and P_b thus obtained are used to calculate the actual applied stress or primary stress on the specimen, using Equation 5-2, described in Section 5.3.2.1. The evaluated primary stress is used for fatigue prediction in Chapter 6.

5.4.1.2 Static data from weld toe strain gauges

Apart from measuring P_m and P_b from static testing, static load data was also collected from the strain gauges connected at the stress concentrating weld toe, to capture any work hardening or shakedown effect due to the local stress field exceeding the yield point of the base material (measured to be 383 MPa, given in Chapter 3, Section 3.3.1). The data has been presented as a stress-strain distribution in Figure 5.16.

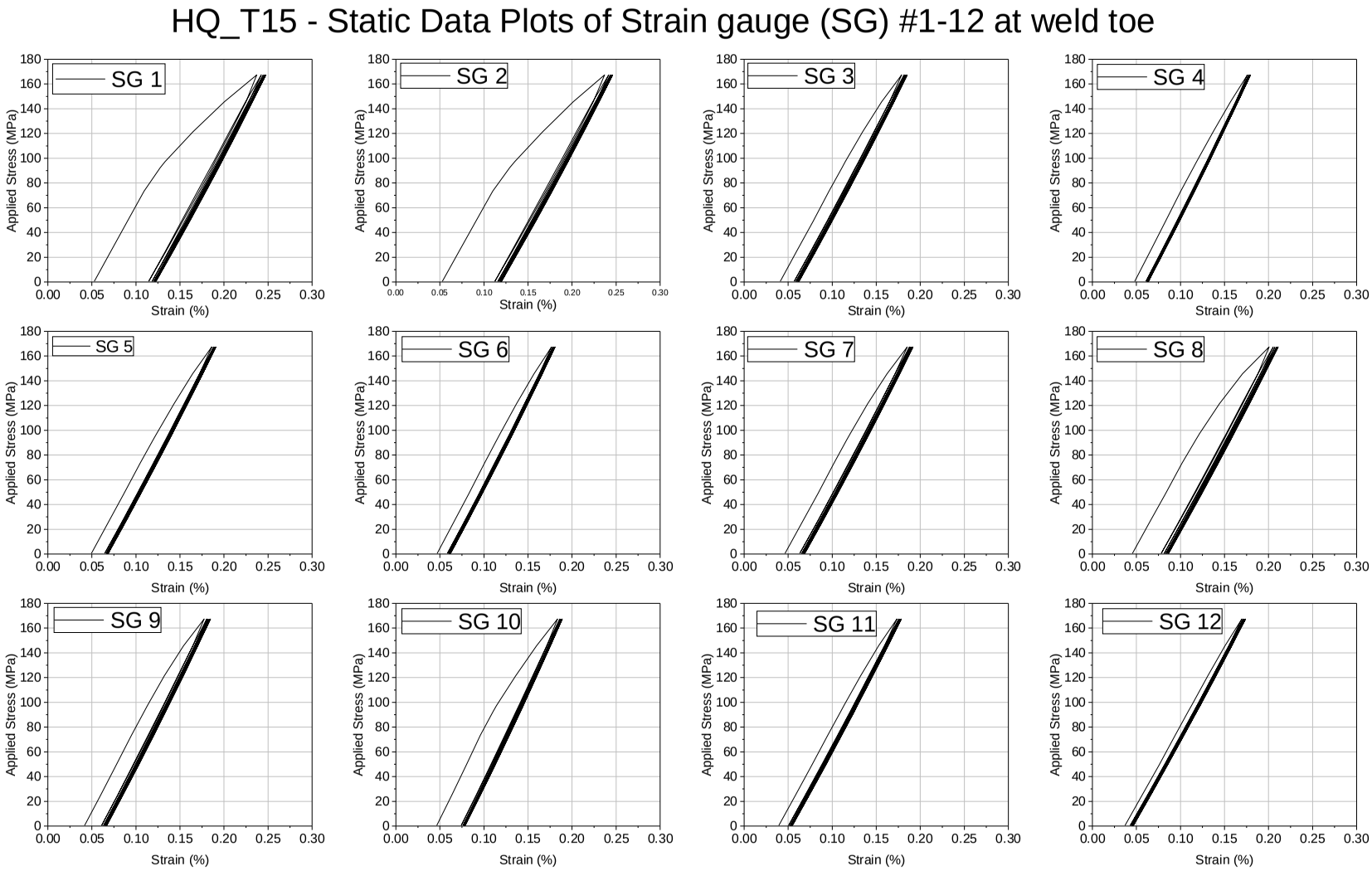

Figure 5.16 HQ_T15 – Static data plots of strain gauges (SG) #1-12 attached near the weld toe.

From the plot, it can be observed that all strain gauges indicate yielding and cyclic softening. This is attributed to the high value of P_b superimposed on the applied nominal stress. For HQ_T15, the value of P_b ranges from 90-129 MPa. Combined with the local stress concentration existing due to the weld toe, it is possible that the local stresses along the direction of applied stress measured by each strain gauge were exceeding the yield point of the base metal (383 MPa) within the applied stress range of 0-166.7 MPa. In the case of maximum applied stress of 166.7 MPa, the actual applied stress or primary stress (sum of P_m and P_b) is 291 MPa. For the local stress to exceed yield, an SCF of only 1.32 is required. Also, the presence of transverse tensile residual stress adds to the overall tensile profile of the local stress field. As the number of cycles increased, the change in maximum strain reduced, showing a decrease in the rate of cyclic softening with an increasing number of cycles. To evaluate the extent of cyclic hardening, strain-controlled tests would be required as detailed in [200]. Such tests were not carried out for this PhD project. Specific strain gauges (SG) have shown yielding, and subsequent hardening at relatively lower applied stresses than others. Two such strain gauges are SG1 and SG2. This behaviour can be attributed to the geometry of the local weld toe, which caused a higher SCF distribution relative to other locations. This is seen in Figure 5.17, which is the distribution of maximum elastic SCF for the specimen HQ_T15. The maximum elastic SCF at the location of SG1 and SG2 are relatively severe.

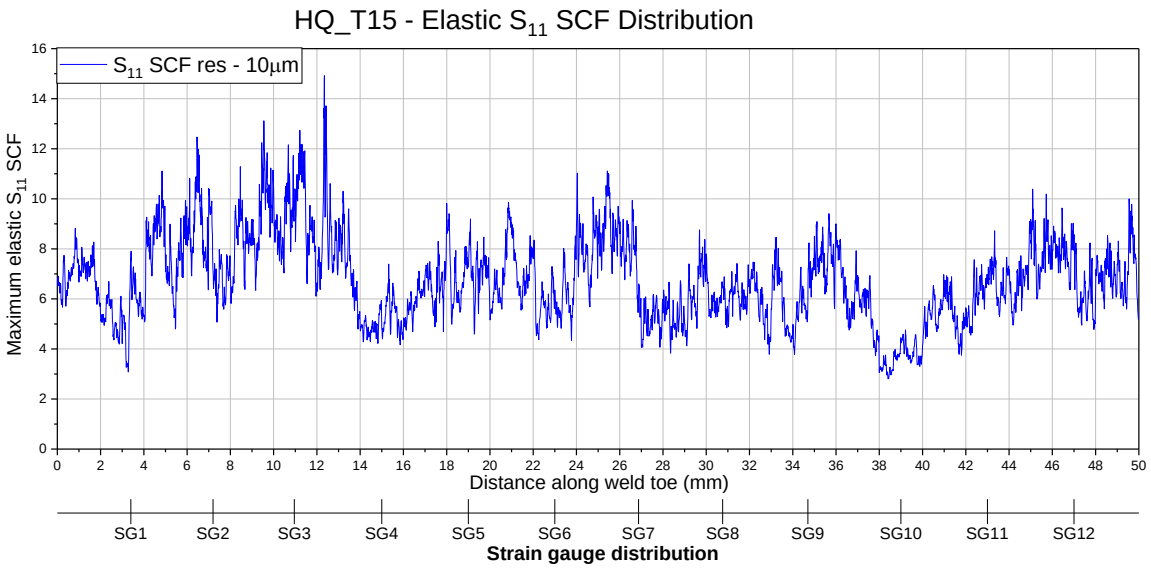

Figure 5.17 HQ_T15 – Elastic S_{11} maximum SCF distribution along the weld toe.

5.4.2 Elastic strain range analysis

A comparative study was done on the effect of WTA on the strain range drops for different crack depths (up to 1 mm) and has been presented graphically in Figure 5.18. The loading parameters for this study was based on a nominal stress range of 220 MPa and a load ratio of 0.1. A nominal stress range of 220 MPa was initially chosen for the fatigue tests, but later it was revised to 150 MPa due

to the significant bending stresses present in each specimen due to weld misalignment. The effect of WTA on strain range drop was observed to not vary with a change in nominal stress range. Therefore, the data for the nominal stress range of 220 MPa has been presented in Figure 5.18. It can be seen that the variation in WTA does not have a discernible effect on the obtained elastic strain range drop for different crack depths. The effect of changing WTR was not evaluated as the most severe case, that is a sharp profile, was considered in the model. Based on these results, a 45 degrees WTA was chosen for subsequent analyses.

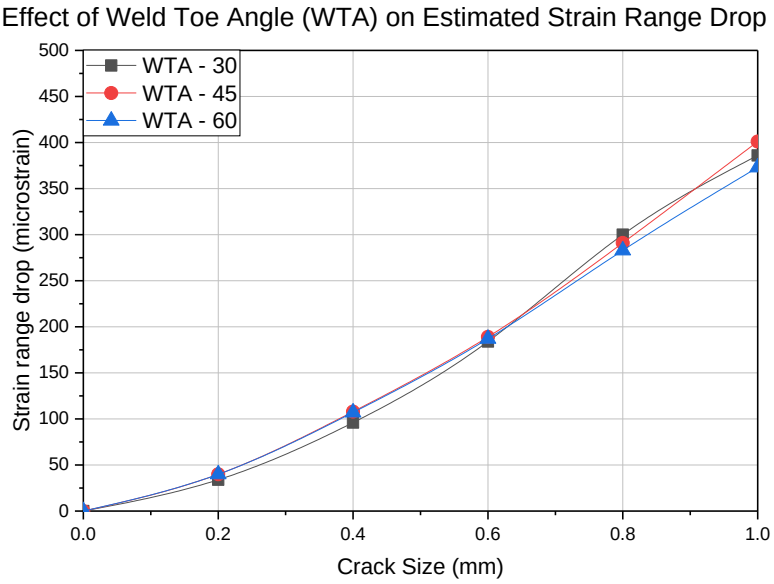

Figure 5.18 Effect of WTA on the estimated elastic strain range drop for different crack depths.

The strain range drop (based on strain averaging over a distance of 1.7-2.7 mm from the weld toe) for varying crack depths was evaluated based on the loading conditions given in Table 5.2, and the data has been presented in Figure 5.19. The data obtained in Figure 5.19 was used in the interrupted tests as well as for beach marking in the tests to failure (both described in Section 5.3.2.5).

Table 5.2 Loading parameters for elastic strain range analysis.

Stress Ratio	Maximum Stress (MPa)	Minimum Stress (MPa)	Stress Range (MPa)
0.1	166.7	16.67	150
0.5	166.7	83.35	83.35

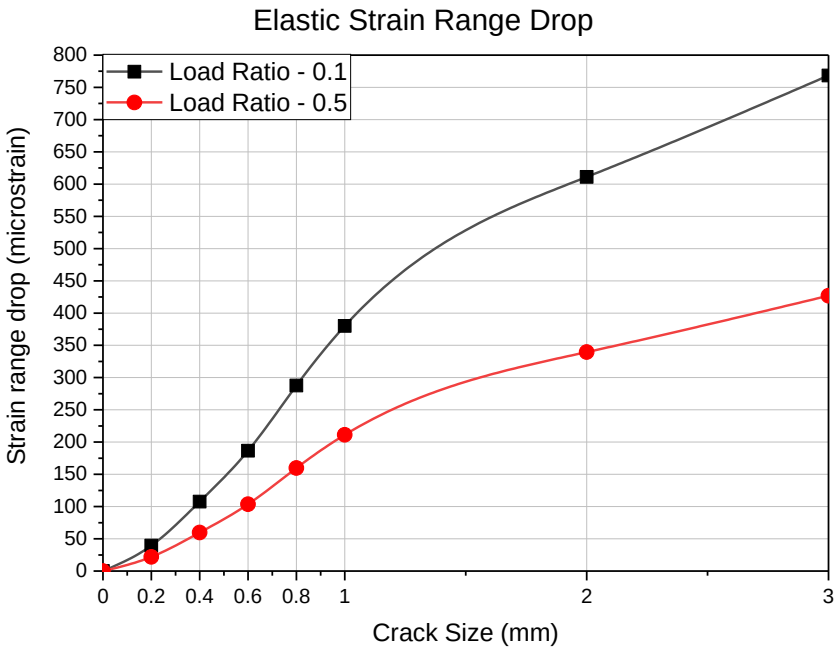

Figure 5.19 Elastic strain range drop for varying crack depths across different load ratios. Please note that only the crack depths for which strain range drop was evaluated have been shown.

5.4.3 Fatigue testing

Seven fatigue tests were carried out in total. The first fatigue test (HQ_T9) was performed at a nominal stress range of 200 MPa, maximum stress of 222 MPa and a load ratio of 0.1. For this specimen, the pre-defined strain range drop was achieved at 87,956 cycles. Considering that this was an HQ specimen, it could be assumed that at the same stress range, LQ specimens (with even higher maximum bending stresses) would exhibit very low FCI and fatigue lives. Based on the results of HQ_T9, the nominal stress range for the remaining six tests, three each of HQ and LQ, was chosen to be 150 MPa with a load ratio of 0.1, as described in Section 5.3.2.5.

The results from six fatigue tests have been analysed for the purpose of this PhD project. Three specimens each of types HQ and LQ were tested. One specimen of each type was tested to failure, and four specimens were interrupted fatigue tests. The interrupt was based on the elastic strain range drop analysis described in 5.4.2. The details of these tests in terms of number of cycles to either failure or crack detection are shown in Table 5.3. It is important to note that for the specimens that were tested to failure, HQ_T13 and LQ_T14, beach marking was performed (as described in Section 5.3.2.5). For beach marking, the load ratio was changed multiple times during the fatigue life of these specimens. Correlations between the strain gauge data and the fatigue crack and fatigue fracture surface are discussed further in this Section. Representative specimens will be discussed individually.

Table 5.3 Fatigue test results.

Test Number	Specimen	Number of Cycles	
		Tested to Failure	Interrupted
10	**LQ_T10**	NA	66,077
11	**HQ_T11**	NA	171,504
12	**LQ_T12**	NA	70,052
13	**HQ_T13**	1,027,588	NA
14	**LQ_T14**	441,720	NA
15	**HQ_T15**	NA	258,112

5.4.3.1 Interrupted testing

Four specimens were not tested until ultimate failure; instead, the test was stopped once a strain range drop of 60-70 με was observed in one of the strain gauges used for monitoring crack growth at the weld toe. The value of the strain range drop is based on the analysis described in Section 5.4.2 and corresponds to a crack depth of 0.3 mm for a load ratio of 0.1 (Figure 5.19). These specimens were later used as 'Scan set 2' for X-ray micro-computed tomography, as described in Chapter 3, Section 3.3.2.2.

In this section, the results of test number 11, labelled HQ_T11, will be presented as representative of the interrupted fatigue tests. As described previously in Section 5.3.2.5, the fatigue test was not started at the chosen test frequency of 5 Hz but was started at 0.5 Hz and ramped up to the maximum test frequency in increments of 0.5 Hz. The test was running at 5 Hz (until the strain range drop interrupt) beyond 4000 cycles.

HQ_T11 was interrupted at 171,504 cycles, when a strain range drop of 60 με was observed at strain gauge number 8. Figure 5.20 presents the strain gauge data recorded in-situ from all twelve strain gauges at the weld toe after Loess smoothing with a span of 5% (of total points recorded) was used to smooth the data [175]. The data was tared to 4,000 cycles, to make any deviations more obvious. SG #8 can be seen to have the most significant drop. Other strain gauges at the weld toe also indicate significant drops in strain range drop, specifically SG #1, #2, #3, #4, and #9. The remaining weld toe strain gauges are seen to exhibit an increase in strain range, which is a direct consequence of the drop as strain will increase in the reduced net section.

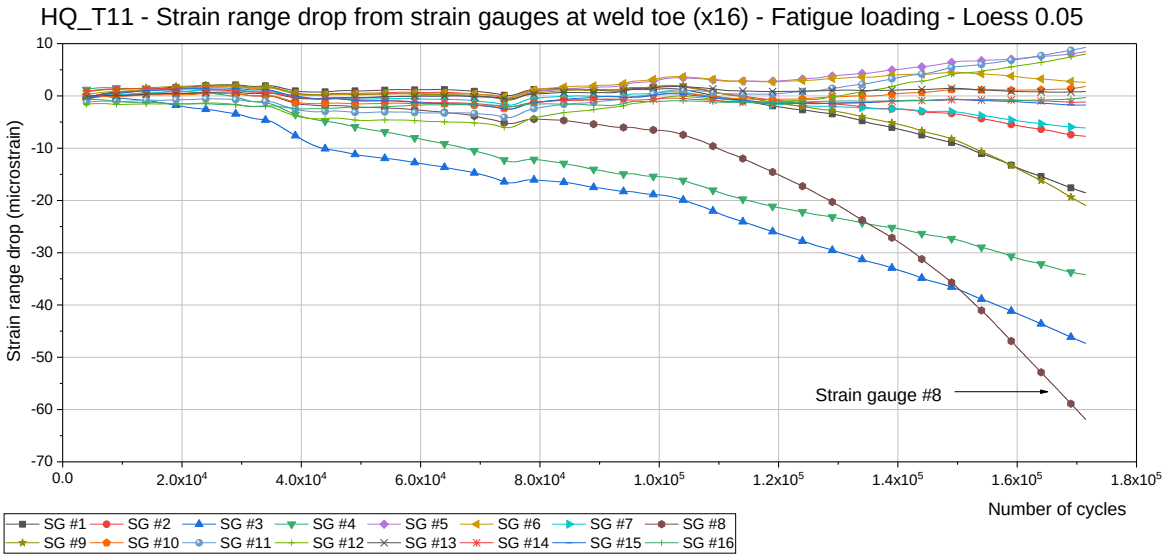

Figure 5.20 HQ_T11 - Strain range drop data. Smoothing done using Loess algorithm.

Figure 5.21 highlights the data from SG #1-9. FCI was seen at SG #3, #4 and #8 at 35,000 cycles, marked as Zone A. It is interesting to note that at the FCI point, all strain gauges show a deflection in the strain range data, but only SG #3, #4, and #8 exhibit a consistent drop. This could possibly be an indication that the initiation of a crack was not only picked up by the strain gauge next to the location of the strain gauge, but also by all the other gauges attached to the specimen, including the strain gauges attached away from the weld toe for measuring P_b and P_m. The load spectrum was observed, and no discernible abrupt change was seen at the resolution at which the load was captured (resolution of 0.01 kN). It could be postulated that the initiation of fatigue cracking caused an instantaneous and minute change in the compliance of the entire specimen, which was picked up by all of the strain gauges. However, this could also be the result of an overshoot or underload in the testing machine.

For the sake of simplicity, the crack detected by #3 and #4 will be henceforth referred to as T11_crack_34, and the crack at SG #8 will be referred to as T11_crack_8. Zone B indicates another such instance in the fatigue life of the specimen where all strain gauges exhibit a change in the strain range at approximately 75,000 cycles, causing the rate of change in strain range to change for approximately 3,000 cycles (until 78,000 cycles), beyond which SG #3, #4 and #8 continued to drop. Zone C indicates a point (101,000 cycles) where the strain range drop rate increased for SG #3, #4 and #8, with SG #8 propagating much faster than SG #3 and #4, resulting in SG #8 reaching the pre-determined strain range drop interrupt of 60 με before the other two strain gauges. Also, at the same point, i.e. 101,000 cycles, the other strain gauges in Figure 5.21 (SG#1-#9) showed a deviation as well. SG #5 and #6 indicated an increase in strain range drop, which is a result of the change in compliance of the specimen, causing a redistribution of applied stresses for maintaining

equilibrium. SG #1, #2, #7 and #9 exhibited drops in strain range, indicating that the cracks T11_crack_34 and T11_crack_8 have increased in surface length enough to result in compliance changes at the adjacent strain gauges. But, the data from SG #5 and #6 suggests that no coalescence is occurring between T11_crack_34 and T11_crack_8, thereby suggesting that the surface crack growth/opening for both cracks is measurably occurring unidirectionally, away from each other. To highlight the phenomena of strain gauge perturbation before crack growth activity, the change in the Loess smoothened strain range drop (dSR_{LOESS}) was plotted to see if the perturbation can be magnified. Figure 5.22 depicts the distribution of dSR_{LOESS} for all sixteen strain gauges. Zones A, B and C identified in Figure 5.21 have been highlighted in the plot for dSR_{LOESS}. A discernible perturbation can be seen in the dSR_{LOES} results, and the same behaviour has been seen in other specimens as well. This behaviour of strain gauges could be used to identify accurately crack initiation and propagation activity. Figure 5.23 is an actual image of HQ_T11 of the weld profile that was monitored using strain gauges. An overlap defect is visible at the location indicated by SG #3 and #4, the stress concentration feature that possibly could have initiated T11_crack_34.

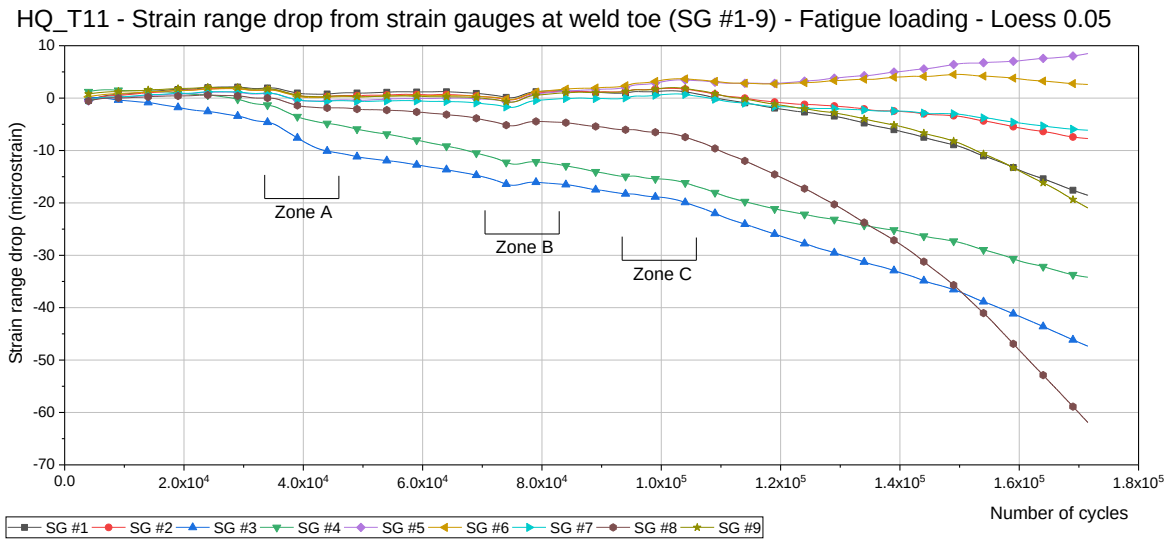

Figure 5.21 HQ_T11 - Strain range drop data for SG #1-9.

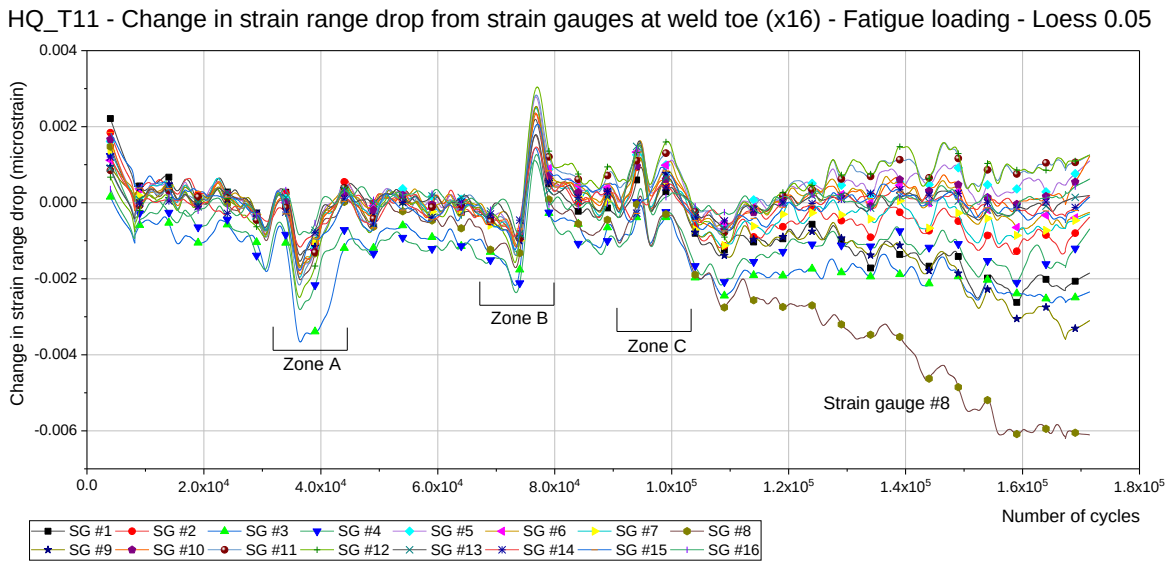

Figure 5.22 HQ_T11 - Change in strain range drop (dSR_{LOESS}) for all strain gauges.

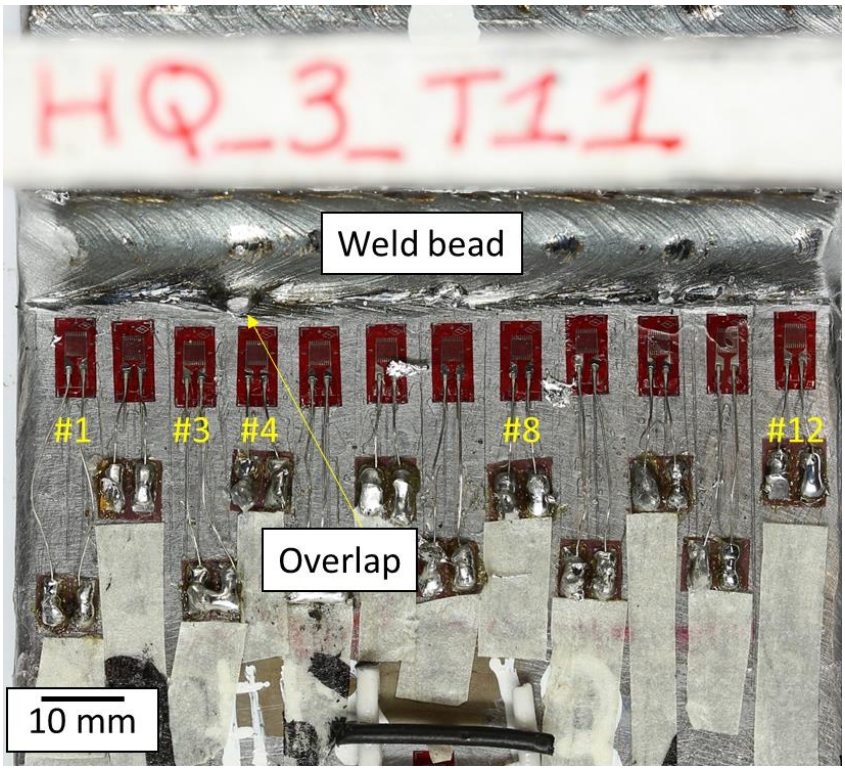

Figure 5.23 HQ_T11 - Actual image of the specimen with the strain gauge array. Left to Right - SG#1 to #12.

Similar to the phenomena described for HQ_T11, the same effect was also seen in HQ_T13. Figure 5.24 is the strain range drop distribution plot (smoothened using Loess algorithm). HQ_T13 was interrupted once SG #5 reached a strain range drop of 70 με was observed at 197,542 cycles. Initiation was seen in Zone A, as marked by the red circle in Figure 5.24. Figure 5.25 is a magnified plot highlighting Zone A, where initiation is observed to have occurred at 54,000 cycles, identified both by change in strain range drop as well as the drop in SG #5 beyond this stage point in the

fatigue life of the specimen, the latter shown in an inset in the same figure. Initiation activity can also be identified by the distribution of dSR_{LOESS} shown in Figure 5.26. A similar perturbation to HQ_T11 is, therefore, seen for HQ_T13. Again, as all the strain gauges showed the same deviation, this could be identified as a momentary compliance change occurring due to crack initiation. Another perturbation is observed to begin at approximately 4,000 cycles. However, this is related to the test machine being ramped up to the maximum test frequency of 5 Hz.

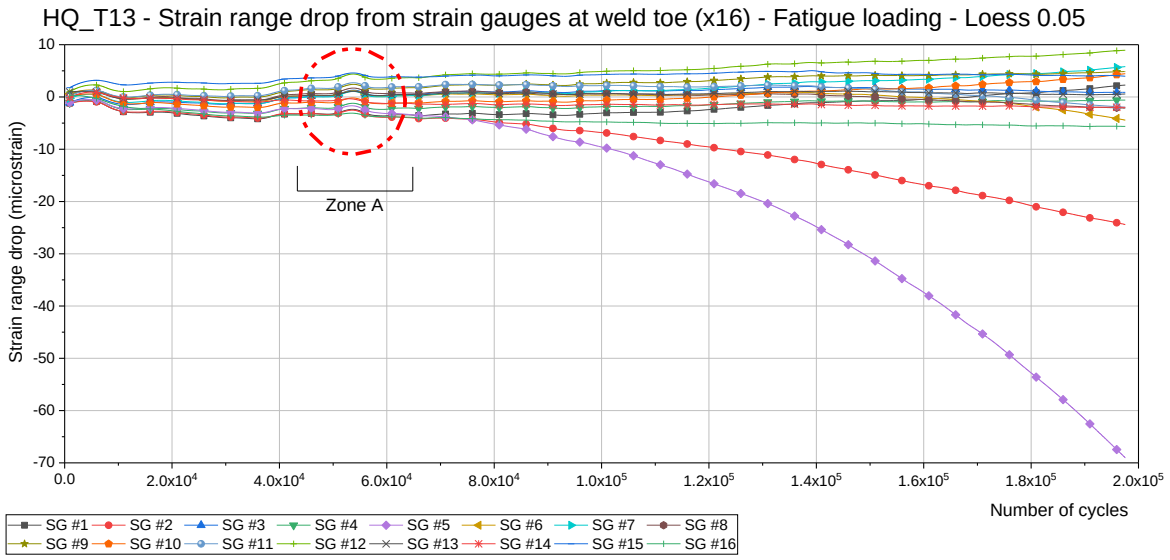

Figure 5.24 HQ_T13 - Strain range drop data. Smoothing done using Loess algorithm.

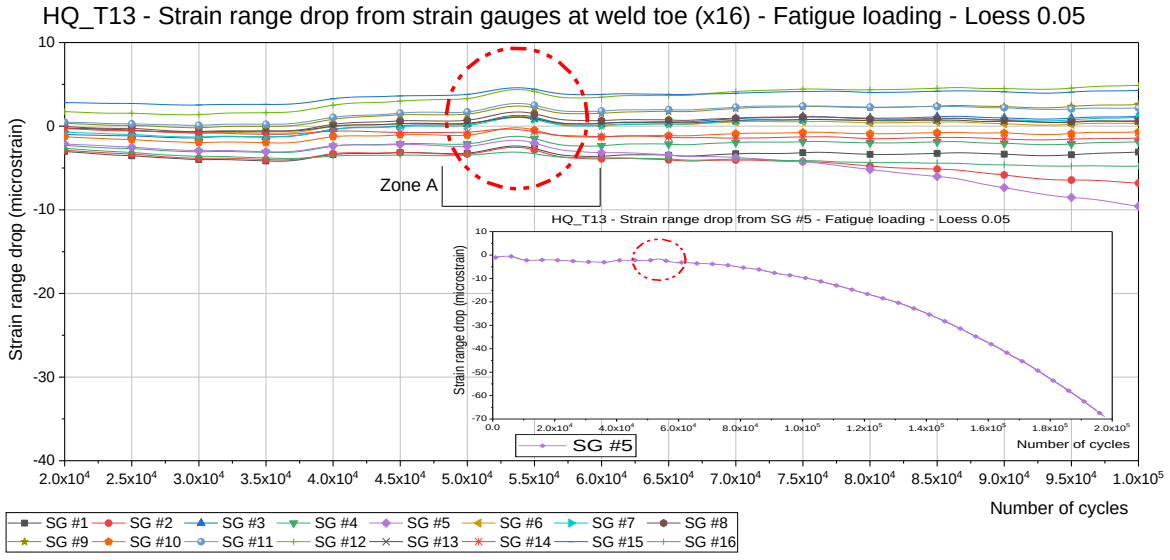

Figure 5.25 HQ_T13 – a magnified plot of strain range drop, highlighting Zone A. Inset is the overall strain range drop plot for SG #5.

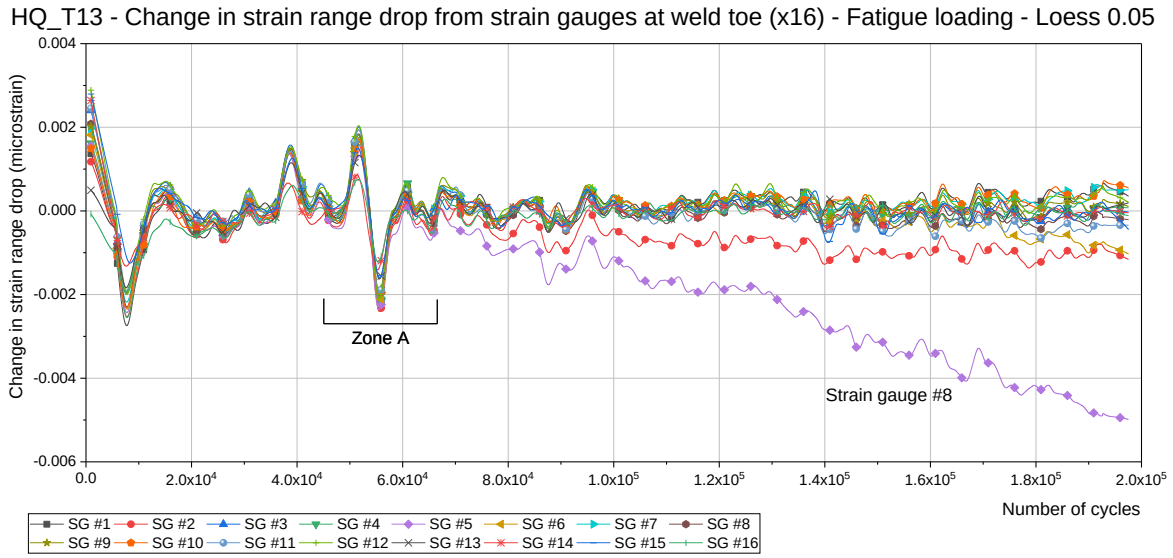

Figure 5.26 HQ_T13 - Change in strain range drop (dSR_{LOESS}) for all strain gauges.

HQ_T13 was one of the specimens that were tested to failure with beach marking, and the events up to the first beach marking stage have been described here (until 197,542 cycles). The fatigue life of the specimen beyond 197,542 cycles until failure at 1,027,588 cycles will be described in Section 5.4.3.2.

5.4.3.2 Test to failure

The results from one representative specimen, HQ_T13, will be presented and discussed in detail and results from the second specimen, LQ_T14, will be presented for evaluating whether the strain gauge results were repeatable across two differently welded (in terms of welding parameters, detailed in Chapter 3, Section 3.3.1.2) specimens. It is essential for the reader to note that there are inconsistencies in the determination of the target strain range drop. Although the methodology is based on using the FE-based elastic strain range drop analysis data for the target strain range drop value, in a few cases, this value was adjusted after an error was measured between the actual strain range drop and the FE estimation. This has been highlighted in the cases that this inconsistency has occurred. However, the strain range drop data was collected for the entirety of fatigue loading, without any bias.

5.4.3.2.1 Results of HQ_T13

HQ_T13 failed at 1,027,588 cycles and a summary of each beach marking stage in provided in Table 5.4.

Table 5.4 HQ_T13 - Details of beach marking stages.

Stage	Load Ratio	Stress Range (MPa)	Number of Cycles (total)	Total strain range drop (με)	Estimated Crack Depth (mm)
Stage-1	0.1	150	197,542	71 (SG #5)	0.3
Stage-2	0.5	83.35	600,685	186 (SG #5)	1
	0.5	83.35	724,498	239 (SG #5)	
Stage-3	0.1	150	779,186	392 (SG #5)	2
Stage-4	0.5	83.35	932,874	89 (SG #4); 452 (SG #5)	3
Stage-5	0.1	150	1,027,588	**TO FAILURE**	

Stage-1, simulating the interrupted fatigue tests, Stage 1 was performed to a target strain range drop of 70 με. 70 με was achieved first on SG #5, which corresponded to an estimated crack depth of 0.3 mm.

Stage-2, the target crack depth was 1 mm, corresponding to a target strain range drop of 170 με at the applied cyclic loads. This was observed after 724,498 cycles at SG #5. During this stage, the strain range drop was consistent and was indicative of stable stage II crack growth behaviour.

Stage-3, the target crack depth was 2 mm, corresponding to a target strain range drop of 230 με at the applied cyclic loads. However, a strain range drop of 150 με was used, which was observed after 54,688 elapsed cycles at SG #5. The strain range drop was reduced, as the strain range drop observed at SG #5 at the start of Stage 3 was much less than that predicted for a crack depth of 1 mm under the Stage 3 cyclic loading conditions from the linear-elastic FEA.

Stage-4, the target crack depth was 3 mm, corresponding to a target strain range drop of 88 με. A drop of 88 με was observed at SG #4 and 60 με at SG #5 after 153,688 elapsed cycles. The test was interrupted here, however in hindsight, it should have been continued until the strain range drop of 88με was observed at SG #5 as the crack at SG #4 corresponded to a total crack depth less than 3 mm. At the end of Stage-4, a replica was taken on the weld toe, as described in Section 3.3.2.3, whilst the specimen was held at a constant load equivalent to a nominal applied stress of ≈ 15 MPa.

Stage-5, the final stage, and the specimen was cycled to complete failure reaching a total of 1,027,588 cycles. No strain data was obtained as the strain gauges were disconnected during the replication process.

Strain range drop distribution and fractography – HQ_T13

Figure 5.27 is the strain gauge distribution across the different beach-marking stages. It can be observed that the largest strain range drops are at SG #5, #6 and #4 respectively. The values of the individual drops for each stage has been shown when possible. Figure 5.28 presents the fatigue fracture surface of HQ_T13, along with the distribution of attached strain gauges (left to right – SG #1-12, same as in Figure 5.27). The middle image has optimised brightness and contrast to better highlight the fracture surface and the crack fronts. Red lines have been drawn to outline the easily identifiable crack fronts for each of the multiple cracks seen. The blue line depicted the boundary between the fatigue fracture surface and the fracture surface when the specimen was being pulled apart in tension for separation, as shown in the bottom schematic in Figure 5.28.

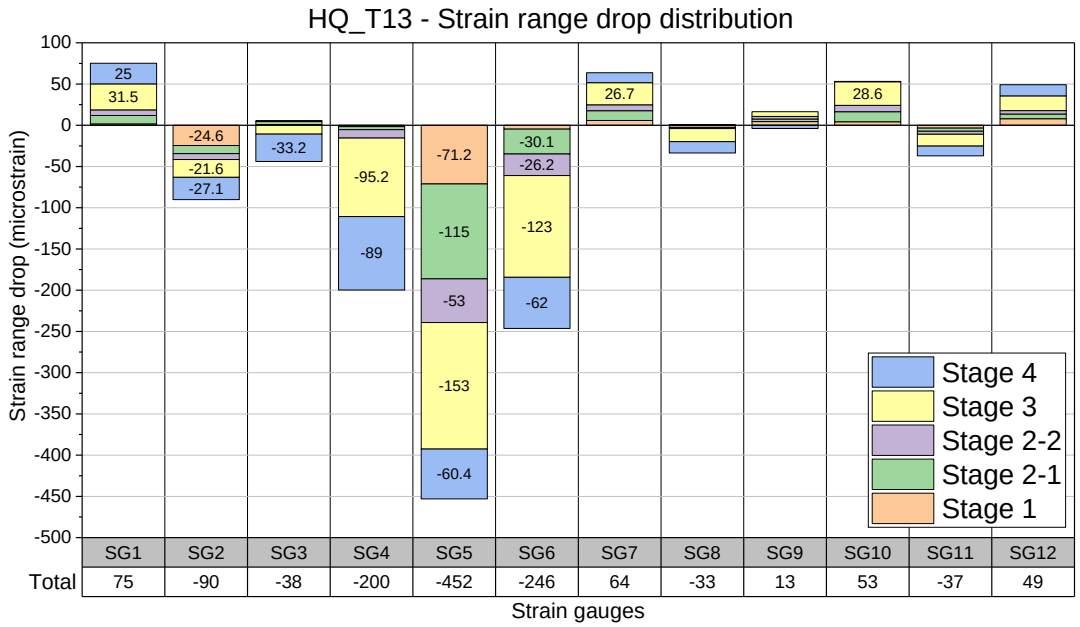

Figure 5.27 HQ_T13 - Strain range distribution across the multiple beach-marking stages.

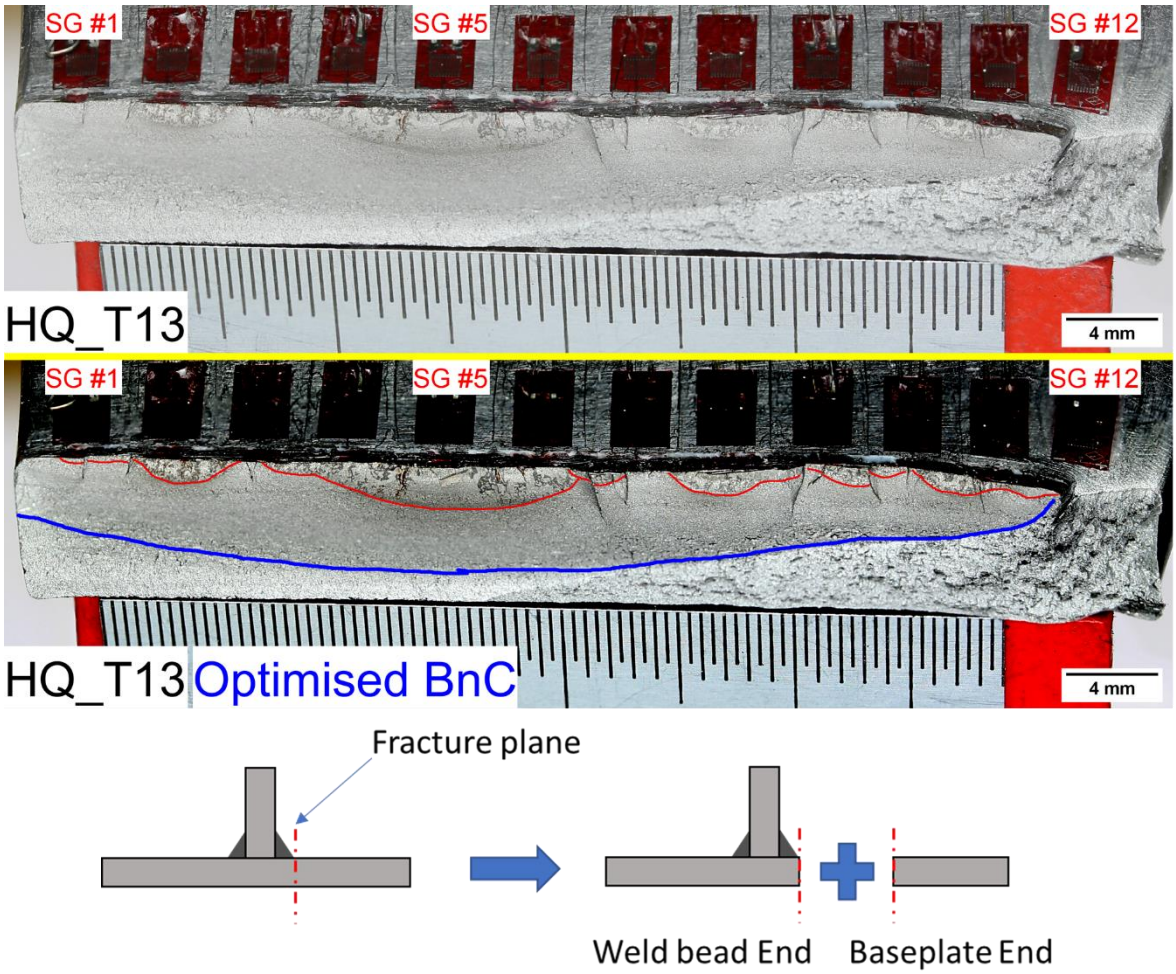

Figure 5.28 HQ_T13 - Fracture surface of the baseplate end of the specimen, highlighting multiple cracking. The middle image is optimised (brightness and contrast) for visualising the fatigue crack fronts. The bottom image is a schematic of how the specimens were labelled after complete fracture.

Comparing Figure 5.27 and Figure 5.28, it is evident that the largest strain range drop seen in the strain gauges corresponds well with the deepest crack observed on the fracture surface, i.e. the strain range drop of SG #5 and the crack underneath the same strain gauge. As this crack grew both in crack depth and length, it was picked up by the strain gauges around SG #5, i.e. SG# #4 and #6. This is also seen in the strain range drop distribution as the largest drops after SG #5 are in these two strain gauges. Therefore, the strain gauge arrangement was successfully able to indicate both the initiation time (in terms of fatigue life), and the location of the largest fatigue crack observed the specimen HQ_T13.

Figure 5.29 is a magnified view of the crack under SG #5. Crack depth and crack length measurements were taken to potentially find a relation between strain range drop and crack depth. It is important to highlight that stage-4 measurements are not visible in this image as they were beyond the image dimensions. The results have been presented in Table 5.5. Also, it should be

noted that the strain range drop for stage-4 is the combined strain range drop for SG #4-6, as the crack length at this stage was approximately 16 mm, symmetric around the centre of the crack, which happened to coincide with the centre of SG #5. Therefore, as strain gauges measure the change in strain, which is effectively the change in compliance of the specimen, both SG #4 and #6 would be expected to detect SG #5 crack growth.

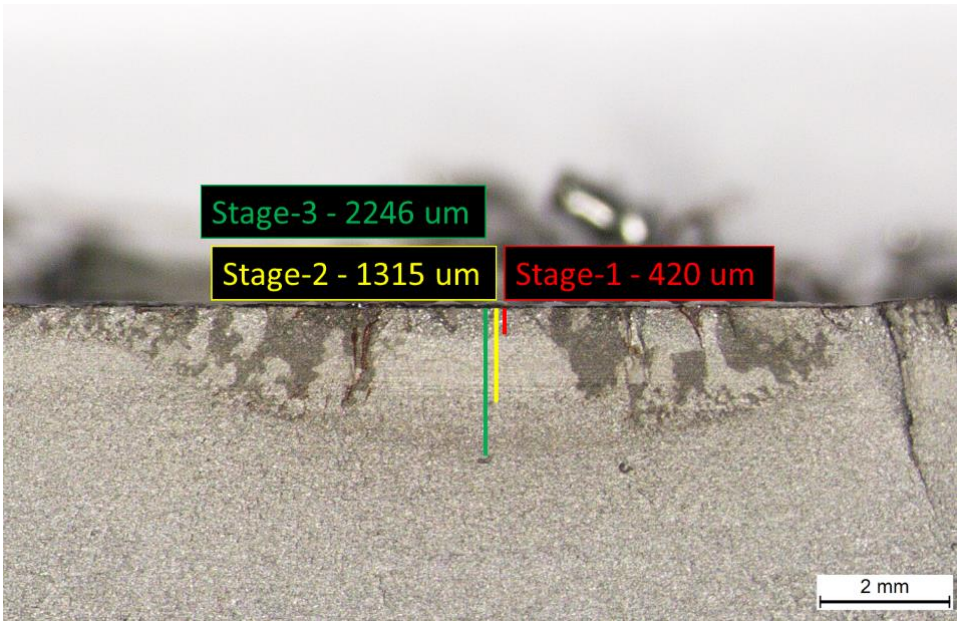

Figure 5.29 HQ_T13 - Fatigue crack under SG #5 annotated with the crack depths at different beach marking stages.

Table 5.5 HQ_T13 - Crack under SG #5 - Strain range drop and crack depth analysis.

Parameters	Stage-1	Stage-2-2 (End)	Stage-3	Stage-4
Load ratio	0.1	0.5	0.1	0.5
Strain range drop (με)	71	168	153	212
Overall crack depth (μm)	420	1315	2246	3894
Overall crack length (μm)	3200	9800	13100	15600
Aspect ratio	0.131	0.134	0.171	0.249
Incremental crack growth (μm)	420	895	931	1648
Incremental crack growth/Strain Drop (μm/με)	0.169	0.188	0.164	0.129

From the data in Table 5.5, the average crack depth versus strain range drop relation is 0.162 μm/με, but comparing the average with each obtained value, the error ranges from +16% to -21%.

The error could be associated with the growth of multiple cracks in the same specimen, resulting in an accumulative change in compliance of the specimen. As the cracks coalesce, the error is compounded by a further decrease in compliance resulting in the other strain gauges recording crack growth with varying crack depth versus strain range drop values. An example of this is the crack under SG #8. Figure 5.30 is an image of a crack that initiated in stage-3, 754,000 cycles. It has grown 240 µm in stage-3 and 990 µm in stage-4. The average crack growth versus strain range drop is 0.04 µm/µε, much lower than the values obtained for SG #5. This is primarily due to the fact that the crack under SG #8 initiated almost 550,000 cycles after the crack under SG #5. The compliance of the specimen at the location of SG #5 has potentially led to the values obtained with strain gauge #8.

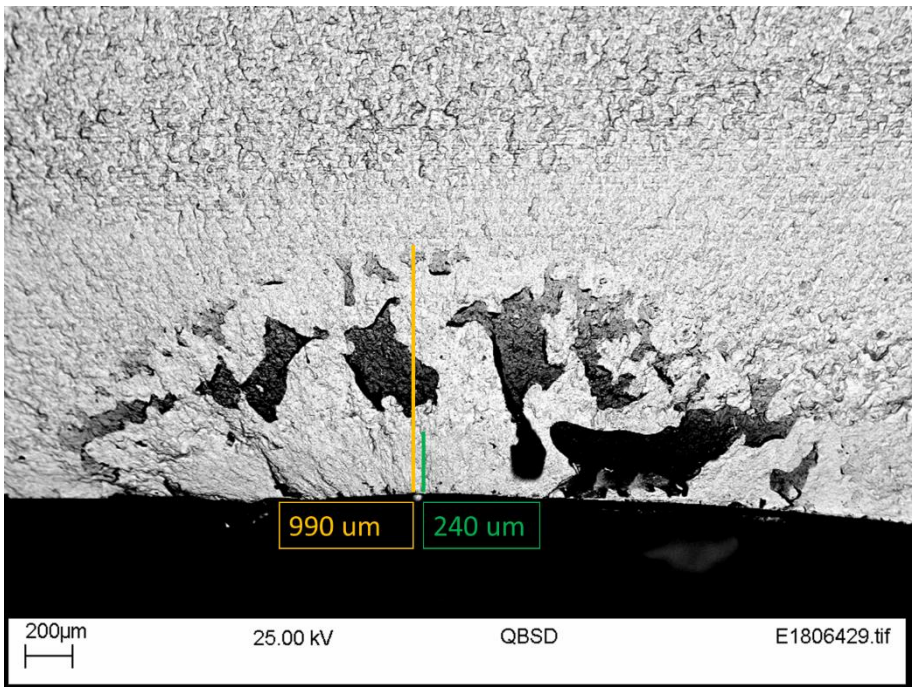

Figure 5.30 HQ_T13 - Crack under SG #8.

5.4.3.2.2 Results of LQ_T14

The data from the beach marking test of LQ_T14 has been presented in Table 5.6. It is important to note that LQ specimens have a total of twenty-four strain gauges for weld toe monitoring. Similar to HQ_T13, there are some inconsistencies in the estimated strain range drop from the FE-based analysis and the actual strain range drop value used to interrupt the test machine for each stage. The strain range drop distribution for each strain gauge across the different beach marking stages has been shown in Figure 5.31. At the end of stage-4, replicas were taken as well, similar to HQ_T13. The specimen was held at 0.5 kN corresponding to 1.3 MPa for taking the replica of the weld bead. Such a low load was used as these were LQ specimens and were showing signs of rapid and multiple

crack growth, as evidenced by the number of strain gauges highlighting substantial crack growth in Figure 5.31.

Figure 5.32 is an image of the fracture surface of LQ_T14, highlighting, amongst other features, the edge crack detected by SG #24. The edge crack was the first fatigue crack to initiate in LQ_T14, at 2,900 cycles. Similar to HQ_T13, the largest strain range drop is directly associated with the deepest crack and initiation. The crack under SG #23 initiated at 312,000 cycles in stage-3, much later than the edge crack. For this reason, even with substantial crack depth, the strain range drop at SG #23 corresponding to the crack under SG #23 was much lower, suggesting the same effect of compliance as in HQ_T13. SG #19 and #20 picked up the cracks underneath with a substantial strain range drop. This is because the initiation of these cracks occurred in stage-2, earlier than the crack under SG #23, and therefore the overall compliance of the specimen at their initiation was not as significant. Also, the multitude of cracks and initiation points seen in Figure 5.32 highlight the severity and number of stress concentrations that are present in the LQ specimen. The relative difference in lives spent at each stage between HQ_T13 and LQ_T14 also show the contrast in welding quality of both specimens, with the LQ specimen having lower lives at each stage.

Table 5.6 LQ_T14 - Details of beach marking stages.

Beach Marking Stage Number	**Load Ratio**	**Stress Range (MPa)**	**Maximum Test Frequency (Hz)**	**Number of cycles (elapsed)**	**Number of Cycles (total)**	**Strain Range Drop overall (micro-strain)**	**Estimated Crack Depth (mm)**
Stage-1	0.1	150	6	38,331	38,331	70 (SG #24)	0.3
Stage-2	0.5	83.35	1	268,750	307,081	150 (SG #24)	1
Stage-3	0.1	150	6	38,111	345,192	215 (SG #5); 140 (SG #24)	2
Stage-4	0.5	83.35	1	67,633	412,825	85 (SG #5); 50 (SG #24)	3
Stage-5	0.1	150	6	28,895	441,720	**TO FAILURE**	

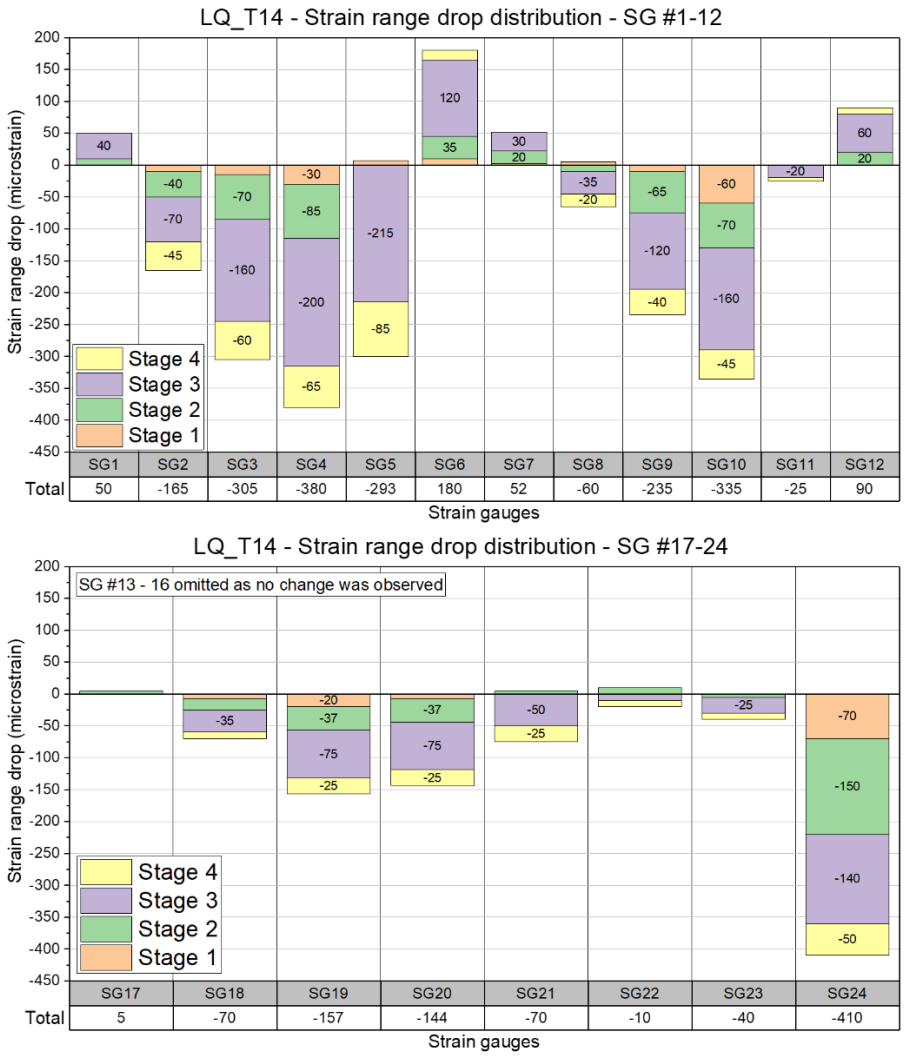

Figure 5.31 LQ_T14 - Strain range distribution across the multiple beach-marking stages.

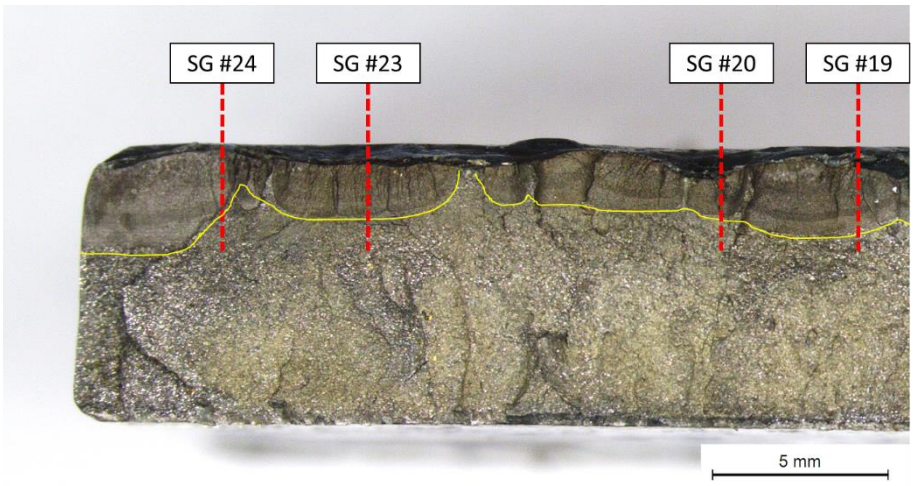

Figure 5.32 LQ_T14 - Fracture surface showing an edge crack detected by SG #24, amongst other fatigue cracking left of the edge of the specimen.

5.5 Summary

The work described in chapter 5 on the use of a strain gauge array technique for FCI detection in fatigue testing of welded specimens can be summarised in the following points –

- The technique of using a strain gauge array, substantiated with similar uses in the literature, has been implemented in-situ during fatigue testing of two different types of welded specimens.
- Misalignment in the specimens was quantified using strategically positioned strain gauges which increases the accuracy of the evaluation of stress that the entire specimen is subjected to – the sum of bending stresses as the specimen is straightened in an axially aligned test machine and the applied (intended for fatigue testing) nominal stress.
- For the purpose of 3D FE stress analysis detailed in chapter 3, some tests were carried out as interrupted tests. The test machine was programmed to trip or interrupt the cyclic loading once a pre-defined strain range drop was reached by any of the attached strain gauges. The value of the strain range drop for interrupting the test was based on a 2D FE elastic strain analysis carried out before the fatigue testing was performed. Although not very accurate (actual crack depth of 420 µm for an estimated crack depth of 300 µm), it provides a numerical approach for determining the interrupt. It is important to note that the analysis was based only on the elastic strain, whereas the strain gauges are measuring both elastic and plastic strain, without any method of isolating the plastic and elastic components of the total strain obtained.
- The use of multiple strain gauges monitoring the entirety of the weld toe provides a data-rich and high-resolution approach to detecting FCI in terms of location, time in fatigue life, and in some cases, crack depth.
    - The fractography images validate the sensitivity of strain gauges to crack initiation and propagation. The largest observed cracks in the fracture surfaces corresponded directly to the largest strain range drops seen in the strain gauge data analysis.
- Inconsistencies were present in the way the value of strain range drop were chosen for interrupting the test during the beach marking process. These inconsistencies related to adjusting for possible errors in the case of specimen HQ_T13, and conservatism in the case of specimen LQ_T14. The latter was due to the relatively low lives of the LQ specimen spent in each beach marking stage.

5.6 Conclusion and future work

To conclude, from the results described in the sections above, it is evident that if strain gauges are used in this data-rich arrangement, FCI can be accurately detected both in terms of location and life and has application in structural integrity problems, where it is critical to identify potential FCI locations during operation accurately. Other phenomena such as plastic shakedown and cyclic hardening or softening can also be obtained from the strain data. Using the array of strain gauges as described in this chapter also helped identify misalignment in the jaws of a testing machine, which otherwise would not have been identifiable if a single strain gauge or an array of strain gauges were attached only at the centre of the specimen.

However, similar to what was observed in chapter 4, it is not possible to accurately quantify the relation between strain range drop and crack depth. This is primarily due to multiple cracking occurring at the weld toe, and therefore, it becomes challenging to isolate the strain range drop for each crack. As cracks grow in both depth and size, they interfere with the strain field of neighbouring strain gauges which further makes it difficult to isolate cracks, especially after coalescence. It is expected in a welded specimen that multiple cracking will occur due to the potentially large number of stress concentrating features present at the weld toe. Like any other crack detection technique, it would be very suited if it was possible to control crack growth by limiting it to a specific location (for example, in the case of notched samples). Also, as strain gauges effectively measure the compliance of the specimen to the applied load, the change in compliance due to a crack that has initiated sooner affects the strain range data obtained from other strain gauges for cracks that initiate relatively later in the overall fatigue life of the specimen.

In terms of future work, the effectiveness of the strain gauge array technique in detecting FCI is apparent and can be used in tests or applications where FCI life is a critical deliverable. The phenomenon described in Section 5.4.3.1, where each strain gauge deviates momentarily as a result of an initiating crack could be further developed in terms of the resolution of crack detection (the depth of the crack when this phenomenon is observed). The use of biaxial or triaxial strain gauges could possibly increase the sensitivity to detect cracks in parts where the loading is not simply transverse to the stress concentrating zone. The 2D FE elastic strain range drop could potentially be carried out using 3D models with the real weld geometry, accounting for the considerable increase in complexity.

Chapter 6 Local Notch Stress-Strain Approach to Fatigue Lifing

6.1 Motivation

The standards available for the fatigue assessment of welded joints primarily deal with procedures based on S-N curves, fatigue crack propagation considerations and experimental evaluation (fatigue testing). However, they lack an appropriate approach for fatigue crack initiation (FCI) estimation for welded joints [5-8, 17]. This may be due to the large number of variables involved in the process of such estimations as well as the difficulty in experimentally validating the obtained results. In FCI estimation, it is crucial to first define what crack initiation is. Radaj et al., 2006 [16] define crack initiation based on the initiation of a crack (usually initiating at the surface) large enough to be detected with any of the experimental methods available for crack detection. The complex microscopic phenomena driving crack initiation can be approximated using macroscopic elastic or elastic-plastic stress and strain analysis based on continuum mechanics, which define the cyclic deformation causing fatigue crack initiation [45].

The assessment can be categorised into global and local approaches to analyse the applied load and resulting stress and strain distributions based on continuum mechanics. The global approach refers to the assessment based on the applied forces or moments and the resultant nominal stress in the critical cross-section and subsequently comparing the obtained stresses with specific critical values such as fully plastic yielding or total fracture of the specimen. The local approaches incorporate the stress and/or strain distribution (as a result of externally applied forces/moments) occurring at local stress concentration features, e.g. a notch, and the material fatigue defined by cyclic deformation [16, 17, 85, 201, 202]. The complete local fatigue strength assessment incorporates both crack initiation and crack propagation; crack initiation is described by notch strain or notch stress approaches and crack propagation is described by the crack propagation approach based on an initiated crack [16].

In Chapter 3, the possibility of capturing the true weld geometry and resultant local stress distributions was presented using a combination of high-resolution X-ray μ-CT and 3D FE stress analysis. Chapters 4 and 5 highlighted two data-rich crack growth monitoring techniques (experimental) to obtain the FCI life of the test specimen. The combination of the work done in these three chapters leads to the following overarching aim of this PhD project –

"To use the local stress-strain approach for the estimation of fatigue crack initiation life and, subsequently, the total life of a welded joint using local stresses obtained from 3D FE stress analysis of the true weld geometry, followed by validation of the results with data-rich experimental methods of crack growth monitoring."

This chapter introduces the steps involved in the fatigue strength assessment of welded joints using the local notch strain approach. Steps include identifying the required material parameters, experimentally derived data and the assumptions that have been made during this project. A critical review of the approach based on the results and findings is presented at the end of this chapter.

6.2 Local notch stress-strain approach – Review

6.2.1 Introduction

In the case of welded joints, it is well known that the stress distribution is not uniform throughout complex structures and local stress concentration features result in a certain degree of plastic flow and constraint of deformation in the vicinity of such notch-like features. Therefore, it becomes more appropriate to consider the *local* notch stress-strain behaviour of these stress concentrating notches and subsequently the strain-life approach to fatigue as these stress concentrations are the primary location of fatigue crack initiation.

6.2.2 Principles of the local notch stress-strain approaches

To understand the application of the local notch stress-strain approach, it is important to highlight the fundamental concepts that were used in this project. Both approaches (local notch stress and local notch strain) can be used separately. The use of the notch stress approach alone is best suited for high-cycle fatigue estimations [16, 202], although the International Institute of Welding (IIW) has published recommendations to implement its use for medium-cycle and low-cycle fatigue ranges [8].

The primary difference between the notch strain approach and the notch stress approach is that the notch stress approach is based on nominal or far-field stresses and elastic stress concentration factors (with associated empirical modifications). The notch strain approach, on the other hand, emphasises the local stress-strain changes and therefore, can account for local yielding due to high stress amplitudes as well as stress concentrations that result in localised elastic-plastic deformation [203].

A similarity between the two approaches is that both require the implementation of the crack growth approach separately, primarily the damage tolerant approach (or fracture mechanics approach) which requires the assumption of an initiated crack of a specific depth. Therefore, in Equation 6-1, both approaches can be used to evaluate the fatigue crack initiation life N_i (i.e. cycles to achieve a crack depth of 0.25 mm [16]), and then the crack propagation approach is used to evaluate the crack propagation life N_p. N_t is the total fatigue life. The evaluation methods described in Section 6.2.2.1 and 6.2.2.2 refer then to the crack initiation life.

$$N_t = N_i + N_p \quad \text{6-1}$$

6.2.2.1 Notch stress approach

Compared with the available global approaches, which primarily focus on nominally smooth-surfaced specimens, the notch stress approach includes the severe effects of stress concentrating features that are present in most engineering components, especially welded joints. The stress distribution and resulting deformation immediately near such a stress concentration will undoubtedly play an essential role in determining when (in the life of the specimen) and where fatigue cracks will initiate and propagate [14].

The stress concentration due to a notch-like feature can be defined using the theoretical elastic stress concentration factor K_t, which is a ratio of the maximum elastic stress locally at the stress concentrating feature and the far-field (nominal) stress. This can be easily calculated using analytical solutions (e.g. Peterson's library of analytical solutions for SCF evaluation first published in 1974 [204]) as well as FE analysis assuming purely elastic behaviour throughout the material being considered.

It has been observed that under fatigue loading conditions, the actual stress concentration factor effective at the notch is lower than the theoretically predicted elastic stress concentration factor [8, 14, 16, 17, 83, 106, 202, 205-208]. Due to this, the elastic stress concentration factor is replaced with the fatigue notch factor K_f when considering fatigue problems. The relation between K_f and K_t is denoted by the material-dependent notch sensitivity index q, which is defined in Equation 6-2 [14, 16, 209].

$$q = \frac{K_f - 1}{K_t - 1} \quad \text{6-2}$$

The value of q varies from zero up to unity, reflecting no notch effect and the full effect of the notch as predicted by elasticity theory [14] respectively. Its value is generally greater for high strength steels than for low strength steels [16].

The relation between K_f and K_t in the case of notch-like features is established using the microstructural notch support hypothesis [16]. In this hypothesis, the actual stress concentration due to a notch-like feature is lower than the theoretical elastic stress concentration factor, with the degree of variation depending on the geometry of the notch and material properties [14]. For welded joints, three hypotheses are widely used [16] and are as follows:

1. Stress averaging approach originally presented by Neuber [210-212], with application-based modifications published later [213-215].
2. Critical distance approach published by Peterson, 1950 [216].
3. Highly stressed volume approach proposed by Kuguel, 1961 [217].

In this project, the critical distance approach proposed by Peterson [204, 209, 216] will be used. In work done by Lawrence et al., 1975 and 1978 [218, 219] an empirically derived relation between the theoretical elastic stress concentration factor K_t and fatigue notch factor K_f was suggested and is shown in Equation 6-3.

$$K_f = 1 + \frac{(K_t - 1)}{1 + \frac{a^*}{\rho}} \quad \text{6-3}$$

Where,

a^*	Critical distance
ρ	Notch radius

The parameter a^* is a material constant and depends on the strength and ductility of the material. It can also be empirically approximated from the ultimate tensile strength of the material σ_{UTS} for steels using the relation given in Equation 6-4 [218-221].

$$a^* \approx 0.025\left(\frac{2068}{\sigma_{UTS}}\right)^{1.8} \approx \frac{10870}{\sigma_{UTS}^2} \quad \text{6-4}$$

To solve the issue of variability in the value of notch radius ρ due to the irregular geometry of the weld, the worst case scenario was proposed by Lawrence et al., 1978 [218] where the critical notch radius ρ_c for maximum K_f or $K_{f\,max}$ is equal to the critical distance $(\rho_c = a^*)$. Figure 6.1 highlights the difference between calculated K_t for a specific butt weld geometry and the K_f for the same geometry for two different kinds of steels.

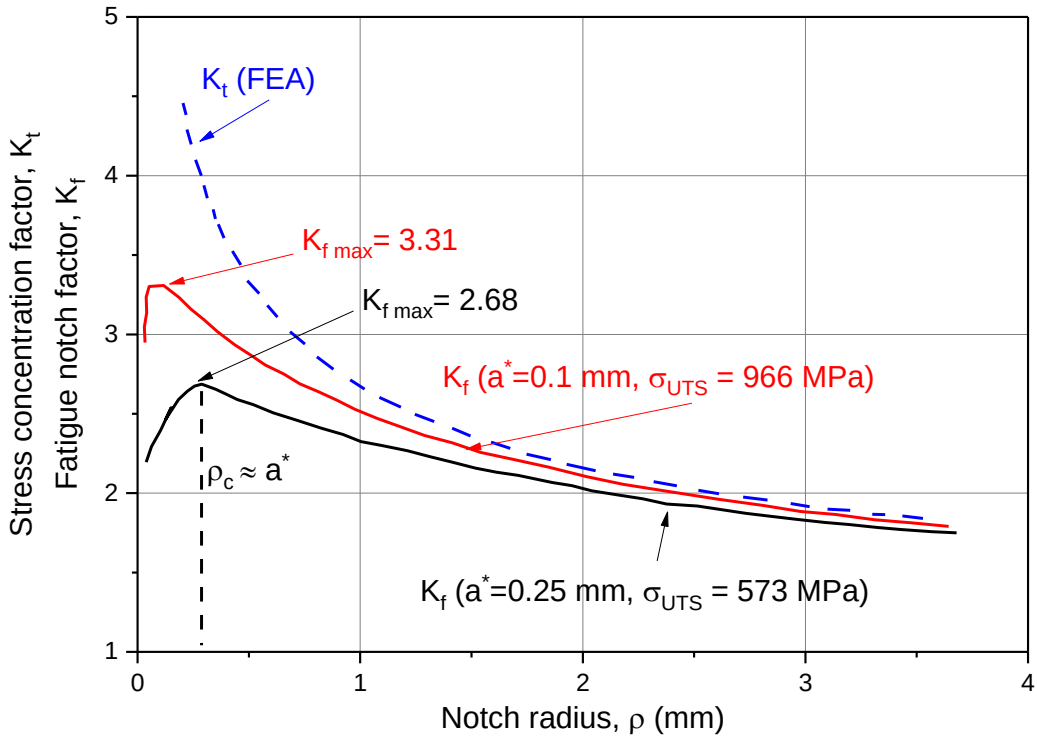

Figure 6.1 Elastic stress concentration factor calculated using FEA and fatigue notch factor of a specific butt weld geometry for two different structural steels. Adapted from [16], originally from [221].

To incorporate mean stress effects on fatigue life, various models are available in the literature which provide a combination of the applied stress amplitude and resulting mean stress. Some well-known models are the Gerber 1874 [222], Goodman 1899 [223] and Soderberg 1939 [224] relations, to name a few. As an example, the modified Goodman relation given in Equation 6-5 can be modified to incorporate K_f to give Equation 6-6 [14]. For welded joints with tensile residual stresses, the mean stress is taken to be equal to the residual stress [205].

$$\sigma_a = \sigma_{a|\sigma_{m=0}} \left\{1 - \frac{\sigma_m}{\sigma_{UTS}}\right\} \tag{6-5}$$

$$\sigma_a = \frac{\sigma_{a|\sigma_{m=0}}}{K_f} \left\{1 - \frac{K_f \sigma_m}{\sigma_{UTS}}\right\} \; for \; \left(K_f . \sigma\right)_{max} < \sigma_{ys} \tag{6-6}$$

Where,

σ_a	Stress amplitude
σ_m	Mean stress
$\sigma_{a\|\sigma_{m=0}}$	Stress amplitude (for a finite life) for fully-reversed loading
σ	The instantaneous value of stress at any point along the cyclic far-field stress distribution
σ_{ys}	Uniaxial yield stress

σ_{UTS} Ultimate tensile strength

The value of the equivalent stress amplitude for nonzero mean stress, σ_a, if exceeding the empirically obtained endurance limit of the materials, can be used in the Basquin equation to obtain the number of load reversals to failure, $2N_f$ [14, 225].

$$\sigma_a = \sigma_f'(2N_f)^b \quad 6\text{-}7$$

Where,

σ_f' Fatigue strength coefficient (approximately equal to the fracture strength of the material).

b Fatigue strength exponent or Basquin exponent.

N_f Number of load reversals to failure (FCI).

Apart from the steps highlighted in Section 6.2.2.1, there are other variations of the notch stress approach available, with the IIW recommendations being a useful resource on how to implement the different versions [8, 17]. Based on the steps highlighted in this section, one can estimate the fatigue stress life of a component. The elastic stress concentration factor K_t can be evaluated either by using analytical solutions or FEA. Chapter 3 describes how both methods were used to calculate K_t from 3D models of the weld toe geometry.

6.2.2.2 Notch strain approach

To evaluate service fatigue life of the fatigue crack initiation stage for medium- and low-cycle lifetimes, the notch strain approach was developed. Fundamentally, the notch strain approach relates the local elastic-plastic strain occurring in the immediate vicinity of a notch root to the strain-life of an unnotched specimen of the same material [14, 16]. Figure 6.2 presents a schematic of the relation.

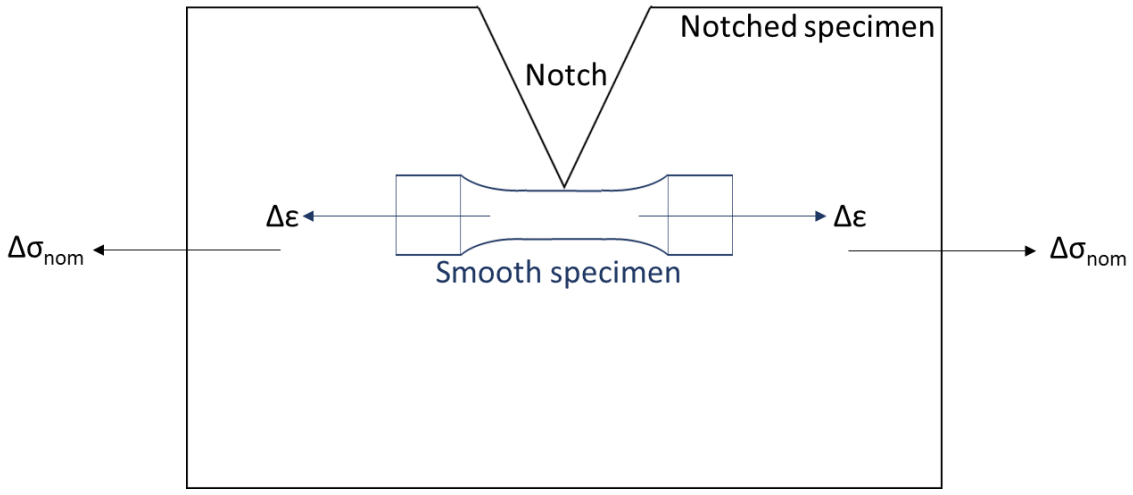

Figure 6.2 Schematic of the local notch strain approach where the stress-strain behaviour at the vicinity of the notch root is considered to be the same as that of a smooth specimen of the same material properties. Adapted from [16].

To describe the changes in stress distribution due to the geometry of the notch-like feature, the relation given in Equation 6-3 is used to calculate the fatigue notch factor K_f. The stress-strain response of the material is taken from a stable hysteresis loop obtained from axial strain-controlled tests of a specimen of the same material. The total strain range $\Delta\varepsilon$ can be broken down into its elastic and plastic components, $\Delta\varepsilon_{el}$ and $\Delta\varepsilon_{pl}$, respectively, as shown in Equation 6-8.

$$\Delta\varepsilon = \Delta\varepsilon_{el} + \Delta\varepsilon_{pl} \quad 6\text{-}8$$

The initial local stress-strain relation at the root of the notch-like feature can be defined with the Ramberg- and Osgood [226] monotonic stress-strain curve described by Equation 6-9, proceeding from the initial residual stress state, to a stress state on the Neuber hyperbola [227], defined by Equation 6-10. Subsequent cyclic stress-strain loops are described by the hysteresis branches of the Ramberg and Osgood cyclic stress-strain curve [226], modified according to Masing [228], as shown in Equation 6-11 and ending at the Neuber hyperbola in a reversed stress-strain diagram, Equation 6-12 [16]. Thus, the far-field nominal stress-strain can be related to the local stress-strain at the root of the notch-like feature using Neuber's rule [227].

$$\varepsilon = \frac{\sigma}{E} + (\frac{\sigma}{K})^{\frac{1}{n}} \quad 6\text{-}9$$

$$\sigma\varepsilon = (\frac{K_f \sigma_{nom}}{1-R} + \sigma_{res})^2 \frac{1}{E} \quad 6\text{-}10$$

$$\Delta\varepsilon = \frac{\Delta\sigma}{E} + 2\left(\frac{\Delta\sigma}{2K'}\right)^{1/n'} \quad 6\text{-}11$$

$$\Delta\sigma\Delta\varepsilon = \left(K_f \Delta\sigma_{nom}\right)^2 \frac{1}{E} \quad 6\text{-}12$$

Where,

ε	Total local strain
σ	Total local stress
E	Elastic modulus
K	Static strength coefficient
n	Static strain-hardening exponent
σ_{res}	Initial residual stress
$\Delta\sigma$	Total local stress range
$\Delta\varepsilon$	Total local strain range
K'	Cyclic strain-hardening coefficient
n'	Cyclic strain-hardening exponent

Based on the cyclic and tensile properties of the material, the local stress and strain can be calculated. Based on the strain data thus obtained, the strain-life of the notched specimen can be defined in terms of the total strain amplitude ε_a at the notch root, which is a sum of the elastic and plastic strain amplitudes, $\varepsilon_{a\,el}$ and $\varepsilon_{a\,pl}$ respectively, as shown in Equation 6-13. Equation 6-13 can be rewritten in terms of total, elastic and plastic strain range, as shown in Equation 6-14. The elastic strain range is used in the Basquin relation [225] in Equation 6-15, with a mean stress effect modification suggested by Morrow [229] in Equation 6-16. The plastic strain range is used in the Coffin-Manson relationship [230, 231] in Equation 6-17. The total strain amplitude can, therefore, be used in the combined relationship to evaluate the number of reversals to crack initiation, Equation 6-18.

$$\varepsilon_a = \varepsilon_{a\,el} + \varepsilon_{a\,pl} \tag{6-13}$$

$$\frac{\Delta\varepsilon}{2} = \frac{\Delta\varepsilon_{el}}{2} + \frac{\Delta\varepsilon_{pl}}{2} \tag{6-14}$$

$$\frac{\Delta\varepsilon_{el}}{2} = \frac{\sigma_f'}{E}\left(2N_f\right)^b \tag{6-15}$$

$$\frac{\Delta\varepsilon_{el}}{2} = \frac{\left(\sigma_f' - \sigma_m\right)}{E}\left(2N_f\right)^b \tag{6-16}$$

$$\frac{\Delta\varepsilon_{pl}}{2} = \varepsilon_f'\left(2N_f\right)^c \tag{6-17}$$

$$\frac{\Delta\varepsilon}{2} = \frac{\Delta\varepsilon_{el}}{2} + \frac{\Delta\varepsilon_{pl}}{2} = \frac{\left(\sigma_f' - \sigma_m\right)}{E}\left(2N_f\right)^b + \varepsilon_f'\left(2N_f\right)^c \tag{6-18}$$

Where the newly introduced parameters are,

σ_m	*Mean stress*

ε_f' *Fatigue ductility coefficient*

c *Fatigue ductility exponent*

The various material parameters used in Equation 6-18 can be obtained either from cyclic axial strain-controlled tests or can be estimated from empirical relations available in the literature and are given below from Equation 6-19 to 6-25 [16, 221, 232-236].

$$\sigma_f' \approx \sigma_{UTS} + 342 \quad \text{6-19}$$

$$\sigma_{UTS} \approx 3.42 H_{BRIN} \quad \text{6-20}$$

$$b \approx -\frac{1}{6} log \frac{2(H_{BRIN} + 100)}{H_{BRIN}} \quad \text{6-21}$$

$$K' \approx 1.65 \sigma_{UTS} \quad \text{6-22}$$

$$n' \approx \frac{b}{c} \quad \text{6-23}$$

$$\varepsilon_f' \approx \left(\frac{\sigma_f'}{K'}\right)^{\frac{1}{n'}} \quad \text{6-24}$$

$$c \approx -0.58 \quad \text{6-25}$$

6.2.3 Notch stress-strain approach – Notable use in recent literature

To assess the use of the notch stress-strain approach presented in section 6.2.2, certain relevant applications from the literature are listed below to highlight the continuing relevance of this approach that has been evolving for more than 70 years.

- **Reference** – Janosch et al., 1998 [237]

  Approach used – Notch stress approach

  Summary – The use of local notch stresses for predicting the fatigue strength of non-load carrying fillet welded joints, specifically looking at the distribution of undercuts and its impact on the endurance limit of the joints.

- **Reference** – Seeger et al., 2008 [238]

  Approach used – Notch stress-strain approach

  Summary – The use of notch stress-strain approach for spot-weld joints. The microstructural support effect is considered to estimate the notch stresses. The failure criterion was set as a crack depth of 0.25 mm.

- **Reference** – Karakas et al., 2008 [239]

  Approach used – Notch stress approach

Summary – The effective notch stress approach [17] was used with fictitious notch radii of 1.0 mm and 0.05 mm for wrought magnesium alloy welded joints. Conventionally 1.0 mm was suggested by Radaj [16, 240]. A 2D FE model of the weld toe with the fictitious radius was used to evaluate the resulting linear elastic stress concentration factor.

- **Reference** – Pedersen et al., 2010 [106]
  Approach used – Notch stress approach
  Summary – The accuracy and inherent conservatism of the notch stress approach was evaluated based on the results of a large number of fatigue test results that were extracted from the literature. SCF values were obtained using FEA of ideal weld geometries. Recommendations were made based on the results obtained from the application of the notch stress approach to different kinds of welded joints, specifically butt welds and fillet welds.
- **Reference** – Bruder et al., 2012 [201]
  Approach used – Notch stress-strain approach
  Summary – Similar to the work done by Pedersen et al. [106], an evaluation of both nominal and local stress approaches were carried out to review their effectiveness in fatigue assessment of seam welds. A large number of fatigue tests were carried out at different participating institutions. A notable highlight of this work is the variation of the fictitious notch radius in the effective notch stress approach and using it in an FE model of the true weld geometry.
- **Reference** - Saiprasertkit et al., 2012 [241]
  Approach used – Notch stress-strain approach
  Summary - Modified version of the effective notch stress approach, with the conventional application of the approach described in [17] primarily for high-cycle fatigue regimes. The fictitious radius concept of the conventional effective notch stress approach is implemented, but local strain data (or effective notch strain) is used instead of elastic stress (or effective notch stress) for fatigue estimates in the medium- to low-cycle fatigue regimes.
- **Reference** - Remes, 2013 [44]
  Approach used – Notch strain approach
  Summary – The notch strain approach was used to evaluate the life to crack initiation and a discrete crack growth model for crack propagation was used which also considered the effect of the material's microstructure on the stress-strain state and fatigue damage accumulation along the crack growth path [45]. The actual weld notch geometry in the butt-welded joints was considered in the 2D FE modelling.
- **Reference** – Lang et al., 2016 [114]
  Approach used – Notch stress approach
  Summary – An attempt has been made to use the notch stress approach with 'real' notch stresses by capturing the actual weld toe geometry using optical laser scanning for FE-based

linear elastic stress analysis. An implicit gradient model has been developed, which is a modification of the stress gradient model (proposed initially by Siebel and Stieler [242] as a hypothesis for explaining the microstructural support approach based on the work done by Zhang, 2012 [243].

- **Reference** – Savaidis et al., 2016 [108]

  Approach used – Notch stress-strain approach

  Summary – The notch strain approach has been used in conjunction with the effective notch stress approach, where the notch radius has been chosen to be a fictitious radius to remove singularity effects during linear-elastic stress calculations at the root of the notch. The approach has been implemented on a welded joint which forms a part of a vehicle axle casing, with the experimental loading conditions (in terms of stress ratio) varied according to the different scenarios during the operation of the component being examined.

- **Reference** – Łagoda et al., 2017 [244]

  Approach used – Notch stress-strain approach

  Summary – A comparison of the different kinds of notches that are possible in a welded joint were examined. The effect of the geometry of the notch and the material heterogeneity on the fatigue notch factor were studied with a notch-free or smooth specimen. The changes in geometry were incorporated in the FE model for calculating local stress-strain data, whereas the material heterogeneity was considered in the values of the parameters used in the analytical fatigue estimation based on the notch stress-strain approach.

- **Reference** – Dong et al., 2018 [245]

  Approach used – Notch stress-strain approach

  Summary –Compressive weld toe residual stresses induced from ultrasonic impact treatment was incorporated into the notch stress-strain approach. To incorporate the resultant initial residual stress state, the original beginning point of the stress-strain relationship of the material was adjusted, resulting subsequently in a different cyclic stress-strain relationship used for describing the local stress-strain state at the notch root.

- **Reference** – Ladinek et al., 2018 [42]

  Approach used – Notch strain approach

  Summary – The critical points of this work lie in the choice of using the real weld toe geometry captured using 3D laser scanning and subsequently developing a 3D FE model of the weld for stress evaluation. Both linear-elastic and elastic-plastic calculations were carried out. The stress analysis was validated by comparing the stress concentrations predicted in the FE model to the cracks detected using the dye penetrant technique (a non-destructive technique (NDT) for detecting surface-breaking flaws in a component).

6.2.4 Summary

An introduction to the way the notch stress-strain approach has developed has been outlined to provide context to the work that has been done in this project. This leads to the next section, which describes how the approach was executed in this PhD project.

6.3 Notch stress-strain approach – Methodology

This section describes the processes undertaken to implement the notch stress-strain approach along with the experimental data that has been described in Chapters 3, 4 and 5. A flowchart describing the methodology has been provided in Appendix D.1.

6.3.1 Material properties

Material properties from the tensile tests performed in Section 3.3.1.1. were used to derive the notch stress-strain approach parameters described in Section 6.2.2.

Table 6.1 Tensile properties of S355 J2+N structural steel (from Section 3.3.1.1).

Young's Modulus	Yield Strength (0.2% proof)	Ultimate Tensile Strength (UTS)
190 GPa	383 MPa	535 MPa

Hardness measurements were initially performed using a Vickers micro-hardness tester, the readings were converted from Vickers Hardness units (HV) to Brinell Hardness values (HB) [246] to allow derivation of the parameters described in Section 6.2.2. The hardness measurements have been divided into two sets based on the experiments described in Chapters 4 and 5 –

1. For the specimens tested in Chapter 4, hardness tests had been carried out previously by Crump, 2017 [9], also referred to as scan set 1 in Chapter 3 Section 3.3.1. Average values for each zone of the weld – base metal (BM), heat-affected zone (HAZ) and weld metal (WM) – for the different weld variations – semi-automated or manual welder; solid- or metal-core electrode – that were fatigue tested and analysed have been provided in Table 6.2.

Table 6.2 Range of hardness values (in HV) of scan set 1, taken from [9].

Hardness Parameters (in HV)	Specimen Type (scan set 1)			
	SM_MAG	SA_MAG	MM_MAG	MA_MAG
Base metal (BM)	160-180	160-180	160-180	160-180
Heat-affected zone (HAZ)	190-220	200-230	190-220	190-220
Weld metal (WM)	210-240	210-240	180-210	180-210

2. For the specimens tested in Chapter 5, also referred to as scan set 2 in Chapter 3 Section 3.3.1, Vickers micro-hardness measurements were carried out according to BS EN ISO 6507 [247]. Indents were spaced 300 µm from each other, and a force of 5 N ($HV_{0.5}$) and dwell time of 10 seconds was used. Average hardness test results have been presented in Table 6.3. The data is divided into the different weld zones and the two welded joint variations – high-quality and low-quality welds. For the LQ specimen, the value was 220 HV as compared to 270 HV for the HQ specimen.

Table 6.3 Range of hardness values (in HV) of scan set 2.

Hardness Parameters (in HV)	Specimen Type (scan set 2)	
	HQ	LQ
Base metal (BM)	160-185	160-185
Heat-affected zone (HAZ)	260-280	190-220
Weld metal (WM)	210-240	190-210

6.3.2 Material parameters for notch stress-strain approach

The parameters that are required to ultimately obtain N_f - Equation 6-7 for notch stress approach and Equation 6-18 for notch strain approach – can be obtained from the empirical relationships described in Section 6.2.2. The cyclic parameters can also be obtained from cyclic uniaxial strain-controlled tests, as obtained in work done by Silva et al., 2019 [248] for fatigue estimation using the notch stress-strain approach.

The empirical relations described in Equations 6-19 to 6-25 are based on the Uniform Material Law (UML) [233] and additional modifications [16, 221, 232-236]. In recent literature, further

modifications have been suggested based on the statistical analysis of material test data of a variety of steels (and other metals) [34, 37, 39, 249, 250]. Ladinek et al., 2018 [43] used the modifications suggested by Fatemi et al., 2000 [34] and Fatemi et al., 2012 [37] for notch strain-based fatigue estimation using the real weld toe geometry (obtained using 3D laser scanning of the weld toe) for S355 J0 structural steel, similar to that tested in this project - Equations 6-26 to 6-33. The values of fatigue strength exponent *b* (Equation 6-32) and fatigue ductility exponent *c* (Equation 6-33) have been given as constants in [34, 37, 43] based on the Muralidharan-Manson Modified universal slopes method suggested by Muralidharan et al., 1988 [251].

$$\sigma_{UTS} = 0.0012(HB)^2 + 3.3(HB) \quad 6\text{-}26$$

$$\sigma_{ys} = 0.0039(HB)^2 + 1.62(HB) \quad 6\text{-}27$$

$$K' = 9.8 \times 10^{-3}(HB)^2 - 1.26(HB) + 705 \; for \left(\frac{\sigma_{UTS}}{\sigma_{ys}}\right) \leq 1.2 \quad 6\text{-}28$$

$$K' = 4.09(HB) + 613 \; for \left(\frac{\sigma_{UTS}}{\sigma_{ys}}\right) > 1.2$$

$$n' = -0.37log\left[\frac{3 \times 10^{-4}(\sigma_{ys})^2 - 0.15(\sigma_{ys}) + 526}{3 \times 10^{-4}(\sigma_{UTS})^2 + 0.23(\sigma_{UTS}) + 619}\right] for \left(\frac{\sigma_{UTS}}{\sigma_{ys}}\right) \leq 1.2 \quad 6\text{-}29$$

$$n' = -0.37log\left[\frac{0.75(\sigma_{ys}) + 82}{1.16(\sigma_{UTS}) + 593}\right] for \left(\frac{\sigma_{UTS}}{\sigma_{ys}}\right) > 1.2$$

$$\sigma_f' = 4.25(HB) + 225 \quad 6\text{-}30$$

$$\varepsilon_f' = \frac{0.32(HB)^2 - 487(HB) + 191000}{E} \quad 6\text{-}31$$

$$b = -0.09 \quad 6\text{-}32$$

$$c = -0.56 \quad 6\text{-}33$$

In the review by Troshchenko et al., 2010 [39], various methods of evaluating the Basquin-Coffin-Manson equation parameters were analysed in terms of their respective conservatism in fatigue estimates when compared with experimental data. Troshchenko et al. concluded that the Meggiolaro-Castro Averaged parameters method suggested by Meggiolaro et al., 2004 [252] provided the best statistical agreement (with experimental data for steel) amongst the methods tested, and these have been given in Equations 6-34 to 6-37. For cyclic strain-hardening coefficient *K'* and cyclic strain-hardening exponent *n'*, Equations 6-38 and 6-23, respectively, were suggested.

$$\sigma_f' = 1.5\sigma_{UTS} \quad 6\text{-}34$$

$$\varepsilon_f' = 0.45 \quad 6\text{-}35$$

$$b = -0.09 \quad \text{6-36}$$

$$c = -0.59 \quad \text{6-37}$$

$$K' = \frac{\sigma_f'}{\left(\varepsilon_f'\right)^{n'}} \quad \text{6-38}$$

Based on the different use of material parameters in the literature for essentially the same problem, three sets of empirical relations will be used to estimate FCI lives and compared with the experimentally observed data. The three sets are as follows:

1. Uniform Material Law and associated modifications - Equations 6-19 to 6-25.
2. Hardness based values (Lopez-Fatemi and Roessle-Fatemi), along with Muralidharan-Manson Modified universal slopes methods – Equations 6-26 to 6-33.
3. Meggiolaro-Castro Averaged parameters method for Basquin-Coffin-Manson – Equations 6-34 to 6-38. Two other sub-variations are possible in this set in the method used to obtain the σ_{UTS} –
    a. σ_{UTS} based on actual tensile test data.
    b. σ_{UTS} based on hardness-based data and Equation 6-20.

6.3.3 Evaluation of stress concentration factor, K_t

One of the primary parameters required to estimate the lives of the tested welded joints is the stress concentration factor, K_t. Chapter 3 describes the 3D FE-based stress analysis which used X-ray micro-computed tomography derived 3D geometries to obtain the local stresses at weld toes, which are known to be the primary location of fatigue crack initiation for non-load carrying joints [8]. In addition, the X-ray micro-computed tomography enabled detailed measurement of the local weld toe geometry of the scanned specimens. Both these outputs presented in Chapter 3 enable the evaluation of K_t from the following two methods –

1. Directly obtain K_t from 3D FE stress analysis. This can be either –
    a. Linear elastic K_t.
    b. Elastic-plastic K_t. However, the elastic-plastic K_t will be directly used to replace the fatigue notch factor K_f in the empirical relations. The elastic-plastic stress analysis theoretically should replace the requirement to implement the microstructural support effect.

Both stress states will be evaluated, and their statistical accuracy with experimental data will be compared.

2. Obtain K_t empirically from the weld toe geometry evaluations based on other findings. The following relations will be used –

   a. SCF relation for double-sided welded joint and in tension load, suggested by Crump, 2017 [9], equations 6-39 and 6-40.

$$K_t = A\rho^{\left(B+\frac{C}{\alpha}\right)} + \frac{D}{\alpha}\ for\ \alpha < 60° \quad \text{6-39}$$

$$K_t = E\rho^{\left(F+\frac{G}{\alpha}\right)} + H\ for\ \alpha \geq 60° \quad \text{6-40}$$

A = 1.799147 B = -0.397380 C = 0.082591 D = −0.051320

E = 1.107283 F = -0.410437 G = -0.015951 H = 0.683463

Where,

ρ Weld toe radius from weld geometry measurement

α Weld toe angle from weld geometry measurement

   b. Solution for linear-elastic stress concentration factor suggested by Hellier et al., 2014 [104] based on evaluating 2D FE stress analyses of welded joints.

$$\begin{aligned} K_t = {} & 0.889 - 0.302\alpha + 3.44\left(\frac{\rho}{T}\right) + 0.529\left(\frac{L}{T}\right) + 0.012\alpha^2 + 104\left(\frac{\rho}{T}\right)^2 \\ & - 0.633\left(\frac{L}{T}\right)^2 - 0.614\alpha^3 + 0.18\left(\frac{L}{T}\right)^3 - 0.018\left(\frac{L}{T}\right)^4 - 35.5\alpha\left(\frac{\rho}{T}\right) \\ & - 0.153\alpha\left(\frac{L}{T}\right) + 4.38\left(\frac{\rho}{T}\right)\left(\frac{L}{T}\right) + 30.6\alpha^2\left(\frac{\rho}{T}\right) - 0.219\alpha^2\left(\frac{L}{T}\right) \\ & - 64.3\alpha\left(\frac{\rho}{T}\right)^2 + 0.041\alpha\left(\frac{L}{T}\right)^2 - 54.5\left(\frac{\rho}{T}\right)^2\left(\frac{L}{T}\right) + 0.595\left(\frac{\rho}{T}\right)\left(\frac{L}{T}\right)^2 \\ & + \alpha^{0.68}\left(\frac{\rho}{T}\right)^{-0.299}\left(\frac{L}{T}\right)^{0.263} \end{aligned} \quad \text{6-41}$$

Limits -

$$30° \leq \alpha \leq 60° \qquad 0.01 \leq \frac{\rho}{T} \leq 0.066 \qquad 0.3 \leq \frac{L}{T} \leq 4.0$$

Where,

L Weld leg length (in millimetres)

T Base plate thickness (in millimetres)

6.3.4 Evaluation of fatigue notch factor, K_f

For the evaluation of the fatigue notch factor, K_f, the following methods can be implemented –

1. Equation 6-3.

2. As suggested in Section 6.3.3, K_f will be replaced by the elastic-plastic K_t.

6.3.5 Implementation of the approach

To implement the approach, a MATLAB code was developed which incorporated the notch stress-strain approach and the variations in the input parameters which were statistically analysed.

6.3.6 Crack propagation approach

Once the FCI life, or N_i, has been evaluated based on the notch stress-strain approach, the N_p, or crack propagation life in Equation 6-1 can be calculated using the crack propagation approach. Software developed by TWI Ltd, CRACKWISE, which is based on BS 7608 [6], can be used in estimating propagation lives beyond FCI based on a Paris law type integration between an initial crack depth and a final crack length. To implement this approach, an appropriate initial crack depth will need to be defined, and the value of initial crack depth, a_i, was taken from the experimental data obtained in Chapters 4 and 5.

6.4 Notch stress-strain approach – Results and Discussion

6.4.1 Fatigue Test Results

The seven data points shown in the SN curve in Figure 6.3 represent the specimens that were tested up to the FCI life and consequently scanned using X-ray μ-CT. Although the number of data points is small, it is notable that the scatter in the FCI lives of the “high quality” weld specimens tested at a higher applied stress range (HQ_T6, HQ_T7 and HQ_T8 – also named Test 6, Test 7 and Test 8, respectively) appears considerably greater than for the equivalent “high quality” specimens tested at a lower stress range (HQ_T11, HQ_T15). In comparing the weld quality at the lower stress level only, it is clearer that the “low quality” welds (LQ_T10, LQ_T12) do show lower FCI lifetimes than the “high quality” welds.

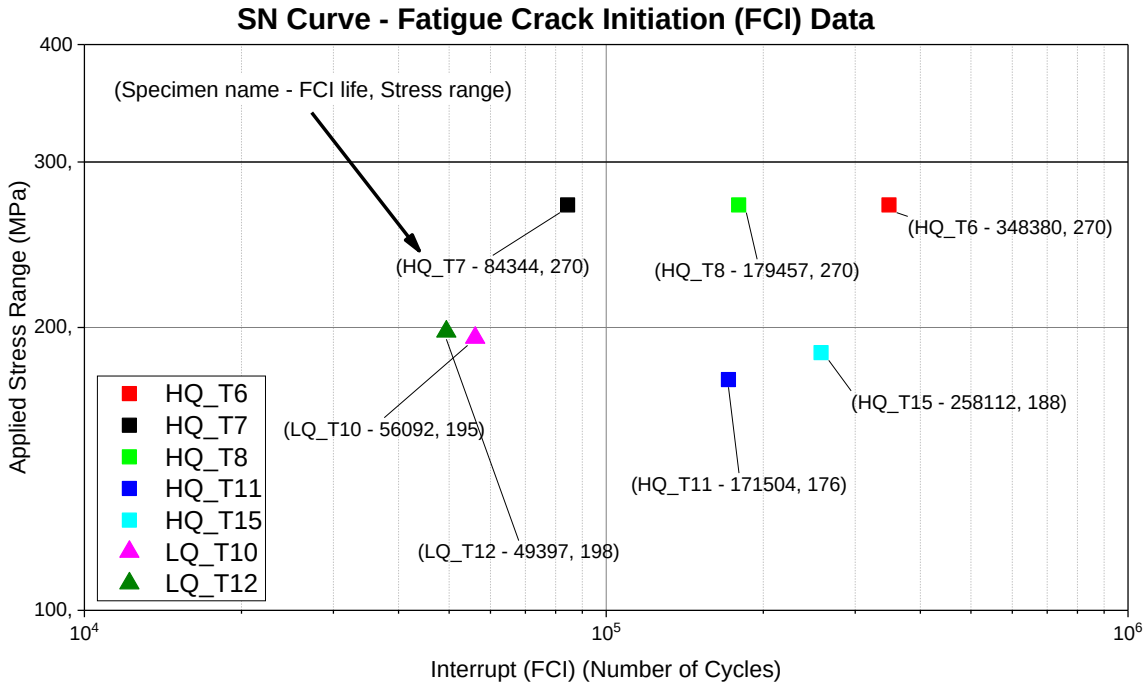

Figure 6.3 SN curve depicting the experimentally derived FCI lives, based on the methodologies described in Chapters 4 and 5.

6.4.2 Materials Parameter Variations

The results of variation in the material parameters for the notch stress-strain approach that have been evaluated are presented in this section. It is important to note that the following relations used are common across all the variations –

- Relations for evaluating monotonic and cyclic stress-strain properties –
    - Ramberg-Osgood relations, Equations 6-9 and 6-11
    - Neuber's rule and hyperbola, Equations 6-10 and 6-12.
- Evaluating the number of load reversals to failure - Coffin-Manson-Basquin relationship with Morrow's correction for mean stress), Equation 6-18.
- Empirically derived critical distance, a^*, Equation 6-4.
- Analytical evaluation of fatigue notch factor, K_f, Equation 6-3 (except in Section 6.4.2.7).

The key parameters and relations that are unique to each variation have been highlighted in the description of each variation. The results for one sample (HQ_T7) are systematically provided for comparison. Although the predictions may potentially vary (in accuracy) for each specimen, the results for one specimen are shown to aide the understanding of each variation.

6.4.2.1 UML_C1

The primary features of variation UML_C1 are as follows:

1. The ultimate tensile strength (UTS) of the material has been taken from the tensile test results.
2. The relations categorised as Uniform Material Law (UML) given in equations 6-19 - 6-25 have been used to calculate material parameters, except for the value of the UTS of the material.
3. The value of fatigue notch factor (K_f) is evaluated using the critical distance approach, Equation 6-3.

The linear elastic stress concentration factor (K_t) distribution in the direction of the applied nominal stress (S_{xx} or S_{11}) has been taken from scan set 1 and scan set 2, as described in Chapter 3. Hardness values have been taken from Table 6.2 and Table 6.3. As the K_t distribution was taken along the weld toe, initially the FCI lives were estimated for each of the available values of K_t for all the three zones - base metal (BM), heat-affected-zone (HAZ) and weld metal (WM). Figure 6.4 is one example of the kind of distributions that have been obtained for each combination of process variation, test specimen, microstructural zone and stress-field. Figure 6.4 presents the predicted FCI life along the weld toe of HQ_T7 (scan set 1) based on the obtained elastic S_{11} K_t using base-metal hardness values along with the distribution of the elastic S_{11} K_t along the same weld toe. It can be seen clearly that the higher predicted FCI lives are for correspondingly lower values of elastic S_{11} K_t. The region of the weld toe, which was indicated by the ACPD crack detection technique (described in Chapter 4) to be the region of FCI for HQ_T7, has been highlighted in red.

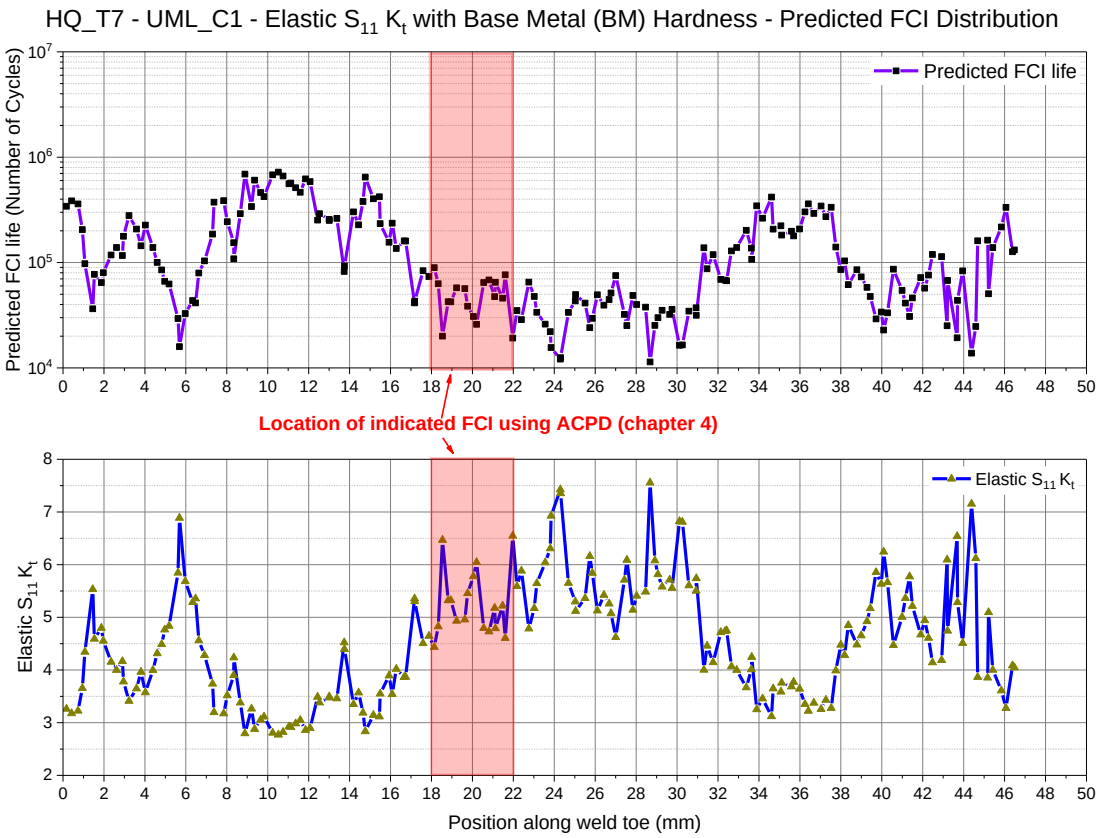

Figure 6.4 Top - FCI prediction distribution in HQ_T7 based on UML_C1 and elastic S_{11} K_t and BM hardness data. Bottom – Distribution of elastic S_{11} K_t along the same weld toe. The FCI location that was indicated by the crack detection method used – ACPD (Chapter 4) – has been highlighted.

Table 6.4 provides a comparison of the predicted FCI life from UML_C1 (BM hardness data) with the actual experimentally obtained data for HQ_T7. Although the maximum S_{11} K_t was obtained at the location of 28.68 mm along the weld toe (in Figure 6.4), the region indicated by the ACPD crack detection technique had the lowest predicted FCI life (corresponding to the maximum S_{11} K_t) of 19,200 cycles, which is a conservative result (by a factor of 4.4). The average predicted FCI life across the region (an area of 2 mm) was 49,400 cycles (a factor of 1.7). Table 6.5 provides a comparison of the predicted FCI lives when the hardness values of all the three microstructural zones (BM, HAZ, WM) are considered. BM gives the most conservative results, with WM being the least conservative. However, it is important to highlight that as the actual tensile test data (from tensile tests) was used for this test, this comparison is not fully representative, as the tensile tests were carried out only for the base metal (BM).

Table 6.4 Comparison of predicted FCI life versus actual (experimental) FCI life for HQ_T7 – UML_C1 - elastic S_{11} K_t – BM Hardness.

HQ_T7 – UML_C1 - elastic S_{11} K_t – BM Hardness		**Position along weld toe**	**Actual (Experimental FCI Life)**
Maximum elastic S_{11} K_t across entire weld toe	7.56	28.68 mm	84,344 cycles (Probe-5 of ACPD array with maximum measured crack depth of 0.23 mm)
Minimum predicted FCI life	11,400 cycles		
Region indicated by crack detection technique			
Maximum elastic S_{11} K_t in region	6.55	21.97 mm	
Average elastic S_{11} K_t in region	5.28		
Minimum predicted FCI life in region	19,200 cycles		
Average predicted FCI life in region	49,400 cycles		

Table 6.5 HQ_T7 – UML_C1 - elastic S_{11} K_t – Comparison of predicted FCI lives based on different hardness values.

UML_C1	**Hardness**		
Parameters	**BM**	**HAZ**	**WM**
Minimum predicted FCI life in region	19,200 cycles	20,900 cycles	22,600 cycles
Factor of actual FCI life	4.4	4.04	3.73
Average predicted FCI life in region	49,400 cycles	55,500 cycles	61,500 cycles
Factor of actual FCI life	1.7	1.5	1.4

6.4.2.2 UML_C2

The primary features of variation UML_C2 are as follows:

1. The ultimate tensile strength (UTS) of the material has been taken from hardness results (Table 6.2 and Table 6.3).
2. The relations categorised as Uniform Material Law (UML) given in equations 6-19 - 6-25 have been used to calculate material parameters.
3. The value of fatigue notch factor (K_f) is evaluated using the critical distance approach, Equation 6-3.

The distribution of predicted FCI life with elastic S_{11} K_t distribution along the weld toe can be found in the Appendix D.2.1. Table 6.6 provides a comparison of the predicted FCI lives with the actual FCI life, and Table 6.7 provides a comparison based on the hardness of the different microstructural zones. It is important to reiterate that the UTS of the material is now based on the hardness results for each microstructural zone, and therefore the predicted FCI lives for HAZ and WM are relatively more representative when compared with UML_C1.

Table 6.6 Comparison of predicted FCI life versus actual (experimental) FCI life for HQ_T7 – UML_C2 - elastic S_{11} K_t – BM Hardness.

HQ_T7 – UML_C2 - elastic S_{11} K_t – BM Hardness		**Position along weld toe**	**Actual (Experimental FCI Life)**
Maximum elastic S_{11} K_t across entire weld toe	7.56	28.68 mm	84,344 cycles (Probe-5 of ACPD array with maximum measured crack depth of 0.23 mm)
Minimum predicted FCI life	7,700 cycles		
Region indicated by crack detection technique			
Maximum elastic S_{11} K_t in region	6.55	21.97 mm	
Average elastic S_{11} K_t in region	5.28		
Minimum predicted FCI life in region	13,300 cycles		
Average predicted FCI life in region	35,700 cycles		

Table 6.7 HQ_T7 – UML_C2 - elastic S_{11} K_t – Comparison of predicted FCI lives based on different hardness values.

UML_C2	**Hardness**		
Parameters	**BM**	**HAZ**	**WM**
Minimum predicted FCI life in region	13,300 cycles	9,500 cycles	7,200 cycles
Factor of actual FCI life	6.34	8.88	11.71
Average predicted FCI life in region	35,700 cycles	27,800 cycles	23,100 cycles
Factor of actual FCI life	2.4	3.0	3.6

6.4.2.3 NEWMAT_C3

The primary features of variation NEWMAT_C3 are as follows:

1. Material parameters and cyclic properties have been empirically obtained from the equations given in Section 6.3.2, Equations 6-26 - 6-33. This is the reason behind using the prefix “NEWMAT” in the identification.
2. The value of fatigue notch factor (K_f) is evaluated using the critical distance approach, Equation 6-3.

The distribution of predicted FCI life with elastic $S_{11}\,K_t$ distribution along the weld toe can be found in the Appendix D.2.2. Table 6.8 provides a comparison of the predicted FCI lives with the actual FCI life, and Table 6.9 provides a comparison based on the hardness of the different microstructural zones. A similar trend to that seen for UML_C2 is present here as well (decrease in predicted FCI life with increasing hardness across the multiple microstructural zones).

Table 6.8 Comparison of predicted FCI life versus actual (experimental) FCI life for HQ_T7 – NEWMAT_C3 - elastic $S_{11}\,K_t$ – BM Hardness.

HQ_T7 – NEWMAT_C3 - elastic $S_{11}\,K_t$ – BM Hardness		**Position along weld toe**	**Actual (Experimental FCI Life)**
Maximum elastic $S_{11}\,K_t$ across entire weld toe	7.56	28.68 mm	84,344 cycles (Probe-5 of ACPD array with maximum measured crack depth of 0.23 mm)
Minimum predicted FCI life	5,500 cycles		
Region indicated by crack detection technique			
Maximum elastic $S_{11}\,K_t$ in region	6.55	21.97 mm	
Average elastic $S_{11}\,K_t$ in region	5.28		
Minimum predicted FCI life in region	9,200 cycles		
Average predicted FCI life in region	22,700 cycles		

Table 6.9 HQ_T7 – NEWMAT_C3 - elastic S_{11} K_t – Comparison of predicted FCI lives based on different hardness values.

NEWMAT_C3	Hardness		
Parameters	**BM**	**HAZ**	**WM**
Minimum predicted FCI life in region	9,200 cycles	8,400 cycles	7,800 cycles
Factor of actual FCI life	9.17	10.04	10.81
Average predicted FCI life in region	22,700 cycles	21,800 cycles	21,500 cycles
Factor of actual FCI life	3.7	3.9	3.9

6.4.2.4 COMPOSITE_C4

The primary features of variation COMPOSITE_C4 are as follows:

1. Material parameters and cyclic properties have been empirically obtained from the equations given in Section 6.3.2, Equations 6-26 - 6-29 and the suggestions of Meggiolaro et al., 2004 [252], Equations 6-34-6-37. The parameters used for the Basquin-Coffin-Manson Equation 6-18 (σ_f', ε_f', b and c) are different from NEWMAT_C3.
2. For cyclic strain-hardening coefficient K', Equation 6-38 was used.
3. For cyclic strain-hardening exponent n', Equation 6-23 was used.
4. The value of fatigue notch factor (K_f) is evaluated using the critical distance approach, Equation 6-3.

The distribution of predicted FCI life with elastic S_{11} K_t distribution along the weld toe can be found in the Appendix D.2.3. Table 6.10 provides a comparison of the predicted FCI lives with the actual FCI life, and Table 6.11 gives a comparison based on the hardness of the different microstructural zones. As the value of fatigue ductility coefficient ε_f' was kept constant as compared to NEWMAT_C3, a small increase in predicted FCI life with increasing hardness across the three microstructural zones was observed (increasing order of hardness – BM < HAZ < WM).

Table 6.10 Comparison of predicted FCI life versus actual (experimental) FCI life for HQ_T7 – COMPOSITE_C4 - elastic S_{11} K_t – BM Hardness.

HQ_T7 – COMPOSITE_C4 - elastic S_{11} K_t – BM Hardness		Position along weld toe	Actual (Experimental FCI Life)
Maximum elastic S_{11} K_t across entire weld toe	7.56	28.68 mm	

Minimum predicted FCI life	2,500 cycles		84,344 cycles (Probe-5 of ACPD array with maximum measured crack depth of 0.23 mm)
Region indicated by crack detection technique			
Maximum elastic S_{11} K_t in region	6.55	21.97 mm	
Average elastic S_{11} K_t in region	5.28		
Minimum predicted FCI life in region	4,300 cycles		
Average predicted FCI life in region	10,900 cycles		

Table 6.11 HQ_T7 – COMPOSITE_C4 - elastic S_{11} K_t – Comparison of predicted FCI lives based on different hardness values.

COMPOSITE_C4	**Hardness**		
Parameters	**BM**	**HAZ**	**WM**
Minimum predicted FCI life in region	4,300 cycles	4,500 cycles	4,900 cycles
Factor of actual FCI life	19.61	18.74	17.21
Average predicted FCI life in region	10,900 cycles	12,200 cycles	14,100 cycles
Factor of actual FCI life	7.8	6.9	6.0

6.4.2.5 NEWMAT_C5

The primary features of variation NEWMAT_C5 are as follows:

1. Material parameters and cyclic properties have been empirically obtained from the equations given in Section 6.3.2, Equations 6-26 - 6-33, similar to NEWMAT_C3.
2. The value of elastic S_{11} K_t is estimated using the captured weld toe geometry from the solutions suggested by Crump, 2017 [9], Equations 6-39 and 6-40. The additionally required inputs were the following –
    a. Weld toe angle (in degrees).
    b. Weld toe radius (in millimetres).
3. The value of fatigue notch factor (K_f) is evaluated using the critical distance approach, Equation 6-3.

Table 6.12 provides a comparison of the predicted FCI lives with the actual FCI life. According to NEWMAT_C5, the highest value of K_t lies within the region indicated by ACPD but values of K_t very close to the maximum K_t have been indicated in other regions as well (e.g. K_t of 2.938 at 25.16 mm). It is evident from the results that NEWMAT_C5 is very non-conservative, as the predicted FCI life in

the region indicated by the ACPD crack detection technique is approximately three times the observed FCI life. This could potentially be due to the high-quality of welding performed for HQ_T7, along with the possibility of the critical stress-concentrating feature not being captured accurately (e.g. a microscopic notch which may not significantly affect weld toe angle or weld toe radius) in capturing weld toe geometry. Also, the use of fatigue notch factor (K_f) compounds this effect as it effectively reduces the stress concentration further. This degree of relative non-conservatism makes this model variation unacceptable. A possible way of increasing the accuracy of NEWMAT_C5 is by combining it with another variation, NEWMAT_C7, Section 6.4.2.7. This is discussed in Section 6.4.3.3. It is, however, important to note that the comparison of data for only one specimen is not representative of the entire set of welded joints that have been examined in this study, but is primarily to show the challenges that can be very specific to a particular specimen.

Table 6.12 Comparison of predicted FCI life versus actual (experimental) FCI life for HQ_T7 – NEWMAT_C5 – weld toe geometry based elastic S_{11} K_t – BM Hardness.

<table>
<tr><th colspan="2">HQ_T7 – NEWMAT_C5 - elastic S_{11} K_t (from weld toe geometry) – BM Hardness</th><th>Position along weld toe</th><th>Actual (Experimental FCI Life)</th></tr>
<tr><td colspan="2">Maximum elastic S_{11} K_t across entire weld toe</td><td colspan="2" rowspan="2">Detected in the indicated region. See results below.</td><td rowspan="6">84,344 cycles (Probe-5 of ACPD array with maximum measured crack depth of 0.23 mm)</td></tr>
<tr><td colspan="2">Minimum predicted FCI life</td></tr>
<tr><td colspan="3">Region indicated by crack detection technique</td></tr>
<tr><td>Maximum elastic S_{11} K_t in region</td><td>2.94</td><td rowspan="4">18.3 mm</td></tr>
<tr><td>Average elastic S_{11} K_t in region</td><td>2.68</td></tr>
<tr><td>Minimum predicted FCI life in region</td><td>234,600 cycles</td></tr>
<tr><td>Average predicted FCI life in region</td><td>272,800 cycles</td></tr>
</table>

6.4.2.6 NEWMAT_C6

The primary features of variation NEWMAT_C6 are as follows:

1. Material parameters and cyclic properties have been empirically obtained from the equations given in Section 6.3.2, Equations 6-26 - 6-33, similar to NEWMAT_C3.
2. The value of elastic S_{11} K_t is estimated using the captured weld toe geometry from the solutions suggested by Hellier, 2014 [104], Equation 6-41. The additionally required inputs were the following –
    a. Weld toe angle (in degrees).

b. Weld toe radius (in millimetres).
c. Weld leg length (in millimetres).
d. Base plate thickness (in millimetres).

3. The value of fatigue notch factor (K_f) is evaluated using the critical distance approach, Equation 6-3.

Table 6.13 provides a comparison of the predicted FCI lives with the actual FCI life. Relative to NEWMAT_C5, the results are even more non-conservative and potentially suffer from the same issues.

Table 6.13 Comparison of predicted FCI life versus actual (experimental) FCI life for HQ_T7 – NEWMAT_C6 – weld toe geometry based elastic S_{11} K_t – BM Hardness.

HQ_T7 – NEWMAT_C6 - elastic S_{11} K_t (from weld toe geometry) – BM Hardness		**Position along weld toe**	**Actual (Experimental FCI Life)**
Maximum elastic S_{11} K_t across entire weld toe	*Detected in the indicated region. See results below.*		84,344 cycles (Probe-5 of ACPD array with maximum measured crack depth of 0.23 mm)
Minimum predicted FCI life			
Region indicated by crack detection technique			
Maximum elastic S_{11} K_t in region	2.52	18.3 mm	
Average elastic S_{11} K_t in region	2.35		
Minimum predicted FCI life in region	488,100 cycles		
Average predicted FCI life in region	513,300 cycles		

6.4.2.7 NEWMAT_C7

The primary features of variation NEWMAT_C7 are as follows:

1. Material parameters and cyclic properties have been empirically obtained from the equations given in Section 6.3.2, Equations 6-26 - 6-33, similar to NEWMAT_C3.
2. Fatigue notch factor K_f has not been evaluated. The stress concentration factor K_t is directly used in the predictions.

In this method, the value of stress concentration factor K_t can be evaluated either using FE analysis or weld toe geometry extraction. Therefore, it is discussed in terms of further possible combinations in Section 6.4.3.

6.4.3 Important combinations of applied variations

Due to the way in which the analysis has been developed, it is possible to combine the variations discussed in Section 6.4.2 to see if more appropriate predictions can be achieved for the example of specimen HQ_T7.

6.4.3.1 Combination 1 (COM1) - NEWMAT_C7 and the use of FE-based elastic S_{11} K_t

In this combination, FE-based elastic S_{11} K_t is used in the variation NEWMAT_C7. Table 6.14 provides a comparison of the predicted and experimentally obtained FCI lives. The results are very conservative.

Table 6.14 Comparison of predicted FCI life versus actual (experimental) FCI life for HQ_T7 – COM1 – BM Hardness.

HQ_T7 – COM1 – FE-based elastic S_{11} K_t – BM Hardness		**Position along weld toe**	**Actual (Experimental FCI Life)**
Maximum elastic S_{11} K_t across entire weld toe	7.56	28.68 mm	84,344 cycles (Probe-5 of ACPD array with maximum measured crack depth of 0.23 mm)
Minimum predicted FCI life	1,000 cycles		
Region indicated by crack detection technique			
Maximum elastic S_{11} K_t in region	6.55	21.97 mm	
Average elastic S_{11} K_t in region	5.28		
Minimum predicted FCI life in region	1,600 cycles		
Average predicted FCI life in region	3,800 cycles		

6.4.3.2 Combination 2 (COM2) - NEWMAT_C7 and the use of FE-based elastic-plastic maximum principal stress S_{maxpr} K_t

In this combination, FE-based elastic-plastic maximum principal stress (S_{maxpr}) K_t is used in the variation NEWMAT_C7. Fatigue notch factor has not been used. Table 6.15 provides a comparison of the predicted and experimentally obtained FCI lives. The overall maximum K_t is seen at the same location as the other methods with similar degrees of conservatism to UML_C2 and NEWMAT_C3. However, the results in the region indicated by the crack detection technique are non-conservative.

Table 6.15 Comparison of predicted FCI life versus actual (experimental) FCI life for HQ_T7 – COM2 – BM Hardness.

HQ_T7 – COM2 - FE-based elastic-plastic S_{maxpr} K_t – BM Hardness		**Position along weld toe**	**Actual (Experimental FCI Life)**
Maximum elastic-plastic S_{maxpr} K_t across entire weld toe	4.24	28.7 mm	84,344 cycles (Probe-5 of ACPD array with maximum measured crack depth of 0.23 mm)
Minimum predicted FCI life	7,800 cycles		
Region indicated by crack detection technique			
Maximum elastic S_{11} K_t in region	2.27	18.5 mm	
Average elastic S_{11} K_t in region	2.03		
Minimum predicted FCI life in region	141,000 cycles		
Average predicted FCI life in region	284,600 cycles		

6.4.3.3 Combination 3 (COM3) – NEWMAT_C5 and NEWMAT_C7

In this combination, the weld toe geometry based K_t from the work of Crump, 2017 [9] described in NEWMAT_C5 is used in NEWMAT_C7. Fatigue notch factor is not used. Table 6.16 provides a comparison of the predicted and experimentally obtained FCI lives, and Table 6.17 gives the distribution with change in hardness across microstructural zones. The results of COM3 show that this combination is a relatively close estimate of the experimentally obtained results (whilst still being conservative), as compared to other explored methods. In Section 6.4.4, a detailed evaluation of COM3 is made with the aid of the available experimental data.

Table 6.16 Comparison of predicted FCI life versus actual (experimental) FCI life for HQ_T7 – COM3 – BM Hardness.

HQ_T7 – COM3 - elastic S_{11} K_t (from weld toe geometry) – BM Hardness		**Position along weld toe**	**Actual (Experimental FCI Life)**
Maximum elastic S_{11} K_t across entire weld toe	*Detected in the indicated region. See results below.*		84,344 cycles (Probe-5 of ACPD array
Minimum predicted FCI life			
Region indicated by crack detection technique			

Maximum elastic S_{11} K_t in region	2.94	18.3 mm	with maximum measured crack depth of 0.23 mm)
Average elastic S_{11} K_t in region	2.68		
Minimum predicted FCI life in region	38,100 cycles		
Average predicted FCI life in region	61,000 cycles		

Table 6.17 HQ_T7 – COM3 - Comparison of predicted FCI lives based on different hardness values.

COM3	**Hardness**		
Parameters	**BM**	**HAZ**	**WM**
Minimum predicted FCI life in region	38,100 cycles	49,500 cycles	64,500 cycles
Factor of actual FCI life	2.21	1.7	1.3
Average predicted FCI life in region	61,000 cycles	81,900 cycles	109,900 cycles
Factor of actual FCI life	1.4	1.03	0.77

6.4.3.4 Combination 4 (COM4) – NEWMAT_C6 and NEWMAT_C7

In this combination, the weld toe geometry based K_t from the work of Hellier et al., 2014 [104] described in NEWMAT_C6 is used in NEWMAT_C7. Fatigue notch factor is not used. Table 6.18 provides a comparison of the predicted and experimentally obtained FCI lives and Table 6.19 provides the distribution with change in hardness across microstructural zones. Compared with COM3, the results of COM4 are less conservative.

Table 6.18 Comparison of predicted FCI life versus actual (experimental) FCI life for HQ_T7 – COM4 – BM Hardness.

HQ_T7 – COM4 - elastic S_{11} K_t (from weld toe geometry) – BM Hardness		**Position along weld toe**	**Actual (Experimental FCI Life)**
Maximum elastic S_{11} K_t across entire weld toe	*Detected in the indicated region. See results below.*		84,344 cycles (Probe-5 of ACPD array with maximum measured
Minimum predicted FCI life			
Region indicated by crack detection technique			
Maximum elastic S_{11} K_t in region	2.52	18.3 mm	
Average elastic S_{11} K_t in region	2.24		

Minimum predicted FCI life in region	81,500 cycles		crack depth of 0.23 mm)
Average predicted FCI life in region	117,200 cycles		

Table 6.19 HQ_T7 – COM4 - Comparison of predicted FCI lives based on different hardness values.

COM4	**Hardness**		
Parameters	**BM**	**HAZ**	**WM**
Minimum predicted FCI life in region	81,500 cycles	111,500 cycles	152,200 cycles
Factor of actual FCI life	1.03	0.76	0.55
Average predicted FCI life in region	117,200 cycles	164,700 cycles	230,100 cycles
Factor of actual FCI life	0.72	0.51	0.37

6.4.4 Summary table (Table 6.20)

Table 6.20 Summary of variations and combinations used.

<table>
<tr><th>Name</th><th>UTS</th><th>Parameters</th><th>Value of strain-life Equation 6-18 parameters</th><th>K_t</th><th>K_f</th></tr>
<tr><td>UML_C1</td><td>Tensile test</td><td colspan="2" rowspan="2">Hardness-based relations (UML equations 6-19 - 6-25)</td><td rowspan="4">Linear elastic solutions</td><td rowspan="4">Critical Distance Approach, Equation 6-3</td></tr>
<tr><td>UML_C2</td><td>Hardness-based relations (UML)</td></tr>
<tr><td>NEWMAT_C3</td><td rowspan="2">Hardness-based relations (Equations 6-26 - 6-33)</td><td>Hardness-based relations (Equations 6-26 - 6-33)</td><td>Constant -Ladinek [43] and Fatemi [34, 37]</td></tr>
<tr><td>COMPOSITE_C4</td><td>Different from NEWMAT_C3</td><td>Constant - Meggiolaro [252]</td></tr>
</table>

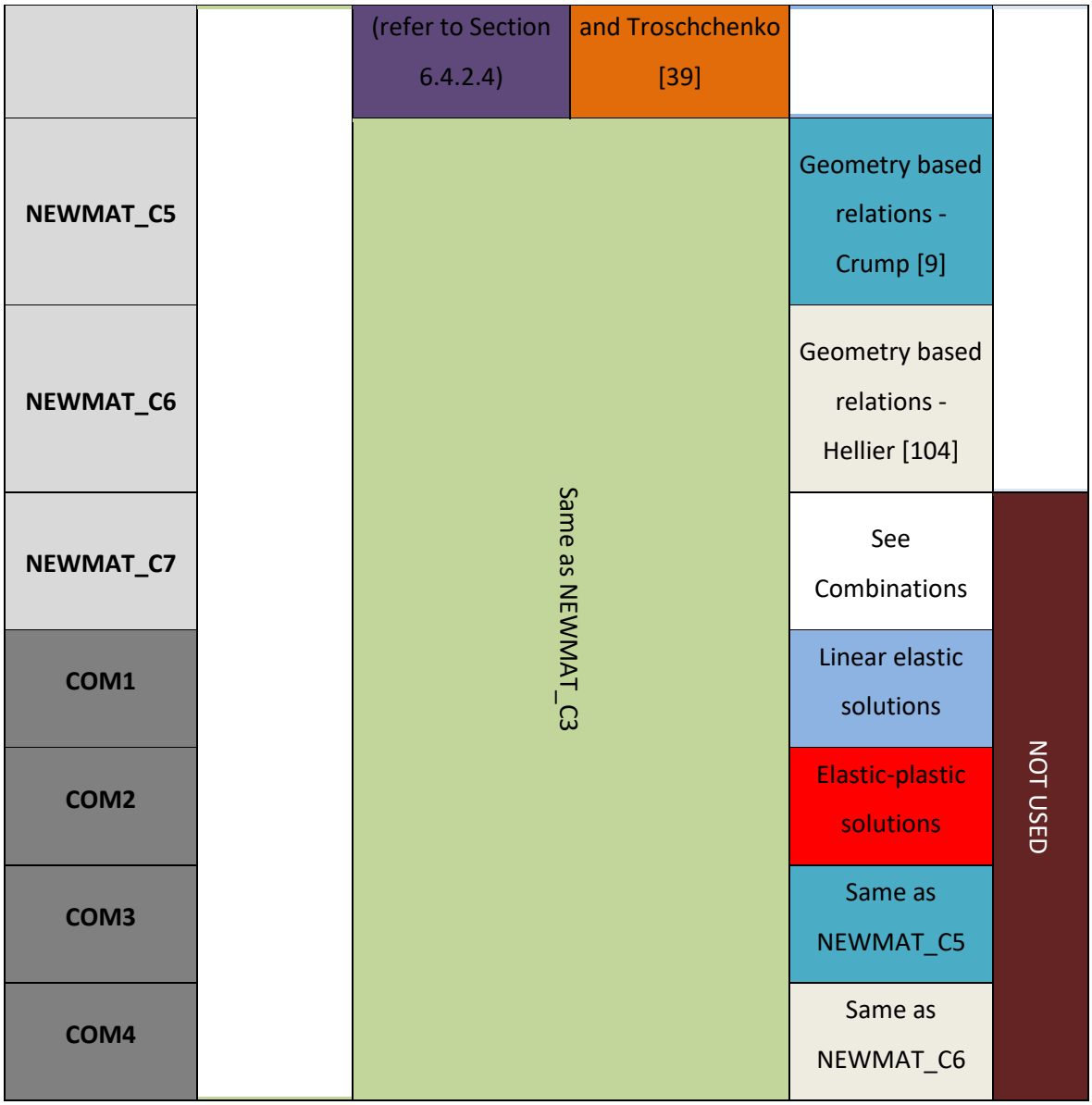

6.4.5 Discussion

6.4.5.1 Overview of results

To statistically represent the variations and combinations of the notch stress-strain approach presented in Section 6.4.2 and 6.4.3, respectively, their results have been compared with the experimentally derived FCI lives, Figure 6.5. It is important to note that the FCI predictions have only been made in the regions where evidence of crack growth was obtained using crack detection techniques. In the cases where the experimental FCI life was based on a crack depth of 0.3 mm, the FCI life at a crack depth of 0.25 mm has been used. Results of all three microstructural zones have been presented for comparison. From an overview, a considerable variation in conservatism (very conservative to highly non-conservative results) can be observed. Some key observations are as follows:

- Variations C1-C4 have consistently given conservative results, as they are based on using fatigue notch factor K_f (based on the critical distance approach) obtained from linear elastic 3D FEA stress concentration factor K_t. Out of these, C1 is the least conservative methodology as it only uses the UTS obtained from the tensile test of the base metal. For this reason, the results for the HAZ and WM zones for C1 have not been shown in Figure 6.5.
- Variations C5 and C6 have consistently been non-conservative. These methodologies are based on using the weld toe geometry measurements to obtain analytically the value of K_t, and hence K_f. The analytical solutions are based on 2D FE modelling of welded joints [9, 104] for obtaining the "best-fit" relation between the weld toe geometry and SCF (K_t). As the microstructural support effect of the notch is taken into consideration (by using K_f), the results tend to be less conservative. This effect is seen when the predicted FCI lives of C5 and C6 are compared with COM3 and COM4, which remove the consideration of K_f and directly use the weld geometry-based K_t for predictions. COM3 is essentially similar to the work done by Crump, 2017 [9], with the only difference being that COM3 used the hardness-based empirical relations suggested in [34, 37, 43] for evaluating specific material properties. No values are available for C6 and COM4 for the LQ specimens as the weld toe angle for the LQ specimens fell outside the validity range of the applied analytical solution [104].
- COM1 gave the most conservative results as it directly uses the linear elastic 3D FE-based K_t for fatigue analysis, without Neuber's microstructural notch support effect.
- The results of COM2 were also conservative, except for HQ_T7 which displayed an uncharacteristically low FCI life (from experiments) relative to the other high quality (HQ) welded specimens tested. As it is based on elastic-plastic 3D FE-based K_t, it is a more accurate representation of the stress distributions in the weld, especially due to near-yield magnitude maximum applied stresses (a combination of bending and membrane stress) at the weld toe.
- Except for C5 and COM3, all variations and combinations have effectively predicted the low FCI lives of the LQ specimens, with substantial conservatism. The results of C5 and COM3 for the LQ specimens can be attributed to the fact that such weld geometries were not examined in the work on which the analytical solutions are based [9]. The LQ specimens were intentionally manufactured in a certain way to examine if irregular weld geometries could also be characterised using the methodologies used in this PhD project.

A) HQ_T6, HQ_T7, HQ_T8 – from scan set 1.

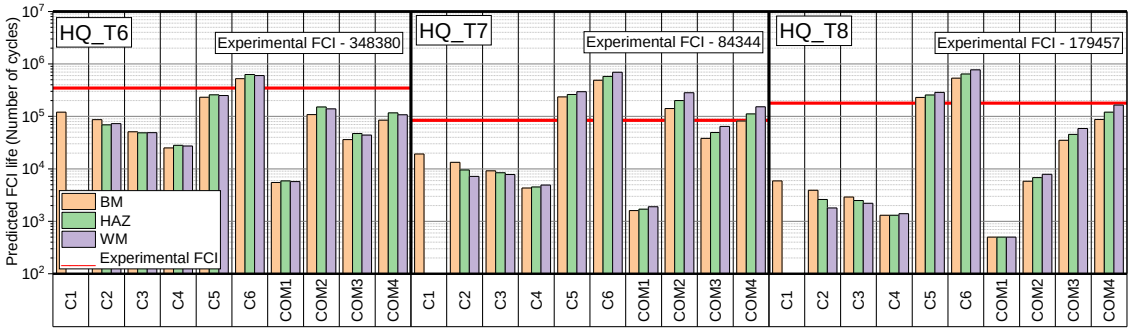

B) HQ_T11 and HQ_T15 – from scan set 2.

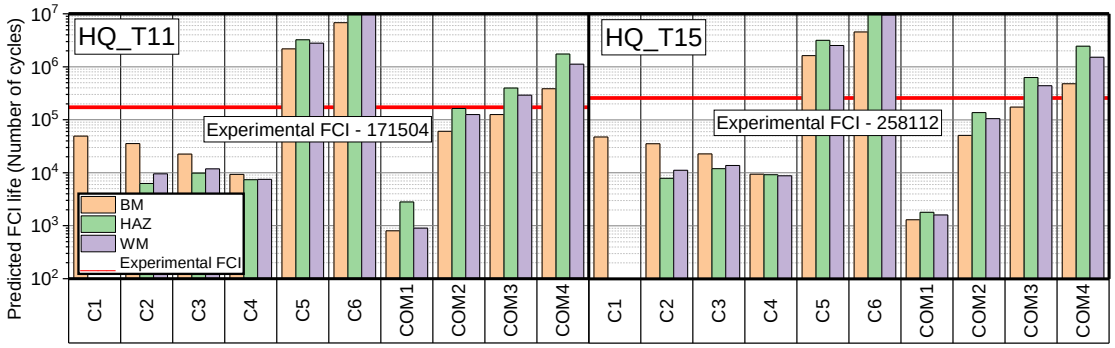

C) LQ_T10 and LQ_T12 – from scan set 2.

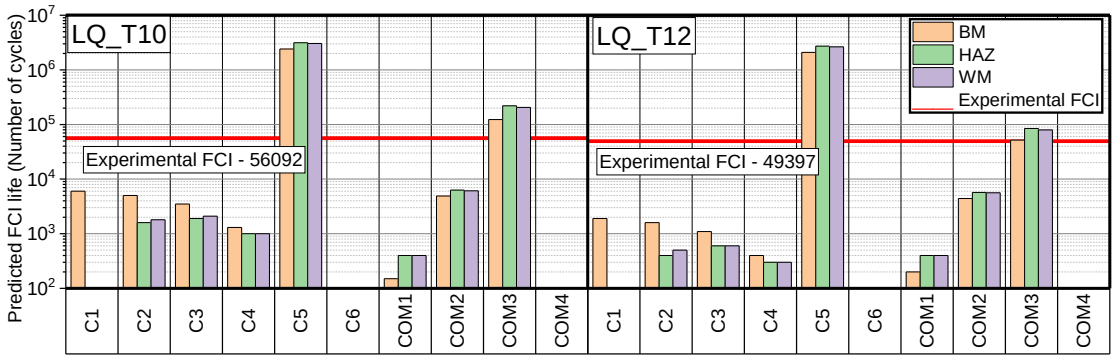

Figure 6.5 Comparison of the predicted FCI lives using the variations and combinations of the notch stress-strain approach with the experimentally obtained FCI life for each scanned specimen.

To better depict the accuracy of the results shown in Figure 6.5, the deviation of the predicted results from the experimental data was extracted as a factor *f*, similar to that suggested by Ladinek et al., 2018 [42], Equation 6-42. The value of the deviation factor will effectively never be below 1. A shortcoming of this approach is that the degree of conservatism in the predicted result is masked, as a prediction of half the actual experimental life has the same deviation factor as that of a prediction which is double of the actual result.

$$f = \max\left(\frac{FCI_{experimental}}{FCI_{predicted}}; \frac{FCI_{predicted}}{FCI_{experimental}}\right) \quad \text{6-42}$$

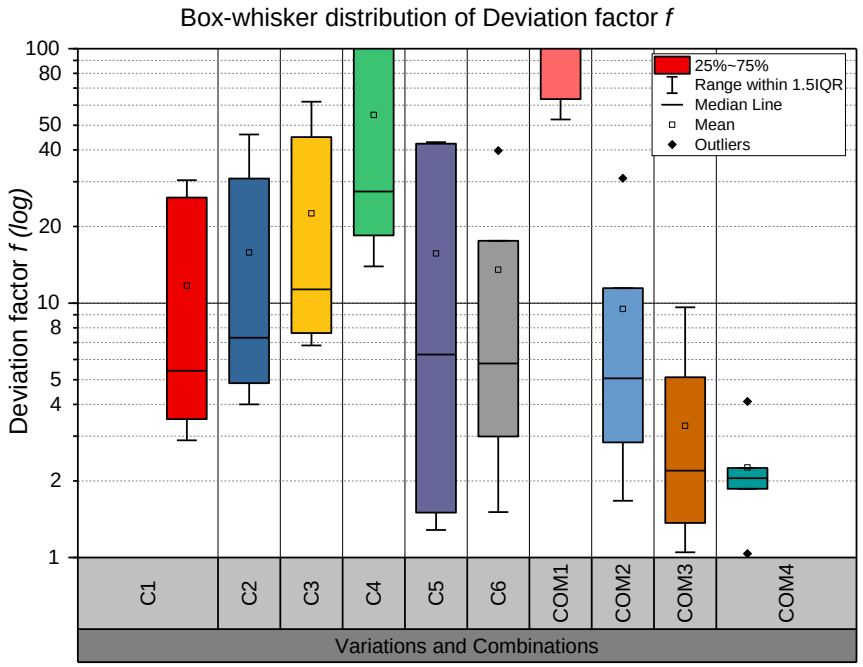

Figure 6.6 Box-whisker distribution of the deviation factor *f* for each attempted variation and combination of the notch stress-strain approach.

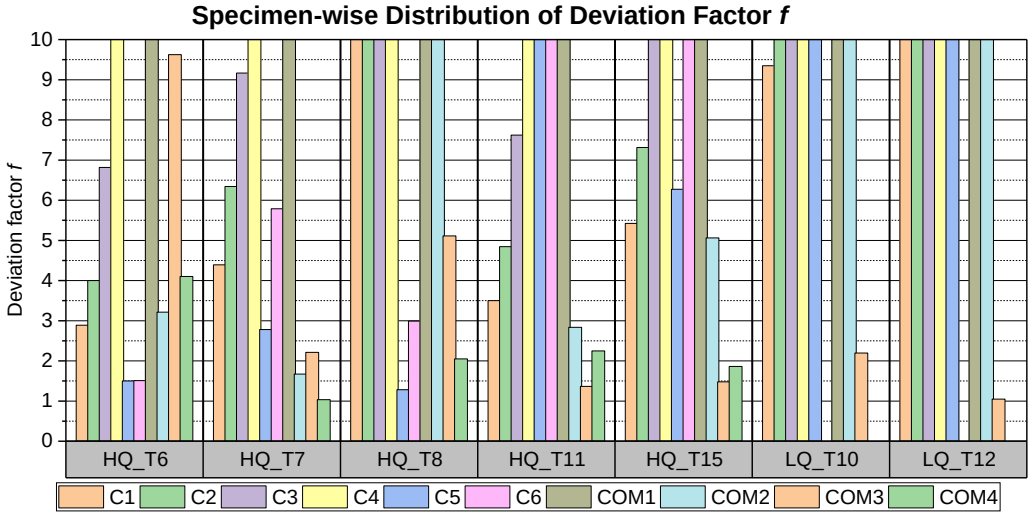

Figure 6.7 Specimen-wise distribution of deviation factor *f*.

Figure 6.6 is a box-whisker distribution of the deviation factor *f* for each of the variations and combinations that have been attempted in this work. The maximum has been set at 100, as large values of *f* were observed in cases where the predicted FCI lives were very conservative, especially in the cases of the LQ specimens, as seen in Figure 6.7. It is essential to iterate that in both crack detection techniques, FCI life is denoted by a drop of ACPD voltage or strain gauge range. Intuitively, the initial deflection occurred earlier (in terms of fatigue life) than the experimental FCI data

presented in Figure 6.3, as the latter considers initiation to be the growth of a technical crack of 0.25 mm depth. For the LQ specimens, the beginning of the strain gauge range drop was within 2000 cycles. The initial deflection can be identified retrospectively by investigating the rate of change of either the measured PD voltage (for ACPD) or strain range (for strain gauges).

Table 6.21 gives a comparison of the FCI lives for each specimen adjusted for time of the first indication of cracking. Based on this data, the deviation factor distribution has been calculated again and is shown in Figure 6.8 and Figure 6.9. The distribution of the deviation factor is considerably less compared to that obtained in Figure 6.6 and Figure 6.7. This raises an important question about what should be considered as fatigue crack initiation. The definition of a technical crack of 0.25 mm is based on the use of the critical distance approach, which is based on this assumption [16, 204, 209, 216, 218, 219]. However, if the critical distance approach is not used, and the weld-toe geometry based SCF values (either from weld toe geometry-based analytical solutions for SCF, or 3D FE-based stress analysis of the real weld toe geometry) is used directly in Neuber's Rule [227] (as performed in variation C7), the definition of crack initiation is not clearly specified.

In the results shown in Figure 6.8, the results of COM2, which combines elastic-plastic 3D FE-based values of K_t combined with C7 (no use of K_f) are promising, as the results were all conservative and the median of the deviation factor results is approximately 2.5. The results are similar to what has been achieved in work done by Ladinek et al., 2018 [42, 43], where elastic-plastic FE stress-strain analysis was also implemented in the strain-life equation, Equation 6-18, for FCI life predictions.

However, it is important to highlight that the work of Ladinek et al. was based on a large set of fatigue tests of a consistent setup (in terms of material, weld type, type of fatigue test and testing machine). The geometry was captured using optical laser scanning, which is relatively faster to implement and does not require any material cutting, as compared with X-ray µ-CT. Also, FCI detection was achieved using liquid dye-penetrant, a visual non-destructive technique for inspection of surface-breaking flaws. Consequently, the tests were stopped based on surface crack length (2-5mm), as compared with the use of crack depth (used in this project) which requires post-analyses or FE-based predictions as described in Chapters 4 and 5. The use of a visual dye-penetrant based detection technique reduces the time taken for preparation of each sample, compared with the high-resolution crack detection systems, thus allowing relatively more tests to be undertaken in the same period of time. However, the large range of crack lengths that were identified as FCI incorporates a significant amount of variation in terms of crack depth – for a crack aspect ratio of 0.2, this corresponds to a crack depth variation of 0.4 to 1 mm. Such a variation in crack depth could potentially correspond to a significant variation in what is denoted as FCI life, as Table 6.21 shows a considerable difference in the number of cycles for the first indication of crack initiation and the

growth of a pre-defined technical crack. Comparatively, the methodology used in this PhD project for defining and identifying FCI life provides additional data, as both the initial indication of crack initiation as well as the life to technical crack growth can be extracted for evaluation.

Table 6.21 Comparison of experimental FCI lives for technical crack with FCI lives based on the first indication of the crack detection technique.

Specimen	Crack Detection Technique	FCI life based on technical crack depth of 0.25 mm	FCI life based on first indication of crack detection technique	Number of cycles for crack growth
HQ_T6	ACPD – drop in PD voltage	348,380 cycles	261,000 cycles	87,380 cycles
HQ_T7		84,344 cycles	49,000 cycles	35,344 cycles
HQ_T8		179,457 cycles	67,000 cycles	112,457 cycles
HQ_T11	Strain Gauge – drop in strain range	171,504 cycles	80,000 cycles	91,504 cycles
HQ_T15		258,112 cycles	47,000 cycles	211,112 cycles
LQ_T10		56,092 cycles	2,500 cycles	53,592 cycles
LQ_T12		49,397 cycles	1,800 cycles	47,597 cycles

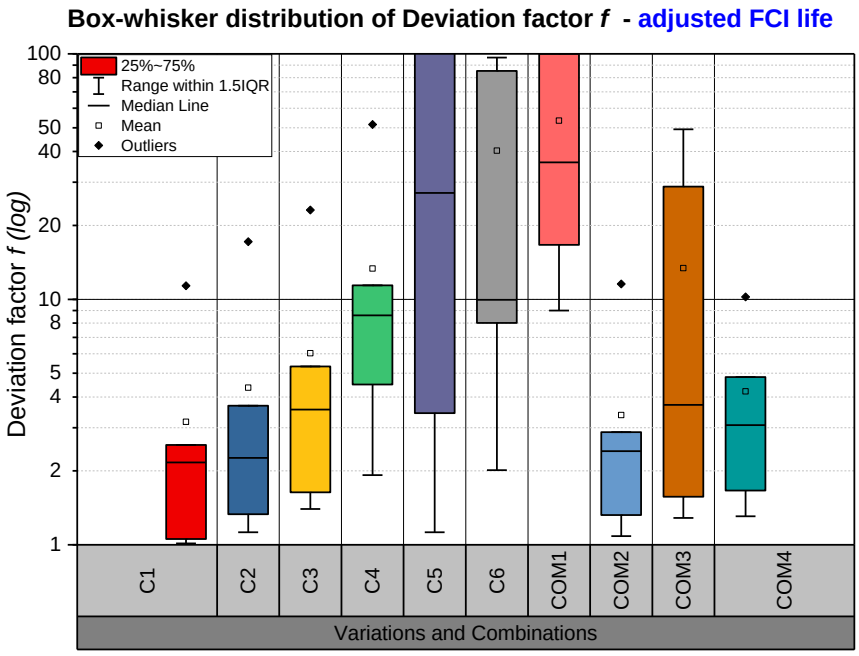

Figure 6.8 Box-whisker distribution of the deviation factor *f* based on adjusted experimental FCI life (Table 6.21).

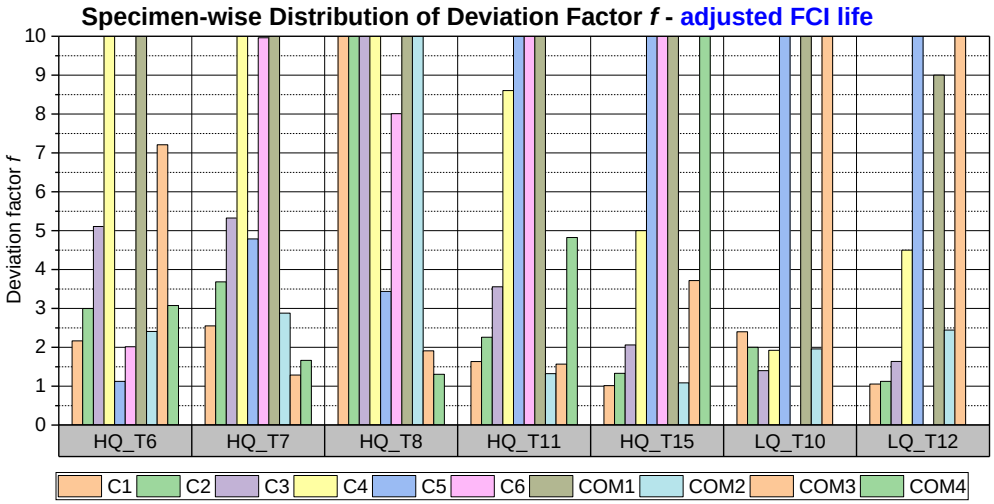

Figure 6.9 Specimen-wise distribution of deviation factor *f* based on adjusted experimental FCI life (Table 6.21).

Figure 6.10 presents an SN plot with the SN curve for BS 7608 Class F welds [6] along with the FCI lives obtained from the experimental data both for technical crack growth and the first indication of crack growth from the crack detection techniques, as well as the predictions from COM2. It is important to note that the Class F data is for total life. As expected, the results for the LQ specimens is relatively worse than the HQ specimens, apart from the COM2 prediction for HQ_T8, which is significantly conservative. This is the outlier data point seen in Figure 6.8 for the distribution of COM2.

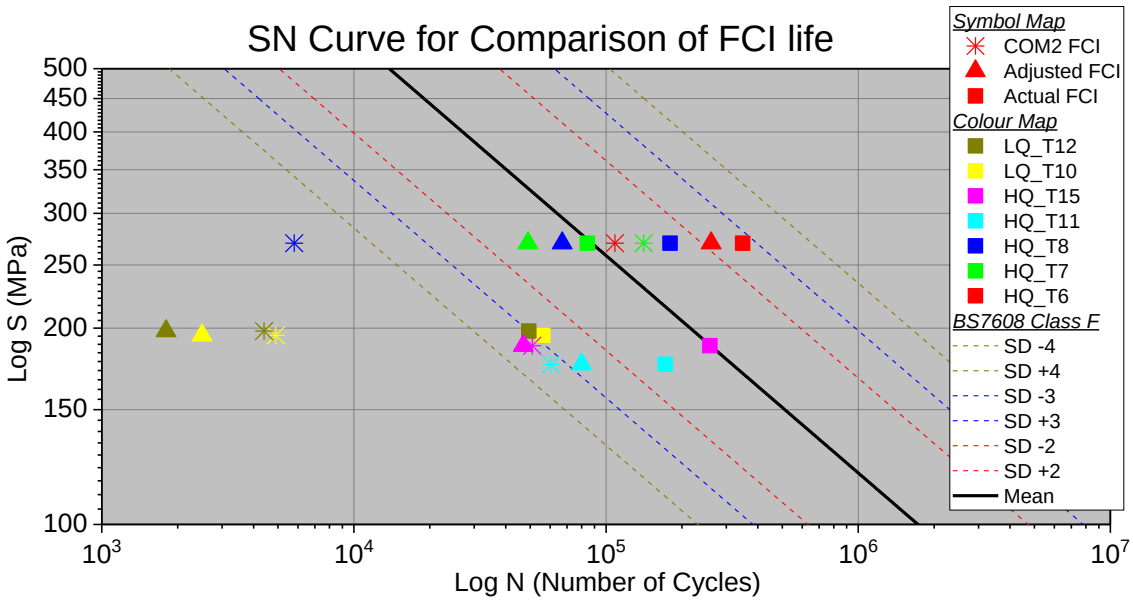

Figure 6.10 Log SN Curve for comparing FCI lives obtained for the growth of a technical crack, adjusted FCI based on the first indication of crack detection techniques and the predictions from variation COM2.

6.4.5.2 The use of fatigue notch factor, K_f

Another aspect which needs to be highlighted is the empirical approach utilised to obtain the fatigue notch factor, K_f. The critical distance approach effectively lowers the value of K_f in relation to K_t, to highlight the microstructural support effect [209]. However, the maximum value of K_f that can be obtained is not at the sharpest notch, as can be seen for an example from specimen HQ_T11 in Figure 6.11, where the value of K_t, obtained from elastic-plastic 3D FE-based stress analysis, is kept constant. The current definition of the critical distance approach, therefore, is not able to represent the effect of severe microscopic notches which were captured in this project using high-resolution X-ray µ-CT.

The relation for the critical distance a^* given in Equation 6-4 is based on empirical data obtained between 1978-1983 [218-221]. Figure 6.11 shows that the value of K_f increases with increasing notch radius, which would lead to lower FCI lives with increasing notch radius. This is the opposite of what is an established understanding where a decrease in notch radius (or weld toe radius) is linked to increased stress concentration and consequently, poorer fatigue performance [101, 141, 253-256]. This is also substantiated by the development of post-weld treatments such as peening, which are carried out to effectively increase the weld toe radii distribution (along with introducing compressive residual stresses) for improving fatigue performance [94, 254].

Figure 6.12 shows the distribution of fatigue notch factor when weld toe geometry based analytical solutions are used to calculate the linear elastic stress concentration factor K_t (weld toe angle is kept constant at 45 degrees). This plot more closely resembles Figure 6.1, as both plots are based on geometry-based K_t calculations, as compared with Figure 6.11. The predicted FCI lives based on K_f (variation C5), and K_t (combination COM3) are also shown in Figure 6.12 and predictions above 10^7 cycles are considered to be runouts. The severe effect of the fatigue notch factor on the conservatism (K_f-based FCI predictions are significantly non-conservative) of the FCI predictions are evident, as the difference between the two predictions is substantial up to a notch radius of 1 mm. It is important to note that the coincidence of the two FCI predictions at a notch radius of 1 mm forms the basis of fictitious notch rounding approaches, where ideal weld geometries are assumed with an effective notch radius of 1 mm for endurance limit predictions, and in some cases, medium-high cycle fatigue [8, 17].

The effect of the fatigue notch factor approach explained above thus raises questions about whether it can be used when attempting to predict FCI lives within the medium-high cycle fatigue regime, i.e. below 10^6 cycles with satisfactory statistical agreement with experimentally obtained data. This is primarily the reason why variation C7 was developed (where the stress concentration factor K_t is directly used for FCI estimations), especially in the case of elastic-plastic solutions where

plastic deformation causes the magnitude of K_t to not reach the same distribution of numerical values as elastic solutions, as can be seen for the linear-elastic solutions (Chapter 3, Section 3.5.4.2).

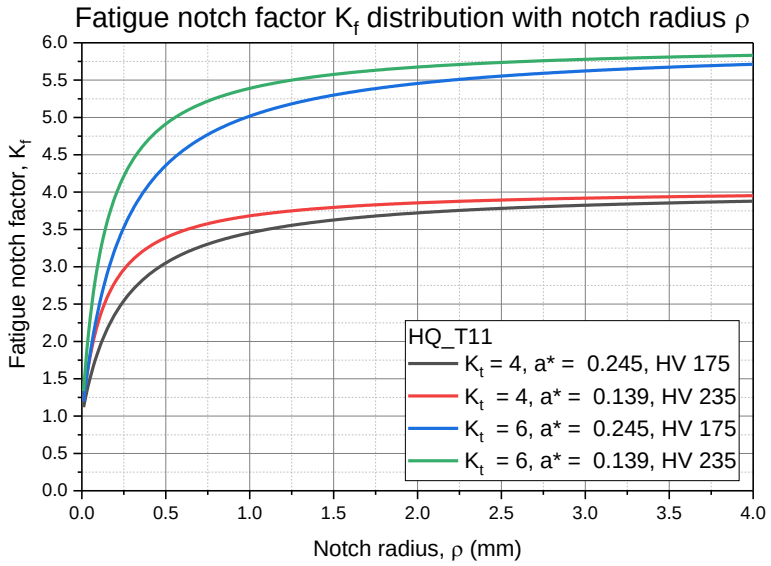

Figure 6.11 Fatigue notch factor distribution with variation in critical distance *a** and notch radius for two values of stress concentration factor, K_t.

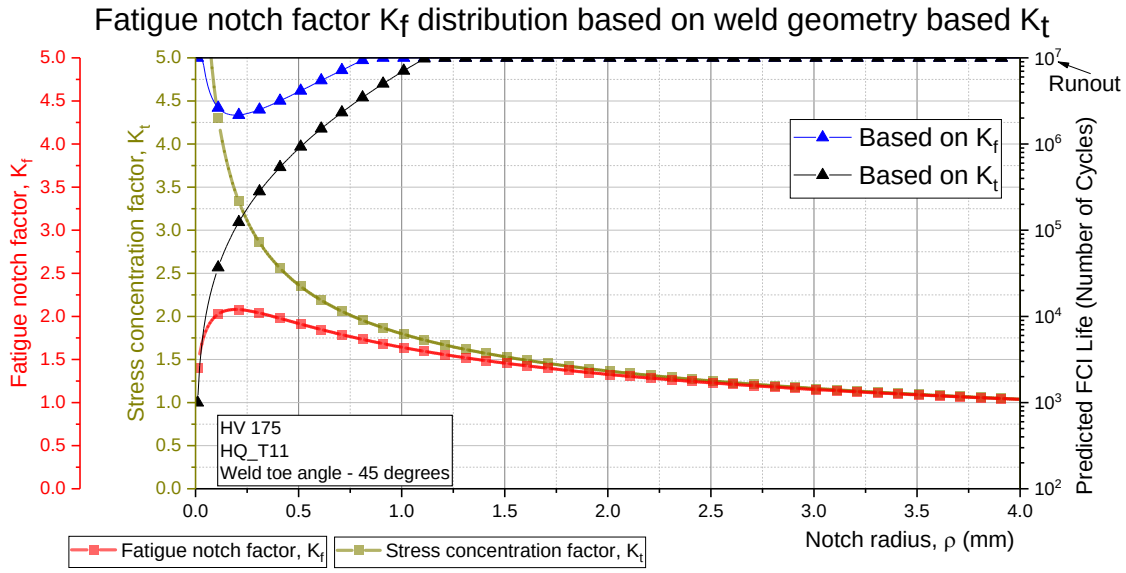

Figure 6.12 Fatigue notch factor distribution based on weld geometry based elastic stress concentration factor analytical solutions of Crump, 2017 [9] (used in variation C5).

6.4.5.3 Effect of microstructural zone

In the work described in Section 6.4, the three different microstructural zones present in a welded joint were considered in terms of their hardness maps. In some cases, the differences in the Vickers hardness distribution was significant, resulting in considerably different FCI life estimates.

Therefore, it becomes crucial to identify the specific microstructural properties that would need to be considered for fatigue analysis. Figure 6.13 presents a distribution of K_t versus the estimated FCI life for the applied stress ranges (using variation C7, which ignores the fatigue notch factor) for BM and HAZ for scan set 2 specimens. The scan set 2 specimens have also been indicated. The difference between the two microstructural zones is significantly lower for the LQ specimens as compared with the HQ specimens due to the larger range of magnitude of K_t exhibited by the LQ specimens. At such large values of K_t, the effect of varying hardness values is relatively less. However, the predicted FCI lives for the HQ specimens changes by a factor of between 2-3 due to the difference in the hardness values. In this project, the most severe effects of geometry were considered, but Figure 6.13 highlights the potential variability in FCI predictions based on the chosen microstructural zone for analysis.

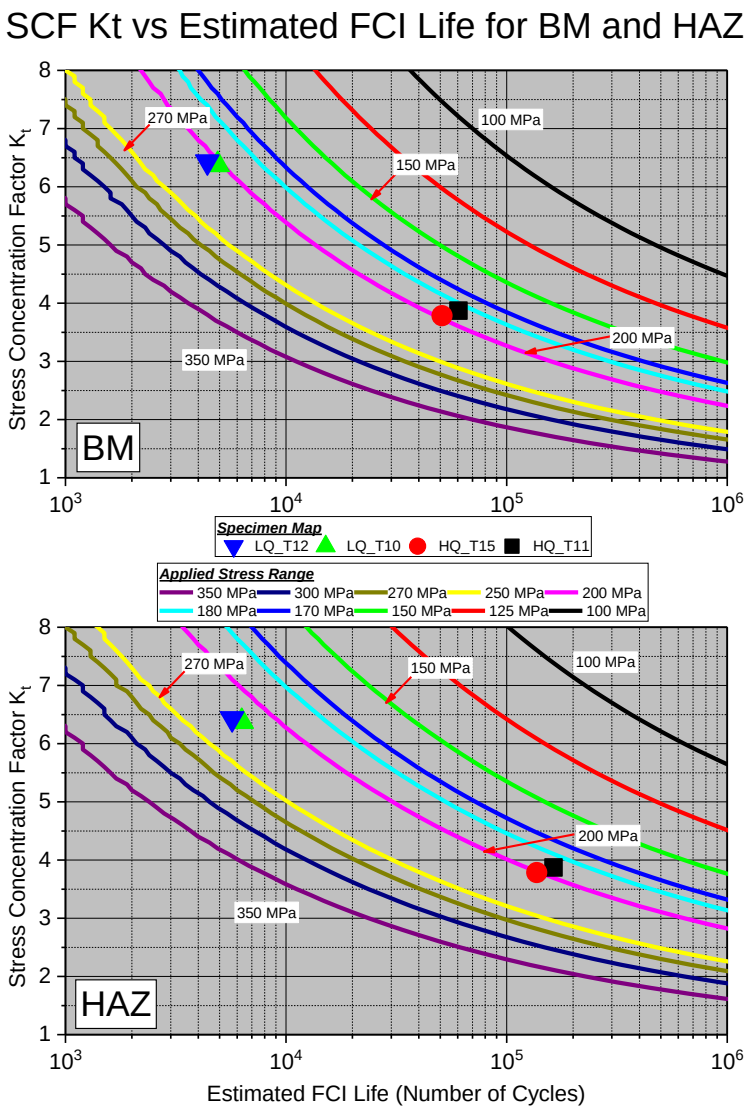

Figure 6.13 SCF K_t versus estimated FCI life (COM2) plot for BM (top) and HAZ (bottom) hardness maps for scan set 2. Specimens tested in scan set 2 have been indicated with their maximum value K_t and estimated COM2-based FCI life.

6.4.5.4 Crack Propagation Approach

To compute the crack propagation life, N_p, for each specimen the damage tolerant fracture mechanics approach in BS7910 was used in the commercially available software CRACKWISE. For the interrupted specimens, the value of N_p could not be validated as the specimens were not tested to final failure. The data has been presented in Table 6.22. It is important to note that the results obtained from CRACKWISE do not take into consideration the effect of crack coalescence, which may manifest in different forms in each of the specimens. This is evident in the results of the LQ specimens, which presented multiple instances of crack coalescence as compared with the HQ specimens. The total life data have been plotted in an SN curve for comparison with BS7608 Class F SN distribution [6], Figure 6.14. The results show reasonable agreement with the Class F mean curve, except for HQ_T6.

Table 6.22 Fatigue life data

Specimen	**Crack Initiation Life (N_i) for technical crack (0.25 mm crack depth) – obtained from experimental data (Number of cycles)**	**Estimated Crack Propagation Life (N_p) – obtained from CRACKWISE® (Number of cycles)**	**Estimated Total Life (N_t) – based on Equation 6-1 (Number of cycles)**
HQ_T6	348,380	30,866	379,246
HQ_T7	84,344	31,360	115,704
HQ_T8	179,457	30,300	209,757
HQ_T11	171,504	120,523	292,027
HQ_T15	258,112	104,832	362,944
LQ_T10	56,092	96,928	153,020
LQ_T12	49,397	93,782	143,179

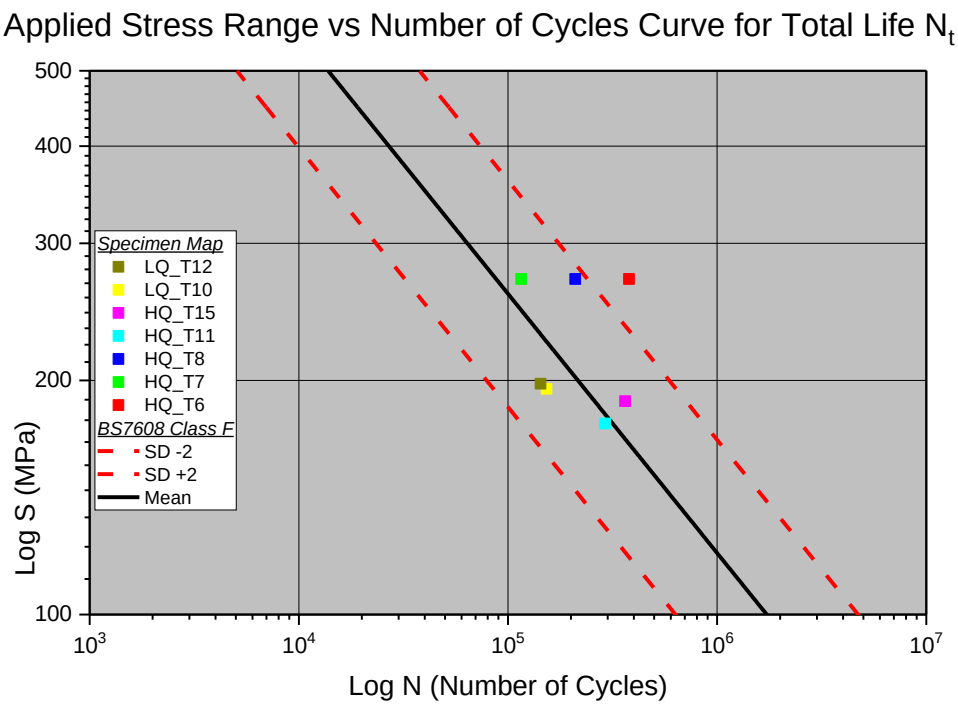

Figure 6.14 SN Curve depicting the total life obtained in Table 6.22 compared with the standard BS7608 [6] Class F SN curve. SD is the standard deviation distribution for class F.

6.5 Notch stress-strain approach – Summary

In this chapter, the notch stress-strain approach was implemented with results from the weld geometry-stress analysis carried out in Chapter 3. Results from both 3D FE-based stress analysis as well as weld toe analytical SCF solutions were used for FCI life predictions. Based on the available literature regarding the notch stress-strain approach, multiple variations and combinations were formulated in the form of a MATLAB program to attempt to identify the combination which provides the closest agreement (but still sufficiently conservative) with experimentally obtained FCI lives. The results from each of these variations were compared with each other as well as the experimental data. Deviation from experimental data was quantitatively analysed to identify any potential trends across the entire dataset. It is important to note that due to the small number of fatigue tests that were performed, the conclusions drawn cannot be truly definitive, but certainly aid in identifying the direction for potential future work on this subject. Based on the results obtained, the following conclusions have been made –

- The large scatter in the results obtained from each variation and combination highlight the large uncertainty that can be introduced into the FCI estimation process when choosing a workflow for the implementation of the notch stress-strain approach. As material parameters were not derived from strain-controlled low-cycle fatigue tests but rather from empirical relations, the

degree of uncertainty inherent in the derivation of each parameter can potentially become significant. This makes it difficult to standardise the procedure as it seems from the literature that different researchers have essentially used different variations of the notch stress-strain approach to get satisfactory results based on the data they are predicting [42, 108, 141, 201, 241, 244, 245, 248, 257], as the comparison of estimations and experimental data is effectively retrospective.

- With the high-resolution weld toe geometry measurement techniques available, the heterogeneity of the weld profile is captured in even greater detail. The increased level of detail results in capturing weld defects that result in severe stress concentrating areas. The classic notch stress-strain approach based on Neuber's work and the microstructural notch support effect [210-212, 227] has been widely accepted and utilised. However, as seen in Section 6.4.5.2, the implementation of the fatigue notch factor results in inconsistent estimations. For this purpose, the stress concentration factor derived directly from the 3D FE stress analysis or weld toe geometry-based analytical solutions are used. The combination COM2 (a combination of C7 with elastic-plastic stress solutions) gave satisfactory results. However, more tests would be required to validate this conclusion statistically.
- In this work, the hardness maps of all three microstructural zones were considered, and FCI estimations were made based on all three zones. The most conservative results of the three were analysed for each variation. However, for increased accuracy in the approach, it would be recommended to carry out strain-controlled low-cycle fatigue tests for each of the microstructural zones.
- The HQ specimens were manufactured with different welding parameters, and no pattern was seen, which could link the welding parameters with the fatigue estimation results. The most significant effect in this work is that of the variation in weld geometry.
- The LQ specimens, which were intentionally manufactured with deep undercuts and large weld toe angles gave (as expected) much lower fatigue crack initiation lives. Apart from the weld geometry-based analytical solutions, the remaining variations of the notch stress-strain approach predicted the poor fatigue performance satisfactorily (within a deviation factor of 2). As the weld geometry-based analytical solutions are based on 2D FE linear elastic stress analysis on a specific set of weld geometries, it is possible that the geometry of the LQ specimens were either -
    - outside of the validation range of the solutions, in the case of Hellier et al., 2014 [104] used in C6 and COM4, or
    - not within the range of the different geometries that were analysed to develop the solutions suggested by Crump, 2017 [9]

To summarise, this Chapter attempted to combine the work described in Chapters 3, 4 and 5 to develop an understanding of the potential of the notch stress-strain approach for FCI prediction in combination with the available high-resolution techniques currently accessible in industry for weld toe geometry identification as well as fatigue crack detection. It was seen that variations in the results are unavoidable based on the empirical relations chosen for implementing the approach. To be able to standardise this approach as other global approaches are [5, 6, 8, 17], the available empirical relations would have to be improved with more fatigue test data and state-of-the-art weld geometry methods, as have been used in this project.

Chapter 7 Conclusions and future work

7.1 Conclusions

The complex problem of fatigue of welded joints can be approached by using both global and local approaches. Standardised global approaches are widely used in estimating the total fatigue life of a welded joint. This PhD project has investigated the use of state-of-the-art high-resolution techniques for capturing the true weld toe geometry in order to implement local notch stress-strain approaches which allow the estimation of fatigue crack initiation life. In addition, data-rich versions of the available fatigue crack detection techniques were developed and investigated in order to validate the results obtained from finite element (FE) modelling based on the captured weld toe geometry. The conclusions are grouped based on the objectives mentioned in Chapter 1, Section 1.3.

7.1.1 Objective 1 (Chapter 3)

"Resolve and define weld toe geometry for high-resolution three-dimensional stress analysis of the inherent weld toe flaws during cyclic fatigue loading."

Following on from the work performed by Crump, 2017 [9] on the use of X-Ray micro-computed tomography (μ-CT) on welded joints, this non-destructive technique was also used in this project for capturing the true weld geometry in 3D. Resolutions from 4.9 μm to 10 μm were achieved on specimens of cross-sections 3 x 3 mm and 8 x 8 mm, respectively.

A qualitative analysis of the flaw distribution was performed using μ-CT scans of the weld joints. The flaw distribution was categorised in terms of number, type and size (depth along the vertical axis) of the flaws. It was possible to distinguish high-quality welds from the low-quality welded joints clearly.

The surface of the weld was extracted from the μ-CT scans, which enabled the welded joints to be quantified in terms of their weld toe radius and weld toe angle distribution. The measurement of the weld toe radius is greatly dependent on the method used to extract the distribution. The Lieurade method was found to be heavily reliant on the pre-determined distance required initially to evaluate the weld toe radius. To counter this problem, another method, least mean-squared Pratt's circle fit was used, and the lowest value of the weld toe radius was selected to provide conservative results.

3D FE-based stress-strain analysis was successfully carried out on the volumes of true weld toe geometry obtained from the μ-CT scans using a methodology developed to process the large data-volumes and converting them from the μ-CT raw scan volumes into 3D FE models. Both linear elastic and elastic-plastic stress concentration factors were obtained, which were later used in Chapter 6 for fatigue crack initiation estimations. As expected, the elastic-plastic stress concentration factor ranges were lower than those of the linear elastic stress analysis, as the former also included yielding of the material. The low-quality specimens were characterised to have the largest values of stress concentration factor at the weld toe.

7.1.2 Objective 2a (Chapter 4)

"Accurately detect in-situ fatigue crack initiation life and location using a data-rich fatigue crack growth monitoring technique." – ACPD.

A novel approach of applying the ACPD technique to a welded specimen was developed, which was an improvement on the previously documented applications of this non-destructive crack detection technique. The methodology developed allowed for precise identification of the location of the fatigue crack initiation site as well as the fatigue life of the specimen at the time of fatigue crack initiation. Early crack growth rates could also be obtained from the ACPD data. The methodology can also be applied to other specimens and testing environments where the sensitivity to surface cracking is critical.

The effect of stress on the ACPD data documented in previous use of the technique was also recognised in this study. An additional effect of elastic and/or elastic-plastic strain due to the applied stress and stress concentrating regions was also identified. It was seen that changing the location of the ACPD voltage measuring probes relative to the strain at the region of interest (elastic in regions of no stress concentration, elastic-plastic in regions of stress concentration, especially the weld toe) results in a variation in the relation between measured ACPD voltage and applied stress.

The ACPD technique was found to be sensitive to surface crack initiation, but once a crack had grown beyond a certain crack depth, further increasing the compliance of the test specimen to the applied (constant) load, the effect of stress on ACPD affects the relationship between the change in measured ACPD voltage with crack depth in a variable/non-consistent fashion. This was also augmented by multiple crack growth along the weld toe at various stress concentration features. It is expected in a welded specimen that multiple cracking will occur due to the potentially large number of stress concentrating features present at the weld toe.

7.1.3 Objective 2b (Chapter 5)

"Accurately detect in-situ fatigue crack initiation life and location using a data-rich fatigue crack growth monitoring technique." – Strain gauge array.

From the results obtained in Chapter 5, it was ascertained that if strain gauges are used in the data-rich arrangement described, FCI can be detected accurately both in terms of location and life and so this approach has potential application in structural integrity problems, where it is critical to identify potential FCI locations during operation accurately. Other phenomena such as plastic shakedown and cyclic hardening or softening can also be obtained from the strain data.

As expected from observations in Chapter 4 and the conclusions detailed in Section 7.1.2, it was not possible to quantify the relation between strain range drop and measured (real) crack depth accurately. This is primarily due to multiple cracking occurring at the weld toe, as it becomes challenging to isolate the strain range drop for each crack.

As strain gauges effectively measure the compliance of the specimen in response to the applied load, the change in compliance due to the increase in crack area (and the adjacent decrease in remaining ligament area) due to a crack that has initiated earlier affects the strain range data obtained from other strain gauges for cracks that initiate relatively later in the overall fatigue life of the specimen.

7.1.4 Objective 3 (Chapter 6)

"The use of the local notch stress-strain approach for the estimation of fatigue crack initiation life and, subsequently, the total life of a welded joint with local stresses obtained from 3D FE stress analysis of the true weld geometry, followed by validation of the results with data-rich experimental methods of crack growth monitoring."

Multiple variations and combinations of the local notch stress-strain approach documented in the available literature (detailed in Chapter 6) were implemented in the form of a MATLAB program. The weld toe geometry-based stress concentration factors obtained in Chapter 3 were used in the notch stress-strain approach, and the results obtained were compared with the experimental results from Chapters 4 and 5. The increase in the accuracy of experimental techniques to detect the early onset of fatigue crack initiation further improves understanding the predictions obtained from the local notch stress-strain approach.

The scatter obtained from the different variations and combinations of the approaches highlights the influence of material parameters that are obtained empirically from material hardness-based

characterisation. The possibility of standardising such an approach is, therefore, challenging. Global approaches that are available as standardised fatigue lifing estimations require relatively fewer parameters.

The inconsistent estimations obtained from the use of fatigue notch factors based on the critical distance approach have been highlighted and the results indicate that better estimations are obtained if the stress concentration factors derived from the weld toe geometry-based analyses are used. The use of elastic-plastic FE-based stress analysis provides satisfactory results when directly used in the notch stress-strain approach.

The estimation approach was clearly able to distinguish between the LQ and HQ specimens when FE-based stress analysis was used in calculating the stress concentration factor, and predicted significantly lower lives for the LQ specimens, as validated by the experimental results obtained in Chapter 4. The weld toe geometry based analytical solutions for stress concentration factor were not as successful for the geometries exhibited by the LQ specimens are possibly beyond the range of geometries on which the analytical solutions are based.

7.2 Future work

Based on the results and findings in this study, some avenues of further improvement are evident, as well as further research questions that would enhance significantly the investigations performed in this study. They have been outlined below.

- The 3D FE-based stress analyses for both linear elastic and elastic-plastic stress-strain distributions were based on applying a static load equal to the maximum stress that the specimens were subjected to during experimental fatigue loading. To account for material hardening/softening effects and the role of residual stresses in the elastic-plastic FE-based stress analysis, the accuracy of the analysis could be further improved if the load was applied cyclically during the FE processing. This was not performed in this study as the computational cost of cyclic loading was too great. Additionally, the incorporation of residual stresses into the modelling process would also increase the accuracy of the stress-strain analysis. This work concentrated on the effect of only the inhomogeneous weld toe geometry distribution along the length of the welded joint, but future work could address the loading state more realistically.
- To understand the effects of stress during the implementation of the ACPD crack detection technique, further testing is required where different orientations of the ACPD voltage measurement probes and stress concentration areas (regions of elastic or elastic-plastic strain) could be tested in both load- and strain-control. The relation of strain and its effect on the

magnetic properties of the material (magnetic permeability of the material impact the sensitivity of the ACPD) needs to be further investigated in order to provide stress-based corrections for using ACPD for quantitative crack growth monitoring. It can be estimated from the findings of the study that the effects of stress would be lower if the fatigue testing were carried out under strain- or displacement-control, as the increase in compliance of the specimen due to crack growth would be compensated by lowering the load applied by fatigue testing machine. As the loads applied during this study combined with the stress concentration at the weld toe pushed the stress-field beyond yield magnitude, understanding the stress effect on ACPD in fully elastic regimes would also shed further light on the effectiveness of the ACPD crack detection technique. Such studies on fully understanding the effect of applied stress on ACPD could potentially increase the range of applications where the technique can be used. The combination of DCPD and ACPD is also a topic for further research, as ACPD can be used to detect the fatigue crack initiation and early crack growth stage, continuing with DCPD measurements for stable crack growth.

- The effectiveness of the strain gauge array technique in detecting FCI was presented in this study and could potentially be used in tests or applications where FCI life is a critical deliverable. The 2D FE elastic strain range drop estimation study (performed to establish an estimate for strain range drop corresponding to a pre-defined crack depth or length) could potentially be carried out using 3D models with the real weld and crack geometry, resulting in a considerable increase in complexity. With 3D modelling, the occurrence of multiple crack initiation sites can also be incorporated. The phenomenon where each strain gauge of the strain gauge array deviates momentarily at the exact instance of an initiating crack could be further evaluated to see whether it is merely an effect of the specific testing machine's feedback loop or if it can be repeated in other testing configurations as well. The use of biaxial or triaxial strain gauges in such an array could potentially increase the sensitivity to detect cracks in parts or structures where the applied loading is not uniaxial.
- The accuracy of fatigue estimation approaches (global and local) can be further investigated and improved using these improved FCI detection techniques.
- In the case of the local notch stress-strain approach, where the estimations are heavily dependent on material parameters, the accuracy can be further improved by carrying out strain-controlled low-cycle fatigue tests for each of the microstructural zones of a welded joint (The practicalities of obtaining suitable specimens exhibiting the HAZ and weld metal microstructure also need to be considered). However, it is important to highlight that such tests are not always feasible due to added complexity in the analysis of the results. Thus, such tests will need to be conducted in conjunction with empirical assessments to allow practical

estimations, and well-defined scatter boundaries to allow such local approaches to be standardised, similar to the current global approaches.

- Due to the nature of the work carried out in Chapters 3, 4 and 5 (high-resolution and data-rich), a considerable amount of time was required to create programs and algorithms to process the large volume of data generated. As a result, the number of specimens that could be feasibly tested was low (seven). This is clearly not enough to thoroughly investigate the possibilities of the local notch stress-strain approach that was applied in this study. As the workflow and algorithms have now been documented in this study, future work could potentially concentrate on testing a wider range of welded joints to understand the potential of a data-rich FCI detection technique, a high-resolution true weld geometry capturing methodology and the local notch approach for predicting the life to fatigue crack initiation of a welded joint. Some examples of potential welded joints are as follows:
    - Steel as-welded MAG weaved,
    - Steel MAG welded, weld toe peened using HFMI.
    - Steel MAG welded with low-temperature transformation electrode.
    - Aluminium as-welded MIG.

Appendix A**(Chapter 3)**

A.1 2D Weld Toe Geometry Extraction

A.1.1 ImageJ Macro

```
/to make skeletonised images, but open each image one by one.
//number of slices processing
num_slices=9600;
for (k=1; k<=num_slices; k++)
{
    //to adjust for file name
    if (k<=9)
    {
        open("D:/Somsubhro/CT/2017/2017_HQ_T6/FIJI Processing/T6_830x910x9600_000"+k+".tif");
    }
    else if ((k>9) && (k<100))
    {
        open("D:/Somsubhro/CT/2017/2017_HQ_T6/FIJI Processing/T6_830x910x9600_00"+k+".tif");
    }
    else if ((k>99) && (k<1000))
    {
        open("D:/Somsubhro/CT/2017/2017_HQ_T6/FIJI Processing/T6_830x910x9600_0"+k+".tif");
    }
    else
    {
        open("D:/Somsubhro/CT/2017/2017_HQ_T6/FIJI Processing/T6_830x910x9600_"+k+".tif");
    }
    run("Smooth (3D)", "method=Gaussian sigma=1.000");
    close("skeletonise*");
    selectWindow("Smoothed");
    run("Find Edges");
    run("Skeletonize (2D/3D)");
    // to remove the lines along the edges of the image
    makeRectangle(41, 51, 521, 527);
    run("Specify...", "width=820 height=900 x=5 y=5");
    run("Crop");

// to adjust for file name
if (k<=9)
    {
        saveAs("Tiff", "D:\\Somsubhro\\CT\\2017\\2017_HQ_T6\\FIJI_Processed\\SKtn_T6_820x900x9600_000"+k+".tif");
    }
    else if ((k>9) && (k<100))
    {
        saveAs("Tiff", "D:\\Somsubhro\\CT\\2017\\2017_HQ_T6\\FIJI_Processed\\SKtn_T6_820x900x9600_00"+k+".tif");
    }
    else if ((k>99) && (k<1000))
    {
        saveAs("Tiff", "D:\\Somsubhro\\CT\\2017\\2017_HQ_T6\\FIJI_Processed\\SKtn_T6_820x900x9600_0"+k+".tif");
    }
    else
    {
        saveAs("Tiff", "D:\\Somsubhro\\CT\\2017\\2017_HQ_T6\\FIJI_Processed\\SKtn_T6_820x900x9600_"+k+".tif");
```

```
49.     }
50.     close();
51.     close();

}
```

A.1.2 MATLAB Code

Main Code

Settings

```
% Set scale of image 1 pix = xx mm
searchRegion.scale = 10e-3;

% WTC search region wrt the break point
searchRegion.WTC.left = 150;
searchRegion.WTC.right = 150;

% WTA
searchRegion.WTA.height = 1.75; %in mm
searchRegion.WTA.height = searchRegion.WTA.height/searchRegion.scale; % in px

thresholds.WTA = 20; % degrees

% WTR
searchRegion.WTR.Pratt.pathLength = 0.25; %mm
searchRegion.WTR.Pratt.pathLength = searchRegion.WTR.Pratt.pathLength/searchRegion.scale;
%in px

searchRegion.WTR.Lieurade.pathLength = 0.425; %mm
searchRegion.WTR.Lieurade.pathLength =
searchRegion.WTR.Lieurade.pathLength/searchRegion.scale; %in px

searchRegion.WTR.smooth = 0.4; %mm
searchRegion.WTR.smooth = searchRegion.WTR.smooth/searchRegion.scale; %in px

% Fit method
fit_method.type = 'best-fit';
fit_method.range = 0.5; %in mm
fit_method.range = 0.5/searchRegion.scale; %in px

% Allow plots
plotOptions.originalImage = 0;
plotOptions.on = 1;
plotOptions.visible = 'off';
plotOptions.save = 1;

%To deal with stop start
custombegin = input('Serial of first beginning image: ');
customend = input('Serial of final image: ');
```

Run program

Define the folder with images Get the current folder

```
main_folder = pwd();
% Get the name of parent folder
% Look for occurance of \
idcs = strfind(main_folder, '\');
if isempty(idcs) %If windows uses / instead - check for it
    idcs = strfind(main_folder, '/');
end
% This is the parent folder
main_folder = main_folder(1:idcs(end)-1);

im_folder = uigetdir(main_folder, 'Select image folder');

% Get a list of all .tif files in that folder
im_list=dir([im_folder '/*.tif']);

% Define the root of image name
root_name = inputdlg('Give the root of the file (name until the numbering of images start',
'name', 1, {im_list(1).name});

% Number of images in the folder
im_num = size(im_list,1);

% Define range of images to be processed
im_range = custombegin:customend;
% im_range = 6;

WTA = nan(1, length(im_range));
flag_WTA = zeros(1, length(im_range));
WTR = nan(2, length(im_range));
% save WTR data for both methods
saveWTR = nan(2, length(im_range));
angleCheck=nan(1, length(im_range));

for pt = im_range
    IMG_NUM=pt;
    if pt<=9
        IMG_NUM=['000' int2str(IMG_NUM)];
    end
    if ((pt>9) && (pt<100))
        IMG_NUM=['00' int2str(IMG_NUM)];
    end
    if ((pt>99) && (pt<1000))
        IMG_NUM=['0' int2str(IMG_NUM)];
    end
    if ((pt>999) && (pt<10000))
        IMG_NUM=['' int2str(IMG_NUM)];
    end
    % Load an image
    currFilename = [root_name{1},num2str(IMG_NUM),'.tif'];
    im = imread([im_folder,'\',currFilename]);
    % Trim image (white edges)
    % im = im(2:end-2,2:end-2);

    % Show the image
    if plotOptions.originalImage
        figure();
        imshow(im);
    end
```

```
    % Get coordinates of skeletonised edge
    [idx] = find(im ~= 0);
    [Y,X] = ind2sub(size(im), idx);

    % Flip Y coordinates
    Y = size(im,1)-Y;

    % Calculate WTC
    [WTC, WTCBackGrad] = getWTC(X, Y, searchRegion.WTC, fit_method, plotOptions);
    % Calculate WTA
    [WTA(pt), WTABackGrad] = getWTA(X, Y, WTC, searchRegion, plotOptions);

    % Check the angle between WTA and WTC back gradient
    angleCheck(pt) = atan2d(norm(cross([WTCBackGrad, 0], [WTABackGrad,
0])),dot(WTCBackGrad, WTABackGrad));
    if angleCheck(pt) < thresholds.WTA
        flag_WTA(pt) = 1;
    end

    % Calculate WTR with the two methods
    WTR(1,pt) = getWTR(X, Y, WTC, searchRegion, plotOptions, 'Pratt');
    WTR(2,pt) = getWTR(X, Y, WTC, searchRegion, plotOptions, 'Lieurade');

    saveWTR(1,pt) = WTR(1,pt);
    saveWTR(2,pt) = WTR(2,pt);

    if plotOptions.on
        if WTR(1,pt) < WTR(2,pt)
            plotFitCircle(X, Y, WTC, searchRegion, plotOptions, 'Pratt')
        else
            plotFitCircle(X, Y, WTC, searchRegion, plotOptions, 'Lieurade');
        end
            currentFig = gcf;
            if plotOptions.save
                saveFitFigures(im_folder, currentFig, [root_name{1},num2str(pt)],
plotOptions);
            end
    end

end

WTA(flag_WTA==0) = NaN;
% WTA along weld
figure();
plot(im_range*searchRegion.scale, WTA);


% WTR along weld
% Chose smaller of the two radii
WTR = min(WTR,[],1);
figure();
plot(im_range*searchRegion.scale, WTR);
% Smooth WTR along the weld toe
WTR = movmean(WTR, searchRegion.WTR.smooth);
hold on;
plot(im_range*searchRegion.scale, WTR, '--r', 'LineWidth', 2);
legend('Raw data', 'Smoothed along length')
```

Pratt Circle Fit

```
function Par = CircleFitByPratt(XY)

%--------------------------------------------------------------------------
%
%     Circle fit by Pratt
%      V. Pratt, "Direct least-squares fitting of algebraic surfaces",
%      Computer Graphics, Vol. 21, pages 145-152 (1987)
%
%     Input:  XY(n,2) is the array of coordinates of n points x(i)=XY(i,1), y(i)=XY(i,2)
%
%     Output: Par = [a b R] is the fitting circle:
%                           center (a,b) and radius R
%
%     Note: this fit does not use built-in matrix functions (except "mean"),
%           so it can be easily programmed in any programming language
%
%--------------------------------------------------------------------------

n = size(XY,1);      % number of data points

centroid = mean(XY);   % the centroid of the data set

%     computing moments (note: all moments will be normed, i.e. divided by n)

Mxx=0; Myy=0; Mxy=0; Mxz=0; Myz=0; Mzz=0;

for i=1:n
    Xi = XY(i,1) - centroid(1);  %  centering data
    Yi = XY(i,2) - centroid(2);  %  centering data
    Zi = Xi*Xi + Yi*Yi;
    Mxy = Mxy + Xi*Yi;
    Mxx = Mxx + Xi*Xi;
    Myy = Myy + Yi*Yi;
    Mxz = Mxz + Xi*Zi;
    Myz = Myz + Yi*Zi;
    Mzz = Mzz + Zi*Zi;
end

Mxx = Mxx/n;
Myy = Myy/n;
Mxy = Mxy/n;
Mxz = Mxz/n;
Myz = Myz/n;
Mzz = Mzz/n;

%    computing the coefficients of the characteristic polynomial

Mz = Mxx + Myy;
Cov_xy = Mxx*Myy - Mxy*Mxy;
Mxz2 = Mxz*Mxz;
Myz2 = Myz*Myz;

A2 = 4*Cov_xy - 3*Mz*Mz - Mzz;
A1 = Mzz*Mz + 4*Cov_xy*Mz - Mxz2 - Myz2 - Mz*Mz*Mz;
A0 = Mxz2*Myy + Myz2*Mxx - Mzz*Cov_xy - 2*Mxz*Myz*Mxy + Mz*Mz*Cov_xy;
A22 = A2 + A2;

epsilon=1e-12;
ynew=1e+20;
```

```
IterMax=20;
xnew = 0;

%    Newton's method starting at x=0

for iter=1:IterMax
    yold = ynew;
    ynew = A0 + xnew*(A1 + xnew*(A2 + 4.*xnew*xnew));
    if (abs(ynew)>abs(yold))
        disp('Newton-Pratt goes wrong direction: |ynew| > |yold|');
        xnew = 0;
        break;
    end
    Dy = A1 + xnew*(A22 + 16*xnew*xnew);
    xold = xnew;
    xnew = xold - ynew/Dy;
    if (abs((xnew-xold)/xnew) < epsilon), break, end
    if (iter >= IterMax)
        disp('Newton-Pratt will not converge');
        xnew = 0;
    end
    if (xnew<0.)
        fprintf(1,'Newton-Pratt negative root:  x=%f\n',xnew);
        xnew = 0;
    end
end

%    computing the circle parameters

DET = xnew*xnew - xnew*Mz + Cov_xy;
Center = [Mxz*(Myy-xnew)-Myz*Mxy , Myz*(Mxx-xnew)-Mxz*Mxy]/DET/2;

Par = [Center+centroid , sqrt(Center*Center'+Mz+2*xnew)];

end    %    CircleFitByPratt
```

Obtain WTA

```
function [WTA, WTAfit] = getWTA(X, Y, WTC, searchRegion, plotOptions)
    % Find where is the point searchRegion.WTA.height above the WTC
    topEnd = Y(WTC)+searchRegion.WTA.height;
    topEndIdx = find(Y>topEnd,1);

    % Ensure that the point exists
    if isempty(topEndIdx)
        error('WTA cannot be computed with given path length')
    end

    % Fit straight line between the point and WTC
    WTAfit = polyfit(X(topEndIdx:WTC), Y(topEndIdx:WTC), 1);
    WTAfit = WTAfit(1); %Get gradient value
    % Calculate angle between the horizontal line and the gradient
    WTA = atan2d(norm(cross([1,0,0], [-1 -WTAfit,0])),dot([1,0], [-1 -WTAfit]));
    % WTA is the complementary angle (to 180deg)
    WTA = 180-WTA;
    % Plot the gradient line
    if plotOptions.on
        plotX = [X(topEndIdx), X(WTC)];
        plotY = [Y(WTC)+(X(topEndIdx)-X(WTC))*WTAfit, Y(WTC)];
```

```
        plot(plotX, plotY, '--m')
    end
    % Convert WTAfit to a vector
    WTAfit = [-1 -WTAfit];
end
```

Obtain WTC

```
function [WTC, WTCBackGrad] = getWTC(X, Y, searchRegion, fit_method, plotOptions)

searchRegion.start = findchangepts(Y, 'MaxNumChanges', 1, 'Statistic', 'linear');

% Define search region (break point +- ranges)
searchRegion.runRange = searchRegion.start-
searchRegion.left:searchRegion.start+searchRegion.right;

% Predefine angle output
angleOut = zeros(1, length(searchRegion.runRange));

% Loop over all points
for pt = 1:length(searchRegion.runRange)
    % Backwards vector
    dy_back = getSlope(X, Y, searchRegion.runRange(pt), 'backward', fit_method);
    % Forwards vector
    dy_forw = getSlope(X, Y, searchRegion.runRange(pt), 'forward', fit_method);
    % Angle between the two
    angleOut(pt) = getAngle(dy_back, dy_forw);
end

% Plot the vectors at the WTC (lowest angle between two vectors)
% figure();
% plot(searchRegion.runRange,angleOut);
[~,WTC] = min(angleOut); % Get WTC
WTC = searchRegion.runRange(WTC); % Convert it back to X coordinate
if plotOptions.on
    plotPtGradients(X,Y, WTC, fit_method, plotOptions)
end
WTCBackGrad = getSlope(X, Y, WTC, 'backward', fit_method);

end
```

Help functions

```
function dy = getSlope(X, Y, pos, dir, method)

% Get slope of a line on either side of the point [X(pos), Y(pos)]

switch method.type
    case 'best-fit'
        switch dir
            case 'forward'
                Xfit = X(pos:pos+method.range);
                Yfit = Y(pos:pos+method.range);
                dy = polyfit(Xfit, Yfit, 1);
                dy = [1 dy(1)]; %Convert to vector going from the point to right
            case 'backward'
                Xfit = X(pos-method.range:pos);
                Yfit = Y(pos-method.range:pos);
```

```
                dy = polyfit(Xfit, Yfit, 1);
                dy = [-1 -dy(1)]; %Convert to vector going from the point to left right
        end
    case 'secant'
        switch dir
            case 'forward'
                a = (Y(pos+method.range)-Y(pos))/(X(pos+method.range)-X(pos));
                dy = [1 a];
            case 'backward'
                a = (Y(pos)-Y(pos-method.range))/(X(pos)-X(pos-method.range));
                dy = [-1 -a];
        end
end

end

function alpha = getAngle(grad_back, grad_forw);
    % Calculate the angle  (combination of cross and dot products
    % definitions)
    alpha = atan2d(norm(cross([grad_forw,0], [grad_back,0])),dot(grad_forw, grad_back));
    if alpha < 0
        alpha = 360+alpha;
    end
end

function [] = plotPtGradients(X,Y, pt, fit_method, plotOptions)
    dy_back = getSlope(X, Y, pt, 'backward', fit_method);
    dy_forw = getSlope(X, Y, pt, 'forward', fit_method);

    % Compute angle between the two gradients
    theta = getAngle(dy_back, dy_forw);

    %  ============ Plot the test point vectors + angle
    figure('Visible', plotOptions.visible); axis equal

    % Plot withing number of ranges (nrg) of best fit range
    plot(X, Y, '-k');
%     plot(X(pt-nrg*fit_method.range:pt+nrg*fit_method.range),...
%          Y(pt-nrg*fit_method.range:pt+nrg*fit_method.range), '-k');
    hold on;
    scatter(X(pt), Y(pt), '^b', 'filled');
    % Backwards gradient
    Xplot = X(pt-fit_method.range:pt);
    Yplot = Y(pt)+(Xplot-X(pt))*(-dy_back(2));
    plot(Xplot, Yplot, '-r');

    % Forwards gradient
    Xplot = X(pt:pt+fit_method.range);
    Yplot = Y(pt)+(Xplot-X(pt))*dy_forw(2);
    plot(Xplot, Yplot, '-r');
end
```

Obtain WTR

```
function [WTR, circProp] = getWTR(X, Y, WTC, searchRegion, plotOptions, method);


% Calculate distance between each point on the profile and WTC
dist = sqrt((X-X(WTC)).^2+(Y-Y(WTC)).^2);
```

```
% Select a method for the WTR calculation
switch method
    case 'Pratt'
        % Define region of interest
        % First point exceeding distance threshold (left bound)
        leftBound = find(dist<searchRegion.WTR.Pratt.pathLength, 1, 'first');
        % Last point exceeding distance threshold (right bound)
        rightBound = find(dist<searchRegion.WTR.Pratt.pathLength, 1, 'last');
        % Create list of XY coordinates of points in the range
        XY = [X(leftBound:rightBound), Y(leftBound:rightBound)];

        % Use external function to fit a circle with Pratt technique
        prattParams = CircleFitByPratt(XY);

        % Get radius
        WTR = prattParams(3); %in px
        WTR = WTR*searchRegion.scale; %in mm

        circProp = prattParams;
    case 'Lieurade'
        % First point exceeding distance threshold (left bound)
        leftBound = find(dist<searchRegion.WTR.Lieurade.pathLength, 1, 'first');
        % Last point exceeding distance threshold (right bound)
        rightBound = find(dist<searchRegion.WTR.Lieurade.pathLength, 1, 'last');
        % Calculate R as half the distance between the two bounds
        WTR = sqrt((X(rightBound)-X(leftBound)).^2+(Y(rightBound)-Y(leftBound)).^2)/2;
        WTR = WTR*searchRegion.scale; %scale to mm

        dirVec = [X(rightBound)-X(leftBound) Y(rightBound)-Y(leftBound)];

        circProp = [X(leftBound)+dirVec(1)/2, Y(leftBound)+dirVec(2)/2,...
                    sqrt((X(rightBound)-X(leftBound)).^2+(Y(rightBound)-
Y(leftBound)).^2)/2];
end



end
```

Plot Fitting Circle

```
function [] = plotFitCircle(X, Y, WTC, searchRegion, plotOptions, method);
[~, circProp] = getWTR(X, Y, WTC, searchRegion, plotOptions, method);

angleRange = linspace(0,360,360);

X = circProp(1)+cosd(angleRange)*circProp(3);
Y = circProp(2)+sind(angleRange)*circProp(3);

plot(X, Y, '-g');

end
```

Save the Fitting Figures

```
function []=saveFitFigures(im_folder, currentFig, currFilename, plotOptions);
```

```
if 7~=exist([im_folder,'\figs'],'dir')
    mkdir([im_folder,'\figs']);
end

ax1 = gca;
grid(ax1, 'on');
xlabel('X coord [px]');
ylabel('Y coord [px]');

legend('Weld profile', 'WTC', 'WTC back gradient', 'WTC forward gradient',...
        'WTA line fit', 'WTR fit');
set(ax1, 'FontSize', 14);
axis(ax1, 'equal');

saveas(currentFig, [im_folder,'\figs\',currFilename], 'png')
```

A.2 3D FEA CT Volume Pre-processing

A.2.1 ImageJ Macro

```
//run("Image Sequence...", "open=[D:\\Somsubhro\\CT\\2017\\20170716_Test7_HMX_1371_SC\\ \\20170818_Test7_FINAL_CROPPEDnROT97_1139x967x1001_0001.tif] sort");
//obtain dimension of the MATLABed image
run("Select None");
run("Set Measurements...", "area mean bounding redirect=None decimal=3");
run("Measure");
orig_width = getResult("Width");
orig_height = getResult("Height");
//the values below have been taken from the excel sheet called - 20171031_Test7_Step1_Measurements.xlsx
//Take the values from there, and edit the values below.
stepA = 820;
stepB = 820;
stepC = 581;
//STEP-A
width2 = orig_width;
height2 = orig_height + stepA;
run("Canvas Size...", "width="+width2+" height="+height2+" position=Bottom-Center");
run("Invert", "stack");
//STEP-B
width3 = width2 + stepB;
height3 = height2;
run("Canvas Size...", "width="+width3+" height="+height3+" position=Top-Right");
//STEP-C
width4 = width3;
height4 = height3 + stepC;
run("Canvas Size...", "width="+width4+" height="+height4+" position=Top-Center");
run("Invert", "stack");
run("Set Scale...", "distance=1 known=0.004878 unit=mm");
//change file name below before running macro
//run("Image Sequence... ", "format=TIFF name=20170927_Test7_FINAL_"+width4+"x"+height4+"x151_ start=1 save=[D:\\Somsubhro\\CT\\2017\\20170716_Test7_HMX_1371_SC\\04_concatenated_volume\\Image Analysis\\Image_sequence_result_2\\20170927_Test7_FINAL_3721x3085x1000_0001.tif]");
```

A.2.2 MATLAB Code

```
%Image Extender - Line Adder - Line Shader - Multi Image
%For n>1 number of images. BETA version

clc;
clear all;
close all;

res = input('Resolution in microns :'); %Input resolution of image

weldth = input('Weld thickness in mm :');
xmm = input('x extension in mm :'); %Define x in mm
zmm = input('z extension in mm :'); %Define z in mm

num_images = round((weldth * 1000)/res);
x = round((xmm * 1000) / res); %value of x in pixels
z = round((zmm * 1000) / res); %value of z in pixels

ya=[num_images,2]; %Array storing position of point A
yb=[num_images,2]; %Array storing position of point B
```

```
lineangle = [num_images,2]; %Array storing angles of the line
```

Populating ya and yb

```
    wb1=waitbar(0, 'Ya and Yb array population progress');

    for k1=1:num_images
        waitbar(k1/(num_images),wb1);
        IMG_NUM1=k1;
        if k1<=9
            IMG_NUM1=['000' int2str(IMG_NUM1)];
        end
        if ((k1>9) && (k1<100))
            IMG_NUM1=['00' int2str(IMG_NUM1)];
        end
        if ((k1>99) && (k1<1000))
            IMG_NUM1=['0' int2str(IMG_NUM1)];
        end
        if ((k1>999) && (k1<10000))
            IMG_NUM1=['' int2str(IMG_NUM1)];
        end

        %Read original image
        img1=['Image_Sequence/20171030_Test7_773x700x9708_' IMG_NUM1 '.tif'];
        Im_in1=imcomplement(imread(img1));

    % Get size of the original image
    [szy, szx] = size(Im_in1);

    %Find point A (First column + Find first row to be black)
    %Saves position of A of each image
    ya(k1,1)=k1;
    xa = 1;
    ya(k1,2) = (find(Im_in1(:,1)==0, 1, 'first'));

    %Find point B (Last column + Find first row to be black);
    %Saves position of B of each image
    yb(k1,1)=k1;
    xb = szx;
    yb(k1,2) = find(Im_in1(:,szx)==0, 1, 'first');

    %Define increased picture size
    Im_out1 = uint8(255*ones(x+szy, x+szx+z));

    %Put original image in new image
    Im_out1(x+1:end,x+1:x+szx) = Im_in1;
end

%Defined the point where all the extended lines will connect up with.
new_y = median(ya(:,2));
```

Reading multiple images and picking up the coordinates of points.

```
wb=waitbar(0, 'Image Extender Progress');
for k2=1:num_images
```

```
    waitbar(k2/(num_images),wb);
    IMG_NUM2=k2;
    if k2<=9
        IMG_NUM2=['000' int2str(IMG_NUM2)];
    end
    if ((k2>9) && (k2<100))
        IMG_NUM2=['00' int2str(IMG_NUM2)];
    end
    if ((k2>99) && (k2<1000))
        IMG_NUM2=['0' int2str(IMG_NUM2)];
    end
    if ((k2>999) && (k2<10000))
        IMG_NUM2=['' int2str(IMG_NUM2)];
    end

    %Read original image
    img2=['Image_Sequence/20171030_Test7_773x700x9708_' IMG_NUM2 '.tif'];
    Im_in2=imcomplement(imread(img2));

    % Get size of the original image AGAIN
    [szy, szx] = size(Im_in2);

    %Define increased picture size AGAIN
    Im_out2 = uint8(255*ones(x+szy, x+szx+z));

    %Put original image in new image AGAIN
    Im_out2(x+1:end,x+1:x+szx) = Im_in2;

    %Fill the right hand side by going through columns and inserting black
    %pixels at the level from point B
    % Mind that original point B has now coordinates [xb+x, yb+b]

    for pt = 1:z
        Im_out2(x+yb(k2,2):end,x+szx+pt) = 0;
    end
```

For adding line to image

```
    h_im = imshow(Im_out2);

    %assigning the line to a handle for the line. The line is drawn from the
    %evaluated xa,ya to a point decided by analysing the xa,ya for all the
    %images.

    hLine = imline(gca,[1 (xa+x)],[(new_y) (ya(k2,2)+x)]);

    %Storing the angle of the line
    % lineangle = atan2({{ya+x}-{90+x}},{{xa+x}-{1}})*180/pi; this is
    % essentially what is written below
    lineangle(k2,1) = k2;
    lineangle(k2,2) = atan2(ya(k2,2)+x-new_y,xa+x-1)*180/pi;

    %creating a binary mask for the line
    BinarkMask = createMask(hLine,h_im);

    % Burn line into image by setting it to 0 wherever the mask is true.
    Im_out2(BinarkMask) = 0;
```

For shading the area below the line black.

```
    %using polyfit to calculate the coefficients m and c of the equation
    %y=mx+c describing the line drawn above. Inputs are the two points that are
    %used to create the line.

    eqcoeff = polyfit([xa xa+x],[new_y x+ya(k2,2)],1);

    %using the line defined above to identify pixels to be changed to 0.
    for pt2 = 1:x
        vary = eqcoeff(1)*pt2 + eqcoeff(2);
        Im_out2(round(vary):end,pt2) = 0;
    end

    Im_out3 = imcomplement(Im_out2);

    %Save image to Image_sequence_result
    im_write=['Image_sequence_result\20171031_Test7_MATLABed_9708_' IMG_NUM2 '.tif'];
    imwrite(Im_out3,im_write);

    close all;
end
```

A.3 Simpleware ScanIP automated mesh creation script (Python)

```
from scanip_api import *
import os

WD = "D:\\Somsubhro\\CT\\2018\\HQ3T11_WELD_BEAD\\05_scanIP\\1-900" # folder containing files to process
XYZ = (2161, 2566, 100) # image size in pixels in (X, Y, Z) format
XYZ_SIZE = 0.01 # pixel spacing in mm
PIXEL_TYPE = ImportOptions.UnsignedCharPixel  # pixel type
FILE_TYPE = ImportOptions.BinaryFile # file type
BYTE_ORDER = ImportOptions.LittleEndian # byte order

def process_and_mesh(file, count):
        #Threshold
        App.GetDocument().Threshold(1, 255, Doc.CreateNewMask, App.GetDocument().GetSliceIndices(Doc.OrientationYZ), Doc.OrientationYZ)

        #Mask renaming
        App.GetDocument().GetMaskByName("Mask 1").SetName("WELD_SECTION")

        #Cavity fill filter
        App.GetDocument().ApplyCavityFillFilter()

        #Island removal filter
        App.GetDocument().ApplyIslandRemovalFilter(2000)

        # 2018-12-28 20:09:20 - Recursive Gaussian filter
        App.GetDocument().ApplyRecursiveGaussianFilter(Doc.TargetMask, False, Sigma(1, 1, 1))

        #FE model creation
        App.GetDocument().CreateFeModel("Model 1")

        #Part creation
        App.GetDocument().GetModelByName("Model 1").AddMask(App.GetDocument().GetGenericMaskByName("WELD_SECTION"))

        #Model renaming
        App.GetDocument().GetModelByName("Model 1").SetName("CAVISL2000RG_3ROI_CYL_CUB")

        # 2018-12-17 18:44:19 - Model configuration modification
        App.GetDocument().GetActiveModel().SetHigherOrder(True)

        #Model configuration modification
        App.GetDocument().GetActiveModel().SetEditAdvancedParametersManuallyOnPart(App.GetDocument().GetActiveModel().GetPartByName("WELD_SECTION"), True)

        # 2018-12-17 19:18:59 - Model configuration modification
        App.GetDocument().GetActiveModel().SetAdditionalMeshQualityImprovementAllowOffSurface(False)

        # 2018-12-17 19:19:09 - Model configuration modification
        App.GetDocument().GetActiveModel().SetTargetMinimumEdgeLengthOnPart(App.GetDocument().GetActiveModel().GetPartByName("WELD_SECTION"), 0.5)

        # 2018-12-17 19:19:11 - Model configuration modification
        App.GetDocument().GetActiveModel().SetTargetMaximumErrorOnPart(App.GetDocument().GetActiveModel().GetPartByName("WELD_SECTION"), 0.05)

        # 2018-12-17 19:19:14 - Model configuration modification
        App.GetDocument().GetActiveModel().SetMaximumEdgeLengthOnPart(App.GetDocument().GetActiveModel().GetPartByName("WELD_SECTION"), 0.5)

        # 2018-12-17 19:19:16 - Model configuration modification
```

```
55.         App.GetDocument().GetActiveModel().SetSurfaceChangeRateOnPart(App.GetDocument
    ().GetActiveModel().GetPartByName("WELD_SECTION"), 60)
56.
57.         # 2018-12-17 19:19:20 - Model configuration modification
58.         App.GetDocument().GetActiveModel().SetTargetNumberElementsAcrossLayerOnPart(A
    pp.GetDocument().GetActiveModel().GetPartByName("WELD_SECTION"), 0.7)
59.
60.         #Contact to boundary creation (SURFACE)
61.         App.GetDocument().GetActiveModel().AddSurfaceContact(App.GetDocument().GetAct
    iveModel().GetPartByName("WELD_SECTION"), Model.Xmax)
62.         ##Name of contact surface created - "SF_WELD_SECTION_WITH_XMAX"
63.
64.         ###NODE SETS FOR BOUNDARY CONDITION
65.         #Node set to boundary creation
66.         App.GetDocument().GetActiveModel().AddNodeSet(App.GetDocument().GetActiveMode
    l().GetPartByName("WELD_SECTION"), Model.Xmin)
67.
68.         #Node set to boundary creation
69.         App.GetDocument().GetActiveModel().AddNodeSet(App.GetDocument().GetActiveMode
    l().GetPartByName("WELD_SECTION"), Model.Ymax)
70.
71.         #Node set to boundary creation
72.         App.GetDocument().GetActiveModel().AddNodeSet(App.GetDocument().GetActiveMode
    l().GetPartByName("WELD_SECTION"), Model.Zmin)
73.
74.         # 2017-11-06 14:04:37 - Node set to boundary creation
75.         App.GetDocument().GetActiveModel().AddNodeSet(App.GetDocument().GetActiveMode
    l().GetPartByName("WELD_SECTION"), Model.Zmax)
76.
77.         ###MESH REFINEMENT ZONES
78.         #INTERNAL ROI CYLINDER
79.         #+FE Free mesh refinement volume creation #INTERNAL
80.
81.         zcentre=count+0.5 #changed value based on new file size
82.
83.         ##Enter the values here
84.         xposition=10.715956
85.         yposition=16.76995
86.         xaxispos=0.345171
87.         yaxispos=0.927276
88.         zaxispos=0.144972
89.         angle=355.091644
90.
91.         #+FE Free mesh refinement volume creation
92.         App.GetDocument().GetActiveModel().CreateFeFreeMeshRefinementVolume(Doc.Cylin
    der, Vector3D(xposition, yposition, zcentre), Vector3D(0.2, 0.2, 10), Vector3D(xaxisp
    os, yaxispos, zaxispos), angle, True)
93.
94.         #+FE Free mesh refinement name modification
95.         App.GetDocument().GetModelByName("CAVISL2000RG_3ROI_CYL_CUB").GetFeFreeMeshRe
    finementVolumeByName("Cylinder1").SetName("INT_CYL")
96.
97.         #EXTERNAL ROI CYLINDER 1
98.         #+FE Free mesh refinement volume creation
99.         App.GetDocument().GetActiveModel().CreateFeFreeMeshRefinementVolume(Doc.Cylin
    der, Vector3D(xposition, yposition, zcentre), Vector3D(0.4, 0.4, 10), Vector3D(xaxisp
    os, yaxispos, zaxispos), angle, True)
100.
101.          #  +FE Free mesh refinement name modification
102.          App.GetDocument().GetModelByName("CAVISL2000RG_3ROI_CYL_CUB").GetFeFreeMesh
    RefinementVolumeByName("Cylinder1").SetName("EXT1_CYL")
103.
104.          #  +FE Free mesh refinement mesh size modification
105.          App.GetDocument().GetModelByName("CAVISL2000RG_3ROI_CYL_CUB").GetFeFreeMesh
    RefinementVolumeByName("EXT1_CYL").SetMeshSize(0.02)
106.
107.          #EXTERNAL ROI CYLINDER 2
108.          #+FE Free mesh refinement volume creation
```

```
109.          App.GetDocument().GetActiveModel().CreateFeFreeMeshRefinementVolume(Doc.Cyl
    inder, Vector3D(xposition, yposition, zcentre), Vector3D(1.0, 1.0, 10), Vector3D(xaxi
    spos, yaxispos, zaxispos), angle, True)
110.
111.          #  +FE Free mesh refinement name modification
112.          App.GetDocument().GetModelByName("CAVISL2000RG_3ROI_CYL_CUB").GetFeFreeMesh
    RefinementVolumeByName("Cylinder1").SetName("EXT2_CYL")
113.
114.          #  +FE Free mesh refinement mesh size modification
115.          App.GetDocument().GetModelByName("CAVISL2000RG_3ROI_CYL_CUB").GetFeFreeMesh
    RefinementVolumeByName("EXT2_CYL").SetMeshSize(0.04)
116.
117.          #Mesh generation
118.          App.GetDocument().GenerateMesh()
119.
120.  def main():
121.      for root, dirs, files in os.walk(WD):
122.          count=0
123.          for file in files:
124.              if file.endswith(".raw"):
125.                  ## import
126.                  App.GetInstance().ImportRawImage(
127.                      os.path.join(WD, file),
128.                      PIXEL_TYPE,
129.                      XYZ[0], XYZ[1], XYZ[2],
130.                      XYZ_SIZE, XYZ_SIZE, XYZ_SIZE,
131.                      0,
132.                      FILE_TYPE,
133.                      BYTE_ORDER,
134.                      CommonImportConstraints().SetWindowLevel(0, 0).SetCrop(0, 0, 0,
     XYZ[0], XYZ[1], XYZ[2]))
135.
136.                  ## process and mesh
137.                  process_and_mesh(file, count)
138.                  count=count-1.000
139.                  ## export, save and close
140.                  doc = App.GetDocument()
141.                  doc.ExportAbaqusVolume(os.path.join(root, file[:-
    4] + '.inp'), False)
142.                  doc.SaveAs(os.path.join(root, file[:-4] + '.sip'))
143.                  doc.Close()
144.
145.  main()
```

A.4 Script for converting mesh input file into ABAQUS analysis input file (Python)

```
# -*- coding: mbcs -*-
#
# Abaqus/CAE Release 6.13-1 replay file
# Internal Version: 2013_05_16-03.28.56 126354
# Run by sc24g14 on Wed Nov 08 09:04:37 2017
#
from abaqus import *
from abaqusConstants import *

from caeModules import *

import os

#remember to change the folder below
os.chdir(r"D:\Somsubhro\CT\2018\HQ3T11_WELD_BEAD\06_ABAQUS\abaqus_processed_INP_STACK") ##this has backward slash

#number of files and corresponding slices in the folder
begin=1
num_files=48
total_slices=num_files*100

for i in range(0,num_files):

    # display the currently running file number
    desc='Currently running file number - %d' %(begin+i)
    print(desc)

    #session.viewports['Viewport: 1'].setValues(displayedObject=a)

    model_name='%s_HQ3T11_RAW_%s_%s' %((begin+i),(100*(begin-1+i)+1),(100*(begin+i)))

    #remember to check the folder below
    inp_name='D:/Somsubhro/CT/2018/HQ3T11_WELD_BEAD/06_ABAQUS/scanIP_INP_STACK/%s_HQ3T11_RAW_%s_%s.inp' %((begin+i),(100*(begin-1+i)+1),(100*(begin+i)))

    mdb.ModelFromInputFile(name=model_name, inputFileName=inp_name) ##input has forward slash

    #assigning to a variable
    a = mdb.models[model_name].rootAssembly

    #Step creation
    mdb.models[model_name].StaticStep(name='Load', previous='Initial', maxNumInc=1000, initialInc=0.1)



    #LOAD
    region = a.surfaces['SF_WELD_SECTION_WITH_XMAX']
    mdb.models[model_name].Pressure(name='LOAD', createStepName='Load', region=region, magnitude=-100.0)

    #Boundary conditions
    #Xmin
    region = a.sets['NS_WELD_SECTION_WITH_XMIN']
    mdb.models[model_name].EncastreBC(name='XMIN', createStepName='Initial',
        region=region, localCsys=None)

    #Ymax
    region = a.sets['NS_WELD_SECTION_WITH_YMAX']
```

```
    mdb.models[model_name].YsymmBC(name='YMAX', createStepName='Initial',
        region=region, localCsys=None)

    #Zmax
    region = a.sets['NS_WELD_SECTION_WITH_ZMAX']
    mdb.models[model_name].ZsymmBC(name='ZMAX', createStepName='Initial',
        region=region, localCsys=None)

    #Zmin
    region = a.sets['NS_WELD_SECTION_WITH_ZMIN']
    mdb.models[model_name].ZsymmBC(name='ZMIN', createStepName='Initial',
        region=region, localCsys=None)

    a.regenerate()

    mdb.Job(name=model_name, model=model_name, description='', type=ANALYSIS,
        atTime=None, waitMinutes=0, waitHours=0, queue=None, memory=90,
        memoryUnits=PERCENTAGE, getMemoryFromAnalysis=True,
        explicitPrecision=SINGLE, nodalOutputPrecision=SINGLE, echoPrint=OFF,
        modelPrint=OFF, contactPrint=OFF, historyPrint=OFF, userSubroutine='',
        scratch='', multiprocessingMode=DEFAULT, numCpus=1, numGPUs=0)

    mdb.jobs[model_name].writeInput(consistencyChecking=OFF)
```

A.5 Different types of flaws counted and measured

A.5.1 Notch-like undercut

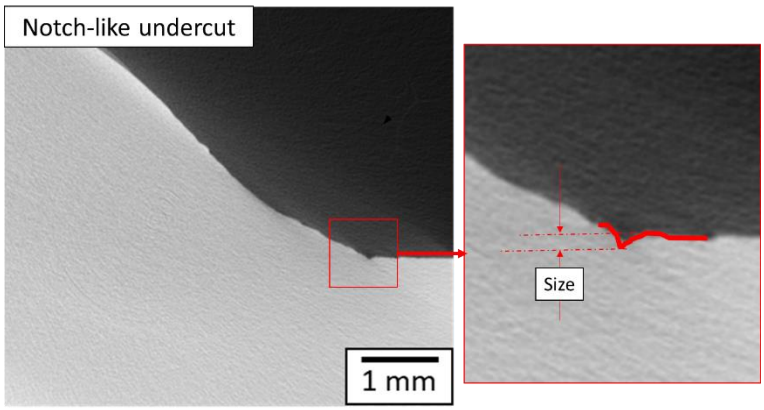

A.5.2 Internal flaw

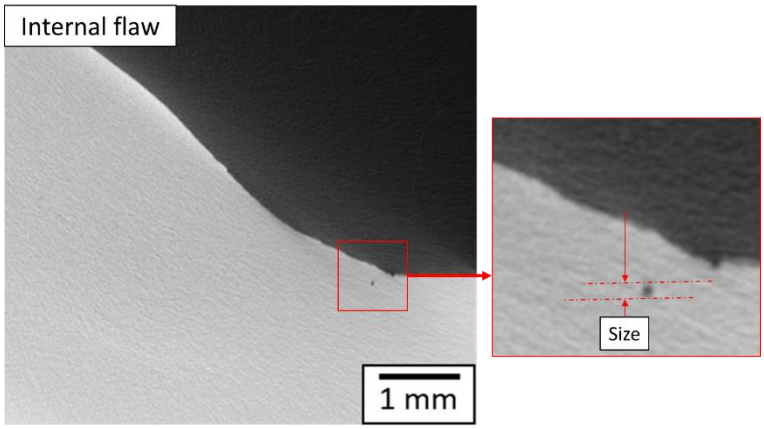

A.5.3 Cold lap

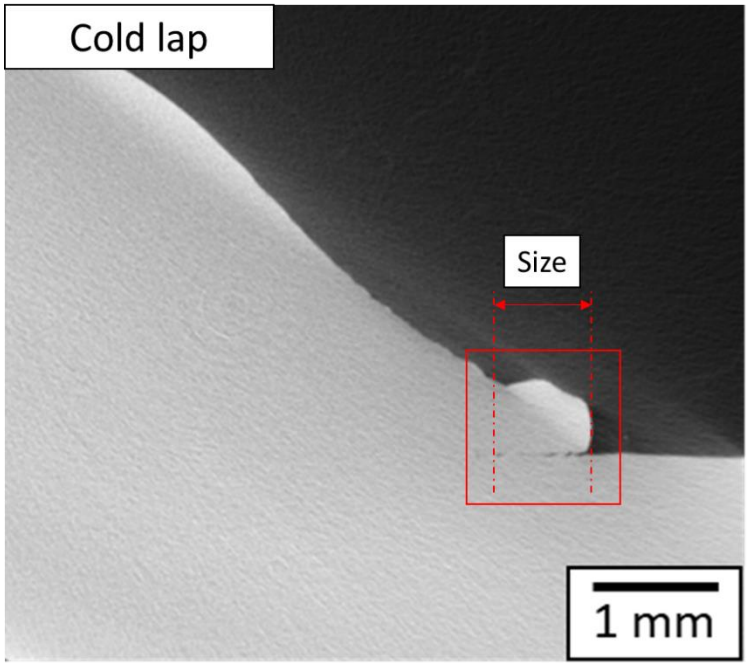

A.5.4 Spatter-like

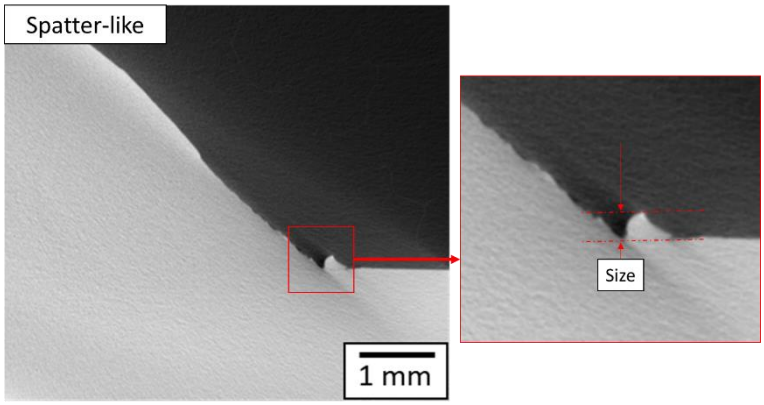

A.6 Script for submitting ABAQUS jobs to IRIDIS (University of Southampton HPC) for solving (BASH)

```
#!/bin/bash

#SBATCH --nodes=4                ### Number of nodes requested
#SBATCH --ntasks-per-node=40     ### Tasks per node
#SBATCH --time=24:00:00                  ### wall time
#SBATCH --dependency=afterany:317955          ###dependency

### mail aleter at start, end and aborton of execution
#SBATCH --mail-type=ALL
#SBATCH --mail-user=sc24g14@soton.ac.uk

#SBATCH -p batch

ABQ_INPUT=1_HQ1T15_RAW_1_100.inp                      # input file name
ABQ_NAME=1_HQ1T15_RAW_1_100                           # job name

# Abaqus doesn't seem to pull the nodelist correctly

node_list=$(scontrol show hostname ${SLURM_NODELIST} | sort -u)

mp_host_list="["
for host in ${node_list}; do
            mp_host_list="${mp_host_list}['$host',
${SLURM_CPUS_ON_NODE}],"
done

mp_host_list=$(echo ${mp_host_list} | sed -e "s/,$/]/")

### Build Environment file
env_file=abaqus_v6.env
cat << EOF > ${env_file}
scratch="$PWD"
mp_mode=MPI
mp_host_list=${mp_host_list}
EOF

### Need to unset SLURM's Global Task ID
unset SLURM_GTIDS

### load Abaqus
module load abaqus/6.14

### ABAQUS parallel execution
abaqus job=$ABQ_NAME input=$ABQ_INPUT cpus=${SLURM_NTASKS} mp_mode=mpi
interactive
```

A.7 Script for converting ABAQUS analysis output (.ODB) files into report (.RPT) files for specific quantities (Python)

```
#Load libraries
from abaqus import *
from abaqusConstants import *
from caeModules import *
from driverUtils import executeOnCaeStartup
import numpy as np

import os
os.chdir(
    r"D:\Somsubhro\CT\2018\HQ1T15_WELD_BEAD\06_ABAQUS\scratch")


# Import the ODB file
for i in range(0,50):

    # display the currently running file number
    desc='Currently running file number - %d' %(i+1)
    print(desc)

    name_odb = 'D:/Somsubhro/CT/2018/HQ1T15_WELD_BEAD/06_ABAQUS/HQ1T15_DATA_EXTRACTION/ELASTIC_CALC/ELASTIC_ODB_STACK/%s_HQ1T15_RAW_%s_%s.odb' %((i+1),(100*i+1),(100*(i+1)))

    o1 = session.openOdb(name_odb)

    #Viewport to make Abaqus write the .rpt file

    session.viewports['Viewport: 1'].setValues(displayedObject=o1)

    #This is to create an .rpt file which contains the output data.
    name_rpt = 'D:/Somsubhro/CT/2018/HQ1T15_WELD_BEAD/06_ABAQUS/HQ1T15_DATA_EXTRACTION/ELASTIC_CALC/MISES_RPT_STACK/%s_HQ1T15_RAW_%s_%s.rpt' %((i+1),(100*i+1),(100*(i+1)))

    # this is to create an ELEMENT_NODAL .rpt file.
    session.fieldReportOptions.setValues(printMinMax=OFF)
    session.writeFieldReport(
        fileName=name_rpt,
        append=ON, sortItem='Node Label', odb=o1, step=0, frame=1,
        outputPosition=ELEMENT_NODAL, variable=(('S', INTEGRATION_POINT, ((
        INVARIANT, 'Mises'), )), ))


    #Close ODB
    session.odbs[name_odb].close(

        )
```

A.8 Script for extracting SCF distribution from ABAQUS input and output report files (MATLAB)

Create an enveloping for loop which covers the whole code, and runs it for the number of files available.

```
masterlist='20180215_TEST6_TITLES_LIST.xlsx';

masterdata = importdata(masterlist,'\t');

totalnum = length(masterdata.textdata(:,1));

wb1=waitbar(0, 'Overall Progress');

for count=1:totalnum
```

```
    %Clear all variables
    clear numval valarray maxarray rpt_path inp_path fid fid2 inpbuffer line_num INPdata
cylCentre correctNodes outputData sortData numval2 valarray2

    fprintf('0. Now beginning File No. %d \n', count);
    waitbar((count)/(totalnum),wb1);

    s_No = count;
    slice_First = ((count-1)*150+1);
    slice_Last = ((count)*150);
```

Read stress S11

```
    % as the last file has a different set of slice numbers.
    if count==65
        rpt_path='RPT_STACK\65_Test6_RAW_9601_9691.rpt';
    else
        rpt_path=['RPT_STACK\' num2str(s_No) '_Test6_RAW_' num2str(slice_First) '_'
num2str(slice_Last) '.rpt'];
    end

    RPT = importdata(rpt_path, ' ', 22); %the middle bit is the delimiter
```

Beginning fix of ELEMENT_NODAL rpt file

```
    numval = unique(RPT.data(:,2)); %count of unique node labels

    %Placing in variables otherwise "length(variable)" description in a for
    %loop takes a lot of time.

    j = length(numval);

    k = length(RPT.data(:,3));


    %array which will have all the maximum values
    maxarray = zeros(j,2);

    %first column of maxarray should be the list of node labels
    maxarray(:,1)=numval(:,1);
```

```
    %this is to set a flag at the index of RPT.data(2nd column - node
    %labels). As soon  as the countall for loop touches a point where the
    %node label changes value, it stores that index and uses it to jump to
    %that point in the next for loop. Saves a few iterations.
    countend=1;


    %looping over the total number of values I eventually need (unique node
    %labels)



    for countnode = 1:j

        %waitbar(countnode/j,wb3); %taking too much time. Don't use
        %waitbars inside massive for loops.

        % ever changing max value which fastens the for loop process
        max_now=0;

        %looping over the actual set of data (consisting of repeated node
        %labels)
        for countall = countend:k

            % if the node label sticks to countnode (1, 2, .....), it saves
            % the values for one particular node label, and ultimately we
            % take the max later.
            if RPT.data(countall,2) == countnode
                max_now = max(max_now,RPT.data(countall,3));
                continue; %brings the control back to the top of the loop.

            % this elseif is used to save the indice where the node label
            % changes. It is saved in countend which is used in looping.
            elseif RPT.data(countall,2) == countnode+1
                countend = countall;
                break;
            end
        end


        %saving the max value for a particular node label into the max
        %array.
        maxarray(countnode,2) = max_now;

    end

    fprintf('1. Done importing data (Node_label and S11) - file No. %d \n', count); %to
keep track of where the code is
```

Read X Y Z coordinates from INP

```
    %Read the file (take scanIP generated INPs, not abaqus processed INPs)
    if count==65
        inp_path='INP_STACK\65_Test6_RAW_9601_9691.inp';
    else
        inp_path=['INP_STACK\' num2str(s_No) '_Test6_RAW_' num2str(slice_First) '_'
num2str(slice_Last) '.inp'];
    end
```

```
    fid = fopen(inp_path, 'r');

    fprintf('2. fopen done - file No. %d \n', count); %to keep track of where the code is

    %saving the input file in a variable
    inpbuffer = textscan(fid, '%s', 'delimiter', '\n');

    fprintf('3. text scan done - file No. %d \n', count'); %to keep track of where the code
is

    %Define Header
    header='*NODE';

    %finding the line in inp file
    line_num = find(strcmp(inpbuffer{1}, header), 1, 'first');

    %to adjust with the scanip .inp file
    line_num = line_num+3;
    fclose(fid);
    fprintf('4. line found - file No. %d \n', count); %to keep track of where the code is

    %should open it again as otherwise it was giving errors. This is to
    %take the data from INP file into MATLAB.
    fid2 = fopen(inp_path, 'r');
    INPdata = textscan(fid2, '%f, %f, %f, %f', 'Headerlines', line_num); %the '%f's define
the columns.
    INPdata = [INPdata{1}, INPdata{2}, INPdata{3}, INPdata{4}];
    fclose(fid2);

    fprintf('5. INP file read - file No. %d \n', count); %to keep track of where the code
is
```

Define cylinder for interest

```
    %The cylinder definition can be picked from the Coordinate calculator for
    %scanIP
    %In masterdata variable, columns 4 and 5 describe the X and Y
    %coordinate of the ROI cylinder centre resp.
    cylCentre = [masterdata.data(count,4), masterdata.data(count,5)];
    radius = 1;
```

Find coordinates close to the defined centre of cylinder

```
    %Uses a pythagoras theorem logic.
    correctNodes = find(sqrt((cylCentre(1)-INPdata(:,2)).^2+(cylCentre(2)-
INPdata(:,3)).^2)<radius^2);

    fprintf('6. Correct nodes found - file No. %d \n', count); %to keep track of where the
code is
```

Find order of Node labels in RPT and INP data

```
    [~,~,listOrder] = intersect(maxarray(:,1), INPdata(:,1));
```

```
    fprintf('7. Order of labels done - file No. %d \n', count); %to keep track of where the
code is
```

Output data only for valid nodes

```
    outputData = [INPdata(listOrder(correctNodes),4), maxarray(correctNodes,2)];

    fprintf('8. Output data created - file No. %d \n', count); %to keep track of where the
code is

    %sorting it by node label to keep it simple
    sortData = sortrows(outputData,1);
```

Calculations of max values

```
    %defining resolution of max SCF extraction
    maxres = 0.05; % in mm

    %number of iterations
    numval2 = round((max(sortData(:,1)))/(maxres));

    sDn = length(sortData(:,1));

    %defining empty arrays
    valarray2 = NaN(sDn,1);
    mainarray = zeros(numval2,5);

    wb2=waitbar(0, 'Max Value Finding Process');

    %two for loops -
    %first loop runs for the number of values that you need. This is to be able
    %to define the max-resolution defined limits between which I need the max
    %SCF.

    for i = 1:numval2
        waitbar(i/numval2,wb2);
        lim1 = ((i-1)*maxres);
        lim2 = (i*maxres);

        %second loop runs for the entire length of the sortData array, and
        %checks for z coordinates which lie beteween the limits defined above.
        %Then, prints that value into valarray
        for j = 1:sDn
            if sortData(j,1) >= lim1 && sortData(j,1) <= lim2
                valarray2(j,1) = sortData(j,2);
            end
        end
        % back in the first loop, only the maximum values are written into
        % maxarray by evaluating the max of the valarray from the previous
        % loop.
        % the if is for the last file again. Make sure to change it
        % accordingly for each scan.
        if count==65
            mainarray(i,1) = ((i+((count-1)*(numval2+5))-1)*0.05);
            mainarray(i,2) = max(valarray2);
            mainarray(i,3) = mean(valarray2,'omitnan');
            mainarray(i,4) = median(valarray2,'omitnan');
            mainarray(i,5) = std(valarray2,'omitnan');
```

```
        else
            mainarray(i,1) = ((i+((count-1)*numval2)-1)*0.05);
            mainarray(i,2) = max(valarray2);
            mainarray(i,3) = mean(valarray2,'omitnan');
            mainarray(i,4) = median(valarray2,'omitnan');
            mainarray(i,5) = std(valarray2,'omitnan');
        end

        maxFile = '20180301_Test6_STAT_SCF_Distribution_NEW.txt';

        %zeroing valarray so that maxarray takes the max after each iteration.
        valarray2 = NaN(sDn,1);
    end

    dlmwrite(maxFile,mainarray,'-append','newline','pc','delimiter','\t');

    %delete the wait bar for max value progress
    delete(wb2);
end

delete(wb1);
fprintf('DONE');
```

A.9 Specimen-wise elastic SCF distributions from 3D FE analysis

A.9.1 HQ_T6

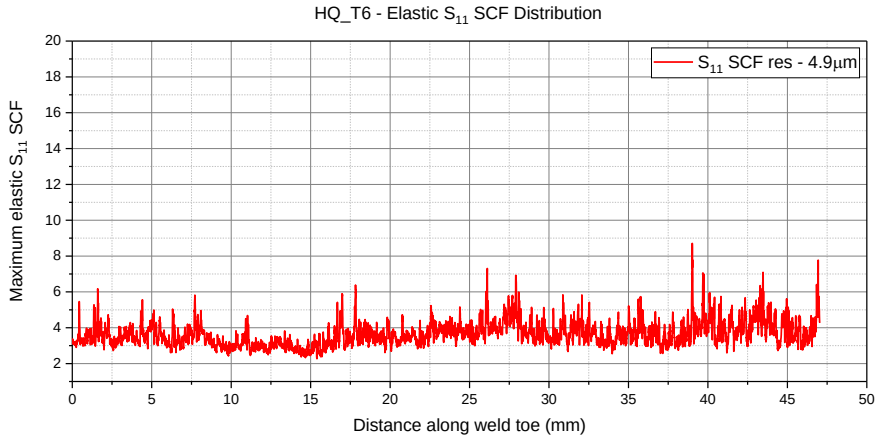

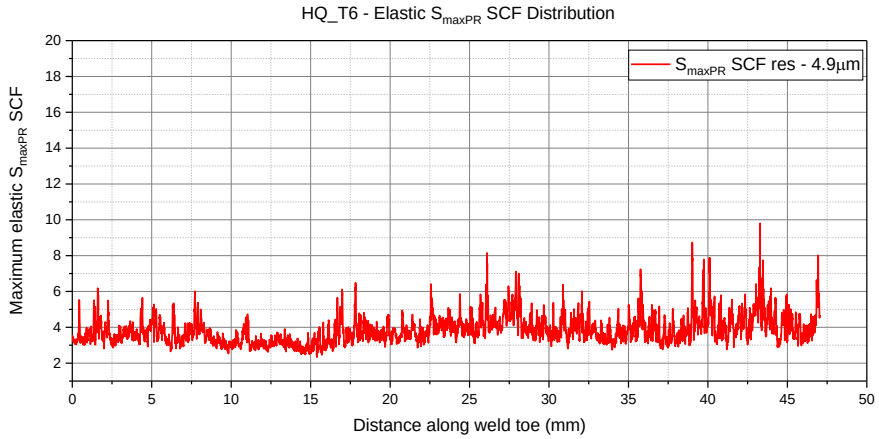

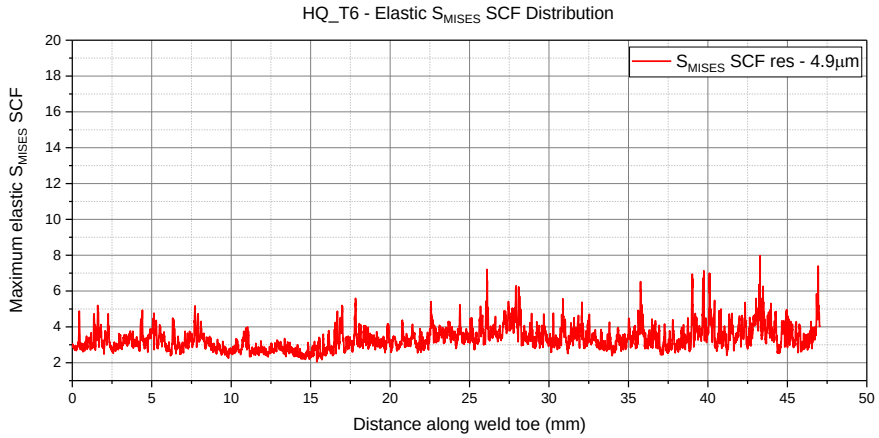

A.9.2 HQ_T7

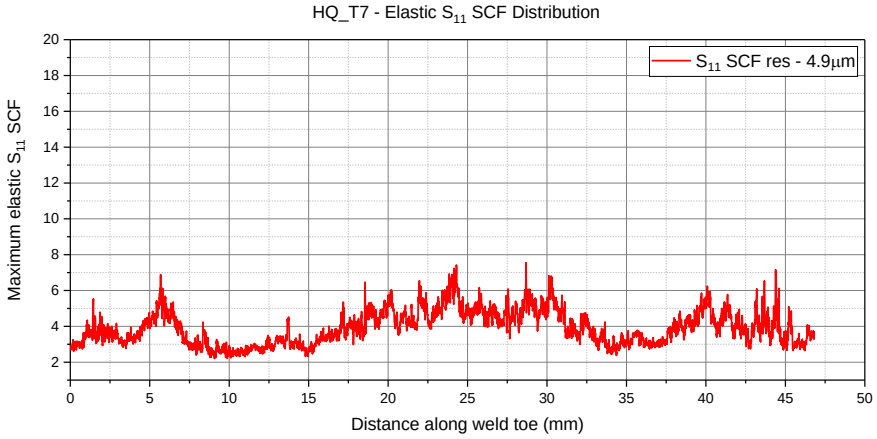
HQ_T7 - Elastic S11 SCF Distribution
S11 SCF res - 4.9µm
Maximum elastic S11 SCF
Distance along weld toe (mm)

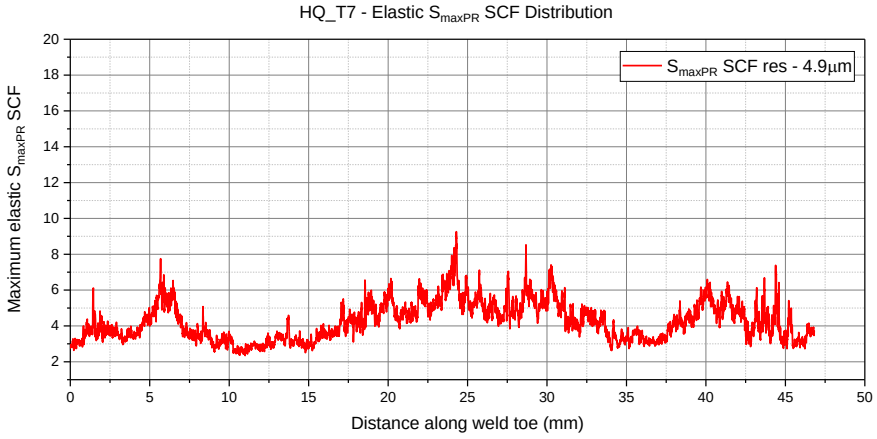
HQ_T7 - Elastic SmaxPR SCF Distribution
SmaxPR SCF res - 4.9µm
Maximum elastic SmaxPR SCF
Distance along weld toe (mm)

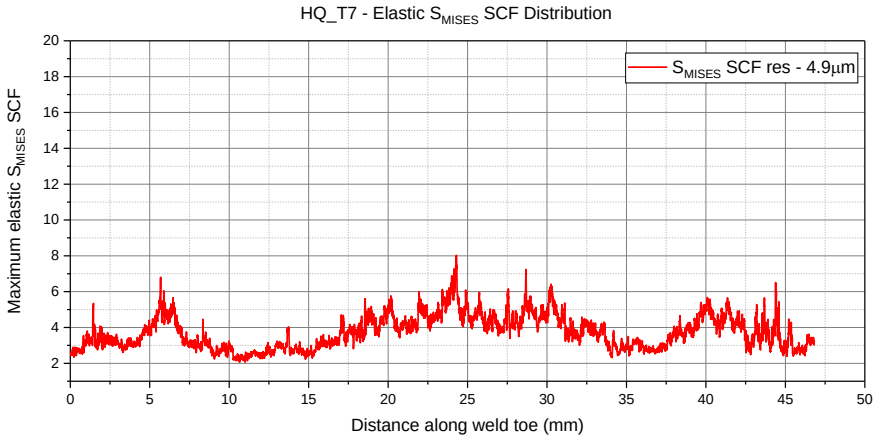
HQ_T7 - Elastic SMISES SCF Distribution
SMISES SCF res - 4.9µm
Maximum elastic SMISES SCF
Distance along weld toe (mm)

A.9.3 HQ_T8

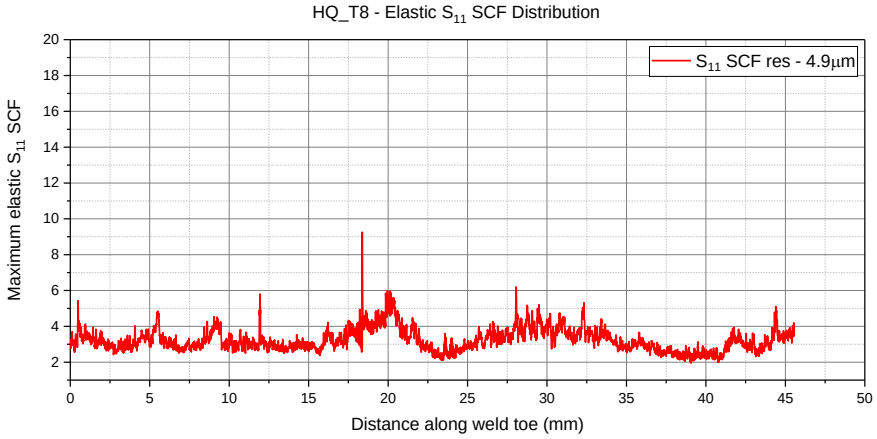
HQ_T8 - Elastic S11 SCF Distribution
S11 SCF res - 4.9µm
Maximum elastic S11 SCF
Distance along weld toe (mm)

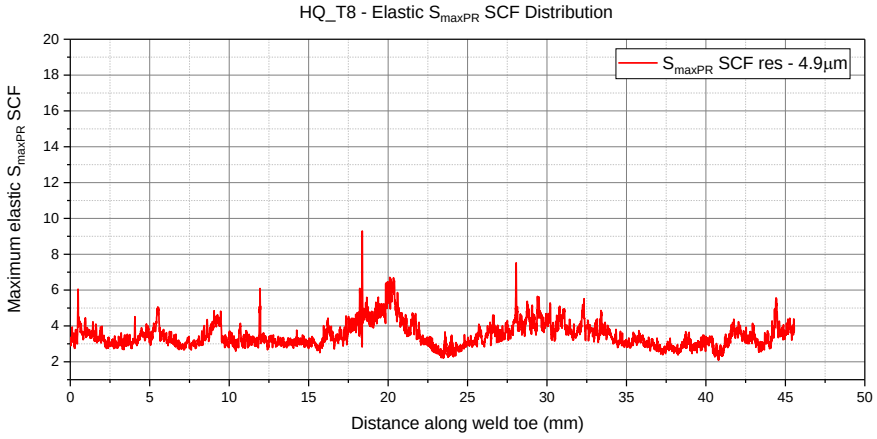
HQ_T8 - Elastic SmaxPR SCF Distribution
SmaxPR SCF res - 4.9µm
Maximum elastic SmaxPR SCF
Distance along weld toe (mm)

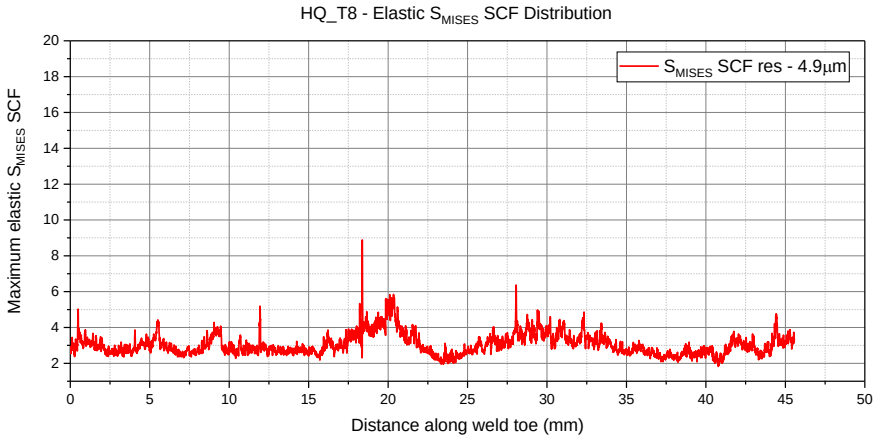
HQ_T8 - Elastic SMISES SCF Distribution
SMISES SCF res - 4.9µm
Maximum elastic SMISES SCF
Distance along weld toe (mm)

A.9.4 HQ_T11

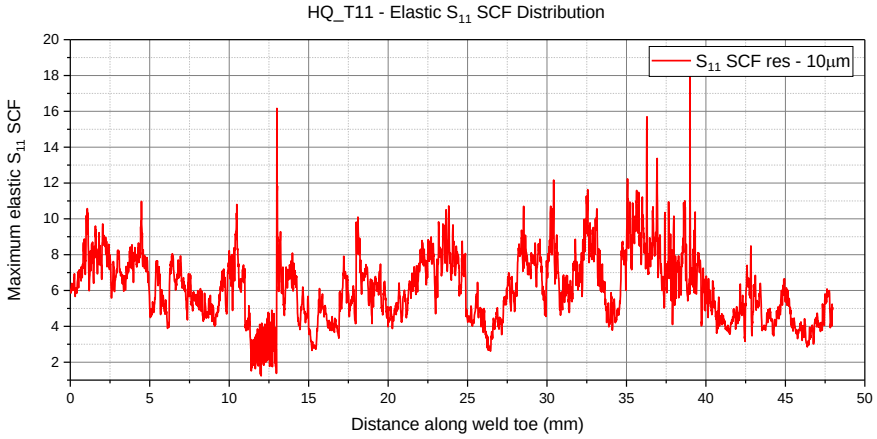
HQ_T11 - Elastic S11 SCF Distribution
S11 SCF res - 10µm
Maximum elastic S11 SCF
Distance along weld toe (mm)

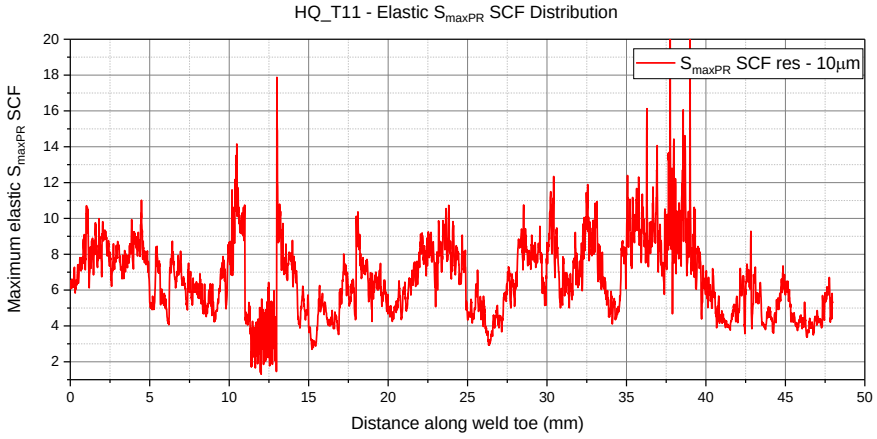
HQ_T11 - Elastic SmaxPR SCF Distribution
SmaxPR SCF res - 10µm
Maximum elastic SmaxPR SCF
Distance along weld toe (mm)

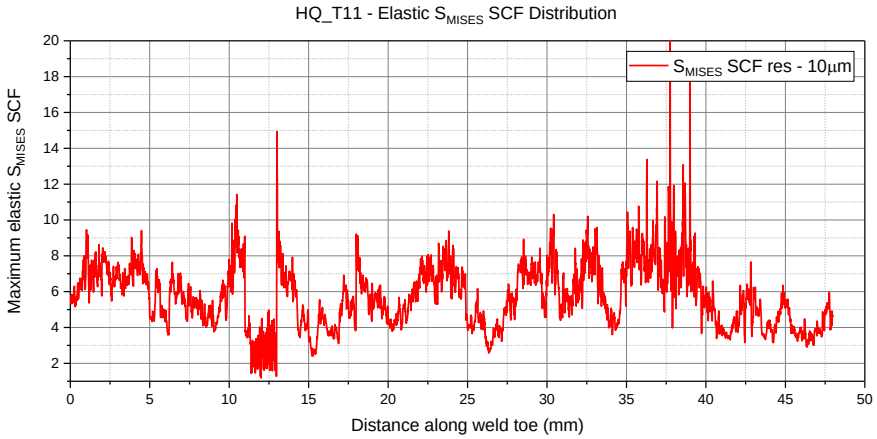
HQ_T11 - Elastic SMISES SCF Distribution
SMISES SCF res - 10µm
Maximum elastic SMISES SCF
Distance along weld toe (mm)

A.9.5 HQ_T15

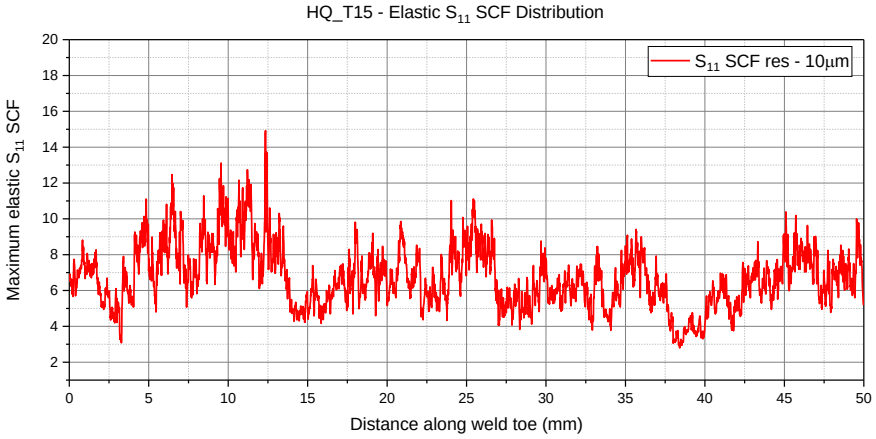
HQ_T15 - Elastic S11 SCF Distribution
S11 SCF res - 10µm
Maximum elastic S11 SCF
Distance along weld toe (mm)

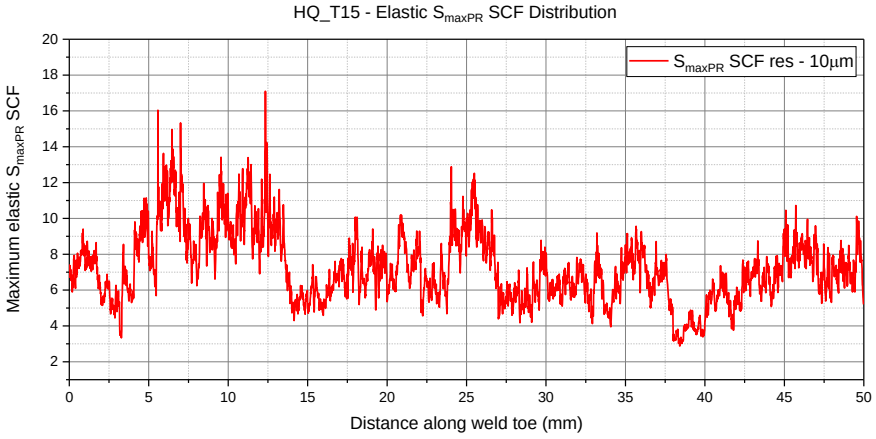
HQ_T15 - Elastic SmaxPR SCF Distribution
SmaxPR SCF res - 10µm
Maximum elastic SmaxPR SCF
Distance along weld toe (mm)

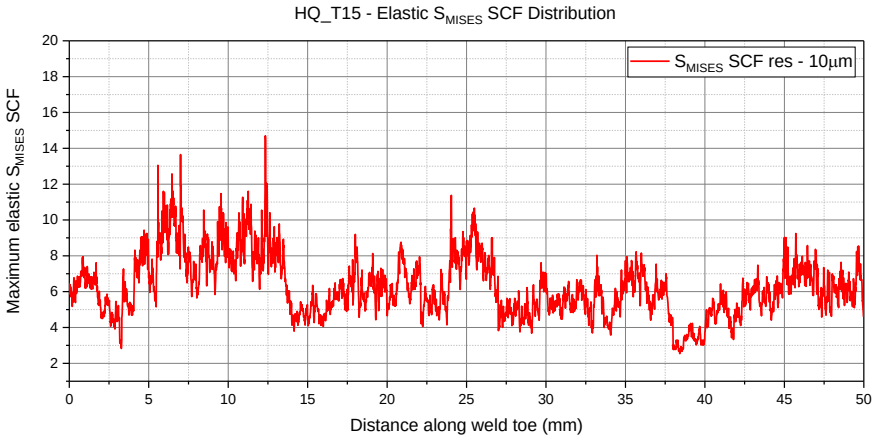
HQ_T15 - Elastic SMISES SCF Distribution
SMISES SCF res - 10µm
Maximum elastic SMISES SCF
Distance along weld toe (mm)

A.9.6 LQ_T10

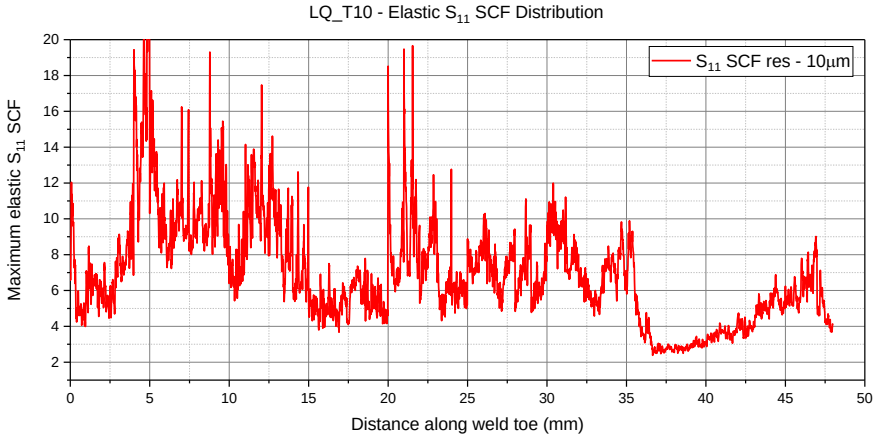
LQ_T10 - Elastic S11 SCF Distribution
S11 SCF res - 10μm
Maximum elastic S11 SCF
Distance along weld toe (mm)

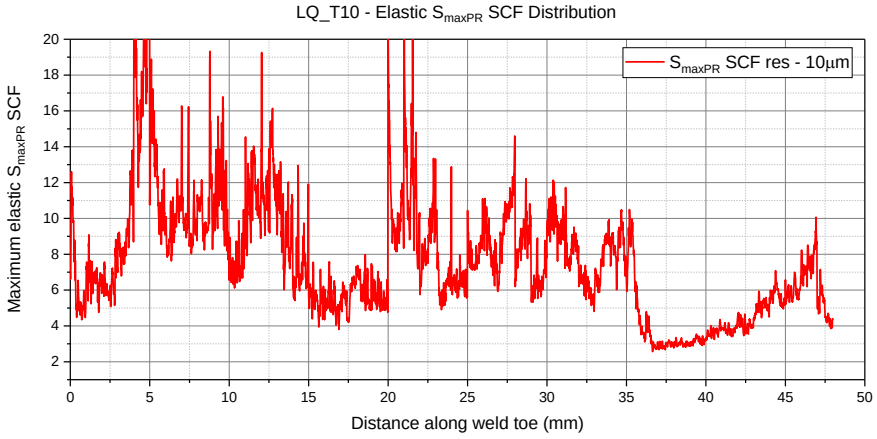
LQ_T10 - Elastic SmaxPR SCF Distribution
SmaxPR SCF res - 10μm
Maximum elastic SmaxPR SCF
Distance along weld toe (mm)

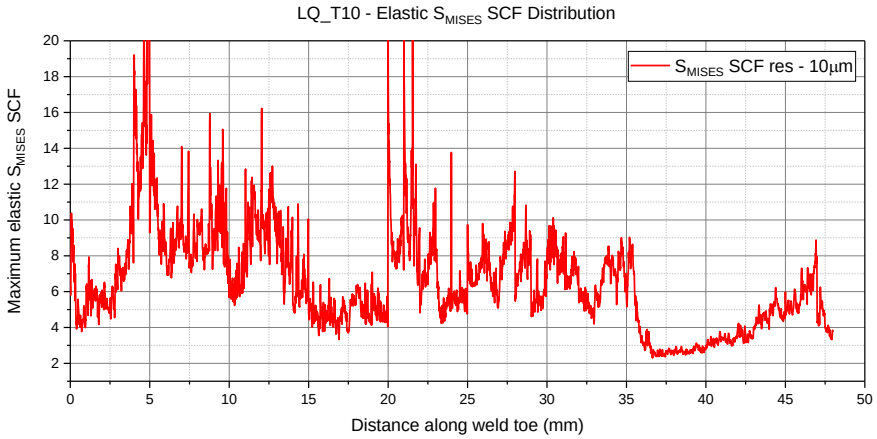
LQ_T10 - Elastic SMISES SCF Distribution
SMISES SCF res - 10μm
Maximum elastic SMISES SCF
Distance along weld toe (mm)

A.9.7 LQ_T12

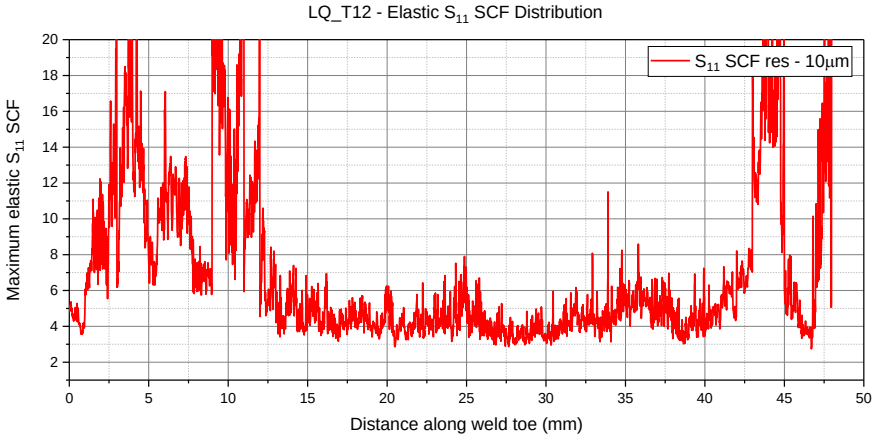
LQ_T12 - Elastic S_{11} SCF Distribution
S_{11} SCF res - 10μm
Maximum elastic S_{11} SCF
Distance along weld toe (mm)

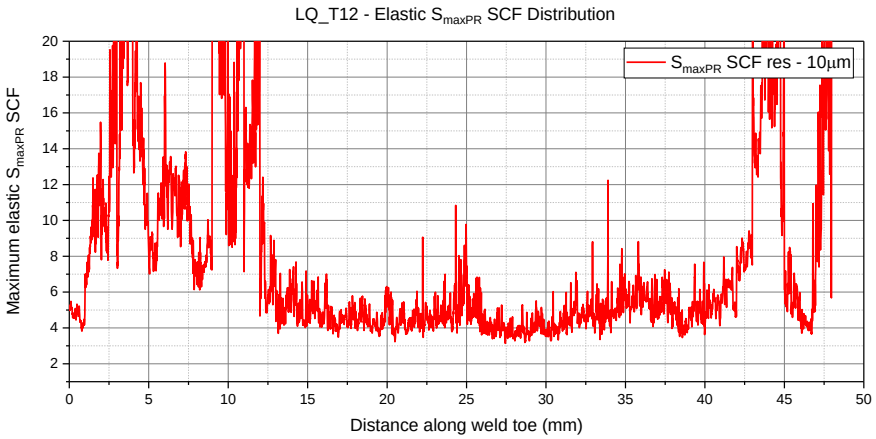
LQ_T12 - Elastic S_{maxPR} SCF Distribution
S_{maxPR} SCF res - 10μm
Maximum elastic S_{maxPR} SCF
Distance along weld toe (mm)

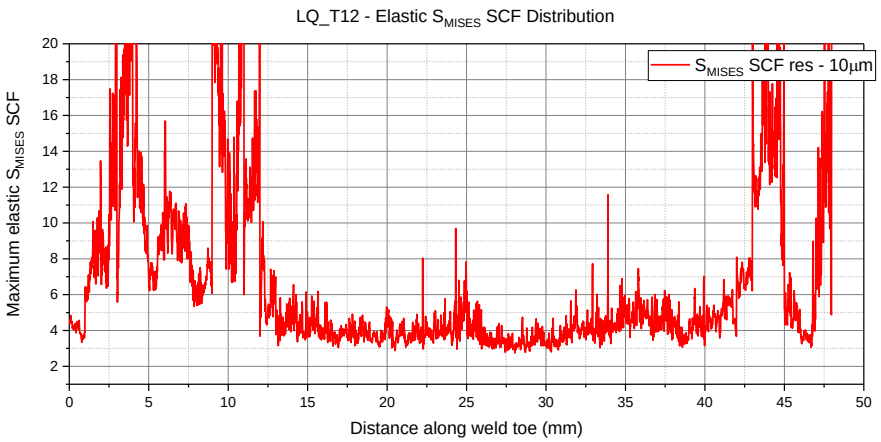
LQ_T12 - Elastic S_{MISES} SCF Distribution
S_{MISES} SCF res - 10μm
Maximum elastic S_{MISES} SCF
Distance along weld toe (mm)

A.10 Specimen-wise elastic-plastic SCF and strain distributions from 3D FE analysis

A.10.1 HQ_T6

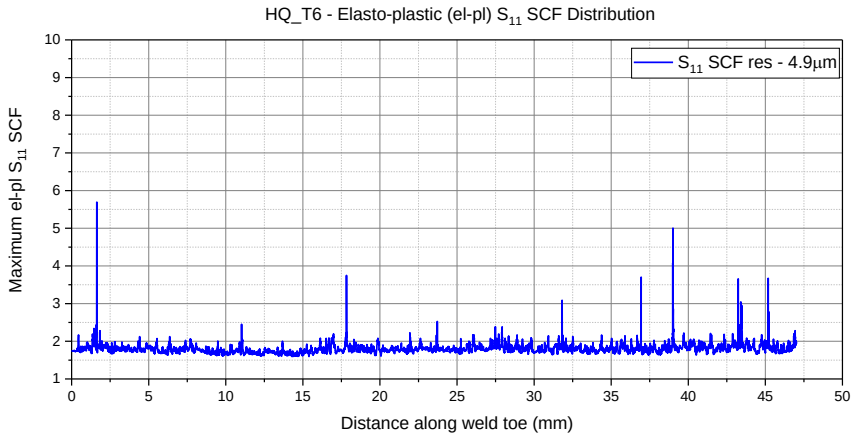

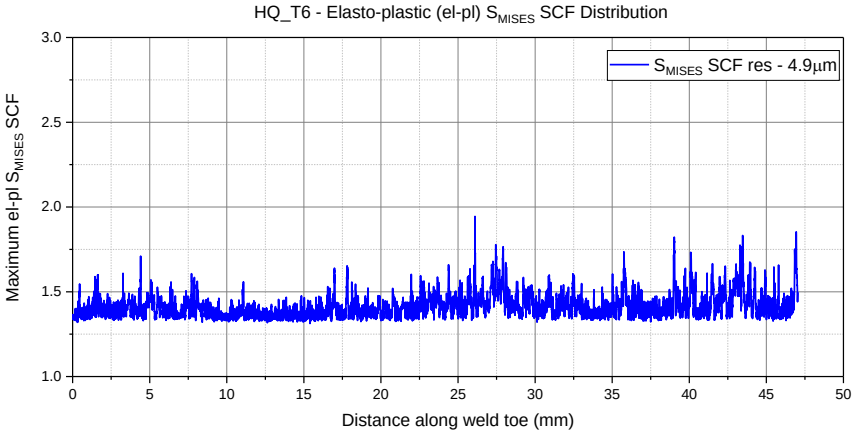

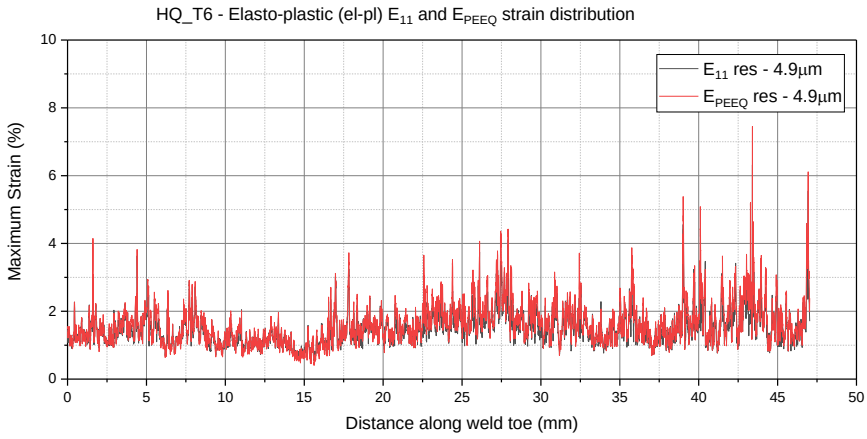

A.10.2 HQ_T7

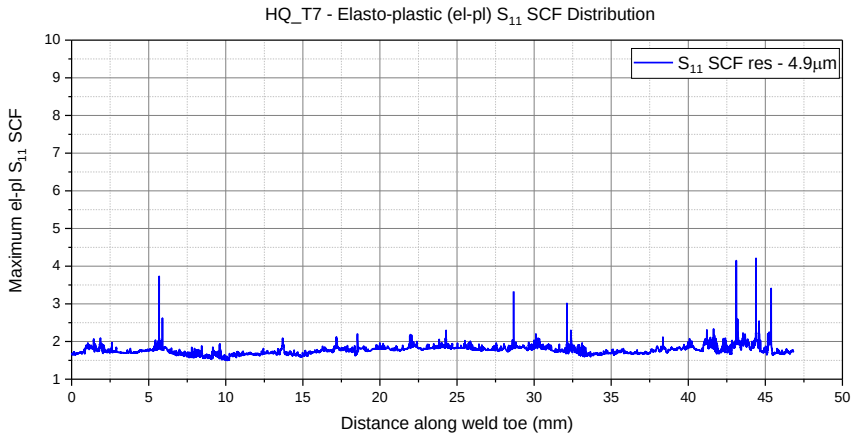
HQ_T7 - Elasto-plastic (el-pl) S11 SCF Distribution
S11 SCF res - 4.9µm
Maximum el-pl S11 SCF
Distance along weld toe (mm)

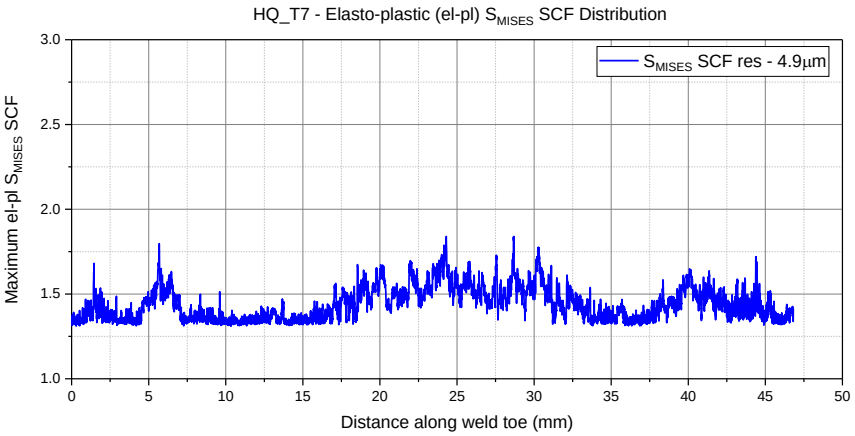
HQ_T7 - Elasto-plastic (el-pl) SMISES SCF Distribution
SMISES SCF res - 4.9µm
Maximum el-pl SMISES SCF
Distance along weld toe (mm)

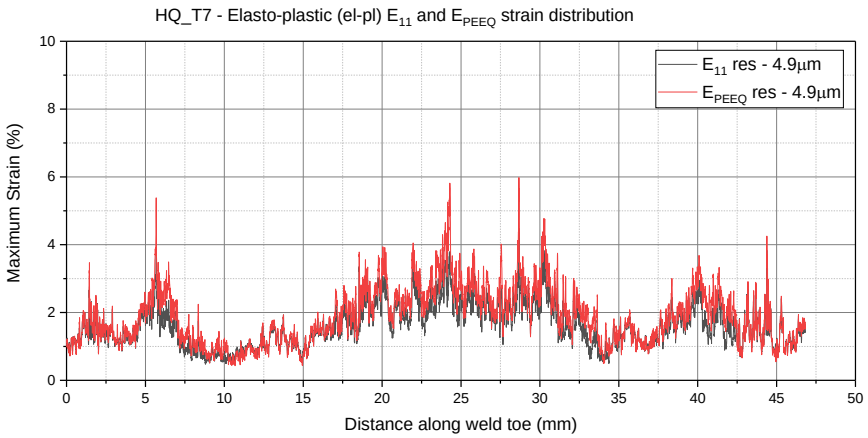
HQ_T7 - Elasto-plastic (el-pl) E11 and EPEEQ strain distribution
E11 res - 4.9µm
EPEEQ res - 4.9µm
Maximum Strain (%)
Distance along weld toe (mm)

A.10.3 HQ_T8

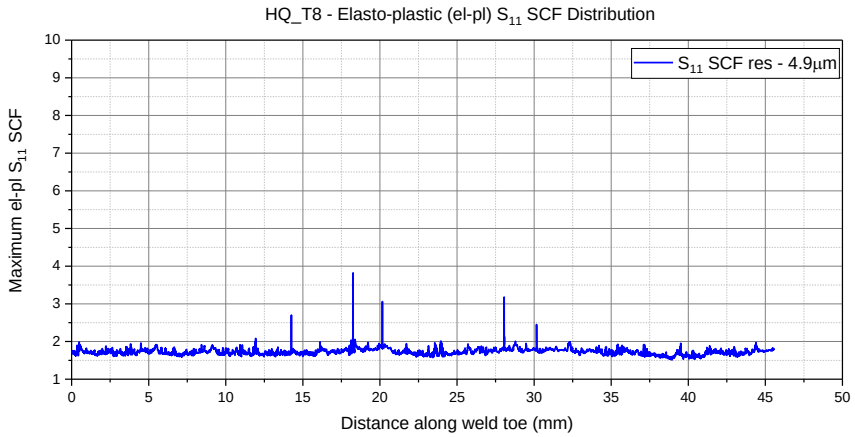
HQ_T8 - Elasto-plastic (el-pl) S11 SCF Distribution
S11 SCF res - 4.9µm
Maximum el-pl S11 SCF
Distance along weld toe (mm)

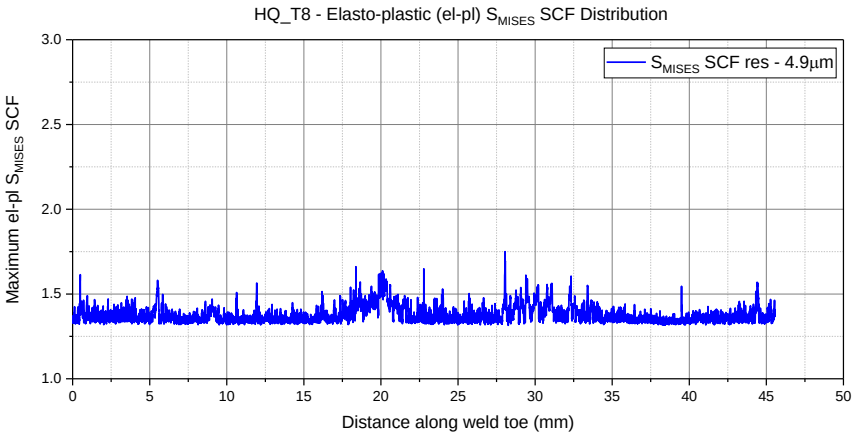
HQ_T8 - Elasto-plastic (el-pl) SMISES SCF Distribution
SMISES SCF res - 4.9µm
Maximum el-pl SMISES SCF
Distance along weld toe (mm)

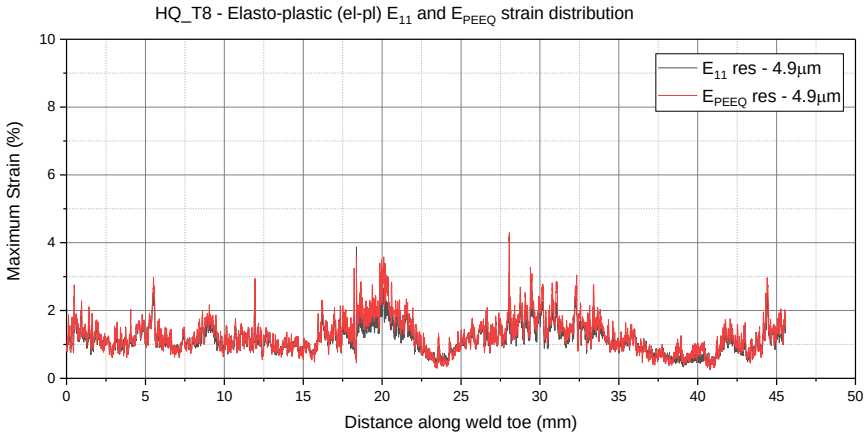
HQ_T8 - Elasto-plastic (el-pl) E11 and EPEEQ strain distribution
E11 res - 4.9µm
EPEEQ res - 4.9µm
Maximum Strain (%)
Distance along weld toe (mm)

A.10.4 HQ_T11

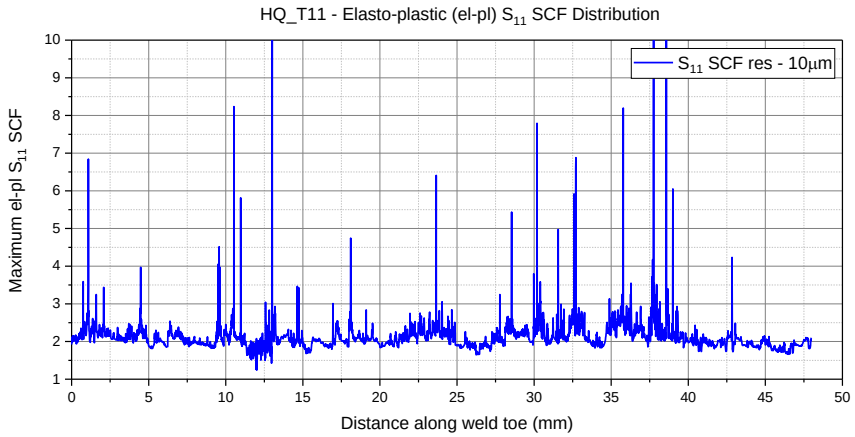
HQ_T11 - Elasto-plastic (el-pl) S11 SCF Distribution
S11 SCF res - 10μm
Maximum el-pl S11 SCF
Distance along weld toe (mm)

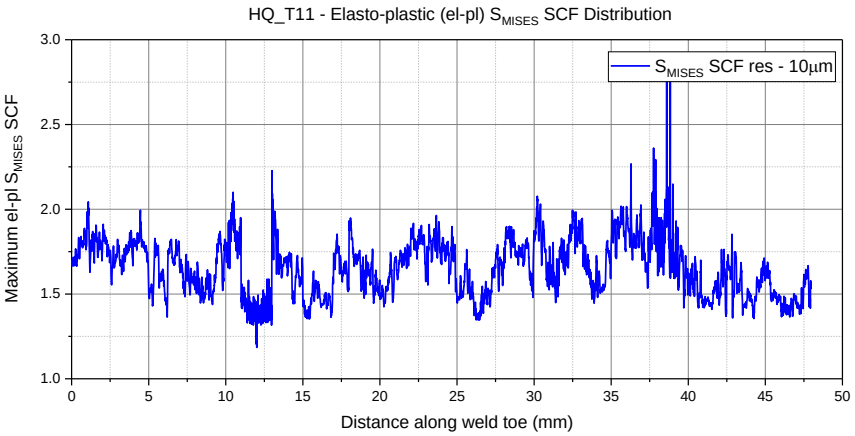
HQ_T11 - Elasto-plastic (el-pl) SMISES SCF Distribution
SMISES SCF res - 10μm
Maximum el-pl SMISES SCF
Distance along weld toe (mm)

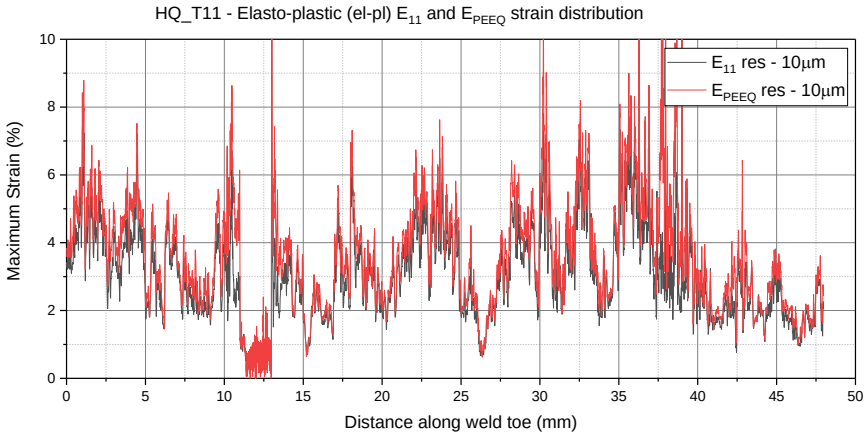
HQ_T11 - Elasto-plastic (el-pl) E11 and EPEEQ strain distribution
E11 res - 10μm
EPEEQ res - 10μm
Maximum Strain (%)
Distance along weld toe (mm)

A.10.5 HQ_T15

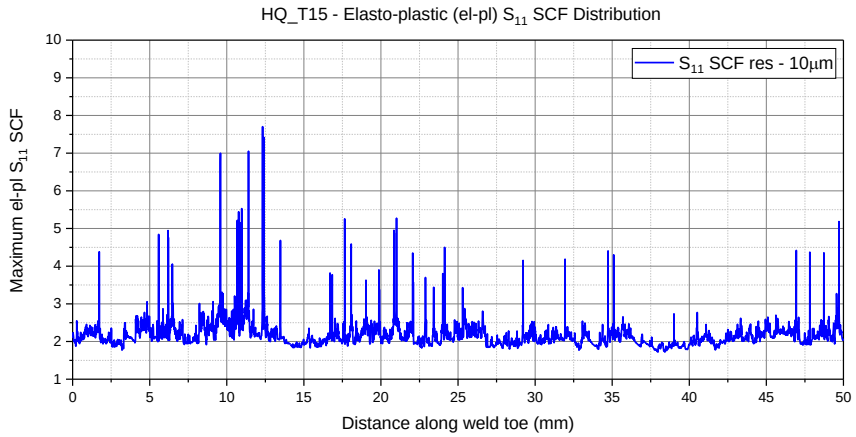
HQ_T15 - Elasto-plastic (el-pl) S11 SCF Distribution
S11 SCF res - 10μm
Maximum el-pl S11 SCF
Distance along weld toe (mm)

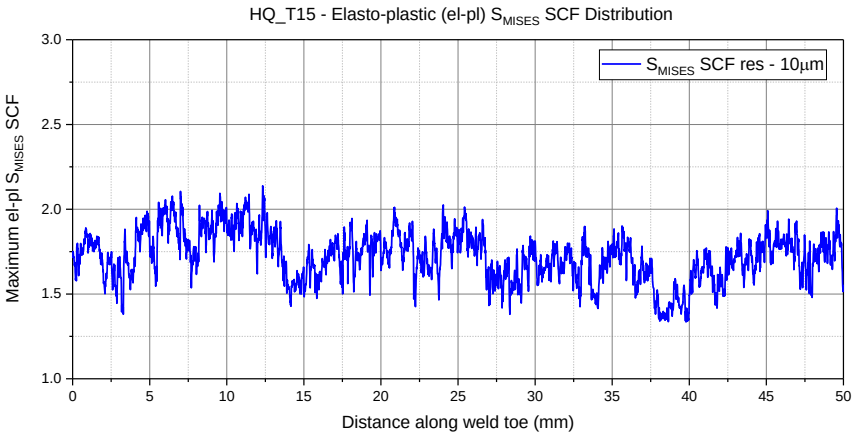
HQ_T15 - Elasto-plastic (el-pl) SMISES SCF Distribution
SMISES SCF res - 10μm
Maximum el-pl SMISES SCF
Distance along weld toe (mm)

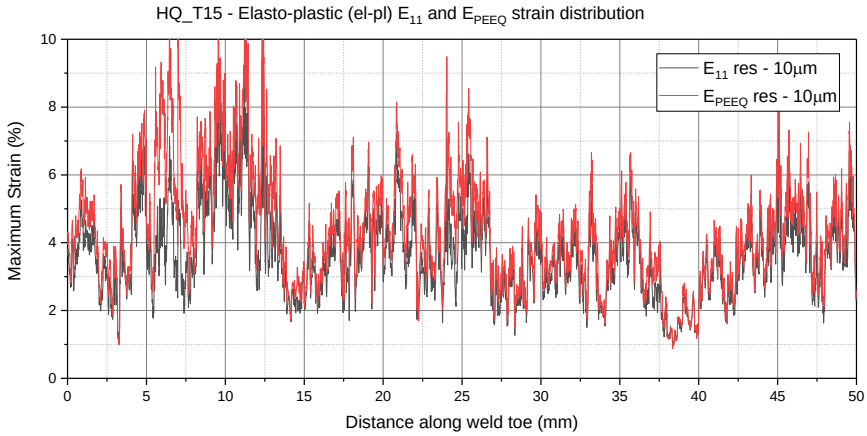
HQ_T15 - Elasto-plastic (el-pl) E11 and EPEEQ strain distribution
E11 res - 10μm
EPEEQ res - 10μm
Maximum Strain (%)
Distance along weld toe (mm)

A.10.6 LQ_T10

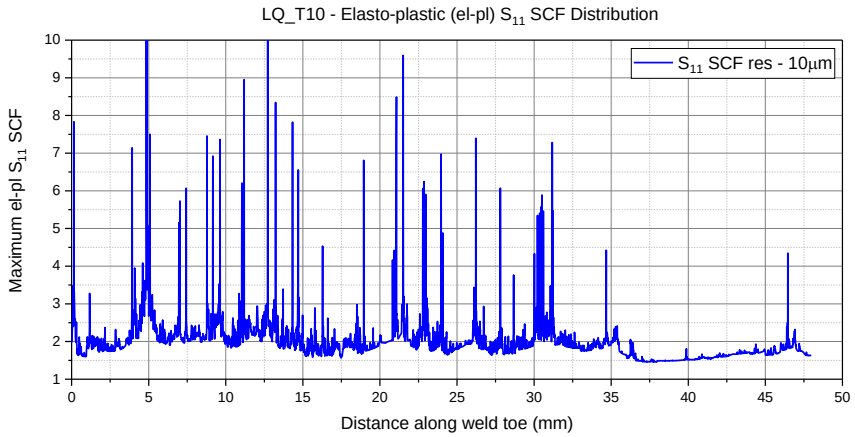
LQ_T10 - Elasto-plastic (el-pl) S11 SCF Distribution
S11 SCF res - 10µm
Maximum el-pl S11 SCF
Distance along weld toe (mm)

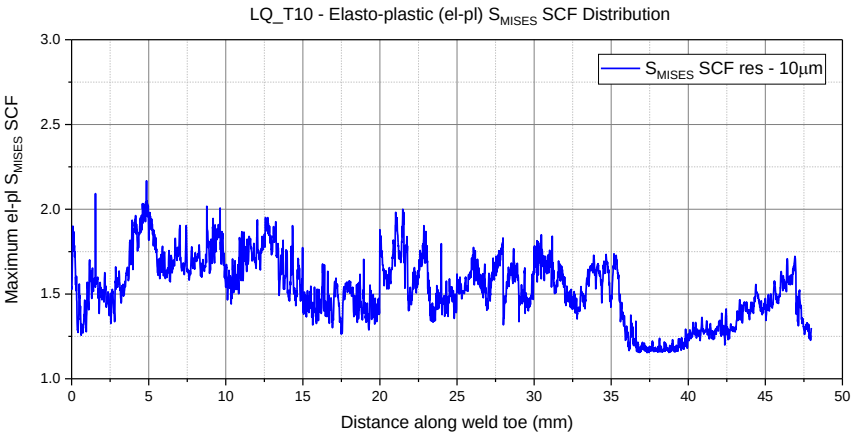
LQ_T10 - Elasto-plastic (el-pl) SMISES SCF Distribution
SMISES SCF res - 10µm
Maximum el-pl SMISES SCF
Distance along weld toe (mm)

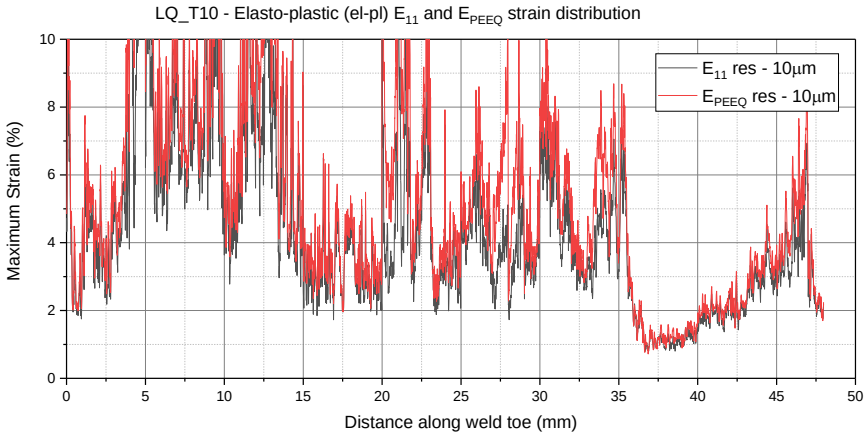
LQ_T10 - Elasto-plastic (el-pl) E11 and EPEEQ strain distribution
E11 res - 10µm
EPEEQ res - 10µm
Maximum Strain (%)
Distance along weld toe (mm)

A.10.7 LQ_T12

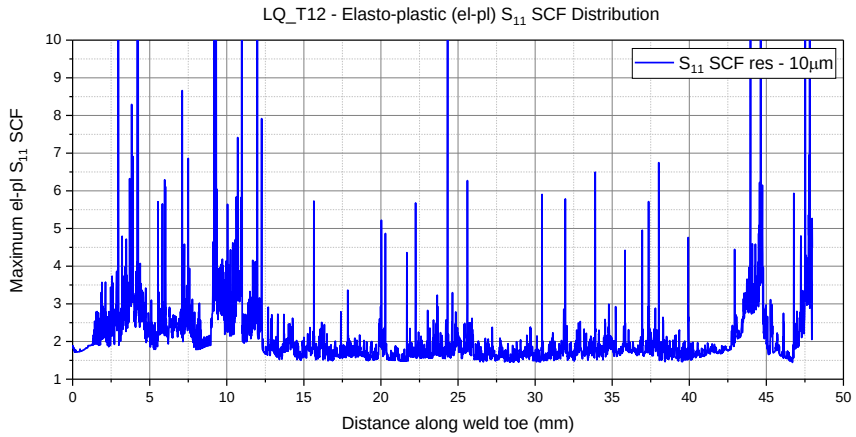
LQ_T12 - Elasto-plastic (el-pl) S11 SCF Distribution
S11 SCF res - 10μm
Maximum el-pl S11 SCF
Distance along weld toe (mm)

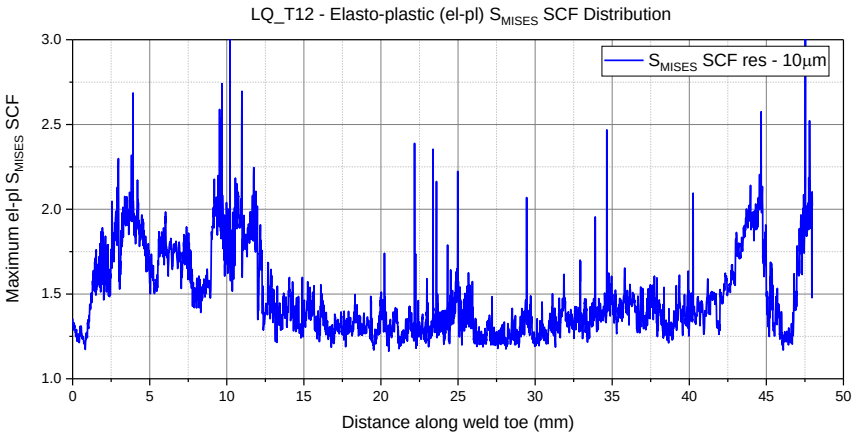
LQ_T12 - Elasto-plastic (el-pl) SMISES SCF Distribution
SMISES SCF res - 10μm
Maximum el-pl SMISES SCF
Distance along weld toe (mm)

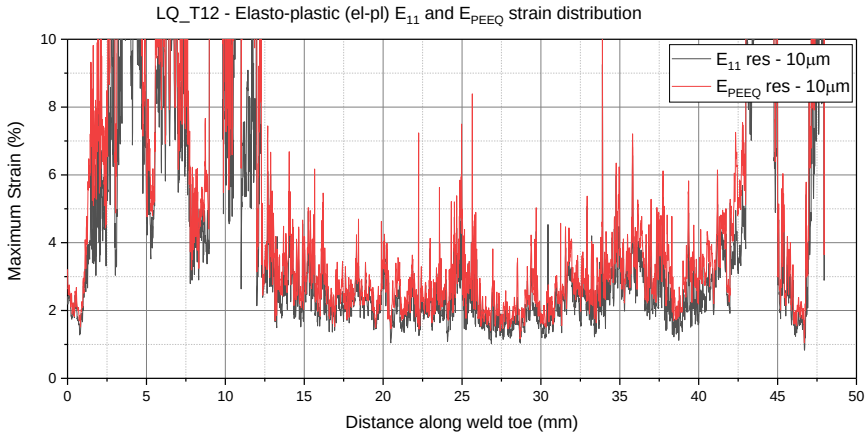
LQ_T12 - Elasto-plastic (el-pl) E11 and EPEEQ strain distribution
E11 res - 10μm
EPEEQ res - 10μm
Maximum Strain (%)
Distance along weld toe (mm)

Appendix B **(Chapter 4)**

B.1 Fatigue test loading data for experiment set 1

Parameters	Specimen Identification		
	HQ_T3	**HQ_T4**	**HQ_T5**
Breadth (B) (mm)	51.44	51.13	54.00
Width (W) (mm)	8.11	7.90	8.10
Cross-sectional area (mm^2)	417.2	403.9	437.4
σ_{max} (MPa)	300	300	300
P_{max} (kN)	125.2	121.2	131.2
Load Ratio R	0.1	0.1	0.1
P_{min} (kN)	12.5	12.1	13.1
P_{mean} (kN)	68.8	66.6	72.2
$P_{amplitude}$ (kN)	56.3	54.5	59.0
	HQ_T6	**HQ_T7**	**HQ_T8**
Breadth (B) (mm)	52.00	50.40	52.10
Width (W) (mm)	8.00	8.00	8.00
Cross-sectional area (mm^2)	416.0	403.2	416.8
σ_{max} (MPa)	300	300	300
P_{max} (kN)	124.8	121.0	125.0
Load Ratio R	0.1	0.1	0.1
P_{min} (kN)	12.5	12.1	12.5
P_{mean} (kN)	68.6	66.5	68.8
$P_{amplitude}$ (kN)	56.2	54.4	56.3

B.2 Fatigue testing ACPD data for experiment set 1

B.2.1 HQ_T3 (Tested to failure)

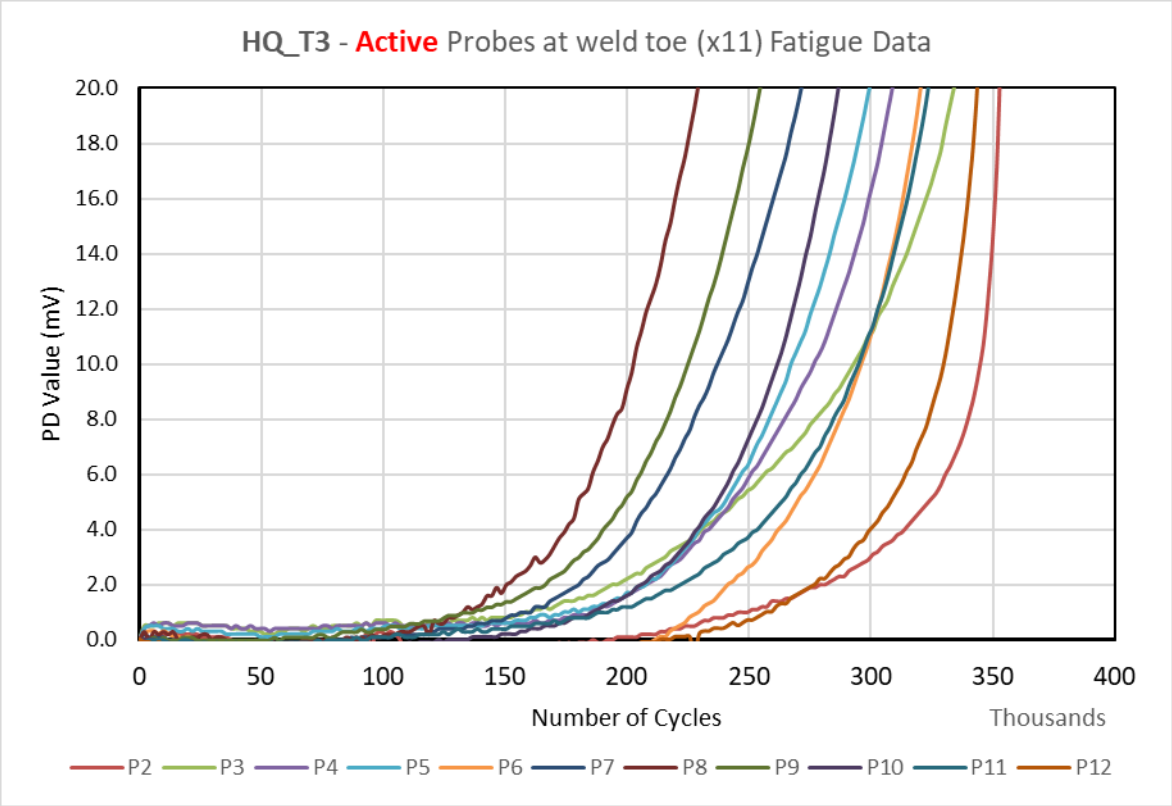

B.2.2 HQ_T4 (Tested to failure)

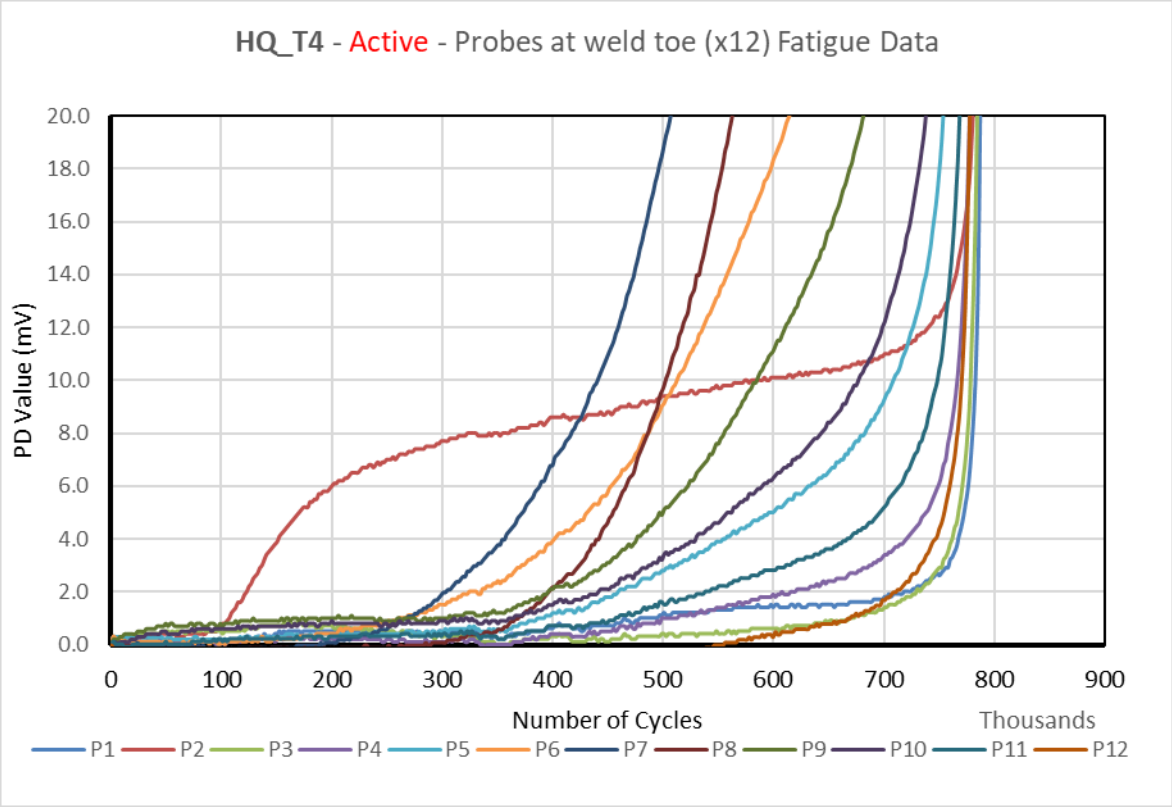

B.2.3 HQ_T6 (Interrupted)

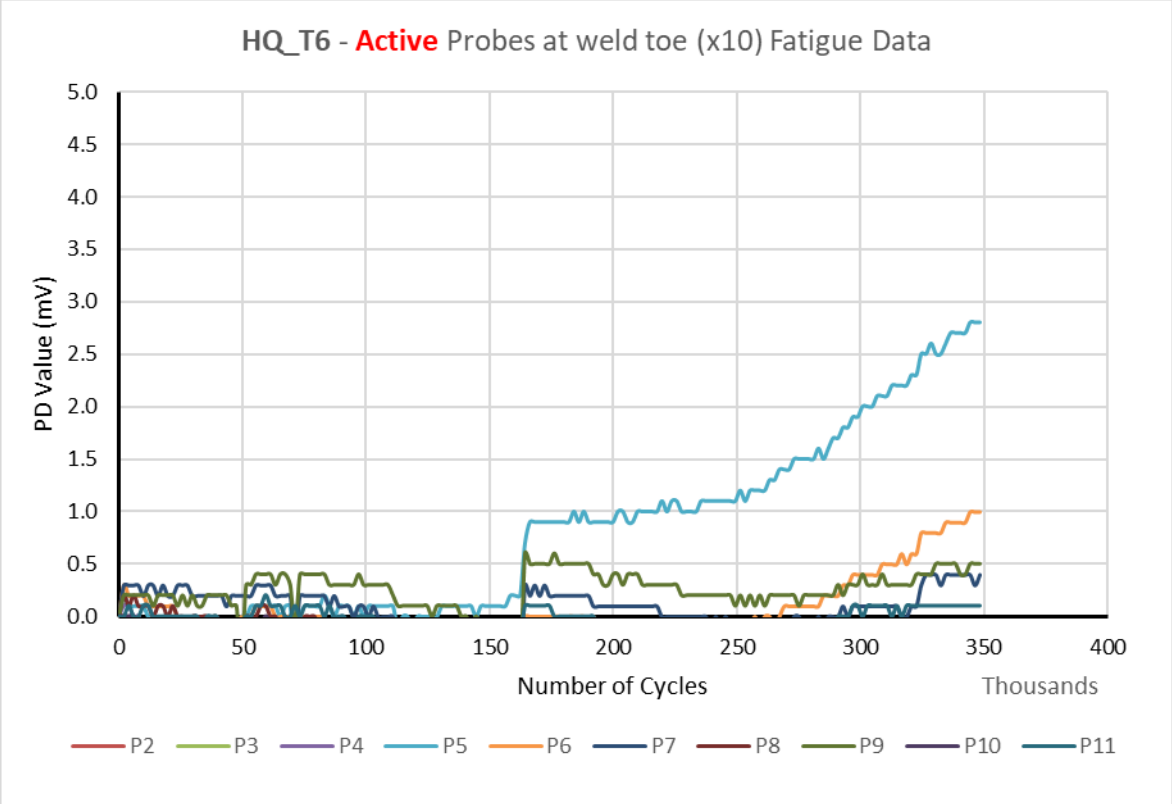

B.2.4 HQ_T7 (Interrupted)

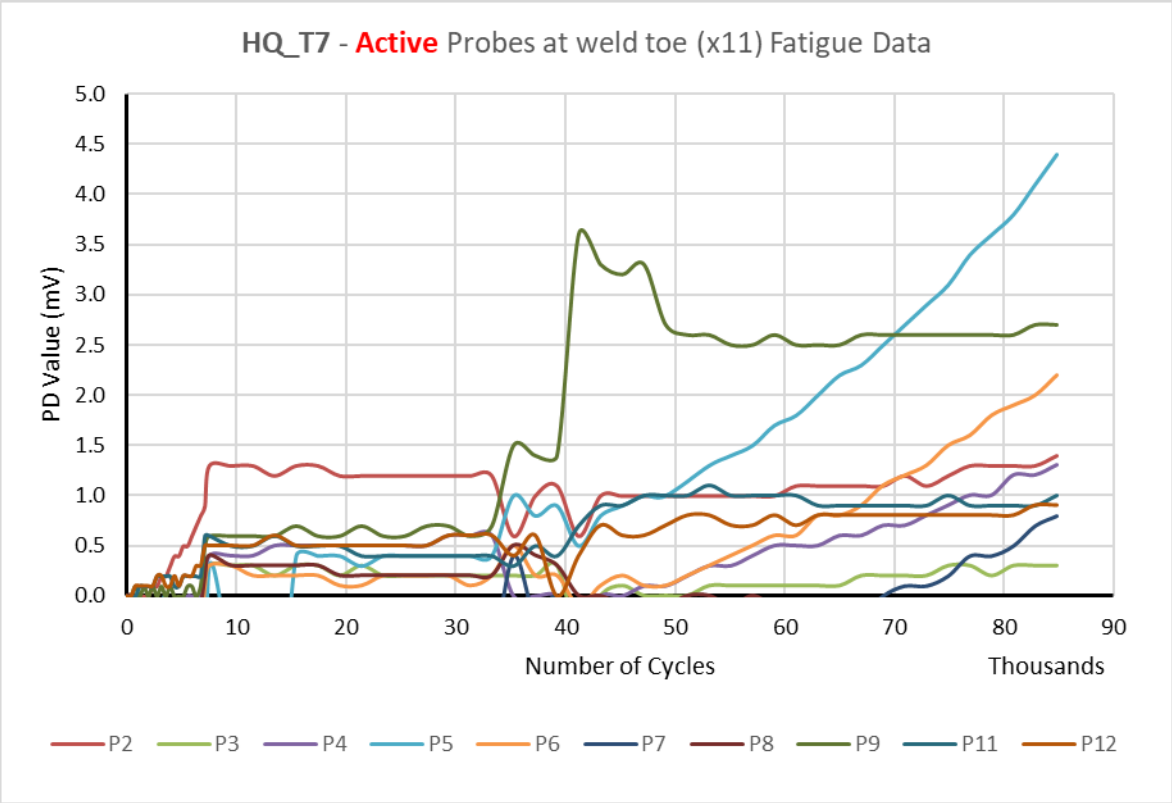

B.2.5 HQ_T8 (Interrupted)

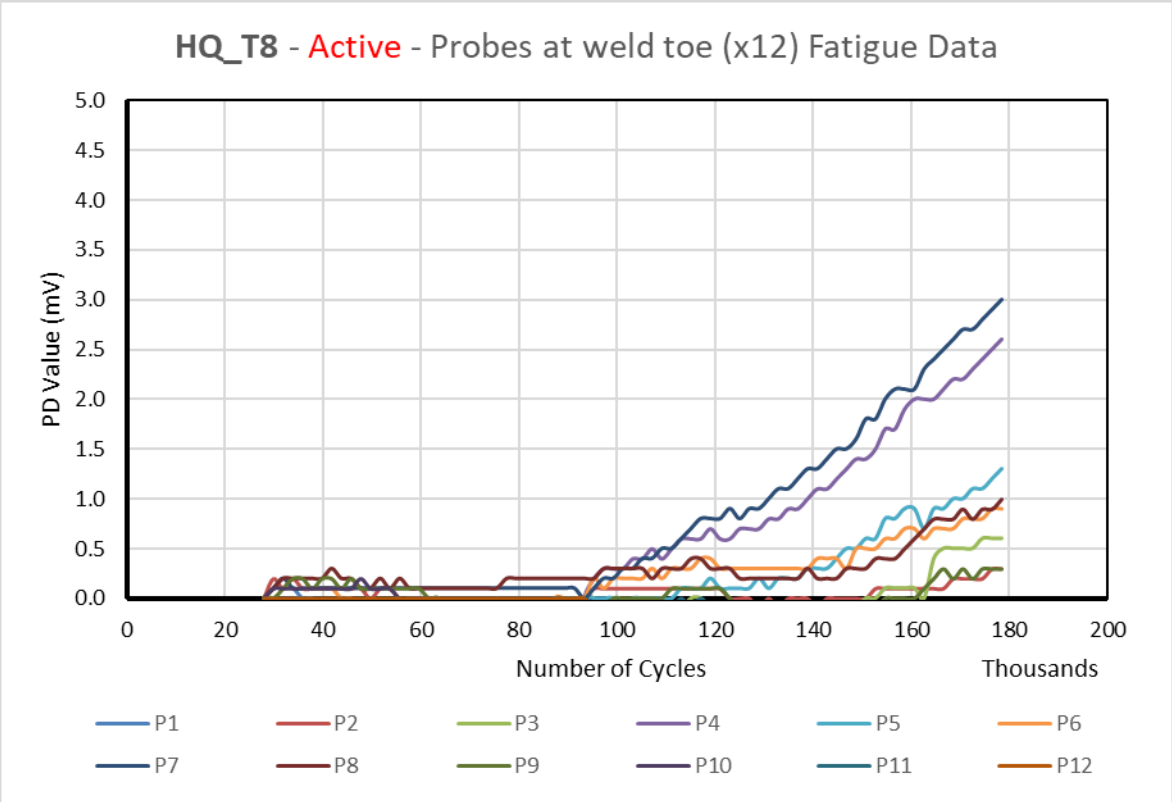

Appendix C **(Chapter 5)**

C.1 Fatigue test loading data for experiment set 2

Parameters	Specimen Identification		
	HQ_T11	**HQ_T13**	**HQ_T15**
Breadth (B) (mm)	7.75	7.8	7.8
Width (W) (mm)	50.6	51.1	53.1
Cross-sectional area (mm^2)	392.15	398.58	414.18
σ_{max} (MPa)	166.67	166.67	166.67
P_{max} (kN)	65.4	66.4	69
Load Ratio R	0.1	0.1	0.1
P_{min} (kN)	6.54	6.64	6.9
P_{mean} (kN)	35.97	36.52	37.95
$P_{amplitude}$ (kN)	29.43	29.88	31.05
	LQ_T10	**LQ_T12**	**LQ_T14**
Breadth (B) (mm)	7.8	7.8	7.8
Width (W) (mm)	50.6	50.5	50.5
Cross-sectional area (mm^2)	394.7	393.9	393.9
σ_{max} (MPa)	166.67	166.67	166.67
P_{max} (kN)	66	65.6	65.6
Load Ratio R	0.1	0.1	0.1
P_{min} (kN)	6.6	6.56	6.56
P_{mean} (kN)	36.3	36.08	36.08
$P_{amplitude}$ (kN)	29.7	29.52	29.52

C.2 Static loading data from experimental set 2

C.2.1 HQ_T13

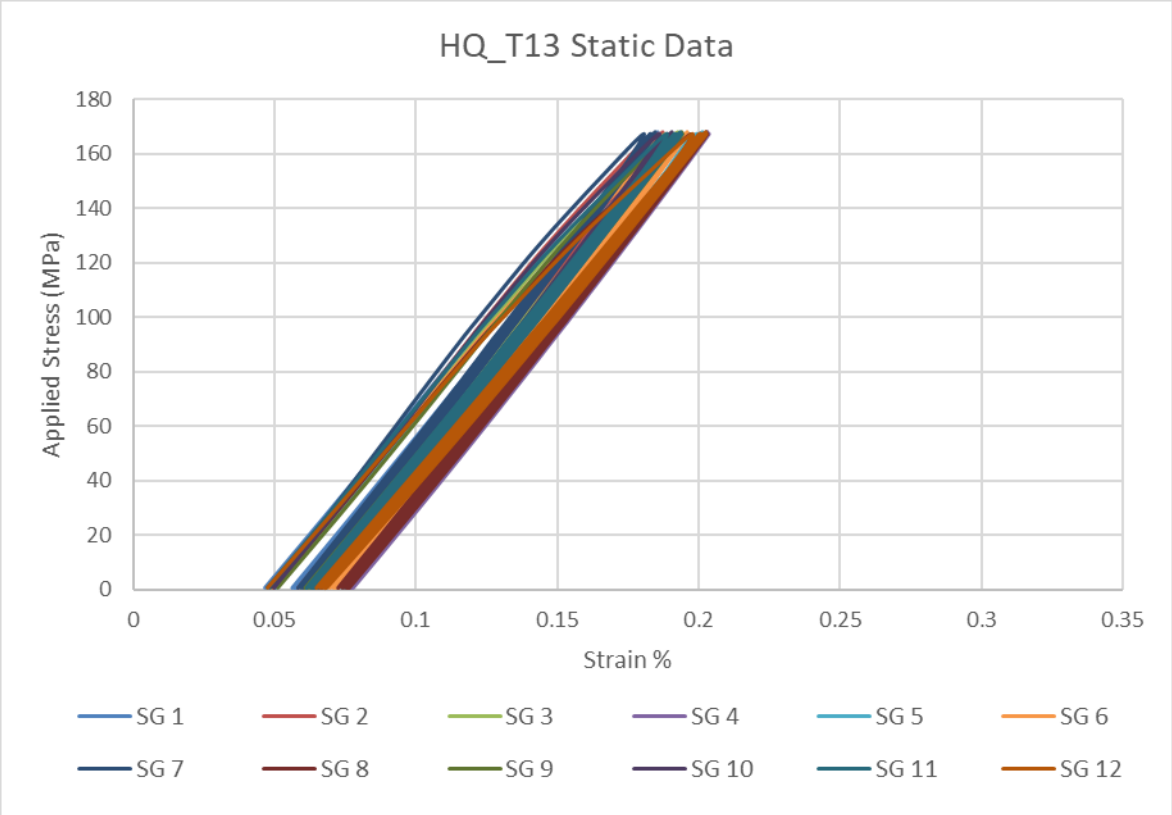

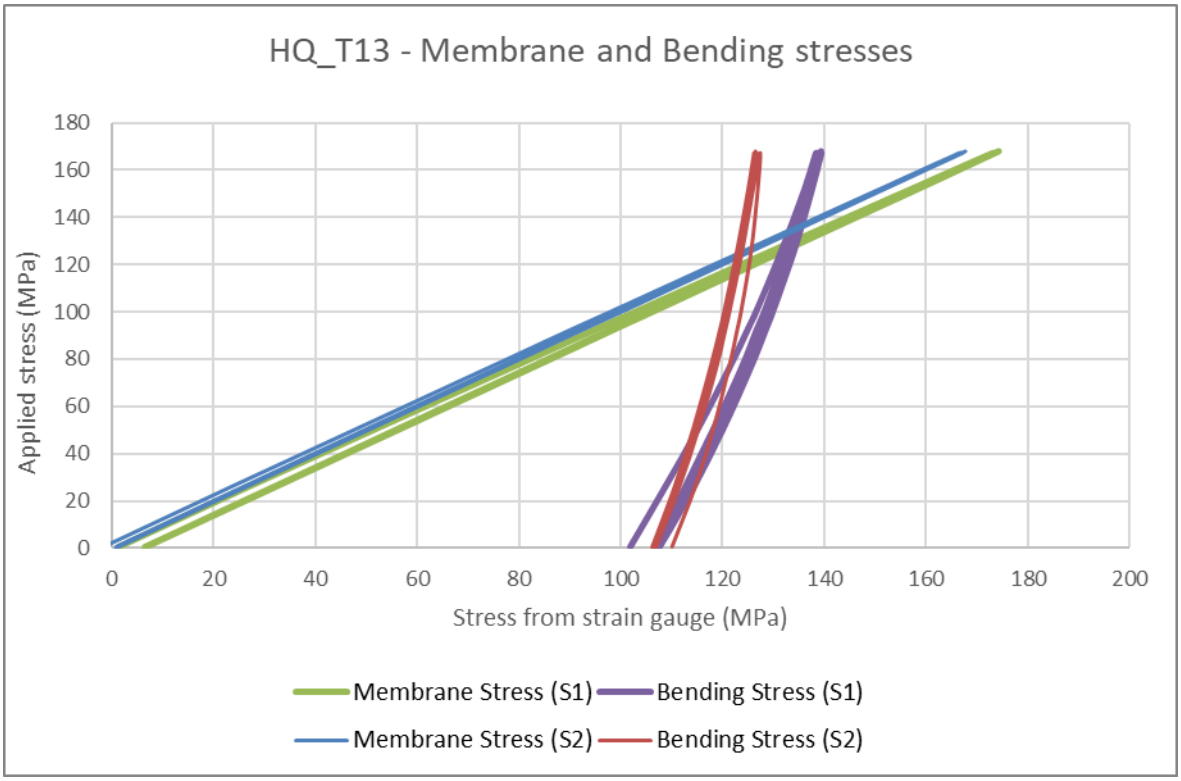

C.2.2 LQ_T14

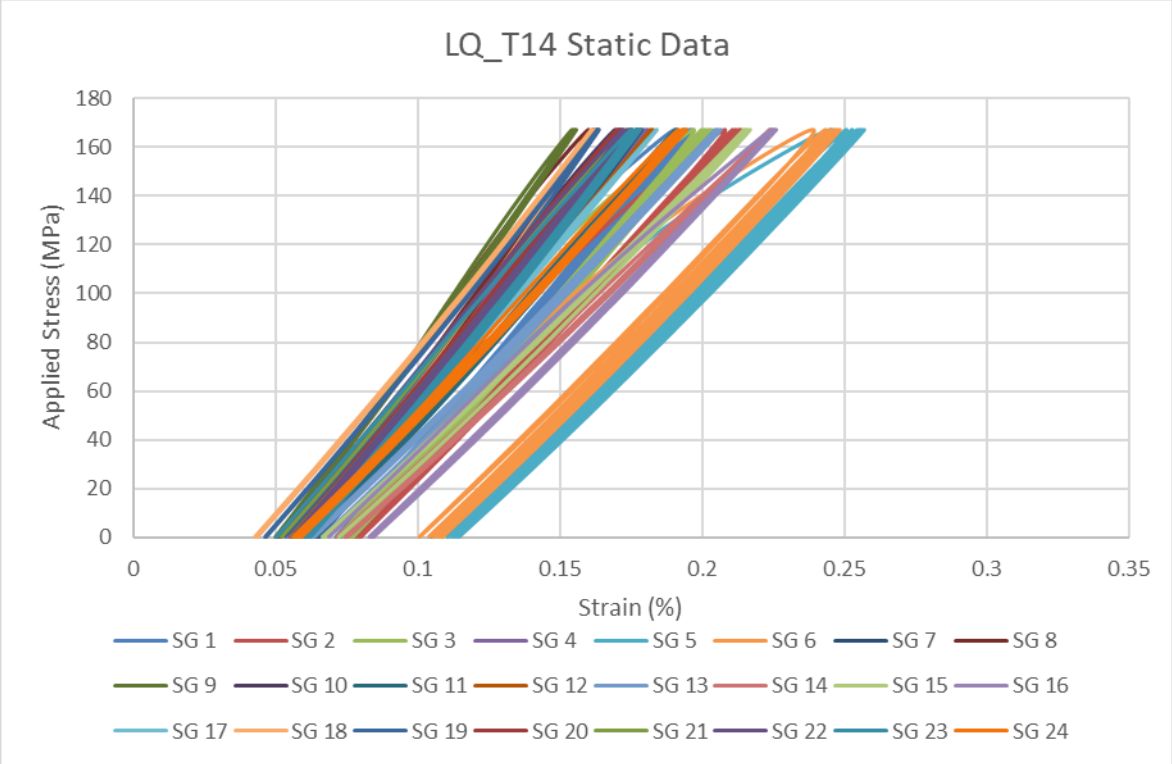
LQ_T14 Static Data
Applied Stress (MPa)
180
160
140
120
100
80
60
40
20
0
0
0.05
0.1
0.15
0.2
0.25
0.3
0.35
Strain (%)
SG 1
SG 2
SG 3
SG 4
SG 5
SG 6
SG 7
SG 8
SG 9
SG 10
SG 11
SG 12
SG 13
SG 14
SG 15
SG 16
SG 17
SG 18
SG 19
SG 20
SG 21
SG 22
SG 23
SG 24

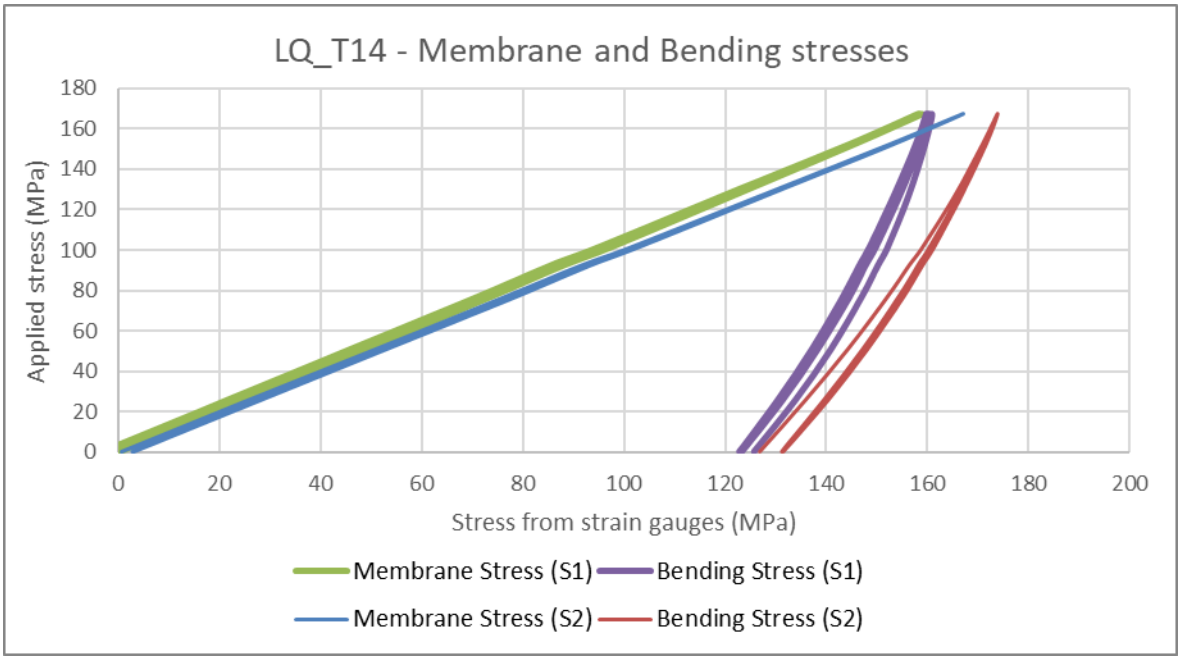
LQ_T14 - Membrane and Bending stresses
Applied stress (MPa)
180
160
140
120
100
80
60
40
20
0
0
20
40
60
80
100
120
140
160
180
200
Stress from strain gauges (MPa)
Membrane Stress (S1)
Bending Stress (S1)
Membrane Stress (S2)
Bending Stress (S2)

C.2.3 HQ_T11

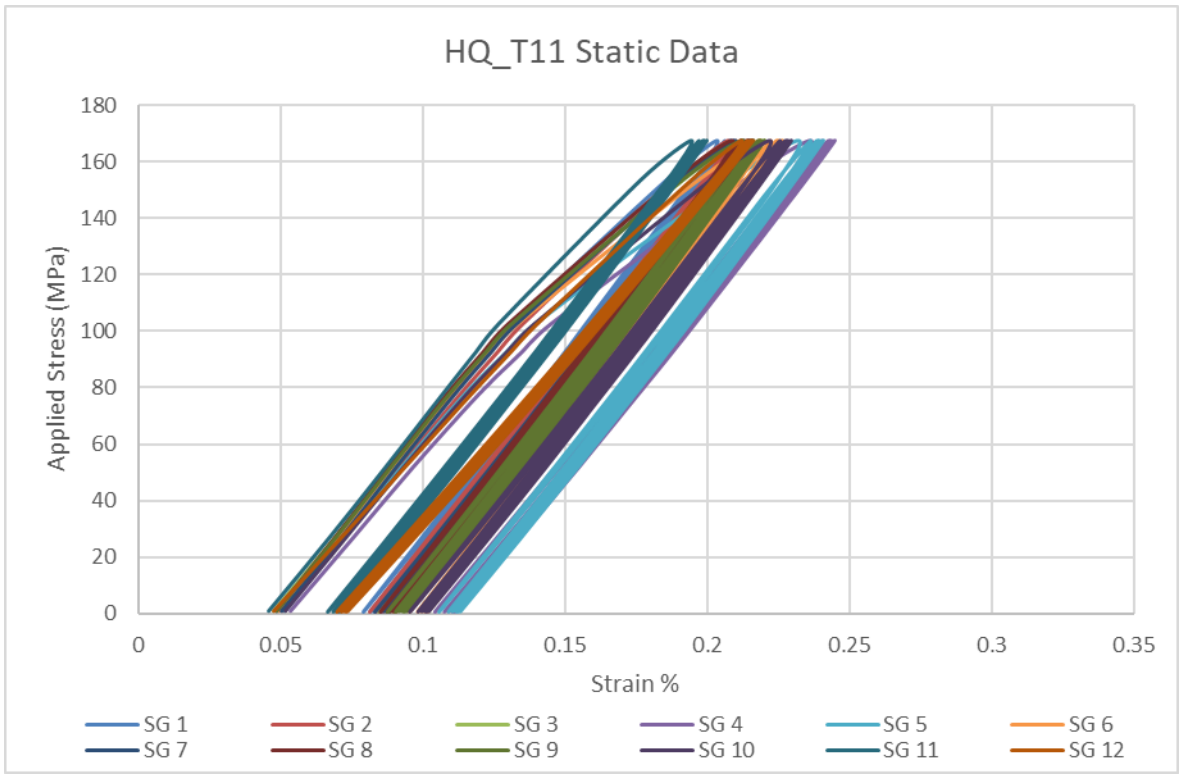
HQ_T11 Static Data
Applied Stress (MPa)
180
160
140
120
100
80
60
40
20
0
0
0.05
0.1
0.15
0.2
0.25
0.3
0.35
Strain %
SG 1
SG 2
SG 3
SG 4
SG 5
SG 6
SG 7
SG 8
SG 9
SG 10
SG 11
SG 12

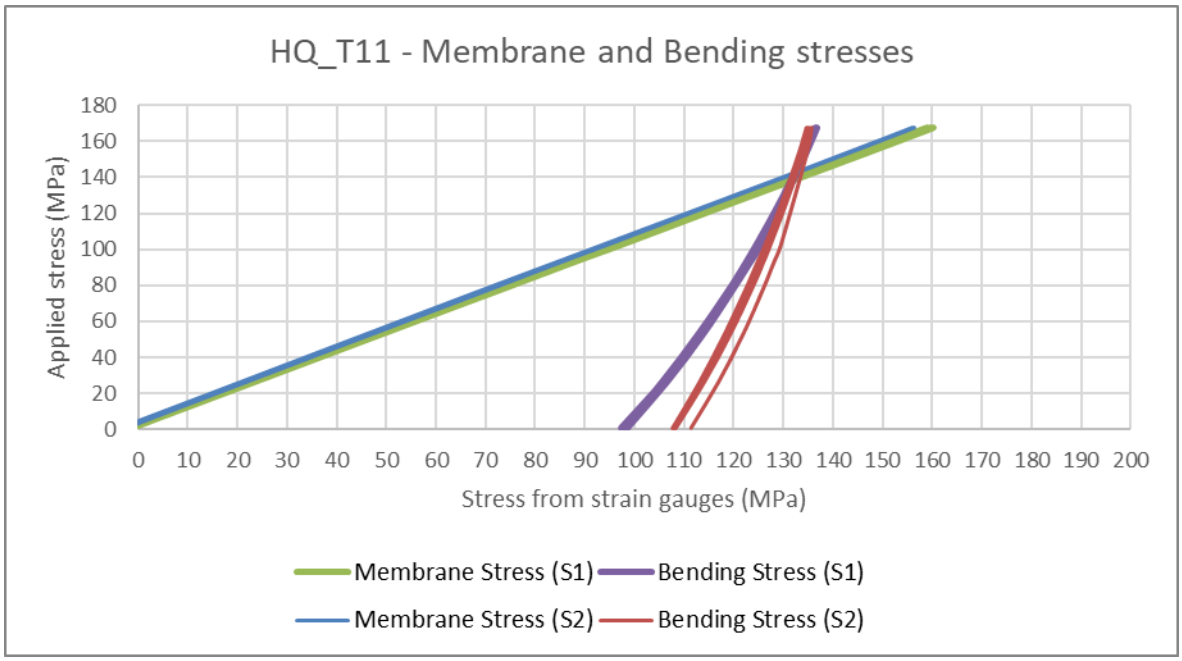
HQ_T11 - Membrane and Bending stresses
Applied stress (MPa)
180
160
140
120
100
80
60
40
20
0
0 10 20 30 40 50 60 70 80 90 100 110 120 130 140 150 160 170 180 190 200
Stress from strain gauges (MPa)
Membrane Stress (S1)
Bending Stress (S1)
Membrane Stress (S2)
Bending Stress (S2)

C.2.4 HQ_T15

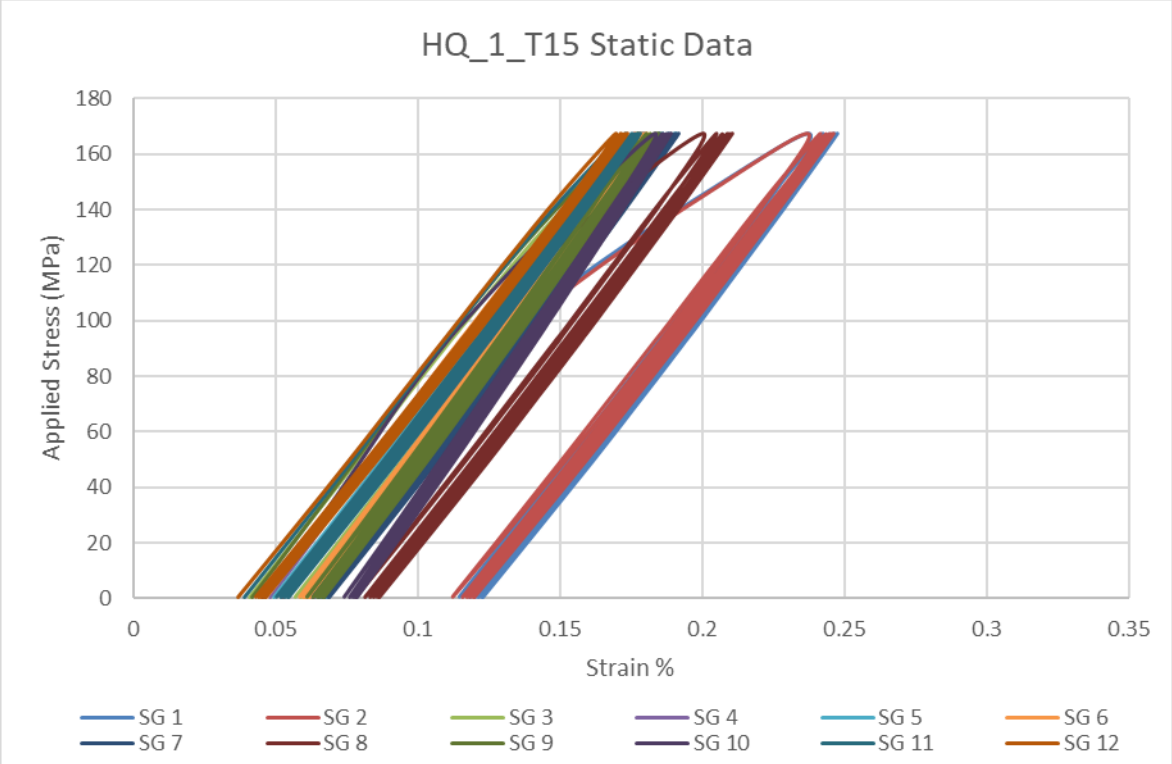
HQ_1_T15 Static Data
Applied Stress (MPa)
180
160
140
120
100
80
60
40
20
0
0
0.05
0.1
0.15
0.2
0.25
0.3
0.35
Strain %
SG 1
SG 2
SG 3
SG 4
SG 5
SG 6
SG 7
SG 8
SG 9
SG 10
SG 11
SG 12

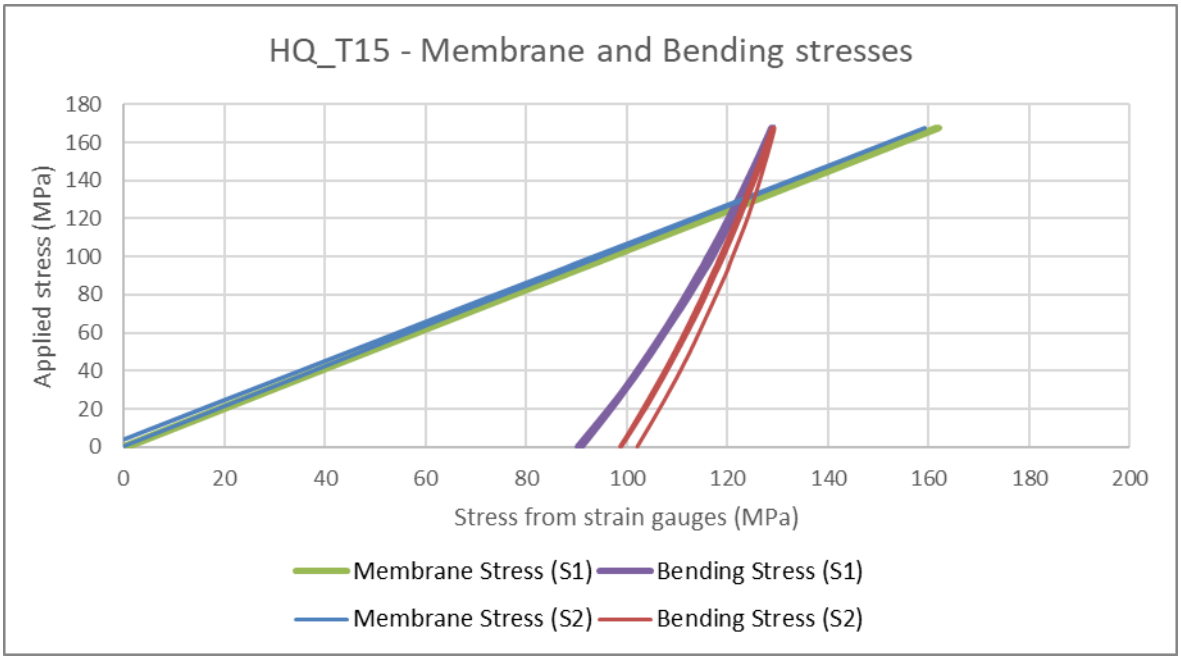
HQ_T15 - Membrane and Bending stresses
Applied stress (MPa)
180
160
140
120
100
80
60
40
20
0
0
20
40
60
80
100
120
140
160
180
200
Stress from strain gauges (MPa)
Membrane Stress (S1)
Bending Stress (S1)
Membrane Stress (S2)
Bending Stress (S2)

C.2.5 LQ_T10

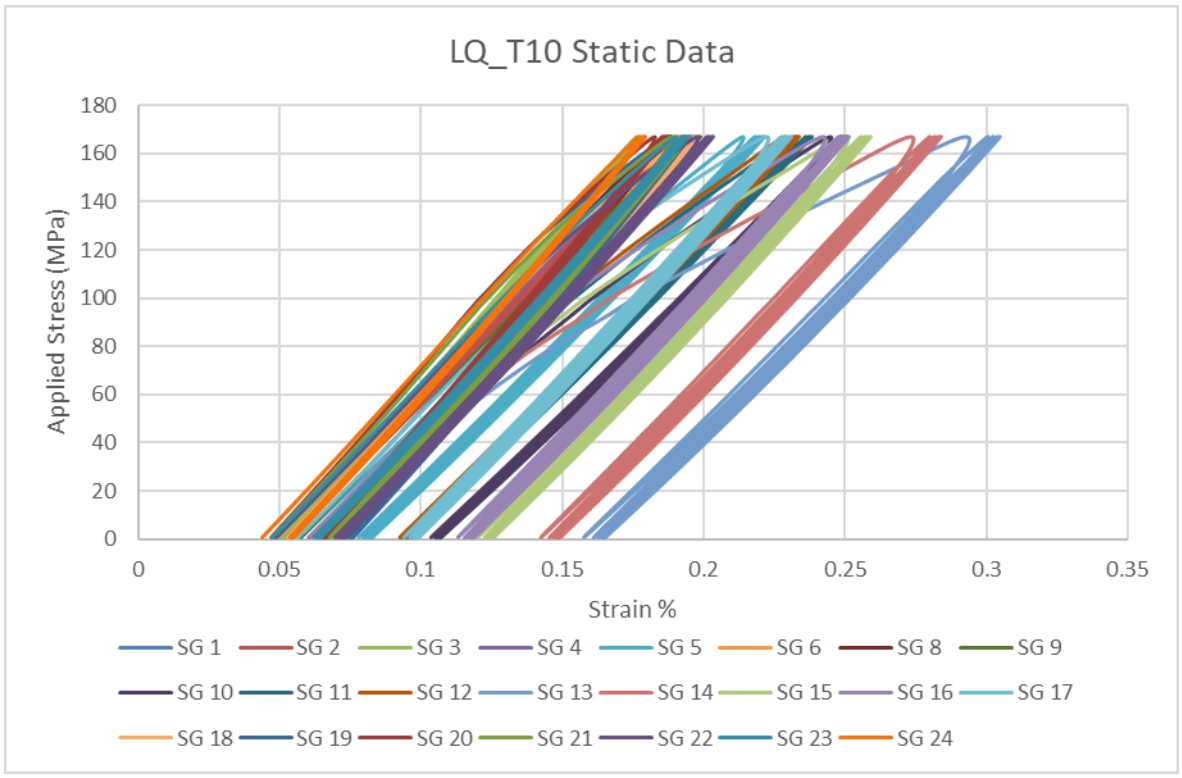
LQ_T10 Static Data
Applied Stress (MPa)
180
160
140
120
100
80
60
40
20
0
0
0.05
0.1
0.15
0.2
0.25
0.3
0.35
Strain %
SG 1
SG 2
SG 3
SG 4
SG 5
SG 6
SG 8
SG 9
SG 10
SG 11
SG 12
SG 13
SG 14
SG 15
SG 16
SG 17
SG 18
SG 19
SG 20
SG 21
SG 22
SG 23
SG 24

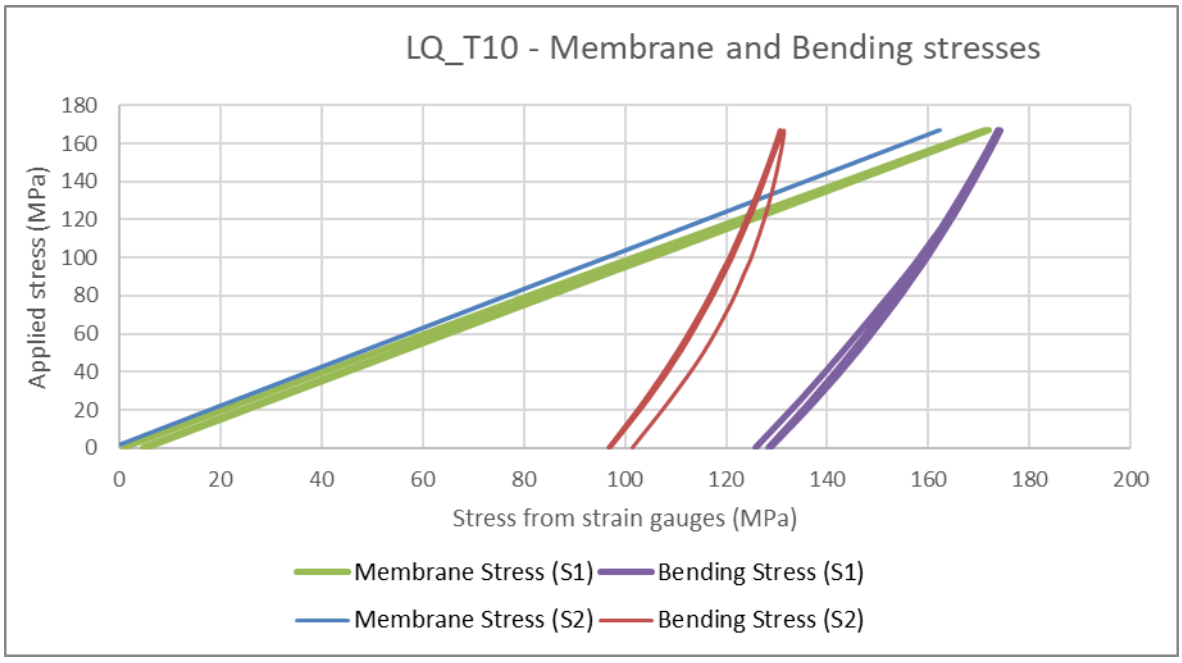
LQ_T10 - Membrane and Bending stresses
Applied stress (MPa)
180
160
140
120
100
80
60
40
20
0
0
20
40
60
80
100
120
140
160
180
200
Stress from strain gauges (MPa)
Membrane Stress (S1)
Bending Stress (S1)
Membrane Stress (S2)
Bending Stress (S2)

C.2.6 LQ_T12

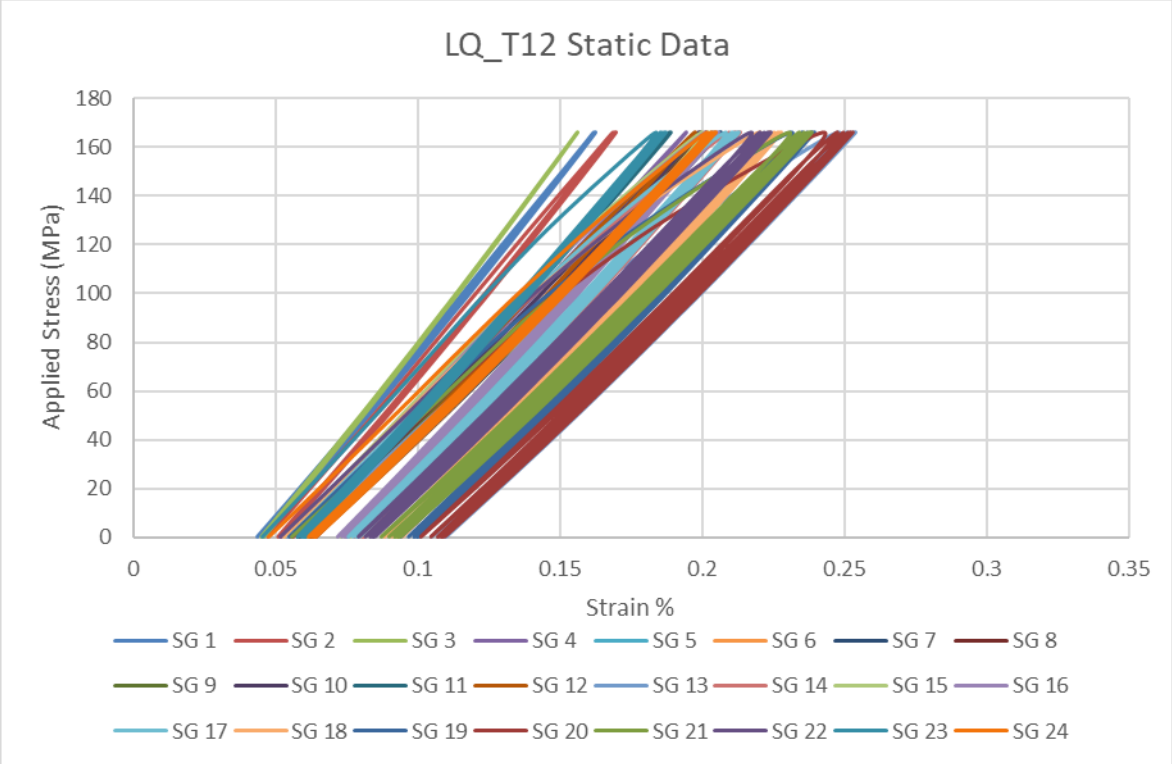
LQ_T12 Static Data
Applied Stress (MPa)
180
160
140
120
100
80
60
40
20
0
0
0.05
0.1
0.15
0.2
0.25
0.3
0.35
Strain %
SG 1
SG 2
SG 3
SG 4
SG 5
SG 6
SG 7
SG 8
SG 9
SG 10
SG 11
SG 12
SG 13
SG 14
SG 15
SG 16
SG 17
SG 18
SG 19
SG 20
SG 21
SG 22
SG 23
SG 24

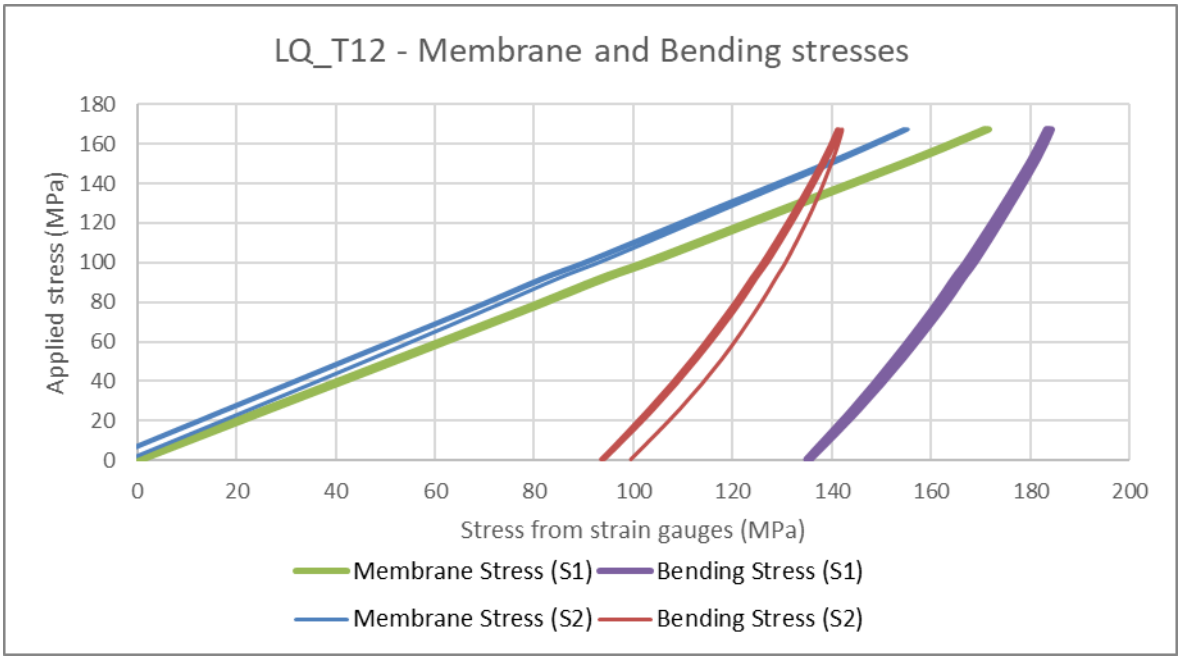
LQ_T12 - Membrane and Bending stresses
Applied stress (MPa)
180
160
140
120
100
80
60
40
20
0
0
20
40
60
80
100
120
140
160
180
200
Stress from strain gauges (MPa)
Membrane Stress (S1)
Bending Stress (S1)
Membrane Stress (S2)
Bending Stress (S2)

C.3 Fatigue testing Strain Gauge data for experiment set 2

C.3.1 HQ_T13 (Tested to failure) – First stage

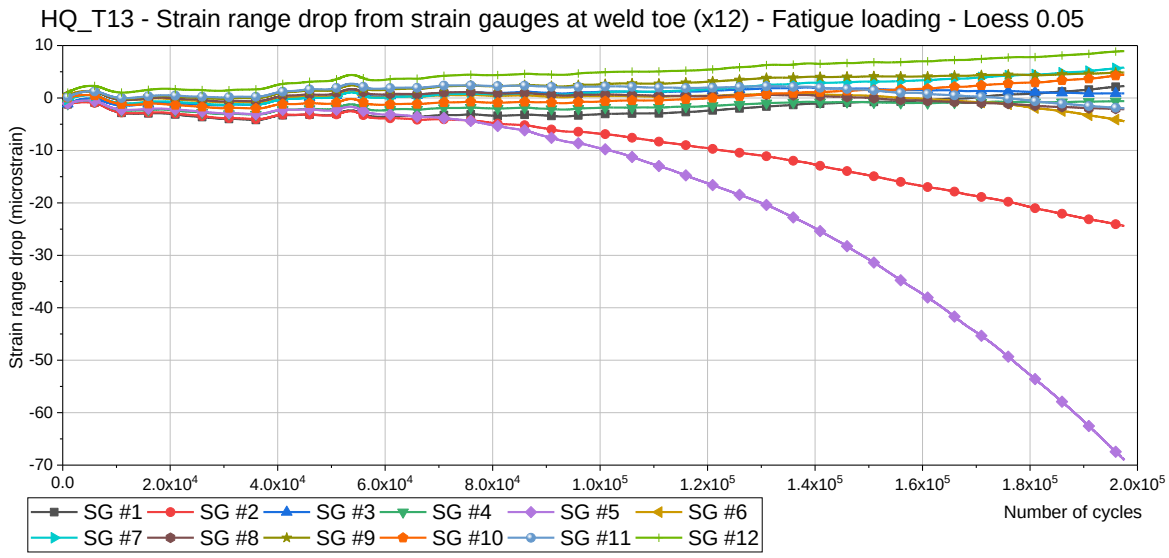

C.3.2 LQ_T14 (Tested to failure) – First stage

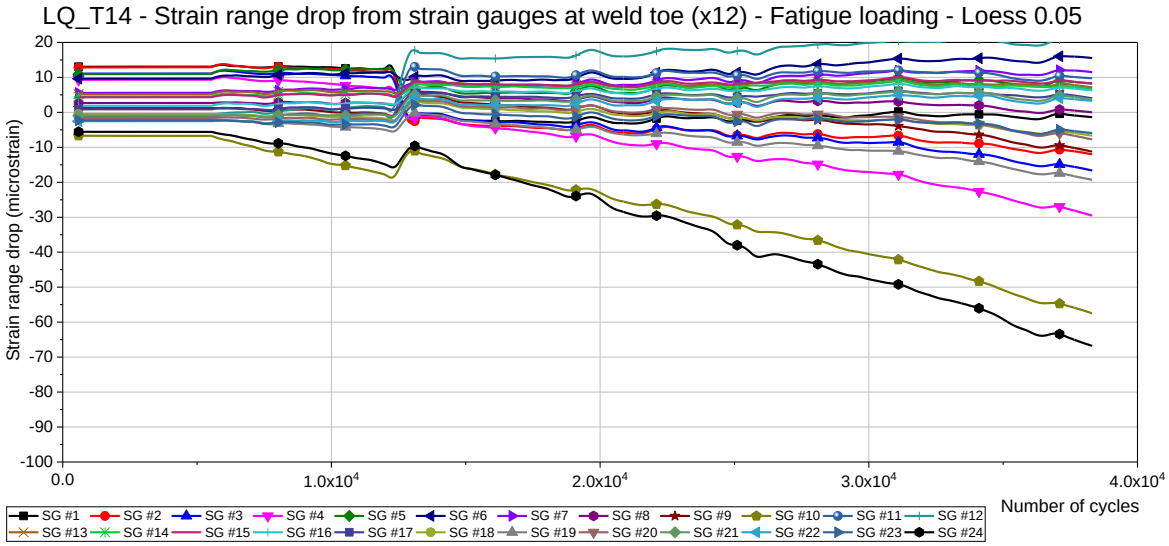

C.3.3 HQ_T11 (Interrupted)

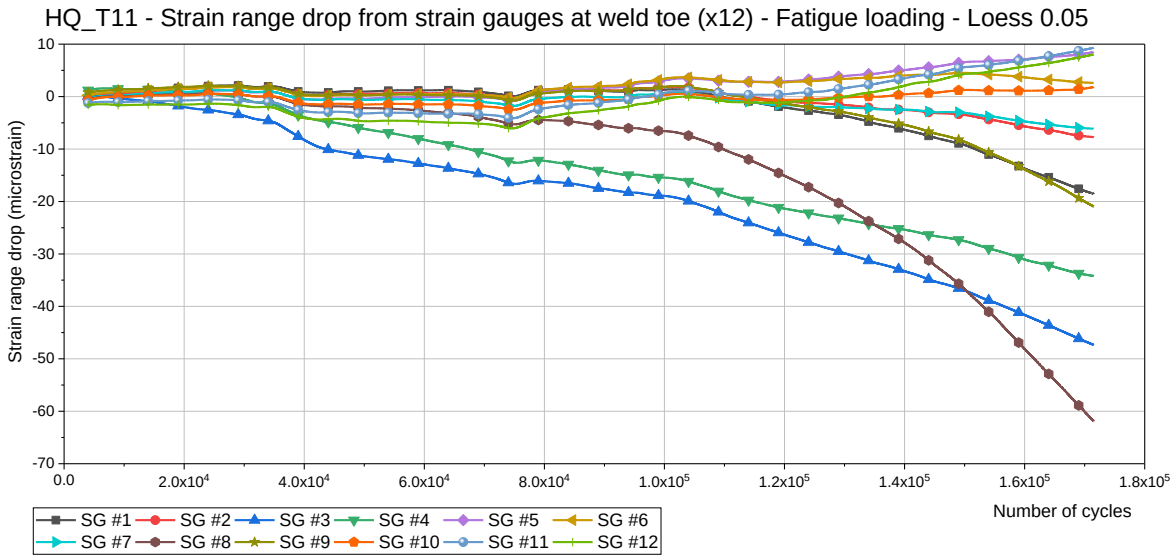

C.3.4 HQ_T15 (Interrupted)

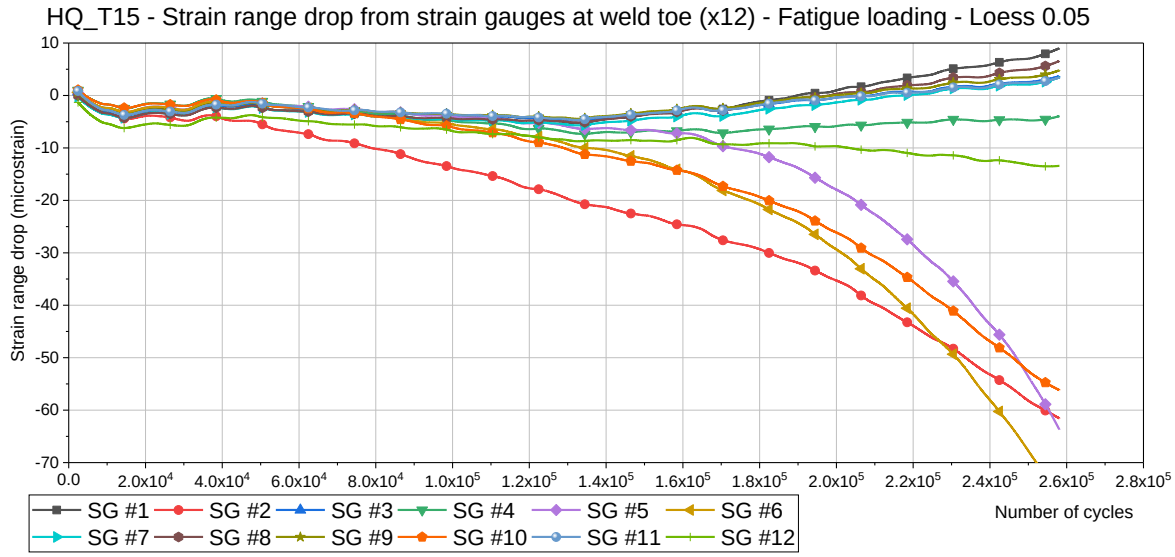

C.3.5 LQ_T10 (Interrupted)

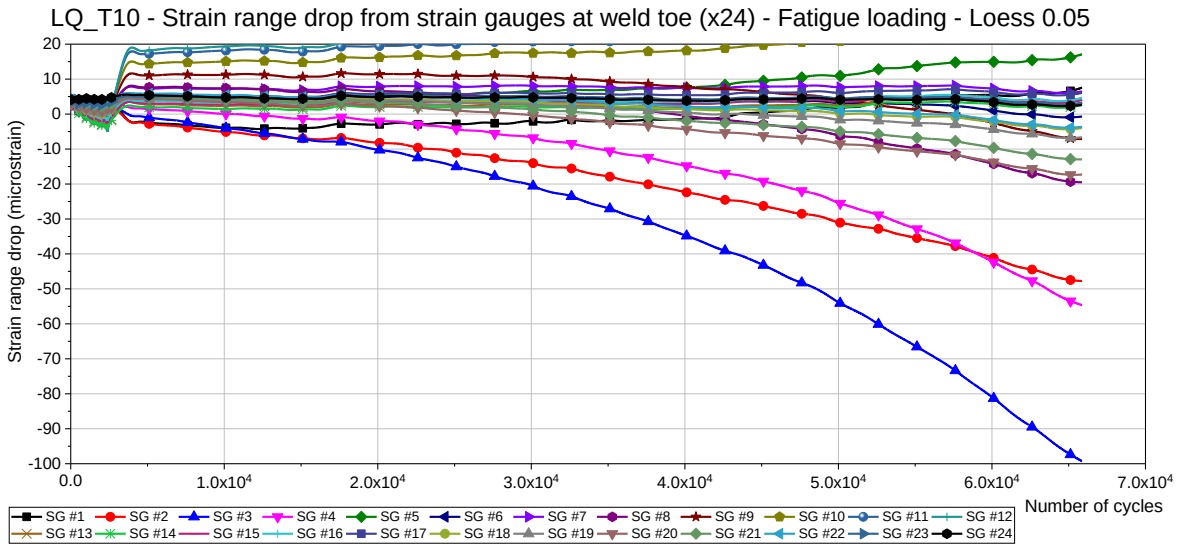

C.3.6 LQ_T12 (Interrupted)

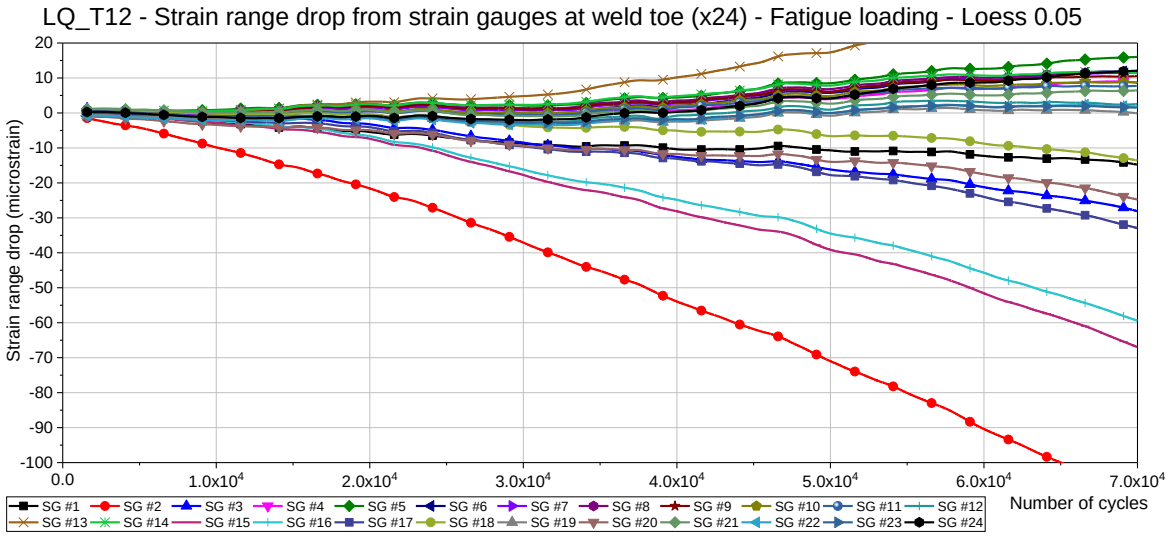

Appendix D**(Chapter 6)**

D.1 Flowchart of the application of notch stress-strain approach

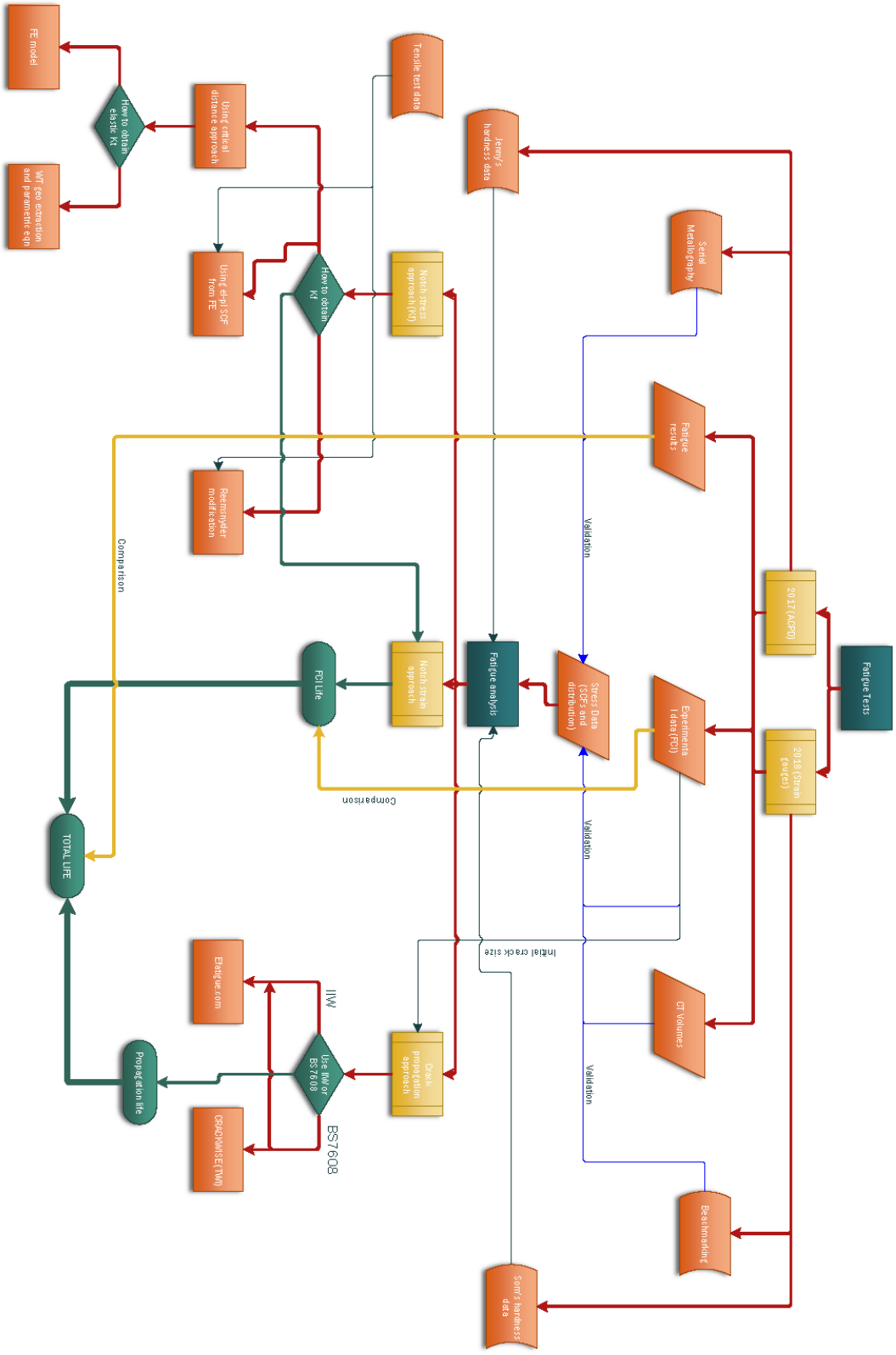

D.2 FCI Prediction Distribution

D.2.1 UML_C2

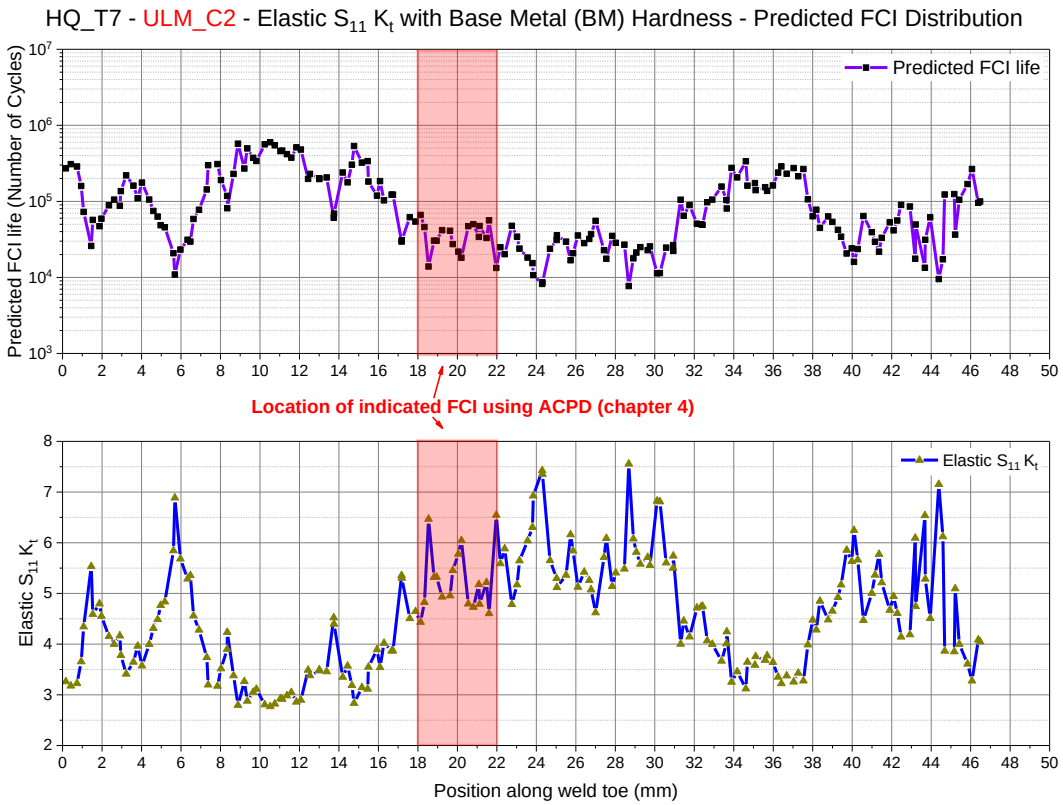

D.2.2 NEWMAT_C3

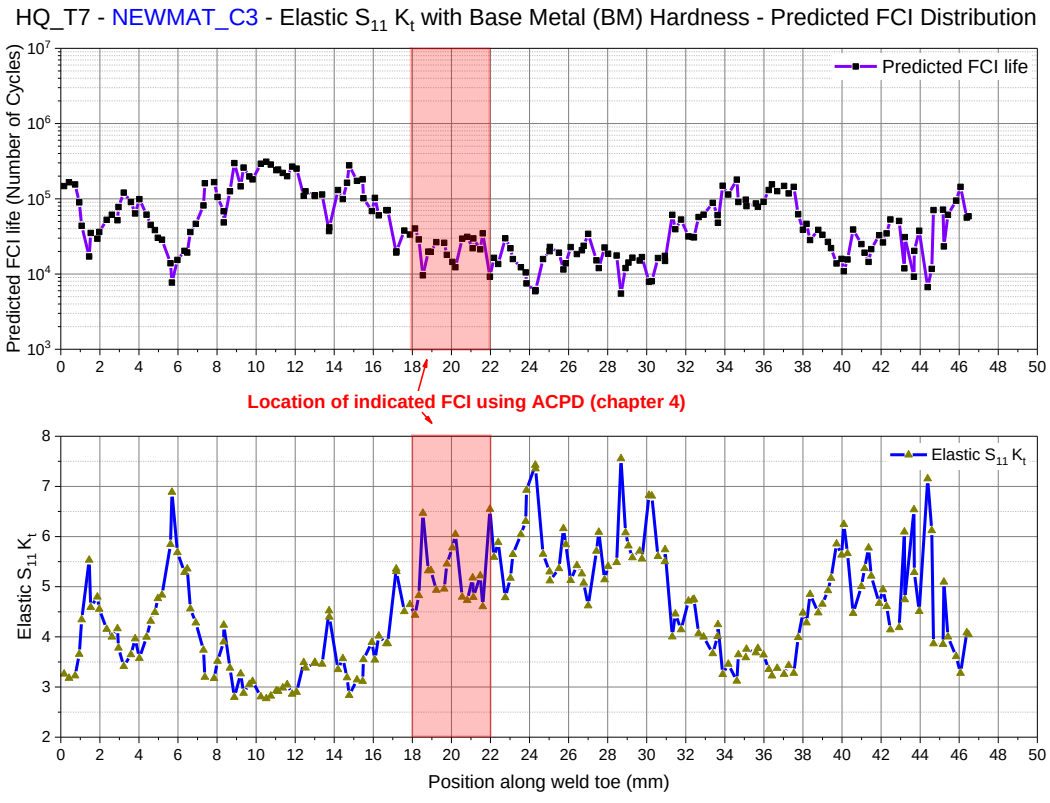

D.2.3 COMPOSITE_C4

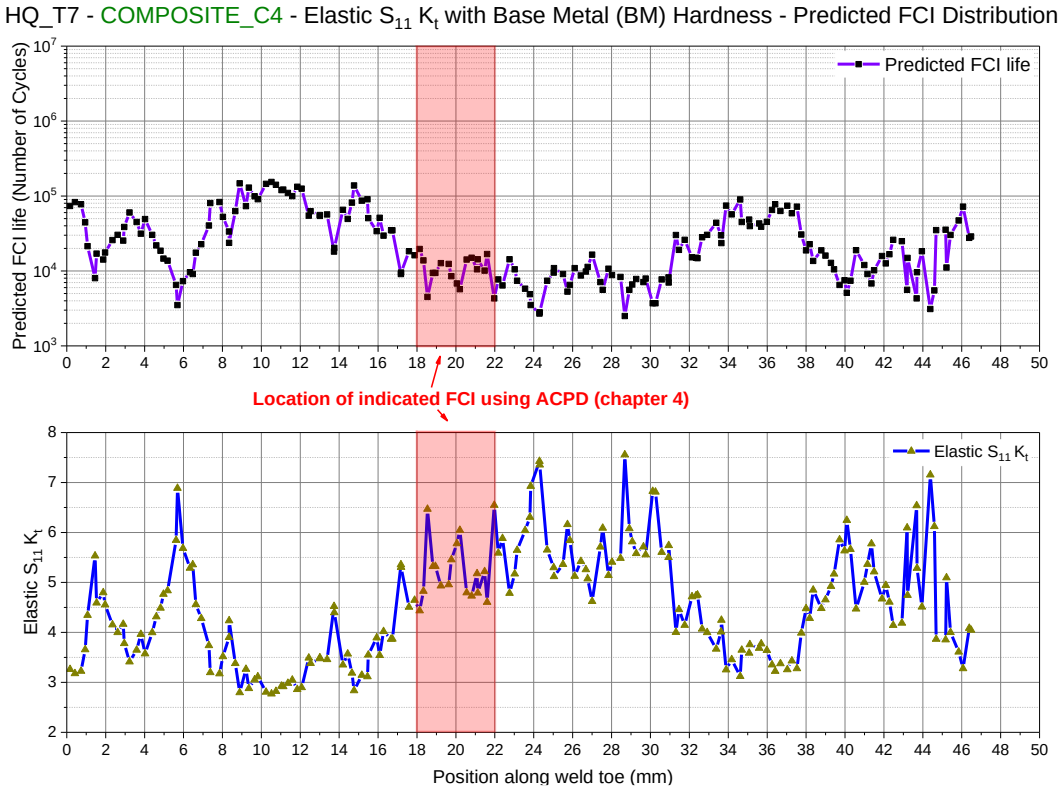

D.2.4 NEWMAT_C7

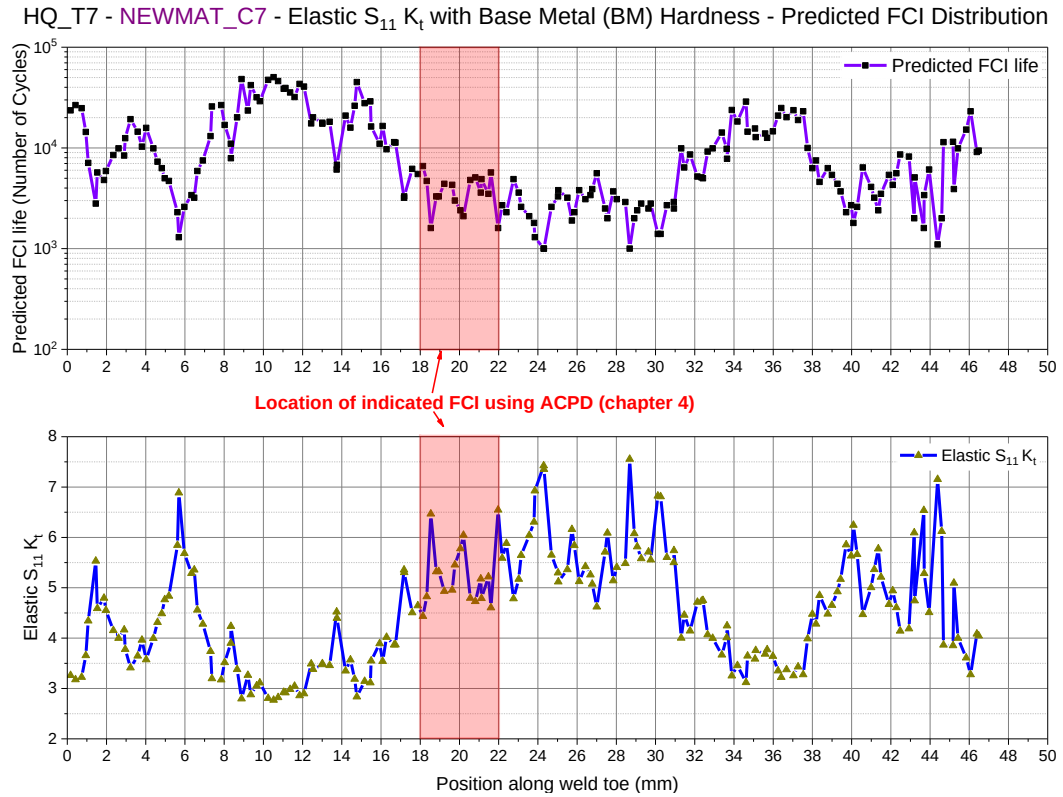

References (Numbered)

[1] H. O. Fuchs and R. I. Stephens, *Metal fatigue in engineering*: Wiley, 1980.

[2] K. Macdonald, *Fracture and Fatigue of Welded Joints and Structures*. Cambridge, UK: Elsevier Science, 2011.

[3] BSI, "BS EN 1011-1:2009 Welding. Recommendations for welding of metallic materials. General guidance for arc welding," ed: The British Standards Institution, 2009.

[4] BSI, "PD ISO/TR 14345:2012 - Fatigue - Fatigue testing of welded components - Guidance," The British Standards Institution, UK2012.

[5] BSI, "BS 7910-2013 Guide to methods for assessing the acceptability of flaws in metallic structures," ed: The British Standards Institution, 2013.

[6] BSI, "BS 7608-2014+A1-2015-Guide to fatigue design and assessment of steel products," ed: The British Standards Institution, 2015.

[7] CEN, "EN 1993-1-9:2005 Eurocode 3: Design of steel structures - Part 1-9: Fatigue," ed. Brussels, 2005.

[8] A. F. Hobbacher, *Recommendations for Fatigue Design of Welded Joints and Components*, 2 ed.: Springer International Publishing, 2016.

[9] J. Crump, "A Review and Investigation on the Effect of Welding Parameters on Weld Toe Geometry, Stresses and Fatigue," EngD Thesis, University of Southampton, Southampton, UK, 2017.

[10] S. Rajaram, "Welding Equipment and Supplies: The Global Market," bcc Research 2016.

[11] S. J. Maddox, *Fatigue strength of welded structures*, 2nd ed. Cambridge: Abington Publishers, 1991.

[12] T. R. Gurney, *Fatigue of welded structures*. Cambridge: Cambridge University Press, 1979.

[13] E. F. Signes, R. G. Baker, J. D. Harrison, and F. M. Burdekin, "Factors affecting the fatigue strength of welded high strength steels," *British Welding Journal,* pp. 109-116, 1967.

[14] S. Suresh, *Fatigue of Materials*, Second ed. Cambridge: Cambridge University Press, 1998.

[15] W. Fricke, "Fatigue analysis of welded joints: state of development," *Marine Structures,* vol. 16, pp. 185-200, 2003.

[16] D. Radaj, C. M. Sonsino, and W. Fricke, *Fatigue strength assessment of welded joints by local approaches*, 2nd ed. Cambridge: Woodhead Publishing, 2006.

[17] W. Fricke, "IIW Recommendations for the Fatigue Assessment of Welded Structures by Notch Stress Analysis: IIW-2006-09," in *IIW Recommendations for the Fatigue Assessment of Welded Structures by Notch Stress Analysis*, ed: Woodhead Publishing, 2012, pp. 2-41.

[18] P. G. Forrest, "Chapter I - Introduction," in *Fatigue of Metals*, P. G. Forrest, Ed., ed: Pergamon, 1962, pp. 1-11.

[19] T. Anderson, *Fracture Mechanics*, 3rd Edition ed. Boca Raton: CRC Press, 2005.

[20] G. R. Irwin, "Plastic zone near a crack and fracture toughness," in *Proceedings of the Seventh Sagamore Ordnance Materials Conference*, New York: Syracuse University, 1960, pp. 63-78.

[21] ASTM, "ASTM E399 - 17: Standard test method for linear-elastic plane-strain fracture toughness K of metallic materials," ed: ASTM International, 2017.

[22] S. Suresh and R. O. Ritchie, "Propagation of short fatigue cracks," *International Metals Reviews,* vol. 29, pp. 445-475, 1984/01/01 1984.

[23] J. R. Rice, "A Path Independent Integral and the Approximate Analysis of Strain Concentration by Notches and Cracks," *Journal of Applied Mechanics,* vol. 35, pp. 379-386, 1968.

[24] J. Lancaster, *Handbook of Structural Welding*. Cambridge, UK: Abington Publishing, 1992.

[25] M. Puschner, *5 Jahrtausende Schweissen: Eine Frühgeschichte der Schweisstechnik*. Düsseldorf: DVS Media GmbH, 1986.

[26] H. B. Cary, *Modern Welding Technology*. Englewood Cliffs, N.J.: Prentice-Hall, 1979.

[27] Techblogsearch.com. (18/08/2016). *MIG/MAG Welding - GMAW Process*. Available: http://techblogsearch.com/a/migmag-welding-gmaw-process.html

[28] J. F. Lancaster, *Metallurgy of Welding*, 6th ed. Abington, Cambridge: Abington Publishing, 1999.

[29] W. S. Association. (2016, 02/08/2016). World Steel Association - World Steel in Figures 2016. Available: http://www.worldsteel.org/media-centre/press-releases/2016/

[30] ASM, "Alloying: Understanding the Basics (#06117G)," ASM International, Ohio, USA, 2001.

[31] ASM, *Metals Handbook*, 9th ed. vol. 9. Materials Park, OH: American Society for Metals, 1985.

[32] P. Zubko and L. Pešek, "Prediction of Tensile Properties Based on Hardness Measurement," *Key Engineering Materials,* vol. 606, pp. 35-38, 2014.

[33] E. J. Pavlina and C. J. Van Tyne, "Correlation of Yield Strength and Tensile Strength with Hardness for Steels," *Journal of Materials Engineering and Performance,* vol. 17, pp. 888-893, 2008/12/01 2008.

[34] M. L. Roessle and A. Fatemi, "Strain-controlled fatigue properties of steels and some simple approximations," *International Journal of Fatigue,* vol. 22, pp. 495-511, 2000/07/01/ 2000.

[35] P. Zubko and L. Pešek, "Correlation between Hardness and Fatigue Properties," *Key Engineering Materials,* vol. 662, pp. 197-200, 2015.

[36] J. Li, Z.-f. Yao, and Z.-p. Zhang, "Multiaxial Fatigue Life Prediction for Steels Based on Some Simple Approximations," *Journal of Materials Engineering and Performance,* vol. 24, pp. 185-193, 2015/01/01 2015.

[37] Z. Lopez and A. Fatemi, "A method of predicting cyclic stress–strain curve from tensile properties for steels," *Materials Science and Engineering: A,* vol. 556, pp. 540-550, 2012/10/30/ 2012.

[38] R. Basan, M. Franulovic, D. Rubeša, and I. Prebil, "Implementation of strain-life fatigue parameters estimation methods in a web-based system," *Procedia Engineering,* vol. 10, pp. 2363-2368, 2011/01/01/ 2011.

[39] V. T. Troshchenko and L. A. Khamaza, "Strain-life curves of steels and methods for determining the curve parameters. Part 1. Conventional methods," *Strength of Materials,* vol. 42, pp. 647-659, 2010.

[40] H. Remes, "Strain-based approach to fatigue strength assessment of laser-welded joints," PhD, Department of Applied Mechanics, Aalto University, Aalto, Finland, 2008.

[41] D. Ye, X. Tong, L. Yao, and X. Yin, "Fatigue hardening/softening behaviour investigated through Vickers microhardness measurement during high-cycle fatigue," *Materials Chemistry and Physics,* vol. 56, pp. 199-204, 1998/10/15/ 1998.

[42] M. Ladinek, A. Niederwanger, R. Lang, J. Schmid, R. Timmers, and G. Lener, "The strain-life approach applied to welded joints: Considering the real weld geometry," *Journal of Constructional Steel Research,* vol. 148, pp. 180-188, 2018/09/01/ 2018.

[43] M. Ladinek, A. Niederwanger, and R. Lang, "An individual fatigue assessment approach considering real notch strains and local hardness applied to welded joints," *Journal of Constructional Steel Research,* vol. 148, pp. 314-325, 2018/09/01/ 2018.

[44] H. Remes, "Strain-based approach to fatigue crack initiation and propagation in welded steel joints with arbitrary notch shape," *International Journal of Fatigue,* vol. 52, pp. 114-123, 2013/07/01/ 2013.

[45] H. Remes, P. Varsta, and J. Romanoff, "Continuum approach to fatigue crack initiation and propagation in welded steel joints," *International Journal of Fatigue,* vol. 40, pp. 16-26, 2012/07/01/ 2012.

[46] M. Leitner, T. FÖSsl, M. Stoschka, and W. Eichlseder, "Evaluation of fillet weld properties and fatigue behaviour in dependence of welding parameters," *Archives of Civil and Mechanical Engineering,* vol. 11, pp. 651-660, 2011.

[47] C. Casavola and C. Pappalettere, "Discussion on local approaches for the fatigue design of welded joints," *International Journal of Fatigue,* vol. 31, pp. 41-49, 2009.

[48] D. Ye and Z. Wang, "An approach to investigate pre-nucleation fatigue damage of cyclically loaded metals using Vickers microhardness tests," *International Journal of Fatigue,* vol. 23, pp. 85-91, 2001/01/01/ 2001.

[49] P. Moore and G. Booth, *The Welding Engineer's Guide to Fracture and Fatigue*. Cambridge: Woodhead Publishing, 2015.

[50] J. W. Fisher, *Fatigue and Fracture in Steel Bridges: Case Studies*: Wiley Interscience, 1984.

[51] R. C. McClung, "A literature survey on the stability and significance of residual stresses during fatigue," *Fatigue & Fracture of Engineering Materials & Structures,* vol. 30, pp. 173-205, 2007/03/01 2007.

[52] S. J. Maddox, "Fatigue design rules for welded structures," in *Fracture and Fatigue of Welded Joints and Structures*, K. A. Macdonald, Ed., ed Cambridge, UK: Elsevier Science, 2011.

[53] K. Iida and M. Takanashi, "Relaxation of welding residual stresses by reversed and repeated loadings," *Welding in the World, Le Soudage Dans Le Monde,* vol. 41, pp. 314-327, 1998.

[54] K. Jacobus, R. E. DeVor, and S. G. Kapoor, "Machining-induced residual stress: Experimentation and modeling," *Journal of Manufacturing Science and Engineering, Transactions of the ASME,* vol. 122, pp. 20-31, 2000.

[55] M. M. El-Khabeery and M. Fattouh, "Residual stress distribution caused by milling," *International Journal of Machine Tools and Manufacture,* vol. 29, pp. 391-401, 1989.

[56] E. K. Henriksen, *Residual stresses in machined surfaces*: ASME, 1948.

[57] W. Jiang, W. Woo, G.-B. An, and J.-U. Park, "Neutron diffraction and finite element modeling to study the weld residual stress relaxation induced by cutting," *Materials & Design,* vol. 51, pp. 415-420, 2013/10/01/ 2013.

[58] V. Dattoma, M. De Giorgi, and R. Nobile, "On the evolution of welding residual stress after milling and cutting machining," *Computers & Structures,* vol. 84, pp. 1965-1976, 2006/11/01/ 2006.

[59] J. L. Grover, "Initial flaw size estimating procedures for fatigue crack growth calculations," in *International Conference on Fatigue of Welded Construction*, Brighton, 1987, pp. 275-285.

[60] G. Meneghetti, D. Marini, and V. Babini, "Fatigue assessment of weld toe and weld root failures in steel welded joints according to the peak stress method," *Welding in the World,* vol. 60, pp. 559-572, 2016.

[61] H. L. J. Pang, "Analysis of weld toe profiles and weld toe cracks," *International Journal of Fatigue,* vol. 15, pp. 31-36, 1993.

[62] V. V. Yakubovskii and I. J. Valteris, "Geometrical parameters of butt and fillet welds and their influence on the welded joint fatigue life," *IIW Document XIII,* pp. 1326–89, 1989.

[63] R. Bell, O. Vosikovsky, and S. A. Bain, "The significance of weld toe undercuts in the fatigue of steel plate T-joints," *International Journal of Fatigue,* vol. 11, pp. 3-11, 1989/01/01/ 1989.

[64] W. R. Cherry, "Stress concentration factors in main members due to welded stiffeners," *Welding Journal,* vol. 20, 1941.

[65] W. Kenyon, W. B. Morrison, and A. G. Quarrel, "The fatigue strength of welded joints in structural steels," *British Welding Journal,* vol. 13, 1966.

[66] D. J. Hayes and S. J. Maddox, "The stress intensity factor of a crack at the toe of a fillet weld," *The Welding Institute Research Bulletin,* vol. 13, 1972.

[67] J. A. Martins Ferreira and C. A. Moura Branco, "Influence of the radius of curvature at the weld toe in the fatigue strength of fillet welded joints," *International Journal of Fatigue,* vol. 11, pp. 29-36, 1989.

[68] C. M. Branco, S. J. Maddox, V. Infante, and E. C. Gomes, "Fatigue performance of tungsten inert gas (TIG) and plasma welds in thin sections," *International Journal of Fatigue,* vol. 21, pp. 587-601, 1999/07/01/ 1999.

[69] J. L. Otegui, U. H. Mohaupt, and D. J. Burns, "Effect of weld process on early growth of fatigue cracks in steel T joints," *International Journal of Fatigue,* vol. 13, pp. 45-58, 1991.

[70] C.-H. Lee, K.-H. Chang, G.-C. Jang, and C.-Y. Lee, "Effect of weld geometry on the fatigue life of non-load-carrying fillet welded cruciform joints," *Engineering Failure Analysis,* vol. 16, pp. 849-855, 2009.

[71] Z. Barsoum and B. Jonsson, "Influence of weld quality on the fatigue strength in seam welds," *Engineering Failure Analysis,* vol. 18, pp. 971-979, 2011.

[72] C.-Y. Hou, "Fatigue analysis of welded joints with the aid of real three-dimensional weld toe geometry," *International Journal of Fatigue,* vol. 29, pp. 772-785, 2007.

[73] M. M. Alam, Z. Barsoum, P. Jonsén, A. F. H. Kaplan, and H. Å. Häggblad, "The influence of surface geometry and topography on the fatigue cracking behaviour of laser hybrid welded eccentric fillet joints," *Applied Surface Science,* vol. 256, pp. 1936-1945, 2010.

[74] R. Lang, G. Lener, J. Schmid, and M. Ladinek, "Welded seam evaluation based on 3D laser scanning – Practical application of mobile laser scanning systems for surface analysis of welds – Part 1," *Stahlbau,* vol. 85, pp. 336-343, 2016.

[75] G. Lener, R. Lang, M. Ladinek, and R. Timmers, "A numerical method for determining the fatigue strength of welded joints with a significant improvement in accuracy," *Procedia Engineering,* vol. 213, pp. 359-373, 2018/01/01/ 2018.

[76] M. J. Ottersböck, M. Leitner, M. Stoschka, and W. Maurer, "Analysis of fatigue notch effect due to axial misalignment for ultra high-strength steel butt joints," *Welding in the World,* vol. 63, pp. 851-865, 2019/05/01 2019.

[77] R. M. Andrews, "The effect of misalignment on the fatigue strength of welded cruciform joints," *Fatigue and Fracture of Engineering Materials and Structures,* vol. 19, pp. 755-768, 1996.

[78] H. Jakubczak and G. Glinka, "Fatigue analysis of manufacturing defects in weldments," *International Journal of Fatigue,* vol. 8, pp. 51-57, 1986/04/01/ 1986.

[79] S. J. Maddox, *Fitness-for-purpose Assessment of Misalignment in Transverse Butt Welds Subject to Fatigue Loading*: Welding Institute, 1985.

[80] S. Berge and H. Myhre, "Fatigue strength of misaligned cruciform and butt joints," *Norwegian Maritime Research,* vol. 5, pp. 29-39, 1977.

[81] S. J. Maddox, "Background to BS7608:2014," *TWI Ltd, Cambridge,* 2014.

[82] E. Niemi, W. Fricke, and S. J. Maddox, *Fatigue Analysis of Welded Components: Designer's Guide to the Structural Hot-Spot Stress Approach*: Woodhead Publishing, 2006.

[83] D. Radaj, *Design and Analysis of fatigue-resistant welded structures*. Cambridge: Abington Publishers, 1990.

[84] I. Poutiainen, P. Tanskanen, and G. Marquis, "Finite element methods for structural hot spot stress determination—a comparison of procedures," *International Journal of Fatigue,* vol. 26, pp. 1147-1157, 2004.

[85] C. M. Sonsino, W. Fricke, F. de Bruyne, A. Hoppe, A. Ahmadi, and G. Zhang, "Notch stress concepts for the fatigue assessment of welded joints – Background and applications," *International Journal of Fatigue,* vol. 34, pp. 2-16, 2012.

[86] C. M. Sonsino, "A Consideration of Allowable Equivalent Stresses for Fatigue Design of Welded Joints According to the Notch Stress Concept with the Reference Radii r_{ref} = 1.00 and 0.05 mm," *Welding in the World,* vol. 53, pp. R64-R75, 2009.

[87] A. F. Hobbacher, "Chapter 4 - The use of fracture mechanics in the fatigue analysis of welded joints," in *Fracture and Fatigue of Welded Joints and Structures*, K. A. Macdonald, Ed., ed: Woodhead Publishing, 2011, pp. 91-112.

[88] J. L. Otegui, H. W. Kerr, D. J. Burns, and U. H. Mohaupt, "Fatigue crack initiation from defects at weld toes in steel," *International Journal of Pressure Vessels and Piping,* vol. 38, pp. 385-417, 1989.

[89] T. Lassen, "The effect of the welding process on the fatigue crack growth," *Welding Journal,* vol. 69, pp. 75S-81S, 1990.

[90] R. Bell and O. Vosikovsky, "Fatigue life prediction of welded joints for offshore structures under variable amplitude loading," *Journal of Offshore Mechanics and Arctic Engineering,* vol. 115, pp. 123-130, 1993.

[91] M. D. Chapetti and J. L. Otegui, "A technique to produce automatic welds with enhanced fatigue crack propagation lives under transverse loading," *International Journal of Pressure Vessels and Piping,* vol. 70, pp. 173-181, 1997.

[92] M. D. Chapetti and J. L. Otegui, "Controlled toe waviness as a means to increase fatigue resistance of automatic welds in transverse loading," *International Journal of Fatigue,* vol. 19, pp. 667-675, 1997.

[93] M. Leitner, M. Ottersböck, S. Pußwald, and H. Remes, "Fatigue strength of welded and high frequency mechanical impact (HFMI) post-treated steel joints under constant and variable amplitude loading," *Engineering Structures,* vol. 163, pp. 215-223, 2018/05/15/ 2018.

[94] H. C. Yildirim, G. B. Marquis, and Z. Barsoum, "Fatigue assessment of high frequency mechanical impact (HFMI)-improved fillet welds by local approaches," *International Journal of Fatigue,* vol. 52, pp. 57-67, 2013/07/01/ 2013.

[95] ASTM, "ASTM E3024/E3024M - 19, Standard Practice for Magnetic Particle Testing for General Industry," ed. West Conshohocken, PA: ASTM International, 2019.

[96] BSI, "BS ISO 12108:2012 Metallic materials. Fatigue testing. Fatigue crack growth method," ed: British Standards, 2012.

[97] M. Neçar, "Detecting and measuring flaws using electric potential techniques," *Journal of Quality in Maintenance Engineering,* vol. 9, pp. 160-175, 2003/06/01 2003.

[98] K. Takeuchi, "Locations of strain gauges for fatigue analysis of welded joints (2)," *Welding International,* vol. 26, pp. 655-664, 2012.

[99] A. Hobbacher, "Recommendations for fatigue design of welded joints and components," *IIW Document XIII,* 2008.

[100] X. Niu and G. Glinka, "Stress-intensity factors for semi-elliptical surface cracks in welded joints," *International Journal of Fracture,* vol. 40, pp. 255-270, 1989.

[101] X. Niu and G. Glinka, "The weld profile effect on stress intensity factors in weldments," *International Journal of Fracture,* vol. 35, pp. 3-20, 1987.

[102] F. P. Brennan, W. D. Dover, R. F. Karé, and A. K. Hellier, "Parametric equations for T-butt weld toe stress intensity factors," *International Journal of Fatigue,* vol. 21, pp. 1051-1062, 1999.

[103] A. F. Hobbacher, "Stress intensity factors of welded joints," *Engineering Fracture Mechanics,* vol. 46, pp. 173-182, 1993.

[104] A. K. Hellier, F. P. Brennan, and D. G. Carr, "Weld toe SCF and stress distribution parametric equations for tension (membrane) loading," in *Advanced Materials Research* vol. 891-892, ed, 2014, pp. 1525-1530.

[105] J. L. Otegui, D. J. Burns, H. W. Kerr, and U. H. Mohaupt, "Growth and coalescence of fatigue cracks at weld toes in steel," *International Journal of Pressure Vessels and Piping,* vol. 48, pp. 129-165, 1991.

[106] M. M. Pedersen, O. Ø. Mouritsen, M. R. Hansen, J. G. Andersen, and J. Wenderby, "Re-analysis of fatigue data for welded joints using the notch stress approach," *International Journal of Fatigue,* vol. 32, pp. 1620-1626, 2010/10/01/ 2010.

[107] Y. Kim, J.-S. Oh, and S.-H. Jeon, "Novel hot spot stress calculations for welded joints using 3D solid finite elements," *Marine Structures,* vol. 44, pp. 1-18, 2015.

[108] G. Savaidis and M. Malikoutsakis, "Advanced notch strain based calculation of S–N curves for welded components," *International Journal of Fatigue,* vol. 83, pp. 84-92, 2016/02/01/ 2016.

[109] T. Shiozaki, N. Yamaguchi, Y. Tamai, J. Hiramoto, and K. Ogawa, "Effect of weld toe geometry on fatigue life of lap fillet welded ultra-high strength steel joints," *International Journal of Fatigue,* vol. 116, pp. 409-420, 2018/11/01/ 2018.

[110] T. Nykänen, G. Marquis, and T. Björk, "A simplified fatigue assessment method for high quality welded cruciform joints," *International Journal of Fatigue,* vol. 31, pp. 79-87, 2009.

[111] E. Harati, L. Karlsson, L. E. Svensson, and K. Dalaei, "The relative effects of residual stresses and weld toe geometry on fatigue life of weldments," *International Journal of Fatigue,* vol. 77, pp. 160-165, 2015.

[112] E. Harati, M. Ottosson, L. Karlsson, and L.-E. Svensson, "Non-destructive measurement of weld toe radius using Weld Impression Analysis, Laser Scanning Profiling and Structured Light Projection methods," presented at the First International Conference Welding Non Destructive Testing, Tehran, Iran, 2014.

[113] J. Raujol-Veillé, D. Thévenet, C. Doudard, S. Calloch, and H. Minnebo, "Rapid method for low cycle fatigue properties: thickness effect on the fatigue crack initiation life of welded joints," *Fatigue & Fracture of Engineering Materials & Structures,* vol. 38, pp. 1492-1506, 2015.

[114] R. Lang and G. Lener, "Application and comparison of deterministic and stochastic methods for the evaluation of welded components' fatigue lifetime based on real notch stresses," *International Journal of Fatigue,* vol. 93, pp. 184-193, 2016/12/01/ 2016.

[115] E. Sato, H. Matsukiyo, A. Osawa, T. Enomoto, M. Watanabe, J. Nagao*, et al.*, "Characteristic x-ray generator and its applications," in *Optical Engineering + Applications*, 2008, p. 5.

[116] E. N. Landis and D. T. Keane, "X-ray microtomography," *Materials Characterization,* vol. 61, pp. 1305-1316, 2010.

[117] S. Stock, *MicroComputed Tomography: Methodology and Applications*: CRC Press, 2008.

[118] R. M. Kessler, J. R. J. Ellis, and M. Eden, "Analysis of Emission Tomographic Scan Data: Limitations Imposed by Resolution and Background," *Journal of Computer Assisted Tomography,* vol. 8, 1984.

[119] S. R. Stock, "Recent advances in X-ray microtomography applied to materials," *International Materials Reviews,* vol. 53, pp. 129-181, 2008/05/01 2008.

[120] B. J. Connolly, D. A. Horner, S. J. Fox, A. J. Davenport, C. Padovani, S. Zhou*, et al.*, "X-ray microtomography studies of localised corrosion and transitions to stress corrosion cracking," *Materials Science and Technology,* vol. 22, pp. 1076-1085, 2006/09/01 2006.

[121] D. Shiozawa, Y. Nakai, T. Kurimura, Y. Morikage, H. Tanaka, H. Okado*, et al.*, "Observation of Cracks in Steels Using Synchrotron Radiation X-Ray Micro Tomography," *Journal of the Society of Materials Science, Japan,* vol. 56, pp. 951-957, 2007.

[122] J. Kastner, B. Harrer, G. Requena, and O. Brunke, "A comparative study of high resolution cone beam X-ray tomography and synchrotron tomography applied to Fe- and Al-alloys," *NDT & E International,* vol. 43, pp. 599-605, 2010/10/01/ 2010.

[123] M. Jovanović, L. Kosec, and B. Zorc, "Examination of weld defects by computed tomography," *Metalurgija,* vol. 51, pp. 233-236, 2012.

[124] E. Gamboa, M. Giuliani, and O. Lavigne, "X-ray microtomography observation of subsurface stress corrosion crack interactions in a pipeline low carbon steel," *Scripta Materialia,* vol. 81, pp. 1-3, 2014/06/15/ 2014.

[125] G. Ziółkowski, E. Chlebus, P. Szymczyk, and J. Kurzac, "Application of X-ray CT method for discontinuity and porosity detection in 316L stainless steel parts produced with SLM technology," *Archives of Civil and Mechanical Engineering,* vol. 14, pp. 608-614, 2014/08/05/ 2014.

[126] J. Y. Meng, M. A. Chen, S. Liu, F. C. Zhang, and L. H. Qian, "3D investigation of fatigue crack morphology and crack growth of iron-based materials via synchrotron X-ray CT," vol. 833, ed, 2015, pp. 154-157.

[127] D. Seo, H. Toda, M. Kobayashi, K. Uesugi, A. Takeuchi, and Y. Suzuki, "Three-dimensional investigation of void coalescence in free-cutting steel using X-ray tomography," *ISIJ International,* vol. 55, pp. 1483-1488, 2015.

[128] X. An, M. Brambilla, A. Dobson, and O. Francois, "An application of computed tomography inspection on butt weld of super duplex umbilical tube," in *Annual Offshore Technology Conference*, Houston, Texas, USA, 2015, pp. 2669-2681.

[129] F. Farhad, D. Smyth-Boyle, X. Zhang, I. Wallis, and D. Panggabean, "Laboratory apparatus for in-situ corrosion fatigue testing and characterisation of fatigue cracks using X-ray micro-computed tomography," *Fatigue & Fracture of Engineering Materials & Structures,* vol. 41, pp. 2629-2637, 2018/12/01 2018.

[130] R. F. Hamade and A. M. R. Baydoun, "Nondestructive detection of defects in friction stir welded lap joints using computed tomography," *Materials & Design,* vol. 162, pp. 10-23, 2019/01/15/ 2019.

[131] M. Piazza, T. H. Burns, J. Medford, and T. Shie, "Validation of computed tomography technology for pipeline inspection," in *Proceedings of the Biennial International Pipeline Conference, IPC*, 2018.

[132] BSI, "BS EN 10025-2:2004 Hot rolled products of structural steels. Technical delivery conditions for non-alloy structural steels," ed, 2004.

[133] BSI, "BS EN ISO 6892-1:2016 Metallic materials. Tensile testing. Method of test at room temperature," ed: BSI, 2016.

[134] BSI, "BS EN ISO 17632:2015 Welding consumables. Tubular cored electrodes for gas shielded and non-gas shielded metal arc welding of non-alloy and fine grain steels. Classification," ed: BSI, 2015.

[135] BSI, "BS EN ISO 14341:2011 Welding consumables. Wire electrodes and weld deposits for gas shielded metal arc welding of non alloy and fine grain steels. Classification," ed: BSI, 2011.

[136] SONATS, "Fatigue Life Improvement Of Welded Structures By Ultrasonic Needle Peening (White Paper)," 2016.

[137] ASTM, "ASTM E1441-11, Standard Guide for Computed Tomography (CT) Imaging," ed. West Conshohocken, PA: ASTM International, 2011.

[138] J. Kittler and J. Illingworth, "Minimum error thresholding," *Pattern Recognition,* vol. 19, pp. 41-47, 1986/01/01/ 1986.

[139] I. Sobel and G. Feldman, "A 3x3 Isotropic Gradient Operator for Image Processing," 1968.

[140] T.-C. Lee, R. L. Kashyap, and C.-N. Chu, "Building skeleton models via 3-D medial surface axis thinning algorithms," *CVGIP: Graph. Models Image Process.,* vol. 56, pp. 462-478, 1994.

[141] Z. Mikulski and T. Lassen, "Fatigue crack initiation and subsequent crack growth in fillet welded steel joints," *International Journal of Fatigue,* vol. 120, pp. 303-318, 2019/03/01/ 2019.

[142] E. Harati, M. Ottosson, L. Karlsson, and L.-E. Svensson, "Non-destructive measurement of weld toe radius using Weld Impression Analysis, Laser Scanning Profiling and Structured Light Projection methods," *Dept. of Engineering Science, University West, Sweden,* 2014.

[143] D. Radaj, C. M. Sonsino, and W. Fricke, "Recent developments in local concepts of fatigue assessment of welded joints," *International Journal of Fatigue,* vol. 31, pp. 2-11, 2009.

[144] D. Bowness and M. M. K. Lee, *Fracture Mechanics Assessment of Fatigue Cracks in Offshore Tubular Structures*: HSE Books, 2002.

[145] H. Lieurade, I. Huther, and D. Lebaaillif, "Weld quality assessment as regard to fatigue," in *IIW Commission XIII*, Centre Technique des Industries Mecaniques 2002.

[146] V. Pratt, "Direct least-squares fitting of algebraic surfaces," 1987, pp. 145-152.

[147] P. Lazzarin and R. Tovo, "A Notch Intensity Factor Approach to the Stress Analysis of Welds," *Fatigue & Fracture of Engineering Materials & Structures,* vol. 21, pp. 1089-1103, 1998/09/01 2002.

[148] D. Bowness and M. M. K. Lee, "Prediction of weld toe magnification factors for semi-elliptical cracks in T–butt joints," *International Journal of Fatigue,* vol. 22, pp. 369-387, 2000.

[149] H. P. Lehrke, "Calculating of stress concentration factors for welded joints," *Konstruktion,* 1999.

[150] J. L. Chaboche, "A review of some plasticity and viscoplasticity constitutive theories," *International Journal of Plasticity,* vol. 24, pp. 1642-1693, 2008/10/01/ 2008.

[151] Simulia, "Abaqus 6.13 Documentation," ed, 2014.

[152] C. You, B. Y. He, M. Achintha, and P. A. S. Reed, "Numerical modelling of the fatigue crack shape evolution in a shot-peened steam turbine material," *International Journal of Fatigue,* vol. 104, pp. 120-135, 2017/11/01/ 2017.

[153] C. You, "Fatigue lifing approaches for shot peened turbine components," PhD Doctoral Thesis, University of Southampton, 2017.

[154] K. A. Soady, "Reducing conservatism in life assessment approaches: Industrial steam turbine blade to disc interfaces and the shot peening process," EngD, University of Southampton, Southampton, 2013.

[155] Synopsys, *Simpleware ScanIP Reference Guide*, 2017.

[156] G. Project. *What is Bash?* Available: https://www.gnu.org/software/bash/manual/html_node/What-is-Bash_003f.html

[157] ASTM, "ASTM E647-15e1, Standard Test Method for Measurement of Fatigue Crack Growth Rates," ed. West Conshohocken, PA: ASTM International, 2015.

[158] G. M. Wilkowski and W. A. Maxey, "Review And Applications Of The Electric Potential Method For Measuring Crack Growth In Specimens, Flawed Pipes, And Pressure Vessels," in *ASTM Special Technical Publication*, 1983, pp. 266-294.

[159] R. P. Wei and R. L. Brazil, "An Assessment of A-C and D-C Potential Systems for Monitoring Fatigue Crack Growth," presented at the ASTM Special Technical Publications No. 738, 1980.

[160] M. Ltd., "Practical Aspects of the ACPD Technique, User Manual," ed.

[161] J. R. Rudlin and R. Kare, "Crack Depth Measurement using an Advanced ACPD Technique on a Large Tubular Joint," in *Impact of Non-Destructive Testing*, C. Brook and P. D. Hanstead, Eds., ed Oxford: Pergamon, 1990, pp. 221-230.

[162] G. P. Gibson, "The use of alternating current potential drop for determining J-crack resistance curves," *Engineering Fracture Mechanics,* vol. 26, pp. 213-222, 1987.

[163] S. Tiku, N. J. Marchand, and B. Unvala, "An advanced multiple frequency ACPD system for crack detection and calibration," *ASTM Special Technical Publication,* vol. 1318, pp. 56-70, 1997.

[164] T. V. Venkatsubramanian and B. A. Unvala, "An AC potential drop system for monitoring crack length," *Journal of Physics E: Scientific Instruments,* vol. 17, pp. 765-771, 1984.

[165] N. Okumura, T. V. Venkatasubramanian, B. A. Unvala, and T. J. Baker, "Application of AC potential drop technique to the determination of R curves of tough ferritic steels," *Engineering Fracture Mechanics,* vol. 14, pp. 617-625, 1981.

[166] A. Wojcik, M. Waitt, and A. S. Santos, "The use of the potential drop technique for creep damage monitoring and end of life warning for high temperature components," *Materials at High Temperatures,* vol. 34, pp. 458-465, 2017/11/02 2017.

[167] W. D. Dover, G. Glinka, and R. Collins, "Automated Crack Detection and Monitoring of Crack Shape in Tubular Welded Joints and T-Butt Welds," presented at the International Conference on Non Destructive Testing in the Fitness for Purpose Assessment of Welded Constructions, 1984.

[168] R. Collins, W. D. Dover, and D. H. Michael, "The Use of a.c. Field Measurement for Non Destructive Testing.," *Research Techniques in NDT,* vol. VIII, pp. 211-267, 1985.

[169] N. Net. (2010, Accessed - 03/04/2019). *NDT Forum*. Available: https://www.ndt.net/forum/thread.php?msgID=33215

[170] B. Fereidooni, M. R. Morovvati, and S. A. Sadough-Vanini, "Influence of severe plastic deformation on fatigue life applied by ultrasonic peening in welded pipe 316 Stainless Steel joints in corrosive environment," *Ultrasonics,* vol. 88, pp. 137-147, 2018/08/01/ 2018.

[171] H. C. Yildirim and G. B. Marquis, "A round robin study of high-frequency mechanical impact (HFMI)-treated welded joints subjected to variable amplitude loading," *Welding in the World,* vol. 57, pp. 437-447, 2013.

[172] H. C. Yildirim and G. B. Marquis, "Overview of fatigue data for high frequency mechanical impact treated welded joints," *Welding in the World,* vol. 56, pp. 82-96, 2012.

[173] M. S. H. Leung, J. Corcoran, and P. B. Nagy, "The influence of the dynamic magnetoelastic effect on potential drop measurements," *NDT & E International,* vol. 102, pp. 153-160, 2019/03/01/ 2019.

[174] K. Chen, F. P. Brennan, and W. D. Dover, "Thin-skin AC field in anisotropic rectangular bar and ACPD stress measurement," *NDT & E International,* vol. 33, pp. 317-323, 2000/07/01/ 2000.

[175] W. S. Cleveland, "Robust Locally Weighted Regression and Smoothing Scatterplots," *Journal of the American Statistical Association,* vol. 74, pp. 829-836, 1979/12/01 1979.

[176] S. J. Maddox, "An analysis of fatigue cracks in fillet welded joints," *International Journal of Fracture,* vol. 11, pp. 221-243, 1975/04/01 1975.

[177] J. Rice, "Plastic yielding at crack tip," in *Procs. 1st Int. Conf. on Fracture*, Sendai, 1965, p. 283.

[178] J. Schijve, "Analysis of the fatigue phenomenon in aluminium alloys," *NRL-TR M2122,* 1964.

[179] G. R. Irwin, "Analysis of stresses and strains near the end of a crack traversing a plate," *Journal of Applied Mechanics,* vol. 24, pp. 361-4, 1957.

[180] Y. Murakami, *Stress Intensity Factors Handbook*: Elsevier Science Limited, 1987.

[181] P. J. E. Forsyth, "A unified description of micro and macroscopic fatigue crack behaviour," *International Journal of Fatigue,* vol. 5, pp. 3-14, 1983/01/01/ 1983.

[182] Y. Ochi, A. Ishii, and S. K. Sasaki, "An Experimental And Statistical Investigation Of Surface Fatigue Crack Initiation And Growth," *Fatigue & Fracture of Engineering Materials & Structures,* vol. 8, pp. 327-339, 1985.

[183] Y. Z. Wang, K. Ebtehaj, D. Hardie, and R. N. Parkins, "The behaviour of multiple stress corrosion cracks in a Mn-Cr and a Ni-Cr-Mo-V steel: I—Metallography," *Corrosion Science,* vol. 37, pp. 1651-1675, 1995/11/01/ 1995.

[184] B. Y. He, O. L. Katsamenis, B. G. Mellor, and P. A. S. Reed, "3-D analysis of fatigue crack behaviour in a shot peened steam turbine blade material," *Materials Science and Engineering: A,* vol. 642, pp. 91-103, 2015/08/26/ 2015.

[185] J. E. Spowart, "Automated serial sectioning for 3-D analysis of microstructures," *Scripta Materialia,* vol. 55, pp. 5-10, 2006/07/01/ 2006.

[186] S. I. Lieberman, A. M. Gokhale, and S. Tamirisakandala, "Reconstruction of three-dimensional microstructures of TiB phase in a powder metallurgy titanium alloy using montage serial sectioning," *Scripta Materialia,* vol. 55, pp. 63-68, 2006/07/01/ 2006.

[187] H. Singh and A. M. Gokhale, "Visualization of three-dimensional microstructures," *Materials Characterization,* vol. 54, pp. 21-29, 2005/01/01/ 2005.

[188] P. Clement, J. P. Angeli, and A. Pineau, "Short Crack Behaviour In Nodular Cast Iron," *Fatigue & Fracture of Engineering Materials & Structures,* vol. 7, pp. 251-265, 1984.

[189] E. E. Simmons, "Material Testing Apparatus," U.S. Patent No. 2,292,549, 1942.

[190] A. C. Ruge, "Strain Gauge," U.S. Patent No. 2,350,972, 1944.

[191] S. Keil, *Technology and Practical Use of Strain Gages With Particular Consideration of Stress Analysis Using Strain Gages*: Wilhelm Ernst & Sohn, Verlag für Architektur und technische Wissenschaften GmbH & Co. KG, 2017.

[192] H. J. Grover, "The use of electric strain gages to measure repeated stresses," *Proceeding of SESA,* pp. 110-115, 1943.

[193] C. O. Dohrenwend and W. R. Mehaffey, "Measurement of dynamic strain," *Journal of Applied Mechanics,* pp. A85–A92, 1943.

[194] K. Hoffman, *An Introduction to Measurements using Strain Gages*. Darmstadt: Hottinger Baldwin Messtechnik GmbH, 1989.

[195] Y. Verreman and B. Nie, "Short Crack Growth and Coalescence Along the Toe of a Manual Fillet Weld," *Fatigue & Fracture of Engineering Materials & Structures,* vol. 14, pp. 337-349, 1991.

[196] J. J. Janosch, "Investigation into the fatigue strength of fillet welded assemblies of E-36-4 steel as a function of the penetration of the weld subjected to tensile and bending loads," *Welding Journal (Miami); (United States),* pp. Medium: X; Size: Pages: 355s-365s, 1993.

[197] A. O. Lukashevich, V. A. Leonets', and L. M. Chaus, "Strain-Gauge Method of Detecting Subcritical Fatigue Cracks in Low-Carbon Steel Welds," *Strength of Materials,* vol. 47, pp. 467-473, 2015.

[198] BSI, "BS 6888:1988 Methods for calibration of bonded electrical resistance strain gauges," ed, 1988.

[199] R. Branco, F. V. Antunes, J. D. Costa, F. P. Yang, and Z. B. Kuang, "Determination of the Paris law constants in round bars from beach marks on fracture surfaces," *Engineering Fracture Mechanics,* vol. 96, pp. 96-106, 2012/12/01/ 2012.

[200] BSI, "BS 7270:2006 Metallic materials. Constant amplitude strain controlled axial fatigue. Method of test," ed, 2006.

[201] T. Bruder, K. Störzel, J. Baumgartner, and H. Hanselka, "Evaluation of nominal and local stress based approaches for the fatigue assessment of seam welds," *International Journal of Fatigue,* vol. 34, pp. 86-102, 2012/01/01/ 2012.

[202] D. Radaj, "Review of fatigue strength assessment of nonwelded and welded structures based on local parameters," *International Journal of Fatigue,* vol. 18, pp. 153-170, 1996/04/01/ 1996.

[203] N. E. Dowling, "Mechanical Behavior of Materials: Engineering Methods for Deformation, Fracture, and Fatigue," 3rd ed. ed. Upper Saddle River, NJ :: Pearson Prentice Hall ;, 2007.

[204] R. E. Peterson, *Stress concentration Factors*. New York: John Wiley and Sons Inc., 1974.

[205] Y.-L. Lee, M. E. Barkey, and H.-T. Kang, *Metal Fatigue Analysis Handbook: Practical Problem-Solving Techniques for Computer-Aided Engineering*. Waltham, MA: Butterworth-Heinemann, 2012.

[206] R. G. Tryon and A. Dey, "Reliability-based model for fatigue notch effect," *SAE Technical Papers,* 2003.

[207] R. Olivier, V. B. Köttgen, and T. Seeger, "Schweissverbindung (welded joints) II, FKM Forschungshefte 180," Forschungskuratorium Maschinenebau, Frankfurt/M,1994.

[208] R. Olivier, V. B. Köttgen, and T. Seeger, "Schweissverbindung (welded joints) I, FKM Forschungshefte 143," Forschungskuratorium Maschinenebau, Frankfurt/M,1989.

[209] R. E. Peterson, "Notch sensitivity," *Metal Fatigue,* pp. 293-306, 1959.

[210] H. Neuber, "Über die Berücksichtigung der Spannungskonzentration bei Festigkeitsberechnungen," *Konstruktion,* vol. 20, pp. 245-251, 1968.

[211] H. Neuber, "Theory of Notch Stresses: Principle for Exact Stress Calculations," J. W. Edwards, Ann Arbor, MI,1946.

[212] H. Neuber, *Kerbspannungslehre*. Berlin: Springer-Verlag, 1937, 1958, 1985.

[213] D. Kujawski and J. L. K. Teo, "A Generalization of Neuber's Rule for Numerical Applications," *Procedia Structural Integrity,* vol. 5, pp. 883-888, 2017/01/01/ 2017.

[214] S. T. and H. P., "Generalized Application of Neuber's Rule," *Journal of Testing Evaluation,* vol. 8, pp. 199-204, 1980.

[215] T. Topper, R. M. Wetzel, and J. Dean Morrow, *Neuber's Rule Applied to Fatigue of Notched Specimens* vol. 4, 1967.

[216] R. E. Peterson, "Relation between stress analysis and fatigue of metals," *Proc. SESA,* vol. 11, pp. 199-206, 1950.

[217] R. Kuguel, "A relation between theoretical stress concentration factor and fatigue notch factor deduced from the concept of highly stressed volume," *ASTM Proc.,* vol. 61, pp. 732-748, 1961.

[218] F. V. Lawrence, R. J. Mattos, Y. Higashida, and J. D. Burk, "Estimating the Fatigue Crack Initiation Life of Welds," *Fating Testing of Weldments, ASTM STP 648,* pp. 134-158, 1978.

[219] R. J. Mattos and F. V. Lawrence, *Estimation of the fatigue crack initiation life in welds using low cycle fatigue concepts*. Urbana: University of Illinois, 1975.

[220] F. V. Lawrence, P. C. Wang, and H. T. Corten, "An Empirical Method for Estimating the Fatigue Resistance of Tensile-Shear Spot Welds," 1983.

[221] F. V. Lawrence, N.-J. Ho, and P. K. Mazumdar, "Predicting the fatigue resistance of welds," *Annual Review of Materials Science,* vol. 11, pp. 401-425, 1981.

[222] H. Gerber, "Bestimmung der zulassigen Spannungen in Eisen-konstructionen," *Zeitschrift des Bayerischen Architeckten und Ingenieur-Vereins,* vol. 6, pp. 101-110, 1874.

[223] J. Goodman, *Mechanics applied to Engineering*. London: Longmans Green, 1899.

[224] C. R. Soderberg, "Factor of safety and working stress," *Transactions of the American Society of Mechanical Engineers,* vol. 52, pp. 13-28, 1939.

[225] O. H. Basquin, "The exponential law of endurance tests," in *ASTM 10*, 1910, pp. 625-630.

[226] W. Ramberg and W. R. Osgood, "Description of stress–strain curves by three parameters," NACA, 1943.

[227] H. Neuber, "Theory of Stress Concentration for Shear-Strained Prismatical Bodies With Arbitrary Nonlinear Stress-Strain Law," *Journal of Applied Mechanics,* vol. 28, pp. 544-550, 1961.

[228] G. Masing, "Eigenspannungen und Verfestigung beim Messing," in *International Congress of Applied Mechanics*, Zürich, 1926, pp. 332-335.

[229] J. D. Morrow, "Cyclic plastic strain energy and fatigue of metals," *Internal Friction, Damping, and Cyclic Plasticity, ASTM STP 378,* pp. 45-86, 1965.

[230] L. F. Coffin, Jr., "A study of the effect of cyclic thermal stresses on a ductile metal," *Transactions of ASME,* vol. 76, pp. 931-950, 1954.

[231] S. S. Manson, "Behavior of materials under conditions of thermal stress," in *Heat transfer symposium*, The University of Michigan Engineering Research Institute, Ann Arbor, 1953, pp. 9-75.

[232] T. Seeger, "Grundlagen für Betriebsfestigkeitsnachweise (Fundamentals for service fatigue strength assessments)," in *Stahlbau Handbuch (Handbook of Structural Engineering)* vol. 1B, ed. Köln: Stahlbau-Verlagsgesellschaft, 1996, pp. 5-123.

[233] A. Baümel and T. Seeger, *Materials Data for Cyclic Loading, Suppliment 1*. Amsterdam: Elsevier Science, 1990.

[234] C. Boller and T. Seeger, *Materials Data for Cyclic Loading, Part A-E*. Amsterdam: Elsevier Science, 1987.

[235] J. Y. Yung and F. V. Lawrence, "Analytical and graphical aids for the fatigue design of weldments," *Fatigue Fract Engng Mater Struct,* vol. 8, pp. 223-241, 1985.

[236] F. V. Lawrence and P. K. Mazumdar, "Application of strain-controlled fatigue concepts to the prediction of weldment fatigue life," *Kurzzeitschwingfestigkeit und elastoplastisches Werkstoffverhalten,* vol. DVM-Bericht 105, pp. 469-478, 1979.

[237] J. J. Janosch and S. Debiez, "Influence of the shape of undercut on the fatigue strength of fillet welded assemblies - application of the local approach," *Welding in the World, Le Soudage Dans Le Monde,* vol. 41, pp. 350-360, 1998.

[238] T. Seeger, S. Greuling, J. Brüning, P. Leis, C. M. Sonsino, and D. Radaj, "Bewertung lokaler Berechnungskonzepte zur Ermüdungsfestigkeit von Punktschweißverbindungen, FAT Report 196," Forschungsvereinigung Automobiltechnik e.V. (FAT) Schriftenreihe, Frankfurt am Main, 2005.

[239] Ö. Karakas, C. Morgenstern, and C. M. Sonsino, "Fatigue design of welded joints from the wrought magnesium alloy AZ31 by the local stress concept with the fictitious notch radii of rf=1.0 and 0.05mm," *International Journal of Fatigue,* vol. 30, pp. 2210-2219, 2008/12/01/ 2008.

[240] D. Radaj, *Ermüdungsfestigkeit – Grundlagen für Leichtbau, Maschinen- und Stahlbau (Fatigue Strength – Fundamentals for Light-Weight Design, Mechanical and Structural Engineering)*, 2nd ed. Berlin: Springer-Verlag, 2003.

[241] K. Saiprasertkit, T. Hanji, and C. Miki, "Fatigue strength assessment of load-carrying cruciform joints with material mismatching in low- and high-cycle fatigue regions based on the effective notch concept," *International Journal of Fatigue,* vol. 40, pp. 120-128, 2012/07/01/ 2012.

[242] E. Siebel and M. Stieler, "Ungleichförmige Spannungsverteilung bei schwingender Beanspruchung," *VDI-Zeitschrift,* vol. 97, pp. 121-126, 1955.

[243] G. Zhang, "Method of effective stress for fatigue: Part I – A general theory," *International Journal of Fatigue,* vol. 37, pp. 17-23, 2012/04/01/ 2012.

[244] T. Łagoda, P. Biłous, and Ł. Blacha, "Investigation on the effect of geometric and structural notch on the fatigue notch factor in steel welded joints," *International Journal of Fatigue,* vol. 101, pp. 224-231, 2017/08/01/ 2017.

[245] Y. Dong, Y. Garbatov, and C. Guedes Soares, "Fatigue crack initiation assessment of welded joints accounting for residual stress," *Fatigue & Fracture of Engineering Materials & Structures,* vol. 41, pp. 1823-1837, 2018/08/01 2018.

[246] ASTM, "ASTM E140-12B(2019)e1, Standard Hardness Conversion Tables for Metals Relationship Among Brinell Hardness, Vickers Hardness, Rockwell Hardness, Superficial Hardness, Knoop Hardness, Scleroscope Hardness, and Leeb Hardness," ed. West Conshohocken, PA: ASTM International, 2019.

[247] BSI, "BS EN ISO 6507-1:2018 Metallic materials. Test Method," ed: The British Standards Institution, 2018.

[248] A. L. L. da Silva, J. A. F. O. Correia, A. M. P. de Jesus, G. Lesiuk, A. A. Fernandes, R. Calçada*, et al.*, "Influence of fillet end geometry on fatigue behaviour of welded joints," *International Journal of Fatigue,* vol. 123, pp. 196-212, 2019/06/01/ 2019.

[249] K.-S. Lee and J.-H. Song, "Estimation methods for strain-life fatigue properties from hardness," *International Journal of Fatigue,* vol. 28, pp. 386-400, 2006/04/01/ 2006.

[250] K. S. Kim, X. Chen, C. Han, and H. W. Lee, "Estimation methods for fatigue properties of steels under axial and torsional loading," *International Journal of Fatigue,* vol. 24, pp. 783-793, 2002/07/01/ 2002.

[251] U. Muralidharan and S. S. Manson, "A Modified Universal Slopes Equation for Estimation of Fatigue Characteristics of Metals," *Journal of Engineering Materials and Technology,* vol. 110, pp. 55-58, 1988.

[252] M. A. Meggiolaro and J. T. P. Castro, "Statistical evaluation of strain-life fatigue crack initiation predictions," *International Journal of Fatigue,* vol. 26, pp. 463-476, 2004/05/01/ 2004.

[253] K. S. Tsang, J. H. L. Pang, and H. J. Hoh, "Influence of Weld Toe Radii on Fatigue Life Prediction," *MATEC Web Conf.,* vol. 165, p. 22025, 2018.

[254] D. Tchoffo Ngoula, H. T. Beier, and M. Vormwald, "Fatigue crack growth in cruciform welded joints: Influence of residual stresses and of the weld toe geometry," *International Journal of Fatigue,* vol. 101, pp. 253-262, 2017/08/01/ 2017.

[255] F. P. Brennan, P. Peleties, and A. K. Hellier, "Predicting weld toe stress concentration factors for T and skewed T-joint plate connections," *International Journal of Fatigue,* vol. 22, pp. 573-584, 2000/08/01/ 2000.

[256] K. Iida and T. Uemura, "Stress concentration factor formulae widely used in Japan," *Fatigue and Fracture of Engineering Materials and Structures,* vol. 19, pp. 779-786, 1996.

[257] V. Chmelko, M. Margetin, and M. Harakal', "Notch effect of welded joint," *MATEC Web Conf.,* vol. 165, p. 21003, 2018.